The study of Rydberg gas chemistry by fast flow glow discharge mass spectrometry.

Dickinson, Paul Michael

The Study of Rydberg Gas Chemistry by Fast Flow Glow Discharge Mass Spectrometry

by

Paul Michael Dickinson

Submitted to the University of Wales in Fulfilment of the Requirements for the Degree of Doctor of Philosophy

Swansea University, 2008

ProQuest LLC.
789 East Eisenhower Parkway
P.O. Box 1346
Ann Arbor, MI 48106 – 1346

Summary

This study concerns the analysis of processes occurring within, and fundamental characteristics of the flowing afterglow of a fast flowing direct current glow discharge plasma by both mass spectrometric and electrical diagnostic techniques. The evidence presented within this thesis indicates that the glow discharge plasma studied contains a high density of very highly excited state, Rydberg species. Classically, glow discharge plasma is considered to be a partially ionised gas, the chemistry of which is dominated by processes involving charged particles (ions and electrons). However, under the conditions of the fast flow glow discharge source it is thought that the formation and stabilisation of Rydberg atoms is highly favourable, and thus the plasma chemistry can be described by a Rydberg gas model. Theoretical thermodynamic and kinetic data based on calculations (unpublished at the time of submission) performed by Dr R. S. Mason which corroborate this model are also presented.

Studies of the influence of the magnitude and polarity of applied the ion exit bias on the electrical properties of the flowing afterglow plasma and active discharge region were undertaken, often in situ with mass spectrometric measurements. Comparison of the electrical and mass spectrometric measurements has provided valuable information about the properties of the Rydberg gas plasma and the ionisation processes within the afterglow plasma. The results of the electrical studies (current and double probe measurements) could not be explained for an ion electron medium.

The reactions of secondary gases (H_2, CO, CO_2, N_2, CF_4 and CH_4) and organic vapours to the flowing afterglow plasma have been studied for a range of conditions. The results of which cannot all be explained by ion-molecule processes, and seemingly conform to the Rydberg gas model.

Acknowledgements

At this point I'd like to thank the people who made this possible and helped me get through the last 8 years of university. Firstly, thank you Rod for giving me the chance to join the GPIC group and guiding me in the right direction when I got lost. Thank you to my family who have encouraged me to complete this work (sometimes quite pointedly). Particular thanks go to Kev, who has also helped keep me sane throughout. Thank you to JT and Brian Cooper for putting up with my sometimes regular requests for technical assistance. Cheers to the touch rugby boys for an outlet for excess energy on a Friday. Thanks also to Damon and Kate for the odd trip to the pub and the distracting "funny" emails. Thank you to Ted Clarke for making comprehensive school chemistry seem more interesting than it actually is. Finally, thank you to EPSRC and Swansea University for funding.

Table of Abbreviations

AAS	Atomic Absorption Spectroscopy
ac	Alternating Current
ACT	Asymmetric Charge Transfer
ADS	Anode Dark Space
AES	Atomic Emission Spectroscopy
AG	Anode Glow
Ar^m	Argon $^3P_2$ or $^3P_0$ Metastable State
APCI	Atmospheric Pressure Chemical Ionisation
Ar^R	Argon Rydberg State
CCD	Charge Coupled Device
CDS	Cathode Dark Space
CI	Chemical Ionisation
CID	Collisionally Induced Dissociation / Decomposition
dc	Direct Current
DVM	Digital Voltmeter
ED	Extended Discharge
EP	Extended Plasma
EI	Electron Impact
ESA	Electrostatic Analyser
ESI	Electrospray Ionisation
FAG	Flowing Afterglow
FT	Fourier Transformation
FIMS	Field Ionisation Mass Spectrometry
FFGD	Fast Flowing Glow Discharge
FTICR	Fourier Transform Ion Cyclotron Resonance
GC	Gas Chromatography
GD	Glow Discharge
GDMS	Glow Discharge Mass Spectrometry
GDOES	Glow Discharge Optical Emission Spectroscopy
ICPMS	Inductively Coupled Plasma Mass Spectrometry

I_d	Discharge Current
I_P	Ionisation Potential
ITMA	Ion Trap Mass Analyser
KE	Kinetic Energy
LC	Liquid Chromatography
LCMS	Liquid Chromatography Mass Spectrometry
MCA	Multi Channel Analyser
MS	Mass Spectrometry
n	Principal Quantum Number
NG	Negative Glow
NIST	National Institute of Standards and Technology
N_n	Plasma/Rydberg Atom Density
OES	Optical Emission Spectroscopy
P	Source Pressure
PC	Positive Column
PEEK	Poly-Ether-Ether-Ketone
ppm	Parts Per Million
PSI	Pounds per Square Inch
PTFE	Poly-Tetra-Fluoro-Ethane
PVC	Polyvinyl Chloride
QMA	Quadrupole Mass Analyser
QMF	Quadrupole Mass Filter
rf	Radio Frequency
RGA	Residual Gas Analysis
sccm	Standard Centimetres Cubed per Minute
SCT	Symmetric Charge Transfer
SIMS	Secondary Ion Mass Spectrometry
τ	Plasma Residence Time
t	Time
T	Temperature
T_e	Electron Temperature
TOF	Time of Flight
UIR	Unidentified Infra Red

V_d	Discharge Voltage
V_c	Cone Voltage
V_{cell}	Cell Bias or Cell Volume
$V_{cylinder}$	Cylinder Lens Bias
V_{einzel}	Einzel Lens Bias
ZEKE	Zero Electron Kinetic Energy

Contents

Chapter 3 – Development of the Fast Flow Glow Discharge Mass Spectrometer

Chapter 1

Introduction

1.1 Introduction

The simplest form of glow discharge (GD) ion source is a cell which contains gas at a low pressure and two electrodes. Application of a potential or radiofrequency between the two electrodes leads to partial ionisation of the discharge gas i.e. plasma formation. The glow discharge is so-called due to the characteristic emission of light. The earliest glow discharge research was performed by Faraday, who developed many of the terms used today (anode, cathode, etc), in the 1830s[1]. In 1886, Goldstein observed positive rays (beams of positive ions), or "kanalstrahlen", which Wien[3] later analysed by magnetic deflection. Further studies by Thomson[4] illustrated that the separation of these "positive rays" was allowed due to the different mass-to-charge ratios of the species being analysed, and hence mass spectrometry (MS) was born.

GD-MS is particularly useful for analysis of solid samples[5] where the sample is the cathode. One major advantage of this is that little sample preparation is required, and therefore sample throughput can be quicker and there are less sources of contamination. There are many forms of discharge sources, including inductively coupled plasma (ICP)[6] and pulsed[7] sources each with analytical advantages. Use of plasma MS as a detector for techniques such as gas chromatography[8,9] has expanded the usefulness of GD sources. However, no single GD source has proved to be universally suitable.

Mason et al.[10-15] have developed a direct current fast flow glow discharge (FFGD) ion source, most commonly operated in coaxial geometry. The discharge gas flows between the anode and the cathode pin and the high gas flow rate extends the plasma downstream towards the ion exit orifice. The use of a fast gas flow aids transportation of cathode material, therefore improving the analytical sensitivity through reduction of diffusional losses to the cell walls. Fundamental studies[10-21] have shown that the classical model of the GD plasma as a partially ionised gas consisting of ions (positive and negative), electrons and neutral species which is overall neutrally charged[22] cannot account for all observations. However, the Rydberg gas model developed within this group[9-20] has been shown to account for many of the discrepancies observed. So far however, this model has not been adopted by the scientific community. The work in this thesis was done in order to attempt to harden the evidence for the Rydberg gas

hypothesis. An unpublished theory developed by R. S. Mason from first principles is described in chapter 2 which shows that the Rydberg gas state of matter is the thermodynamically most stable for these plasmas under the conditions studied.

Development of the FFGD source has allowed electrical studies of the flowing afterglow (FAG) plasma in situ with mass spectrometric analysis, therefore allowing direct comparison between results[13,14]. Addition of secondary gases downstream of the active discharge allows reactions to be studied without affecting the processes occurring within the active discharge region of the cell. A system for continuous addition of low quantities (ppm or lower) of volatile organic and organometallic compounds has been developed[11,15,21]. It has been shown that the magnitude of the applied ion exit bias determines the degree of sample fragmentation, and therefore the FFGD source can be used as a tuneable source for chemical speciation[11,15,21]. Newman[15,21] hyphenated the technique for GC analysis, further increasing the range of compounds which could be analysed and determined the minimum detection level to be in the sub parts per trillion (ppt) range.

The work presented in this thesis continues the fundamental studies of the FFGD plasma using a low-voltage quadrupole system as well as redeveloping an existing instrument in an attempt to reduce ion losses, allow electrical probe studies and extend the negative ion studies performed previously[11,14]. This work is summarised below:

Chapter two **(Glow Discharge Plasma Theory)** details the development of plasma theory over the last century. The use of GD plasma sources for optical, mass spectrometric and electrical probe studies is discussed, along with technological developments. The conventional ion/electron model of the plasma is described, including its inconsistencies in explaining experimental observations. The excited state model of the GD chemistry is also presented, including the Rydberg gas hypothesis[11-15]. Chapter 2 also describes the new Rydberg gas state of matter hypothesis eluded to above.

Chapter three **(Development of the Fast Flow Glow Discharge Mass Spectrometer)** details the development of the new FFGD instrument built by Dash[14] to remove inherent

problems, improve the sensitivity of the technique by incorporating an ion transfer optic system and to allow electrical probes studies of the flowing afterglow plasma to be performed. Results of the initial experiments are detailed, including the secondary gas mixing efficiency, ion signal enhancement by the incorporation of new ion optic lenses, and reduction of the ion transfer distance. A full overview of the instrument and routine maintenance procedures are also presented.

Chapter four **(The Ion Exit Bias Effect: Clear Evidence for the Rydberg Gas Model)** describes a series of experiments carried out to investigate the influence of the ion exit bias, V_c, on the electrical properties of the FAG plasma. The influence of V_c on the discharge and cone (plasma) currents and electrical double probe measurements (I-V profiles and local plasma potential measurements – described in section 2.8). It is shown that the results cannot be explained by the conventional model[22] of a GD plasma. Based on these results, and the work of Mason et al.[10-21], a Rydberg gas model is presented which accounts for the observed phenomena.

Chapter five **(Ion Kinetic Energy Measurements: Evidence of Ion Formation Processes Inside and Outside the Ion Source)** details experiments performed to test the performance of the kinetic energy lens of the mass spectrometer probe by accelerating ions across the ion exit to mass analyser orifice gap. It is shown that changes to the kinetic energy could be measured, but the absolute kinetic energy values could not be determined. Despite this, it is shown that ions are formed both inside and outside the discharge cell. The relative kinetic energies of the ions have also been used to propose the mechanism for formation of Ar^+, Ar^{2+} and Cu^+.

Chapter six **(Investigation of Ionisation Processes Downstream of the Active Discharge: Mass Spectrometric and Electrical Studies)** describes the influence of the discharge voltage, secondary gas addition and applied ion exit bias on the electrical properties of the plasma and the mass spectra observed. Both positive and negative ion results are illustrated on addition of carbon tetrafluoride and methane, and without secondary gas addition. Although much studied previously, hydrogen addition is

included to show that the results are compatible with previous experiments. Since the results cannot be rationalised using the conventional ion-electron model of the GD plasma, the Rydberg gas model is applied to explain the effects observed. Collection of electrical probe results in situ with mass spectrometric studies allowed direct comparison between the plasma potentials and the formation of ions. This therefore aided determination of the processes occurring within the plasma.

Chapter seven **(Addition of Secondary Gases to the Flowing Afterglow Plasma: Hydrogen, Nitrogen, Carbon Monoxide, Carbon Dioxide and Methane)** describes the analysis of secondary gases on their addition to the flowing afterglow (FAG) plasma (i.e. downstream from the active discharge region). The variation of the mass spectrum with the applied ion exit bias and percentage addition of the secondary gas are discussed. The results taken during this work again do not fit the conventional ion-electron model of the GD plasma, but their adherence to the excited state model is illustrated. This model enables explanation of the anomalous detection of positive ions without corresponding loss of another ion signal, and cation detection despite application of a positive (repulsive) bias to the ion exit cone. In addition, the quenching rate constants for the reaction:

$$Ar^R + M \rightarrow Ar^* + M^*$$

where M is a reagent gas molecule, assuming field ionisation of argon Rydberg state species to be the primary mechanism for formation of Ar^+ have been determined. The rate constants are compared with literature values for the corresponding ion-molecule reaction;

$$Ar^+ + M \rightarrow Ar + M^+$$

with significant differences observed which can be explained through application of the Rydberg gas hypothesis.

Though these secondary gas reactions have been studied previously, the influence of the ion exit bias on the mass spectrum has not been studied. The only exception to this is the addition of methane, for which Mortimer[11] monitored the level of fragmentation of the molecule with the magnitude of the ion exit field strength. This study extends the work of Mortimer[11] to include the application of a positive ion exit bias.

Chapter eight **(Analysis of Organic Vapours)** describes the influence of the ion exit bias on the ions observed on continuous addition of low quantities (ppm) of organic vapours to the FAG plasma. It has previously been observed that the magnitude of the applied ion exit bias determined the degree of fragmentation of a range of organic and organometallic compounds[15,21]. Addition of a continuous flow of organic vapour allowed the chemistry and ionisation processes to be studied. The ability of the technique to distinguish between different functional groups, and between isomers, is discussed based on the observed fragmentation patterns and appearance of molecular ion peaks. The limitations of the technique are also discussed. This work extends that done previously by Newman[15].

Chapter nine **(Conclusions and Further Work)** contains a summary of the main conclusions drawn within the work described in this thesis and suggests further work.

1.2 References

[1] M. Faraday, *Researches in Electricity*, London, 1844

[2] E. Goldstein, *Berl. Ber.*, **39**, 691, 1886

[3] W. Wien, *Verh. Phys. Ges.*, **17**, 1898

[4] J. J. Thomson, *Rays of Positive Electricity and Their Application to Chemical Analysis*, Longmans Green, London, 1913

[5] W. W. Harrison, C. Yang and E. Oxley, *Glow Discharge Plasmas in Analytical Spectroscopy*, ed. R. K. Marcus and J. A. C. Broekaert, John Wiley and Sons, 2003

[6] R. S. Houk, V. A. Fassel, G. D. Flesch et al., *Anal. Chem.*, **52**, 2283, 1980

[7] J. A. Klingler, P. J. Savickas and W. W. Harrison, *J. Am. Soc. Mass Spectrom.*, **1**, 138, 1990

[8] K. Newman and R. S. Mason, *JAAS*, **19**, 1134, 2004

[9] M. Kazuya and E. H. Piepmeier, *Anal. Chem.*, **63**, 1763, 1991

[10] P. D. Miller, PhD Thesis, University of Wales Swansea, 1996

[11] I. P. Mortimer, Ph.D Thesis, University of Wales Swansea, 2000

[12] D. R. Williams, Ph.D Thesis, University of Wales Swansea, 2001

[13] D. J. Mitchell, Ph.D Thesis, University of Wales Swansea, 2002

[14] N. A. Dash, Ph.D Thesis, University of Wales Swansea, 2004

[15] K. Newman, Ph.D Thesis, University of Wales Swansea, 2005

[16] R. S. Mason, P. D. Miller, I. P. Mortimer, *Phys. Rev. E*, **55**, 7462, 1997

[17] R. S. Mason, P. D. Miller, I. P. Mortimer, D. J. Mitchell and N. A. Dash, *Phys. Rev. E*, **68**, 016408, 2003

[18] K. Newman, R. S. Mason, D. R. Williams and I. P. Mortimer, *JAAS*, **19**, 1192, 2004

[19] R. S. Mason, D. R. Williams, I. P. Mortimer, D. J. Mitchell and K. Newman, *JAAS*, **19**, 1177, 2004

[20] K. Newman and R. S. Mason, *JAAS*, **20**, 830, 2005

[21] K. Newman and R. S. Mason, *Rapid Commun. Mass Spectrom.*, **20**, 2067, 2006

[22] B. Chapman, *Glow Discharge Processes*, John Wiley & Sons Ltd., 1980

[23] T. F. Gallagher, *Rydberg Atoms*, Cambridge University Press

[24] R. S. Mason, unpublished work

Chapter 2

Glow Discharge Plasma Applications and Theory

2.1 Introduction

Glow discharge (GD) plasmas have been widely studied, with the majority of the experimental data generated since the advent of more advanced vacuum technology in the 19th century[1]. Advances in vacuum technology, computers and both optical and mass analysers have led to production of a significant increase in plasma research, especially within the last 35 years[2,3,4]. The first ion source for mass spectrometry (MS) was a GD plasma[5]. However, despite the simplicity of the glow discharge (GD) source and its ability to generate ions from a solid sample with little or no preparation, their use had been fairly limited until the 1970s due to the introduction of alternative ion sources such as electron impact (EI)[6]. Since then glow discharge mass spectrometry (GDMS) has become a standard method for metal analysis[6].

GD plasmas have also been extensively studied both electrically and optically. GD plasmas acquired their name from their characteristic emission of light, or glow. Hence, changes to the plasma will induce changes to the emission, which can then be monitored by GD optical emission spectroscopy (OES). OES is a non-invasive technique, from which electron densities and plasma temperatures are derived[6,7,8]. Processing the results can be laborious, and values obtained are averaged over a volume of plasma. On the other hand, Langmuir probe studies[9,10] can be used to measure local plasma properties, since the probe is immersed in the plasma. Early studies utilised a single thin wire electrode and a larger reference electrode. The reference electrode was often one of the discharge electrodes or the cell wall. Later, a double probe technique was developed, allowing electrical studies in which a reference electrode was not available, e.g. in the upper atmosphere[11,12]. The use of electrical probes in plasma diagnostic studies is discussed in section 2.8.

This chapter details the glow discharge structure and the conventional model of GD chemistry, along with the plasma diagnostic techniques used in this investigation, i.e. electrical probe and mass spectrometric techniques. Section 2.6 details the Rydberg gas model of the GD plasma proposed by this group, based on MS and electrical studies[13-18], and a fundamental model (not yet submitted for publication) developed by R. S. Mason is

described in section 2.7. Applications of GD ion sources in analytical science are also discussed.

2.2 Glow Discharge Plasma

2.2.1 Profile of the Glow Discharge

A low pressure (0.1 to 10 Torr) gas discharge, or glow discharge (GD), is formed by application of a high potential difference between two electrodes, the anode and cathode. Application of a dc discharge voltage (typically 0.5 to 1kV) induces electrical breakdown of the discharge gas to form a plasma[19,20]. Analytical GD sources commonly use inert discharge gases to minimise disturbances due to chemical reactions, but reactive gases and mixtures are commonly used in processing plasmas[21] (for etching, thin layer deposition, etc). The glow discharge is a source of ions, electrons and excited neutral species and can therefore be characterised by electrical, mass spectrometric or optical studies[19,22]. In fact, it is the emission of light following de-excitation of excited state species that is responsible for the name of the glow discharge[23].

The glow discharge consists of a series of "glow" and "dark" regions corresponding to luminous and non-luminous regions respectively[22,1,18,24-26]. The architecture of the discharge is dependent on the anode-cathode separation. Figure 2.1 illustrates the regions which can be observed when the electrodes are separated by a relatively large distance. Up to eight distinct regions can be observed, each with characteristic luminous intensity, potential (also illustrated in figure 2.1), field strength, space charge density and current density[22]. The positive column is most affected by variation of the inter-electrode distance. Hittorf reported that, within the limits of an experiment ended prematurely by a cat, the length of the positive column appeared to extend without limit[22,27]. When reducing the anode-cathode distance the length of the positive column decreases before being 'consumed' entirely, along with the Faraday dark space (figure 2.2). These shorter discharges are often used in analytical studies[22]. The size and positions of the various regions are also dependent on the discharge voltage, pressure, current and gas used.

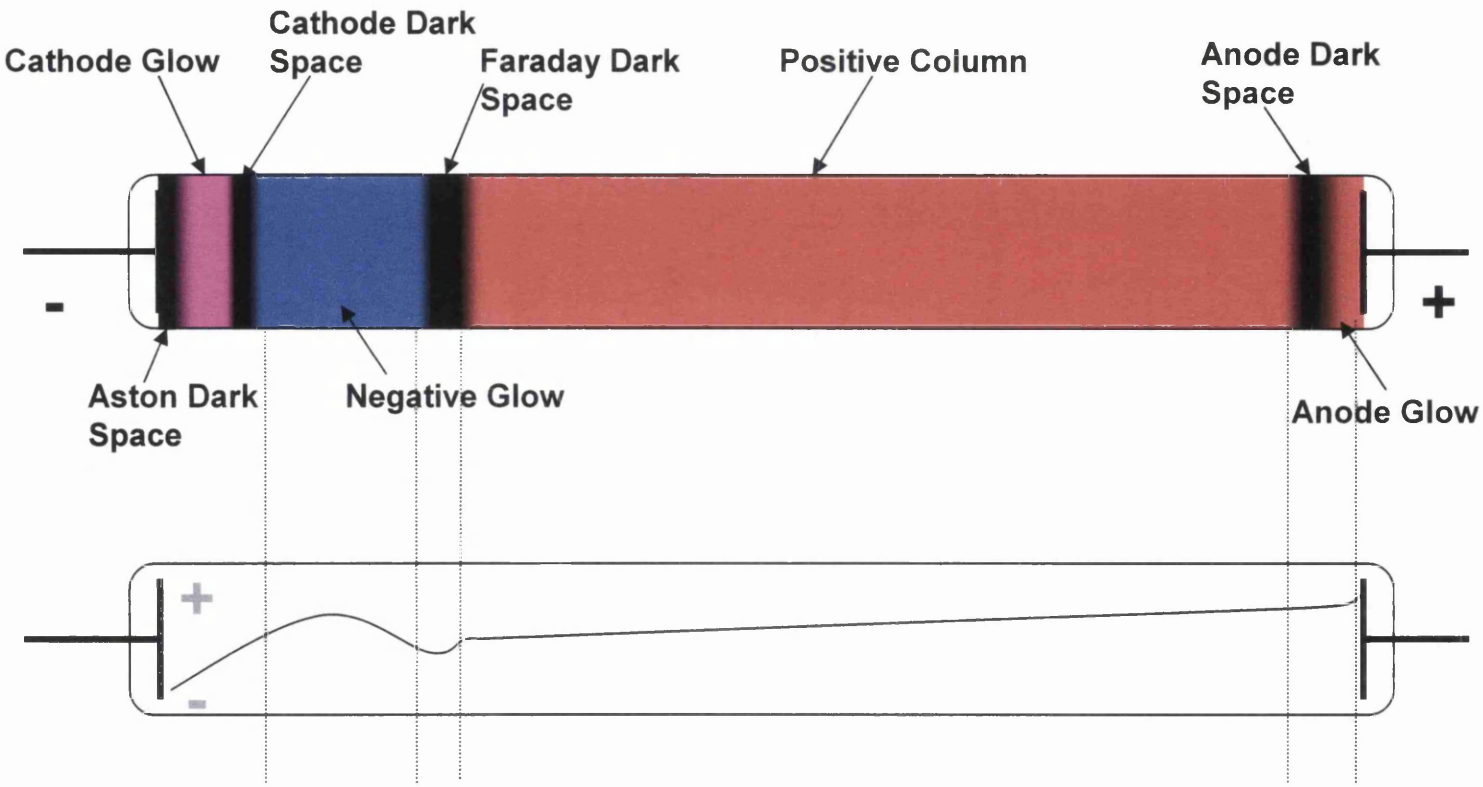

Figure 2.1: Architecture of the glow discharge – regions and potential distributions (colours correspond to an argon discharge, adapted from references 22 and 18)

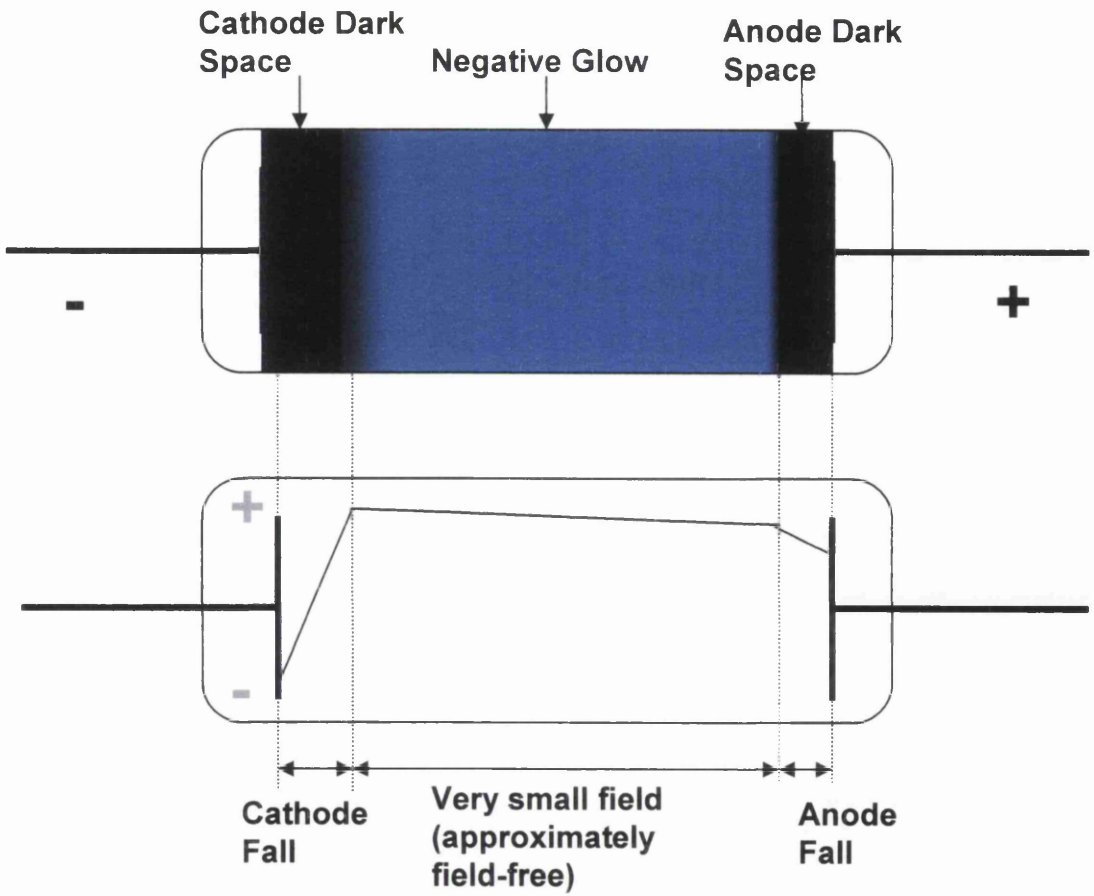

Figure 2.2: Architecture of the analytical glow discharge – regions and potential distributions (colour corresponds to an argon discharge, adapted from references 18 and 6)

2.2.1.1 Cathode Dark Space (CDS)

The CDS is a thin dark layer directly in front of the cathode. It is not completely non-luminous but is much darker than the glow regions and therefore appears dark to the eye. The CDS itself consists of a number of dark and light layers[6]. Within this region there is a steep potential gradient (close to the magnitude of the discharge voltage). This gives rise to another name for this region, the cathode fall. Due to this potential, positive ions are accelerated towards the cathode, giving rise to secondary electron emission. These electrons are accelerated across the cathode fall, leading to ionisation and excitation of discharge gas and cathode ions, leading to further electron release. Despite loss of electrons to the walls and cathode, the ions formed are again accelerated towards the cathode and the discharge is therefore self-sustaining[22,6]. At 1 Torr pressure, most of the ions are in fact converted by charge transfer to fast atoms before hitting the cathode[29]. The weak glow of the CDS occurs due to excitation, and subsequent de-excitation of discharge gas atoms[6]. Excitation can occur via energy transfer from electrons, fast ions or excited neutral atoms (described in more detail in sections 2.3 and 2.4). Due to collisions at the cathode a cathode glow can also be observed close to the surface[6].

The width of the cathode dark space, d, can be determined empirically using equations 2.1 and 2.2[1,29]:

$$d = \frac{A}{P} + \frac{B}{J^{1/2}} \qquad \textit{equation 2.1}$$

$$Pd = A + \frac{DB}{V_d - C} \qquad \textit{equation 2.2}$$

where P is the cell pressure (mTorr), d is the CDS width (cm), J is the current density (mA cm^{-2}), V_d is the discharge voltage (V) and A, B, C and D are constants for specific cathode/discharge gas combinations[1]. When V_d is constant d is inversely proportional to P. Similarly, when P is constant, d is inversely proportional to V_d. Therefore, as V_d and

P are decreased the width of the CDS increases. When the CDS width is approximately half the inter-electrode distance the discharge is extinguished[29].

2.2.1.2 Negative Glow (NG)

The NG is a large, bright, approximately field-free region next to the CDS[6]. Electrons accelerated through the CDS lose energy through collisions within the NG, leading to excitation and ionisation of discharge gas and sputtered cathode atoms. Since the electrons are not accelerated in this region, and due to electron release caused by electron impact ionisation in the CDS, a wide range of electrons with a wide range of energies (from thermal energies through to energies corresponding to acceleration across the full cathode fall potential) are present. Therefore, the probability of a collision leading to excitation rather than ionisation is higher[6]. De-excitation of these excited states produces the characteristic glow. The colour of the glow regions is dependent on the discharge gas[28,30]. Electrons lose energy as they cross the NG and eventually have insufficient energy to induce excitation. Therefore, the light emission intensity decreases further from the cathode[6]. The number of positive and negative charge carriers are considered to be approximately equal, resulting in charge neutrality. Diffusion is considered to be the dominant charge transport mechanism[6].

2.2.1.3 Faraday Dark Space

The Faraday dark space is not always present in analytical discharges (figure 2.2) as discussed earlier in this section (page 11). Transport of electrons through this region is induced by a small positive field[6].

2.2.1.4 Positive Column (PC) (classical free ion-electron theory)

As described in section 2.2.1, the existence and length of the positive column is highly dependent on the length of the anode-cathode separation. The PC is not as bright as the negative glow due to the lower electron energies at this point. The PC is

electrically neutral and electron transport is facilitated by the presence of a small electric field. The electrons accelerated in this field do not gain as much energy as those in the anode fall, hence the lower degree of excitation[6]. The electron energy distribution in this region is reckoned to be approximately Maxwellian[6].

2.2.1.5 Anode Region

The character of the anode dark space is dependent on whether the discharge is run in the long (figure 2.1) or analytical form (figure 2.2), and hence with which glow region (NG or PC) it is in contact[6]. For an analytical discharge the anode dark space is in contact with the NG and electrons emerging from the NG impinge on the anode. As electrons travel much faster than ions a build up of negative charge occurs at the anode surface and the anode acquires a negative space charge[1]. When this occurs, electrons are repelled from the anode and positive ions are attracted, forming an anode sheath. Electrons retaining their energy from acceleration across the cathode fall should have enough energy to traverse this sheath (anode fall), thereby sustaining the discharge[1]. When the anode dark space is in contact with the PC (figure 2.1) the electron energies are considerably lower and a small attractive field acts to accelerate the electrons towards the anode.

2.2.2 GD Source Geometries

The design of the glow discharge cell can be changed depending on the analytical application. There are six main discharge geometries which produce different discharge characteristics.

2.2.2.1 Planar Diode Geometry

The Planar diode geometry (figure 2.3a) was designed by Coburn, and allows analysis of samples in disk or foil form[31]. The anode and cathode are parallel. To allow mass spectrometric studies a small hole in the anode acts as the ion exit aperture.

2.2.2.2 Grimm/Obstructed Cathode Geometry

The obstructed cathode geometry (figure 2.3b) was designed by Grimm[32] and is used extensively for optical emission spectroscopy (OES). The anode is positioned very close to the cathode (less than the width of the cathode dark space away[6]). Due to this, the sputtering area on the cathode is limited to the region enclosed by the anode, and hence it is "obstructed"[20]. The source has also been shown to be suitable for mass spectrometry[33,34]. Anodic sampling results in a narrow ion energy distribution, an thus this source is well suited to mass analysis by quadrupole mass spectrometers[2].

2.2.2.3 Co-axial Cathode Geometry

The co-axial cathode configuration (figure 2.3c) is the most common geometry for GD-MS applications[6,20]. The exposed length of cathode pin is enclosed within the cylindrical anode. Typically operating conditions are 800-2500 V, 0.5 to 4 mA and 0.5 to 5 Torr[20]. Non-conducting samples must be mixed with a conducting host matrix and compacted. As with the obstructed discharge source a narrow ion energy distribution is observed and therefore this configuration is suitable for analysis using quadrupole instruments[20]. Optical studies can be performed by incorporating quartz windows into the cell walls.

2.2.2.4 Hollow Cathode Geometry

The hollow cathode configuration[35] (figure 2.3d) is suitable for GD-MS applications and is widely used for optical studies[20,36]. The cathode is a cylinder with one end sealed, within which the discharge is struck. This source benefits from increased sputtering, ionisation and excitation, and therefore yields good analytical sensitivity[6]. However, the source has a disadvantage, in that samples must be machined into the required cathode configuration. This may not be possible for all sample materials. Hollow cathode discharges are rarely used for mass spectrometric studies due to sampling difficulties[37]

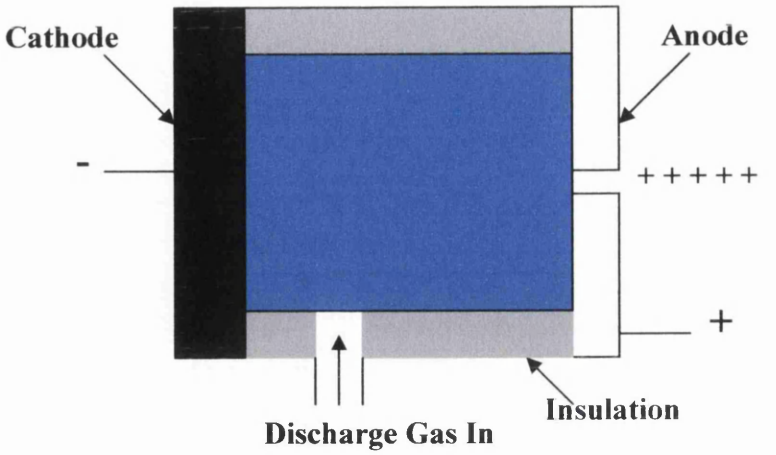

Figure 2.3a: Planar geometry

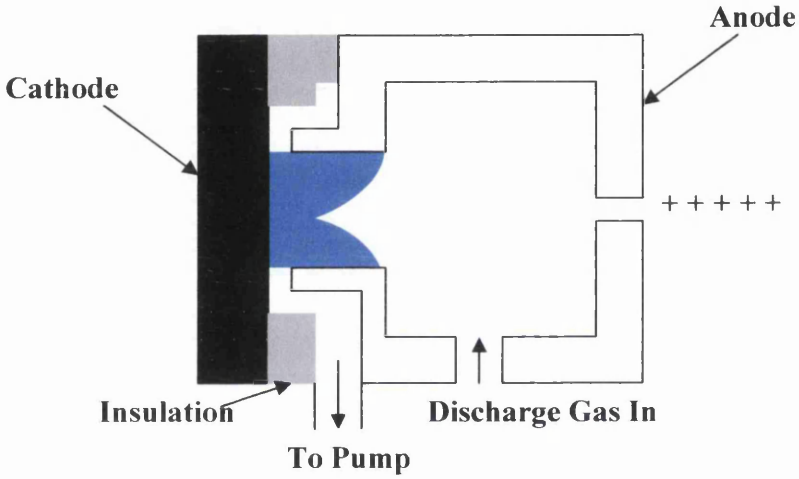

Figure 2.3b: Grimm/Obstructed geometry

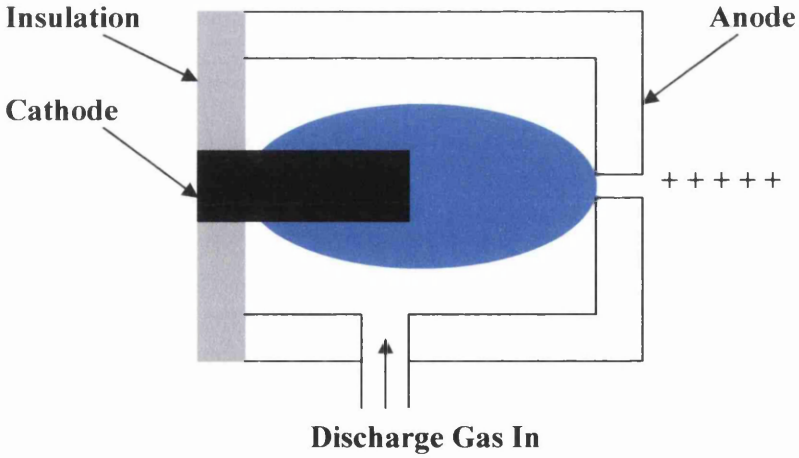

Figure 2.3c: Co-axial geometry

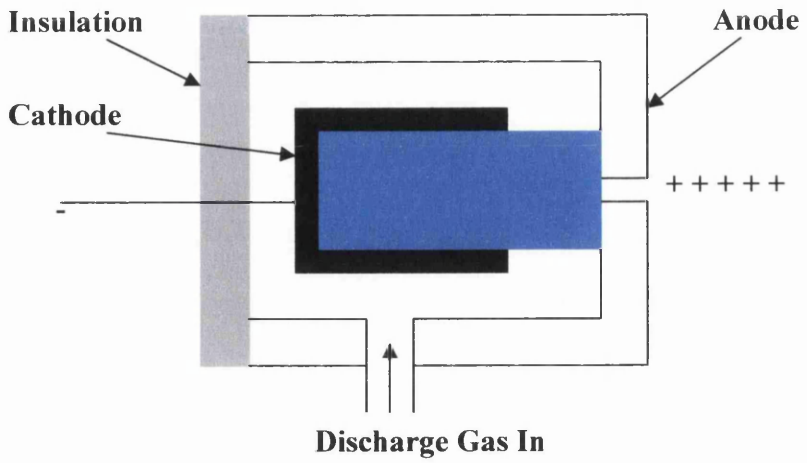

Figure 2.3d: Hollow cathode geometry

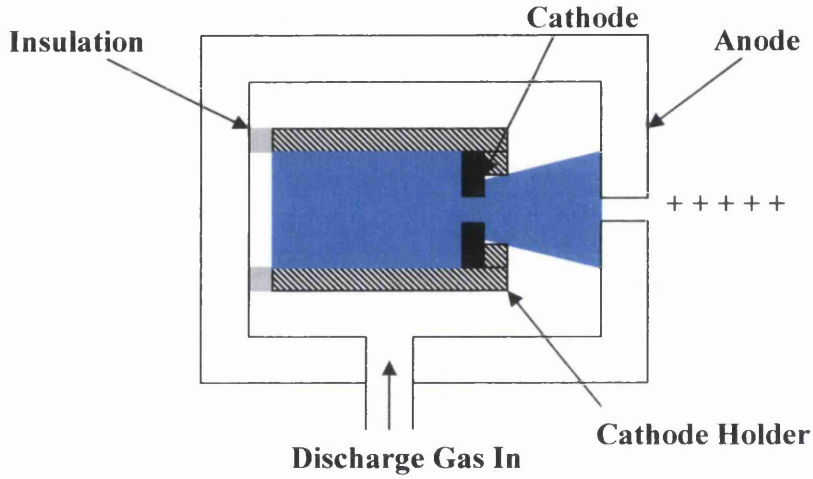

Figure 2.3e: Hollow cathode plume geometry[11]

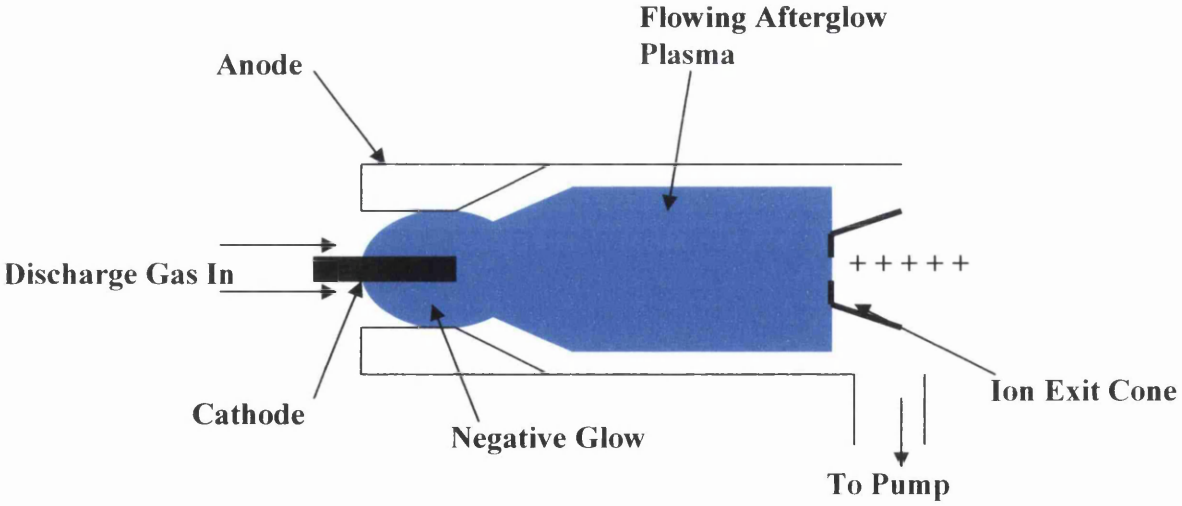

Figure 2.3f: Co-axial fast flow glow discharge (FFGD) source

and is not suitable for use with quadrupole mass analysers due to the wide distribution of ion energies[38].

2.2.2.5 Hollow Cathode Plume

The hollow cathode plume discharge source (figure 2.3e) is similar to the hollow cathode source and was designed by Marcus and Harrison primarily for atomic emission spectroscopy (AES)[39-42]. In this configuration the sample takes the form of a disk with a 1.5mm orifice at the base of the hollow cathode[20]. The sample is mounted in a cylindrical graphite support. A plume of plasma is ejected from the cathode orifice and ions can be sampled through the anode.

2.2.2.6 Fast Flow Glow Discharge (FFGD) Source

The previous source configurations are all 'static', i.e. the discharge gas flow rate is very low (< 5 sccm) and diffusion is the dominant transport mechanism. More recent developments have used a flowing discharge gas[33-46]. The use of a flowing gas increases the cathode erosion rate by reducing back diffusion of sputtered cathode material. Gough[43] reported that use of a high discharge gas flow in a discharge source of Grimm geometry led to approximately 25-fold increase in cathode atom concentration. This is of significant value, particularly in optical spectroscopy, where the analyte atom concentration directly influences the signals observed. A commercially available jet assisted source, Atomsource[44], was attached to a quadrupole mass spectrometer by Kim et al.[45,46]. Ions formed within the discharge were sampled through a sampling cone, to which bias could be applied to aid ion extraction[45]. To maintain a suitable discharge pressure when using a high gas flow rate additional pumping is required.

More recently, a fast flow glow discharge (FFGD) ion source (figure 2.3f) has been developed within this group using co-axial[13,47] and Grimm[15] discharge geometries. As with the source developed by Kim et al.[45], a cone shaped ion exit was incorporated, to which an extraction bias can be applied to improve sampling efficiency from the flowing afterglow (FAG) plasma (this mode has been referred to as extended plasma[16]). In this

mode the active discharge is confined to a small volume within the anode region. However, the high gas flow rates used (commonly up to 500 sccm) extend the plasma downstream to form a FAG plasma. Alternatively, the cone can act as the anode when running the source in an extended discharge (ED) configuration[16]. The high gas flow rate acts to aid transport of cathode material from the discharge region, therefore also increasing the cathode erosion rate. The technique has been successfully coupled to a high voltage magnetic sector[13,47] and low voltage quadupole[16,17] instruments. Recently, a collaborative project has led to production of the first commercial FFGD ion source for high purity analysis[48].

2.2.3 Modes of Operation

2.2.3.1 Direct Current (dc)

This mode of operation is the oldest and simplest method of powering a glow discharge, in which a dc bias (commonly 0.5 to 1.5 kV) is applied between the anode and cathode. Electric currents are typically a few to several hundred milliamps[6] (dependent on discharge voltage, source geometry and pressure). However for cathode analysis the sample must be a conducting material or compressed with a conducting material to form the cathode[20]. If the sample was non-conducting the cathode surface would charge up preventing positive ions bombarding[6]. Developments by Mason et al. allow samples to be analysed in vapour form through addition directly into the FAG plasma of the fast flowing dc glow discharge[13,15-17,18]. Using this method it is not necessary for the sample to be conducting and sample addition does not influence the active discharge.

2.2.3.2 Radio Frequency (rf)

Direct current glow discharges cannot be used to analyse non-conducting materials due to 'charging up' of the cathode surface to floating potential[22]. It was proposed that this problem could be overcome through the use of an alternating current (ac) glow discharge. In this system the positive charge accumulated during one half-cycle is neutralised by electron bombardment during the next half cycle. However, the time over

which the electrodes charge up is significantly lower than the length of a half cycle of a standard mains-powered (50Hz) GD and therefore the system is not very effective[22]. Radio frequency discharge sources can be used to analyse both conducting and non-conducting samples directly. This is because the positive charge accumulated during one half-cycle is neutralised by negative charge accumulation during the next half cycle[6].

On application of the rf power the target electrode is initially negatively biased and therefore positive ion bombardment occurs. The electrode bias rises towards zero. However, the movement of ions is significantly slower than electron flow and therefore if the discharge is of sufficiently high frequency ($\geq$ 1 MHz[22,49]) the target electrode will still be negatively charged when the alternating supply voltage is reversed. At this point the bias on the target electrode becomes positive, but not the full magnitude of the supply voltage due to the initial negative bias. During the next half cycle the much higher rate of electron motion induces a higher negative bias than was achieved in the first half cycle due to the faster electron motion. By this process the sample electrode is negatively charged for the majority of the time and positive ion bombardment occurs in a similar manner to a dc glow discharge[22,50].

The ionisation efficiency of rf glow discharges, compared with dc discharges, allows analysis at much lower pressures for the same discharge current[6]. RF powered glow discharge sources for mass spectrometry were introduced by Coburn and Kay[3]. Since then, rf powered sources have been coupled to all of the common types of mass spectrometer[51-55] and to optical electronic spectroscopy (OES)[56,57].

2.2.3.3 Pulsed Glow Discharge

The third mode of operation is the pulsed GD, for which both rf and dc sources can be produced[6]. Pulsed GD systems have the advantage of running at higher discharge voltages and currents, and therefore increasing the production of atoms, ions and photons, without the overheating, thermal emissions and discharge instability which can occur when running in continuous mode[58]. In pulsed mode the heat generated during the "on" cycle dissipates during the "off" cycle and therefore prevents overheating. The first pulsed GDMS instrument was built Harrison et al[58]. It was determined that the sputter

yield and ion signal were higher than observed for a continuous dc discharge for the same average current. One particularly useful feature of the pulse profile was the observation of ions related to gaseous impurities in the pre-peak period and cathode ions in the afterpeak region. Thus, interference in the mass spectrum due to the presence of gaseous impurities is minimised. For instance, the ion signals for silicon (m/z = 28 and 29) coincide with the masses of N_2 and N_2H/COH. Using the pulsed system the gaseous impurities can be separated from the cathode ion signals.

It was established that ion formation within the pre-peak, plateau and afterpeak regions occurred by different mechanisms[59,60]. In the pre-peak region ionisation formation of discharge gas related ions occurs by electron impact ionisation. In the plateau region ionisation and excitation are thought to occur through a mixture of electron impact, Penning processes and charge transfer. In the afterpeak region, after termination of the discharge ion formation occurs predominately by Penning ionisation, hence the observation of the cathode ions which commonly have lower ionisation potentials than the metastable states of the discharge gas[61]. This has recently been applied to chemical identification since the technique can provide atomic (pre-peak), fragment (mainly plateau) and parent molecular (afterpeak) ion information in a single pulse width[59,60,62]. To date, the pulsed GD source is the only plasma source which has produced sample parent molecular ion peaks solely and separately from corresponding elemental and structural ions[60].

2.3 GDMS – Mass Analysers

The GD ion source was the first ion source used for mass spectrometry[63]. Since its conception by Thomson[63] significant developments have been made to the instrumentation available for mass spectrometric studies. Mass spectrometry is a very useful analytical tool due to its high sensitivity, versatility, ease of use and straightforward spectral analysis. However, the technique does have the disadvantage of requiring a very low pressure for operation, and therefore high performance pumps are required and sample flow from the ion source is limited by a small sampling orifice.

The earliest mass analyser, the so-called parabola spectrograph[63], used a magnetic field to deflect and separate "positive rays" from a gas discharge based on their mass to charge (m/z) ratio. Since the inception of mass spectrometry a number of different types of mass analyser have become commercially available. The major mass analysers are described in the following sections. The quadrupole mass analyser (QMA) and sector mass analyser are described in more detail due to their use within this group.

2.3.1 Quadrupole Mass Analysers

Quadrupole mass analysers are made up of four parallel rods with circular or hyperbolic cross section[64,65]. They are widely used due to their low cost, availability, simplicity and small size. The technique was first developed in the early 1950s[65,66], and the instrument became commercially available in 1968[65]. The ion beam is sent axially between the rods and the ions are forced to oscillate perpendicularly to the axis by a superimposed radiofrequency field. The amplitude of oscillation is dependent on the mass to charge ratio (m/z) of the ion, allowing ions of a single mass to be focussed through the mass filter. Ions of different m/z are lost to the rods. Inclusion of pre- and post-quad lenses removes a fraction of the undesired ions, thereby reducing the deposition of sample material on the quadrupole rods[67]. The pre-quad lens in the V. G. PlasmaQuad system is used to reduce the fringing fields at the QMA entrance so that low energy ions are not prevented from entering[64].

Aside from the advantages listed above, the QMA can scan for single ions or complete mass ranges faster than other mass analysers. Due to the cost of mass spectrometric analysis, a high throughput is desirable. The speed of the technique is also particularly useful for time dependent processes such as depth profiling[68] and chromatographic analysis[18,65]. QMAs also operate at low voltages, and it is therefore not necessary to float the ion source and gas lines at a high potential.

However, QMAs are commonly capable of only unit mass resolution. Thus it is not possible to distinguish between ions of the same nominal mass. Knowledge of isotope patterns can often reduce this problem. It is also common for quadrupole instruments to be limited to approximately 300 amu,[64] prohibiting their use in analysis of higher mass

ions. Analysis of high mass molecules can be achieved via fragmentation, either within the ion source[18,69] or via triple quadrupole MS, whereby ions are selectively fragmented in collision cells[20]. The QMA also exhibits discrimination in favour of low mass species. Therefore, quantitative studies require calibration of the instrument to account for this bias.

Despite its limitations, the QMA has been used extensively for GDMS applications[64]. The first commercially available mass spectrometer was produced by VG Isotopes (now Thermo Elemental) in the 1980s[70]. More recently, inductively coupled plasma (ICP) quadrupole-based instruments have become available[65].

2.3.2 Magnetic Sector Mass Analysers

Magnetic sector mass spectrometers with Nier-Johnson (forward) geometry[71] were the first commercially available mass spectrometers. Magnetic sector instruments induce separation of ions of different m/z in a magnetic field according to their momentum. This process was first observed by Wien in 1898[72] and was the principle for the first mass spectrometric studies performed by J. J. Thomson[63] in the early 20th century. Coupling of the technique with an electrostatic energy filter also permits separation of ions according to their kinetic energies. The energy filter can be placed before or after the magnetic sector, and these instruments are said to have 'forward' or 'reverse' geometry respectively. As these instruments have two regions of ion separation they are referred to as double focussing instruments. The first commercial GDMS instrument was the VG 9000 double focussing mass spectrometer[20]. Recently, a commercially available FFGD instrument has been produced[48].

Magnetic Sector instruments offer far greater resolution than quadrupole instruments, and therefore the problem of isobaric interference[64] is overcome. However, the resolution of these analysers is commonly restricted in order to maintain high sensitivity. The sensitivity of the instrument for elemental analysis has been reported to be in the range of 1 to 10 ppb (by weight)[20,73]. Sector instruments do not favour detection of low mass ions as quadrupole instruments do, and therefore quantitative analysis is simpler.

Sector instruments are large, expensive instruments, complicated to operate and repair, and scan rates are generally slower than those of quadrupole instruments. Due to the high potentials involved, it is necessary to float the ion source and the gas lines at the analyser potential. This is potentially dangerous and restricts modifications to the instrument, such as adaptation for chromatographic analysis.

2.3.3 Other Mass Analysers

This section details further mass analysers which have not been used within this laboratory, they are: time of flight (TOF), ion trap and Fourier transform ion cyclotron resonance (FTICR) mass analysers.

The concept of the linear TOF analyser was proposed in 1946[74] and the design was first published in 1948[75]. The first commercial linear TOF instrument was produced by Bendix in 1958[65]. The principle of the TOF analyser was to separate ions according to their mass. The velocity acquired by an ion on application of a fixed accelerating potential is inversely proportional to the square of its mass. Therefore, ions traversing a set field free distance will be separated according to their mass and will reach the detector at different times[64], i.e. they are temporally resolved. The technique operates in pulses, since continual addition of ions would prevent ion separation. The longer the pulse time, the greater the degree of interference from ions transmitted after the pulse start time. The creation of the reflectron TOF mass analyser[76] was an important development, as it corrects for the kinetic energy distribution of ions within the spectrometer.

TOF analysers are capable of very fast spectral acquisition, with thousands of mass scans per second possible. This is particularly useful for depth profiling, since the each scan is representative of the chemical composition at a fractionally lower depth. The mass range of the TOF analyser is greater than that of other techniques, allowing analysis of larger compounds[65,77]. However, the resolution of the TOF analyser is relatively low, and therefore isobaric interference can be a problem. As with quadrupole mass spectrometry, tandem mass spectrometry (triple quadrupole mass spectrometry in the case of the QMA) can be used to reduce the isobaric interference. Recently TOFMS has been

used as a detector for a pulsed GD source[59,60,78,79]. Over a short pulse (< 1 second timescale) it was possible to determine molecular, structural and elemental information. Molecular and fragment ions were formed at different times, and therefore isobaric interference was minimised. The signal to noise ratio is also significantly enhanced due to the high repetition rate which can be achieved[78].

FTICR mass spectrometry originated with the development of the Omegatron instrument built in 1948[64]. Hipple et al. described the first application of ICR in mass spectrometry a year later[65,79], and FTICRMS was first reported in 1974[80]. In a cyclotron ions are forced to move in a circular trajectory in a magnetic field. Application of a radiofrequency resonant with ion motion (which is mass dependent) increases the energy of the ions and allows them to escape their orbit. Scanning a wide range of frequencies over a set time allows a complete spectrum to be generated.

FTICR has the highest resolution of the techniques (in excess of 650,000 $m/\Delta m$)[81], and therefore isobaric interference is negligible. The spectral acquisition rate is fast, and a complete scan of frequencies can be achieved in < 0.1 ms[55]. However, FTICR mass spectrometers are very large, complex and expensive. Thus, their use has been very limited relative to the previously discussed instruments. Barshick and Eyler[82] reported the coupling of a GD source to an FTICR analyser in 1992, though the detection limits measured were several orders of magnitude higher than those attainable using a magnetic sector instrument. A year later they reported a 15-fold increase in the ion signals[83]. Zientek and Eyler later reported that the sensitivity towards low abundance ions can be significantly improved by removing unwanted high abundance ions[84].

The ion trap mass analyser (ITMA) was described by Paul and Steinwedel in 1960[85,86]. The operating principle is similar to that for the QMA, but a three dimensional field is used instead of a two dimensional one. The cell consists of a ring electrode positioned between two curved end plates. As with the FTICR analyser, a radiofrequency is used to expel selected ions. The ions are contained within the field and expelled according to their masses in order to generate the spectrum[64].

The ITMA is simple, relatively inexpensive and has fast scan rates. The size of the ITMA makes it suitable for production of hand-held mass spectrometers[87]. Handheld mass spectrometers are of growing interest due to their potential for rapid in-situ chemical analysis with high sensitivity and specificity. Such instruments have wide range of possible applications in monitoring local environments[88], e.g. air quality or industrial waste gases. One further advantage is that the analyser operates at relatively high pressures (several mTorr[87] rather than the high vacuum required for other systems). Thus, coupling to GD sources, which operate at higher pressures, is less complicated. As with the FTICR analyser, isobaric interferences are removed by the selected storage and expulsion of ions. Recently ion trap mass spectrometers have been coupled to glow discharge sources for analysis of oxidation of hydrocarbons by ozone[89,90].

2.4 GDMS – Applications in Chemical Analysis

2.4.1 Solid Analysis

As previously discussed, GDMS is a fast and easy way to analyse solid samples with little sample preparation. The sample is often incorporated as the cathode in pin or disk form (machined from bulk sample or compressed from powder). Mass spectrometry is a very sensitive technique, and is therefore suitable for analysis of trace impurities in metals, semiconductors, etc. Similarly, the chemical composition of a sample can be monitored as the cathode is eroded. This process is called depth profiling, and can be used to determine the composition of even very thin films. Problems due to surface contamination, e.g. due to oxidation, can be overcome by allowing a pre-sputter period to remove the surface layer prior to analysis[20]. The processes responsible for atomisation and ionisation of the cathode sample in the cathode fall are discussed in section 2.5.

Analysis of non-conducting samples can be achieved using both rf and dc glow discharges. Using an rf powered discharge, the sample can be run in its pure, non-conducting form[22]. However, as described in section 2.2.3.2, non-conducting samples cannot be used in a dc source due to 'charging up' of the cathode surface[22]. Non-conducting powder samples can be mixed with a conducting host matrix and compacted into a disk or pin as before. This preparation is time consuming and can introduce

contaminants to the cathode. Also, some samples may not be easily converted into powder. One alternative method is the "secondary cathode" technique[91]. A thin metallic mask is placed over the non-conducting sample, with a small aperture exposing the non-conducting surface to the plasma. The sputtered metal can be deposited on the non-conducting surface. Subsequent sputtering of the sample surface is energetic enough to eject sample material from layers below the deposited metal. This technique has been used for analysis of a range of samples including atmospheric particulate matter[92], sediments[93,94], glass[91], and metal oxides[95].

2.4.2 Detector for Gas Chromatography (GC)

The first use of a GD as a detector for gas chromatography (measuring voltage changes across the detector as the sample eluted from the column) was reported by Harley and Pretorius in 1956[23]. Recent studies of GDMS as a detector for GC have focussed primarily on the ability of the technique to extract elemental composition and structural information quickly and easily[18,59,60,62,69,97-99]. The high power of Inductively coupled plasma (ICP) MS means that samples may be completely atomised and ionised[59,100], though reduction of the ICP power allows larger fragment[101], but not parent molecular, ions to be formed. EI ion sources are also used, but atomisation is not normally possible. However, different compounds have characteristic mass spectra which can be compared against library spectra, allowing chemical speciation. Obviously, this relies on the presence of the compound within the mass spectral library.

Lewis et al.[59,60,62,69] have utilised the pulsed-GD technique developed by Harrison[58] to extract elemental, structural and parent molecular ion information for organic compounds separately within a single pulse profile. Thus, in one example it was possible to obtain elemental, structural and parent ion mass spectra of o-dichlorobenzene within 5 ms of pulse initiation[14]. Lewis et al. observed three distinct temporal regions:

1) the pre-peak, where atomic ions are formed,
2) plateau, where fragment molecular ions were formed, and
3) after-peak, where the parent molecular ions were observed.

It was proposed that atomisation in the pre-peak region was induced by EI ionisation. In the plateau region ionisation could occur via EI, charge exchange or Penning ionisation, since the lower energies of charge exchange and Penning ionisation meant that less fragmentation was observed. After termination of the plasma power charged particles quickly recombine to form excited states. Formation of metastable state species leads to further Penning ionisation, therefore yielding mainly Parent molecular ions[60]. The fragmentation patterns observed during the plateau time regime were similar to, but not the same as standard NIST[102] 70 eV EI mass spectra. This was attributed to the influence of charge transfer and Penning ionisation processes[60]. The short time over which information is gathered means that the pulsed technique is suitable for analysis of GC eluted compounds. Detection limits for toluene, with methanol solvent, were as low as several hundred ppb or several hundred pg[103].

The use of gas sampling GDMS for atomic and molecular mass spectrometry was also demonstrated by Guzowski et al.[104-106]. This was allowed by switching the polarity of the discharge electrodes with rates up to 100 Hz. In atomic mode, the best detection limits determined were 1-25 fg of analyte per second[106]. However, the detection limits in molecular mode were somewhat higher; 7-140 pg/s.

The most recent studies in Swansea have highlighted use of the FFGD ion source for tuneable fragmentation of organic[18,97,99] and organometallic[18,98] compounds. It was found that changing the bias applied to the ion exit orifice relative to the anode changed the degree of fragmentation of the molecule. This can provide valuable structural information about the compound being analysed. On application of a negative ion exit bias (V_c) fragmentation is induced, with the degree of fragmentation increasing with increasing negative V_c. However, on application of a low negative, zero or a small positive bias the molecular ion peak reaches its maximum intensity. Thus, monitoring the mass spectral variation as V_c is scanned allows elemental, structural and parent molecular ion information to be determined. Addition of the GC eluent to the FAG plasma rather than the active discharge minimises the collisional fragmentation of the molecules within the main body of the plasma. The fragmentation process, discussed in detail in chapter 8, is believed to occur in the thin sheath around the ion exit cone. Detection limits for

halogen ions were measured between 0.3 and 66.5 pg[97]. On addition of organotin compounds, detection limits as low as 0.2 to 0.4 pg were determined[18,98].

Newman also observed that the plasma conditions, i.e. discharge voltage, and residence time also influenced the degree of fragmentation[18,97] of some organic and organotin compounds. Not surprisingly, increasing the magnitude of the discharge voltage, and therefore the energy of the plasma increased the fragmentation.

2.4.3 Study of Plasma Properties and Ionisation Processes

One of the major focuses of this group has been the study of secondary gas addition to the GD plasma[18,13-17]. The FFGD technique was designed in part to allow a greater degree of control over the GD plasma conditions than is offered by older GD source designs[13,14]. One of the most interesting aspects for fundamental studies of plasma processes is the isolation of the active discharge to the upstream end of the discharge cell. Thus, the addition of secondary gases downstream of the active discharge, i.e. to the flowing afterglow (FAG) plasma allows the study of plasma reactions without disturbing the discharge. The flowing gas prevents back diffusion of the secondary gases and aids the transfer of excited state and ionic species towards the ion exit orifice.

In recent investigations[15-17] secondary gases and organic vapours have been added to the FAG plasma of the FFGD 20 mm upstream of the ion exit orifice, allowing time for gas mixing. The technique, and its use in this study, is discussed in later chapters. Through mass spectrometric analysis of ions emanating from the GD cell, Mason et al.[18,97-99,13-17,107-109] have ascertained that ion-molecule reactions and Penning ionisation involving argon metastable states cannot account for the variation in ion intensities on addition of secondary gases. In most cases there has been anomalous formation or loss of ion signals without corresponding loss of, or formation of, another ion signal. However, Penning ionisation and ion-molecule processes cannot be ruled out in all cases.

As described in section 2.4.2, variation of the ion exit bias allows tuneable fragmentation of organic vapours added downstream of the active discharge via a GC or continuous flow inlet. Understanding the processes occurring within the ion exit sheath, and the influence of the magnitude and polarity on these processes is one of the keys to

understanding the chemistry of the FFGD plasma. The Rydberg gas model developed by Mason is described in detail in section 2.7 and chapter 4. The continuous vapour inlet system developed by Newman[18] is also described in detail later in this thesis (chapter 7). The inlet allows a continuous flow of organic or organometallic vapour, carried by He, into the FAG plasma. Whereas GC is the preferred technique for chemical analysis, the sample is introduced as a small plug of material, and therefore the time over which the reaction chemistry can be studied is very low. Thus, the continuous flow technique allows study of reactions within the flowing plasma.

2.5 Glow Discharge Processes – Conventional Model

2.5.1 Cathodic Sputtering

Atomisation of the cathode occurs via a process called cathodic sputtering[20,22]. Sputtering is caused by a mixture of fast ions and atoms bombarding the cathode[110,111]. For a source pressure of approximately 1 Torr the bombardment flux is overwhelmingly composed of fast neutral atoms formed via charge transfer (equation 2.3) in the cathode dark space[29,112-114]. Discharge gas ions are accelerated across the cathode fall and symmetric charge transfer can lead to formation of fast neutral discharge gas atoms[115]. The resulting discharge gas ions will also be accelerated towards the cathode and may themselves undergo symmetric charge transfer, leading to the formation of fast neutral atoms with a range of kinetic energies[110,116].

$$Ar^{+}_{\rightarrow} + Ar \rightarrow Ar_{\rightarrow} + Ar^{+} \qquad \textit{(equation 2.3)}$$

If the energy transferred during a collision exceeds the binding energy of atoms at the cathode surface formation of atomic vapour can occur[22]. The number of atoms released per bombarding particle is the 'primary sputter yield' and is dependent on the energy transferred and the masses and types of the bombarding and target species[116-118] (discussed in more detail below). The major processes which occur in the cathode fall region are illustrated in figure 2.4.

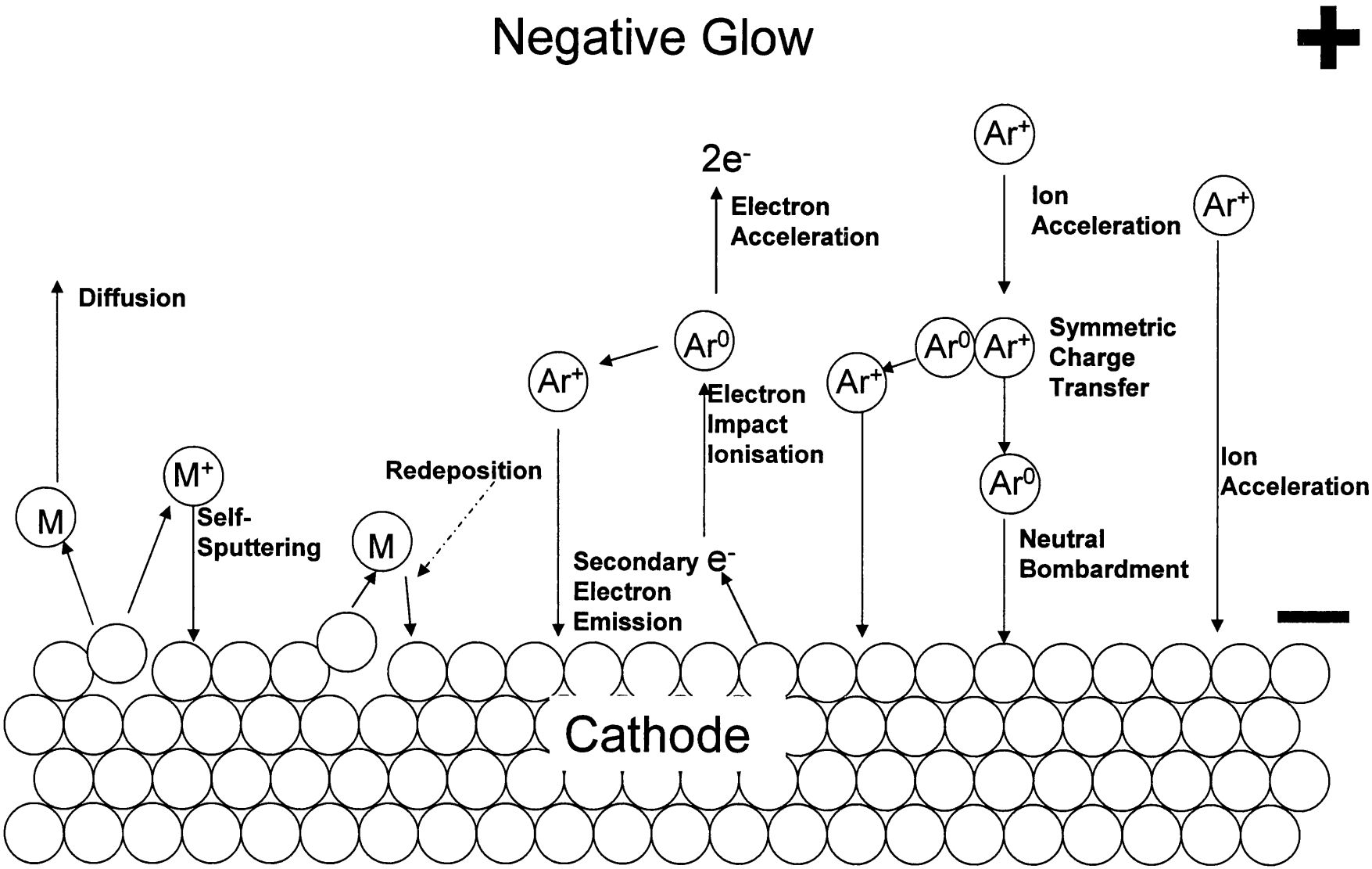

Figure 2.4: Sputtering and cathode fall chemistry (adapted from references 17 and 18)

Sputter released cathode atoms diffuse away from the cathode surface. These atoms can undergo a number of processes. Cathode atoms may diffuse to, and be deposited on, the walls of the discharge cell (including the anode). Collisions within the discharge act to reduce the energy of the atoms to the thermal energy of the surrounding gas and redeposition of sputtered material on the cathode can occur[112]. In a static glow discharge it has been estimated that up to 90% of sputtered material is redeposited on the cathode surface[119]. Alternatively, electron impact ionisation due to release of secondary electrons during bombardment of the surface may occur, leading to "self-sputtering"[120] of the cathode. Self-sputtering will also occur if positive ions are ejected from the surface on bombardment by high energy species. Electrons released from the cathode surface and from electron impact ionisation within the cathode fall are accelerated into the NG region where they undergo ionisation and excitation processes[20].

Due to the redeposition of cathode material the true sputter yield (i.e. total number of atoms ejected from the surface per incident particle) cannot be determined[6]. However, a net sputter yield can be determined empirically[20] or estimated from theoretical calculations[121] and computer simulations[122]. The discharge conditions, sample type, contamination and discharge gas are all significant in the sputtering efficiency. The discharge voltage determines the initial kinetic energy of the discharge gas ions and therefore the energy of ions and fast neutral species bombarding the cathode surface. The discharge pressure controls the collision frequency in the cathode fall and therefore the rate of charge exchange and redeposition of cathode material. The nature of the discharge gas determines the momentum transfer during a collision[123]. The binding energy, and therefore the sputter yield, of the cathode surface atoms is dependent on the cathode material. The sputter yield is reduced by any formation of an oxide or nitride layer on the cathode surface[6,124]. Therefore, to ensure that the atomic vapour released is representative of the cathode material, sufficient time must be allowed for the system to equilibrate prior to analysis[20].

2.5.2 Excitation and Ionisation

The conventional model of the GD plasma, based on the work of authors such as Townsend[123,124] and Langmuir[125], is that of a partially ionised gas[22], i.e. ions, electrons and neutral species in both ground and excited states. In this section the major excitation and ionisation processes are discussed.

2.5.2.1 Electron Bombardment

Ionisation (equations 2.4 and 2.5) and excitation (equations 2.6 and 2.7) of cathode and discharge gas atoms can occur by bombardment by electrons accelerated across the cathode fall. The energy of the bombarding electrons is dependent on the point of release within the cathode fall and any loss of energy due to collisions within the cathode sheath or NG region. If the electrons do not have enough energy to induce ionisation, excitation to a range of states is possible.

$$Ar^0 + e^-_f \rightarrow Ar^+ + 2e^-_s \qquad \textit{(equation 2.4)}$$

$$Cu^0 + e^-_f \rightarrow Cu^+ + 2e^-_s \qquad \textit{(equation 2.5)}$$

$$Ar^0 + e^-_f \rightarrow Ar^*, Ar^{**}, Ar^R + e^-_s \qquad \textit{(equation 2.6)}$$

$$Cu^0 + e^-_f \rightarrow Cu^*, Cu^{**}, Cu^R + e^-_s \qquad \textit{(equation 2.7)}$$

The superscript ^{0} indicates ground state electronic configuration, * and ** indicate unspecified excited states, and ^{R} represents highly excited Rydberg states. The subscript $_f$ and $_s$ denote fast and slow species respectively. The minimum excitation energy for Ar is 11.55 eV[17,18], and therefore this is the lowest electron energy which can induce excitation of argon. The argon first excited state, or metastable state, is higher in energy than many cathode element ionisation energies. Therefore, to excite cathode atoms significantly less energy is required.

2.5.2.2 Charge Transfer

Ionisation can occur via charge transfer (equations 2.8 and 2.9). Symmetric charge transfer (SCT)[22] (i.e. electron transfer between species with the same chemical composition) between argon and Ar^+ is known to occur readily[126]. This process has already been shown to be important in cathodic sputtering by fast atoms (section 2.3.1). If the two species are not chemically equivalent the process is known as asymmetric charge transfer (ACT)[22]. This process does not increase the degree of ionisation but could lead to a greater degree of sample (cathode or secondary gas) ion formation.

$$Ar^+ + Ar \rightarrow Ar + Ar^+ \qquad \textit{(equation 2.8)}$$

$$Ar^+ + Cu \rightarrow Ar + Cu^+ \qquad \textit{(equation 2.9)}$$

ACT tends to be less efficient than SCT[22] due to the greater difference between the ground state energy levels of the argon and resultant ions. When the energies of the two ions differ the resultant ion exists in an excited state which can go on to react, fragment or relax through photon emission or energy transfer.

2.5.2.3 Penning Ionisation

Energy transfer from an excited state neutral species to a second neutral species in ground or an excited state can induce Penning ionisation. For instance, the energy of the argon first excited, or metastable, state ($^3P_2$, 11.55 eV[17,18]) is higher than the ionisation potential of many cathode species (e.g. ionisation energies – Cu – 7.73 eV, V – 6.75 eV)[127]. Therefore, energy transfer from argon excited states to cathode atoms can directly induce ionisation. Examples of Penning ionisation processes are illustrated in equations 2.10 and 2.11. It has been noted that the energy transfer from one argon metastable state atom to another could induce ionisation (equation 2.12)[128,129]. However, this is not thought to be an important due to the low probability of a collision between two metastable state species[130].

$$Cu + Ar^* \rightarrow Ar + Cu^+ + e^- \qquad \textit{(equation 2.10)}$$

$$A^* + B^* \rightarrow A + B^+ + e^- \qquad \textit{(equation 2.11)}$$

(where A and B are unspecified elements)

$$Ar^* + Ar^* \rightarrow Ar + Ar^+ + e^- \qquad \textit{(equation 2.12)}$$

If the energy transferred during a collision is not sufficient to induce ionisation then excitation may occur (equation 2.13).

$$A^* + B^0 \rightarrow A^{0,*'} + B^* \qquad \textit{(equation 2.13)}$$

Argon is often chosen as a discharge gas because its metastable state energies are higher than the first ionisation energies of most elements but lower than the second[22]. Therefore, Penning ionisation selectively produces singly charged ions and spectral interpretation is simpler.

Energy transfer from argon metastable states could also induce dissociation of molecular species such as methane (equation 2.14). Alternatively, associative ionisation could occur (equation 2.15). This process may be responsible for the formation of polyatomic argon-containing ion species[131].

$$Ar^* + AB \rightarrow Ar + A^+ + B^* + e^- \qquad \textit{(equation 2.14)}$$

$$Ar^* + M \rightarrow ArM^+ + e^- \qquad \textit{(equation 2.15)}$$

2.5.2.4 Electron Attachment

Negative ion formation can occur via attachment of the slow electrons, produced from electron impact ionisation, to neutral species. Electron attachment is known to occur more readily to excited state, rather than ground state, neutrals[132-135]. This is discussed in more detail in section 2.6. Pinnaduwage et al.[132-135] concluded that only dissociative electron attachment occurred (equation 2.16), i.e. only fragment ions were observed. However, Mortimer[14] observed parent ion peaks for both CCl_4 and O_2. Cu^-

was also observed, although Ar^- was not, due to the very low electron affinity of Ar. It is possible that the molecular ions observed by Mortimer formed through recombination processes, although this cannot be confirmed.

$$AB^0, AB^* + e^-_s \rightarrow AB^-, AB^{*-} \rightarrow A^- + B \qquad \textit{(equation 2.16)}$$

2.5.2.5 Formation of the Main Discharge Related Ions

Taking the Cu/Ar GD as an example, the mechanisms of formation for the major discharge related species have been proposed by a number of authors through application of the conventional plasma model. As previously discussed, the argon and cathode (Cu) ion species are thought to be formed predominately by electron impact and Penning ionisation respectively.

Water can be present as an impurity in the discharge gas or adsorbed onto the surface of the cell wall or cathode. The formation of the water related ion species may therefore be dependent on the region in which they are formed. If water is introduced into the active discharge region it is possible that H_2O^+ and OH^+ are formed via electron bombardment as shown in equations 2.17 and 2.18

$$H_2O + e^- \rightarrow H_2O^+ + 2e^- \qquad \textit{(equation 2.17)}$$

$$H_2O + e^- \rightarrow OH^+ + H + 2e^- \qquad \textit{(equation 2.18)}$$

However, in the FAG plasma of the FFGD electron energies are unlikely to be sufficient to induce ionisation of ground state water molecules. The ionisation potential of water (12.61 eV)[127] is also higher than the energies of the argon $^3P_2$ and $^3P_0$ metastable state species, therefore Penning ionisation can only occur through energy transfer from higher excited states of argon (equation 2.19), or to water molecules already in excited states (equation 2.20).

$$H_2O + Ar^{**} \rightarrow H_2O^+ + Ar + e^- \qquad \textit{(equation 2.19)}$$

$$H_2O^* + Ar^* \rightarrow H_2O^+ + Ar + e^- \qquad \textit{(equation 2.20)}$$

Other possible Penning processes include the formation of ArH^+ and H_3O^+ (equations 2.21 and 2.22 respectively), wherein proton transfer occurs.

$$H_2O + Ar^* \rightarrow ArH^+ + OH + e^- \qquad \textit{(equation 2.21)}^{136,137}$$

$$H_2O^* + H_2O^* \rightarrow H_3O^+ + OH + e^- \qquad \textit{(equation 2.22)}^{138}$$

However, both ions may be formed via ion molecule reactions (equations 2.23 to 2.25).

$$H_2O + Ar^+ \rightarrow ArH^+ + OH \qquad \textit{(equation 2.23)}^{136}$$

$$H_2O^+ + H_2O \rightarrow H_3O^+ + OH \qquad \textit{(equation 2.24)}^{139,140}$$

$$ArH^+ + H_2O \rightarrow Ar + H_3O^+ \qquad \textit{(equation 2.25)}^{136}$$

One other ion of interest is the argon dimer cation. Two competing processes have been proposed to account for its formation, a) the Hornbeck-Molnar reaction[131] and b) a three-body ion molecule reaction[136,138]. The Hornbeck-Molnar process (equation 2.26) is a two-body process which commonly occurs within the positive column of the GD. One or both of the argon atoms could be in metastable states, but this cannot be confirmed and would be highly dependent on the concentration of argon metastable state species within the plasma.

$$Ar^* + Ar^{0,*} \rightarrow Ar_2^+ + e^- \qquad \textit{(equation 2.26)}$$

The second process (equation 2.27) is an ion-molecule reaction with a third colliding body (Q) acting to remove the excess energy from the process.

$$Ar^* + Ar + Q \rightarrow Ar_2^+ + Q + e^- \qquad \textit{(equation 2.27)}$$

2.5.3 The Positive Column Plasma: Classical Free Ion-Electron Model

There are hundreds of papers with regard to this topic, but the fundamental principles are outlined in many textbooks such as references 1 and 22. The positive column is thought to be the closest there is to an ideal plasma. It is a partially ionised gas, containing equal numbers of ions and electrons, and is therefore essentially a neutral medium. When an electrically floating surface (such as a disconnected electrode) is brought into contact with it, there is a separation of charge due to the faster movement of electrons compared to ions. The surface therefore adopts a negative potential relative to the plasma[22]. This decelerates the electrons and accelerates the cations such that their rates of migration towards the surface are equal. The steady state potential is called the sheath potential.

When the discharge current of the GD passes through the positive column of the discharge, the electrons are thought to have a higher average energy than the kinetic energy of the ions, but for purposes of the model are considered to have a Maxwell-Boltzmann distribution[22]. In a 'cold' plasma such as a GD, the ion kinetic energies are thought to be close to that of the gas temperature, and usually assumed to be so. The electron temperature, T_e, is much higher[22]. A direct current can therefore pass through to the anode by virtue of the high energy tail of electrons which can overcome the negative sheath field, which must form according to this model.

In a steady state 'static' gas GD the ions and electrons find their way towards the anode by diffusion[6,20,22]. In a column GD, ions and electrons are lost from the plasma by radial diffusion to the walls of the discharge cell[22]. Recombination to ground state atoms is a relatively very slow process in an atomic discharge, and diffusion will be the main loss mechanism. Yet, in the axial direction the plasma density remains essentially constant[22]. To sustain this, the theory requires that re-ionisation must occur constantly along the length of the column. The ionisation (by electron impact) can only be achieved by very high energy electrons, since in argon, for example, the ionisation energy is 15.76 eV[127].

A small positive field develops along the axis which aids the drift of free electrons towards the anode. There must therefore be a small net drift of positive ions from the anode towards the Negative Glow[1]. There must therefore also be a net production of ions at the anode.

Modellers use a combination of the Poisson equation[22] (to calculate the fields due to electrostatic charges of free ions and electrons present) and the transport equations[1] (to model the movement of charge). One consequence of these is that the current flowing through the plasma to the anode must be directly proportional to the plasma density. In all models to date, these conditions are assumed, and the results are critically dependent on the electron temperature adopted. The participation of excited states is largely dismissed as being important because of their short lifetimes and relatively small concentrations (even the metastable states of Ar). However, there are a number of inconsistencies with the conventional model of the positive column plasma, as follows:

1) As fast electrons (created by acceleration through the cathode fall) pass through the NG and the PC they undergo collision, with increasing probability, the closer they get towards the anode. The electron temperature would therefore tend to decrease, unless the electrons are continuously re-energised. The only source of energisation is the positive field along the axis. In a gas such as Ar, at 1 Torr, the fields are usually $<< 1$ V cm^{-1} (see references 16 and 17, and chapter 6).
2) Ionisation of Ar requires very high energy electrons, but these have the highest probability of collision and de-energisation. Chapman[22] reckons that, to provide sufficient energy, the electrons must survive the journey from the cathode to the anode with very few collisions. This may work when the anode is immersed in the NG (and therefore relatively close to the cathode), but becomes increasingly unlikely down a column. It has been suggested that perhaps the electrons are carried by means of an electrostatic 'wave' motion of the plasma (again see reference 22).
3) In nearly all experimental studies of the dc GD, there is an upturn in voltage at the anode (see chapter 4 and references 16 and 17). This contravenes the above theory. Chapman[22] summarises two possible conditions under which this might

happen: (i) if the surface area of the electrode is << the cross sectional area of the plasma carrying the current, and (ii) when there is a very high coefficient of secondary electron emission at the anode surface.

In previous work by the group, it is shown that the upturn in voltage often occurs in our plasmas without either of the conditions (i) and (ii) above pertaining[16,17,141].

4) It will be shown in chapter 4 that the condition that the plasma is of equal density along the axial direction is not true. On the contrary, it declines exponentially as seems inherently likely.
5) It will also be shown in chapter 4 that the condition that the current flow is dependent on the plasma density is not true. It has been suggested previously that the current flows through a Rydberg gas by charge transfer[16]. The way this can explain all the experimental data is also outlined.

2.6 Rydberg Atoms

Despite the volume of work on plasma processes published, no single model has been proposed which can explain the processes which occur in the glow discharge. However, over the last decade work within this group[13-18] has led to the formulation of a Rydberg gas model which can explain the phenomena observed using the FFGD and many other systems. Secondary gases can be added to the FAG plasma, allowing the chemistry of the plasma to be studied without disturbing the active discharge region. Many of the results from these studies[13-18] cannot be explained by conventional ion-molecule or Penning ionisation processes. This section outlines the Rydberg gas theory and its application to ion formation and electrical properties of the GD.

2.6.1 What is a Rydberg Atom?[142]

Rydberg atoms are atoms in states of high principal quantum number, n, and the Rydberg electron has an energy close to or greater than the ionisation potential of the

species. According to the Bohr model, the Rydberg electron is very loosely bound to the ionic core, as the electron binding energy decreases as $1/n^2$. Rydberg atoms are also very large, as the electron orbit increases as n^2.[142,143] The geometric cross section of a Rydberg atom, assuming the Rydberg electron has a circular orbit, therefore increases as n^4. Due to their high energies and large size, the effects of collisions and the presence of fields, electric and magnetic, are exaggerated. Whilst Rydberg atoms have always played an important role in atomic spectroscopy, it is only since the 1970s that they have been studied intensely. Two factors have aided the study of Rydberg atoms: 1) development of quantum theory and 2) development of techniques which can efficiently produce Rydberg atoms. Interest increased with the invention of the tuneable dye laser, as it is now possible to excite large numbers of atoms to a single, well defined Rydberg state[144,145].

When the Rydberg electron is at outer points of its orbit it is influenced only by the charge of the ionic core. However, when the electron is in an elliptical orbit it passes closer to the core and the distribution of the positive charge becomes important[142].

The formation of Rydberg atoms (A^R) can be achieved in a number of ways, including charge exchange[146] (equation 2.28), electron impact excitation (equation 2.29), photoexcitation[147] (equation 2.30), recombination reactions (equation 2.31 to 2.33), or a combination of the processes[142].

$$A^+ + B \rightarrow A^R + B^+ \qquad \textit{(equation 2.28)}$$

$$e^- + A \rightarrow A^R + e^- \qquad \textit{(equation 2.29)}$$

$$h\upsilon + A \rightarrow A^R \qquad \textit{(equation 2.30)}$$

$$e^- + AM^+ \rightarrow A^R + M \qquad \textit{(equation 2.31)}$$

$$e^- + A^+ + M \rightarrow A^R + M \qquad \textit{(equation 2.32)}^{151}$$

$$e^- + A^+ \leftrightarrow A^{**} \rightarrow A^R + h\upsilon \qquad \textit{(equation 2.33)}^{152}$$

where M is present to remove energy from the system by dissociative or collisional quenching, A^{**} is a doubly excited, autoionising, Rydberg state and hυ is a photon.

Electron impact excitation[150,151] is simple but inefficient and non-selective. It is not possible to specify the energy transferred during the collision, and therefore excitation to a variety of excited states, or even ionisation, can occur. Charge exchange requires

production and acceleration of ions into a collision gas, leading to formation of fast excited state species. As with electron impact, it is not possible to specify the energy transferred during the collision. However, photoexcitation (optical pumping) allows specific excitation of atoms by controlling the frequency of the laser light. This technique is mainly used for excitation of alkali and alkaline earth atoms, because for most other atoms the energy required to excite to the first excited state is too high[145]. This problem can be overcome using a collisional-optical process. Collisional techniques are used to excite atoms to metastable states, and optical pumping can selectively excite these states to Rydberg states.

At high n, the energy spacings between Rydberg levels are so small that the influence of black body radiation cannot be ignored. The result of strong coupling between Rydberg atoms and the thermal radiation is rapid energy transfer by black body radiation induced dipole transitions[152-154], i.e. the system is in thermal equilibrium.

2.6.2 Effect of Electric Fields

Whilst ground states are relatively unaffected by small electric fields (ground state atoms can be polarised, but large fields are required to induce changes in principal quantum number), small electric fields can distort Rydberg atoms, changing the electron energy (the Stark effect) or even inducing ionisation[142]. Introduction of a small electric field induces polarisation of Rydberg state species. The Rydberg electron is weakly held in orbit a long way from the ionic core and therefore distortion of the electron orbit readily occurs. A positive Stark shift results in localisation of the electron on the upfield side of the atom, whilst a negative shift results in the electron being localised on the downfield side.

Stark broadening induces red (n+1) and blue (n) shifts[142]. Red states ionise at the classical ionisation limit, whereas higher fields are required to ionise blue states. For hydrogen the blue and red states of differing n levels cross. However, for non-hydrogenic species blue and red states are coupled by their slight overlap at the core and therefore a series of avoided crossings occur[142]. Non-hydrogenic states decay more rapidly by ionisation and radiative decay. Field ionisation is an efficient and selective

method of Rydberg state detection, with the energy of the Rydberg state determining the field required to induce ionisation.

2.6.3 Collisions with Neutral Atoms and Molecules[142]

Due to the large separation between the Rydberg electron and the ionic core, Rydberg atoms are quite transparent to most collision partners[142]. Collisions can involve the ionic core *and* the Rydberg electron, or just one. Collisions with ground state neutral atoms are short-range, compared to the size of a high n Rydberg atom, polarisation interactions. These collisions are elastic, as the atom has no energetically accessible states, and only translational energy can be transferred. Collisions with diatomic, non-polar molecule such as nitrogen are also short range, but the probability of interaction is increased due to the size of the molecule. Vibrational energy transfer is also possible with diatomic molecules[142].

Interactions with slightly more polar species such as CO are longer range electron-dipole and electron-quadrupole interactions. However, the most important process is still the electron-induced dipole interaction[142]. Collisions with larger polar molecules such as SF_6 occur readily, due to strong dipole-electron interactions and the large physical size of the molecule. Larger molecules also allow translational, vibrational and rotational energy transfer. However, it is not clear whether polar molecules interact only with the Rydberg electron, or with the Rydberg atom as a whole.

Collision angular momentum, l, mixing occurs rapidly during collisions (equation 2.34), leading to higher l states of the same n[155-160]:

$$Ar^R(n,l) + Q \rightarrow Ar^R(nl') + products \qquad \textit{(equation 2.34)}$$

where Q is the species with which the Rydberg atom collides and n is the principal quantum number. There appear to be no strong Δl or Δm selection rules[142]. Electron-dipole coupling interactions with polar molecules leads to $\Delta J \pm 1$ transitions. This is a resonant energy transfer process, i.e. there is no change to the translational energy. Rotational de-excitation of the molecule is favourable because 1) the dense packing

makes resonance more likely, and 2) rotational excitation requires energy transfer from the Rydberg electron, which is less likely at the outer turning point than at smaller orbital radii. Hotop and Niehaus[161] observed collisional ionisation of Rydberg atoms by electron transfer to highly polar molecules, but not to non-polar molecules. This is because only the highest rotational states can induce the ΔJ-1 transitions required to induce ionisation.

Whilst the majority of the collisions considered concern interactions with the Rydberg electron, there is evidence of collisions with the ionic core. One such process is the deflection of lithium Rydberg atoms due to collisions between gases and the solid ionic core[162].

2.6.3.1 Ionisation Processes

2.6.3.1.1 Electron Attachment

Due to the low binding energy of the Rydberg electron it is possible for electron transfer to occur during a collision. This can lead to formation of negative molecular ions (equation 2.35)[163], fragmentation (dissociative electron attachment)[164-166] (equation 2.36) or simply ionisation of the Rydberg atom if autodetachment follows (equation 2.37)[142]. For high n Rydberg atoms the attaching rate constants (attachment to molecules) are identical to free electron attachment[167,168]. However, at low n the rate constant falls below that for free electron attachment. Electron transfer from Rydberg atoms is often used where very low electron energies are required in order to prevent dissociation, such as studies of clusters[169].

$$BC + A^R \rightarrow BC^- + A^+ \qquad \textit{(equation 2.35)}$$

$$BC + A^R \rightarrow B + C^- + A^+ \qquad \textit{(equation 2.36)}$$

$$BC + A^R \rightarrow A^+ + BC^- \rightarrow BC + e^- \qquad \textit{(equation 2.37)}$$

Equation 2.38 illustrates a process called Coulomb trapping. The ion pair cannot overcome the binding (Coulomb) potential, and therefore deactivation or formation of neutral products is likely to occur. However, dissociative electron attachment provides translational energy to the fragments, and may therefore overcome Coulomb trapping.

$$BC + A^R \rightarrow BC^-.A^+ \qquad \textit{(equation 2.38)}$$

2.6.3.1.2 Associative Ionisation

Excluding transfer of kinetic energy, associative ionisation is the only way a collision with a ground state atom can ionise a Rydberg atom. Associative ionisation (equation 2.39) can only occur if the energy of the Rydberg state exceeds the minimum energy of the dimer ion[142].

$$B + A^R \rightarrow BA^+ + e^- \qquad \textit{(equation 2.39)}$$

Associative ionisation with polar molecules is less likely to occur as *l* mixing, i.e. formation of atoms of different angular momentum but the same principal quantum number, readily occurs and is preferred[142].

2.6.3.1.3 Penning Ionisation

Penning ionisation involving metastable state species was previously discussed in section 2.5. It is also possible for Penning ionisation processes involving Rydberg atoms to occur (equation 2.40)[170].

$$Rb^* + Rb^R \rightarrow Rb^+ + Rb + e^- \qquad \textit{(equation 2.40)}$$

where Rb^* is the rubidium 5p state. Penning ionisation of molecules has also been reported in collisions with Rydberg atoms[171]:

$$A^R + XY \rightarrow A^{0(*)} + XY^+ + e^- \qquad \textit{(equation 2.41)}$$

$$A^R + XY \rightarrow A^{0(*)} + X^+ + Y + e^- \qquad \textit{(equation 2.42)}$$

where ^{0}, * and ^{R} are ground, excited and Rydberg states respectively.

2.6.4 Charged Particle Collisions

The cross sections for collisions between charged particles and Rydberg atoms are by far the largest due to the long range ion-electron interaction. Δl and Δn state changing collisions (equation 2.43), ionisation (equation 2.44) and charge exchange (equation 2.45) are all possible[142].

$$A^R\, nl + B^+ \rightarrow A^R\, n'l' + B^+ \qquad \textit{(equation 2.43)}$$

$$A^R + B^+ \rightarrow A^+ + e^- + B^+ \qquad \textit{(equation 2.44)}$$

$$A^R + B^+ \rightarrow A^+ + B^R\, n'l' \qquad \textit{(equation 2.45)}$$

where nl and $n'l'$ denote the n and l states of the Rydberg atom. The cross section for collisions with electrons is also large due to their charge[142]. Ionisation and state changing (l and n) collisions are again possible. Collisions of 'slow' electrons with Rydberg atoms have been reported by Pinnaduwage et al[132-135]. The authors reported that dissociative electron attachment processes (e.g. equations 2.46 and 2.47) were responsible for anion formation in a glow discharge plasma. Associative electron attachment was not found to occur. The authors also reported that electron attachment to excited state species, particularly Rydberg states, is far more efficient than to ground state species.

$$AB^R + e^- \rightarrow A^- + e^- + B \qquad \textit{(equation 2.46)}$$

$$AB^R + e^- \rightarrow A^- + B^+ \qquad \textit{(equation 2.47)}$$

2.6.5 Resonant Rydberg-Rydberg Collisions

Transfer of internal energy, not translational energy, requires a precise match of the energy intervals in the two collision partners. Thus, internal energy transfer between Rydberg state species, in which the energy levels are very closely spaced, can occur readily[145]. Resonant electronic to vibrational, and rotational to electronic energy transfer

have both been observed.[172,173]. Collisions of combinations of s and d states of alkali metal atoms have been shown to lead to formation of p states. Two such processes are illustrated in equations 2.48[142] and 2.49[174].

$$K\,29s + K\,27d \rightarrow K\,29p + K\,28p \qquad \textit{(equation 2.48)}$$

$$Na\,26s + Na\,26s \rightarrow Na\,26p + Na\,25p \qquad \textit{(equation 2.49)}$$

This implies that the p states are more stable than the s and d states. These processes may be radiative. A radiative collision is a resonant energy transfer collision in which two atoms emit or absorb photons during a collision[175]. Due to their long collision times and large dipole moments, Rydberg atoms provide the ideal system in which to study radiative collisions in a quantitative fashion[142].

2.6.6 Rydberg Molecules

The capacity of the ionic core of Rydberg molecules to "store" energy allows molecular states with internal energies greater than their ionisation potentials to exist for up to microseconds[176]. The excess energy (up to a few eV above the ionisation potential has been reported) resides in rotational and vibrational modes[177-179]. However, when the ionic core is unstable, dissociation of the molecule, leading to formation of a fragment Rydberg state is expected to occur (equation 2.50). When the unstable core dissociates into a fragment ion and a fragment neutral, the Rydberg electron can be expected to stay bound to the fragment ion.

$$AB^{R'} \rightarrow A^{R} + B \qquad \textit{(equation 2.50)}$$

Collisional fragmentation of Rydberg molecules can occur in a similar manner to the fragmentation of ground state molecules in collisions with Rydberg atoms. Equation 2.51 illustrates how such collisions can lead to the formation of neutral radicals.

$$XY^{R} + A \rightarrow X + Y + A \qquad \textit{(equation 2.51)}^{183}$$

2.6.7 Autoionising Rydberg States

Autoionising Rydberg states are atoms in which there are at least two excited state electrons with a combined energy great enough for ionisation to occur[142]. One such species is the 'double-Rydberg' atom, in which two electrons are excited to high-n states. The basic mechanism for autoionisation is superelastic scattering of the Rydberg electron to produce a ground state ion and a more excited atom[142].

2.6.8 Ultra-Cold Rydberg Gases and Rydberg Matter

Ultracold Rydberg gases (< 1 mK)[147] can be produced by exciting cooled and trapped ground state atoms into Rydberg states[181]. Such gases are of particular interest, since the properties of Rydberg gas species are exaggerated due to their large sizes, making changes to spectroscopic measurements clearer. At such low temperatures it also becomes possible to monitor l and m mixing in high principal quantum number, n, Rydberg atoms[181]. The cold Rydberg gas is also a unique environment in which spontaneous formation of a cold plasma (ions and electrons) occurs. Spontaneous ionisation has been studied as a function of Rydberg atom density, N, and temperature (black body radiation). Due to the close proximity of the n levels in Rydberg atoms, exposure to black body radiation can induce excitation to higher excited states, or even ionisation[182]. Thus, the lifetime of Rydberg atoms[181], and the timescale for spectroscopic variations[182], is longer at lower temperatures. The critical Rydberg density at which spontaneous ionisation occurs is dependent on n[183]. Similar studies of high density, but not ultracold, plasmas[184] have also been performed.

In cold Rydberg gases the long range interaction between Rydberg atoms (electric dipole interactions[185]) cannot be ignored, as atom-atom interaction increases with n. Frozen Rydberg gases can be used to study few- or many-body collisions, since even weak interactions induce measurable effects[147,186].

Rydberg matter is of great interest in astrophysics in particular, since it has been proposed as a candidate for the "missing" dark matter[187]. The most obvious characteristic

therefore is that Rydberg matter does not emit or absorb light. Rydberg matter consists of two or three dimensional clusters of spherical Rydberg atoms which, experimentally, form at surfaces[187-189]. Since the radiative lifetimes of Rydberg states are long (10^{-6} s at n = 40, increasing as n^5)[188], and they interact only weakly with light, Rydberg matter essentially fits the requirements. However, it is also proposed that heating of Rydberg matter in the vicinity of stars could explain the unidentified infrared (UIR) bands that are observed from all parts of the universe. Badiei and Holmlid state that the most likely n level for the Rydberg matter to account for this observed radiation is $n \sim 80$[184]. Manykin et al. have calculated lifetimes for Rydberg matter of the order of several hours for some excitation levels[190].

2.7 The Rydberg Gas State of Matter

2.7.1 Introduction

This section details unpublished theoretical calculations, from first principles, performed by Dr. Mason which seemingly confirm the FFGD plasma used in this investigation to be a Rydberg gas. The results also demonstrate that the Rydberg gas can exist as a long lived, stable, state of matter.

2.7.2 Formation of Rydberg Atoms: Kinetic Model

Rydberg atoms in the FFGD plasma are believed to form via ion-electron recombination reactions. For simplicity, a Rydberg gas composed of argon atoms of a single n value will be considered here. The simplest process is direct recombination of Ar^+ and e^-, as shown in equation 2.52. However, there is no way for the excess energy of this process to be removed, and therefore the recombination process is highly unfavourable.

$$Ar^R \leftrightarrow Ar^+ + e^- \qquad \textit{(equation 2.52)}$$

Excess energy can be dispersed via dissociation of molecular ions, such as that in equation 2.53.

$$ArM^+ + e^- \leftrightarrow Ar^R_{nlm} + M \qquad \textit{(equation 2.53)}$$

The mechanism proposed for a pure Ar plasma is therefore in effect the reverse of associative ionisation (see above). The series of possible reactions which are envisaged are:

$$Ar^+ + Ar\ (k_{-1}) \leftrightarrow (k_1)\ (Ar_2^+)^* \qquad \textit{(equation 2.54)}$$

$$(Ar_2^+)^* + e^-\ (k_{-2}) \leftrightarrow (k_2)\ Ar^R_{nlm} + Ar \qquad \textit{(equation 2.55)}$$

$$Ar^R_{nlm} + Ar \rightarrow (k_3)\ Ar^+ + e^- \qquad \textit{(equation 2.56)}$$

$$(Ar_2^+)^* + M \rightarrow (k_4)\ Ar_2^+ + M^* \qquad \textit{(equation 2.57)}$$

$$Ar^R_{nlm} + Q \rightarrow (k_5)\ quenched \qquad \textit{(equation 2.58)}$$

$$Ar_2^+ + e^- \rightarrow (k_6)\ Ar_2^R{}_{vj} \qquad \textit{(equation 2.59)}$$

$$Ar_2^+ + e^- \rightarrow (k_7)\ 2Ar \qquad \textit{(equation 2.60)}$$

Here, v and j are vibrational and rotational quantum numbers, n is the principal quantum number, l is the angular momentum quantum number, m is the magnetic quantum number and k_x is the rate constant for a given reaction process (k_{-x} indicating the rate constant for the reverse process). $(Ar_2^+)^*$, formed in equation 2.54, represents the orbiting collision complex. Since the Ar concentration is effectively constant, the reaction has a pseudo first order rate constant of 2×10^{-7} s^{-1} in Ar at 1 Torr and 310 K. This value was calculated by Mason using the Average Dipole Orientation (ADO) theory[214] to measure the Langevin collision rate constant, k_L (the polarisability of argon is 1.64×10^{-30} m^3)[127] for formation of the excited state association complex, $(Ar_2^+)^*$. Since the concentration of Ar is approximately constant, $k_1 = k_L[Ar]$.[192] The symmetric charge transfer rate constant for Ar under the same conditions is 1.4×10^{-7} s^{-1}.[126] Therefore, the collision complex can undergo charge transfer and then separate, with no effect on the ion population. The complex can also be stabilised by energy transfer (equation 2.57), or undergo ion-electron recombination to form the Rydberg molecule (equation 2.59) or neutral Ar (equation

2.60). The latter process is very fast, and under classical GD plasma conditions the lifetime of Ar_2^+ would be < $3x10^{-4}$ s, and therefore it could not survive[191]. We would therefore expect to find Ar_2^R and Ar^R in the mix, and this would account for the high intensity of Ar_2^+ often seen in the ionised gas.

Equation 2.55 is, kinetically, highly favourable due to the coulombic force of attraction between charged particles. Thus, the cross section is high, even for fast electrons. The classical orbiting collision condition occurs when the attractive electrostatic potential is equal to the net kinetic energy of the system[192]:

$$e^2/(4\pi\varepsilon_0 r) = eV \qquad \textit{(equation 2.61)}$$

where V is the kinetic energy of the free electron in electron volts. The electron collision capture cross section[192] is therefore given by:

$$\sigma = \pi b^2 = 2\pi r^2 = 2\pi e^2/(4\pi\varepsilon_0)^2 \times 1/V^2 \qquad \textit{(equation 2.62)}$$

where b is the impact parameter and r is the orbiting radius. The collision capture rate constant $k_2 = \sigma v$, where v is the electron velocity, given by $v = (2eV/m)^{1/2}$, so that $k_2 = 7.73x10^{-6}/V^{3/2}$ cm^3 s^{-1} $particle^{-1}$. Therefore, even when the average electron energy is 1 eV, the collision capture rate constant is very large, and therefore this would not be the rate determining step. If equation 2.55 represented even just 0.01% of the products of the orbiting complex, the reaction lifetime to create a Rydberg gas from the ion-electron population would be < 0.5 ms.

We would therefore expect a population of Rydberg atoms, if created in a steady state to be given by equation 2.63.

$$[Ar^R]_{ss} = \frac{k_1 k_2 [Ar^+][e^-]}{k_{-1}(k_{-2}+k_3) + k_2 k_3 [e^-] + (k_{-2}+k_3)k_4[Ar] + (k_{-1}+k_2[e^-]+k_4[Ar])[Q]/[Ar]} \qquad \textit{(equation 2.63)}$$

2.7.3 Stability of the Rydberg Gas: Thermodynamic Model

The radiative lifetimes, τ (in seconds), of Rydberg atoms are dependent on the l and n states, and can be determined using equation 2.64[142]:

$$\tau = \alpha n^{4.5} \qquad \textit{(equation 2.64)}$$

where α is a constant which is dependent on the value of l. Thus, Rydberg atoms of higher n levels have longer radiative lifetimes. The p states are the most polarised and have longer lifetimes than the f and d states[142]. In collisions the main interaction is with the Rydberg electron, rather than the ion core. Since direct resonant energy exchange is not possible, the main effect is l m mixing of the electronic state[142], and therefore Rydberg atoms are relatively stable towards collisions. Whilst the lifetimes of individual Rydberg states are relatively short, l m mixing leads to formation of another Rydberg state, therefore retaining the Rydberg gas character.

At high n levels the electron is also susceptible to changes due to black body radiation[142]. Thus, for a monatomic gas in the absence of a strong electric field, assuming the reactions in equations 2.56 to 2.58 to occur much more slowly than those in equations 2.54 and 2.55, the overall system will rapidly reach thermal equilibrium with the surrounding container.

Determination of the equilibrium constant for the dissociation of Ar^R (equation 2.52), K_{ion}, under the conditions of the FFGD plasma is of the utmost importance in proving that the FAG plasma is a Rydberg gas. Determination of K_{ion} from partition functions allows us to calculate the free energy of different n states using equation 2.65[192];

$$\Delta G_n = -RT\ln K_{ion} \qquad \textit{(equation 2.65)}$$

where, ΔG_n is the free energy, R is the gas constant, and T is the temperature, for a Rydberg gas composed solely of states of in energy level n.

The ionisation equilibrium constant is given by:

$$K_{ion} = \frac{[Ar^+][e^-]}{[Ar^R]} = \frac{k_{-1}k_{-2}}{k_1 k_2} \qquad \textit{(equation 2.66)}$$

assuming that in equation 2.63 k_{-1}, k_{-2}, k_1 *and* k_2 are >> k_3 and k_4.

At high n levels the electron spends most of its time away from the ionic core. The energies of high n Rydberg states can then be approximated to those of the H atom and are given as $-Ry/n^2$, where Ry is the Rydberg constant[142]. For the process $Ar^R \rightarrow Ar^+ + e^-$, the equilibrium constant, K_{ion}, can be derived using standard equations in text books[192]:

$$k_{ion} = \frac{\frac{q^{\theta}_{m,A^+}}{N_A}\frac{q^{\theta}_{m,e^-}}{N_A}}{\frac{q^{\theta}_{m,Ar^R}}{N_A}} \exp\left(\frac{-\Delta E}{RT}\right) \qquad \textit{(equation 2.67)}$$

where q values are the molar partition functions of each species under standard pressure (p^{θ} = 1 bar) conditions, N_A is Avogadro's number, ΔE is the dissociation energy, R is the gas constant and T the temperature.

For a monatomic gas:

$$q^{\theta}_m = g\frac{V^{\theta}_m}{\lambda^3} \qquad \textit{(equation 2.68)}$$

where g is the degeneracy of the electronic state of the atom, λ is the thermal wavelength of the atom[192]:

$$\lambda = (h/2\pi mkT)^{1/2} \qquad \textit{(equation 2.69)}$$

where h is Planck's constant, m is the mass of the atom, and k Boltzmann's constant, and V^{θ}_m is the molar volume of an ideal gas. Therefore:

$$K_{ion} = \frac{g_{Ar+}g_{e-}}{g_{Ar^R}} \frac{V^{\theta}_{m,Ar+}V^{\theta}_{m,e-}}{V^{\theta}_{m,Ar^R}N_A} \left(\frac{\lambda_{Ar^R}}{\lambda_{Ar+}\lambda_{e-}} \right)^3 \exp\left(\frac{-Ry}{n^2 RT} \right) \quad (equation\ 2.70)$$

where K_{ion} refers to the ionisation equilibrium constant of a Rydberg gas composed solely of Rydberg atoms with quantum number n. This is chosen to make it easy to deal with. It is an approximation, but it illustrates the principle well. The degeneracy, g, of ground state Ar^+ is considered to be 2, and an electron, 1. The degeneracy of the Rydberg atom, g_{ArR} is n^2.[142]

At low densities, the free ions and electrons behave as an ideal gas, and therefore, for both gases[192]:

$$V^{\theta}_m = RT / p^{\theta} \quad (equation\ 2.71)$$

However, the Rydberg gas does not behave as an ideal gas because of the large volume of the atoms (increases as n^6)[142]. It is assumed that atoms cannot exist within the volume envelope of another, and therefore at high n the gas behaves imperfectly under the same conditions that a ground state gas behaves ideally. At high n, the radius of a Rydberg atom = $a_0 \times n^2$, where a_0 is the Bohr radius (5.292×10^{-11} m). Therefore, the volume occupied by N_n atoms is $\sim N_n(2a_0n^2)^3$, and the net volume available to the gas is equal to $(V\text{-}N_n 8a_0^3 n^6)$. Incorporation into the non-ideal gas equation gives:

$$P(V - N_n 8a_0^3 n^6) = RT \quad (equation\ 2.72)$$

therefore giving an n-dependent molar volume of:

$$V^{\theta}_{m,n} = \frac{RT}{P} + N_A 8a_0^3 n^6 \quad (equation\ 2.73)$$

where N_A is Avogadro's number. Thus, the volume of the Rydberg atom is significantly higher than that of a normal atom, and the molar partition function is increased accordingly. However, as the volume occupied by the Rydberg atoms approaches the

volume of the space within which they are contained, the number of accessible energy states becomes restricted. When the atoms fill the available space they become 'fixed' in space as a crystal (Rydberg matter[33-35]), at which point the translational energy partition function becomes equal to 1. Theoretically this point is reached when:

$$8N_n a_0^3 n^6 = 1\ m^3$$

and

$$n^6 = (8N_n a_0^3)^{-1}$$

Hence, the limit of n depends on N_n. This 'spontaneous ionisation' can be thought of as 'Rydberg gas pressure ionisation'.

Assuming this normally secondary effect to be proportional to the net volume available, as a first approximation we can write:

$$V' = V^{\theta}_{m,n}\left(1 - aV^{\theta}_{m,n}\right) \qquad (equation\ 2.74)$$

where V' is the molar volume corrected for the restricted access, and a is the constant of proportionality. When $n^6 = (8N_n a_0^3)^{-1}$, $q_n = 1$. Since, in this model, $q_n = \frac{V - aV^2}{\lambda^3}$, then $a = 1/V - \lambda^3/V^2$, when $q = 1$.

Therefore, through substitution, and ignoring terms in the resulting equation which are very small, we determine:

$$\alpha = \frac{N_n}{N_A \times 1m^3} \qquad (equation\ 2.75)$$

In equation 2.70, the thermal wavelengths of the Ar^+ and Ar^R cancel because they both have the same mass, hence we can write:

$$K_n = \frac{1}{n^2} \frac{\left(R/P^\theta\right)^2 T^2}{V^\theta_{m,n}} \frac{2(2\pi m_e k)^{3/2} T^{3/2}}{h^3} \exp\left(\frac{-Ry/R}{n^2 T}\right) \quad (equation\ 2.76)$$

where the thermal wavelength of the electron has been replaced by $h/(2\pi m_e kT)^{1/2}$, where m_e is the mass of the electron. Inserting known values:

$$K_n = 5.406 \times 10^{-11} \times T^{7/2} \frac{\exp\left(-157889/n^2 T\right)}{n^2\left(V' - aV'^2\right)} \quad (equation\ 2.77)$$

where $V' = 8.205x10^{-5}\ T + 7.14x10^{-7} n^6\ m^3$ and $a = N_n(m^{-3})/6.022x10^{23}$. Hence, the standard free energy of each Rydberg state, relative to the ionisation level, can be calculated as:

$$\Delta G^\theta_{m,n} = -RT \ln(1/K_n)/1000 \quad kJ\ mol^{-1} \quad (equation\ 2.78)$$

The free energy is dependent on N_n, which will be dependent on the overall plasma density N (ions, electrons and Rydberg atoms of varying n).

Examples of standard free energy curves, calculated by Mason using equations 2.77 and 2.78, at a temperature of 313 K and pressure of 1 Torr are shown for a series of plasma densities in figure 2.5a. It is clear that, despite the close proximity of high n states to the ionisation level, there is a deep free energy well. The standard free energy is a hypothetical parameter extrapolated to pressures of 1 bar, whereas, the pressures of glow discharge plasmas are often much lower, but have the same plasma densities. At a partial pressure of 1 bar the volume of high n Rydberg atoms would exceed the space available to them, and could not therefore exist at this pressure.

The degree of ionisation of the Rydberg gas at low partial pressures can be calculated from[192]:

$$K_n = \frac{x^2}{(1-x)^2} p_n \qquad \textit{(equation 2.79)}$$

where x is the degree of ionisation and p_n is the ratio of the partial pressure of the reaction mixture to 1 bar. In terms of particle densities:

$$p_n = {}^{N_n}\!/_{N^\theta} = N' \qquad \textit{(equation 2.80)}$$

where N_n is the plasma density, assuming the plasma to be free ions and electrons in equilibrium with Rydberg atoms in a single n state, and N^θ is the standard particle density of an ideal gas at 1 bar. Thus we deduce that:

$$x = \left(\frac{1}{1 + N'/K_n} \right)^{1/2} \qquad \textit{(equation 2.81)}$$

Also shown in figure 2.5a is the dependence of the degree of ionisation of the Rydberg gas on n. Similarly, figure 2.5b shows the degree of ionisation at constant pressure and temperature, but different Rydberg gas densities. Within the limits of the plasma densities displayed, the stability of high n Rydberg states is greater at lower densities. This is because at lower densities the Rydberg atoms have a greater volume into which they can expand. Figure 2.6 shows the effect of changing the temperature on the degree of ionisation, for a fixed Rydberg gas density ($N_n = 10^{11}$ cm^{-3}). Since Rydberg atoms are susceptible to n transitions due to black body radiation[142], the Rydberg gas is destabilised by increases in temperature. In this simplified model, each Rydberg n state has been treated as an isolated gas.

This idealistic model implies that, in equilibrium, all plasmas are Rydberg gases under all conditions. This is very unrealistic, and interactions with the environment must be included. The three main interactions are, a) Rydberg atoms interacting with themselves (Rydberg atom pressure ionisation), b) interactions with charged particles and

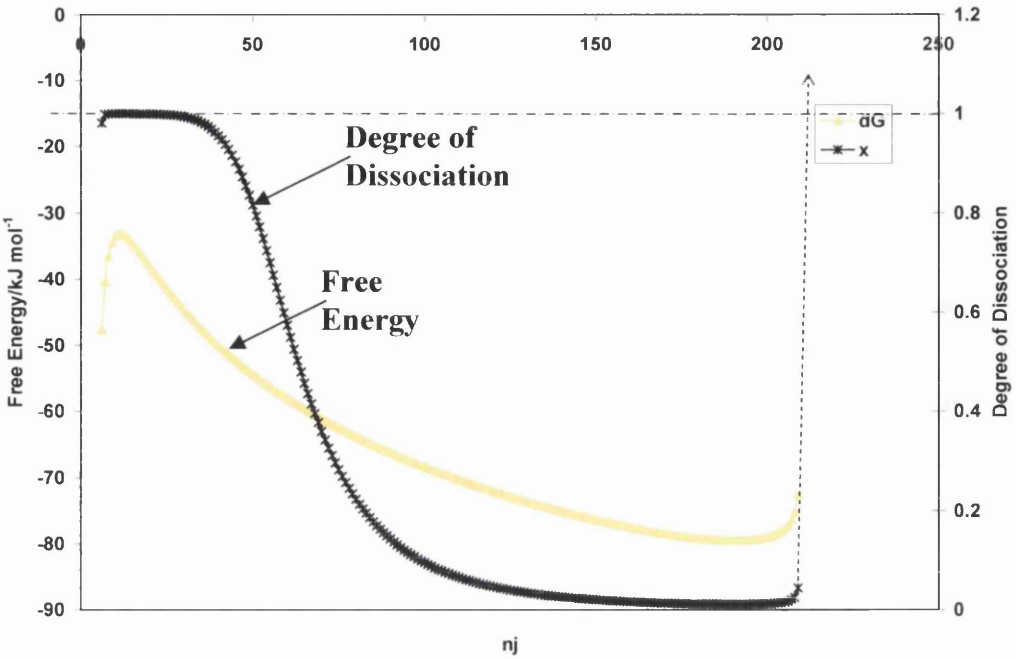

Figure 2.5a: Standard free energy variation with principal quantum number, n, when the plasma density, N = 10^{10} cm^{-3} (P = 1 Torr, T = 313 K)

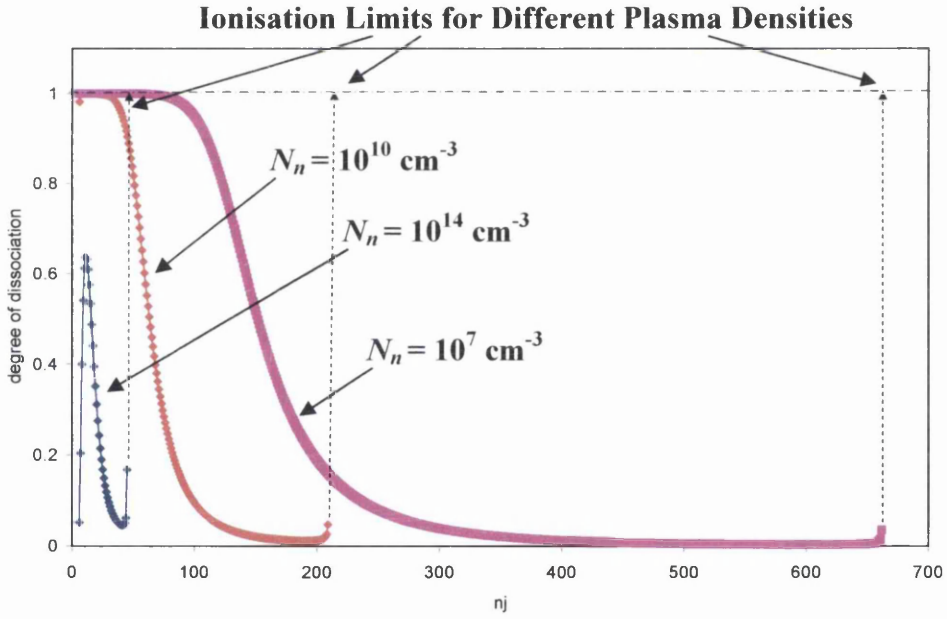

Figure 2.5b: Degree of Rydberg gas ionisation, x, dependence on *n* and the plasma density N_n (P = 1 Torr, T = 313 K)

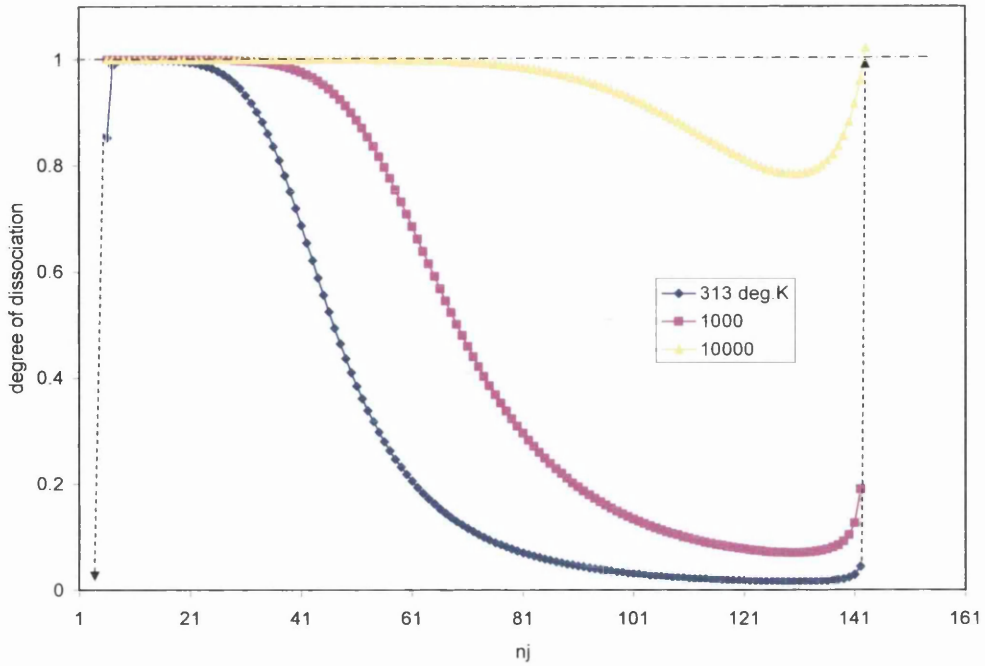

Figure 2.6: Degree of Rydberg gas ionisation, x, dependence on *n* and temperature, T (P = 1 Torr, $N_n = 10^{11}$ cm^{-3})

c) interactions with ground state atoms of the discharge gas. The interaction of Rydberg atoms with themselves, a), has already been discussed.

The influence of b) and c) are more difficult to quantify. However, Dr. Mason has determined theoretical limits based on the available literature, and plans to publish these results in a series of forthcoming papers. Ionisation of Rydberg atoms in collisions with ground state neutral atoms does not readily occur, and therefore this effect is expected to be limited to the highest n Rydberg atoms. At this point the population of neutral gas atoms occupying the space between the Rydberg electron and the ion core may be sufficient to negate the attractive forces between the two, allowing release of the electron from its orbit. It is also worth noting that ionisation in collisions with dipolar molecules occurs far more readily. Mortimer[14] and Dash[17] have reported evidence of this on addition of small quantities of secondary gases such as CO and NO.

Figure 2.5b shows how a high density Rydberg gas is limited to relatively low n values, since the volume into which the atoms can expand is limited. At lower N_n, the distribution shifts to higher n values, i.e. the atoms expand to fill the available space. This will occur until the size of the atom reaches the 'atom pressure ionisation' limit, at which point the Rydberg gas breaks down into ions and electrons. Experimentally, at 1 Torr and 313 K this breakdown occurs when $N_n \approx 10^7$ cm^{-3}.[193] This can occur, for example, as the Rydberg gas expands into the low pressure region outside the GD cell. However, it may need help (field ionisation), because lifetimes of these states are so long[142].

Collisions at surfaces can lead to two major processes, both of which lead to ionisation within the plasma; i) quenching of the atoms, therefore lowering the Rydberg atom density close to the surface, which can lead to 'pressure ionisation', and ii) electron release to the surface, resulting in the characteristic negative potential drop to the discharge cell walls (see chapter 4). This sheath field can also aid ionisation or Rydberg atoms.

In summary, the theoretical calculations performed by Mason show that under a wide range of pressures and plasma densities, including those of the FFGD source, the GD plasma could exist as a very stable Rydberg gas. The estimated ratio of the Rydberg atom concentration in equilibrium with ions and electrons is << 1%.

2.8 Electrical Studies of Glow Discharge Plasmas

Electrical probe studies are a cheap and simple way of directly monitoring local changes to GD properties. Other diagnostic techniques such as spectroscopy give information averaged over a large volume of plasma[194]. GD plasmas are conventionally viewed as a partially ionised gas consisting of ions (positive and negative), electrons and neutral species[22]. Therefore, any change made to the plasma is likely to change the electrical properties e.g. potential gradients and conductivity. Classically, the magnitude of the current flowing through a plasma is monitored on variation of a potential between two electrodes (probes) immersed in the plasma. In early studies, one probe was a very small metallic electrode electrically isolated from the walls of the cell and the second "reference" electrode was commonly a metallic component of the discharge cell, sometimes the anode or cathode[9,10,194]. As only one probe is immersed in the plasma this is called the single probe method (figure 2.7a). Later, a double probe method (i.e. two small metallic probes, electrically isolated from each other and the walls of the cell, immersed in the plasma) was developed by Johnson and Malter[12] (figure 2.7b). A double probe method has been used previously within this group[16,17,141]. Both techniques are discussed below.

2.8.1 Langmuir (Single) Probe Measurements

The single probe is commonly called a Langmuir probe after its designer Irving Langmuir[9,10,195], who in the 1920s made electrical probe studies a powerful plasma diagnostic tool. Langmuir probes are generally cylindrical or spherical, and the geometry of the probe influences the results observed[3]. The technique used by Langmuir and Mott-Smith induces a current through the plasma on application of a potential difference between the probe and the reference electrode. By plotting the induced current against the applied voltage a characteristic s-shaped curve is generated (figure 2.8a). Langmuir found that from this curve it was possible to determine the magnitude of several plasma parameters including the charge carrier concentration, the plasma potential at the probe

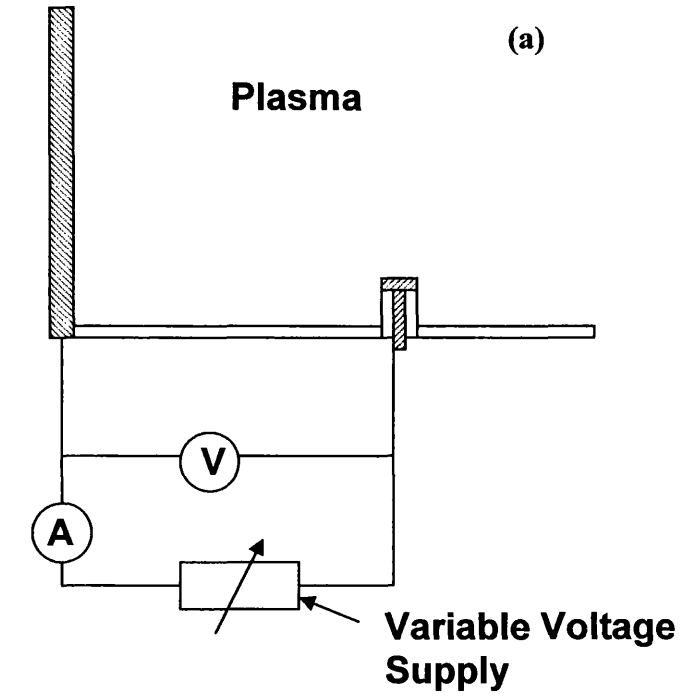

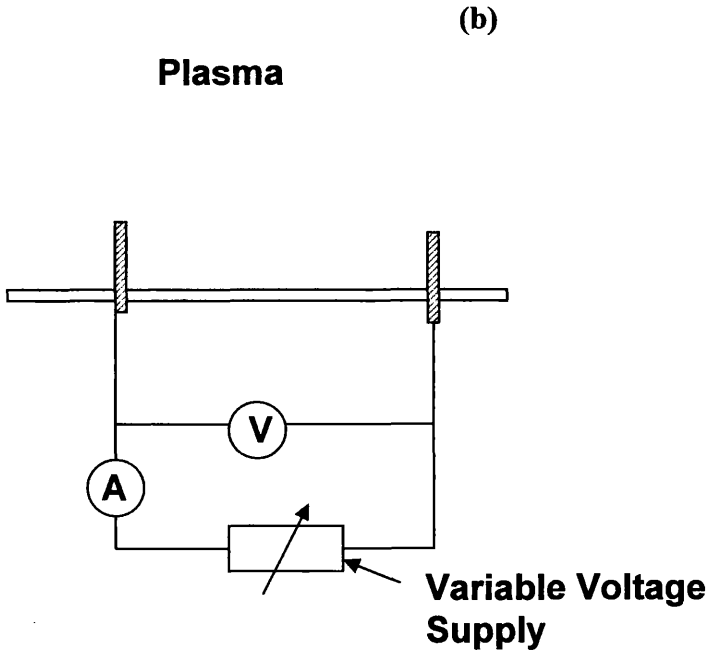

Figure 2.7: Schematics for (a) single and (b) double probe circuitry ((a) based on diagram from reference 2)

position and the electron temperature, T_e[194]. The probe must be very small or it may draw sufficient current to disturb the discharge conditions it is designed to measure[12].

The voltage current (I-V) curves can be divided into 3 regions[7]:

1) When the probe is biased positively with respect to the local plasma potential the flux of all the negative particles to the probe is collected and electron current saturation occurs. This is called the electron saturation region.
2) When the applied potential is lower than the local plasma potential the probe acts as an energy selector, collecting only those electrons which have energies large enough to overcome the retarding potential. This is the electron retardation region.
3) If the applied potential is further negatively biased none of the plasma electrons have enough energy to overcome the retarding potential and all the current measured is due to the positive ions. This is the ion saturation region.

Although collection of I-V data is relatively simple, data analysis is far more complicated, and no single theory is valid for all plasmas. Also, for this technique to apply, several assumptions are made, including:

a) The plasma is infinite, homogeneous and quasineutral in the absence of the probe.
b) Electrons and ions have Maxwellian velocity distributions where T_e is significantly higher than the ion temperature (T_+). The mean free paths of electrons and ions are large compared to all other relevant characteristic lengths.
c) Each charged particle hitting the probe is absorbed and does not react with the probe.
d) The region in front of the probe surface where the plasma parameters deviate from their values in the undisturbed plasma are confined to a sheath with a well defined boundary. Outside of this sheath the potential is assumed to be constant.

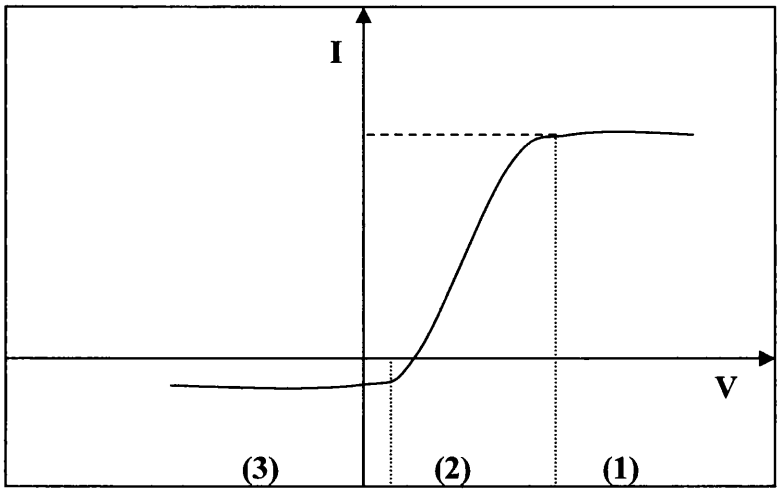

Figure 2.8a: V-I curve generated using the single probe technique (based on figure from reference 2) indicating the (1) electron saturation, (2) electron retardation and (3) ion saturation regions

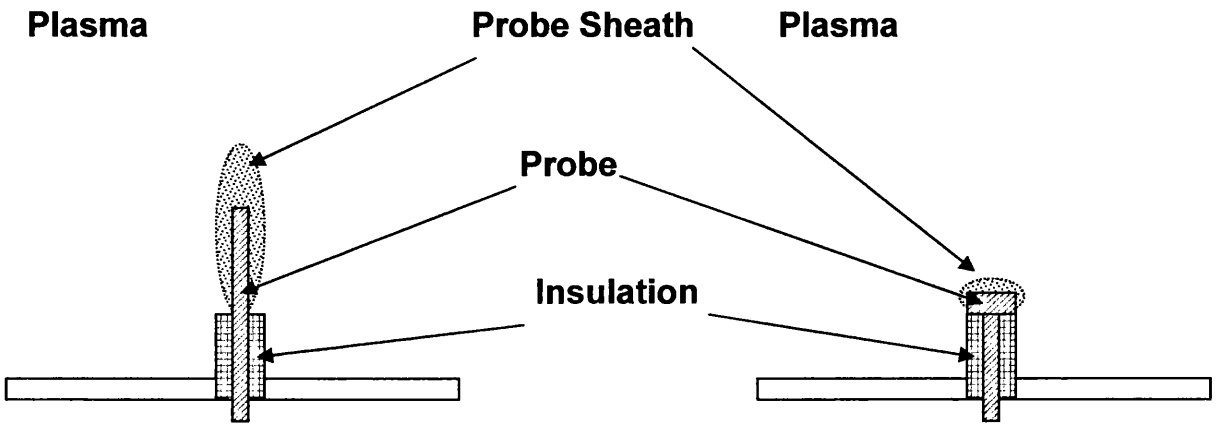

Figure 2.8b: Effective probe surface area increase through formation of a narrow sheath

e) The sheath thickness is small compared with the lateral dimensions of the plane probe. Hence edge effects can be neglected.

It is common that one or more of these assumptions does not apply to a particular plasma system. For instance, the formation of a sheath around the probe can significantly increase the effective surface area (figure 2.8b). This sheath size would also increase with build up of deposited cathode material and therefore assumption e) cannot apply[16,17]. Dowden et al. have also reported conditions where the assumption that the plasma is quasi-neutral (assumption a) does not apply[196]. A GD plasma is not homogeneous, hence the characteristic "glow" and "dark" regions[22] (see section 2.2).

If the electron energy distribution is not Maxwellian, as is often the case[1,2,197], then the electron temperature measured is likely to be that of the "hot" component and therefore, unless the density of "hot" electrons is small, the electron temperature can be significantly overestimated[198,199] (>2% hot electrons can dominate the value of T_e)[200]. Assumption c) is not valid in all higher pressure systems due to the reduction of the ion mean free path[201]. Also, the size of the probe determines the sheath diameter and therefore the sheath diameter may increase beyond the mean free paths of the electrons and ions[194]. Several authors have reported the reaction of plasmas with the probe surface[202-210]. The validity of each of the assumptions is specific to the system studied. Bombardment of the probe by ions or electrons can also lead to secondary electron emission, which would also influence the measured currents[22].

2.8.2 Double Probe Technique

The symmetrical double probe technique was designed by Johnson and Malter[12,211] to allow probe studies where the single probe technique cannot be used. For instance, when a reference electrode is absent or where the space potential is not defined e.g. afterglow and electrodeless atmospheric plasmas. The double probe method uses two small probes "floating" with respect to the discharge system. The double probe technique was based on the system used by Reifman and Dow[11] to study the upper atmosphere (i.e. an

electrodeless plasma). The technique developed by Reifman and Dow[11] used an asymmetrical probe setup.

The probes used are generally very small to minimise disturbance to the plasma[22,194] and to ensure that the probe current does not constitute a significant drain on the plasma[22]. However, the current drawn using the double probe technique can be hundreds of times lower than that for the single probe technique[12]. As with the single probe technique it is common to use cylindrical or spherical probes to minimise disturbance to the plasma. However, the disturbance caused by probes is often localised and therefore has no effect on the quantities being measured[212]. This has been illustrated in recent studies[202] where flat, planar probes have allowed more precise measurement of the ion saturation current and electron temperature.

The applied potential does not influence the plasma potential, only the sheath potential close to the probe surface. Figure 2.9 illustrates how increasing the negative bias on one probe increases the sheath voltage without changing the potential of the bulk plasma.

Despite the problems associated, probe measurements are still a very useful tool in plasma diagnostic studies. For many years the technique was limited to low pressure collisionless plasmas but more recent studies have allowed the technique to be applied to characterisation of[201,213]:

I. non-weakly ionised plasmas;
II. flowing plasmas;
III. higher pressure, collisional, plasmas;
IV. systems where probe-plasma cooling occurs;
V. collection of current; and
VI. systems with strong magnetic fields

2.8.3 Zero-Current Potentiometry

Zero-current potentiometry has been used previously within this group in order to determine the relative potentials of different points within the flowing afterglow plasma

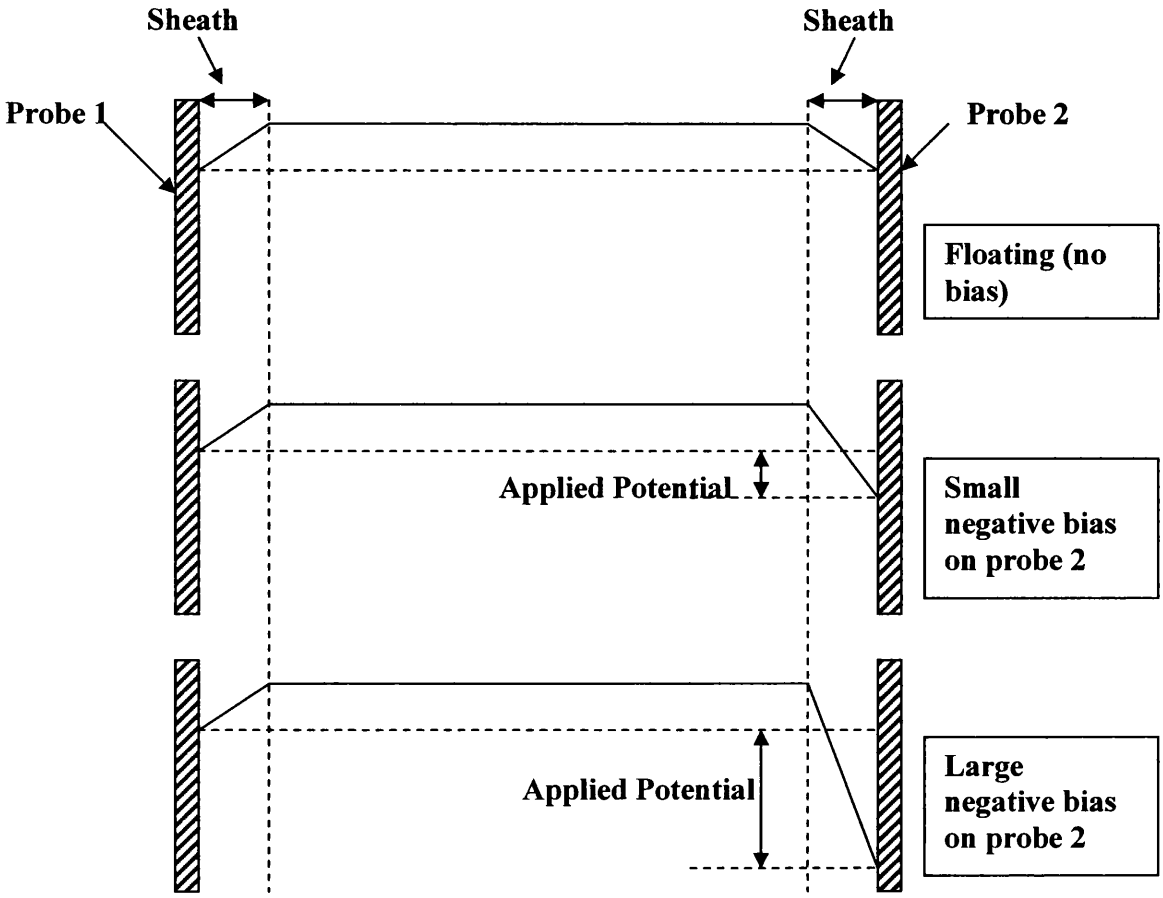

Figure 2.9: Variation of probe sheath potential with applied probe bias (from reference 12)

using the double probe technique[16,17]. To allow this, two lengths of stainless steel tubing (1/16" diameter), insulated from the walls of the discharge cell, protrude into the flowing afterglow (FAG) plasma. The diameter of the probes was chosen to allow one probe to act as an inlet for secondary gas addition and was therefore limited by the available material. The relative potentials of the probes are dependent on their position relative to the active discharge, and therefore a current flows between the two probes. Application of a potential to prevent current flow between the two points determines the zero-current potential, i.e. the potential difference between the two points within the plasma. It is also possible to measure the potential of the ion exit cone and the walls of the discharge cell using the setup illustrated in figure 2.10. The design allows potentiometric studies to be run in situ with mass spectrometric analysis, and therefore the observed changes to the mass spectra have been compared directly with the fields within the FAG plasma. The accuracy of the results obtained is reliant on the sheath potentials being either equal or small compared to other effects, for each of the probes[16]. The experimental procedure is discussed in chapter 4.

2.8.4 Calculating Electron Temperatures

The electron temperature, T_e, is proportional to the mean kinetic energy of free electrons in a GD plasma, assuming the electrons to have Maxwell-Boltzmann energy distribution, by equation 2.82[1,22].

$$\tfrac{1}{2}mu^2 = 3/2kT_e = eV \qquad \textit{(equation 2.82)}$$

where m is the mass of an electron, u is the velocity of the electron and k is the Boltzmann constant. T_e can be calculated from I-V plots such as that in figure 2.11 using equation 2.83[212].

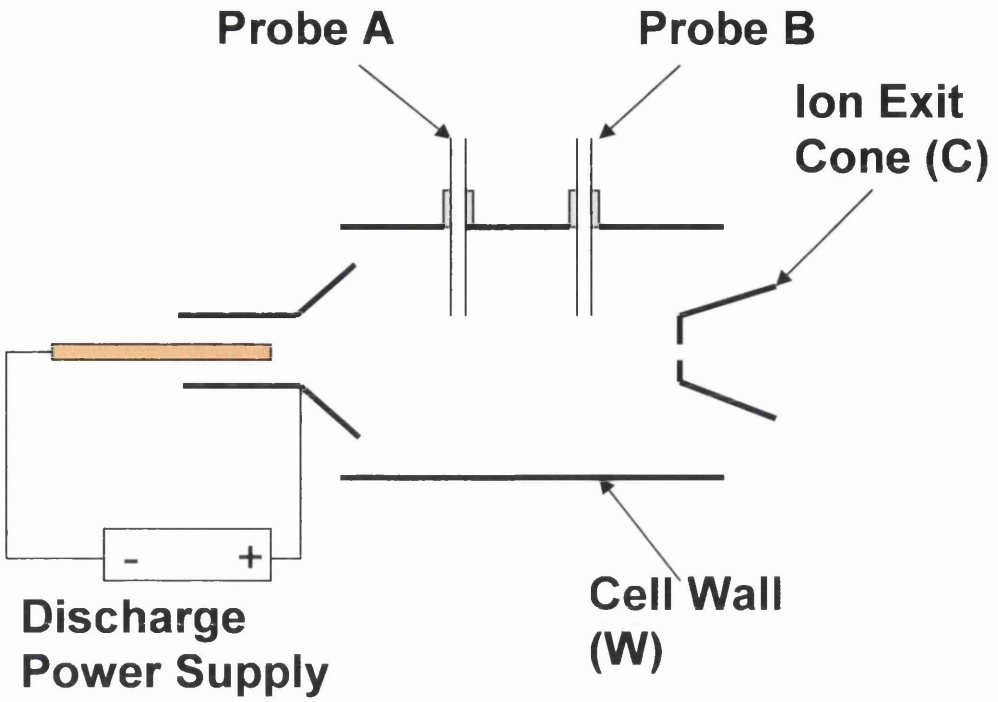

Figure 2.10: Arrangement of probes relative to the discharge and ion exit (not to scale)

$$\frac{dI}{dV} = \frac{\left(\frac{e}{kT_e}\right) i_{1+} . i_{2+}}{i_{1+} + i_{2+}} \qquad \textit{(equation 2.83)}$$

which can be rearranged to:

$$T_e = \frac{\left(\frac{dI}{dV}\right) i_{1+} . i_{2+} . e}{k(i_{1+} + i_{2+})} \qquad \textit{(equation 2.84)}$$

where dI/dV is the gradient of the steepest region of the curve, k is the Boltzmann constant, e is the charge of an electron, and i_{1+} and i_{2+} are illustrated in figure 2.11.

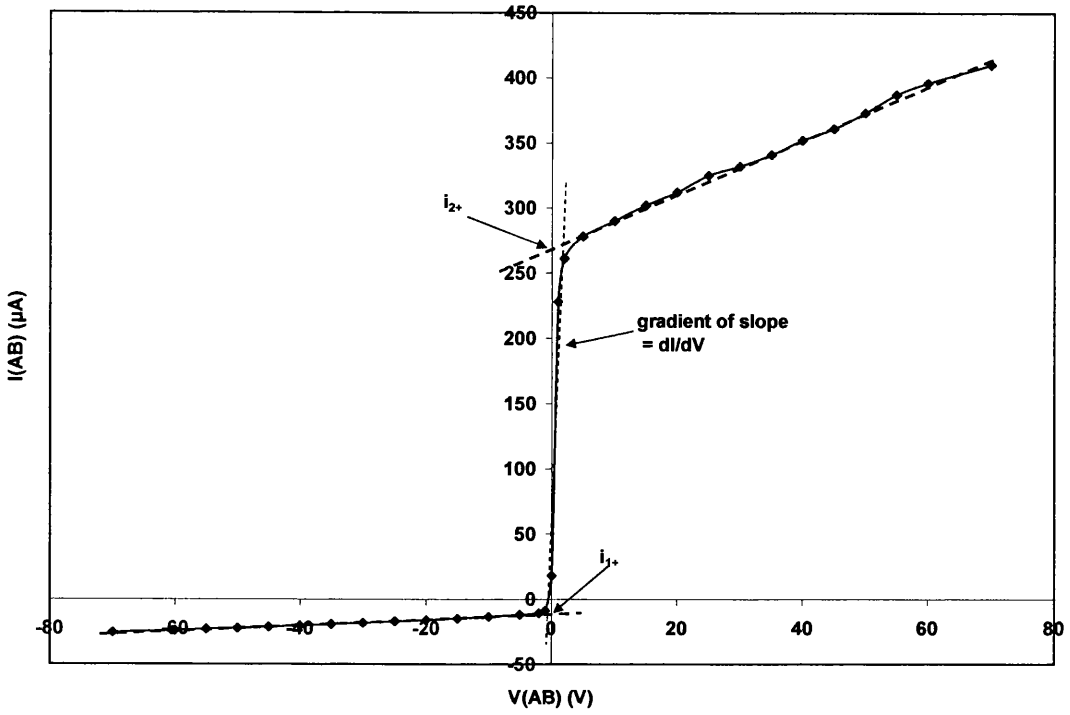

Figure 2.11: Typical I-V profile marked with parameters required for electron temperature calculation

(V_d = 450 V, P = 2 Torr, τ = 3.7 ms, I_d ~ 6.5 mA)

2.9 References

[1] F. Llewellyn-Jones, *The Glow Discharge and an Introduction to Plasma Physics*, Meuthen & Co. Ltd, London, 1966

[2] W. Hang, X. Yan, D. M. Wayne, J. A. Olivares, W. W. Harrison and V. Majidi, *Anal. Chem.*, **71**, 3231, 1999

[3] J. W. Coburn and E. Kay, *Phys. Lett.*, **19**, 350, 1971

[4] W. W. Harrison and C. W. Magee, *Anal. Chem.*, **46**, 1236, 1974

[5] J. J. Thomson, *Rays of Positive Electricity and Their Application to Chemical Analysis*, Longmans Green, London, 1913

[6] A. Bogaerts and R. Gijbels, *Spectrochim. Acta B*, **53**, 1, 1998

[7] A. Bogaerts, A. Quentmeier, N. Jakubowski and R. Gijbels, *Spectrochim. Acta B*, **50**, 997, 1995

[8] D. M. Mehs and T. M. Niemczyk, *Appl. Spectrosc.*, **35**, 66, 1981

[9] I. Langmuir and H. M. Mott-Smith, *Phys. Rev.*, **28**, 727, 1926

[10] I. Langmuir and H. M. Mott-Smith, *Gen. Elec. Rev.*, **26**, 731, 1923

[11] A. Reifman and W. G. Dow, *Phys. Rev.*, **76**, 987, 1949

[12] E. O. Johnson and L. Malter, *Phys. Rev.*, **80**, 58, 1950

[13] P. D. Miller, PhD Thesis, University of Wales Swansea, 1996

[14] I. P. Mortimer, Ph.D Thesis, University of Wales Swansea, 2000

[15] D. R. Williams, Ph.D Thesis, University of Wales Swansea, 2001

[16] D. J. Mitchell, Ph.D Thesis, University of Wales Swansea, 2002

[17] N. A. Dash, Ph.D Thesis, University of Wales Swansea, 2004

[18] K. Newman, Ph.D Thesis, University of Wales Swansea, 2005

[19] W. W. Harrison, C. M. Barshick, J. A. Lingler, P. H. Ratliff and Y. Mei, *Anal. Chem.*, **62**, 943A, 1990

[20] F. L. King and W. W. Harrison, *Mass Spec. Rev.*, **9**, 285, 1990

[21] A. M. Ghorbanzadeh, S. Norouzi and T. Mohammadi, *J. Phys. D.*, **38**, 3804, 2005

[22] B. Chapman, *Glow Discharge Processes*, John Wiley & Sons Ltd., 1980

[23] M. H. Elghazaly and S. Solyman, *J. Quantitative Spectroscopy & Radiative Transfer*, **103**, 260, 2006

[24] E. Nasser, *Fundamentals of Gaseous Ionisation and Plasma Electronics*, Wiley Interscience, New York and London, 1971

[25] J. D. Cobine, *Gaseous Conductors*, Dover, New York, 1958

[26] A. von Engel, *Ionised Gases*, Oxford Univ. Press, 1965

[27] S. C. Brown, in *Gaseous Electronics*, ed. J. W. McGowan and P. K. John, North-Holland, Amsterdam, 1974

[28] E. Brown, *Introduction to Electrical Discharges in Gases*, John Wiley & Sons Ltd., 1966

[29] R. S. Mason, D. M. P. Milton, M. Pichilingi, P. D. J. Anderson and M. T. Fernandez, *Rapid Commun. Mass Spectrom.*, **8**, 187, 1994

[30] G. Francis, *The Glow Discharge at Low Pressure*, in: Handbuch der Physik, vol. 22, ed. S. Flügge, Springer, Berlin, 1956

[31] J. W. Coburn, *Rev. Sci. Instrum.*, **41**, 1219, 1970

[32] W. Grimm, *Spectrochim. Acta B*, **23**, 443, 1968

[33] N. Jakubowski, D. Stuewer, G. Tolg, *Int. J. Mass Spectrom. Ion Proc.*, **71**, 183, 1986

[34] N. Jakubowski, D. Stuewer, W. Vieth, *Anal. Chem.*, **59**, 1825, 1987

[35] F. Paschen, *Ann. Phys.*, **50**, 901, 1916

[36] P. J. Slevin and W. W. Harrison, *Spectrosc. Rev.*, **10**, 201, 1976

[37] W. W. Harrison, C. Yang and E. Oxley, in *Glow Discharge Plasmas in Analytical Spectroscopy*, ed. R. K. Marcus and J. A. C. Broekaert, John Wiley & Sons, 2003

[38] B. L. Bentz, C. G. Bruhn and W. W. Harrison, *J. Mass Spectrom. Ion Phys.*, **28**, 409, 1978

[39] R. K. Marcus and W. W. Harrison, *Spectrochim. Acta B*, **40**, 933, 1985

[40] R. K. Marcus and W. W. Harrison, *Anal. Chem.*, **58**, 797, 1986

[41] R. K. Marcus and W. W. Harrison, *Anal. Chem.*, **59**, 2369, 1987

[42] R. K. Marcus and W. W. Harrison, *Anal. Chem.*, **58**, 972, 1986

[43] D. S. Gough, *Anal. Chem.*, **48**, 1926, 1976

[44] A. E. Bernhard, *Spectroscopy*, **2**, 24, 1987

[45] H. J. Kim, E. H. Piepmeier, G. L. Beck, G. G. Brumbaugh and O. T. Farmer III, *Anal. Chem.*, **62**, 639, 1990

[46] H. J. Kim, E. H. Piepmeier, G. L. Beck, G. G. Brumbaugh and O. T. Farmer III, *Anal. Chem.*, **62**, 1368, 1990

[47] P. D. Miller, D. Thomas, R. S. Mason and M. Liezers, *Recent Advances in Plasma Mass Spectrometry*, ed.G. Holland, Proc. 4th Conf. Plasma Source Mass Spectrom., 91, 1995

[48] Automated GD-MS Project financed by the EU under the Auspices of the 5th Framework Program for Competitive and Sustainable Growth (contract number G6RD-CT 2000-00170), R.S. Mason's group at University of Wales Swansea, V. Hoffmann's group at Institute of Solid State and Material Research, Dresden, Germany, N. Jakubowski's group at Institute for Spectrochemistry and Applied Spectroscopy, Dortmund, Germany and Thermo Elemental (Winsford, UK and Bremen, Germany)

[49] G. S. Anderson, W. N. Mayer and G. K. Wehner, *J. Appl. Phys.*, **33**, 2991, 1962

[50] J. Pispnero, J. M. Costa, R. Pereiro, N. Bordel and A. Sanz- Medel, *Anal. Bioanal. Chem.*, **379**, 17, 2004

[51] D. C. Duckworth and R. K. Marcus, *Anal. Chem.*, **61**, 1879, 1989

[52] R. K. Marcus, P. R. Cable, D. C. Duckworth, M. V. Buchanan, J. M. Pochkowski and R. R. Weller, *Appl. Spectrosc.*, **46**, 1327, 1992

[53] S. A. McLuckey, G. L. Glish, D. C. Duckworth and R. K. Marcus, *Anal. Chem.*, **64**, 1606, 1992

[54] D. C. Duckworth, D. L. Donohue, D. J. Smith, T. A. Lewis and R. K. Marcus, *Anal. Chem.*, **65**, 2478, 1993

[55] D. P. Meyers, M. J. Heintz, P. P. Mahoney, G. Li and G. M. Hieftje, *Appl. Spectrosc.*, **48**, 1337, 1994

[56] T. R. Harville and R. K. Marcus, *Anal. Chem.*, **65**, 3636, 1993

[57] V. Hoffman, H. J. Uhlemann, F. Präßler, K. Wetzig and D. Birus, *Fresenius' J. Anal. Chem.*, **355**, 826, 1996

[58] J. A. Klingler, P. J. Savickas and W. W. Harrison, *J. Am. Soc. Mass Spectrom.*, **1**, 138, 1990

[59] C. L. Lewis, M. A. Moser, D. E. Dale Jr., W. Hang, C. Hassell, F. King and V. Majidi, *Anal. Chem.*, **75**, 1983, 2003

[60] D. Fliegel, R. Waddell, V. Majidi, D. Günther and C. L. Lewis, *Anal. Chem.*, **77**, 1847, 2005

[61] J. A. Strauss, N. P. Ferreira and H. G. C. Human, *Spectrochim. Acta B*, **37**, 947, 1982

[62] V. Majidi, M. A. Moser, C. L. Lewis and F. L. King, *JAAS*, **15**, 19, 2000

[63] J. J. Thomson, *Rays of Positive Electricity and Their Application to Chemical Analysis*, Longmans Green, London, 1913

[64] *Chemical Analysis Vol. 95: Inorganic Mass Spectrometry*, Ed. F. Adams, R. Gijbels and R. Van Grieken, John Wiley & Sons, New York, 1988

[65] E. de Hoffmann and V. Stroobant, *Mass Spectrometry: Principles and Applications, 2nd Edition*, John Wiley & Sons, New York, 2002

[66] W. Paul and H. S. Steinwedel. *Z. Naturforsch.*, **8a**, 448, 1953

[67] *Hiden 301 EQP/EQS quadrupole mass spectrometer manual*, Hiden Analytical Ltd., Warrington, UK, 1993

[68] K. Wittmaack, *Int. J. Mass. Spec. Ion Proc.*, **143**, 19, 1995

[69] C. L. Lewis, M. A. Moser, W. Hang, D. E. Dale, D. C. Hassell and V. Majidi, *JAAS*, **18**, 629, 2003

[70] R. C. Hutton and A. Raith, *JAAS*, **7**, 623, 1992

[71] E. G. Johnson and A. O. Nier, *Phys. Rev.*, **91**, 12, 1953

[72] W. Wien, *Verh. Phys. Ges.*, **17**, 1898

[73] N. E. Sanderson, P. Charalambous, D. J. Hall and R. J. Brown, *Res. Nat. Bur. Standards*, **93**, 426, 1988

[74] W. Stephens, *Phys. Rev.*, **69**, 691, 1946

[75] A. E. Cameron and D. F. Eggers, *Rev. Sci. Instrum.*, **19**, 605, 1948

[76] V. R. Karataev, B. A. Mamyrin and D. V. Smikk, *Sov. Phys.-Tech. Phys.*, **16**, 1177, 1972

[77] D. C. Imrie, J. M. Pentney and J. S. Cottrell, *Rapid Commun. Mass Spectrom.*, **9**, 1293, 1995

[78] W. Hang, C. Baker, B. W. Smith, J. D. Winefordner and W. W. Harrison, *JAAS*, **12**, 143, 1997

[79] H. Sommer, H. A. Thomas and J. A. Hipple, *Phy. Rev.*, **76**, 1877, 1949

[80] M. B. Comisarov and A. G. Marshall, *Chem. Phys. Lett.*, **25**, 282, 1974

[81] C. H. Watson, C. M. Barshick, J. Wronka, F. H. Leukien and J. R. Eyler, *Anal. Chem.*, **68**, 573, 1996

[82] C. M. Barschick and J. R. Eyler, *J. Am. Soc. Mass Spectrom.*, **3**, 122, 1992

[83] C. M. Barschick and J. R. Eyler, *J. Am. Soc. Mass Spectrom.*, **4**, 387, 1993

[84] K. D. Zientek and J. R. Eyler, *JAAS*, **19**, 1513, 2004

[85] W. Paul and H. S. Steinwedel, *US Patent*, 2 939 952, 1960

[86] J. F. J. Todd, *Mass Spectrom. Rev.*, **10**, 3, 1991

[87] L. Gao, Q. Song. R. J. Noll, J. Duncan, R. G. Cooks and Z. Ouyang, *J. Mass Spectrom.*, **42**, 675, 2007

[88] E. R. Badman and R. G. Cooks, *J. Mass Spectrom.*, **35**, 659, 2000

[89] G. A. Uzochuckwu, K. Schimmel, G. B. Reddy, S. Y. Chang and V. Kabadi, *Proc. 2002 National Conf. Environ. Sci. Technol.*, 195, 2003

[90] C. N. Dalton, M. Jaoui, R. M. Kamens et al., *Anal. Chem.*, **77**, 3156, 2005

[91] D. M. P. Milton, *Spectrochim. Acta B*, **48**, 39, 1993

[92] W. Schelles, K. Maes, S. De Gendt and R. Van Grieken, *Anal. Chem.*, **68**, 1136, 196

[93] M. Betti, S. Giannarelli, T. Hiernaut, G. Rasmussen and L. Koch, *Fressenius J. Anal. Chem.*, **355**, 642, 1996

[94] L. A. D. Heras, E. Hrnecek, O. Bildstein and M. Betti, *JAAS*, **17**, 1011, 2002

[95] W. Schelles and R. E. Van Grieken, *JAAS*, **12**, 49, 1997

[96] J. Harley and V. Pretorius, *Nature*, **178**, 1244, 1956

[97] K. Newman and R. S. Mason, *JAAS*, **19**, 1134, 2004

[98] K. Newman and R. S. Mason, *JAAS*, **20**, 830, 2005

[99] K. Newman and R. S. Mason, *Rapid Commun. Mass Spec.*, **20**, 2067, 2006

[100] T. J. Cleland and F. R. Meeks, *Spectrochim. Acta B*, **51**, 1487, 1996

[101] J. W. Waggoner, L. S. Milstein, M. Belkin, K. L. Sutton, J. A. Caruso and H. B. Fannin, *J. Anal. At. Spectrom.*, **15**, 13, 2000

[102] *NIST Chemistry Webbook, NIST Standard Reference Database Number 69,* ed. P.J. Linstromand, W.G. Mallard, National Institute of Standards and Technology, Gaithersburg, MD, 20899, (http://webbook.nist.gov), 2003

[103] D. Fliegel, K. Fuhrer, M. Gonin and D. Günther, *Anal. Bioanal. Chem.*, **386**, 169, 2006

[104] J. P. Guzowski, J. A. C. Broekaert, S. J. Ray and G. M. Hieftje, *JAAS*, **14**, 1121, 1999

[105] J. P. Guzowski and G. M. Hieftje, *JAAS*, **15**, 27, 2000

[106] J. P. Guzowski and G. M. Hieftje, *Anal. Chem.*, **72**, 3812, 2000

[107] R. S. Mason, P. D. Miller and I. P. Mortimer, *Phys. Rev. E*, **55**, 7462, 1997

[108] R. S. Mason, P. D. Miller, I. P. Mortimer, D. J. Mitchell and N. A. Dash, *Phys. Rev. E*, **68**, 016408, 2003

[109] K. Newman, R. S. Mason, D. R. Williams and I. P. Mortimer, *J. Anal. Atom. Spectrom.*, **19**, 1192, 2004

[110] W. D. Davis and T. A. Vanderslice, *Phys. Rev.*, **131**, 219, 1963

[111] I. Abril, A. Gras-Marti and J. A. Valles-Abarca, *Phys. Rev.*, **28**, 3677, 1983

[112] R. S. Mason and M. Pichilingi, *J. Phys. D: Appl. Phys.*, **27**, 2363, 1994

[113] M. van Straaten, PhD Thesis, University of Antwerp, 1993

[114] R. Seeliger, *Z. Phys.*, **119**, 482, 1942

[115] R. S. Mason and R. M. Alcott, *J. Phys. D: Appl. Phys.*, **27**, 2372, 1994

[116] A. Guentherschulze, *Vacuum*, **3**, 359, 1953

[117] J. S. Colligen and G. Carter, *Ion Bombardment of Solids*, Heinemann, London, 1968

[118] W. D. Westwood, *Prog. Surf. Sci.*, **7**, 711, 1976

[119] A. von Hippel, *Ann. Phys.*, **81**, 1043, 1926

[120] W. W. Harrison, in *Inorganic Mass Spectrometry*, ed. F. Adams, R. Gijbels and R. Van Grieken, John Wiley & Sons Ltd., 1988

[121] P. Sigmund, *Phys. Rev.*, **184**, 383, 1969

[122] M. T. Robinson and I. M. Torrens, *Phys. Rev. B*, **9**, 5008, 1974

[123] J. S. Townsend, *Electricity in Gases*, Clarendon Press, Oxford, 1915

[124] J. S. Townsend, *Philos. Mag.*, **11**, 1112, 1932

[125] I. Langmuir, *Phys. Rev.*, **33**, 954, 1929

[126] Y. Ikezoe, S. Matsuoka, M. Takebe and A. Vigiano, *Gas Phase Ion-Molecule Reaction Rate Constants Through 1986*, Mazuren Co. Ltd. Tokyo, Japan, 1987

[127] D. R. Lide, *Handbook of Chemistry and Physics*, CRC Press, 1995

[128] W. Vieth and J. C. Huneke, *Spectrochim. Acta B*, **45**, 941, 1990

[129] A. D. Angstadt, J. Whelan and K. R. Hess, *Michrochem. J.*, **47**, 206, 1993

[130] A. Bogaerts and R. Gijbels, *Phys. Rev. A*, **52**, 3743, 1995

[131] J. A. Hornbeck and J. P. Molnar, *Phys. Rev.*, **84**, 621, 1951

[132] L. A. Pinnaduwage, W. Ding and D. L. McCorkle, *Appl. Phys. Lett.*, **71**, 3634, 1997

[133] W. Ding, D. L. McCorkle and L. A. Pinnaduwage, *J. Appl. Phys.*, **84**, 3051, 1998

[134] L. A. Pinnaduwage and P. G. Datskos, *J. Appl. Phys.*, **84**, 3442, 1998

[135] W. X. Ding, L. A. Pinnaduwage, C. Tav and D. L. McCorkle, *Plasma Sources Sci. Technol.*, **8**, 384, 1999

[136] P. F. Knewstubb and A. W. Tickner, *J. Chem. Phys.*, **36**, 674, 1962

[137] S. E. Kupriyanov, *Sov. Phys. JETP*, **24**, 674, 1967

[138] P. F. Knewstubb and A. W. Tickner, *J. Chem. Phys.*, **36**, 684, 1962

[139] W. Lindinger, *Phys. Rev. A*, **7**, 328, 1973

[140] P. Ding and M. Cottin, *J. Chem. Phys.*, **57**, 537, 1960

[141] D. J. Mitchell, N. A. Dash and R. S. Mason, *Proceedings of the XIVth International Conference on Gas Discharges and their Applications*, **2**, 248, 2002

[142] T. F. Gallagher, *Rydberg Atoms*, Cambridge University Press, 2005

[143] H. E. White, *Introduction to Atomic Spectra*, McGraw-Hill, New York, 1934

[144] P. P. Sorokin and J. R. Lankard, *IBM J. Res. Dev.*, **10**, 162, 1966

[145] T. W. Hansch, *Appl. Opt.*, **11**, 895, 1972

[146] P. M. Koch, *Rydberg States of Atoms and Molecules*, ed. R. F. Stebbings and F. B. Dunning, Cambridge University Press, 1983

[147] K. Singer, M. Reetz-Lamour, T. Amthor, S. Fölling, M. Tscherneck and M. Weidemüller, *J. Phys. B*, **38**, S321, 2005

[148] T. C. Killian, M. J. Lim, S. Kulin, R. Dumke, S. D. Bergeson and S. L. Rolston, *Phys. Rev. Lett.*, **86**, 3759, 2001

[149] T. P. Softley and R. J. Rednall, *J. Chem. Phys.*, **112**, 7992, 2000

[150] J. A. Schiavone, D. E. Donohue, D. R. Herrick and R. S. Freund, *Phys. Rev. A*, **16**, 48, 1977

[151] J. A. Schiavone, S. M. Tarr and R. S. Freund, *Phys. Rev. A*, **20**, 71, 1979

[152] E. J. Beiting, G. F. Hildebrandt, F. G. Kellert, G. W. Flotz, K. A. Smith and F. B. Dunning, *J. Chem. Phys.*, **70**, 3351, 1979

[153] T. F. Gallagher and W. E. Cooke, *Appl. Phys. Lett.*, **34**, 369, 1979

[154] T. F. Gallagher and W. E. Cooke, *Phys. Rev. Lett.*, **42**, 835, 1979

[155] M. Harnafi and B. Dubreuil, *Phys. Rev. A*, **31**, 1375, 1985

[156] R. Kachru, T. F. Gallagher, F. Gounand, K. A. Safinya and W. Sandner *Phys. Rev. A*, **27**, 795, 1983

[157] M. Chapelet, J. Boulmer, J. C. Gauthier and J. F. Deplech, *J. Phys. B*, **15**, 3455, 1982

[158] M. Hugon, F. Gounand, P. R. Fournier and j. Berlande, *J. Phys. B*, **12**, 2707, 1979

[159] F. G. Kellert, K. A. Smith, R. D. Rundel, F. B. Dunning and R. B. Stebbings, *J. Chem. Phys.*, **72**, 6312, 1980

[160] C. Higgs, K. A. Smith, F. B. Dunning and R. B. Stebbings, *J. Chem. Phys.*, **75**, 745, 1981

[161] H. Hotop and A. Niehaus, *J. Chem. Phys.*, **47**, 2506, 1967

[162] C. A. Kocher and A. J. Smith, *Phys. Rev. Lett.*, **39**, 1516, 1977

[163] L. Suess, R. Parthasarathy and F. B. Dunning, *J. Chem. Phys.*, **117**, 11222, 2002

[164] J. A. Stockdale, F. J. Davis, R. N. Compton and C. E. Klots, *J. Chem. Phys.*, **60**, 4279, 1974

[165] R. Parthasarathy, L. Suess, S. B. Hill and F. B. Dunning, *J. Chem. Phys.*, **114**, 7962, 2001

[166] R. Parthasarathy, C. D. Finch, J. Wolfgang, P. Nordlander and F. B. Dunning, *J. Chem. Phys.*, **109**, 8829, 1998

[167] W. P. West, G. W. Foltz, F. B. Dunning, C. J. Latimer and R. F. Stebbings, *Phys. Rev. Lett.*, **36**, 854, 1976

[168] B. G. Zollars, K. A. Smith and F. B. Dunning, *J. Chem. Phys.*, **81**, 3158, 1984

[169] T. Kondow, *J. Phys. Chem.*, **91**, 1307, 1987

[170] L. Barbier and M. Cheret, *J. Phys. B*, **20**, 1229, 1987

[171] I. Dimicoli, R. Botter, *J. Chem. Phys.*, **74**, 2346, 1981

[172] K. A. Smith, F. G. Kellert, R. D. Rundel, F. B. Dunning and R. F. Stebbings, *Phys. Rev. Lett.*, **40**, 1362, 1978

[173] T. F. Gallagher, G. A. Ruff and K. A. Safinya, *Phys. Rev. A*, **22**, 843, 1980

[174] M. J. Renn and T. F, Gallagher, *Phys. Rev. Lett.*, **67**, 2287, 1991

[175] L. I. Gudzenko and S. S. Yakovlenko, *Sov. Phys. Teo. JETP*, **35**, 877, 1972

[176] L. A. Pinnaduwage, *J. Chem. Phys.*, **108**, 6633, 1998

[177] H. Krause and H. J. Neusser, *J. Chem. Phys.*, **99**, 6278, 1993

[178] W. G. Scherzer, H. L. Selzle, E. W. Schlag and R. D. Levine, *Phys. Rev. Lett.*, **72**, 1435, 1994

[179] L. A. Pinnaduwage and F. Zhu, *Chem. Phys. Lett.*, **277**, 147, 1997

[180] G. V. Golubkov, G. K. Ivanov, E. M. Balashov and G. Golubkov, *JETP*, **87**, 56, 1998

[181] A. Walz-Flannigan, J. R. Guest, J. –H. Choi and G. Raithel, *Phys. Rev. A*, **69**, 063405, 2004

[182] T. Amthor, M. Reetz-Lamour, S. Westermann, J. Denskat and M. Weidemüller, *Phys. Rev. Lett.*, **98**, 023004, 2007

[183] S. K. Dutta, D. Feldbaum, Walz-Flannigan, J. R. Guest and G. Raithel, *Phys. Rev. Lett.*, **86**, 3993, 2001

[184] G. Vitrant, J. M. Raimond, M. Gross and S. Haroche, *J. Phys. B*, **15**, L49, 1982

[185] S. Westermann, T. Amthor, A. L. de Oliveira, J. Deiglmayr, M. Reetz-Lamour and M. Weidemüller, *Eur. Phys. J. D*, **40**, 37, 2006

[186] I. Mourachko, D. Comparat, D. de Tomasi, A. Fioretti, P. Nosbaum, V. M. kulin and P. Pillet, *Phys. Rev. Lett.*, **80**, 253, 1998

[187] S. Badiei and L. Holmlid, *Mon. Not. R. Astron. Soc.*, **333**, 360, 2002

[188] L. Holmlid, *J. Phys.: Condens. Matter*, **14**, 13469, 2002

[189] L. Holmlid, *Chem. Phys.*, **237**, 11, 1998

[190] E. A. Manykin, M. I. Ozhovan and P. P. Poluéktov, *Sov. Phys. JETP*, **75**, 602, 1992

[191] L. G. Christophorou, *Electron-Mol*ecule *Interactions and Their Applications Vol. 2*, (p74 table 3), Academic Press Inc., New York, 1984

[192] P. W. Atkins, *Physical Chemistry 5th edition*, Oxford University Press, Oxford, 1997

[193] D. Smith, A. G. Dean and N. G. Adams, *J. Phys. D*, **7**, 1944, 1974

[194] L. Schott, *Plasma Diagnostics*, ed. W. Lochte-Holtgreven, North-Holland Publishing Co., Amsterdam, 1968

[195] I. Langmuir and H. M. Mott-Smith, *Gen. Elec. Rev.*, **27**, 449, 538, 616, 762, 810 (1924)

[196] J. Dowden, P. Kapadia and B. Fenn, *J. Phys. D*, **26**, 1215, 1993

[197] K. T. Chao and T. Y. Tang, *Phys. Rev.*, **68**, 30, 1945

[198] I. H. Hutchinson, *Phys. Fluids*, **30**, 3777, 1987

[199] J. Horacek, R. A. Pitts, P. C. Stangeby, O. Batischev and A. Loarte, *J. Nucl. Mat.*, **313**, 931, 2003

[200] P. C. Stangeby, *Plasma Phys. Control. Fusion*, **37**, 1031, 1995

[201] C. Fanara and I. M. Richardson, *J. Phys. D: Appl. Phys.*, **34**, 2715, 2001

[202] J. Banský, A. Brockhaus, J. Engemann, Y. Yuan, L. Livovský and S. Slosarčík, *Sensors for in-situ Plasma Diagnostics*, Proc. Inter. Symp on Microelectronic, ISHM '95, Los Angeles, CA, USA, p119, 1995

[203] Y. Ye and R. K. Marcus, *Spectrochim. Acta. B*, **50**, 2715, 2001

[204] K. S. Knol, *Philips Res. Rept.*, **6**, 288, 1951

[205] T. A. Anderson, *Phil. Mag.*, **38**, 179, 1947

[206] G. Wehner and G. Medicus, *J. Appl. Phys.*, **23**, 1035, 1952

[207] G. Wehner and G. Medicus, *Phys. Rev.*, **93**, 647, 1954

[208] B. Richelman, *Rev. Sci. Instr.*, **30**, 593, 1959

[209] F. F. Chen, *IRE Trans. Nucl. Sci.*, **8**, 150, 1960

[210] A. G. Coulter and G. S. Higginson, *J. Electron. Control*, **15**, 437, 1963

[211] E. O. Johnson and L. Malter, *Phys. Rev.*, **76**, 1411, 1949

[212] F. F. Chen, *Plasma Diagnostic Techniques*, ed. R. H. Huddlestone and S. L. Leonard, Academic Press Inc., USA, 1965

[213] K. Nagaoka, A. Okamoto, S. Yoshimura and M. Y. Tanaka, *J. Phys. Soc. Jpn.*, **70**, 131, 2001

[214] J. A. Stone, *IJIMS*, **5**, 19, 2002

Chapter 3

Development of the Fast Flow Glow Discharge Mass Spectrometer

3.1 Introduction

The development of a new Fast Flow Glow Discharge (FFGD) mass spectrometer was started by Dr. Neil Dash[1]. The original aim was to build a FFGD mass spectrometer from other instruments within this group in order to study the following aspects of fundamental plasma chemistry within the source[1]:

1) optical emission properties;
2) direct analysis of the kinetic energies of ions exiting the source;
3) negative ion formation in the plasma afterglow on addition of secondary gases;
4) analysis of neutral species emerging from the discharge.

It was hoped that the results using the above techniques could be taken simultaneously to allow direct comparison. Due to time constraints, instrument development and characterisation were incomplete. The project described here is therefore an extension of the above and involved a major rebuild. This chapter describes changes to the instrument and its characterisation. The main objectives were to:

a) remove inherent problems and minimise instrument downtime;
b) adapt the source to allow electrical probe studies;
c) improve ion transmission from the FFGD cell to the mass spectrometer.

3.2 Fast Flow Glow Discharge Mass Spectrometry

The FFGD source was created by Mason et al and the design has evolved within the group over the course of a decade[1-7]. The source was created to improve analytical sensitivity relative to other glow discharge (GD) sources, but particularly to study the fundamental processes occurring within and beyond the GD plasma[2]. The FFGD source was successful in improving sensitivity over static systems since the flowing discharge gas reduces the back diffusion[8] and re-deposition of sputtered material onto the cathode surface[9] as well as aiding the movement of ions and excited states downstream to the mass analyser aperture.

The FFGD plasma is formed by application of a high potential across the fast flowing gas, which leads to electrical breakdown[10] of the gas. The movement of the discharge gas extends the plasma downstream, i.e. beyond the active discharge region. Two different discharge geometries have been used, Grimm[2,4,11,12] (obstructed) and coaxial[1-6] (figure 3.1), although coaxial geometry is preferred due to inefficient sputtering of the cathode using the Grimm geometry under the desired conditions.

A schematic of the first FFGD source built by Miller[2] is shown in figure 3.2. The source, of Grimm geometry, was produced from non magnetic stainless steel (316 grade) and PEEK and ceramic insulators. The cathode was a flat conducting plate (usually copper) fitted into a cap. The source can be operated in two modes; i) Extended Plasma (EP), also known as Flowing Afterglow (FAG) mode, and ii) Extended Discharge (ED) mode. In EP mode the plasma is struck between the cathode and the anode, labelled in figure 3.2, with the fast flowing gas extending the plasma downstream forming a FAG plasma. A bias (V_c) relative to the anode could be applied to the ion exit cone to improve ion extraction from the source. In ED mode the discharge is struck between the cathode and the ion exit cone. Since in ED mode the ion exit cone acts as the only anode surface, an extraction bias cannot be applied. The fast gas flow is allowed by incorporation of the pumping aperture near the ion exit. The more usual static glow discharge source uses a very low gas flow rate to replace that lost through the ion exit aperture.

The discharge region was redesigned in a coaxial configuration to improve sputtering efficiency[2]. The new source, shown in figure 3.3, incorporates a probe to hold, and to take power to the cathode pin. A vacuum interlock was also added to allow cathode replacement without letting the whole source up to atmospheric pressure. Using a coaxial design with a cylindrical pin allows uniform sputtering of the sample. Another important addition illustrated in figure 3.3 is the secondary gas inlet. The secondary gas inlet was added to allow plasma chemistry to be investigated through addition of gases to the FAG plasma near the ion exit. Previous to incorporation it was possible to change only the cathode material and the discharge gas (pure or mixture). The secondary gas inlet has allowed the addition of a number of gaseous chemicals[1-7] and organic vapours[1,3,5,6] to the FAG plasma and the interaction to be monitored through mass spectrometry[1-7] and electrical probe studies[1, 5,6] independent of the discharge creating the plasma. The position and design of the

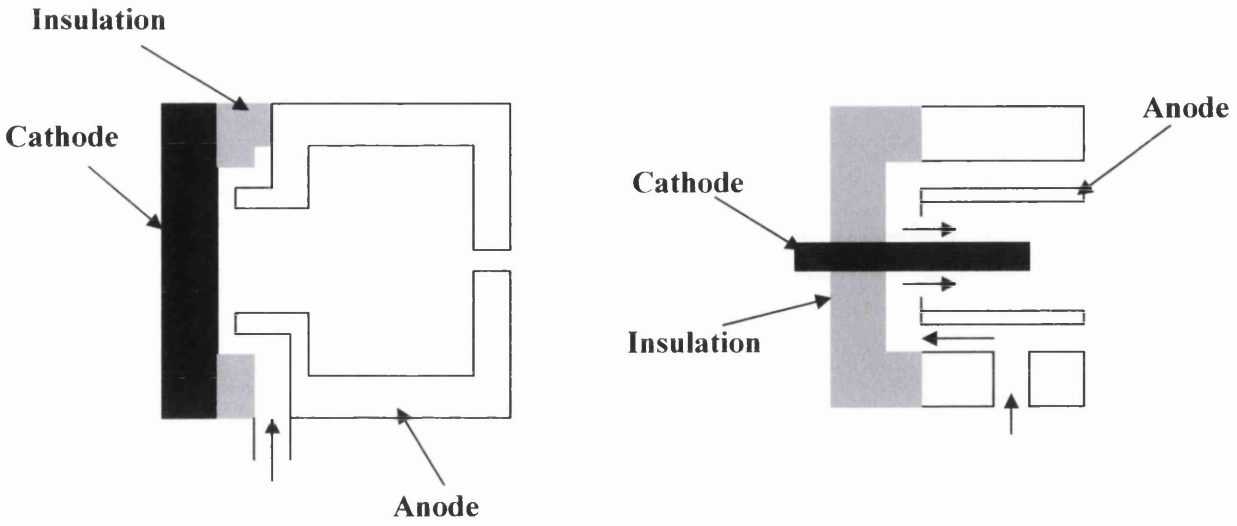

Figure 3.1: Grimm/obstructed (left) and coaxial (right) discharge sources

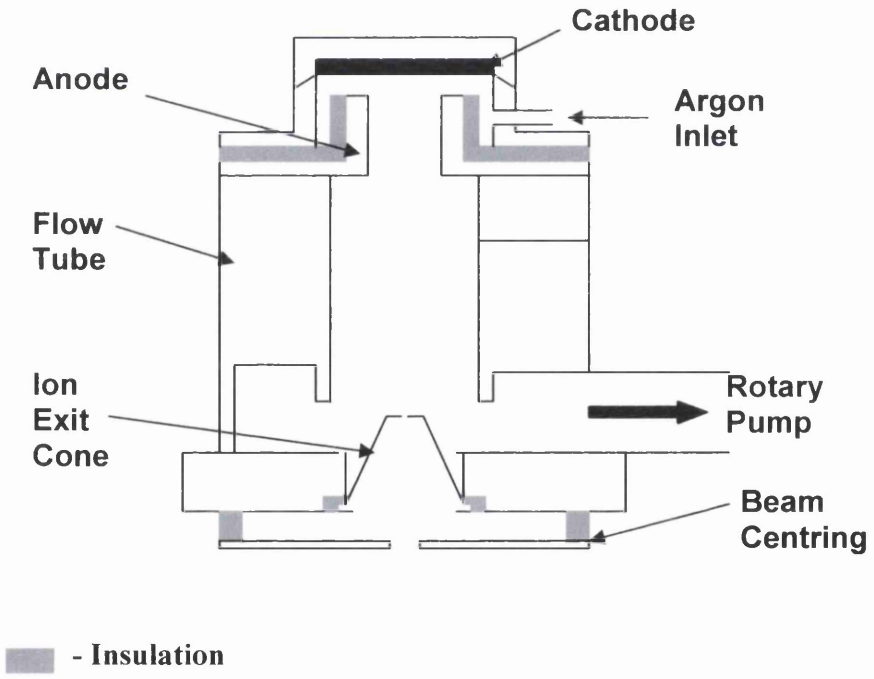

Figure 3.2: Cross sectional diagram of the initial FFGD source design (not to scale) (adapted from reference 2)

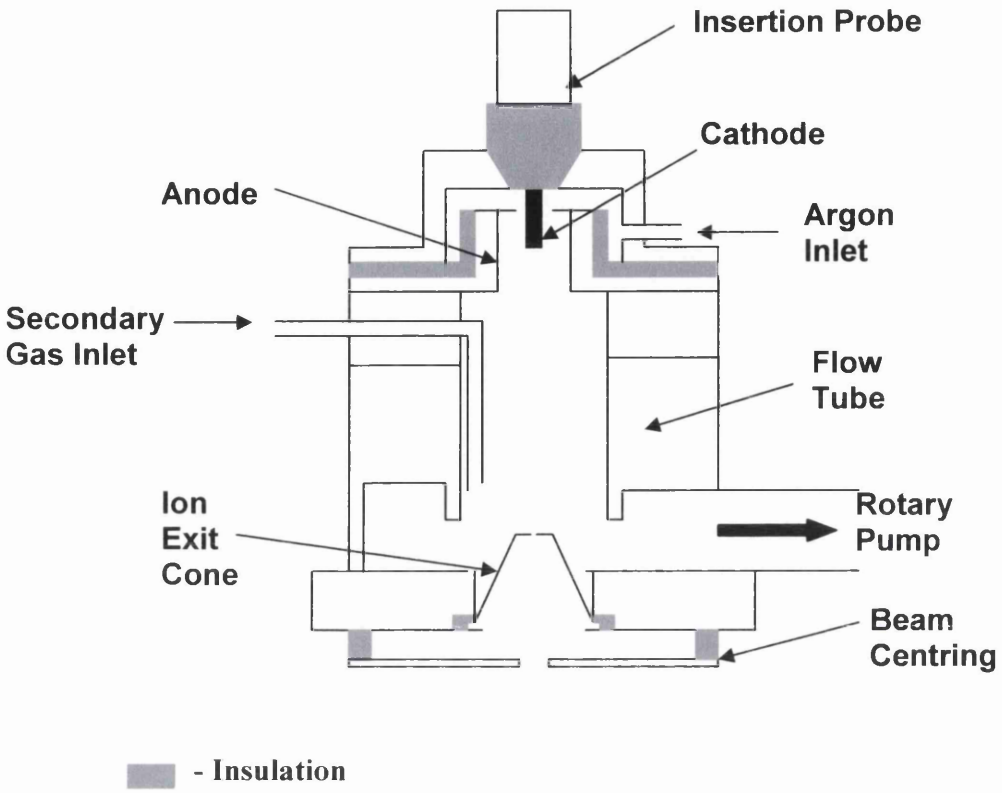

Figure 3.3: Adapted source configuration incorporating coaxial cathode pin and secondary gas inlet (approximately 1:1) (adapted from reference 2)

secondary gas inlet has changed slightly over time to make maintenance simpler and to utilise the inlet as a probe for electrical studies[1,5].

The first FFGDMS instrument incorporated a reconditioned MS9 (AEI) magnetic sector instrument which had undergone extensive modification[13,14]. The second-generation instrument is a reconditioned VG PlasmaQuad II[15] quadrupole mass spectrometer. The instrument was originally an inductively coupled plasma (ICP) instrument, but extensive redevelopment was carried out to allow the fast flow source to be incorporated[4]. Quadrupole instruments are desirable as they are smaller and cheaper than sector instruments, although the mass resolution is usually much lower (in this instrument mass is determined to nearest mass unit). Using a quadrupole instrument there is no need to float the source at a very high voltage, and therefore they are easier to couple to other devices (such as a GC inlet system[6]). One further advantage is that the new source was mounted outside the vacuum chamber of the quadrupole and could be isolated using a slide valve, making maintenance and cathode replacement much simpler. The source for the sector instrument is located within the vacuum housing and therefore the instrument must be let up to atmospheric pressure for most maintenance.

The source design was similar to that for the MS9 instrument. Both Grimm (figure 3.4) and coaxial geometries (figure 3.5) were built, and as with the first source design there was no secondary gas inlet, although one was later added (figure 3.6). The secondary gas inlet was later modified by Newman[6] (figure 3.7) in a similar manner to that by Mitchell[5] shown in figure 3.8 for the first generation instrument. Also illustrated in figure 3.5 is a cell extension piece produced from non-magnetic stainless steel which increased the distance between the pin and the ion exit cone to that used in the first instrument. A major difference is that the ion exit cone is grounded to the instrument case.

Newman[6] also adapted the source to allow addition of organic compounds and reduced gas flow rates. The new inlet system is discussed in detail in chapters 7 and 8. Lower gas flow rates can be achieved by splitting the gas flow in a known ratio[6,16].

As well as studying the ions formed from the plasma it was also desirable to monitor the electrical properties of the plasma. A system was constructed by Mitchell[4] (figure 3.9) based on the double probe method used by Johnson and Malter[17] and Reifman and Dow[18] before them, the basic circuit for which is shown in figure 3.10. In the work carried within this group[1,4] the secondary gas inlet has been

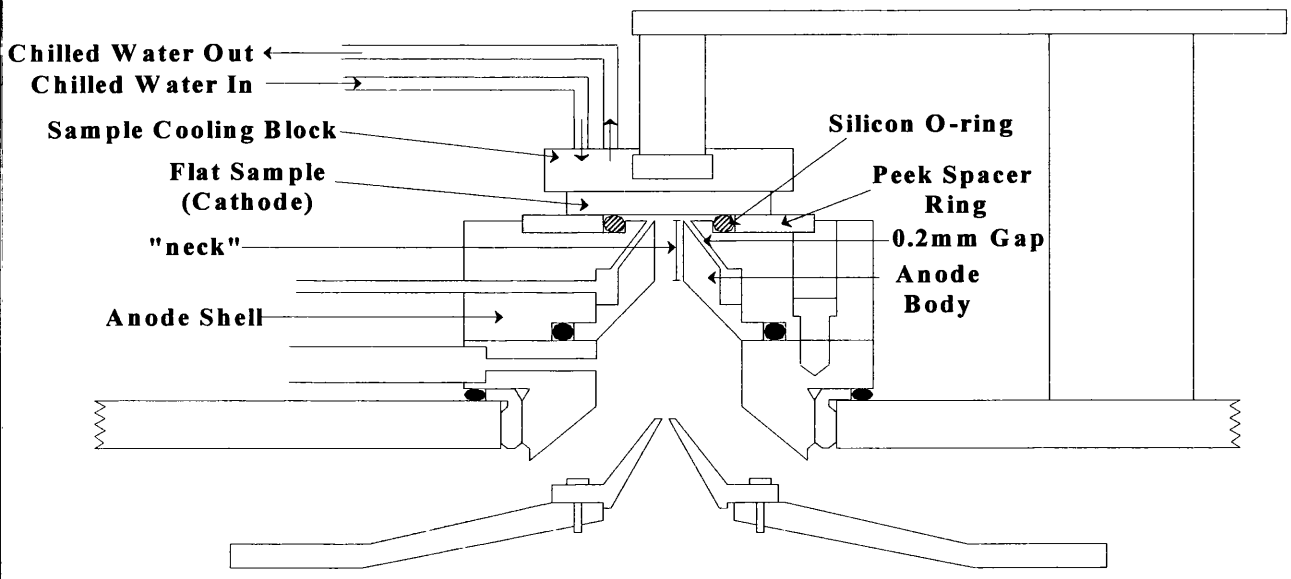

Figure 3.4: Schematic of the initial Grimm FFGD ion source (adapted from reference 6, approximately 1:1)

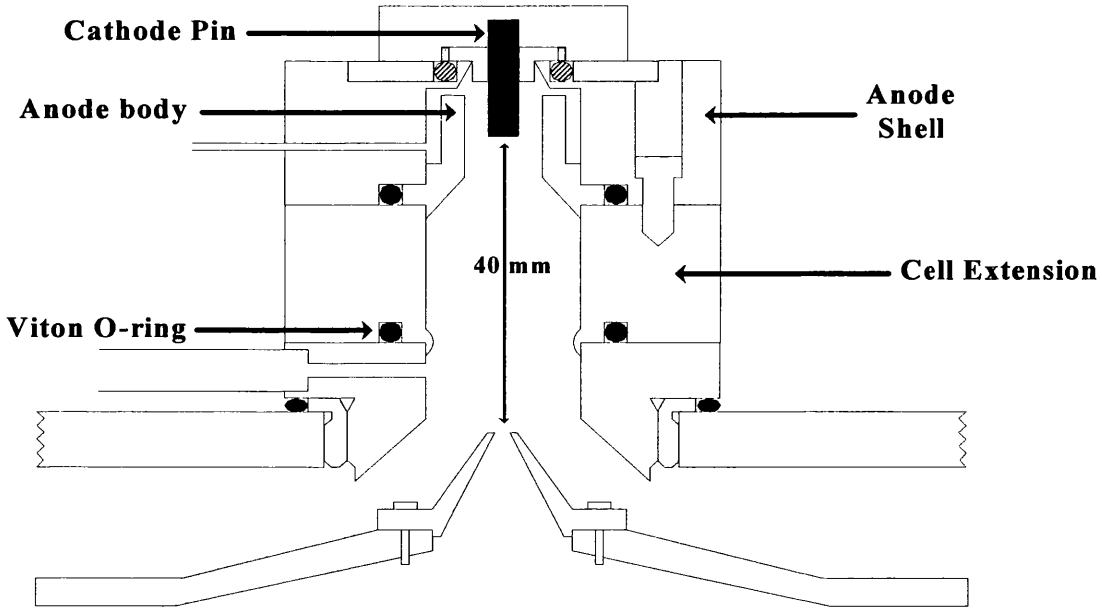

Figure 3.5: Schematic of the FFGD co-axial Ion Source with a cell extension (adapted from reference 6, approximately 1:1)

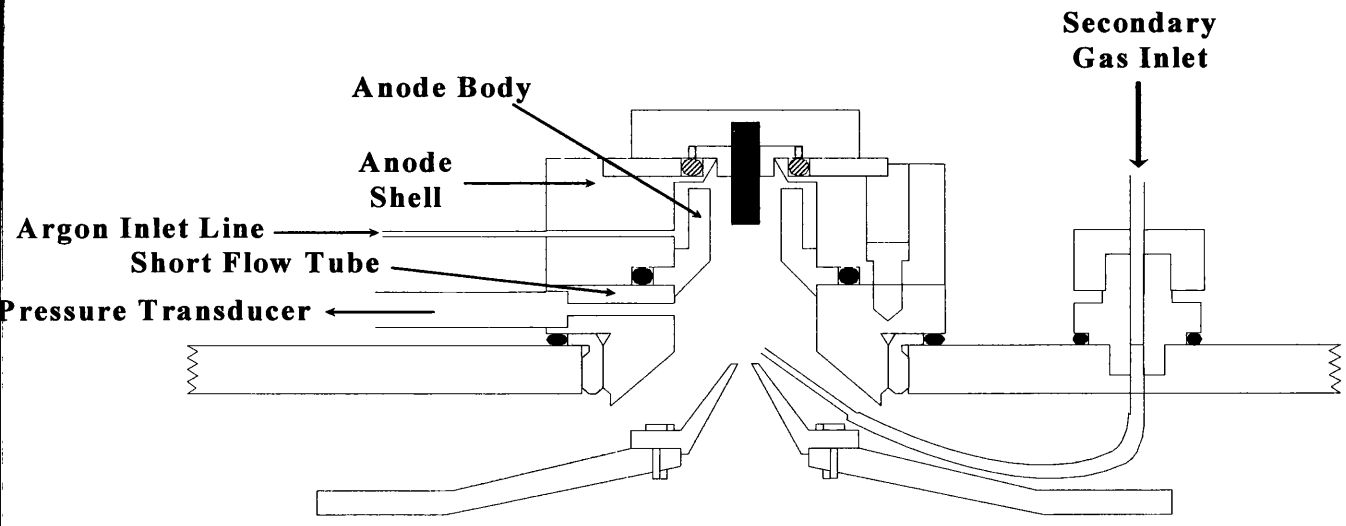

Figure 3.6: Arrangement of the secondary gas inlet (adapted from reference 6, approximately 1:1)

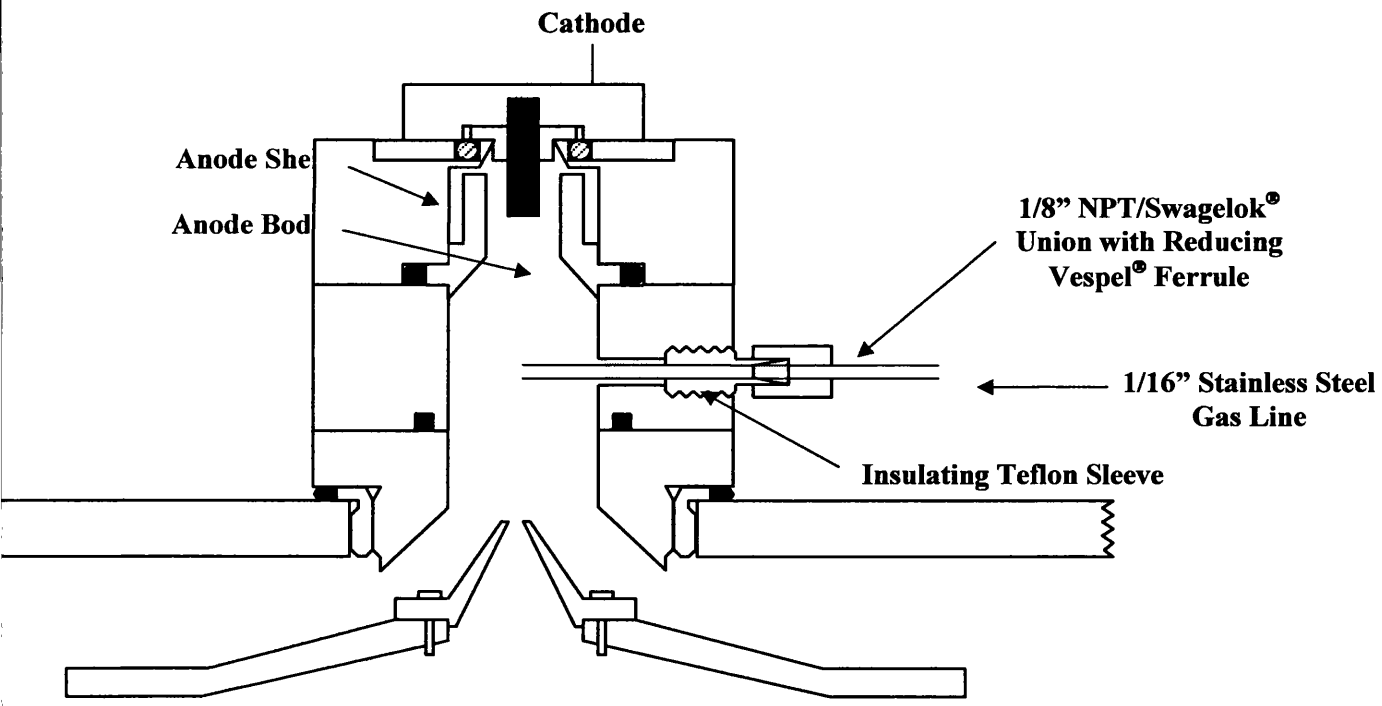

Figure 3.7: Cross-section of the co-axial source showing the modified secondary gas inlet (adapted from reference 6, approximately 1:1)

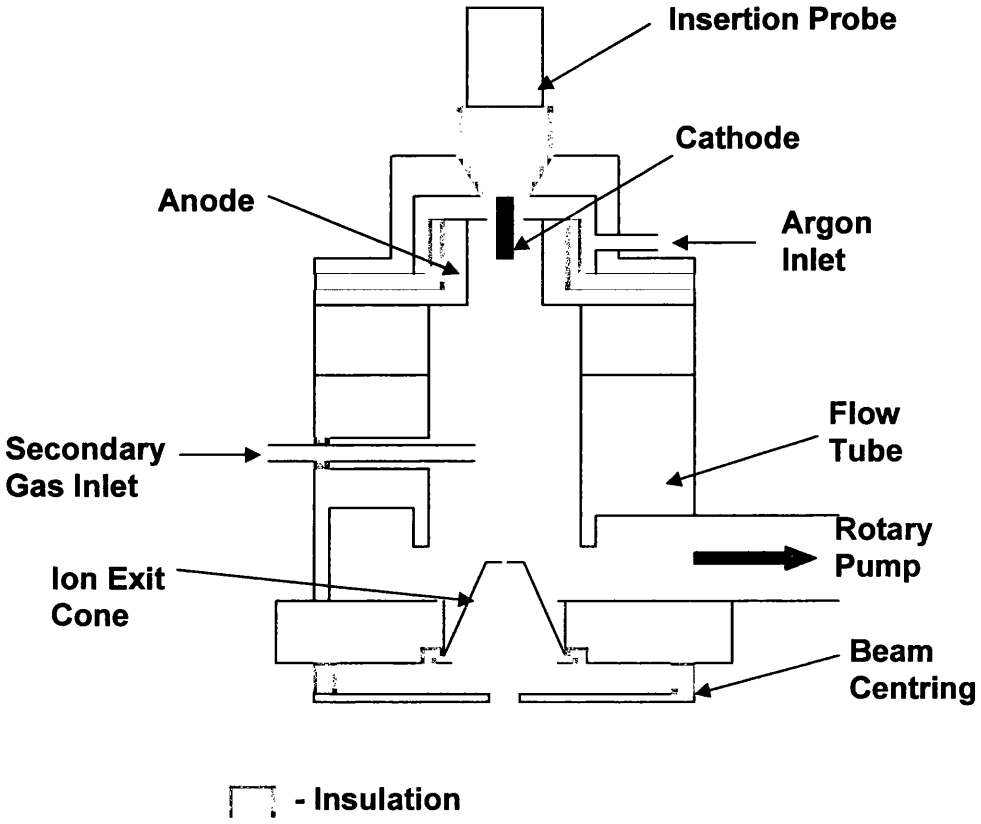

Figure 3.8: Secondary gas inlet design used by Mitchell (approximately 1:1)

used as a probe. This meant that probes A, B and B' (as illustrated in figure 3.9) were all produced from 1/16" tubing to keep the probe areas approximately equal. In contrast, however, Newman[6] performed experiments using copper wire of 0.315 mm diameter in order to minimise disturbance to the plasma.

The FFGD instrument allows a number of parameters to be controlled and therefore allows excellent control of the plasma. The parameters which can be controlled are the discharge voltage (V_d), source pressure (P), argon (discharge gas) flow rate (F_{Ar}), residence time of the gas in the source (τ), secondary gas flow and the ion exit or 'cone' bias (V_c)

3.3 Experimental Methods

3.3.1 Source Maintenance

Throughout the course of this investigation it was necessary to carry out a number of standard procedures to maintain the performance of the FFGD cell and to ensure the consistency of results.

The FFGD source was cleaned at least every 2-3 months, although the time between cleanings was initially dependent on the occurrence of short-circuits due to deposited copper on the insulators. It is also known that deposition of sputtered material on the walls and ion exit cone can induce a decrease in the observed ion intensities[1]. Each source section was cleaned with nitric acid before successive washes with distilled water and methanol (AnalR, Fischer Scientific). For particularly heavy deposition, stainless steel sections of the source have been cleaned using a solution of Decon 90 in an ultrasonic bath, again followed by successive washes with distilled water and methanol.

The cathode pin was replaced daily, and 45 minutes of pre-sputtering was performed to prepare a fresh cathode surface and to allow deposition of a layer of copper on the walls of the discharge cell. This has been shown to stabilise detected ion signals[1,3]. Before insertion the cathode pin was cleaned by immersion in nitric acid followed by successive washes with distilled water and methanol. Cleaning with nitric acid allows removal of surface layers such as copper oxide formed via reactions with atmospheric gases.

Checks for electrical leakage were performed every other day for spectrometric work and every day when performing probe studies.

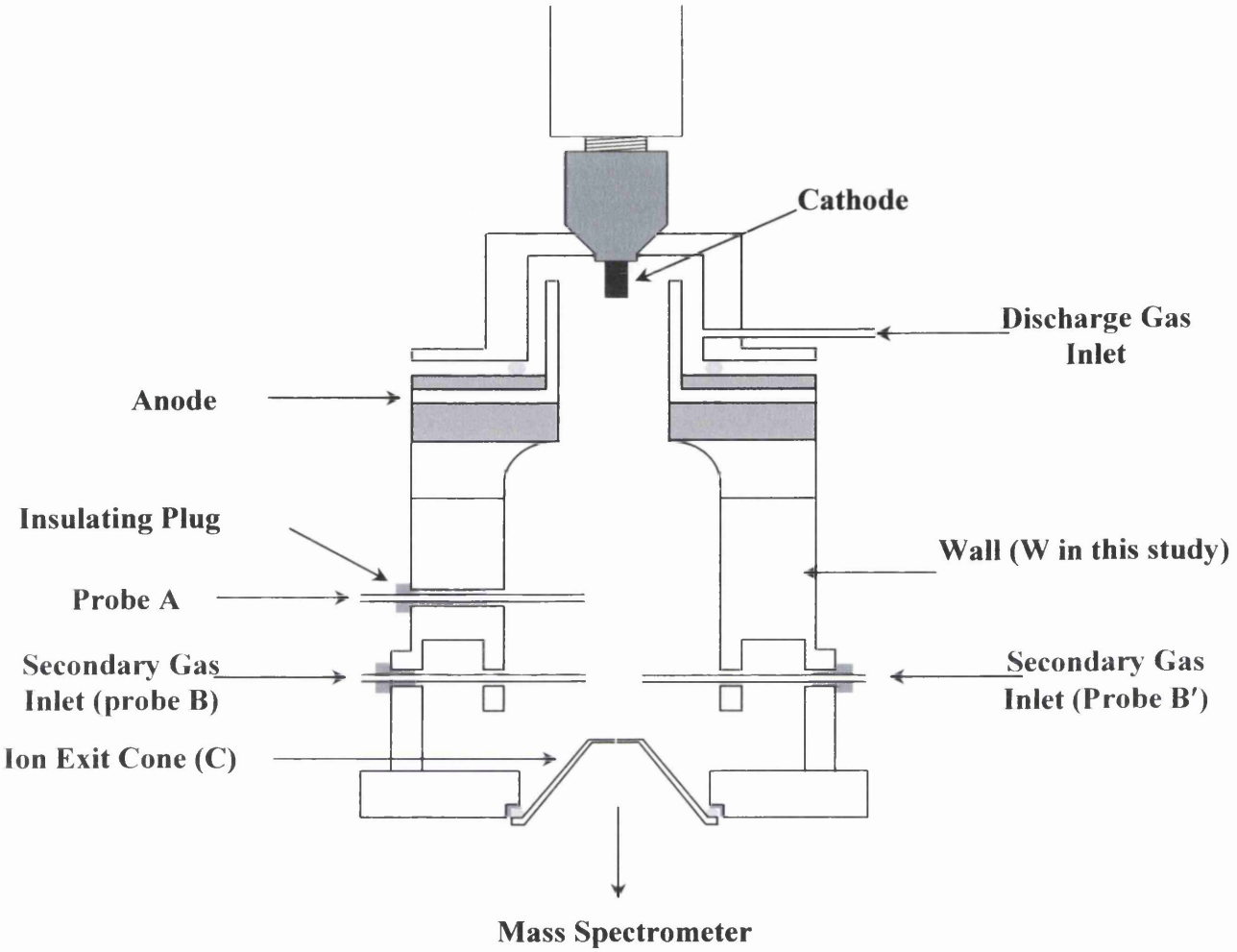

Figure 3.9: Electrical probe arrangement in the first FFGD source (from reference 5, approximately 1:1½)

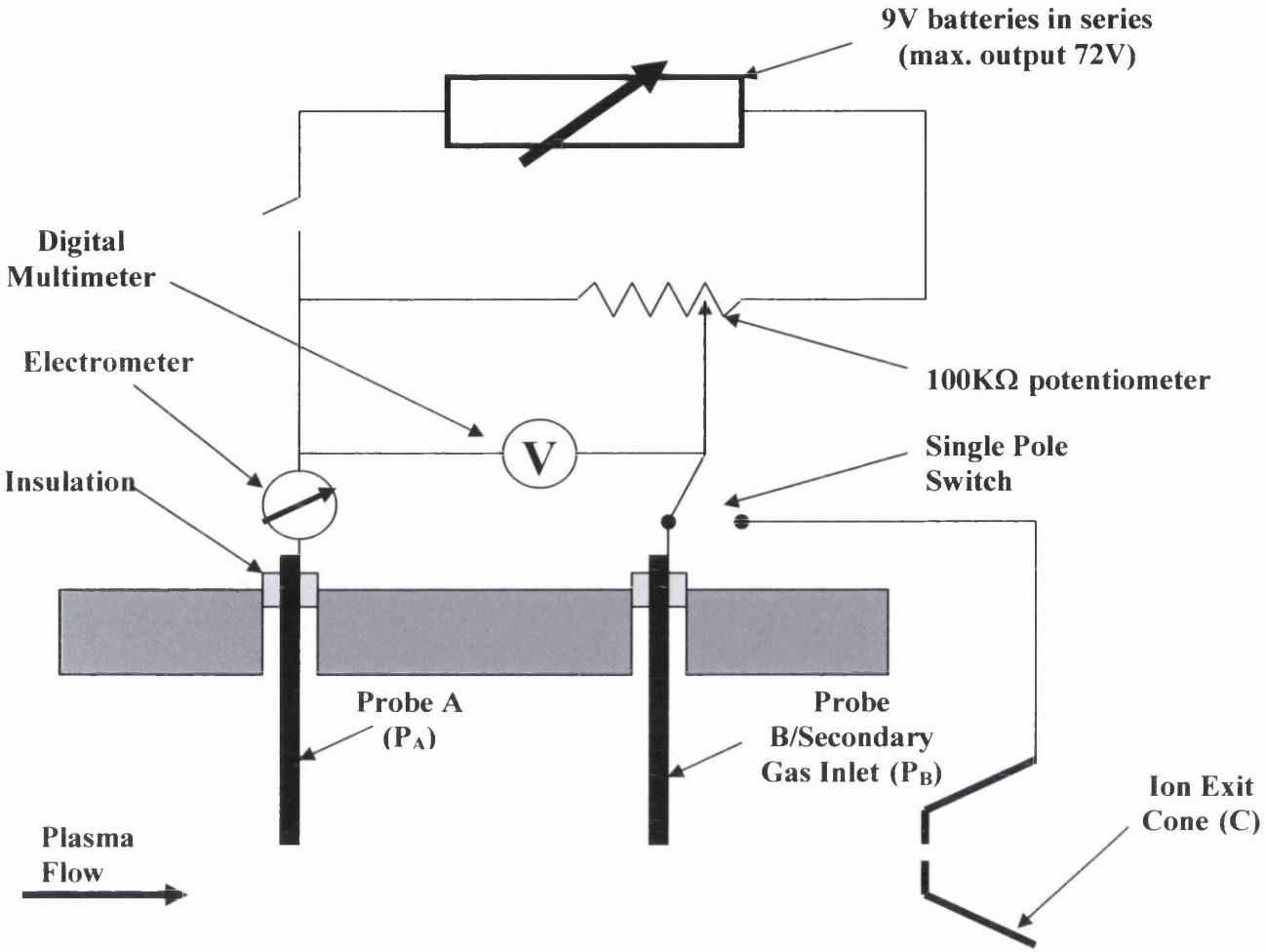

Figure 3.10: Electric Probe Circuit used by Mitchell[4]
(Probes 1/16" diameter stainless steel tubing, distance between probes A and B = 10 mm, distance between probe B and cone = 8 mm)

3.3.2 Gases and Cathode Materials Used

Cathode pins were produced from 3.2 mm copper rod (Goodfellows[19], 99.99%). A list of the gases used and their purities used is shown in table 3.1.

Gas	Supplier	Purity (%)
Argon (Research Grade)	BOC[20]	99.9995
Hydrogen (Research Grade)	BOC[20]	99.9995
Methane (Research Grade)	BOC[20]	99.995
Carbon Tetrafluoride	Fluorochem Ltd[21]	Not specified
Carbon Monoxide (Research Grade)	BOC[20]	99.97
Nitrogen (Research Grade)	BOC[20]	99.9995

Table 3.1: Purity of gases used

3.3.3 Discharge Gas Residence Time

Assuming the discharge gas to traverse the source as a plug, equation 3.1[3] can be used to determine the residence time, τ, of the flowing afterglow plasma (FAG) between the tip of the cathode pin and the tip of the ion exit cone.

$$\tau = \frac{V_{cell} \cdot T_{gas} \cdot P_{source} \cdot 60}{T_{source} \cdot P_{standard} \cdot F_{gas}} \qquad \textit{(equation 3.1)}$$

V_{cell} = the volume of cell between the tip of the cathode pin and the tip of the ion exit cone (17.75 cm^3 since modification, 10.8 cm^3 initially)

T_{gas} = temperature of the argon gas prior to entry into the discharge cell (295 K).

P_{source} = pressure inside the discharge cell (Torr).

T_{source} = temperature inside the discharge cell (~ 310 K).

$P_{standard}$ = pressure of the argon prior to entry into the discharge cell (760 Torr).

F_{gas} = discharge gas flow-rate (sccm). The value 60 is the conversion factor to change sccm into the flow rate per second.

3.2.4 Secondary Gas Addition

The secondary gas flow rate was monitored using a Tylan[22] mass flow meter. However, the flow meter was calibrated using argon and so a conversion factor (supplied with the meter) was often required. The secondary gas flow rates were calculated using equation 3.2.

$$F_R = \frac{CF(R/N_2)}{CF(Ar/N_2)} \times F_{reading} \qquad \textit{(equation 3.2)}$$

where CF is the conversion factor, R is the secondary/reagent gas and F is the gas flow rate.

The secondary gas addition is expressed as a percentage of the total gas flow calculated using equation 3.3.

$$\%\,\text{Secondary Gas} = \left(\frac{F_R}{(F_R + F_{Ar})} \right) \text{x}\,100 \qquad \textit{(equation 3.3)}$$

where *% secondary gas* is the amount of reactant gas added to the FAG plasma, F_R is the secondary/reactant gas flow rate (sccm) and F_{Ar} is the argon (discharge gas) flow rate (sccm).

3.3.5 Discharge Conditions

The FFGD source was designed to allow improved control over the plasma conditions compared with other GD sources. The conditions which are operator controlled are:

1) discharge voltage (V_d);
2) source pressure (P);
3) discharge gas flow rate (F, F_{Ar} or F_{gas});
4) source temperature (T_{source});
5) argon residence time (τ) – determined by P, F and T_{source} (equation 3.1);
6) ion exit bias (V_c);
7) percentage addition of secondary gas.

It was therefore possible to determine the effect of changing each condition individually, though τ is dependent on P, F and T_{source} (equation 3.1). The magnitude of the discharge current I_d was determined by conditions 1 to 6 as well as the surface area of the cathode exposed within the anode region and deposition of materials on the anode wall. This was accounted for by dividing the ion signal obtained by the discharge current value.

Throughout this investigation the source temperature remained approximately constant at 310 K. The source pressure was kept constant during each experiment since it directly affects both the discharge current and the residence time. For investigation of the effect of varying τ the argon flow rate was varied and the pumping rate varied to maintain the source pressure at a constant value. This was achieved by controlling the pumping rate through incorporation of a ball valve[23] in the pumping line prior to the source rotary pump. Table 3.2 illustrates the ranges of values used for each parameter.

Discharge Parameter	Minimum Value	Maximum Value
Discharge Voltage (V)	390	1000
Source Pressure (torr)	0.5	2
Argon Flow Rate (sccm)	70	343
Residence Time (ms)	~2	~24
Ion Exit Bias (V)	0	+/- 64

Table 3.2: Range of discharge conditions studied

3.3.6 Tuning the Mass Spectrometer

When analysing ions formed outside the mass spectrometer probe, ion transfer within the mass analyser (figure 3.11) is optimised by tuning five lenses;

1) Extractor lens (Ext) located just beyond the mass analyser orifice to accelerate ions into the mass spectrometer probe;
2) Lens 1 (L1) focuses the ion beam to allow optimum transmission through the electron impact region to the first focussing lens;

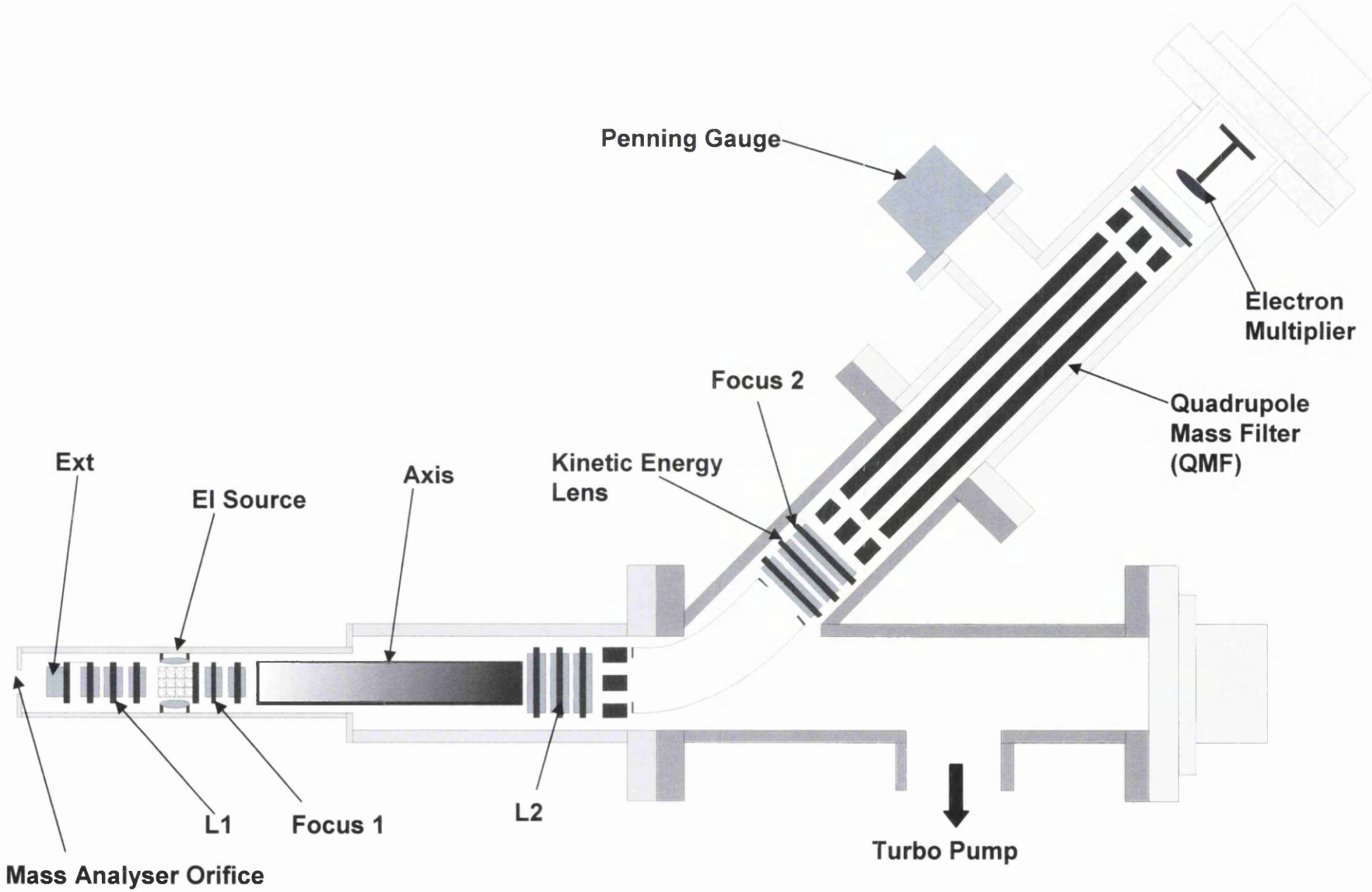

Figure 3.11: Mass analyser and ion optic schematic (adapted from reference 1)

3) Axis (sometimes referred to as the energy filter) is a cylindrical lens for which the voltage is set +/- 40V according to the polarity of the charge on the ions being analysed[24]. It was observed that this value was only applicable assuming that the lens stack was free from contamination;
4) Lens 2 (L2) accelerates the ions towards the electrostatic analyser (ESA) region
5) Kinetic Energy (Energy) lens decelerates the ion beam as it approaches the QMF to allow optimum transmission through the mass analyser.

The variation of ion intensity with applied lens bias could be monitored on the display panel of the instrument console or remotely via a pc using the "map" function of the software. Assuming that the ions were detected from a single source, each map should display a single maximum for ion transmission[24] (figure 3.12). When tuning, the kinetic energy lens was tuned first and the lenses then tuned and retuned in sequence (1 to 5). When the electron impact source was operated, only the last three lenses (3 to 5) required tuning since ion extraction from outside the mass analyser probe was not required.

3.4 The New Instrument

The new FFGD source constructed by Dash[1] (figure 3.13) was of coaxial design based on the most recent designs for the first and second generation instruments, as it was desired that the instrument would produce results similar to those taken on the older instruments. Like the other quadrupole instrument, the source was mounted outside the vacuum housing. All metallic parts of the source except the cathode were produced from non-magnetic stainless steel (316 grade). The details of the instrument are outlined in the following sections along with details of the developments made during this project.

3.4.1 The Active Discharge Region

The active discharge region, shown in figure 3.14 is of coaxial geometry i.e. a pin (cathode) extending through the centre of a stainless steel cylinder (anode). The cathode was machined from 3.2 mm diameter copper rod (Goodfellows[19], Cu rod;

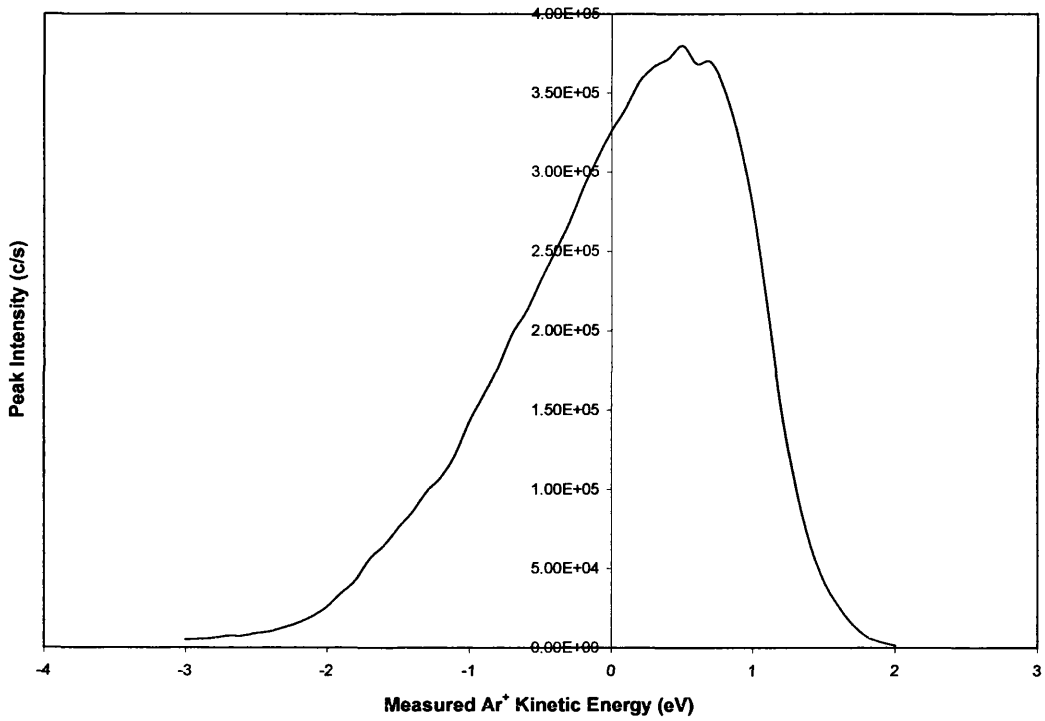

Figure 3.12: Ar^+ kinetic energy map generated using electron impact source with a repeller bias of +3V

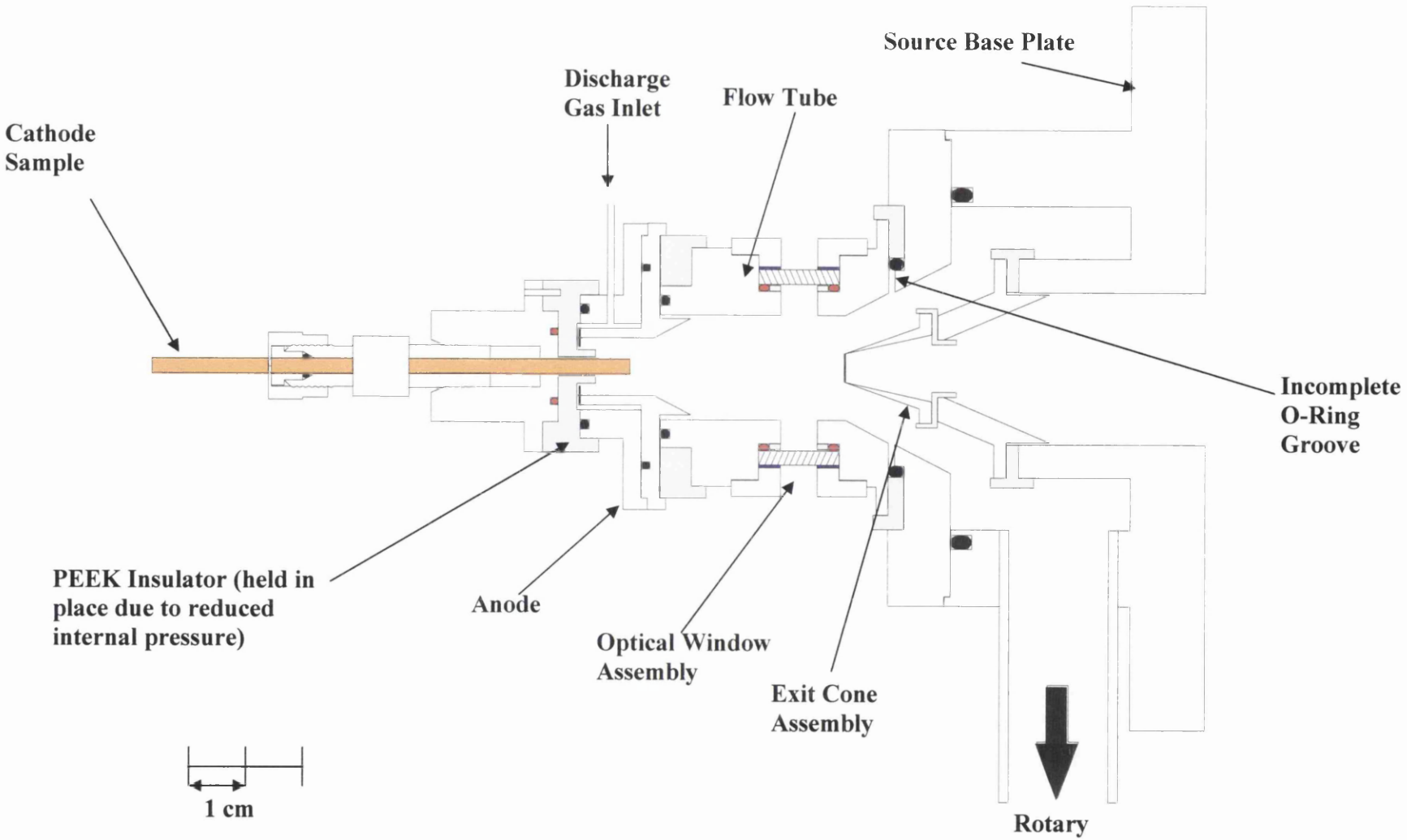

Figure 3.13: Prototype source design (adapted from reference 1)

99.99%) and passed through a 1/8" Cajon[23] fitting to allow the source to be sealed to the limits of helium leak testing. The electrical connection can be made directly to the cathode outside the source via a coaxial plug. The cathode insulator was machined from PEEK (Poly Ether Ether Ketone) rod. The exposed section of cathode extends 7 mm beyond the cathode insulator within the anode region. The cathode was held in position by atmospheric pressure, but only when the source was evacuated. It was sealed to the anode using a Viton O-ring

The anode consists of 2 sections which channel the discharge gas to allow uniform flow around the cathode pin. It is desirable that the gas flow through the source can be modelled as a plug, but due to protrusions the gas flow is disturbed. The gas enters through 1/16" stainless steel tubing and is directed past the cathode insulator and into the anode channel. The insulator between the anode and flow tube was also produced from PEEK, and again this region was sealed using Viton O-rings.

One unavoidable property of the glow discharge is the deposition of sputtered cathode material, in this case copper, on the walls of the discharge cell. However, deposition of a layer of copper on the stainless steel walls is desirable since it presents a fresh clean surface to the plasma (which is sensitive to surface conditions) and it therefore aids the discharge stability[3]. If significant deposition occurs on the cathode insulator however, it is possible for a short-circuit to occur. The discharge power supply is current limited and therefore when a 'short' forms the supply trip is activated. As the source is not isolated from the vacuum region of the instrument by a valve it is necessary to let the whole instrument up to atmospheric pressure for any source maintenance. This is undesirable as it takes several hours for the machine to pump down to a suitable operating pressure. Also, when the instrument is open to atmospheric gases water is absorbed into the walls. Water vapour is very efficient at quenching excited state species[3,25] and therefore causes significant disturbance to the mass spectra produced. Under vacuum, or as the source is heated due to the plasma flow, water vapour is released from the walls into the plasma.

Initially 'shorting' between the anode and cathode was a major problem and therefore it was decided to redesign the insulator. One possible way to reduce the probability of shorting is to prevent contact between the cathode pin and the insulator extending into the anode. In the original design (figure 3.14a) the internal diameter of the insulator was 0.8mm greater than the diameter of the cathode pin. The clearance

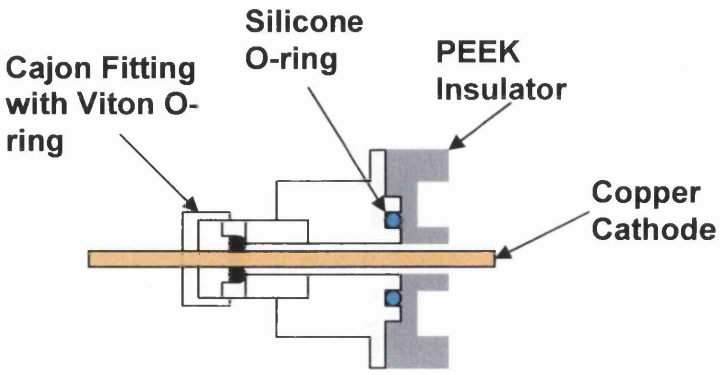

Figure 3.14a: Prototype cathode design

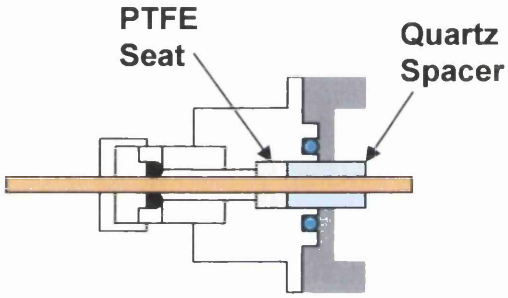

Figure 3.14b: First improved design

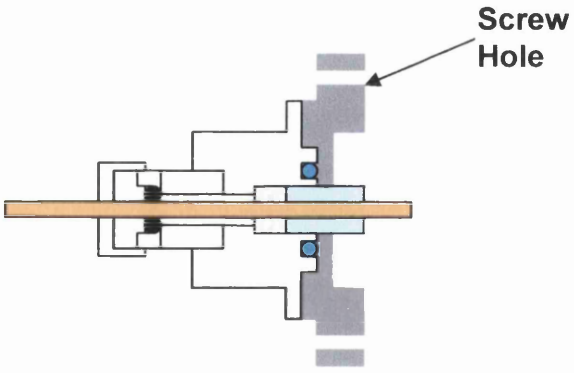

Figure 3.14c: Final cathode design
(Diagrams approximately actual size)

around the pin should have been enough to prevent shorting but due to poor centring of the cathode this was not the case. It was discovered that the pin was poorly supported between the Cajon fitting and the insulator.

The first new design (figure 3.14b) allows the cathode pin to be well centred using a PTFE cylinder within the cathode block to support the pin. However, the clearance around the pin is less than 0.1 mm. The cathode pin was found to be centred more accurately and a significant increase in the time necessary for a short to form was observed. The source should be cleaned every 2 to 3 months (depending on use) to prevent excessive build-up of material on the cell walls, and shorting has only been observed once between cleanings since the new insulator was produced in the first year of this project. As with the original insulator, however, the cathode was still only held in place by atmospheric pressure when the source was pumped.

To overcome this problem and to aid insulation of the anode from the flow tube a new insulator was designed (figure 3.14c). The new design is very similar to that shown in figure 3.14b, but the outer diameter has been increased to allow screw holes to be incorporated. As above, the new insulator significantly reduced shorting. The addition of the screws to support the cathode helps prevent damage to the cathode in the event of loss of pumping. In conclusion, the new cathode insulation meets the requirements for prevention of shorting and improved support of the cathode. The cathode itself is changed at the end of each day to ensure the instrument has time to pump down before it is next used and to ensure that a fresh pin is used each day to minimise discrepancies between results.

3.4.2 The Flow Tube

The flow tube section (figure 3.15a) was 33 mm in length with an internal diameter of 22 mm. The length was important to allow incorporation of quartz windows for optical studies of the flowing afterglow region. The distance between the cathode pin and the tip of the ion exit cone was 39 mm. The window assemblies (illustrated in figure 3.13 but not in 3.15a) were sealed using silicone O-rings. The internal diameter of the flow tube begins to increase downstream to allow pumping around the ion-exit cone, which extends into the flow tube to reduce the cathode-ion exit distance. The secondary gas inlet was produced from 1/16" o.d. non-magnetic stainless steel tubing which entered vertically through a Cajon[23] fitting beneath the

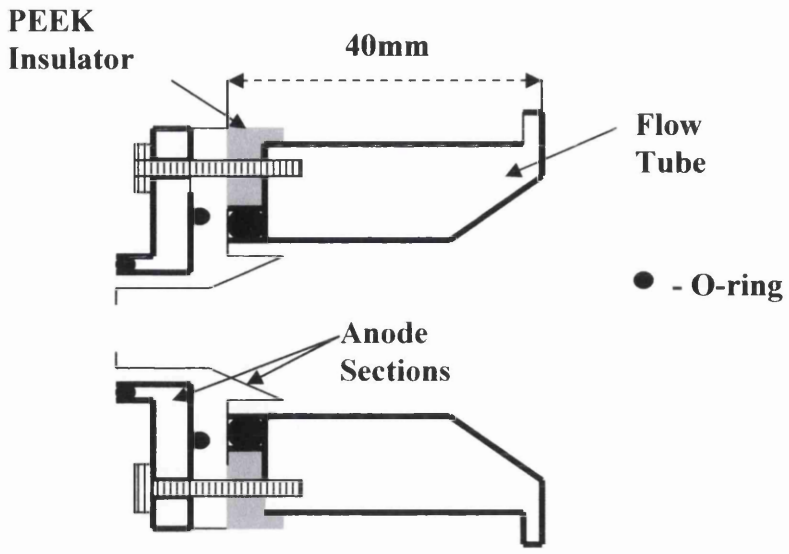

Figure 3.15a: Prototype flow tube design before electrical isolation (approximately 1:1)

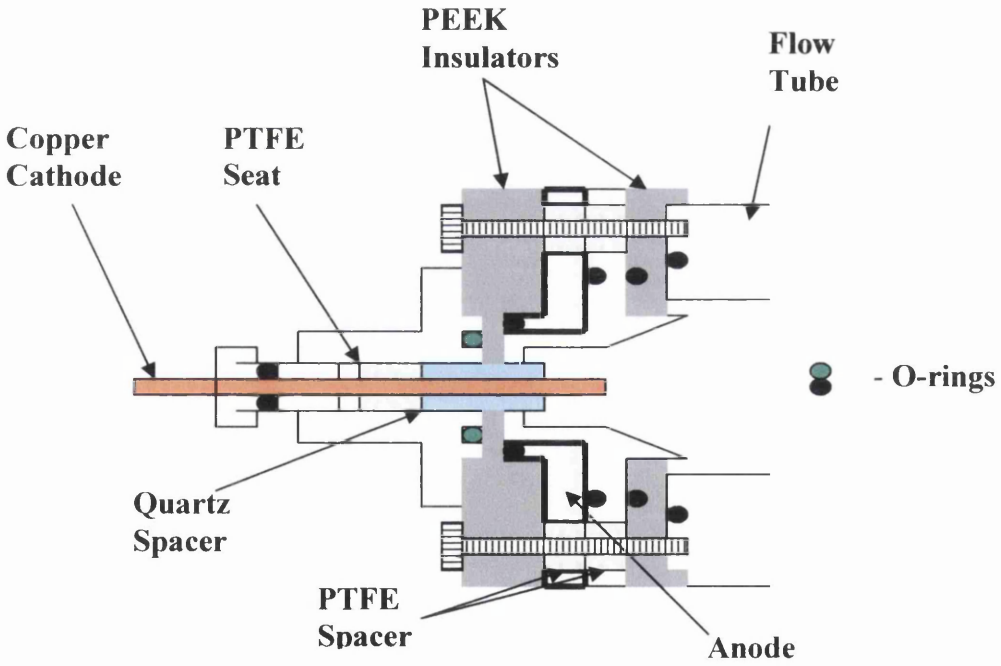

Figure 3.15b: Electrical isolation of anode from flow tube (approximately 1:1)

source and terminated approximately 10 mm inside the flow tube (slightly off centre). The source pressure transducer was mounted on a short length of ¼" o.d. stainless steel tubing extending from the source through a Swagelok[23] fitting at the top of the flow tube. The pressure has to be measured off-axis to avoid disturbance due to the gas flow.

In the prototype design the flow tube was at anode potential. A number of authors have cited the use of one of the vessel walls including the anode or cathode as a reference electrode for electrical probe studies[1,5,26-28]. To achieve this it was necessary to prevent contact through the screws holding the anode in place and to prevent contact between the 2 parts directly. To prevent direct contact, the O-ring groove on the flow tube was removed and a new groove cut into the flow tube body. A new PEEK insulator was produced to fit between the anode and the flow tube. It was necessary to redesign the insulator to allow the joints to be sealed by O-rings (figure 3.15b).

To prevent contact through the screws, tightened into the flow tube walls to support the anode, initially the stainless steel screws were replaced with nylon screws. This did work; however, to provide a gas tight seal it was necessary to tighten the screws to a point at which the nylon screws were distorted and therefore frequent replacement was necessary. To overcome this and to allow the cathode to be held in place even when the source was not being pumped out a new cathode insulator was produced (figure 3.15b). The new PEEK piece insulates the screw heads, but not the thread, from the anode. To overcome this problem, Teflon sleeving was fitted into the anode screw holes. There was no need to modify the cathode or the design of the anode (except to insert the Teflon sleeves) and therefore the original O-rings could be used again. Since introduction of the new insulator the cathode, anode and flow tube have remained insulated from each other between routine source cleaning times. It is now also easier to achieve a good vacuum seal as the cathode is well supported.

In the prototype design the flow tube was insulated from the source flange to ensure that the main body of the source remained electrically isolated from the body of the instrument[1]. To achieve this, a PEEK ring insulator was sandwiched between the flow tube and source flange and nylon screws were used to hold the flow tube in place (figure 3.16). Though the insulator has kept the two sections electrically isolated the incomplete groove for the O-ring meant that there was a small air leak. The presence of air causes a dramatic change to the nature of the discharge[29-32].

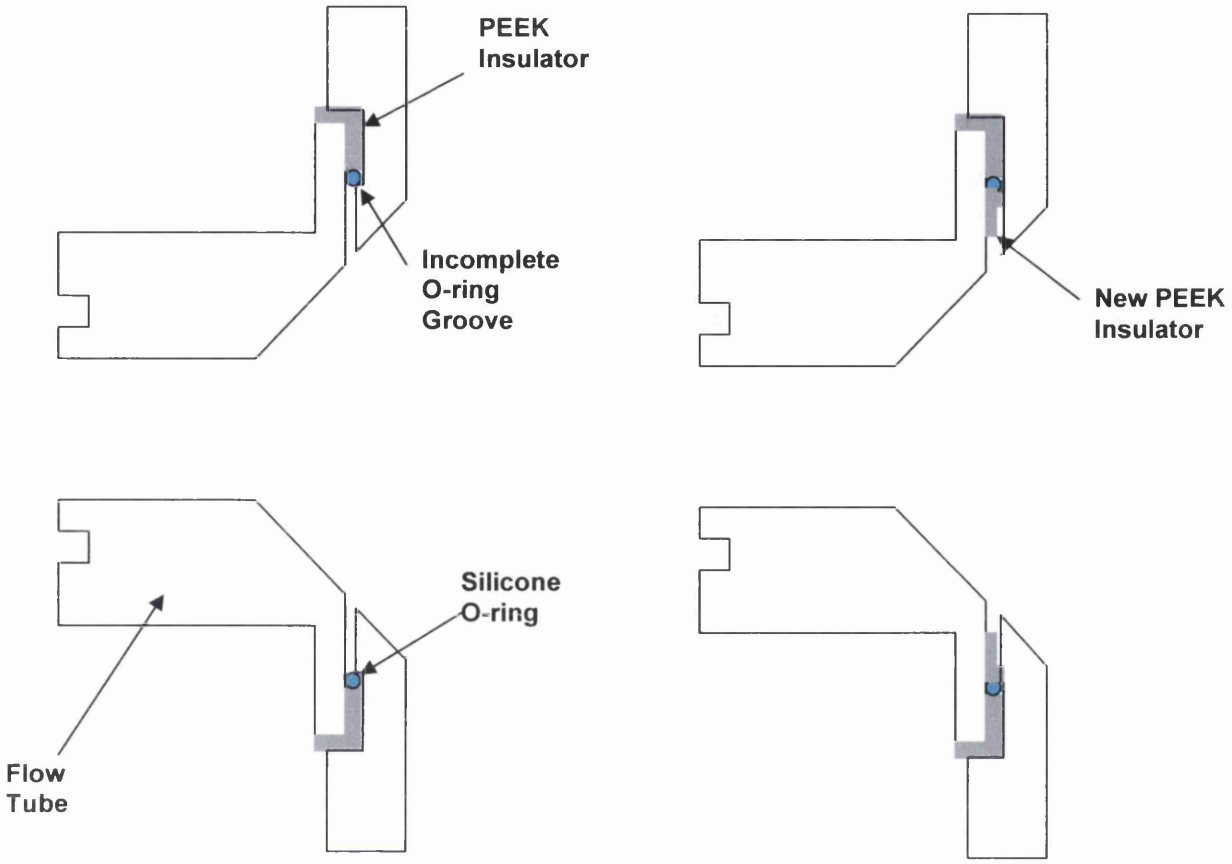

Figure 3.16: Insulating the flow tube from the source flange and sealing connection (approximately 1:1)

Figure 3.16 illustrates how this section was modified to prevent leakage whilst retaining electrical isolation between the two source sections. The original PEEK insulator remained unchanged. However, the source flange was machined to remove the metal lip originally used as the second half of the O-ring groove. To complete the groove a new PEEK ring was machined with the same thickness as the original. A section was cut out of the ring to prevent shorts due to build up of deposited copper from the afterglow. Since modification the source seals to the limits of helium leak testing and no shorts have been observed between routine cleanings of the source, usually 2 - 3 months. This is very much less often than is required for a standard 'static gas' discharge.

The flow tube was later redesigned to improve secondary gas mixing and to allow electrical probe studies. These are discussed in the following sections (3.4.3 and 3.4.4).

3.4.3 The Secondary Gas Inlet System

One way in which it is possible to better understand the processes occurring within the plasma is to monitor the ions formed on addition of secondary gases to the FAG plasma. As detailed in the previous section, the secondary gas inlet entered the source vertically through the base of the flow tube and terminated within the FAG 8 mm in front of the ion exit cone. Upon addition of secondary gases to the afterglow it was observed that a greater addition of gas was required to replicate the effects observed in the other FFGD instruments. It was realized that the efficiency of the gas mixing was greatly reduced due to the close proximity of the pumping aperture (figure 3.17a). Since the gas was entering close to the pumping aperture it is clear that the bulk of the gas was carried away before efficient mixing with the FAG plasma could occur.

Various positions of the secondary gas inlet were tried. A new flow tube was therefore designed and built (figures 3.17b and c) with three possible positions for the secondary gas inlet. One inlet entered the source further upstream (figure 3.17b) (i.e. further from the ion exit). The new design also incorporated 2 inlets positioned at 60° relative to each other closer to the ion exit orifice. As with the original design they terminate slightly off centre, in this case to avoid contact between the 2 inlets. This also expanded the opportunity for electrical probe studies (see section 3.4.4). In the

new design the centre of the gas inlet is positioned 3.9 mm before the ion exit cone (using the original ion exit cone designed by Dash[1], using the new cone, see section 3.4.5, this is increased to 13.4 mm). The position relative to the cone was enforced by the length of the flow tube and the size of the Swagelok[23] fittings used to hold the inlets. It is more desirable to increase the distance between the inlets and the ion exit to allow a longer time for gas mixing and therefore longer for reactions to occur.

The second design investigated used only one inlet the centre of which is 15.9 mm from the ion exit (25.4 mm using the new cone). As previously stated, the further the inlet is from the ion exit the longer the gas mixing time, and therefore the number of collisions between the secondary gas molecules and the afterglow plasma should be greater. Using a source pressure of 0.9 Torr and argon flow rate of 170 sccm the additional mixing time is 5.8×10^{-4} s. Equation 3.1 allows calculation of the plasma gas residence time, τ, flowing through a known volume, V_{cell}, with a known gas flow rate, F_{gas}. The addition of small quantities of secondary gas should not induce a significant change to any of the values in the equation and therefore the average residence time of the secondary gas flowing from the gas inlet to the tip of the ion exit cone may be determined using V_{cell} = volume of the flow tube through which the secondary gas flows.

Equation 3.1 assumes 'plug' flow of the FAG plasma. This is aided by the relatively short length of the flow tube. It is still possible to use the instrument for electrical probe studies in this configuration as the inlet is insulated from the flow tube and protrudes the same distance into the plasma as the probe (A) used previously.

The third design, shown in figure 3.17d, was very similar to the second but incorporates an inlet ring with five holes, each with roughly 0.5 mm internal diameter, pointing upstream. The inlet is in the same position relative to the ion exit as that in the second design. The centre of the ring is in line with the ion exit orifice and the gas should be released into the afterglow over a far wider area therefore further improving gas mixing. One might predict that, as the inlet was designed to improve gas mixing and increase the interaction time, a smaller quantity of gas would be required to have the same effect as either of the previous designs.

To determine the effect of redesigning the secondary gas inlet a known reaction was chosen and performed with each setup. The reaction chosen was the addition of hydrogen to the FAG plasma since it has been widely studied within this group[1-7,33-35] and has a dramatic effect on the Ar^+ ion signal. When hydrogen is added to the

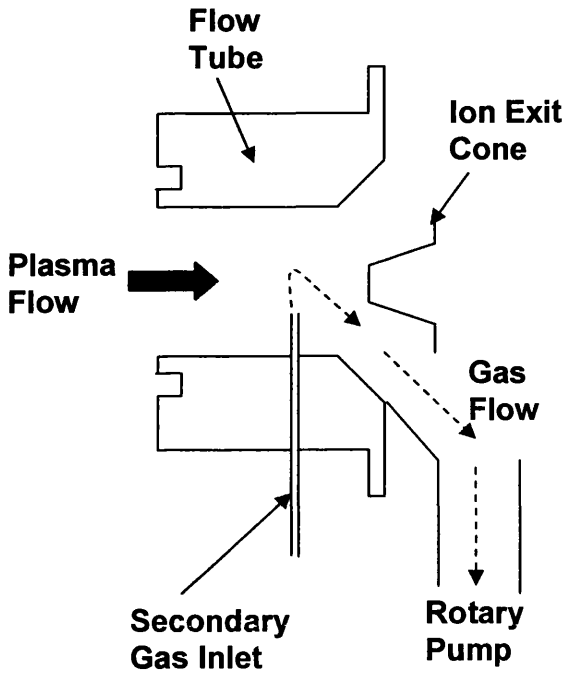

Figure 3.17a: Secondary gas inlet position on prototype 3rd generation instrument (approximately 1:1)

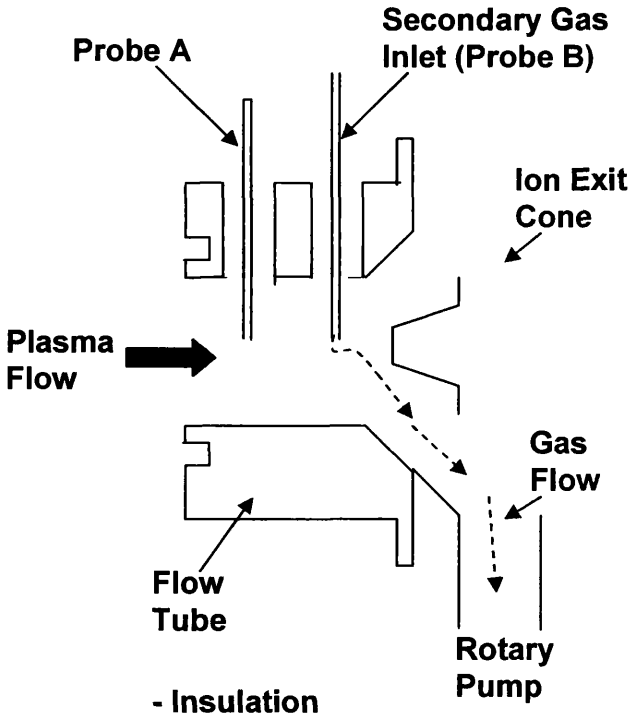

Figure 3.17b: New flow tube secondary gas inlet position (side view, approximately 1:1)

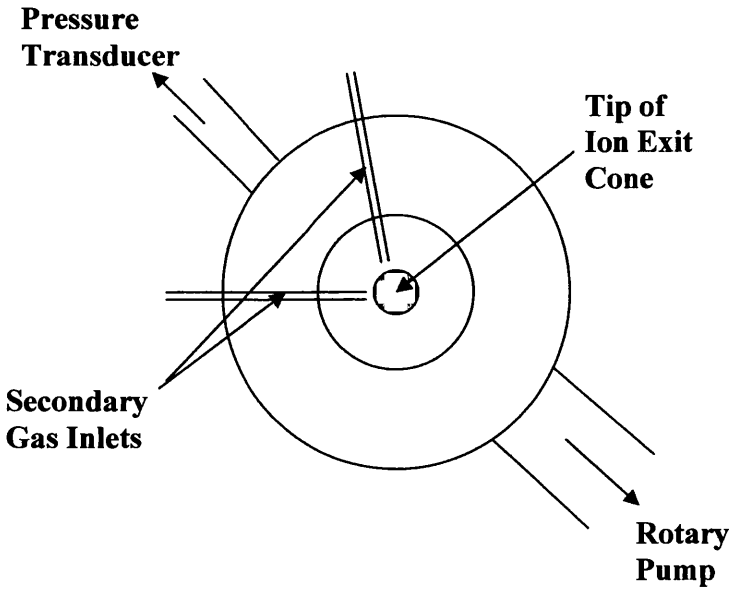

Figure 3.17c: New flow tube secondary gas inlet positions (end view, approximately 1:1)

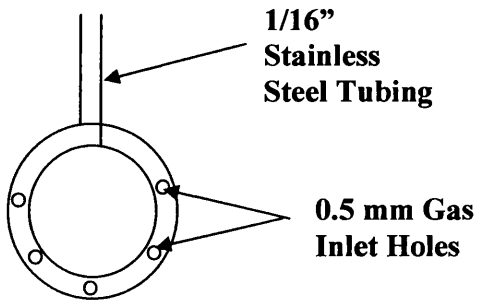

Figure 3.17d: New secondary gas inlet design to improve gas mixing (scale = 1:3)

flowing plasma the observed Ar^+ intensity decreases sharply until it is removed from the spectrum. The amount of hydrogen required for this to occur will depend on the efficiency of the gas mixing and therefore the position of the inlet. Table 3.3 illustrates the amount of hydrogen, as a percentage of the overall gas flow, required to completely quench the Ar^+ ion signal.

Inlet Configuration	Hydrogen Required to Quench Ar^+ Ion Signal (% of the total gas flow)
Prototype (designed by Dash[1])	7.6 ± 0.8
Two inlets close to cone (figures 3.16b and c)	1.73 ± 0.8
Single inlet upstream	4.2 ± 0.8
Ring inlet upstream	3.7 ± 0.8

Table 3.3: Amount of hydrogen, as a percentage of the total gas flow, required to quench the Ar^+ ion signal. (V_d = 800 V, P = 0.9 Torr, F_{Ar} = 170 sccm, τ = 2 ms, V_c = -24 V, cell bias (V_{cell}) = +80 V, cylinder bias (V_{cyl}) = -180 V and einzel lens bias(V_{ein}) = +20 V (einzel, cell and cylinder biases are explained in section 3.3.3)

Since the flowmeter used can measure only to the nearest standard centimetre cubed per minute (sccm) it was not possible to obtain exact values for the hydrogen flow rate at low flows, and therefore exact values for the percentage addition of hydrogen were not possible, hence the large errors indicated in table 3.3 (most significant for low gas flow rates). However, the values measured by the ratemeter show that the most effective quenching is allowed through the two inlets close to the cone. This is probably due to the fact that the hydrogen concentration in the ion exit region is very high due to the position of the gas inlet relative to the cone. It is possible that much of the chemistry occurs within the sheath around the ion exit, and therefore the higher concentration of hydrogen in this region would have a larger effect. The next most effective is the new ring inlet due to the gas distribution via five holes, followed by the single straight inlet in the same position. On restoring the source to its original configuration the amount of hydrogen required to quench the argon ion signal, under the same conditions, was approximately double that for the upstream inlets and more than four times that required using the two inlet system.

The two inlet design clearly does not allow sufficient time for complete mixing with the afterglow plasma before impinging on the ion exit cone.

It was believed that the use of the ring inlet would improve mixing over the straight inlet by improved dispersal for the gas due to the number of points of entry into the FAG plasma and due to the increased turbulence induced around the inlet. However, on analysis it appears that there is very little difference induced by using the ring inlet compared with the straight inlet. The use of a straight inlet was initially preferred as this would cause the minimum disturbance to the flowing plasma. To use the secondary gas inlet for electrical double probe studies it was decided that the probes should have equal surface areas.

It was concluded that to allow sufficient time for gas mixing the upstream inlet is the most appropriate solution. The ring inlet appears to improve the secondary gas mixing over that for a single straight inlet. However, the difference in the mixing efficiencies of the straight and ring inlets was not significant enough for either to be classed as the "best" setup.

3.4.4 Electrical Probe Studies

A double probe setup[17,18,5] is often used to monitor the electrical characteristics of plasma. The system used within this group[1,5,6] can be used to monitor the plasma conditions throughout an experimental run, and therefore variation in plasma potentials can be compared directly with effects on ion intensity. The new flow tube (figure 3.17b and c) was designed to allow electrical probe studies. Vespel 1/8" to 1/16" reducing ferrules insulate the secondary gas inlets and probe A from the flow tube and therefore they are floated at the local plasma potential. The flow tube and ion exit cone were also isolated from surrounding sections to allow their use as electrodes. It was discovered that 1/16" steel tubing and the relevant Swagelok[23] fittings were the smallest readily available. This is not ideal since the probe area is relatively high (49.87 mm^2) although, as Mitchell[5] observed, the results obtained could be used comparatively with others generated using the same instrument.

Since the dimensions used in this instrument were very similar to those used previously[1,5] some comparison can be drawn between the results obtained in this investigation and those obtained using the first generation instrument. In single probe studies such as those performed by Langmuir and Mott-Smith[27,28] a single probe was

immersed in the plasma and biased relative to a larger reference probe (commonly the anode or another vessel wall). In this investigation, and those performed previously by Mitchell[5] and Dash[1], the flow tube wall and the ion exit cone were used as additional probes.

The probe circuitry, constructed by Newman[6], is illustrated in figure 3.10. An electrometer is incorporated to allow measurement of the current flowing between the probes. When a bias is applied between two probes the current flowing between them will change. The use of a number of 9 V batteries connected in series with a potentiometer, and a digital voltmeter (DVM) allows control of the bias with minimal interference. Using the system described it is possible to generate I-V curves as described in section 2.8. It is also possible to determine the relative potentials at four different points within the plasma; these are at:

1. probe A – closest to anode;
2. probe B – gas inlet closest to the ion exit cone;
3. W – the wall of the flow tube;
4. C – the ion exit cone.

Use of the electrical probes has proved to be valuable as an analytical tool, especially since the probe experiment can be run alongside the mass spectrometric studies. Initially there was a problem of short-circuits occurring between the probes (A and B) and the sides of the Swagelok fitting, however, covering the exposed length of probe within the fitting, with silicone rubber tubing, has removed the problem. Very little maintenance was required to keep this setup operational. The probes were cleaned at regular intervals to prevent excessive build-up of sputtered copper which in principle would increase the surface area of the probes, and therefore could influence the results obtained. However, in practice, the areas of the probes are sufficiently large that this is not a problem, which it would have been for very small Langmuir probes.

3.4. 5 The Ion Exit Region

The ion exit region (figure 3.18a) consisted of 2 sections. The ion exit plate was mounted onto a cone attached to a second larger cone. The smaller cone was

insulated from the larger using ceramic washers and nylon tubing to cover the screws, fitting into a Teflon seat. The cone sections were sealed using viton washers. The ion exit plate was produced from a non-magnetic stainless steel (316 grade) disk of 7 mm diameter and 0.05 mm thickness. An ion exit orifice of 0.3 mm diameter was drilled in the centre of the plate. The thickness of the disk is important to prevent channelling the gas and to allow unrestricted expansion of the gas inside the cone. The second cone section was sealed to the source flange using a viton washer. The discharge gas was pumped past the ion exit region by one or two rotary pumps (depending on the required gas flow rate and source pressure).

To allow application of an ion exit bias the smaller cone had to be insulated from the body of the source at all times, although connected in the external electrical circuit. A further objective for this project was investigating the effect of accelerating the ions across the field free region between the ion exit orifice and the inlet to the mass spectrometer. It was hoped that this would reduce the loss of ions and enable the kinetic energy function of the mass spectrometer probe to be checked for accuracy. For this to be possible the FFGD cell had to be floating, and therefore insulated from the main chamber vacuum housing. A new cone and set of insulators were designed to minimise the persistent problem of short-circuiting.

The original cone turned out to be magnetic stainless steel. Magnetic fields could influence formation and passage of ions[36] in the ion exit region. The new cone was produced from non-magnetic stainless steel and incorporated countersunk screw heads to minimise the disturbance to the plasma flow. Another problem with the original design was the small surface area (less than 1mm in width) upon which the front plate, a thin stainless steel disk, had to be spot-welded. It was difficult to position and seal the disk when welding and led to some damage to the cone, so the first new design (figure 3.18b) included a much larger surface area. The external diameter of the seat is 7 mm and the internal diameter is 3 mm therefore leaving 2 mm thickness upon which to weld the plate.

To reduce the number of parts used to seal the cone and isolate it from the ion exit, a Teflon 'top-hat' shaped insulator (figure 3.18c) was produced. This also helped to centre the cone correctly. To insulate the screws from the cone, the holes in the cone were expanded and Teflon pieces were fitted (figure 3.18c). Teflon is distorted when pressure is applied and so the force required to seal the fitting meant that the screws were cutting through the top therefore causing an electrical short-

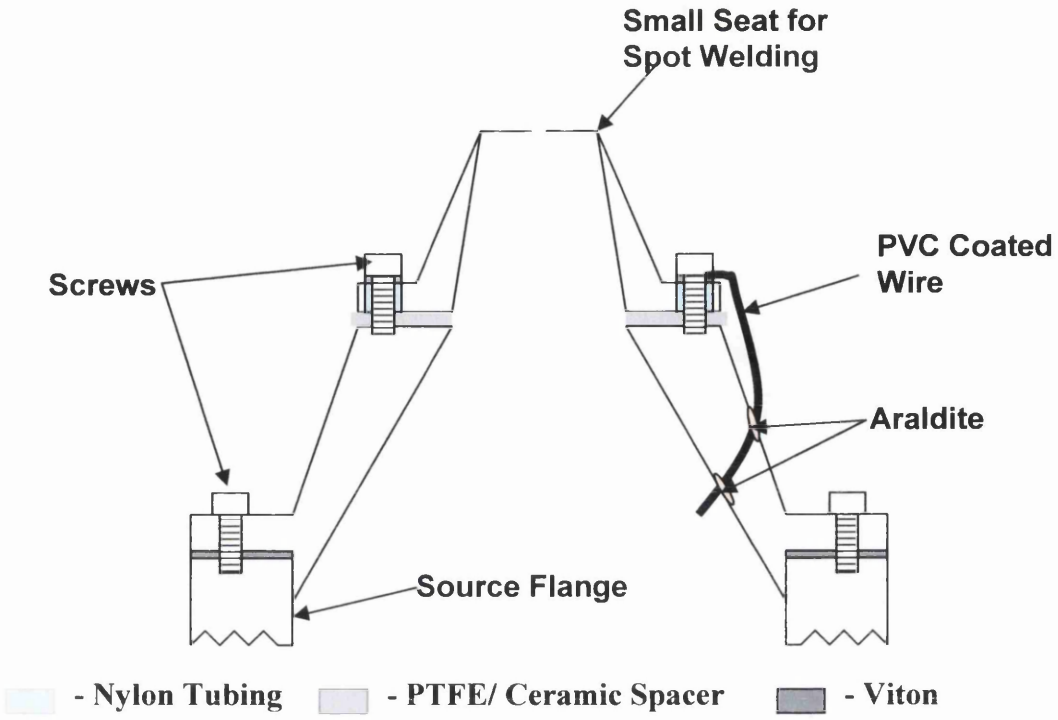

Figure 3.18a: Prototype two-piece cone design (approximately 1:2)

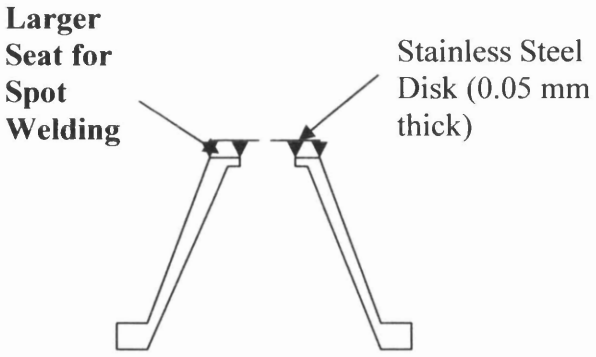

Figure 3.18b: Redesigned front cone allowing easier spot welding (approximately 1:2))

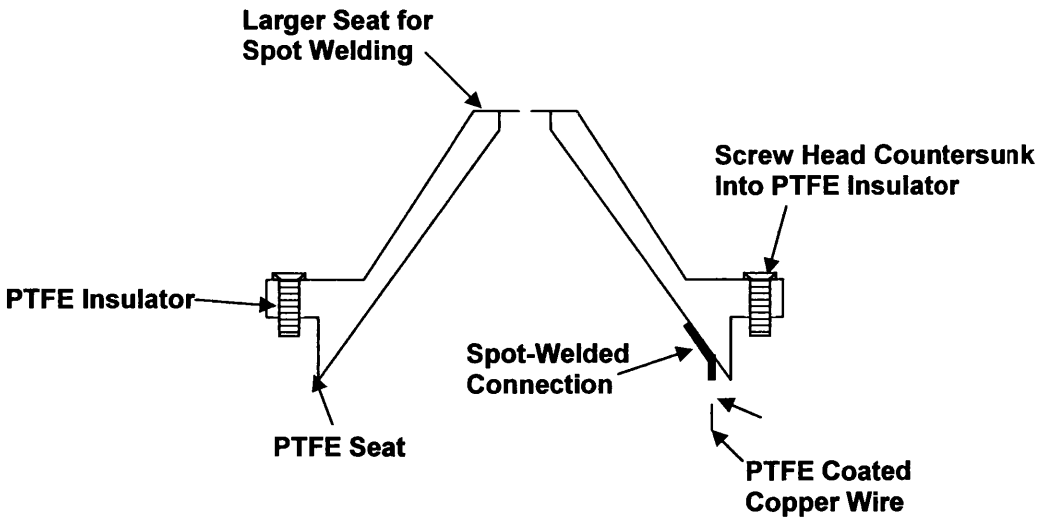

Figure 3.18c: New one-piece ion exit cone (approximately 1:2)

circuit. Unfortunately, this meant that a washer had to be used and therefore the screw head is not completely recessed into the cone. It was decided to use 2 washers – stainless steel on top of Teflon. The purpose of the stainless steel washer is to reduce the distortion of the Teflon washer and allow the screws to be tightened further, to make a good gas seal.

A number of problems observed were due to the original electrical connection to the cone (figure 3.18a). Materials not suitable for use in a vacuum were used including Araldite to seal the hole in the wall through which the wire passed, and the wire itself was coated in PVC. Although these materials are not known to have influenced any of the results it was undesirable and unnecessary to have them present within the instrument. The presence of the wire in the discharge source could also disturb the plasma flow in much the same way as the screw heads used to secure the cone. To overcome these problems the electrical connection in the new cone design (figure 3.18c) is made via a length of wire spot welded inside the cone, outside the FFGD cell and therefore not disturbing the plasma. The PVC coated wire was replaced with Teflon coated wire, which is suitable for use in a vacuum, and the electrical connection was completed using a crimp connector.

Since modification, problems of shorting have been very rare but as the cone is immersed in the flowing plasma the insulators do, after a significant amount of time, become coated in copper. They can then be cleaned in nitric acid, rinsed with distilled water and methanol, and then reused. The spot-welded electrical connection to the cone, although now suitable for use in a vacuum, can be broken relatively easily during maintenance and must be re-welded. The use of non-magnetic stainless steel in the cone construction appears to have made a negligible difference to results.

3.4.6 Gas Transfer System

The gas handling system (figure 3.19) for the new instrument was based on the systems used in the previous FFGD instruments. There were two gas lines to allow delivery of the discharge gas (argon) and the secondary gases. The plasma gas was usually delivered at 40-60 lb/in^2 whilst the secondary gas was delivered at a lower pressure (typically 30 lb/in^2 or below) since much lower secondary gas flow rates are required. All of the gas line used was stainless steel, usually of 1/8" outer diameter, although, ¼" was used where necessary and the gas inlets are 1/16". The gas flow is

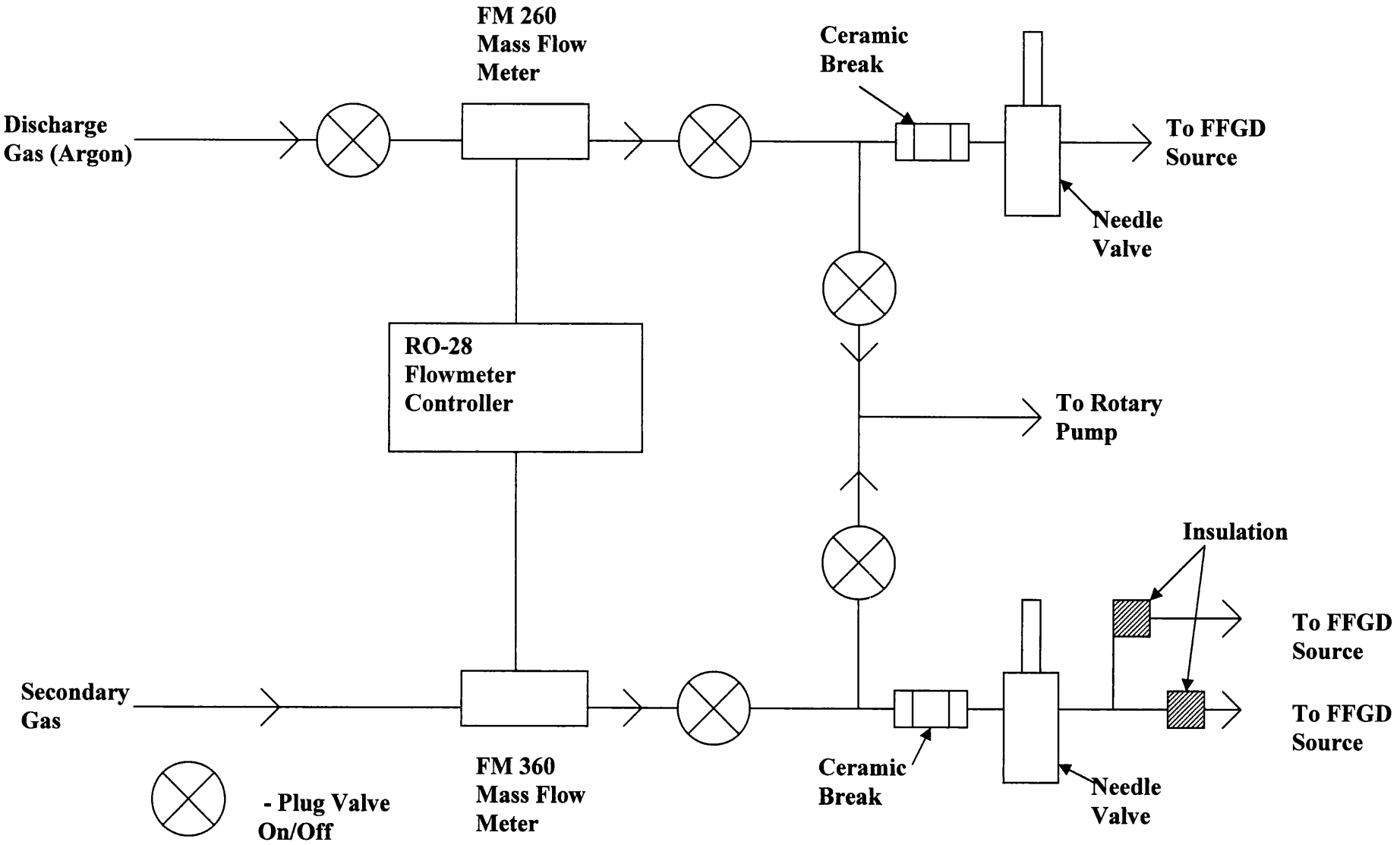

Figure 3.19: Gas transfer system

monitored using Tylan[22] mass flow meters (models FM260 and FM360) and displayed on a Tylan[22] 4 channel controller (Model RO28). The gas flow rates were controlled using a Negretti needle valve[37] for each inlet as it was decided that better control would be allowed than is possible using the electronic mass flow controller function. The needle valves were designed to allow titration of small constant flows of gas. The flow controller was set so that maximum throughput was allowed whilst still monitoring the gas flow rate.

The gas lines can be evacuated using an intermediate purge line which is connected to the source pumps. When not in use the pumped line can be closed off using a plug valve. Due to the high discharge voltage used, the gas lines were isolated from the source using 3 kV ceramic breaks[38]. Originally, as described in section 3.4.3, there was a single secondary gas inlet.

3.4.7 Source Electronics

Figure 3.20 illustrates the electrical circuit for the FFGD source. The glow discharge is powered by a Wallis Hi-Volt[39] (series XRV MK III) power supply. The cathode is biased negatively with respect to the power supply earth. The power supply itself receives its power via an isolating transformer (Legrand[40] model 322). The discharge power supply can deliver a constant voltage (0-5000 V) or constant current (0-10 mA). Throughout this work the supply was only operated in constant voltage mode and the power supply was set to trip if the discharge current was greater than 10 mA. The discharge was usually operated well below 10 mA. The discharge current (I_d) and voltage (V_d) were originally read from analogue meters on the front panel of the supply and a DVM connected to the remote output of the supply. Early in this project it was discovered that neither provided the correct values, and it was therefore necessary to calibrate the DVM. The measured I_d and V_d values now have an error limit of 0.1%.

The source pressure was monitored using a baratron pressure transducer (Datametrics[41] model 1173) mounted onto the flow tube as described in section 3.4.2. The pressure transducer was powered by the same transformer as the source power supply. The flow tube and the pressure transducer were therefore at anode potential. The gas flow rate was measured using a Tylan General[22] flow controller as described

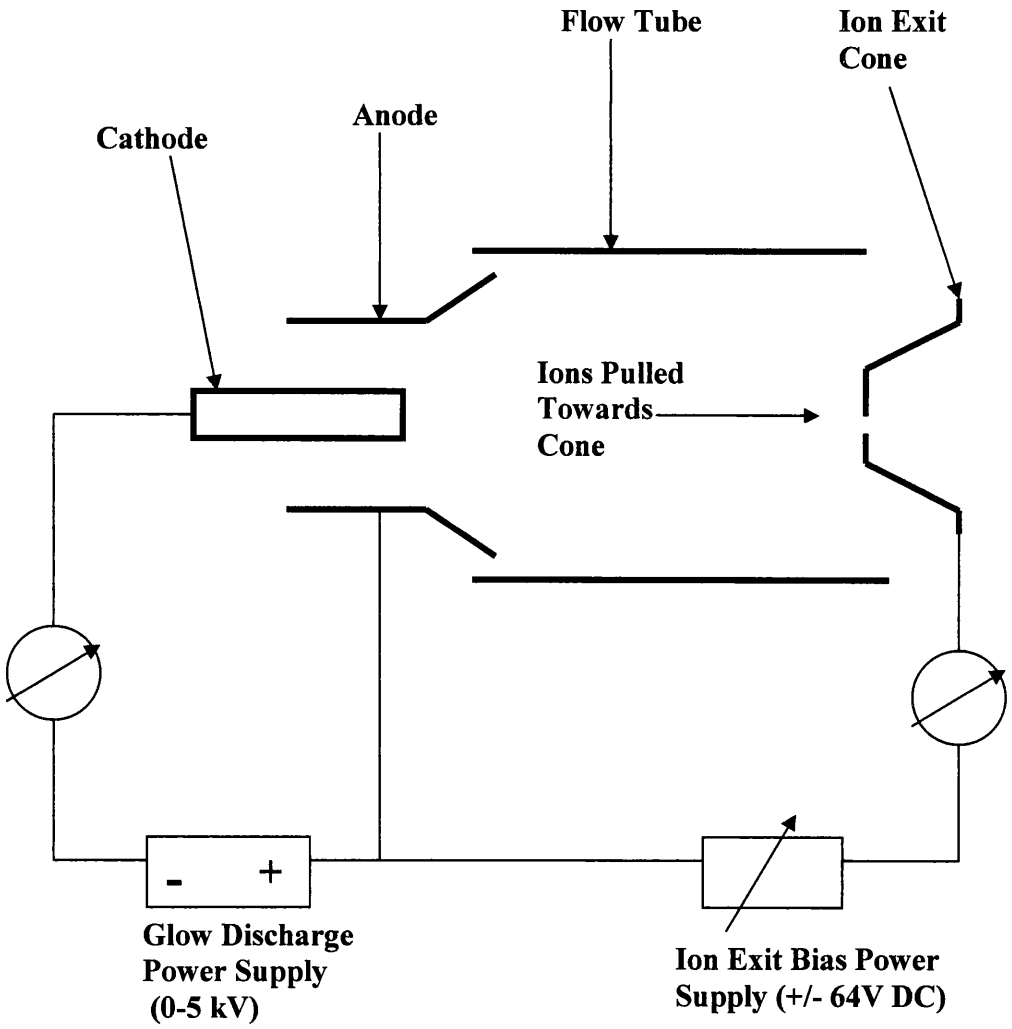

Figure 3.20: FFGD Source Electrical Schematic

in section 3.4.6. The flow controller was run on mains power as the flow meters were insulated from the source.

The ion exit cone was powered using an Isotech[42] model IPS601A power supply, which can provide a potential difference between 0 and 64 V between the anode and the ion exit cone. Switching the connections to the supply reverses the polarity. The ion exit is biased relative to the anode by connecting one terminal to the anode i.e. to bias the cone positively the negative connection on the power supply is connected to the discharge power supply earth. The ion exit power supply is current limited to 1 A. The bias can be read from the analogue display on the unit and the cone current was monitored on a MK6 Avometer[43] incorporated into the circuit between the cone and the power supply during this project.

3.5 Ion Transmission from the Source to Mass Analyser Probe

The ion intensities observed using the third generation instrument were significantly lower than those observed using the second generation instrument and therefore the sensitivity of the technique is reduced. Initial measurements illustrated that the second generation instrument, despite running the same source conditions, could produce signals a factor of 100 higher. This was attributed to a large gap across the "vacuum" region between the discharge cell and the mass spectrometer probe (figure 3.21) in which the ion beam was not focussed. A second problem is the extended nature of the mass analyser probe to allow for kinetic energy analysis. This lowers transmission through the analyser.

In each of the previous instruments the ion beam was continually focussed throughout instrument therefore reducing attenuation losses. Figure 3.21 illustrates the initial configuration of the new instrument. The region between the ion exit orifice and the entrance to the mass spectrometer was field-free, with a distance of 86 mm. These distances were dictated by the instrument to hand. Ions could be observed from the FFGD cell, nevertheless it was thought that the ion transmission could be improved considerably. Three changes were decided:

1) to attempt to reduce the distance between the ion exit and the focusing lenses;
2) accelerate the ions towards the mass spectrometer probe;
3) focus the ion beam to reduce attenuation losses.

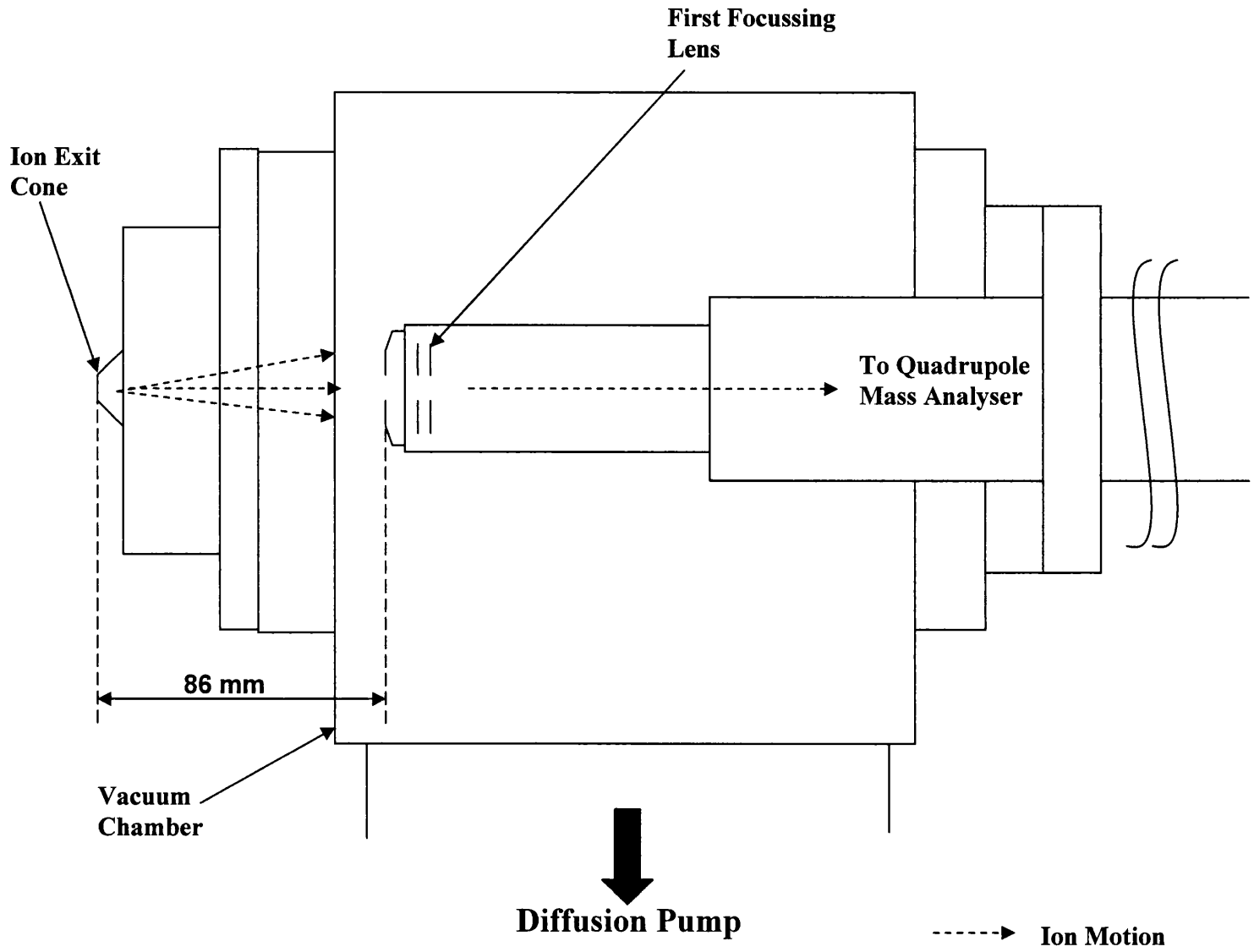

Figure 3.21: Initial configuration of new instrument (approximate scale = 1:2)

3.5.1 Reducing the Cell-Probe Transmission Distance

3.5.1.1 Modification

To reduce the distance between the ion exit orifice and the mass spectrometer probe it was necessary to adapt the mass spectrometer probe quite significantly from the manufacturers design. It was also necessary to electrically 'float' the FFGD cell, and some of the gain was lost by the need to incorporate a polycarbonate flange. Figure 3.22 illustrates the new arrangement. The net reduction of the inter-orifice gap was therefore only 11 mm. The length of the lens cover was reduced to prevent extension beyond the mass spectrometer entrance.

3.5.1.2 Results.

Unfortunately, the reduction of the ion transmission distance coincided with an apparent reduction in the pumping efficiency of the pumps of the main chamber. Since the funding was not available to replace the pumps the maximum pressure at which the source could be operated without exceeding the safe operating pressure for the electron multiplier of the mass analyser was therefore reduced to approximately 0.5 Torr, well below the 1-2 Torr desired. An attempt was made to overcome this problem by designing a cap to fit over the end of the mass spectrometer probe housing, thereby restricting its exposure to the escaping discharge gas. The cap was secured onto the stainless steel cylinder surrounding the probe ion transmission system with three screws. An ion entrance aperture, of smaller diameter than that of the probe orifice, was drilled into the end of the cap. A number of diameters were tested and it was concluded that a 4 mm orifice should be used since it allowed the source to be operated at 1 Torr pressure without exceeding the maximum operating pressure of the electron multiplier in the mass analyser. A lower diameter orifice, despite allowing higher source pressure, is undesirable as the collection of ions would be restricted. However, it became impossible to detect ions from the FFGD cell with this new arrangement.

On reversing the changes made, i.e. increasing the distance between the ion exit and mass analyser orifices the pressure within the mass analyser region was still found to be significantly higher than that observed before modification (for the same source

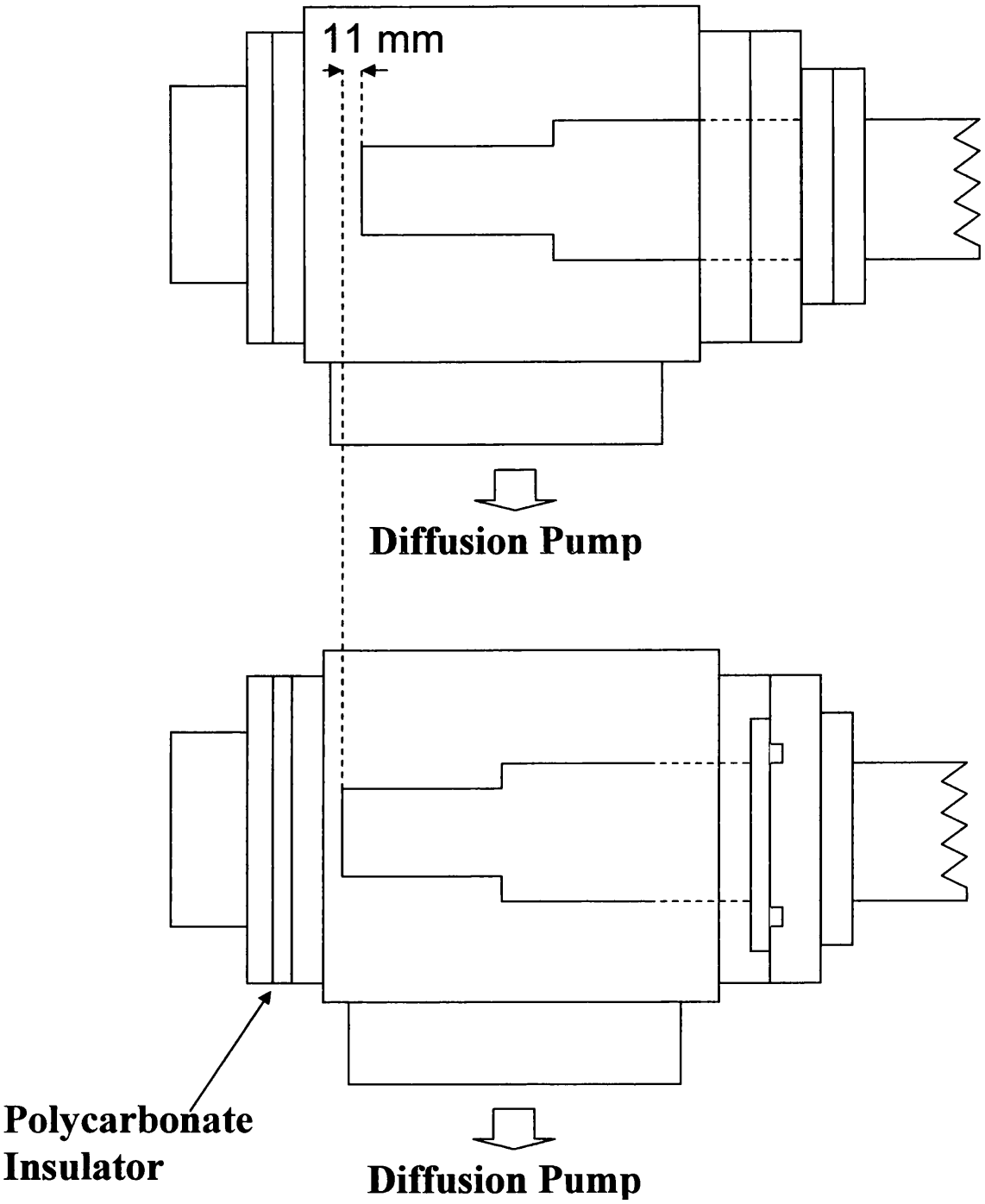

Figure 3.22: Reduction of distance between ion exit orifice and mass spectrometer (scale 3:1)

pressure). As above, it was not possible to detect ions extracted from the FFGD source. This may be due to the increase in argon residence times enforced by the limited gas flow rate and source pressure allowed. In order to allow ion detection it was necessary to provide an accelerating voltage across the inter-orifice gap. One further possibility is that the pressure outside the orifice is still too high and the equilibrium between the Rydberg states and formation of ions and electrons is still strongly in favour of Rydberg states. According to the theory enunciated in section 2.7, the Rydberg gas ionises when the plasma density drops below 10^7 cm^{-3}. If the pumping efficiency in the region of the aperture is insufficient, the Rydberg gas remains stable for a greater distance beyond the aperture and requires the presence of a field to ionise it in time for ions to be collected efficiently by the mass spectrometer probe.

In addition, since it is an expanding plasma, the focusing of such ions when they are created is inefficient. In the high voltage (first generation) instrument the plasma entered into a very high field, which efficiently ionises close to the ion exit aperture. In the second generation instrument there was a much lower field, and this restricted significantly the range of ions formed and detected[4,6]. In this instrument the physical restrictions imposed on us by the apparatus to hand made it impossible to mimic the conditions of the other two instruments. It does however highlight the problems of handling and detecting ions from plasmas

3.5.2 Effect of Biasing the GD Cell with Respect to Mass Analyser Ground

3.5.2.1 Modification

Previously, the system had relied on detecting ions effusing from the ion exit aperture of the GD cell as they impinge on the aperture of the mass analyser which was 86 mm down beam (75 mm after modification). The region between the two sections was effectively field-free, and therefore the ions would be in an expanding envelope and most would not be collected. By floating the glow discharge cell (done by biasing the ion exit cone with respect to earth) it was hoped to encourage ionization of the plasma leaving the source, and the ions could then be accelerated towards the mass spectrometer sampling aperture at the tip of the mass analyser probe. It was hoped to thereby improve the efficiency of collection.

It was expected that increasing the kinetic energy of the ions between the exit of the FFGD cell and the mass analyser aperture would improve ion transmission across the space. This was achieved by biasing the ion exit of the discharge cell with respect to earth (the casing of the mass spectrometer). This is referred to as the cell bias (V_{cell}). To do this, the discharge cell was floated as previously described in section 3.4.5 and the source flange was insulated from the mass spectrometer housing to reduce the effects on the field of a grounded metal surface in close proximity. A polycarbonate insulator was produced along with PTFE top hat shaped insulators to insulate the bolts from the flange (figure 3.23). A good vacuum seal was achieved using a silicone O-ring and a viton gasket.

Figure 3.24 illustrates the discharge cell and cell bias circuitry. The ion exit cone can be biased positively or negatively relative to the casing of the mass spectrometer in order to accelerate positive or negative ions respectively. When the cell is biased positively relative to the mass spectrometer cations leaving the ion exit will be propelled towards the mass spectrometer. For each 1 V increase in V_{cell} the kinetic energy of a singly charged ion increases by 1 eV, and therefore the maximum accelerating potential could not be greater than 100 V since the maximum kinetic energy which could be measured on the instrument was 100 eV. This restriction occurs because the quadrupole loses resolving power due to the reduced time for mass analysis when the ion kinetic energy is too high[44]. Bearing this in mind, it was proposed that this could also serve to calibrate the kinetic energy measurements of ions passing from the GD cell.

3.5.2.2 Results

The first attempt to accelerate the ions between the ion exit and mass analyzer orifices was made prior to modification of the mass spectrometer probe, when application of a relatively small positive cell bias (< +20 V) was found to increase the observed copper ion intensity by up to a factor of ten. Figure 3.25a shows the variation in the major ion peak intensities with the applied cell bias. In this example it was observed that the optimum accelerating bias for detection of copper was +14.95 V and an increase by a factor of 4.9 possible over the intensity observed when V_{cell} was 0 V. Figure 3.25a also illustrates that a second copper ion maximum approximately equal to the first could be achieved on application of $V_c \sim +35$ to +40

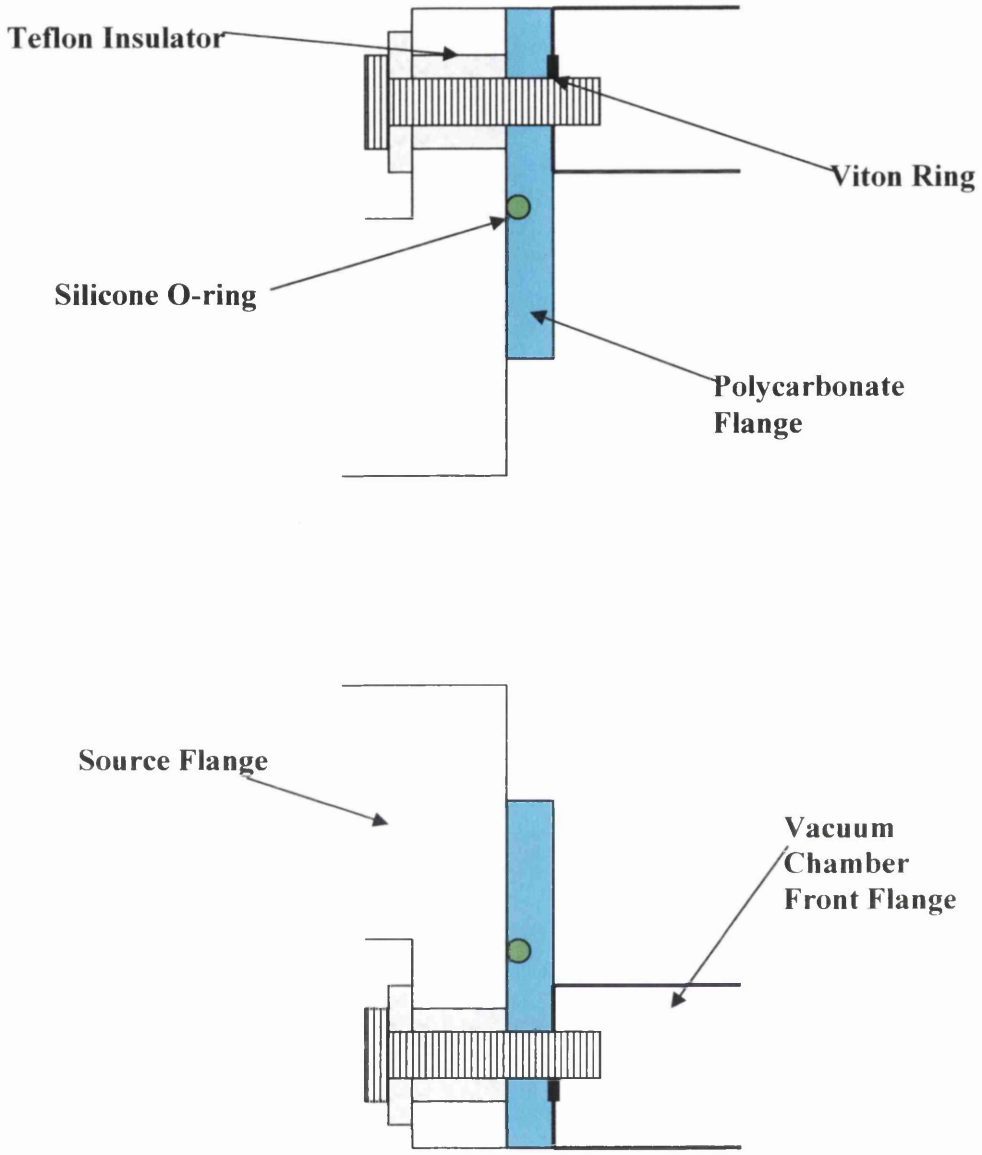

Figure 3.23: Insulating the FFGD cell from the main body of the instrument (scale ≈ 1:1)

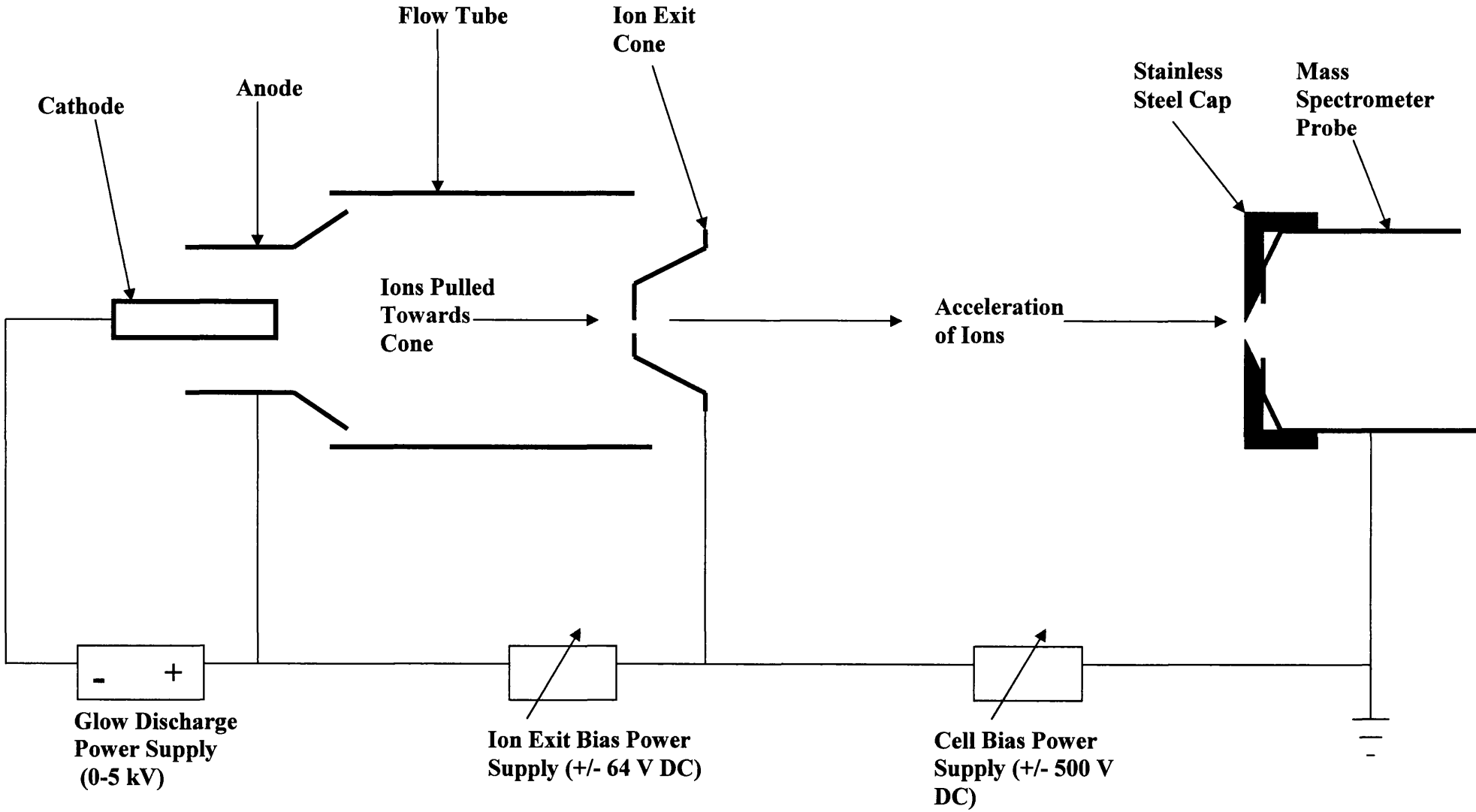

Figure 3.24: Schematic of source and cell bias circuitry

V. Results were however dependent on the discharge conditions and ion exit bias. This illustrates that application of a cell bias can significantly improve ion transmission between the ion exit and mass analyser.

As expected, the variation of the measured relative kinetic energy with applied cell bias gives an almost linear response. Due to problems with the instrument electronics the values for the kinetic energy indicated by the instrument was incorrect at this point.

The variation of ion signal intensity indicates two optimal focussing conditions (A and B). Figure 3.25b illustrates the mass spectra observed when V_{cell} = +14.95 (A) and +39.8 V (B). It was observed that the spectra were very similar, although the signals for the argon related ions, Ar^+ and ArH^+, were significantly reduced on application of a higher cell bias. Besides increasing the ion signal and changes to the relative intensities of the different ions, there was no significant change to the types of ion identity observed. Figure 3.26a illustrates a typical mass spectrum observed without application of an accelerating potential. Initially the major ions detected from the Cu/Ar plasma without addition of a secondary gas were Cu^+, ArH^+, H^+ (though low mass peaks are exaggerated using a quadrupole mass filter) and water related ions. It has also been possible to detect O_2^+ and N_2^+, possibly due to air leaks. Figure 4.4b illustrates a mass spectrum generated on application of a small positive cell bias prior to modification of the mass spectrometer probe. The same species were detected, often at higher intensity and with different relative ion intensities. The spectrum indicates a significant increase in the intensity of the Ar^+ peak intensity (approximately a factor of 5) elevating the signal above a level which could be attributed to background noise.

After modification of the mass analyser probe a significant increase in the observed ion peak intensities was initially observed and it became possible to detect Cu^+ up to 3.7×10^6 c/s. Figure 3.27a illustrates a spectrum generated on optimisation of the cylinder and cell biases for Cu^+ transmission. The structure of the spectrum is very similar to those produced using the prototype instrument design. However, when tuning for optimised Ar^+ detection a significant change to the spectrum was observed. One such spectrum is illustrated in figure 3.27b. Aside from enhancement of the argon ion peak, Ar^{2+} and Ar_2^+ were also detected, where previously the argon and argon dimer ions had only been observed in significant quantities on application of a positive ion exit bias and Ar^{2+} had not been detected.

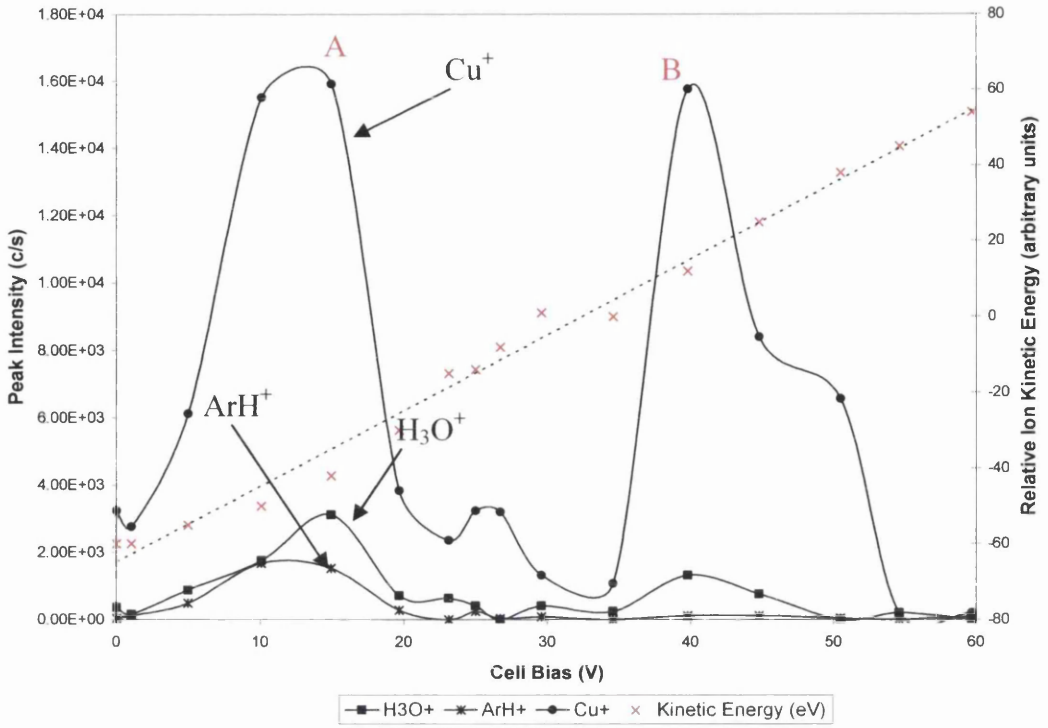

Figure 3.25a: Variation of major ion peak intensities and measured ion kinetic energy as a function of the applied cell bias, prior to mass spectrometer probe modification. The ion intensity maxima, A and B, at V_{cell} = +15 and +40 V were reproducible, but due to problems with the instrument the ion intensities and kinetic energies varied significantly between experimental runs. The small increase in Cu+ intensity when V_{cell} = +25 V was not observed in any other run.

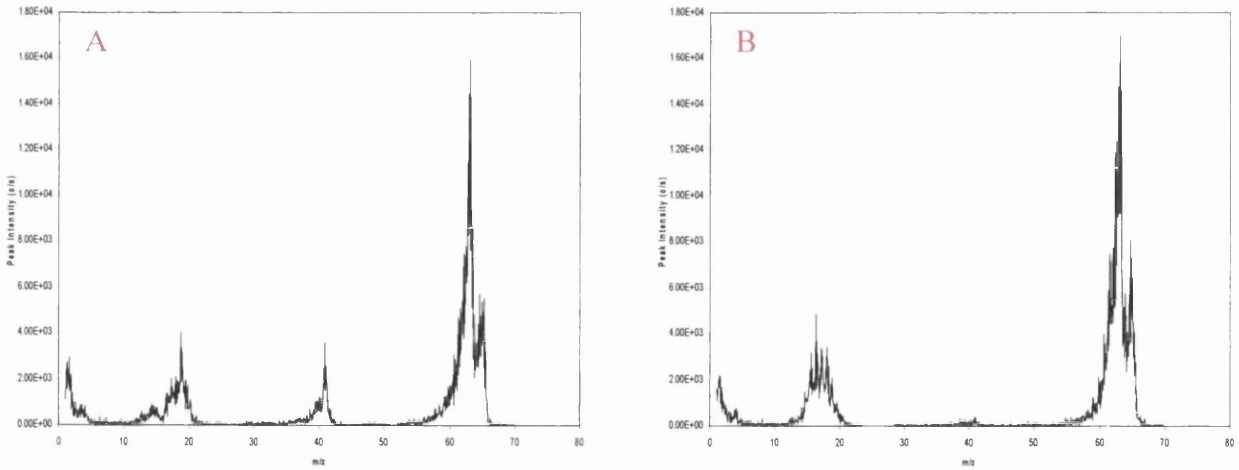

Figure 3.25b: Mass spectra observed at each maximum for copper ion detection

(V_d = 880 V, P = 0.75 Torr, F = 170 sccm, τ = 3.58 ms, V_c = -24 V, $V_{cylinder}$ = +0.5 V, Tuned for Cu^+)

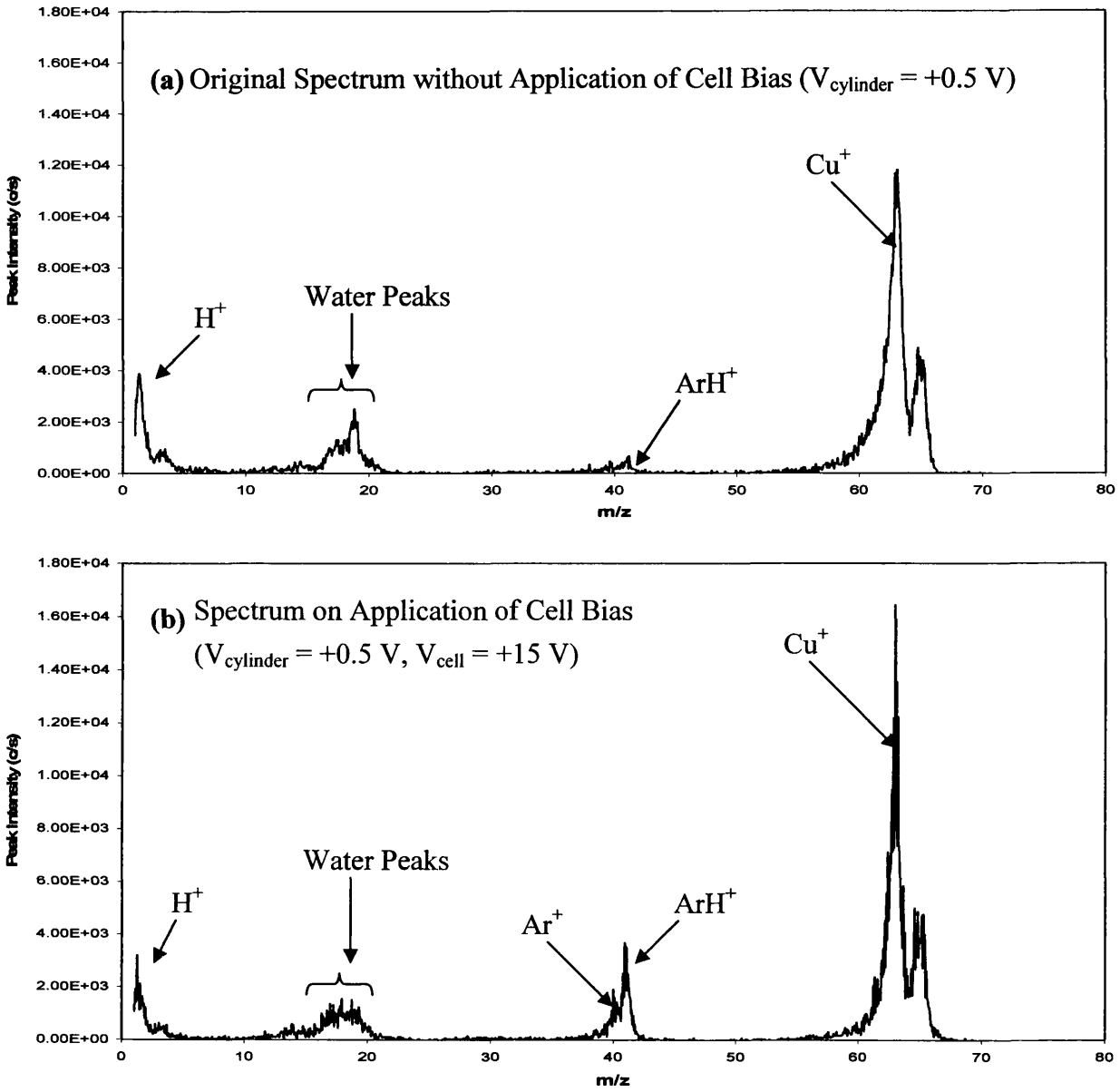

Figure 3.26: Common mass spectra at different stages of instrument modification

(V_d = 880 V, P = 0.75 Torr, τ = 4.78 ms, I_d = 4.27 mA, V_c = -24 V)

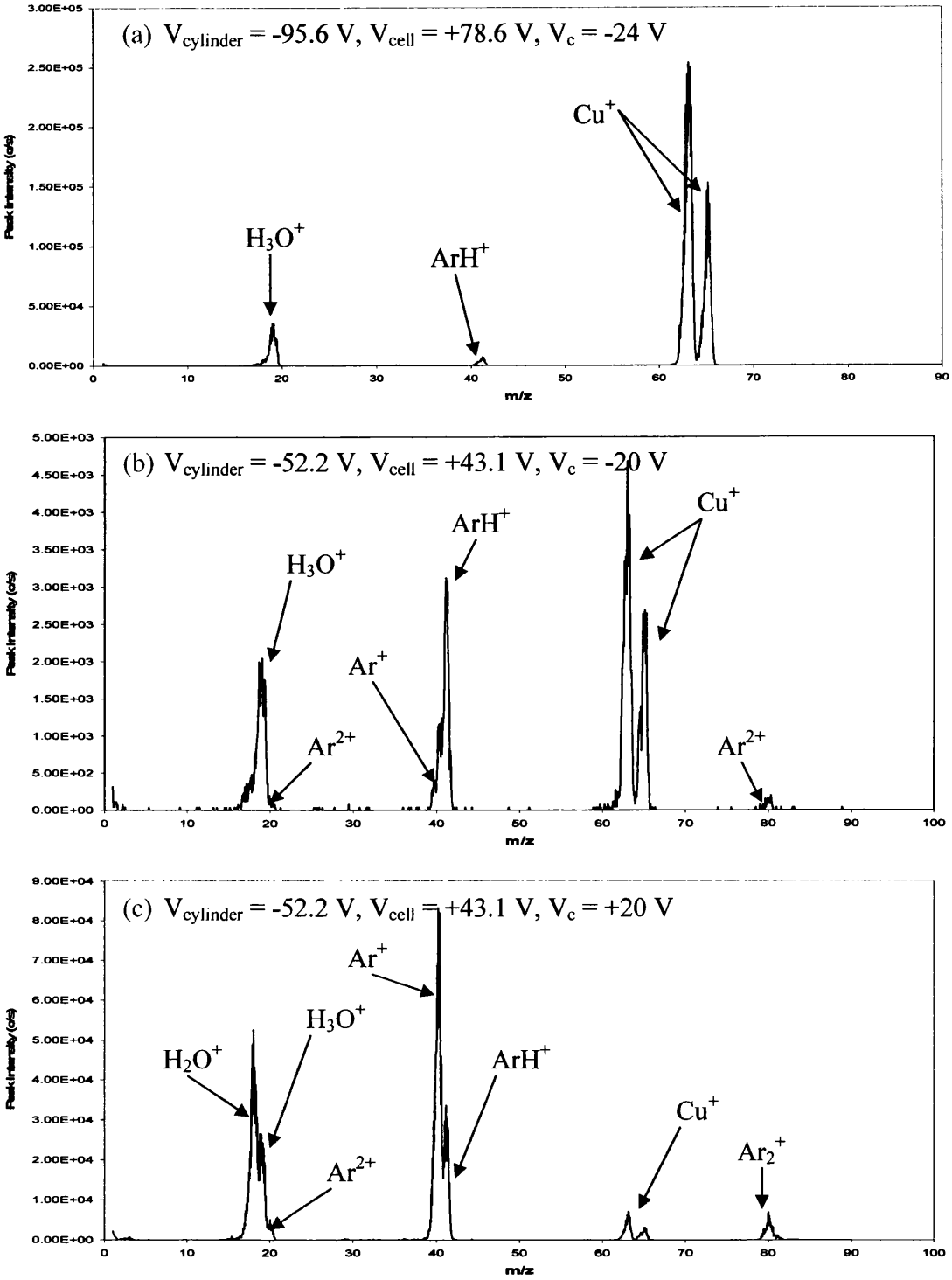

Figure 3.27: Mass spectra generated on optimisation of (a) Cu^+ ion signal (V_c = -24 V), (b) Ar^+ (V_c = -20 V) and (c) Ar^+ (V_c = +20 V)

((a) V_d = 711 V, P = 0.95 Torr, τ= 5.63 ms, I_d = 3.37 mA, (b) V_d = 804 V, P = 0.75 Torr, τ= 5.888 ms, I_d = 2.8 mA, (c) V_d = 804 V, P = 0.75 Torr, τ= 5.88 ms, I_d = 3.7 mA)

Using the instrument in its most recent form cations could be detected on application of $V_{cell} \geq +10$ V and optimisation of the ion signal occurred when V_{cell} was +70 to +80 V. However, significant changes to the ion kinetic energy maps and the mass spectra were observed. Figures 3.27a to c illustrate the mass spectra observed after modification of the mass spectrometer. It is clear that the relative ion intensities were highly dependent on the discharge and focussing conditions. Using the new instrument Ar^+ has been detected above background levels only on application of a positive ion exit bias or when accelerating ions between the ion exit and mass analyser orifices (discussed in chapter 6). This also corresponded with the decrease in the pumping efficiency of the main chamber pump. Ar^+ was one of the major ion peaks observed using the first and second generation instruments[1-6].

Figure 3.27c illustrates a mass spectrum observed on application of a positive V_c. The major peaks observed were Ar^+, Ar^{2+}, Cu^+ and the water related ions. It shows that a significant change to the ionisation process responsible for the ions detected occurred on modification of the instrument as previously Ar^{2+} had not been detected. It has been observed that Ar^+ and Ar^{2+} are prominent in the electron impact (EI) spectrum of argon and in low pressure argon glow discharges[45-48]. We can rule out EI ionisation close to the ion exit orifice as the likely mechanism for Ar^{2+} formation. This is because the EI spectrum of species effusing from the GD cell shows very little or no Cu^+ detection. This is shown in figure 3.28b. A fraction of the plasma gas enters the mass spectrometer probe, where the EI source is used to ionise it. There are plenty of Cu^+ in the spectrum of figure 3.28a, and therefore it has a different ionisation mechanism.

However, the new spectrum is similar to those generated by a low pressure argon discharge[45]. This supports an explanation that the ions detected in figure 3.28a are formed through a secondary discharge outside the glow discharge cell. This is probably due to the inclusion of a new cylindrical extraction lens (discussed below) just beyond the ion exit orifice which was biased negatively with respect to earth and therefore to the cell. This means that a voltage much greater than the cell bias was applied between the ion exit and the cylinder lens. Figure 3.28a also illustrates that the conditions can be tuned to allow the Ar^{2+} peak to become the maximum in the spectrum. Due to the far higher greater energy required to doubly ionise argon this is a very unusual result (Ar – first ionisation potential = 15.76 eV, second ionisation potential = 27.63 eV). Figure 3.28b shows a high energy EI (70 eV) mass spectrum

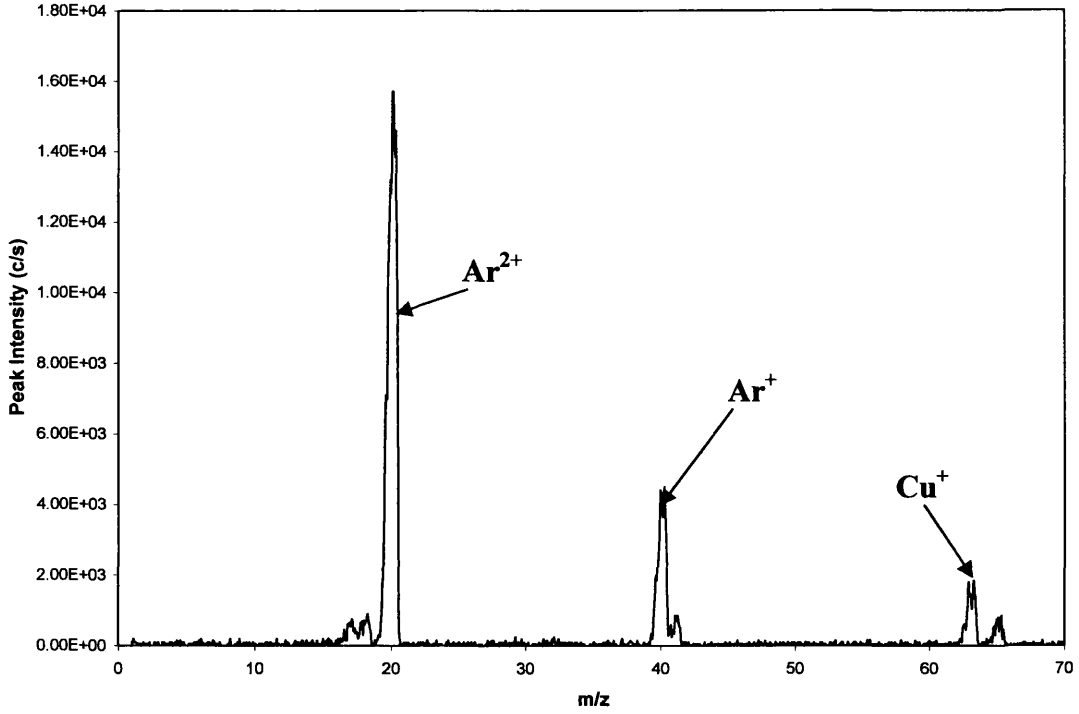

Figure 3.28a: Mass spectrum generated optimising detection of Ar^{2+} (V_d = 990 V, P = 0.8 Torr, τ = 5.68 ms, I_d = 5 mA, V_c = -20 V, V_{cell} = +80 V, $V_{cylinder}$ = -180 V, tuning for Ar^{2+})

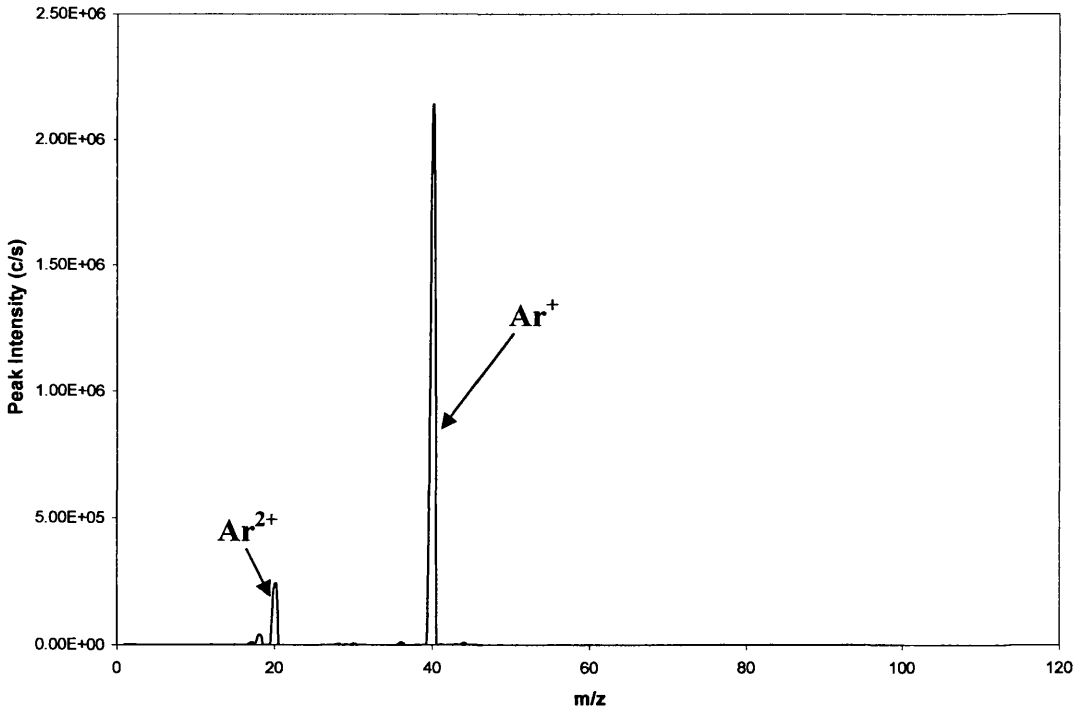

Figure 3.28b: 70 eV electron impact mass spectrum of the residual plasma gas (Source and extraction conditions - V_d = 625 V, P = 0.9 Torr, τ = 7.06 ms, I_d = 5 mA, V_c = +30 V, V_{cell} = +70 V, $V_{cylinder}$ = -180 V, tuning for Ar^{+})

of the residual gas species effusing from the FFGD. Even under "strong" ionising EI conditions (70 eV electron energy) Ar^{2+} was only detected at $1/40^{th}$ of the argon ion intensity. Formation of Ar^{2+} in argon discharges has been reported by Harrison and co-workers in low pressure[49] and dual discharge[50] ion sources. If the ions observed in this investigation were formed outside the FFGD cell via ionisation of highly excited states as proposed then the system could be described as having dual discharge character with formation of a secondary low pressure discharge beyond the GD cell.

If the FAG plasma is a Rydberg gas, Ar^{2+} must originate from a doubly excited Ar^R atom (double Rydberg[36]). The field ionisation conditions would be different from that for Ar^+, and hence the acute sensitivity of the spectrum to the conditions. At long residence times it is possible that the increased probability of collisions between Ar^R atoms allows a Penning process, such as is illustrated in equation 3.4, to occur.

$$Ar^R + Ar^R \rightarrow (Ar_2^R)^* \rightarrow Ar^{R*} + Ar \qquad \textit{(equation 3.4)}$$

The variation of the measured ion kinetic energy and Cu^+ peak intensity with applied cell bias were monitored over the range V_{cell} = -5 to +77.7 V. The results are illustrated in figure 3.29. It was observed that the ion kinetic energy increased linearly with increasing V_{cell}. In this case the magnitudes of the measured energies were consistent with expected values. Application of a positive cell bias was found to increase the Cu^+ ion intensity by a factor of 9 over that measured when the cell was earthed. The maximum copper ion intensity was observed when V_{cell} = +46 to 56 V and above this value a small decrease in ion intensity was observed.

3.5.3 Focusing the Ion Beam

3.5.3.1 Modification

In a further attempt to improve ion transmission across the vacuum region, einzel (figure 3.30a) and cylindrical extraction lenses (cylinder lens) (figure 3.30b) were incorporated. Each lens could be biased with respect to the mass spectrometer earth using a custom built power supply as illustrated in figure 3.31. The cylinder lens design and placement was similar to the extraction lens in the second-generation instrument and was therefore expected to focus the ion beam in the same manner. Four cylinder lengths were tried in this study. Produced from non magnetic stainless

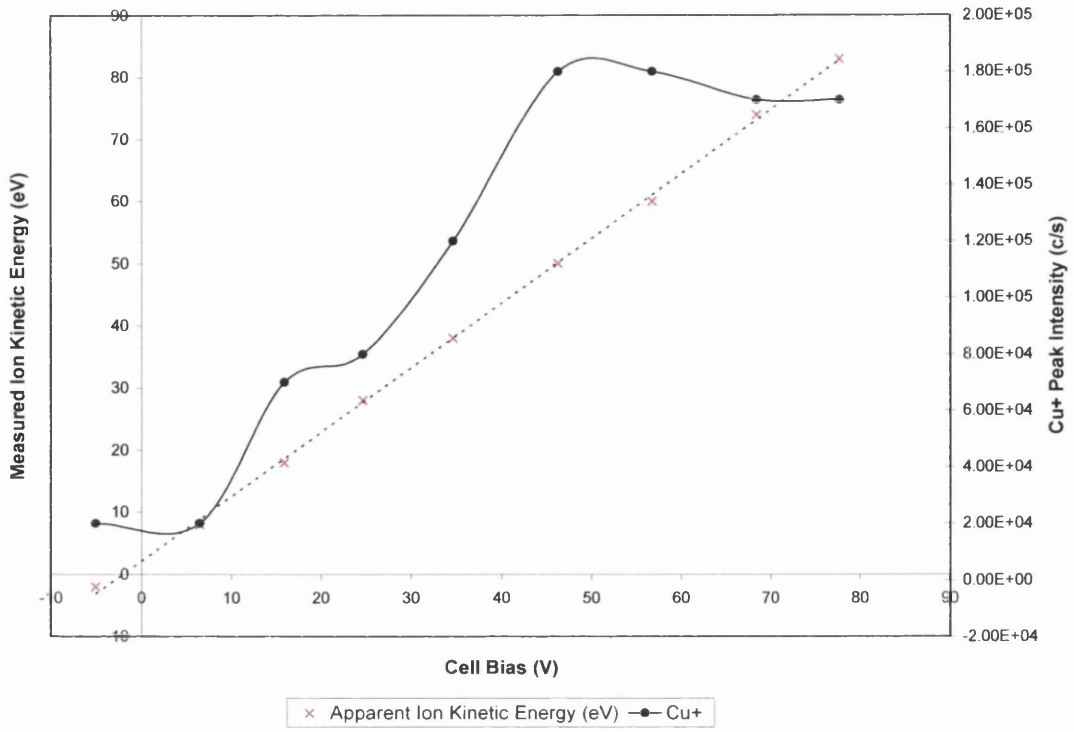

Figure 3.29: Variation of copper ion kinetic energy and peak intensity with applied cell bias. This experiment was not repeated under the same discharge conditions, and due to the deterioration of the performance of the instrument subsequent results differed greatly. This figure is therefore only included to indicate how results changed throughout this work (V_d = 700V, P = 0.95Torr, τ =5.63ms, I_d = 1.67mA, V_c = -24V, $V_{cylinder}$ = +0.5V, tuning for Cu^+)

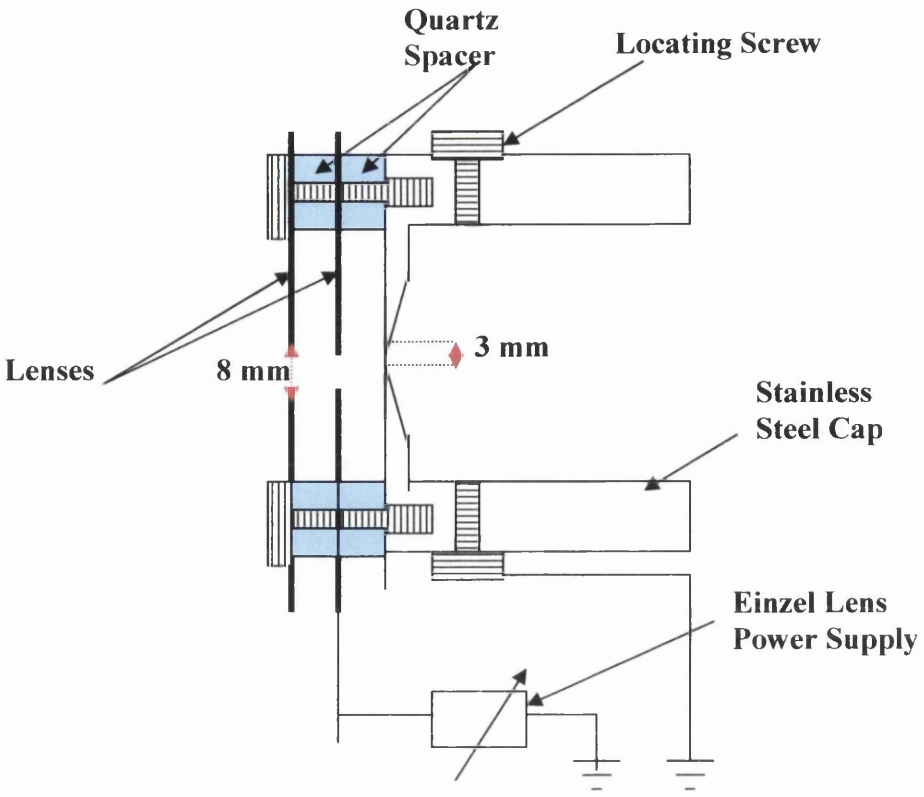

Figure 3.30a: End cap/Einzel lens design

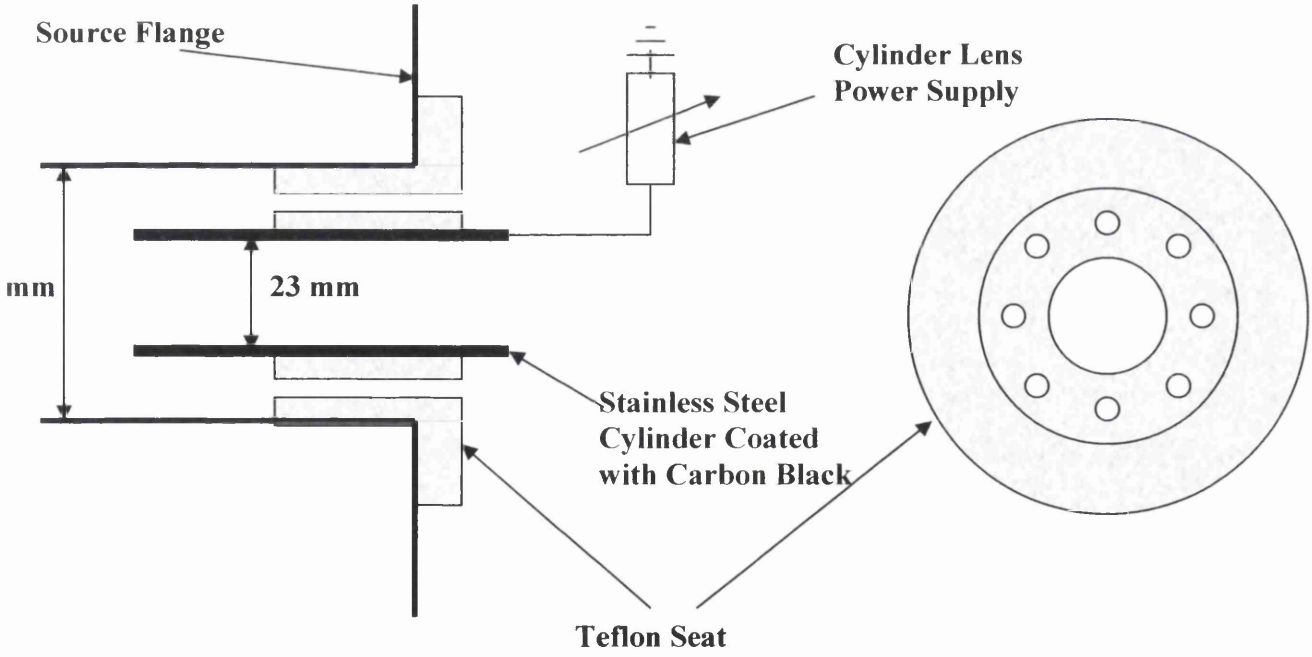

Figure 3.30b: Cylindrical extraction lens design (lenses of 10, 20, 30 and 40 mm length produced)

steel, they were 10, 20, 30 and 40 mm, each with an internal diameter of 23 mm. The length of the cylinder lens determined the position of the end of the cylinder relative to the ion exit orifice. For instance, the ion beam entered the 10 mm lens approximately 45 mm beyond the ion exit orifice.

The interiors were coated with a layer of carbon black to reduce electrostatic effects due to contamination. An aqueous solution was painted onto the interior surfaces and the cylinders were baked overnight at 160 °C. A PTFE spacer was produced to locate the lens within, and insulate it from, the source flange. A number of holes were drilled through the PTFE to improve the pumping efficiency. The electrical connection was made via a length of stainless steel wire spot-welded to the outside of the cylinder. A small groove was etched into the PTFE spacer, which both supports and allows this connection to fit within. Again a crimp connector was used to allow the cylinder to be detached easily.

The Einzel lens (figure 3.30a) was mounted onto the cap developed to reduce the gas flow into the mass spectrometer aperture (discussed in section 3.5.1.2). To complete the Einzel lens two non-magnetic stainless steel disks of 58 and 61 mm diameter were added. Each was 0.5 mm thick and an 8 mm diameter orifice was cut centrally. The disks were separated from each other and the orifice cap by 3 mm using quartz spacers. The spacers also insulated the disks from one another whilst the supporting screws allowed the front plate to be connected to the instrument earth. An electrical connection was made to the lens closest to the mass analyser to allow it to be biased relative to the instrument earth as illustrated in figure 3.31.

3.5.3.2 Influence of Cylinder Lens Bias

The second generation FFGD-MS instrument includes a cylindrical ion extraction lens just beyond the ion exit aperture. A previous attempt to replicate this design on the new instrument was carried out by Dash[1] and a series of experiments and modelling of the system using Simion[51] (ion and electron optics simulator) were performed. Comparing the theoretical and experimental results it was concluded that when the cylinder lens was placed close to the ion exit ion formation was induced outside the source by field ionisation of excited state neutral species. It was demonstrated that use of a shorter lens further from the ion exit could improve ion transmission by focussing the beam rather than inducing ionisation. It was also

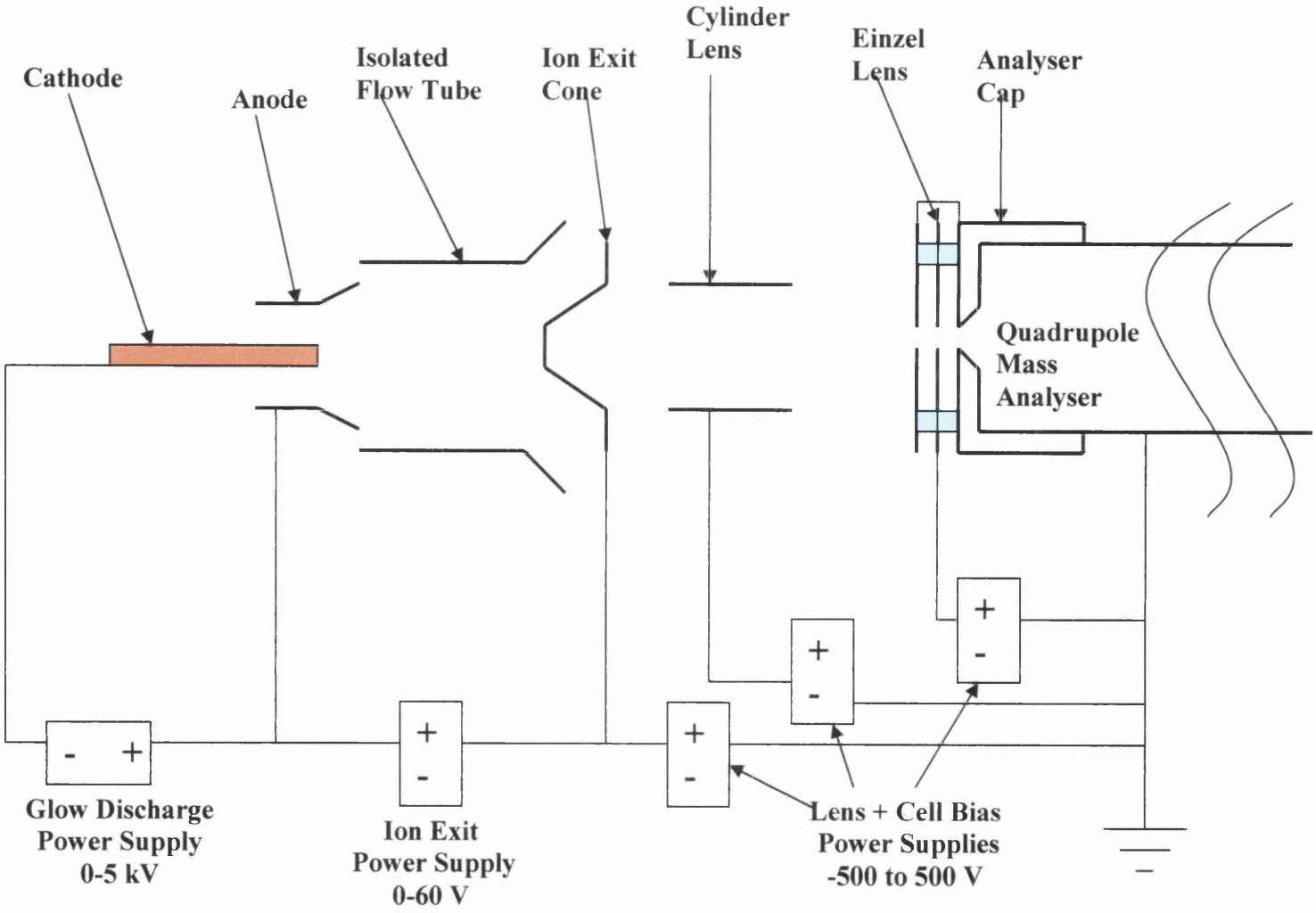

Figure 3.31: Ion focusing lens schematic

observed that the cylinder lens bias could influence the ion kinetic energy maximum, though the observed change was approximately 2 eV over a range of ~350 V.

Application of a -180 V bias on the cylinder lens was found to optimise the major ion intensities when V_{cell} was set for optimum ion transmission (V_{cell} = +70 to +80 V). It was observed that $V_{cylinder}$ influenced the intensities differently for each ion under fixed source conditions (V_d = 1000 V, P = 0.8 Torr, τ = 5.68 ms, V_c = -40 V, V_{cell} = +70 V, 40 mm cylinder lens). The Ar^+ peak intensity was found to increase by up to 25% on application of a cylinder bias of -180V, whilst for the same applied bias the copper ion signal was found to increase by 114% and the Ar^{2+} signal by 83%. It is unclear why the argon ion intensity increased by so much less than the other peaks. On application of $V_{cylinder}$ = -180 V the ion kinetic energy for maximum ion detection was increased by up to 4 eV compared with results observed when $V_{cylinder}$ = 0 V. This is a slightly larger change than that observed by Dash[1] (see above).

The presence of the cylinder lens increased the ion intensities by over 100%. However, it is not clear whether this is due to the focussing effect of the lens or increased field ionisation of Rydberg state species between the ion exit orifice and cylinder lens. When $V_{cylinder}$ = -180 V and V_{cell} = +70 V the potential difference between the two points is 250 V and therefore extensive ionisation of Rydberg state species would be expected. This may explain why the ion intensities were increased.

3.5.3.3 Influence of Einzel Lens Bias

Some increase in the ion signal was achieved using a bias of 10 to 20 V (positive for cation focussing and negative for anions). The effect was found to be significantly less than that of $V_{cylinder}$ and V_{cell}. When the ion signals for Ar^+, Ar^{2+} and Cu^+ were optimised using fixed source conditions, V_{cell} and $V_{cylinder}$ (V_d = 1000 V, P = 0.8 Torr, τ = 5.68 ms, V_c = -40 V, V_{cell} = +70 V, $V_{cylinder}$ = -180V, 40 mm cylinder lens), variation of V_{Einzel} indicated no increase in the observed Ar^+ intensity within the range investigated, whereas on application of V_{Einzel} = -20 V the Cu^+ signal increased by 33% and Ar^{2+} increased by 18%. A variation of 1 eV with a 60 V change in the V_{ein} was observed. Since this is significantly higher than the V_{Einzel} used in this investigation, this effect is therefore negligible.

3.6 The Mass Analyser

The instrument uses a Hiden[24] 301 EQP/EQS quadrupole mass spectrometer, which was originally designed as a plasma sampling tool. The probe can be operated in secondary ion mass spectrometry (SIMS) or residual gas analysis (RGA) mode. RGA mode utilises an electron impact (EI) source within the first lens stack of the mass spectrometer probe to ionise residual gases and is particularly useful for helium leak testing. The probe was also designed to allow direct ion kinetic energy measurement within the analyser probe using an Electrostatic Analyser (ESA). One of the most important properties for an experimental rig such as this is the fact that it operates at a low voltage and therefore auxiliary equipment can be added without difficulty. A rough outline of the instrument is shown in figure 3.32.

The ion beam passes through a focussing lens stack into an ESA which deflects the beam through 45°. The ions are separated by kinetic energy as they pass through the ESA (ions of one kinetic energy are deflected through the ESA whilst the rest collide with the walls) before being separated by mass as they pass through the quadrupole mass filter (QMF). In practice this has not proved to be as effective as it sounds, since ions of a range of masses regularly have the same kinetic energy and will therefore all pass through the ESA. The beam is again focused by a short lens stack before entering the QMF. The QMF in this instrument uses a triple filter, which consists of a pre-filter, the primary mass filter and a post-filter. The pre- and post-filters are rf powered and independent of the primary filter. The pre- and post- filters allow greater control over the entrance and exit fields of the quadrupole, therefore increasing the sensitivity for high mass transmission than would be possible using a single filter[52]. Long term stability is also improved since the majority of deselected ions collide with the pre-filter, therefore minimising contamination of the primary filter. The beam is then deflected again into the multiplier (detech[53] 415GS) which can produce a gain of $5x10^7$ at 2000 V when fresh. A more detailed summary of the instrument was presented by Dash[1].

It was necessary to replace the detector once during the study. This was performed by Hiden Analytical Ltd.[24] whilst the instrument was being reconditioned. Mass calibration was carried out every six months, although very little drift was observed even over this time. To calibrate the mass it was necessary to produce ions with masses in the ranges 15-40 amu and 40-295 amu. An ion of low mass (15-40

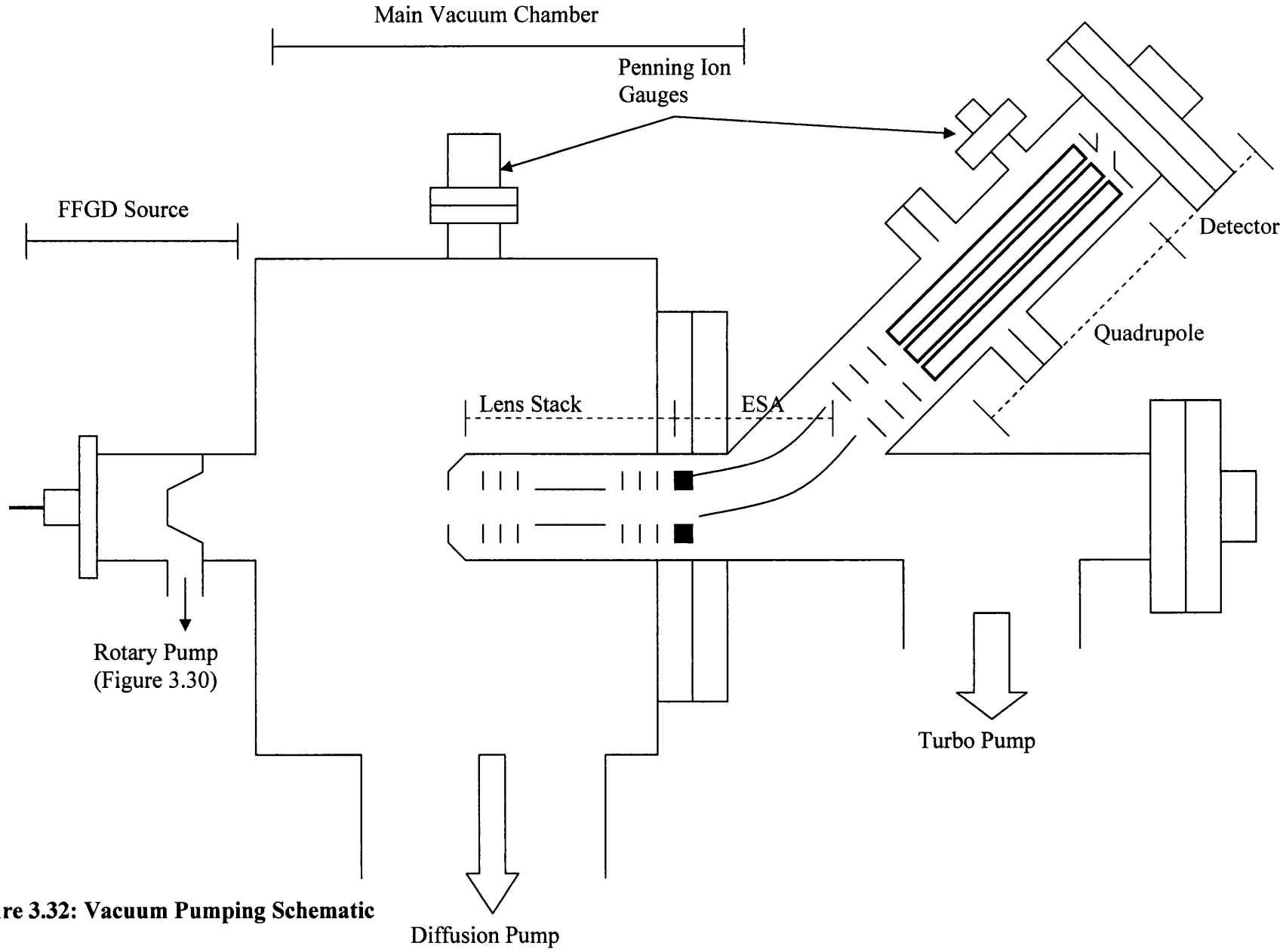

Figure 3.32: Vacuum Pumping Schematic

amu) was selected and a single scan acquired. A cursor was manually moved to the top of the peak therefore assigning the mass. This was repeated in the high mass range (40-295 amu), allowing the console to calibrate the mass readings.

3.7 The Pumping System

The Pumping system for the instrument is shown in figures 3.32 and 3.33. The source can be pumped by one or two two-stage rotary pumps (Leybold[54] Trivac D16B 16 $m^3 h^{-1}$) depending on the required gas flow rate and source pressure. The pumping rate can be controlled using a ball valve (Swagelok[23] 60 series) connected into the pumping line, and therefore the source pressure can be controlled directly. The source pumps are also used to evacuate the gas line via the bypass line illustrated in figure 3.19. An isolation valve was added into the line prior to the second source pump to allow the pump to be turned off when not required to reduce noise levels within the laboratory. The pressure of the pumping line can be monitored close to each pump using Leybold[54] Tr 211 Pirani gauges. The majority of the pumping line was constructed from 1" i.d. copper tubing to maximise gas throughput although a length of neoprene tubing was used to connect the source outlet to the ball valve and a shorter length to connect the ball valve to the copper tubing. Initially a length of bent neoprene tubing was used to connect the ball valve to a length of copper tubing, therefore reducing the pumping efficiency. The length of neoprene tubing connected to the source flange allows simple disconnection, therefore readily allowing maintenance.

Initially the pumps were connected to the copper tubing using lengths of high vacuum hosing which were readily available within the laboratory. Over time these hoses had collapsed at the bend, therefore reducing pumping efficiency, and due to their excessive length created a certain amount of clutter. The new copper tubing significantly reduced the amount of hosing used to connect the pumps. The second source pump is now connected to the isolation valve via a shorter length of flexible stainless steel vacuum hosing. The outlet from the source was ⅔" diameter and therefore the copper tubing used should allow the maximum pumping efficiency. To further reduce clutter the pump exhausts were combined into a single line under the bench rather than the initial four exhaust lines used previously. This has also helped reduce damage to the tubing by preventing contact with high temperatures such as that

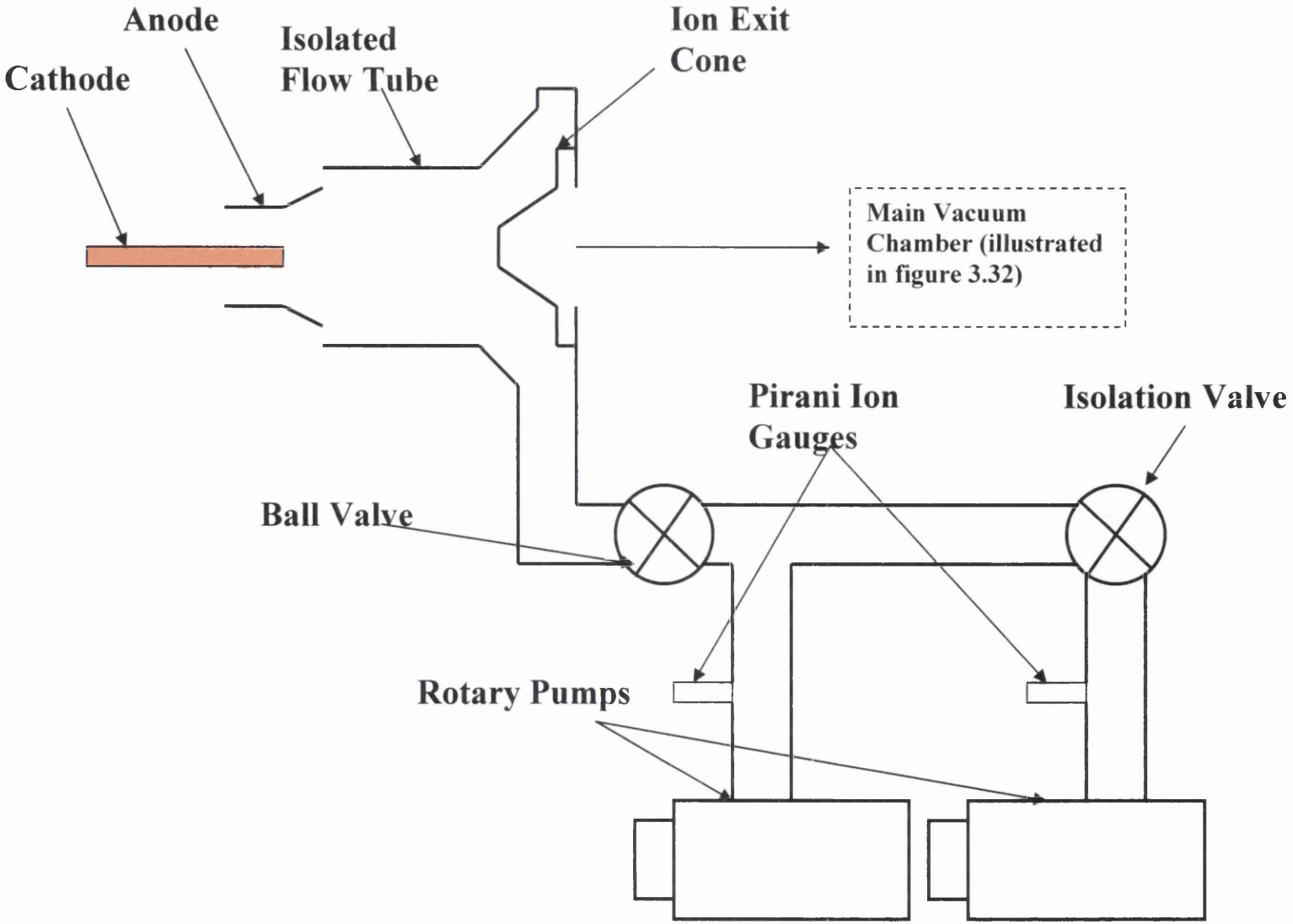

Figure 3.33: Source Pumping System

produced by the diffusion pump heater. Drip trays were also placed under all rotary pumps to prevent loss of oil onto the floor. Despite the modifications to the pumping lines no increase in pumping performance has been observed. It is likely that this is due to the restrictions imposed on gas flow by the source outlet and ball valve internal diameters.

The main vacuum chamber was pumped by an Edwards[55] Diffstak oil diffusion pump (700 l s^{-1}), model 160, through the base of the chamber. The diffusion pump was backed by a Leybold[54] Trivac D16B rotary pump. The vacuum chamber pressure was monitored using a Leybold[50] PR36 Penning gauge and the backing pressure in the rotary pump line was monitored using a Leybold[54] Tr 211 Pirani gauge. The gauges were all controlled by two Leybold[54] Combivac CM31 three channel controllers. Trip relays in the controllers were used to shut down the diffusion pump in the event of a power cut, and a second as overpressure protection for the electron multiplier. The diffusion pump could be isolated using a manual slide valve (VAT[56] series 12) fitted between the pump and the vacuum chamber to allow continued operation when the instrument was allowed up to atmospheric pressure. Typical operating pressures within the main vacuum chamber were $5x10^{-5}$ to $1x10^{-4}$ Torr when the discharge cell was operational and approximately $1x10^{-7}$ Torr when not in use. A vent valve was included in the backing pump line to allow the diffusion pump to be brought up to atmospheric pressure.

The mass analyser section of the instrument was pumped using a Pfeiffer Balzers[53] TPU 060 Turbo pump (56 l s^{-1}) controlled by a Pfeiffer[53] TPC 121 controller. The pressure within the analyser was monitored using a Leybold[50] PR36 Penning gauge. The turbo pump is backed by an Alcatel Pascal 2010 rotary vane pump (9.7 m^3 h^{-1}) and the backing line pressure monitored using a Leybold[50] Tr 211 Pirani gauge connected to one of the Combivac CM31 controllers. When the FFGD cell was in use the analyser pressure was commonly $2x10^{-6}$ to $4x10^{-6}$ Torr and the pressure dropped to $1x10^{-8}$ Torr when the instrument was not in use.

Due to deterioration of the performance of the analyser turbo pump it was necessary to replace the oil reservoir twice during this project. Direct replacement with a ready prepared oil wick allowed this to be done quickly and with little difficulty. The rotary pump oil was changed every 12 months.

3.8: Summary

A number of changes have been made to the FFGD source to remove inherent problems from the original design, in an attempt to improve performance and to allow a wider variety of studies, as follows:

1) significant reduction in electrical leakage through improved insulation design;
2) removal of undesirable materials e.g. magnetic stainless steel;
3) new flow tube to allow electrical probe studies;
4) improved vacuum seal;
5) reduction of flow disturbance around ion exit cone;
6) supported cathode;
7) Improved gas mixing.

The majority of these changes have yielded positive results, although the removal of undesirable materials and reduction in disturbance due to screw heads and wire in the ion exit region do not seem to have had any significant influence on the results obtained.

Further changes were made in an attempt to improve the transmission of ions from between the ion exit and the mass analyser orifice including:

1) reduction of the ion exit-mass analyser orifice distance
2) isolation of the source from the mass spectrometer and application of ion acceleration bias (V_{cell});
3) addition of a cylindrical extraction lens;
4) Addition of an Einzel lens to focus the ion beam into the mass analyser orifice.

The effects of these changes were not as predicted, and unfortunately it was not possible to reverse them due to a serious reduction in pumping efficiency of the large main chamber pump. The accelerating and focussing (Einzel and cylinder lens) potentials have each increased the detected ion intensities. The most significant effect was induced by accelerating the ion beam towards the mass spectrometer probe. After reduction of the inter-orifice distance, ions could only be detected on application of a V_{cell}. The results obtained have also provided us with more information on the

mechanism responsible for ion formation. Prior to the problems detailed above, acceleration of the ions between the discharge cell and mass spectrometer probe led to an increase in the observed ion signals. However, since modification of the mass spectrometer probe to reduce the ion flight distance a substantial decrease in ion intensities has been observed.

Improvements made to the remainder of the instrument include redesign of the pumping setup to improve pumping efficiency and reduce clutter, and reorganisation of, and maintenance to wiring and the general instrument layout. Much of this was performed due to space restrictions and faults diagnosed during relocation of the instrument.

3.9 Further Work

Other improvements to the design were proposed, although, due to the time constraints of the project and effects of changes made to the instrument further adaptation was not possible. The source on this instrument was originally designed[1] with the idea of performing optical studies of the glow discharge, but this was not possible due to problems with the equipment. It was proposed that addition of a fibre optic Charge Coupled Device (CCD) might improve our understanding of the processes occurring within the discharge. However, this did not prove possible during the time of this project.

One of the objectives of this project was to study negative ions formed from organic compounds added to the afterglow plasma using the inlet system designed by Newman[6]. Comparison of positive and negative ion results taken under the same source conditions could yield valuable information about the mechanism of ion formation. This is discussed further in chapter 6, but due to the deterioration of the performance of the mass spectrometer it was not possible to perform this work.

It was also proposed that addition of a slide valve between the discharge cell and the main vacuum chamber could significantly reduce instrument downtime and reduce the amount of water adsorbed onto the walls of the vacuum chamber. Unfortunately, inclusion of a slide valve would increase the cell-analyser distance and reduction of this distance would necessitate production of a new vacuum chamber. This was not possible during the time of this project.

3.10 References

[1] N. A. Dash, PhD Thesis, University of Wales Swansea, 2004

[2] P. D. Miller, PhD Thesis, University of Wales Swansea, 1996

[3] I. P. Mortimer, PhD Thesis, University of Wales Swansea, 2000

[4] D. R. Williams, PhD Thesis, University of Wales Swansea, 2001

[5] D. J. Mitchell, PhD Thesis, University of Wales Swansea, 2002

[6] K. Newman, PhD Thesis, University of Wales Swansea, 2005

[7] P. D. Miller, D. Thomas, R. S. Mason and M. Liezers, *"A New Ion Source For Glow Discharge Mass Spectrometry", The Proceedings of 4th International Conference on Plasma Source Mass Spectrometry, Durham, UK, 11th – 16th September*, ed. G. Holland, Printed BPC Wheatons Ltd., UK, 1994

[8] R. S. Mason and M. Pichilingi, *J. Phys. D.: Appl. Phys.*, **27**, 2363, 1994

[9] A. V. Hippel, *Ann. Phys.*, **81**, 1043, 1926

[10] F. Llewellyn-Jones, *Ionisation and Breakdown in Gases*, Meuthen and Co., 1964

[11] W. Grimm, *Naturwissenschaften*, **54**, 558, 1967

[12] W. Grimm, *Spectrochim. Acta*, **23B**, 433 (1968)

[13] R. S. Mason and D. M. P. Milton, *Int. J. Mass Spectrom. Ion Proc.*, **91**, 209-225, 1989

[14] M. Pichillingi, PhD Thesis, University of Wales Swansea, 1995

[15] Thermo Elemental Ltd. (formerly VG Elemental Ltd. and VG Isotopes Ltd.), Ion Path, Road Three, Winsford, Cheshire, UK

[16] P. W. Atkins, *Physical Chemistry 6th Ed.*, Oxford University Press, 1990

[17] E. O. Johnson and L. Malter, *Phys. Rev.*, **80**, 58, 1950

[18] A. Reifman and W. G. Dow, *Phys. Rev.*, **76**, 987, 1949

[19] Goodfellows Cambridge Ltd., Cambridge Science Park, Cambridge, UK

[20] BOC Edwards, Crawley, West Sussex, UK

[21] Fluorochem Ltd., Old Glossop, Derbyshire, UK

[22] Tylan General UK Ltd., Swindon, Wiltshire, UK

[23] Bristol Valve and Fitting Co. Ltd. (Swagelok), Bristol, UK

[24] Hiden Analytical Ltd., Warrington, UK

[25] J. E. Velazco, J. H. Kolts and D. W. Setser, *J. Chem. Phys.*, **69**, 4357, 1978

[26] L. Schott, *Plasma Diagnostics*, ed. W. Lochte–Holtgreven, North Holland Pub. Co., 1968

[27] I. Langmuir and H. M. Mott-Smith, *Gen. Elec. Rev*, **26**, 731, 1923

[28] I. Langmuir, *The Collected Works of Irving Langmuir*, ed. G. Suits, Pergamon Press, Inc., New York, 1961

[29] R. E. Valiga, D. C Duckworth and D. H. Smith, *Rapid Comm. Mass Spectrom.*, **10**, 305, 1996

[30] P. L. Larkins, *Spectrochim. Acta B*, **46**, 291, 1991

[31] P. H. Ratcliff and W. W. Harrison, *Appl. Spectrosc.*, **49**, 863, 1995

[32] W. Fischer, A. Naoumidis and H. Nickel, *J. Anal. Atom. Spectrom.*, **9**, 375, 1994

[33] R. S. Mason, P. D. Miller and I. P. Mortimer, *Phys. Rev. E*, **55**, 7462, 1997

[34] R. S. Mason, P. D. Miller, I. P. Mortimer, D. J. Mitchell and N. A. Dash, *Phys. Rev. E*, **68**, 016408, 2003

[35] K. Newman, R. S. Mason, D. R. Williams and I. P. Mortimer, *J. Anal. Atom. Spectrom.*, **19**, 1192, 2004

[36] T. F. Gallagher, *Rydberg Atoms*, Cambridge University Press, 2005

[37] Meggit Avionics Valve Dept., Fareham, Hants., UK

[38] Caburn MDC Ltd., Glynde, East Sussex, UK

[39] Wallis Hi-Volt (now Farnell Hi-Volt), Dublin Road, Bognor Regis, West Sussex, UK

[40] Legrand Electric, Ltd., Birmingham, UK

[41] Datametrics Inc. (now Edwards High Vacuum Ltd., ref. 44)

[42] RS Components Ltd. Corby, Northants., UK

[43] Thorn EMI Instruments Ltd., Dover, UK

[44] W. S. Taylor, J. G. Dulak and S. N. Ketkar, *J. Am. Soc. Mass Spectrom.*, **1**, 448, 1990

[45] R. S. Mason, D. M. P. Milton, M. Pichilingi, P. D. J. Anderson and M. T. Fernandez, *Rapid Comm. Mass Spectrom.*, **8**, 187, 1994

[46] J. W. Coburn and E. Kay, *Appl. Phys. Lett.*, **18**, 435, 1971

[47] J. K. Olthoff and R. J. Van Brunt, *J. Appl. Phys.*, **72**, 4566, 1992

[48] J. K. Olthoff, R. J. Van Brunt, S. B. Radovanov, J. A. Rees and R. Surowiec, *J. Appl. Phys.*, **75**, 115, 1994

[49] W. W. Harrison and C. W. Magee, *Anal. Chem.*, **46**, 461, 1974

[50] W. W. Harrison and B. L. Bentz, *Anal. Chem.*, **51**, 1853, 1979

[51] Simion (Version 6), D. A. Dahl, Idaho National Engineering Laboratory, EG & G Idaho Inc., PO Box 1625, Idaho Falls, ID 83415, USA

[52] 3F Series Data Sheet/3FPIC-1, Hiden Analytical Ltd.

[53] Pfeiffer Vacuum GmbH Ltd., Asslar, Germany

[54] Leybold Vacuum Ltd., London, UK

[55] Edwards High Vacuum Ltd., Crawley, West Sussex, UK

[56] VAT Ag Ltd., Haag, Switzerland

Chapter 4

The Ion Exit Bias Effect: Clear Evidence for the Rydberg Gas Model

4.1 Introduction

Section 2.7 outlines the theoretical evidence for the formation and stabilisation of the Rydberg gas state of matter. It was shown theoretically that a Rydberg gas would form under the conditions of the FFGD source used in this investigation. In this chapter the results of electrical studies are presented which can only be explained by modelling the plasma as a Rydberg gas. The influence of the ion exit bias, V_c, on fields and currents within the FAG plasma has been studied by Mitchell[1] in situ with mass spectrometric studies. Unfortunately, due to problems with the present instrument, in situ mass spectrometric and electrical studies were not possible during this investigation. Mitchell[1] studied the effects very carefully, but only for one set of conditions. This work is therefore an extension. Together they give a good idea as to what is happening in these plasmas with regard to the conduction of electric current. The model, presented in section 4.4 outlines the mechanisms for current flow and ion formation within the flowing Rydberg gas.

4.1.1 Error Estimates

The key features of figures of figures 4.3 to 4.6 and 4.7 to 4.9 is how currents probe voltages vary with applied V_c and V_d respectively. Of particular interest in figures 4.5, 4.6, 4.8 and 4.9 is how the profile changes with increased τ (i.e. a longer plasma decay time). Similarly, the key features of figures 4.10 and 4.11/4.12 are how the current flowing between probes A and B is varies with the applied V(AB) and how the profile is influenced by the ion exit bias and argon residence time respectively. The reproducibility of the measured currents and probe potentials is better than ± 14%. Minor fluctuations are evident and are not reproducible between runs, unless stated, and no attempt has been made to rationalise them. A typical run to run reproducibility for a single current and probe potential is given below. The overall effect is the same in each run, but due to the sensitive nature of the plasma to even small changes in discharge conditions small variations are evident.

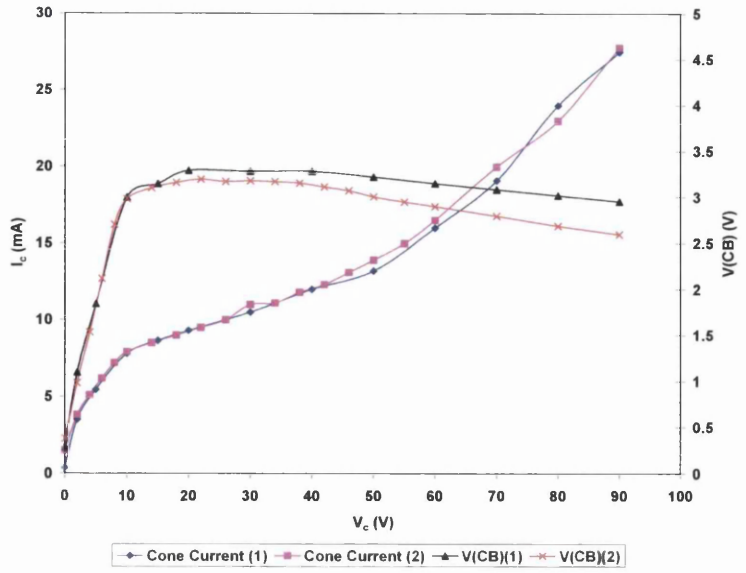

Run to run reproducibility of cone current and V(CB) measurements under the same discharge conditions (V_d = 800 V, τ = 7 ms, P = 0.9 Torr). This example is relevant to figure 4.6.

4.2 The Effect of V_c on the Discharge and Cone Currents

This section details the variation of the discharge and plasma (cone) currents with the applied V_c. This experiment was previously performed by Mitchell[1] on the high voltage instrument. Mitchell[1] observed that application of a positive ion exit bias induced an increase in the cone current. However, application of a negative ion exit bias did not influence the magnitude of the discharge current, and the cone current (flow of ions to the cone) changed very little.

Figure 4.1a illustrates the FFGD source and the points in the circuit at which currents were measured. The variation of each current with changing V_c is shown in figure 4.1b. When V_c was negative the discharge current (I_d) was constant over the whole range, and the current from the cone (I_c) was very low (~ constant within range of V_c investigated). This indicates that the discharge is not influenced by the magnitude of the ion exit bias on application of a negative V_c. The low I_c was expected as previous studies on application of a negative V_c indicated that the ion exit field was localised to a sheath around the ion exit cone[1], and therefore the bias was not expected to influence the glow discharge region. Figure 4.2a illustrates systematically the electron flow through the circuit on application of a negative V_c.

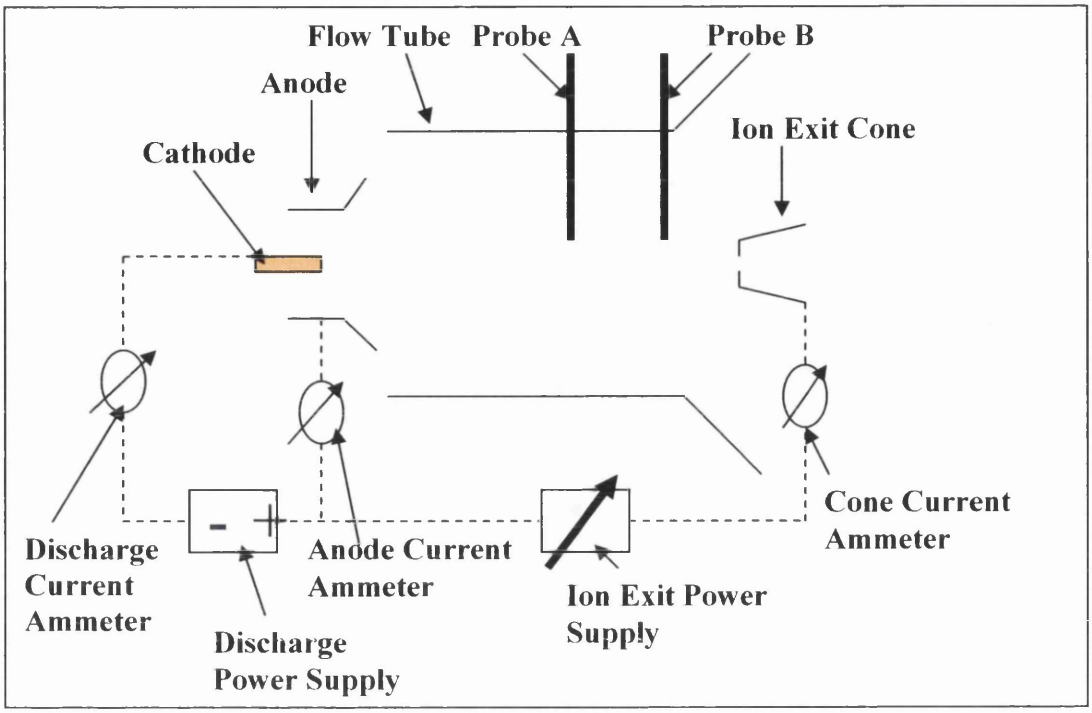

Figure 4.1a: Source diagram illustrating ammeter positions within the electrical circuit

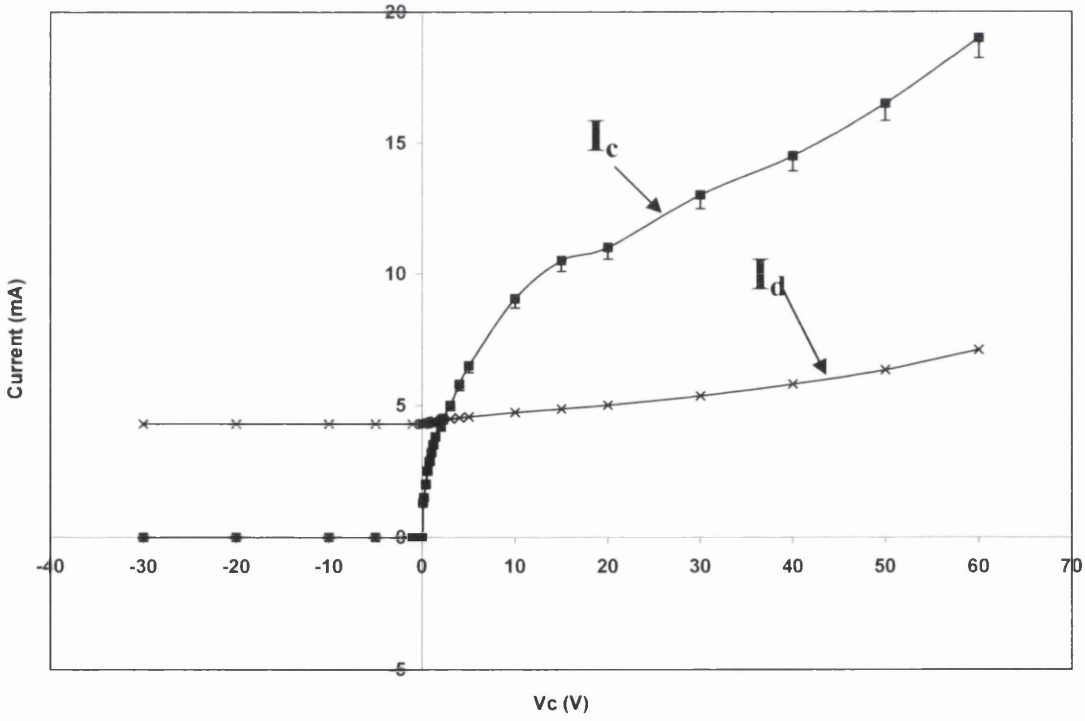

Figure 4.1b: Variation of currents within the system with positive ion exit bias (V_d = 450 V, P = 1.5 Torr, τ = 7.9 ms)

Figure 4.1b shows that on application of a very small positive bias electrons are pulled towards the ion exit cone, therefore reversing the electron flow. However, the magnitude of I_c remained relatively unaffected. Figure 4.2b illustrates schematically the current flow within the source on application of V_c = +0.4 V. It is surprising that application of less than +1 V should have such a significant effect. The conventional model assumes a drift of free ions and electrons present within the plasma induced by the applied V_c. Assuming the FAG plasma to fit the conventional plasma model, one would expect the cone current to be limited by the rate of diffusion of ions through the plasma. In this instance the cone and anode surface areas were approximately equal and therefore the ion saturation currents on application of a positive and negative V_c should be approximately equal. This is not the case here.

Mason and Mitchell[1] proposed that the flow of electrons through the flowing afterglow plasma could occur via electron transfer between argon Rydberg states. Since Rydberg state species have energies close to their ionisation potential, field ionisation occurs close to the ion exit cone. Charge transfer along a chain of Rydberg species as indicated in figure 4.2b could account for the observed currents. It was initially considered that the higher currents observed could be due to the high potential difference between the cathode and the ion exit cone on application of a positive V_c. However, it is clear from the relatively constant value of I_d in figure 4.1b that the current flow is between the cone and the anode of the active discharge.

Continued increase of V_c induced a significant increase in I_c, and when V_c was +2.2 V, I_c was equal to I_d (figure 4.2c). This is illustrated schematically in figure 4.2c as occurring via the charge transfer mechanism[1]. On application of a higher V_c (> +2.2 V), I_c was found to increase to values greater than I_d, with negligible change to the discharge current, and therefore plasma density. If the plasma were an ion-electron medium, an increase in ion concentration within the plasma would be required to induce an increase in the current through the plasma. Therefore, this result clearly does not fit with classical plasma theory. When V_c was $\geq$ +15 V, I_c was more than double the magnitude of I_d. On repeating the experiment at a lower discharge voltage (550 V) the same changes were observed, but the magnitudes of the currents and the voltages required to induce the currents were different. For instance, the V_c when $I_c = I_d$ was +2.2 V for the 750 V discharge, but was +4 V when V_d was 550 V.

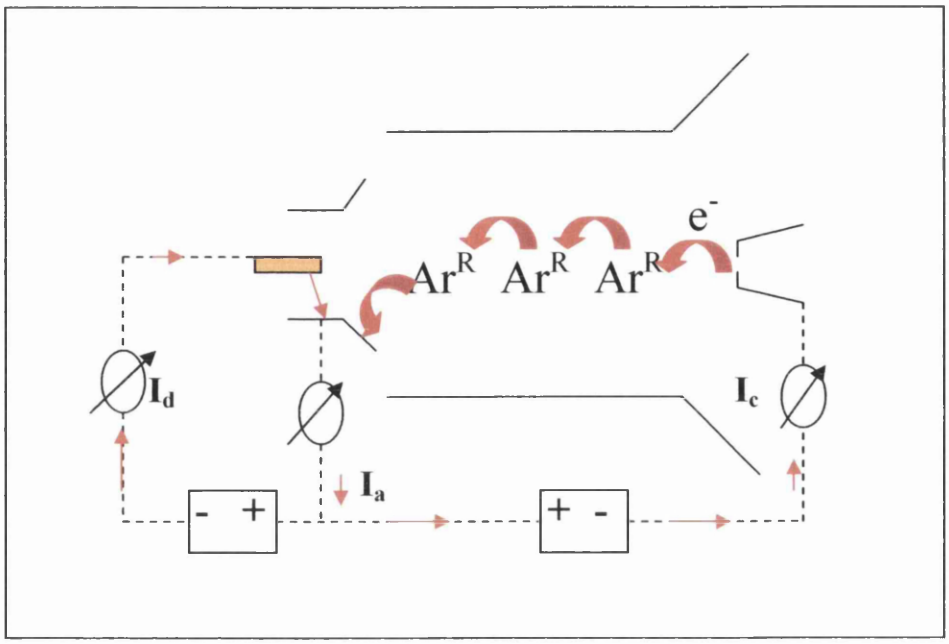

Figure 4.2a: Current flow when a negative ion exit bias is applied

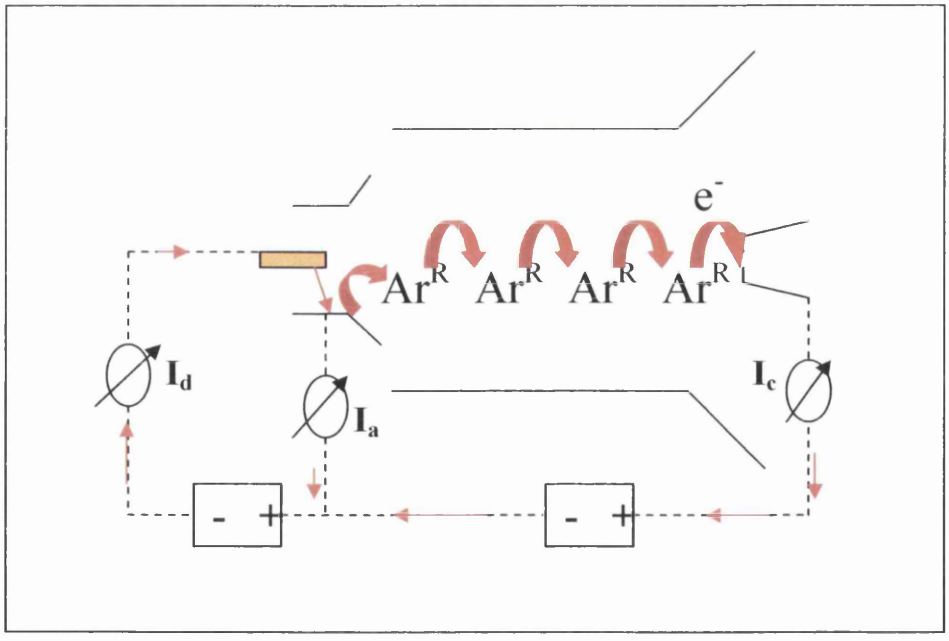

Figure 4.2b: Current flow when ion exit bias = +0.4V

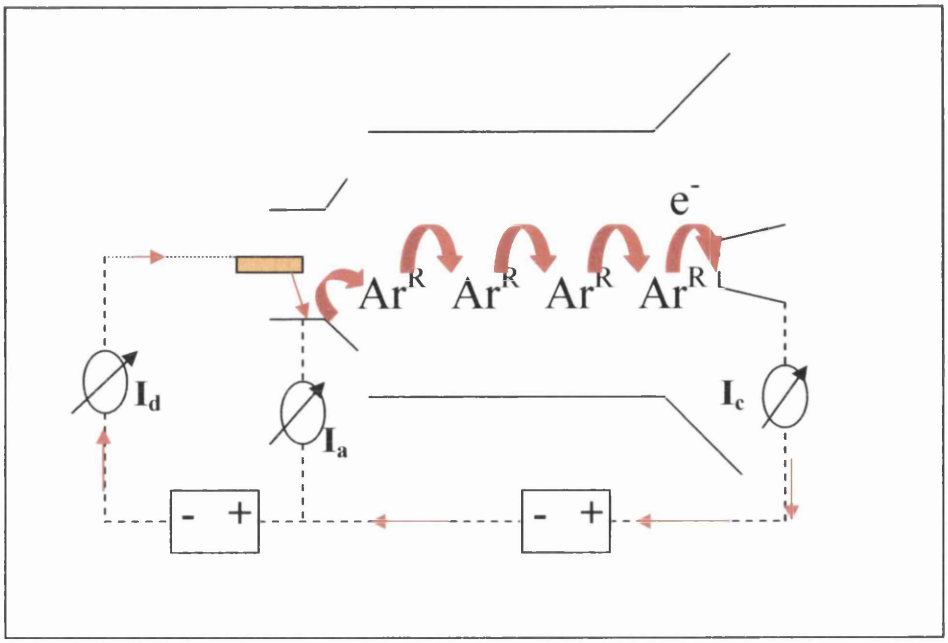

Figure 4.2c: Current flow when ion exit bias = +2.2V

4.3 Double Probe Measurements

In the following results the probe potentials illustrated are the potential of the first probe with respect to the second probe. For instance, if V(AB) = +0.1 V then the potential of probe A is more positive than probe B by 0.1 V when immersed in the flowing plasma.

4.3.1 Influence of a Positive V_c on Local Plasma Potentials

The electrical double probe technique is discussed in section 2.8. Zero-current potentiometry enables the measurement of the potential difference between two electrodes immersed in a plasma. In this study four electrodes were used; 1) probe A (A), 2) probe B (B), the ion exit cone (C) and the flow tube wall (W), as illustrated in figure 3.17b. A, B and W were all (electrically) 'floating'. The technique is very simple and allows the relative potentials of points within the plasma to be measured rapidly. When there is a potential difference between two points in a plasma a current will flow between the two. Therefore, to measure the potential difference an equal and opposite potential must be applied to oppose current flow.

The work in this section follows on from work performed by Mitchell[1] on the high voltage instrument. However, unlike in the previous investigation, the deterioration of the performance of the mass spectrometer meant that mass spectrometric studies could not be performed along side the electrical measurements.

Figures 4.3a and b show the variation of the probe potentials (V(CB), V(AB) and V(WB)), discharge current and cone current with increasing positive V_c. It can be seen in figure 4.3a that V(AB) and V(WB) were very low for all values of V_c. Limits of error were judged to be ± 1 mV, taking into account small errors possible in current measurement and given that the voltmeter used measures to the nearest mV. The variation of the probe potentials was reproducible (though the absolute values are dependent on factors such as cathode wear). Probe A was always more positive than probe B in this experiment. This is opposite to Mitchell's work[1], where the axial field was usually positive in the direction of the cone when electrons flowed downstream towards the cone. V(AB) initially increased on application of a low positive V_c, but decreased again with increasing V_c for $V_c > +10$ V. When $V_c = +110$ V, the

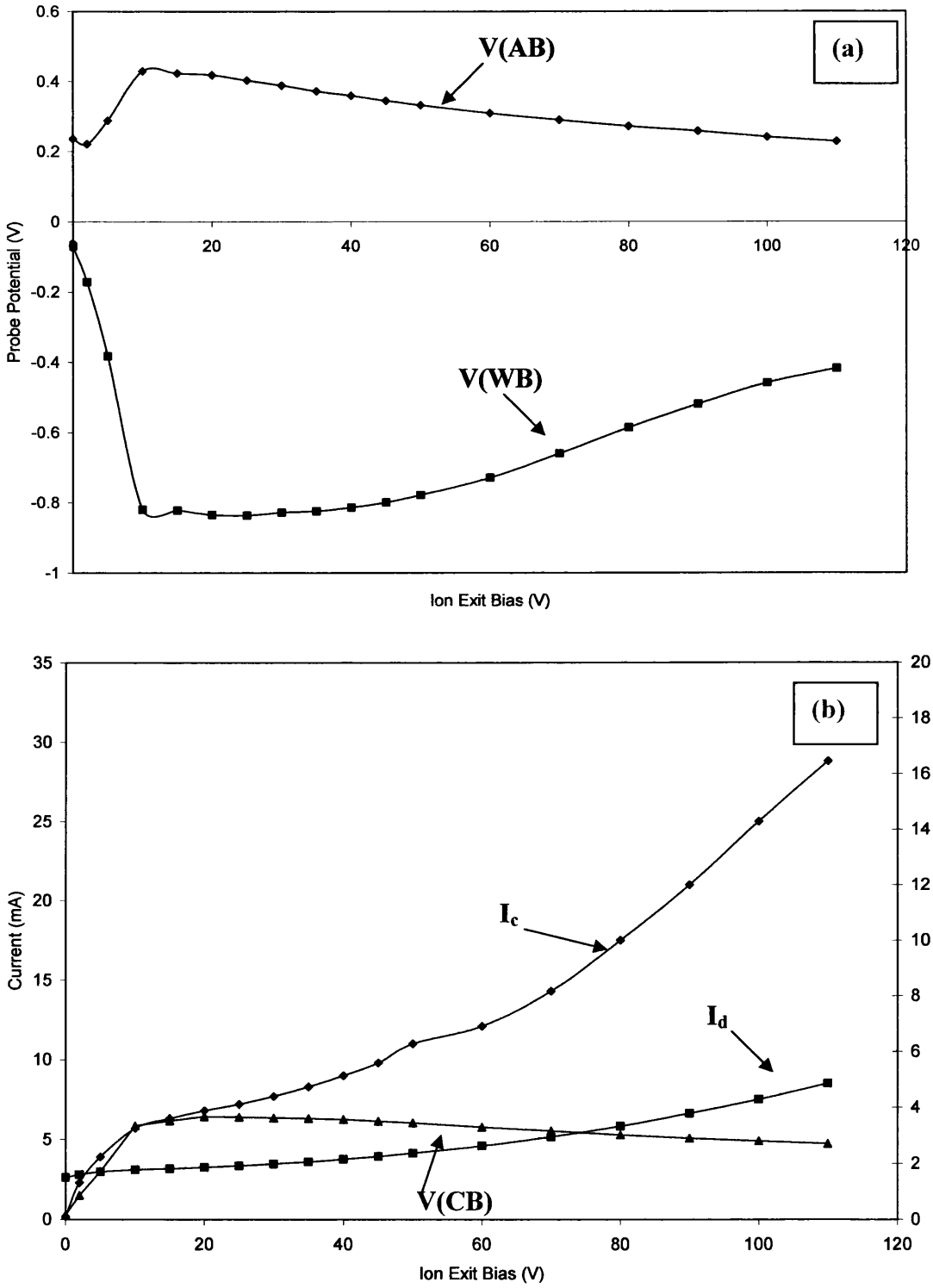

Figure 4.3: Variation of a) V(AB) and V(WB) and b) I_d, I_c and V(CB) with positive V_c (V_d = 700 V, τ = 4.5 ms, P = 0.9 Torr)

magnitude of V(AB) was approximately equal to that when V_c was +2 V. At this potential the cone current, i.e. the current through the plasma, was ~ 29 mA.

W was always more negative than the plasma in these experiments and in this case mirrored the pattern of V(AB), initially becoming more negative, then becoming less negative with increasing V_c for V_c > +10 V. The variation of the currents with V_c shown in figure 4.3b is very similar to that in figure 4.1b and is included to illustrate how changes in V(CB) correspond to changes in the current profiles. Initially V(CB) increased sharply with increasing V_c until V_c = +10 V, at which point both the current and probe potential profiles almost plateau. Whilst the current continues to increase with increasing V_c, V(CB) actually begins to decline. When V_c was +110 V, V(CB) was only +2.71 V. This variation differs greatly from that observed by Mitchell[1]. Mitchell initially observed an increase in the value of V(CB) with increasing V_c, with V(CB) reaching a maximum of V(CB) ~ +20 V, before declining to an approximately constant +13 to 14 V.

Figures 4.4a and b illustrate the variation of the currents and probe potentials on repeating the experiment at higher τ. V(AB) and V(WB) (figure 4.4a) were again very small and both followed the patterns shown in figure 4.3 and described above. The cone and discharge currents, shown in figure 4.4b, also increased in the same manner described above, with both increasing with increasing V_c. It is clear in figure 4.4b that I_c reaches a plateau at ~ V_c = +10 V but increases again for V_c > +18 V. However, unlike the previous example shown in figure 4.3b, there is a jump in both currents between V_c = +95 and 97 V.

The V(CB) variation is significantly different to that shown in figure 4.3b, and initially follows the pattern observed by Mitchell[1]. V(CB) increases with increasing V_c, until V_c = +22 V, above which it drops to a plateau of approximately +15 V. V_c = +22 V is also the point at which the cone current began increasing again after the plateau region. The results of Mitchell[1] had an upper limit V_c = +80 V, and the final section of the curve was not observed. When V_c was > +62 V, V(CB) again increased to ~ +18 V, but this increase did not correspond to any significant change in the cone or discharge currents. For V_c > +74 V, V(CB) began to decline, dropping sharply between V_c = +95 and 97 V, which corresponds to the jump in I_c and I_d described above. For higher V_c, V(CB) is approximately constant (~ +3 V).

The experiment was repeated at τ = 9 ms. Figure 4.5a shows the variation of I_c with increasing V_c at τ = 4.5, 7 and 9 ms. The results show that I_c increases faster at

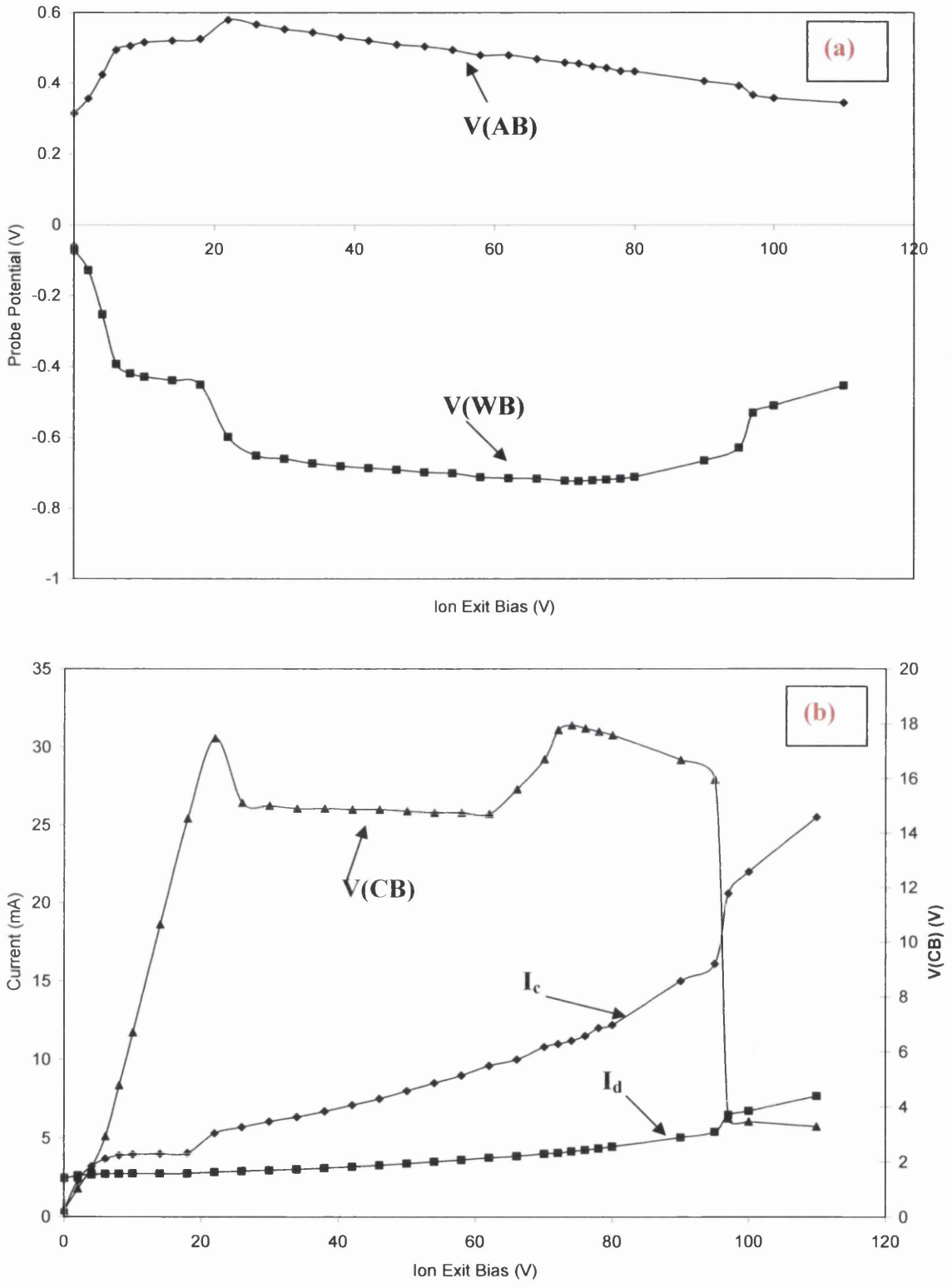

Figure 4.4: Variation of a) V(AB) and V(WB) and b) I_d, I_c and V(CB) with positive V_c (V_d = 700 V, τ = 7 ms, P = 0.9 Torr)

A discussion of the errors associated with the results in this chapter is included in section 4.1.

lower residence times. This is because the current carrier density in the flowing plasma is reduced over time. It should also be noted that the current curves begin to converge to that for 4.5 ms at higher values of V_c, and the point at which it occurs depends on τ. When τ = 7 ms there is a jump in I_c when V_c = +97 V, and when τ = 9 ms a similar jump occurs when V_c = +120 V.

Figure 4.5b shows the variation of V(CB) with increasing positive V_c. As with I_c, the magnitude of V(CB) is initially dependent on τ, but at higher potentials the curves begin to converge, reaching approximately constant values of ~ +3 V. Again, the longer the residence time of the plasma, the higher the magnitude of V_c required to induce the changes to the V(CB) curve.

Figure 4.6a shows the effect of different discharge voltages (constant τ), and therefore varying charge carrier densities on the V_c/I_c curve. The variation of V(CB) under the same conditions is shown in figure 4.6b. Again, the charge carrier density greatly influences the point at which changes to the curves occur, with changes occurring sooner at higher V_d. When V_d = 800 V the curve is the same as that when τ = 4.5 ms, despite the experiment being performed with τ = 7 ms. This again illustrates that the plasma is decaying over time, and that a higher initial charge carrier density or lower τ increases the current which can be carried.

Figure 4.7a shows the variation of V(AB) and V(WB) with V_d at constant V_c. The variation of both potentials was more significant than the examples in figures 4.3 and 4.4. Also, it is seen that for certain values of V_d, V(AB) becomes positive. V(WB) varied in the same way as V(AB), but was negative for all values of V_d.

Figure 4.7b shows the variation of I_c, I_d and V(CB) under the same conditions as 4.7a. For each value of V_d used in figure 4.6b, when V_c was +30 V V(CB) was in the first plateau region of the curve, with V(CB) approximately equal for 600 V $\leq V_d \leq$ 750 V. At very low V_d (< 440 V) V(CB) was > +25 V, and decreasing with increasing V_d. In fact, when V_d = 360 V, V(CB) was 1.7 V greater than V_c. It should not be possible for the cone sheath potential to be greater than the potential applied between the anode and the cone. However, a sheath of this magnitude could form due to the potential difference between the ion exit and the cathode of the active discharge ($V_d + V_c$, since the cone is biased relative to the anode). Between V_d = 420 and 440 V V(CB) fell sharply, and between 500 and 620 V V(CB) was approximately constant (~ +16 V). A second sharp drop in V(CB) was observed between V_d = 640 and 660 V, above which potential there was a slight decrease in V(CB). Above V_d = 440V the

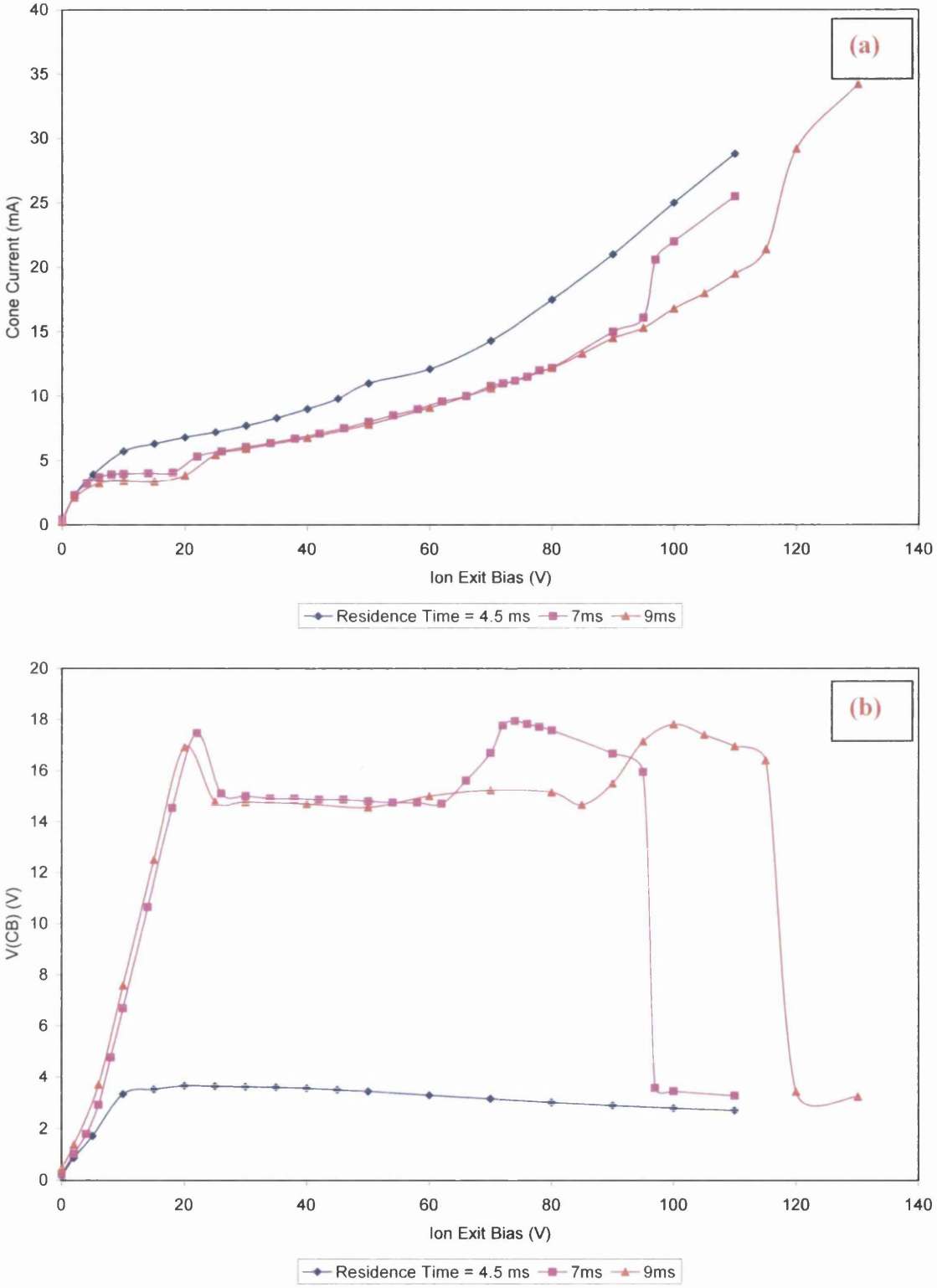

Figure 4.5: Variation of a) cone current and b) V(CB) with ion exit bias (positive relative to anode) and their dependence on argon residence time (V_d = 700 V, P = 0.9 Torr)

A discussion of the errors associated with the results in this chapter is included in section 4.1.

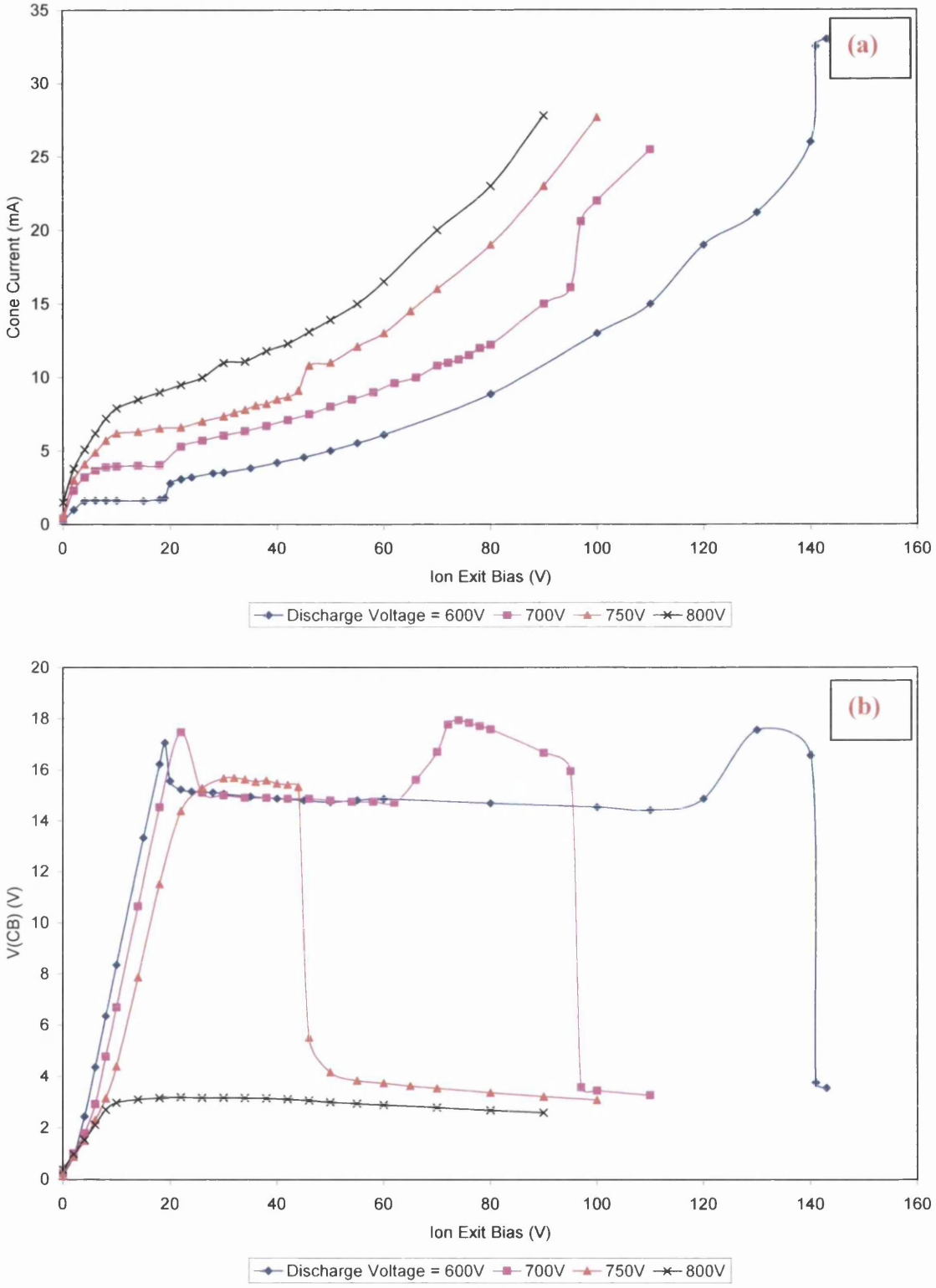

Figure 4.6: Variation of a) I_c and b) V(CB) with ion exit bias (positive relative to anode) and their dependence on the discharge voltage
(τ = 7 ms, P = 0.9 Torr)

A discussion of the errors associated with the results in this chapter is included in section 4.1.

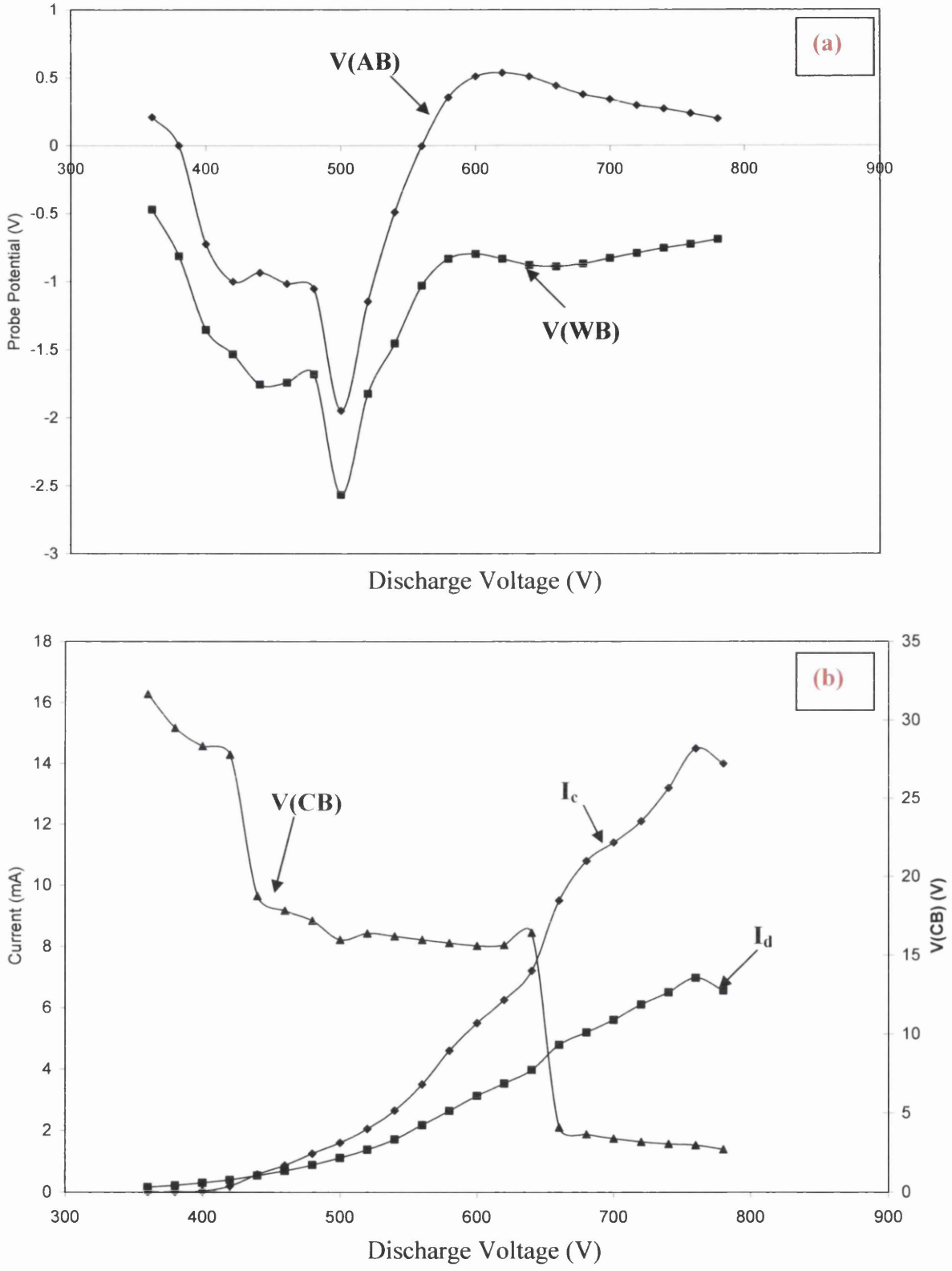

Figure 4.7: Variation of a) V(AB) and V(WB) and b) I_d, I_c and V(CB) with V_d (V_c = +30 V, τ = 4.5 ms, P = 0.9 Torr)

A discussion of the errors associated with the results in this chapter is included in section 4.1.

curve is similar to that shown in figure 4.4b (increasing V_c). Unlike the variation with V_c, there were no significant changes in the cone or discharge currents corresponding to changes in V(CB). With the exception of V_d = 780 V the currents increased with increasing V_d, i.e. with increasing charge carrier density, as expected.

Figure 4.8a shows the variation of I_c with V_d for different residence times. As in figure 4.6a, the variation was dependent on τ, though there is very little difference between the curves when τ = 7 and 9 ms. Errors in the measurement of the argon flow rate due to the flow meter reading (which measures to nearest sccm) are minimised by the use of high flow rates (generally > 100 sccm) and therefore errors in the calculation of τ are unlikely to be important. As before, I_c was greater at low τ than at higher τ, indicating a loss of the current carrying species (ions and electrons or Rydberg atoms) downstream of the active discharge. Similarly, the variation of V(CB) with V_d, shown in figure 4.8b, is the same for each τ, but the changes occur at different values of V_d. In this instance there is very little difference between the results at τ = 7 and 9 ms.

Figure 4.9a shows the variation of I_c with V_d under the same discharge conditions as figure 4.8a, but this time V_c was reduced to +4 V. I_c changed with V_d in the same way as shown in figure 4.8a, but was lower in magnitude due to the smaller potential difference applied across the FAG plasma. However, the variation of V(CB) shown in figure 4.9b was significantly different to that in figure 4.8b. In this instance V(CB) reached a maximum of +8.8 V (at τ = 9 ms), which is more than double V_c. At this point the cone current was very low, as was the discharge current (0.1 mA, not shown). As in figure 4.8b, at a specific V_d there was a sharp decline in V(CB), with a plateau reached at higher values of V_d (in this instance V(CB) remains at approximately +1 V).

4.3.2 Current-Voltage (I-V) Profiles Between Probes A and B

Application of a potential difference between two electrodes immersed in a plasma induces a current. Classically, this is due to the movement of ions and electrons induced by electric fields. The first electrical probe studies were performed by Irving Langmuir[2-4] using a single probe technique. Later Reifman and Dow[5], followed closely by Johnson and Malter[6], used a double probe technique. These techniques are described in more detail in section 2.8. This section details the

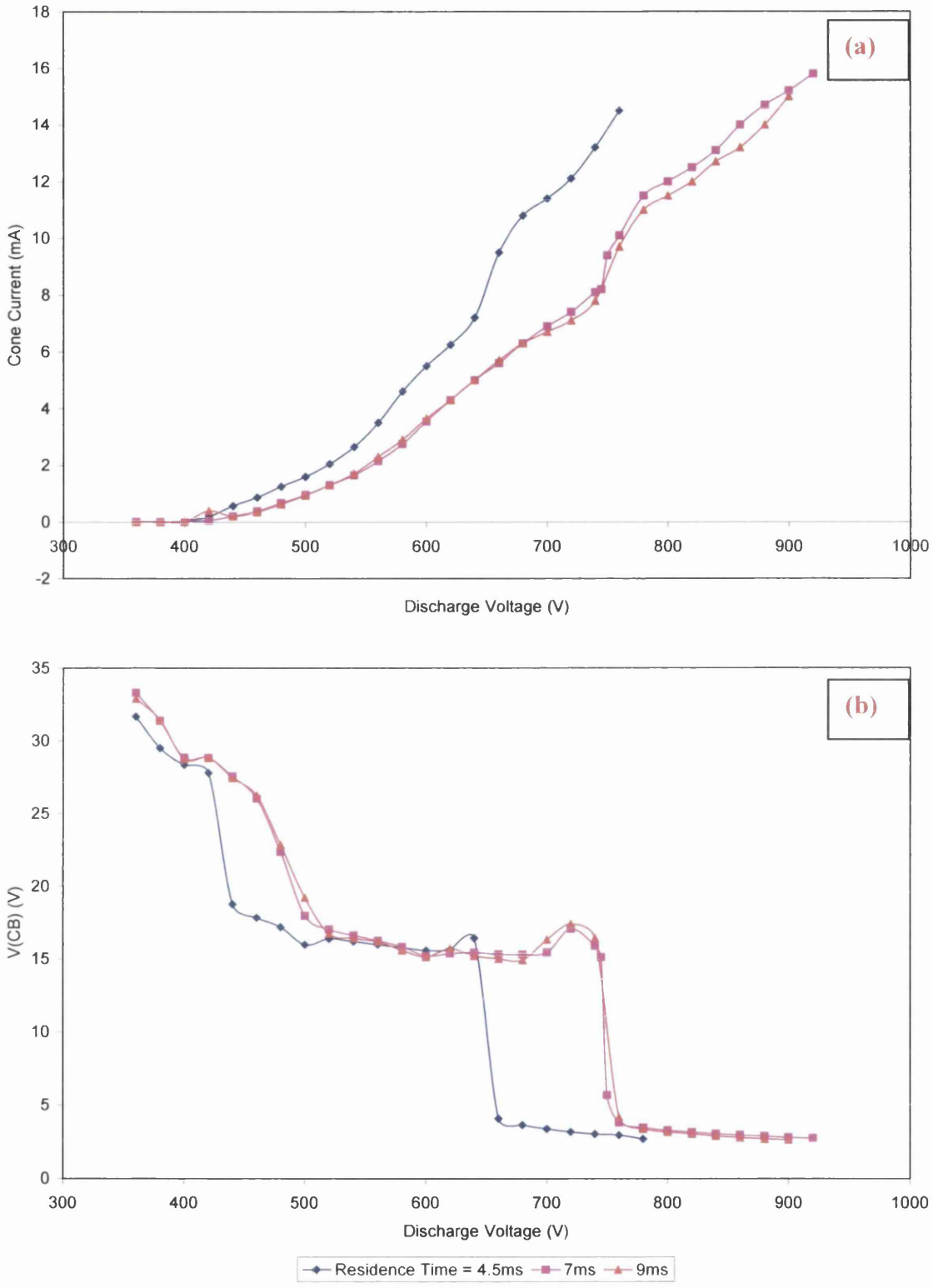

Figure 4.8: Variation of a) I_c and b) V(CB) with V_d, and their dependence on the residence time
(V_c = + 30 V, P = 0.9 Torr)

A discussion of the errors associated with the results in this chapter is included in section 4.1.

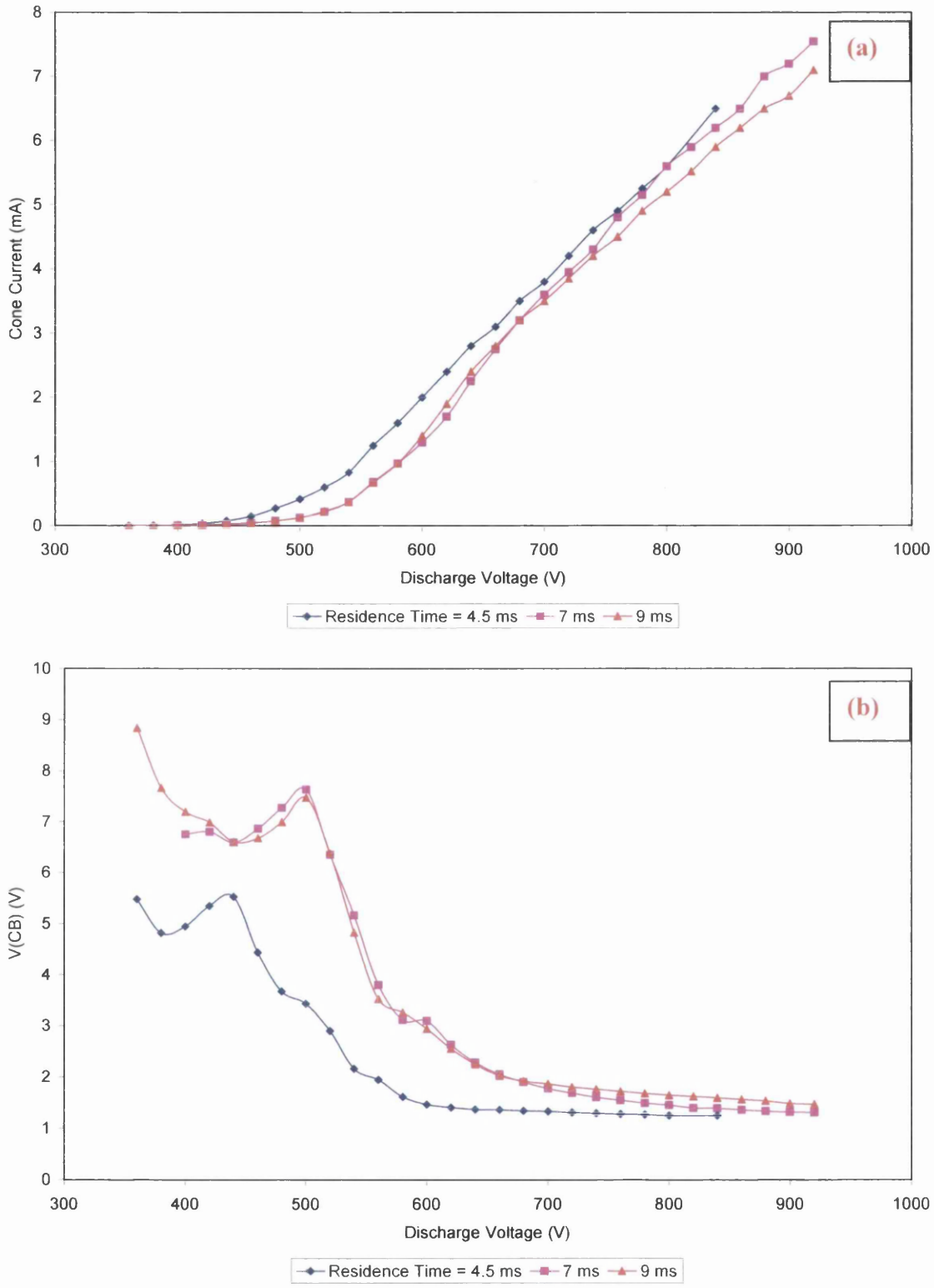

Figure 4.9: Variation of a) I_c and b) V(CB) with ion exit bias (positive relative to anode) and their dependence on the residence time
(V_c = + 4 V, P = 0.9 Torr)

A discussion of the errors associated with the results in this chapter is included in section 4.1.

influence of the ion exit bias and discharge gas residence time on the I-V profiles between (A) and (B) using an approximately symmetrical double probe system. Results taken under extended discharge and static discharge conditions are also presented for comparison.

Figure 2.11 shows the variation of the current between the two probes, I(AB), with the potential difference applied between the two, V(AB), recorded during this investigation. In this instance the value of V(AB) plotted refers to the bias applied to probe B relative to probe A, i.e. when V(AB) is positive, probe B is positive relative to probe A. The curve is similar to those presented by Mitchell[1] in a previous study and to curves typically obtained in Langmuir probe studies (see reference 7). This is unusual as the Langmuir probe technique uses a small probe and a large reference electrode, i.e. the system is assymetrical, but the setup used in this investigation was approximately symmetrical. Thus, based on the results of Johnson and Malter[6] using a symmetrical probe setup, one would expect the curve to also be symmetrical. The I-V profiles presented in this chapter are not as good as figure 2.11 for measuring the magnitudes of i_{1+} and i_{2+} (see section 2.8). Unfortunately, fluctuation of the discharge current when the results in figure 2.11 were recorded meant that the results could not be trusted. This problem was not apparent in more recent studies, but the plateau currents are not as clear.

The I-V curve indicates that when the cathodic electrode is downstream (negative V(AB)) the current is small, but when the cathodic electrode is upstream (positive V(AB)) the current is much larger. The reason for this is the exponential decay of the plasma as it travels down the flow tube.

4.3.2.1 I-V Profile Dependence on V_c

Figures 4.10a to c show the variation of I(AB) with V(AB) under different ion exit conditions and at three different discharge gas residence times. At each residence time investigated, very little difference was observed between the currents induced when V_c was -10, 0 or +10 V. The results were so similar that no consistent order of separation was possible, i.e. it is not possible to say that the maximum current was observed for any one value of V_c. Experiments were also run at V_c = -40 V and +20 V, with negligible difference in the curves obtained, these results have therefore been omitted. Similarly to results presented in section 4.2, the magnitude of the plasma

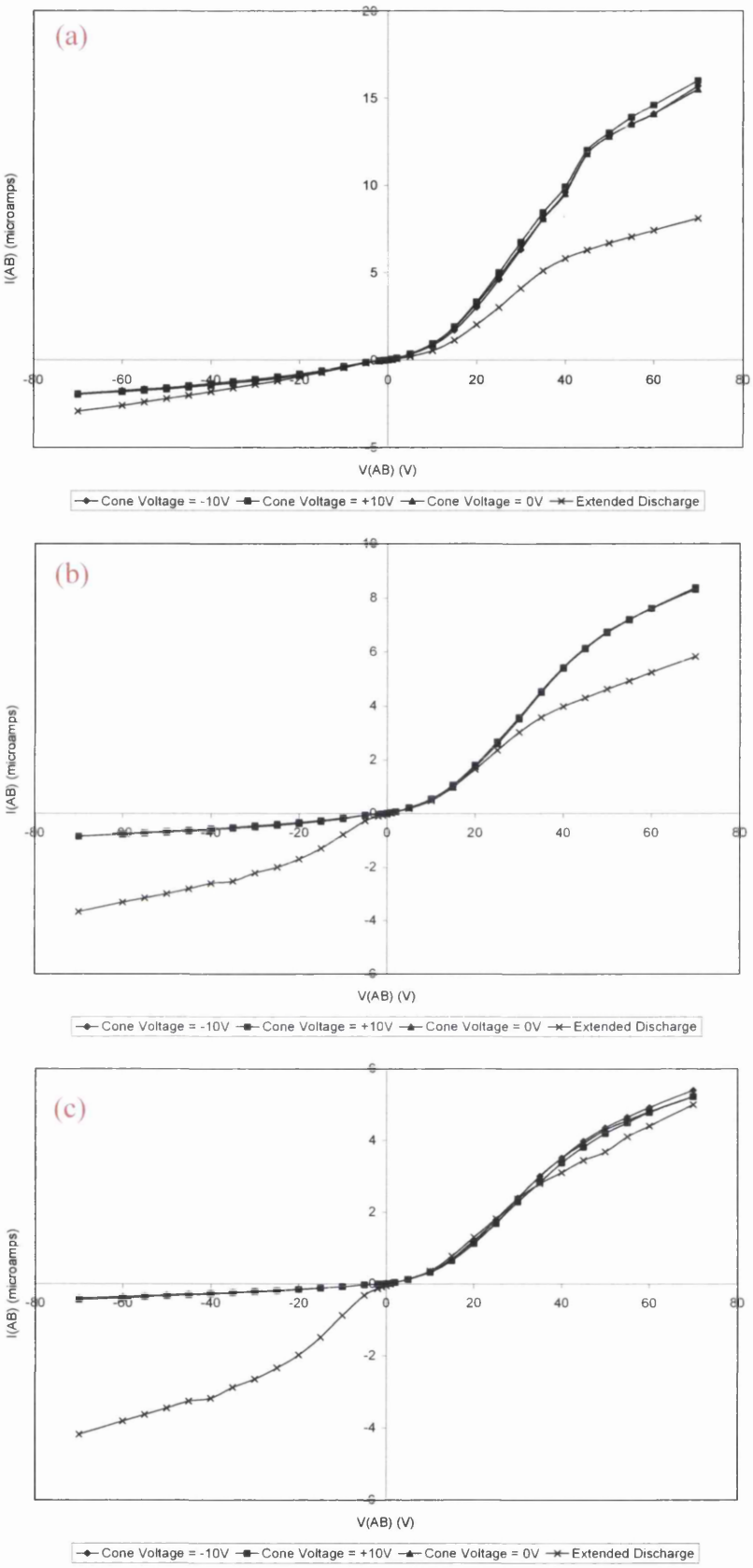

Figure 4.10: Variation of current flow between probes A and B with the bias applied between the two: dependence on ion exit bias when τ is a) 3.7 ms, b) 5.6 ms and c) 7.5 ms (V_d = 450 V, P = 1.5 Torr) (A discussion of the errors associated with the results in this chapter is included in section 4.1)

current was dependent on the direction of electron motion, with larger currents measured with electron motion in the direction of the plasma flow, i.e. when the positively biased electrode is further downstream.

Also illustrated is the current variation under extended discharge (ED) conditions, i.e. when the discharge was struck between the cathode and the ion exit cone. The currents measured under ED conditions were significantly different to those measured within the FAG plasma. The difference between the magnitudes of the current was less dependent on the direction of the plasma flow. However, the induced current was still slightly higher in the direction of the plasma flow.

4.3.2.2 Current-Voltage (I-V) Profile Dependence on τ

Figures 4.11a and b show the variation of I(AB) with V(AB), at three different discharge gas residence times when V_c was +10 V and under extended discharge conditions, respectively. At longer residence times the electron currents measured were lower in both directions. This shows that the charge carrier density decreases over time. As described in section 2.5.3, one of the requirements of the conventional model of a GD plasma is that the plasma density is essentially constant between the electrodes along the axial direction of the current[8]. In the case of the ED (figure 4.11b), the magnitude of I(AB) was less dependent on the direction of the electron motion relative to the plasma flow. Also, when the electron current was flowing upstream, the currents measured were higher at higher τ.

Figure 4.12 shows the I-V profile under 'static' discharge conditions. To achieve this, a discharge gas flow rate of just 3 sccm was used to replace gas lost through the ion exit orifice, and therefore maintain the source pressure. Thus, the argon residence time was approximately 0.9 seconds. The currents when V_c was -10 V, +10 V and 0 V were almost exactly equal and have therefore been shown as a single line. When the flow was fast, the currents measured under extended discharge conditions were less than for the FAG plasma, but when the flow was slow it was the other way around. The currents measured under extended discharge conditions were higher than those measured for the afterglow plasma, but the profile was the same (figure 4.12).

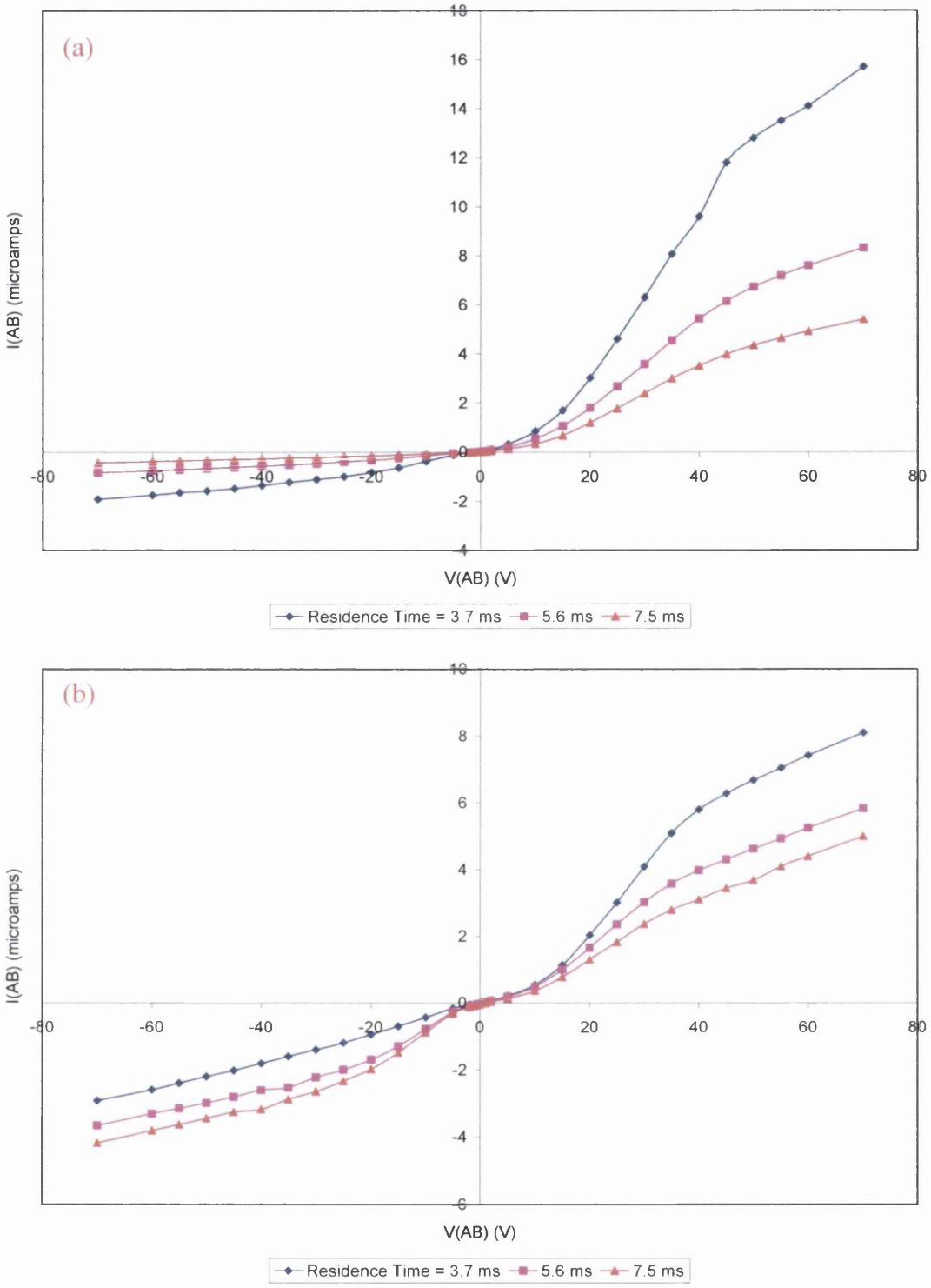

Figure 4.11: Variation of current flow between probes A and B with the bias applied between the two: dependence on τ a) on application of V_c = +10 V and b) in extended discharge mode

(V_d = 450 V, P = 1.5 Torr)

A discussion of the errors associated with the results in this chapter is included in section 4.1.

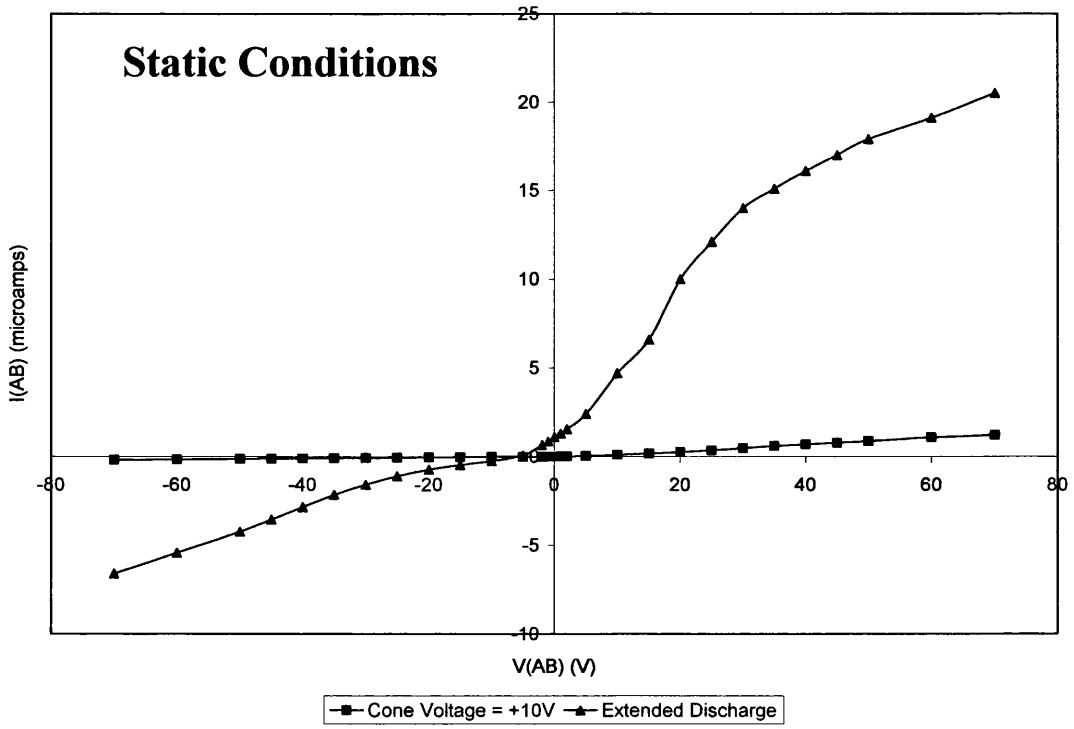

Figure 4.12: Variation of current flow between probes A and B with the bias applied between the two under static discharge conditions a) on application of Vc = +10, -10 and 0V V and b) in extended discharge mode

(V_d = 450 V, P = 2 Torr, $\tau \sim 0.9$ s)

A discussion of the errors associated with the results in this chapter is included in section 4.1.

4.3.2.3 Electron Temperatures

The method for determining "electron temperatures", T_e, is outlined in section 2.8. Classically, T_e values are proportional to the average kinetic energy of free electrons in the GD plasma, assuming the electron velocity distribution to be Maxwellian[8,19], and can be determined from the slope of the I-V curve about the y axis[7]. Values can be presented in Kelvin or eV (to convert from K to eV the value is divided by 11600[8]). Electron temperatures are required to be much higher than ion temperatures, T_i, which in a cold plasma are somewhat above ambient temperature (a value of 500 K is presented as an example in reference 8 for an ambient temperature of 293 K, cf 23200 K for the electron temperature, under static discharge conditions). Tables 4.1 to 4.3 contain a series of electron temperatures calculated in these studies at different residence times and under different ion exit conditions.

V_c (V)	+ 10	0	- 10	Extended Discharge
T_e (minimum) (K)	201	222	211	113
(eV bracketed)	(0.017)	(0.019)	(0.018)	(0.010)
T_e (maximum) (K)	212	227	219	118
(eV bracketed)	(0.018)	(0.020)	(0.019)	(0.010)

Table 4.1: Electron temperatures calculated when τ = 3.7 ms

V_c (V)	+ 10	0	- 10	Extended Discharge
T_e (minimum) (K)	623	566	638	2165
(eV bracketed)	(0.054)	(0.049)	(0.055)	(0.19)
T_e (maximum) (K)	627	571	643	2222
(eV bracketed)	(0.054)	(0.049)	(0.055)	(0.19)

Table 4.2: Electron temperatures calculated when τ = 5.6 ms

V_c (V)	+ 10	0	- 10	Extended Discharge
T_e (minimum) (K)	747	578	664	4833
(eV bracketed)	(0.064)	(0.050)	(0.057)	(0.42)
T_e (maximum) (K)	770	704	701	5352
(eV bracketed)	(0.066)	(0.061)	(0.060)	(0.46)

Table 4.3: Electron temperatures calculated when τ = 7.5 ms

The electron temperature measurements obtained by this method do not fit with the classical model. T_e appears to increase with increasing τ. The opposite would be expected due to increased collisional quenching at a higher τ. At high flow rates they appear to be lower than the temperature of the gas (~ 310 K). This clearly is not realistic. The values at slower flow rates are more realistic, but still very low. The extended discharge at lower flow rates falls into a similar order of measurement to that often quoted in the literature[7,8], but the values are still significantly lower.

It is clear that the electron temperature is highly dependent on τ. As τ was increased the electron temperature appeared to increase dramatically, particularly in ED mode. Since the I-V profiles were very similar for each value of V_c it is no surprise that the electron temperatures calculated were approximately equal. However, some discrepancy was observed due to the errors associated with measuring the gradient of the curve, i_{1+} and i_{2+}.

4.4 The Rydberg Gas Model of the FFGD Plasma

It has been shown above, and in previous publications, that experimental facts do not appear to fit with the conventional model of the GD plasma[1,9]. Mason et al. proposed that all of the results could be rationalised by modelling the GD plasma as a Rydberg gas[1,9]. Mason and Mitchell[1] described the polarisation of Rydberg atoms in the FFGD plasma, leading to the formation of charge transfer chains believed to carry the plasma (cone) current. This section describes the influence of the ion exit bias on the currents within the plasma, and details how the model can be applied to the results shown in the previous sections.

Let us assume the plasma to be a Rydberg gas, consisting of a mixture of high 'n' states, represented here as Ar^R, and other neutral Ar states. The data obtained in this part of the project is fully consistent with that hypothesis. Figure 4.13a illustrates two electrodes at opposite ends of the flowing afterglow plasma. Electrode A is located at the upstream end and electrode E is at the downstream end. In the FFGD system electrode A is the anode of the active discharge region and E is the ion exit cone. The mechanism presented here explains a number of the effects observed on variation of ΔV_E, the bias applied between two electrical probes immersed within the plasma. The variable power supply incorporated into the circuit allows the potential difference to be increased and the polarity of the electrodes to be reversed.

4.4.1 Passage of Current through a Rydberg Gas Plasma

Application of a voltage between electrodes A and E (figure 4.13 a) immersed in a Rydberg gas induces ionisation of Rydberg atoms at the electrode boundaries, and either cations or electrons are collected at the electrodes, depending on their polarity. Electrons released close to the anodic electrode are accelerated to the surface, temporarily leaving behind a layer of cations which prevent further movement of charge. The cations attract electrons from Rydberg atoms[10] within the plasma, leading to charge transfer (figure 4.13b). This occurs throughout the plasma to the cathodic electrode, leaving behind a layer of cations opposite the cathodic surface. This depresses the potential of the cathodic electrode below that of the plasma. Cations are then drawn to the cathodic surface, completing the circuit.

The current is limited by the rate of charge transfer across either the cathodic or anodic boundary layers. When a relatively low current flows, the voltage profile between the electrodes is as illustrated in figure 4.13c. In figure 4.13c ΔV_c is the cathodic sheath potential, ΔV_a is the anodic sheath potential and V_p is the plasma potential. At any point in the plasma the voltage can be thought of as comprising two components: (i) the field emanating from the electrodes, and transmitted by the dielectric behaviour of the medium, and (ii) the electrostatic charge generated by either an excess of either free ions or electrons in the vicinity of a probe. The former is responsible for charge transfer through the main body of the plasma as illustrated in figure 4.13b. With a current flowing, the voltage drop across the plasma, in the absence of (ii), would be that which obeys Ohm's law, with the resistance of the plasma clearly dependent on the concentration of the polarised Rydberg atoms. It is then possible to understand the observed voltage profile as follows.

4.4.2 At the Anodic Electrode (simple case)

The positive surface induces ionisation of Rydberg atoms in the gas layer adjacent to it and attracts electrons, inducing a current to flow across the plasma by charge transfer. This will continue as long as the conditions are conducive to charge migration across the cathodic sheath. Provided the rate of charge transfer through the plasma is as fast as the rate of ionisation, the net concentration of ions at the anode

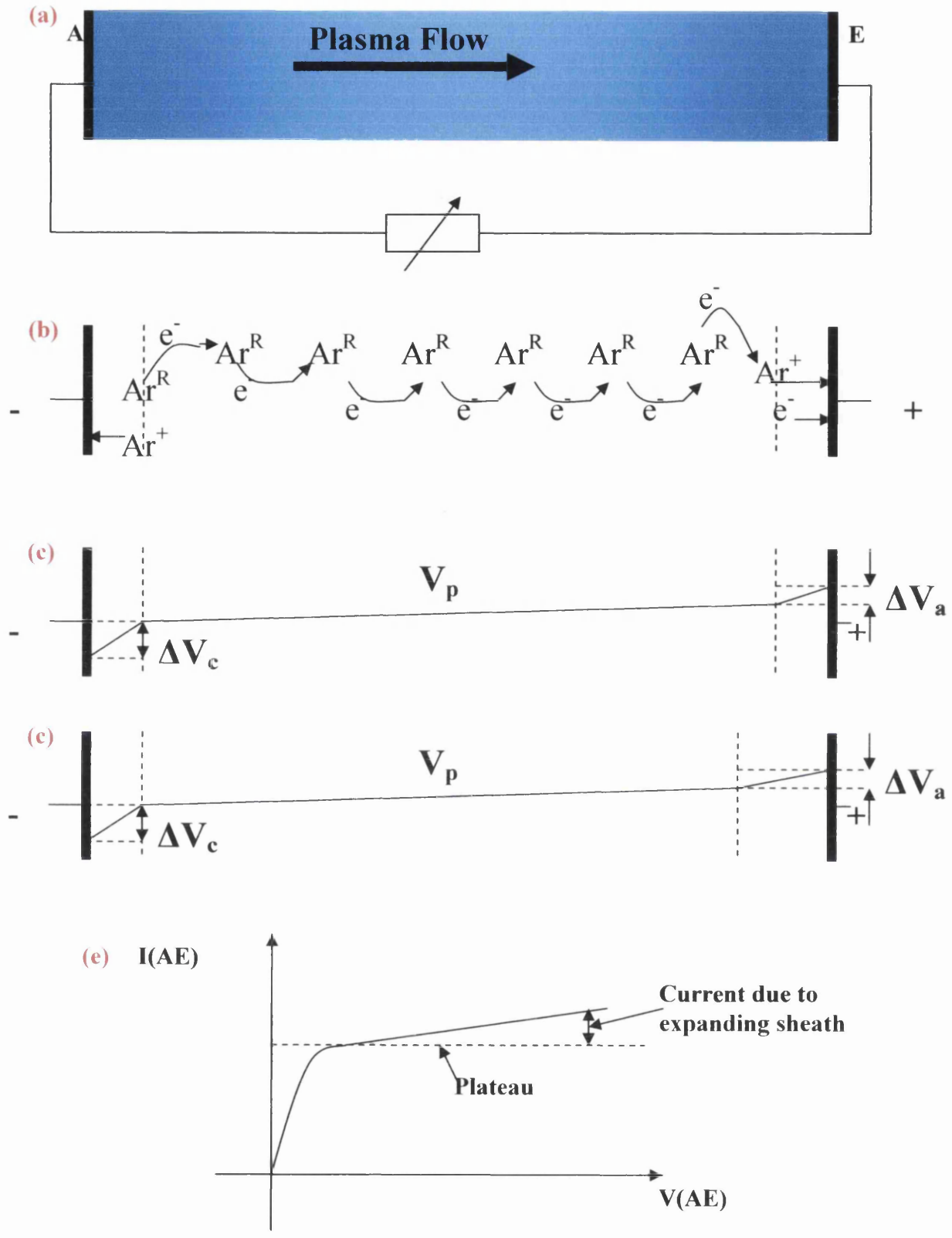

Figure 4.13: Current flow between two electrodes (electrically isolated from the main discharge electrodes) immersed in a Rydberg gas plasma

will be very small, and therefore the contribution V_{ii} (due to effect (ii) in section 4.4.1) will remain negligible. The voltage across the surface layer, V_i (due to effect (ii) in section 4.4.1), is then dependent on the resistance of the surface layer. Since the Rydberg atoms are quenched and ionised at the surface, the surface layer concentration is certain to be much less than in the bulk plasma, and the surface layer resistance much greater. Hence we observe an upturn in the voltage gradient (Ohm's law)[11].

The reaction scheme at the anodic surface layer, ASL, occurs as follows:

$$Ar^{R}_{ASL} + field \rightarrow Ar^{+}_{ASL} + e^{-}_{\rightarrow}\ (Current) \qquad (equation\ 4.1)$$

$$Ar^{R}_{ASL} + surface \rightarrow quenched \qquad (equation\ 4.2)$$

$$Ar^{+}_{ASL} + Ar^{R}_{ASL} \rightarrow Ar^{R'}_{ASL} + Ar^{+}_{ASL} \qquad (equation\ 4.3)$$

$$Ar^{+}_{ASL} + Ar^{R}_{pl} \rightarrow Ar^{R}_{ASL} + Ar^{+}_{pl} \qquad (equation\ 4.4)$$

$$Ar^{+}_{pl} + Ar^{R}_{pl} \rightarrow Ar^{R'}_{pl} + Ar^{+}_{pl} \qquad (equation\ 4.5)$$

etc, where Ar^{R}_{ASL}, $Ar^{R'}_{ASL}$ and Ar^{+}_{ASL} are argon Rydberg states and ions at the ASL and Ar^{R}_{pl}, $Ar^{R'}_{pl}$ and Ar^{+}_{pl} are argon Rydberg states and ions in the plasma. Equations 4.3 to 4.5 are the charge transfer processes responsible for the current flowing between two electrodes immersed in the plasma.

4.4.3 At the Cathodic Electrode (simple case)

The positive charge created at the sheath of the anodic electrode by field ionisation of the Rydberg gas is transferred by rapid charge transfer to the cathode. Hence there is a positive charge build-up on the opposite side of the cathode surface layer (CSL or cathode fall) and the plasma therefore floats at a potential close to that of the anodic surface. This is due to the different migration rates, due to their masses, of ions and electrons. For each electron reaching the anode, a cation must migrate to the cathode. The transfer of positive charge to the cathode surface creates the high negative field across the cathode fall, which provides the ion migratory force. For the electron and ion currents to be equal the fields must be very different.

The reaction scheme at the cathodic surface is as follows:

$$Ar^{+}_{pl} + Ar^{R}_{CSL} \rightarrow Ar^{R}_{pl} + Ar^{+}_{CSL} \qquad (equation\ 4.6)$$

$Ar^{+}_{CSL} \rightarrow$ *cathodic surface* *(equation 4.7)*

where Ar^{R}_{CSL} and Ar^{+}_{CSL} are Rydberg atoms and ions at the CSL.

4.4.4 Increasing the Applied Bias

For simplicity, a plasma of fixed Rydberg density and floating plasma voltage is considered. As the voltage at the anodic electrode is raised, the field across the anode sheath (ΔV_a) increases, increasing the rate of field ionisation at the ASL. This would be expected to increase the current continuously. However, a limit is reached when the rate of ionisation matches the rate at which Rydberg atoms reach the surface layer and the current goes through the plasma. Since no more ions can be created at the surface, a plateau region results. Increasing the anode potential further increases the sheath voltage and the thickness of the surface layer increases as ions are formed deeper into the plasma (figure 4.13d). This increases the number of Rydberg atoms exposed to the field, and hence leads to a further increase in current, though at a slower rate than previously. Since the charge is transferred back to the cathode, and the field created must always be such to match the rate of migration of ions to the cathode to that of electrons across the anode sheath, the plasma voltage adjusts to a point between the two. The current profile appears as in figure 4.13e.

This behaviour is observed for two electrodes immersed in the plasma which are electrically isolated from the anode and cathode of the main discharge. Such results were described in section 4.3.2 (figures 4.10 to 4.12) when probes A and B are immersed in the FAG plasma.

4.4.5 Behaviour when one of the Electrodes is a Reference Electrode

The behaviour is modified when one of the electrodes is the anode of the discharge and the other is located downstream in the FAG plasma (i.e. the ion exit cone in our experiments, which acts like the Langmuir probe in Langmuir probe measurements[2-4]). This is because, as we have observed, at high plasma densities the plasma density decays rapidly as it flows down the flow tube, which causes the plasma density at the anode to be very much greater than at the cone. The plasma density at the anode therefore dictates the level of the plasma voltage, and in effect

fixes the behaviour at the probe (i.e. cone). This is different to classical theory. Apart from the composition of the plasma being a Rydberg gas, the classical theory requires no decay of plasma along the axis[8].

4.4.5.1 Voltage at the probe (cone) negative with respect to the anode; cathodic behaviour

When a negative voltage is applied to the cone, i.e. the cone is the cathodic electrode, a negative field attracts ions to the surface as in section 4.4.3 and electrons at the anode as in section 4.4.2. The flow of electrons to the anode maintains a small positive field across the anode sheath and causes charge transfer through the plasma. The positive charge is rapidly transferred to the cone sheath. This sets the plasma potential close to that of the anodic electrode (the anode in this case), so the whole plasma tends to float at the anode rather than the cathode potential. As the negative cone bias is increased the current increases as before, except that the plasma voltage is no longer free to float continuously down to the level required to maintain equal electrode currents. It is anchored to the high plasma voltage close to the anode surface, set by the main discharge conditions. Due to this, as the negative voltage on the cone increases, although it tends to pull more ions onto the surface, the charge cannot be dissipated by charge transfer to the opposite electrode (because the anode sheath voltage is not free to respond as needed), and the current is therefore rapidly curtailed. The static ion concentration at the CSL opposite the cathode surface must therefore increase to offset the applied negative voltage (thus maintaining the plasma potential at the level set by the anode conditions), but in order to maintain a constant current the thickness of the sheath layer at the cathodic surface must expand to maintain the same ion migration rate. Ions drawn to the surface in front will be held back by the positive charge to rear. Bias differences up to > 100 V can be sustained in this way[1], when the ions accelerated reach very high energies. The voltage profile is illustrated in figure 4.14a, and the current profile in figure 4.14b. At a high enough voltage secondary electron emission at the surface will become important, and a new discharge, as at the main cathode, will occur.

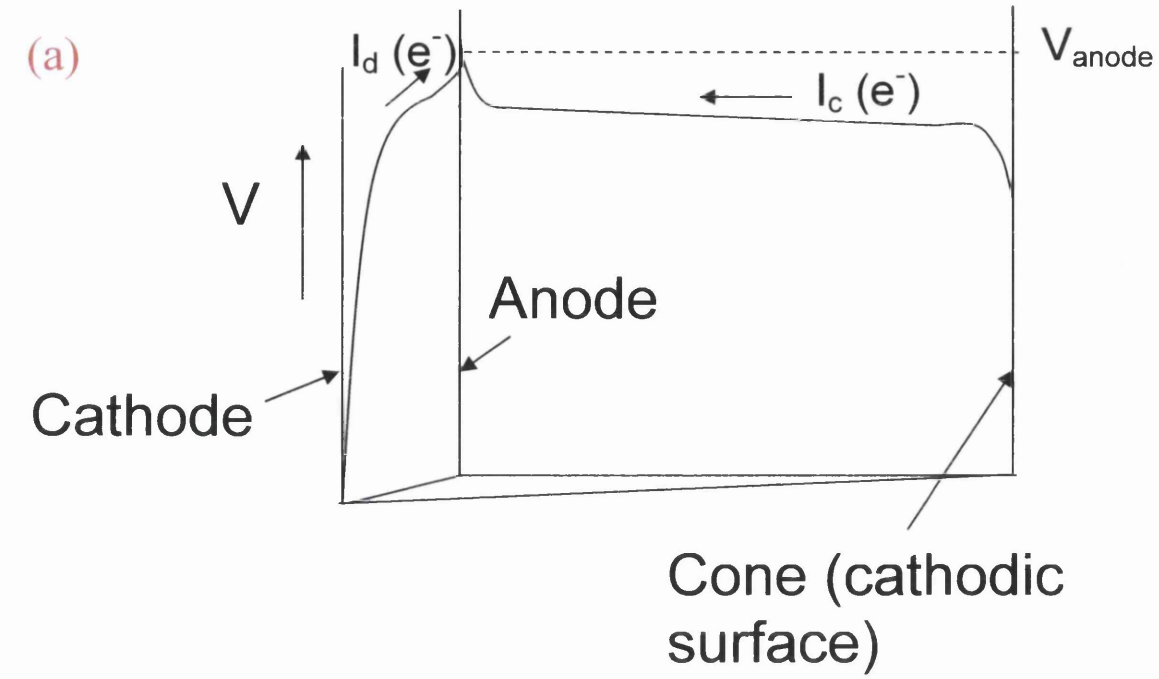

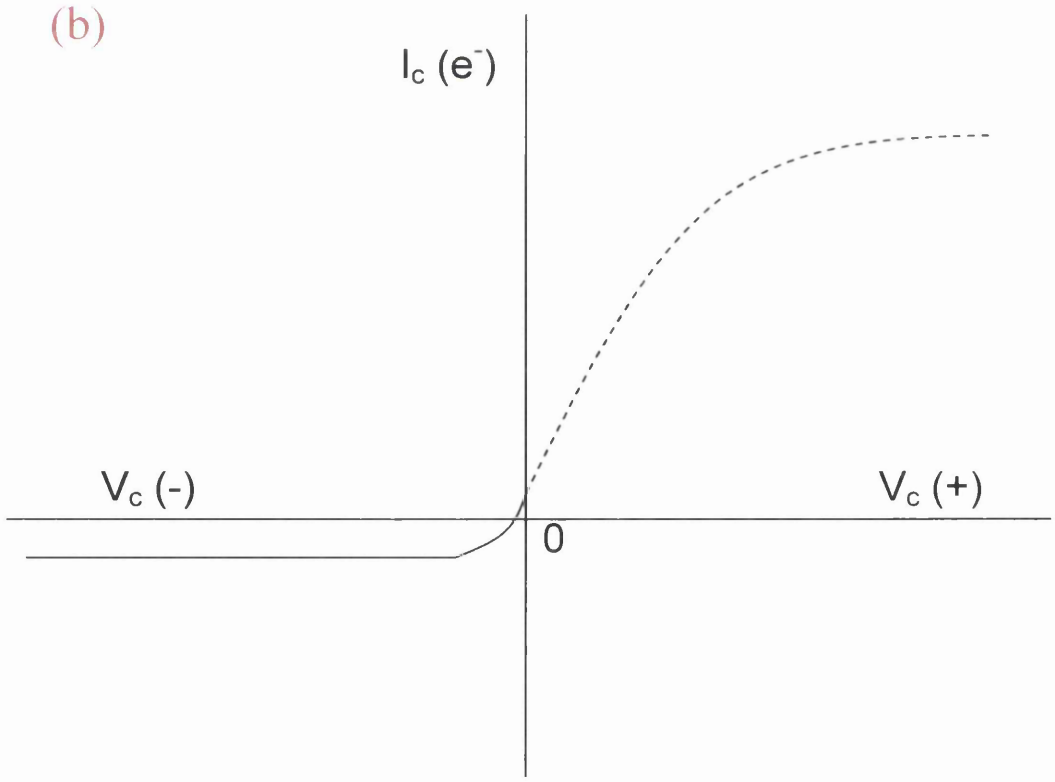

Figure 4.14: (a) electrode potential and (b) cone (plasma) current profiles on application of a negative bias to the ion exit cone of the FFGD source

4.4.5.2 Voltage at the probe (cone) positive with respect to the anode; anodic behaviour, 'simple' case

When the cone is biased positively relative to the anode, the anode becomes the cathodic surface in the secondary circuit. When the bias is zero, in a practical discharge plasma there is always a net current of electrons to the probe from the cathode. The voltage profile at this condition is shown in figure 4.15a. As a positive bias is applied to the cone, electrons are drawn from the plasma by field ionisation of the Rydberg gas and the positive charge is transferred back towards the anode/cathode region of the main discharge, thus raising the plasma potential in the vicinity of the Negative Glow/Positive Column boundary. Since V_p is below V_{anode}, the anode cannot be cathodic to the cone.

Whilst it is difficult to lower the plasma potential in the vicinity of the anode (see section 4.4.5.1), because of the overwhelming effect of the main discharge, in which it is the positive charge at the cathode fall boundary which must be depleted, the same is not true for raising the plasma potential. In this case it requires only that electrons are removed from the anode surface layer closest to the cone (probe). Hence, when the plasma potential is raised above that of the anode potential, by the processes described above, current can pass directly between the anode and the cone, but the portion of the anode surface involved is now cathodic in nature, whilst still continuing to provide the anodic surface for the main discharge. The voltage profile in this instance is as in figure 4.15b.

As in section 4.4.4 the current (I_c) increases in response to field ionisation at the anodic surface (i.e. the cone), which raises the plasma potential at the cathodic surface (the anode) by charge transfer, so that the cation current across the sheath matches the anode sheath current. It appears that this reaches a limit when the rate of field ionisation matches the flux of Rydberg atoms at the cathodic surface. This would explain why in figure 4.4b, between V_c = +8 and +16 V I_c is approximately constant. The current could not increase further without either (a) increasing the rate of ionisation in the ASL, or (b) increasing the rate of secondary electron emission at the cathodic surface. (b) requires very high energy ion or atom bombardment of the surface, and is responsible for sustaining the main glow discharge; the minimum cathodic sheath voltage required is > 300 V. (a) requires electron impact ionisation of the ground state gas (or its impurities), and it is shown here that it is this which occurs

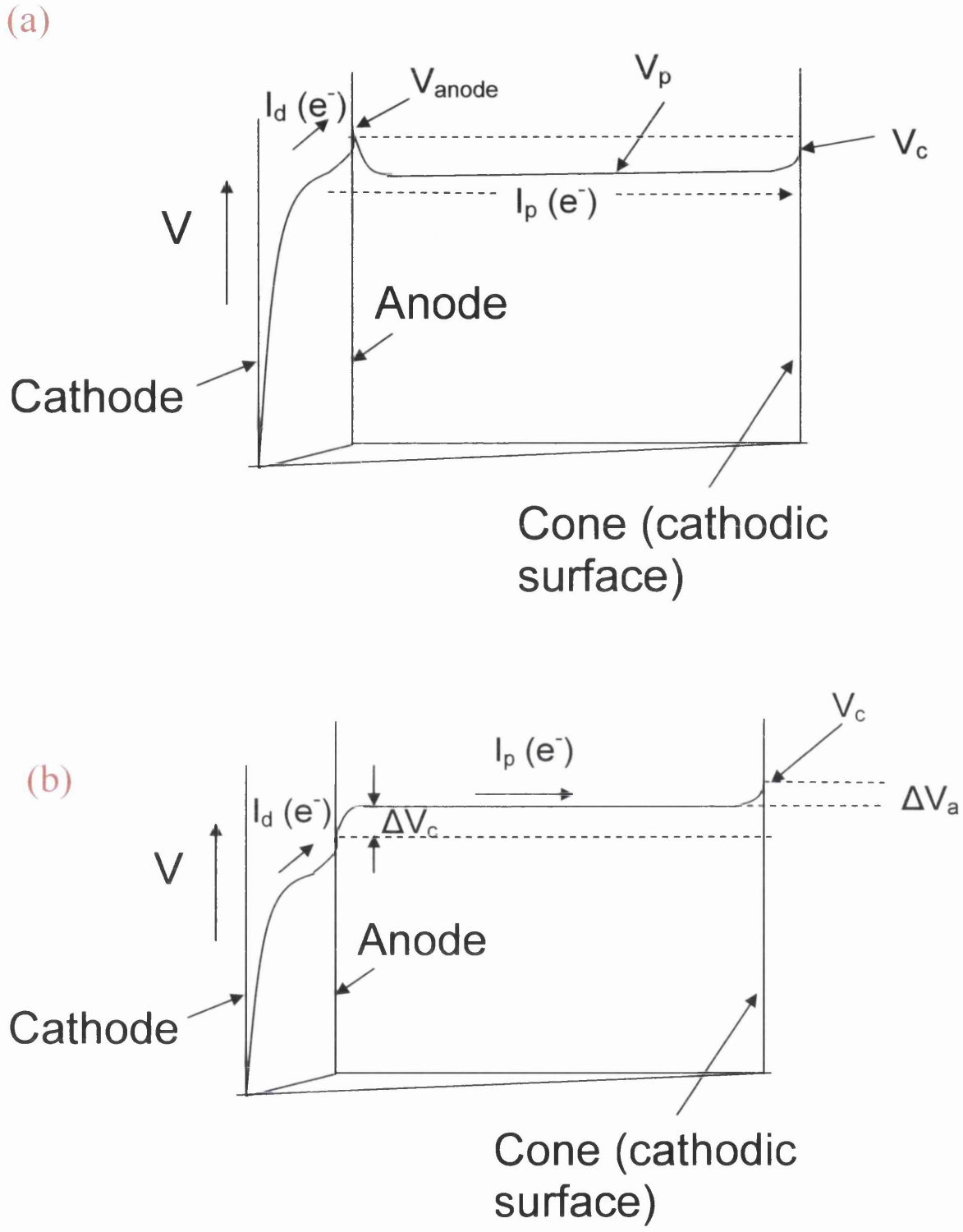

Figure 4.15 electrode potential profiles when a) $V_c = 0$ V and b) V_c is positive with respect to the anode of the main discharge

as the bias voltage is increased. The ionisation potential of Ar is 15.76 eV[13], and therefore electron energies of greater than this are required to ionise Ar. Thus, in figure 4.4, when V_c was > 16 V the current began to increase, and the same effect is observed throughout the results displayed in this chapter. However, lower electron energies are required to ionise metastable state species, Cu (7.73 eV[13]) and gaseous impurities in the plasma. Thus, it is also possible that when V_c is > +8 V EI ionisation of Cu, Ar^m, and trace impurities could occur.

With the above model in mind, the results in figures 4.5a and 4.6a can be explained. Since the FAG plasma is a decaying plasma, the longer the residence time the lower the Rydberg atom density at the ASL (near the cone). Hence, the longer the argon residence time, the lower the magnitude of I_c. Similarly, the density of the plasma is dependent on the discharge voltage, and thus as the discharge voltage is raised the Rydberg atom concentration at the ASL is also increased, therefore increasing I_c.

4.4.5.3 Voltage at the probe (cone) positive with respect to the anode; anodic behaviour, with electron impact ionisation in the ASL

As the bias voltage is increased from zero, the increase in the plasma potential which occurs causes the current to switch from flow between the main cathode (via the NG) to a flow between the anode and the cone. This must be the case because the current through the cathode increases very slowly, whilst that through the cone is very high. Beyond the Rydberg atom flux current limit at the cone, the voltage across the anodic sheath increases without an increase in the current, and therefore the width of the sheath expands (again to maintain the rate of electron migration from the sheath). As it does so electrons are released from the ionising Rydberg atoms further away from the anodic surface. They not only accelerate to a higher energy (because of the increasing sheath potential), but have an increasing chance of collision with the discharge gas. As discussed above, when their energy is > 15.76 eV electron impact ionisation of Ar can occur. When this happens at a sufficient rate a free ion-electron plasma is created within the sheath field. Once this happens, the free ions and electrons will separate according to charge. Electrons quickly migrate towards the anodic surface creating a negative field adjacent to the cone until the rates of migration of free Ar^+ and e^- are matched. This is superimposed on top of the voltage

gradient caused by the charge transfer current. The voltage profile between the anode and the cone is shown in figure 4.16. In this instance, the measured V(CB) value is the net potential difference between probe B and the ion exit cone and not the sheath potential.

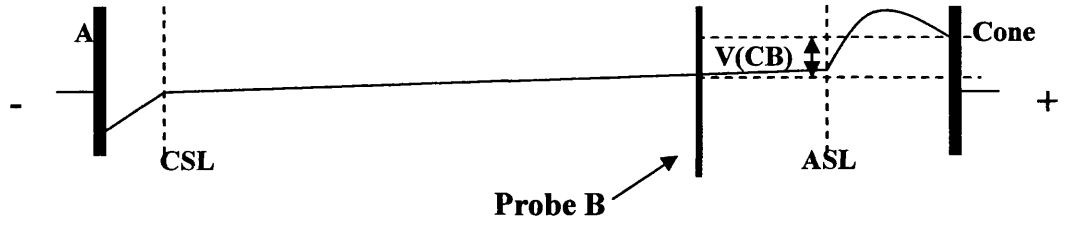

Figure 4.16: Voltage profile between the anode and the ion exit cone on application of V_c > the ionisation potential of Ar.

Without electron impact ionisation in the anodic sheath, the current through the plasma is governed by the steady state condition A (equation 4.8):

$$R_+^{csl} = R_{CT}^{pl} = R_{fi}^{asl} \qquad \textit{(equation 4.8)}$$

where R_+^{csl} is the rate of ion migration across the cathodic sheath, R_{CT}^{pl} is the rate of charge transfer through the plasma, and R_{fi}^{asl} is the rate of field ionisation of Rydberg atoms within the ASL.

With electron impact ionisation, the steady state current is governed by condition B:

$$R_+^{csl} = R_{CT}^{pl} = R_{fi}^{asl} + R_{ei}^{asl} - R_+^{asl} \qquad \textit{(equation 4.9)}$$

where R_{ei}^{asl} is the rate of electron impact ionisation within the anodic sheath, and R_+^{asl} is the rate of cation migration across the negative field created between the layer of free cations and the anodic surface. The latter partially offsets the extra current provided by secondary electrons created by electron impact.

A critical condition can occur when one steady state condition switches to the other. Thus, starting with condition A, as the voltage increases the point is reached when electron impact ionisation leads to a sudden increase in the concentration of the free ion-electron plasma. This creates a negative field at the surface which offsets the

bias below its applied value (figure 4.16). This causes the current to decrease, and hence removes the condition for electron impact ionisation. The system therefore reverts back to condition A. The cycle can then repeat, causing the system to oscillate. The most significant evidence of this effect was the oscillations in ion detection by mass spectrometry in experiments performed by Mitchell[1]. Under condition A, the positive field at the anodic surface (the ion exit cone) prevents extraction of cations from the source, and thus no ions are detected. However, under condition B, the negative field to the cone surface induced by charge separation in the ASL allows transmission of ions formed within the ASL. As soon as the system reverts back to condition A the ion signal is quenched. However, this fluctuation was not observed during the course of this work.

Later in this thesis (chapter 8) it is shown that under positive ion exit conditions ions were formed outside of the FFGD cell by field ionisation of Rydberg atoms in the extraction field beyond the ion exit orifice. As the free ions and electrons exit the GD cell they can recombine to form a Rydberg gas. Recombination is only likely to occur if the excess energy can be lost in collisions or as rovibrational transitions in molecules[13]. During collisional quenching it is possible for molecular Rydberg species to form. The implications of this on the mass spectra observed during this study are discussed in chapters 7 and 8.

4.4.6 Effect of the cone bias on electric fields in the active discharge and FAG plasma

The increase in I_d with increasing positive V_c observed throughout the results in this chapter indicates that on application of a sufficiently high positive V_c, the cone field begins to influence the fields in the active discharge region of the cell. On application of a suitably high V_c, the magnitude of which is dependent on the Rydberg atom density at the ASL (and therefore V_d and τ), there is a jump in I_c which corresponds to a sharp decrease in V(CB) (e.g. figure 4.5). This is possibly due to the creation of a secondary discharge between the anode and the cone. If the ions bombarding the anode (cathodic electrode) transfer enough energy to overcome the work function of the surface material then secondary electron emission from anode surface is possible. When the field across the CSL is > 16 eV, the ions accelerated across the sheath could ionise Ar by electron impact, as occurs in the active discharge.

This is balanced by charge transfer back to the cone as before. It is not possible to tell from the results whether the sheath at the cone is as shown in figure 4.15b or 4.16, but the increase in Rydberg atom density caused by the formation of a secondary discharge reduces the potential required to sustain the current.

It appears that when $\tau = 4.5$ ms a secondary discharge forms when $V_c < 20$ V, and therefore the current and voltage profiles differ significantly from those at longer τ. Similarly, when $\tau = 7$ ms (figure 4.6) the same current and voltage profiles were observed when $V_d = 800$ V, as that when $\tau = 4.5$ ms and $V_d = 700$V. However, since a secondary discharge apparently forms on application of $V_c \sim +10$ V, EI ionisation of Ar in the cathodic and anodic sheaths should not be possible. It is possible that for a short τ or high V_d, there is an increase in the formation of excited state species as well as an increase in sputtered Cu in the flowing plasma. These species could undergo EI ionisation in the anodic sheath, as described for Ar, therefore inducing a similar effect on application of a lower V_c.

On application of a positive V_c one would expect the probe closest to the cone surface (B) to be more positive than that further upstream (A), as it has been in the past[1,9]. Thus, it is unusual that in figures 4.3a and 4.4a probe A was more positive than probe B. This may be explained if the fields close to the anode are distorted due to charge transfer between the anode and the cone. Thus, probe A may be immersed in a region of the plasma which is at a potential higher than that expected. However, the results of this study do not show this conclusively. It is also possible that there is a zero error on the potential measurement which was not realised during this work. On the other hand, the potential of W (cell wall) was always negative with respect to B. When Rydberg atoms are ionised at surfaces the surface tends to become negatively charged due to the faster drift of electrons to it. V(WB) is dependent on the mean electron flux at the wall surface along its length, and the sheath field which forms. Since the wall extends further upstream from B than it does downstream, the sheath field due to ionisation of Rydberg atoms at the upstream (high Rydberg density) end dominates.

4.4.7 Voltage at the cone positive with respect to the anode; effect of Rydberg atom density on the voltage and current profiles

It has already been shown above that the Rydberg density at the ASL (cone sheath) is one of the critical conditions for the changes to the current and voltage profiles. The Rydberg density is dependent on both V_d and τ. Figures 4.7 to 4.9 therefore show the effect of the Rydberg atom density on the current and voltage profiles for a fixed V_c. When V_d is low (~ 400 V) the Rydberg atom density in the FAG plasma will also be low. Since the plasma decays exponentially, the Rydberg atom density at the ASL will be low, and hence I_c is also low. Figure 4.7 shows that as the Rydberg density is increased, and therefore the rate of field ionisation at the ASL is also increased, the Rydberg atom density becomes sufficient for EI ionisation to occur as above, and therefore V(CB) remains constant (see section 4.4.5). When the Rydberg density is further increased, V(CB) drops sharply as described for application of a high V_c.

In the same way, the I-V profiles for the floating probe system were highly dependent on τ. Comparison of the FFGD (figure 4.10) and static discharge conditions (figure 4.12) clearly shows that for a long τ the current which is carried by the FAG plasma is significantly lower than that for a short τ. Figure 4.12 also shows that under static conditions and in extended discharge mode, the plasma density depends on the discharge current, thereby fitting with the widely accepted free ion-electron model[8]. In this instance, this is because the discharge current stabilises the Rydberg gas through formation of charge transfer chains, not because more ions are created.

4.5 I-V Profiles; evidence to support the Rydberg gas model

It is not possible to fully rationalise the data using classical theory. We have already seen from published data that a Rydberg gas is a possibility. We now have a theory to show that such a gas is stable thermodynamically and is likely to form from theoretical consideration of the kinetics (section 2.7). Therefore we use the Rydberg gas theory to explain the data obtained here.

With this in mind, the plasma densities at probes A and B can be calculated. The I-V profiles in figures 4.10 to 4.12 are not symmetrical because, as you would expect

for fixed experimental conditions, the plasma density does decay even when carrying the discharge current. This is contrary to classical theory. Under extended discharge conditions there is still evidence of a reduction in plasma density, despite the fact that the probes are immersed in the active discharge. Figures 4.10 also illustrates that the I-V profile was independent of I_c and V_c, i.e. the plasma density does not change even though I_c changes very significantly. Classical theory requires that the plasma density is directly proportional to the current[8], but here this is clearly not the case.

4.5.1 Plasma Density

Classically, in Langmuir probe studies the plateau regions of the I-V profile are thought to be the ion and electron saturation currents of the Langmuir probe[12]. Since the reference electrode in such experiments is much larger the saturation current of the Langmuir is reached first. Thus, in symmetrical double probe studies the saturation currents should be equal because the probes are of equal surface areas. However, for a decaying Rydberg gas plasma the "plateau" currents, i_{1+} and i_{2+}, can be used to calculate the Rydberg atom densities at points (A) and (B) in the plasma, assuming that the "plateau" current is due to ionisation of all Rydberg atoms at the probe surface.

Equation 4.10 relates the measured current due to Rydberg gas ionisation at probe A, I_{2+}, to the Rydberg atom flux at the probe surface:

$$I_{2+} = F\left[Ar^R\right]_A e.Area \qquad (equation\ 4.10)$$

where F is the discharge gas flow rate (in $cm^3\ s^{-1}$), $[Ar^R]_A$ is the plasma density at probe A, e is the charge on an electron and *Area* is the surface area of the probe (the probe surface areas are considered to be equal, although a small difference in surface area is certain, particularly on deposition of sputtered cathode material). The current due to ionisation of the Rydberg gas at probe B, I_{1+}, and the plasma density at the probe surface, $[Ar^R]_B$ can be related in the same way. I_{1+} and I_{2+} were again measured as indicated in figure 2.11. Using these values, the Rydberg atom densities at each probe have been calculated (the surface area of a probe is 0.47 cm^2) and tabulated below (table 4.4):

Residence Time (ms)	3.7	5.7	7.5
$[Ar^R]_A$ (FAG plasma, Vc = 0 V) ($x10^{12}$ cm^{-3})	8.6 ± 7%	8.2 ± 19%	5.3 ± 17%
$[Ar^R]_B$ (FAG plasma, Vc = 0 V) ($x10^{11}$ cm^{-3})	8.1 ± 45%	5.6 ± 20%	4.4 ± 33%
$[Ar^R]_A$ (Extended Discharge) ($x10^{12}$ cm^{-3})	1.86 ± 10%	3.4 ± 8%	1.85 ± 25%
$[Ar^R]_B$ (Extended Discharge) ($x10^{12}$ cm^{-3})	0.4 ± 43%	3.4 ± 13%	4.89 ± 11%

Table 4.4: Plasma densities at the probe surfaces at different residence times and comparison of results when the probes are immersed in the FAG plasma and active discharge (V_d = 450 V, P = 1.5 Torr)

In the FAG plasma the plasma density at both probes decreases with increasing τ, as expected for a decaying plasma. However, in the ED plasma the density at probe A was affected much less, and the plasma density at probe B actually increased with increasing τ. This increase in plasma density can be rationalised as a result of ion-electron recombination processes within the positive column plasma. The Rydberg gas forms via recombination of ions and electrons as the plasma flows between the anode and cathode.

Assuming that the plasma decays exponentially the decay constant, k_{decay}, can be calculated using equation 4.11[11]:

$$\ln\left(\frac{[Ar^R]_B}{[Ar^R]_A}\right) = -k_{decay}\Delta t \qquad (equation\ 4.11)$$

where Δt is the residence time of the plasma between the two probes. The variation of the decay constant with residence time under fixed discharge voltage and pressure conditions is shown in figure 4.17, for both FAG and ED modes of operation. The decrease in k_{decay} with increasing τ indicates that the plasma becomes more stable at slower flow rates, i.e. lower plasma densities. According to theory (section 2.7), as the plasma density decays, the range of n values for Ar^R moves up. The radiative lifetimes of these states increases as $n^{4.5}$,[10] and therefore the Rydberg gas is stabilised.

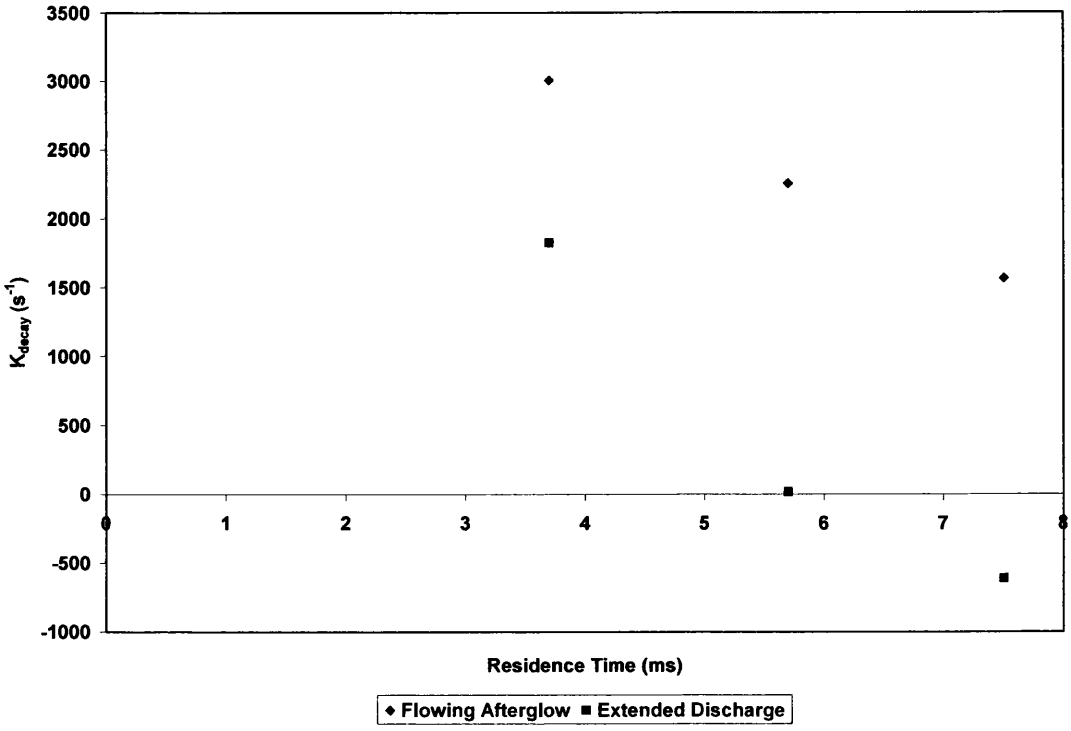

Figure 4.17: Variation of measured (between probes A and B) Rydberg gas decay constant with τ when the probes are immersed in a) the flowing afterglow plasma (FAG mode) and b) the active discharge (ED mode) (V_d = 450 V, P = 1.5 Torr)

Comparison of figures 4.11 a and b shows that when the full discharge current flows, the curves become more symmetrical and therefore the plasma is more stable. According to the theory, the current flows by charge transfer directly between Rydberg atoms. The Rydberg atoms must therefore become highly polarised. We believe that under the conditions of the full discharge current, the polarised medium is effectively held stationary over the time it takes an electron to travel between the cathode and anode. We have seen this stabilisation when adding hydrogen to the plasma carrying the discharge current. When carrying I_d, the plasma is non reactive to H_2[9], but when not carrying I_d (FAG mode) the plasma is rapidly quenched[9].

From figure 4.12 it could perhaps be understood how the plasma, under the normal static gas conditions of an axial glow discharge, might appear to have an almost constant plasma density along its length. In addition, since in the extended discharge the current is increased by increasing the discharge voltage, it is bound to increase the plasma density. Hence, it can be understood why the original theory developed the way it did. However, as we shall see, it is not a necessary condition for the current to flow.

4.6 Conclusions

It has been shown that the majority of the results presented in this chapter cannot be explained by the conventional free ion-electron model of a plasma. An extension of the Rydberg gas model developed by this group has been presented which accounts for all of the results. Some of the most important observations are detailed below:

- The results indicate that the FAG plasma decays as it moves downstream, but conventionally the plasma should be continuously re-energised.
- Field ionisation of Rydberg atoms at the anodic and cathodic boundaries is responsible for the current carried to the electrode surfaces.
- An axially polarised Rydberg charge transfer chain carries I_c through the FAG plasma.
- The upper limit of V(CB) corresponds to the applied cone voltage at which EI ionisation of Ar, and subsequent formation of a free ion-electron plasma, is initiated in the cone sheath (ASL).

- The fast migration of electrons to the cone surface from the free ion-electron plasma leaves a positive boundary layer, thereby forming a negative field to the cone surface. This allows release from the source of a recombining plasma, the Rydberg atoms formed from which can be field or pressure ionised (see section 2.7) outside the GD cell.
- The I-V profiles show that the plasma density was not influenced by the magnitude of V_c despite the large differences in I_c, but classically I_c is proportional to the plasma density.
- The current profiles obtained using a floating probe system differ from those where the anode is a reference electrode, because in the latter case the plasma density at the anode dictates the plasma voltage.
- The Rydberg gas is stabilised at low flow rates (lower Rydberg atom densities) because the range of n states is lifted, thereby increasing the radiative lifetime, which scales as $n^{4.5}$.[10]
- On application of a high V_c, and possibly on increasing the Rydberg density in the flowing plasma, a secondary discharge forms between the ion exit cone and the anode of the active discharge.

4.7 Summary

The results presented in this chapter are in good agreement with those obtained by Mitchell and therefore fit with the Rydberg gas theory previously presented[1]. Extending the range of V_c, V_d and τ for which the results were recorded further strengthen the Rydberg gas model by illustrating the effect of each parameter on the currents and probe potentials, both of which are dependent on the Rydberg atom density, within the plasma.

4.8 References

[1] D. J. Mitchell, Ph.D Thesis, University of Wales Swansea, 2002

[2] I. Langmuir and H. M. Mott-Smith, *Phys. Rev.*, **28**, 727, 1926

[3] I. Langmuir and H. M. Mott-Smith, *Gen. Elec. Rev.*, **26**, 731, 1923

[4] I. Langmuir and H. M. Mott-Smith, *Gen. Elec. Rev.*, **27**, 449, 538, 616, 762, 810 (1924)

[5] A. Reifman and W. G. Dow, *Phys. Rev.*, **76**, 987, 1949

[6] E. O. Johnson and L. Malter, *Phys. Rev.*, **76**, 1411, 1949

[7] L. Schott, *Plasma Diagnostics*, ed. W. Lochte-Holtgreven, North-Holland Publishing Co., Amsterdam, 1968

[8] B. Chapman, *Glow Discharge Processes*, John Wiley & Sons Ltd., 1980

[9] N. A. Dash, PhD Thesis, University of Wales Swansea, 2004

[10] T. F. Gallagher, *Rydberg Atoms*, Cambridge University Press, 1994

[11] P. W. Atkins, *Physical Chemistry 5th edition*, Oxford University Press, Oxford, 1997

[12] D. R. Lide, *Handbook of Chemistry and Physics*, CRC Press, 1995

[13] I. P. Mortimer, PhD Thesis, University of Wales Swansea, 2000

[14] R. S. Mason, P. D. Miller, I. P. Mortimer, *Phys. Rev. E*, **55**, 7462, 1997

[15] I. P. Mortimer, D. J. Mitchell, N. A. Dash and R. S. Mason, *Proceedings of the XIVth International Conference on Gas Discharges and their Applications*, **2**, 260, 2002

[16] F. Llewellyn-Jones, *The Glow Discharge and an Introduction to Plasma Physics*, Meuthen & Co. Ltd, London, 1966

Chapter 5

Ion Kinetic Energy Measurements: Evidence of Ion Formation Processes Inside and Outside the Ion Source

5.1 Introduction

In previous studies by Mason et al.[1-5] it was observed that the magnitude of the ion exit bias had a significant effect on the intensities and kinetic energies of the ions detected. Dash[4] reported that increasing the (negative) ion exit bias induced an almost linear increase in the observed ion kinetic energy for ArH^+, Cu^+ and H_2O^+ (figure 5.1). The kinetic energy lens of the mass analyser accelerates or decelerates ions to optimise transmission through the electrostatic analyser (ESA) (see chapter 3). Since the optimum kinetic energy for ion transmission through the ESA is set, the kinetic energy of an ion can be determined from the accelerating or decelerating potential applied to the kinetic energy lens. The response shown in figure 5.1 indicates that the ions observed were formed within the FFGD cell and therefore gained kinetic energy through acceleration in the ion extraction field close to the ion exit orifice. Taylor[6] observed a linear increase in ion kinetic energy with increasing positive ion exit potential. However, the authors did not make clear the circuitry of the apparatus. It is implied in the paper that the plasma potential is raised as a result of the ion exit bias being increased positively, and it is this that is responsible for the increase in the kinetic energy of ions emerging. In fact, the results presented suggest that the ion exit was biased positively relative to the mass spectrometer earth, therefore accelerating the ion beam into the instrument. The increase in kinetic energy is therefore neither here nor there.

Initial studies on the new instrument concentrated on the detection of cations on application of a negative V_c. This would be expected to accelerate ions towards the ion exit orifice, whereas a positive bias would be expected to repel cations back into the bulk plasma. In the measurements during this project the kinetic energy values turned out to have only limited value due to problems with the instrument electronics (see chapter 3).

5.2 Kinetic Energy Analysis: Where Are Ions Formed?

Figure 5.2a illustrates the typical profile of an ion kinetic energy (KE) map generated using the EI ion source within the mass spectrometer probe itself. It is a single envelope with a distribution of energies to either side of the maximum, indicating ion formation at different points in the EI source, with the ions thereby

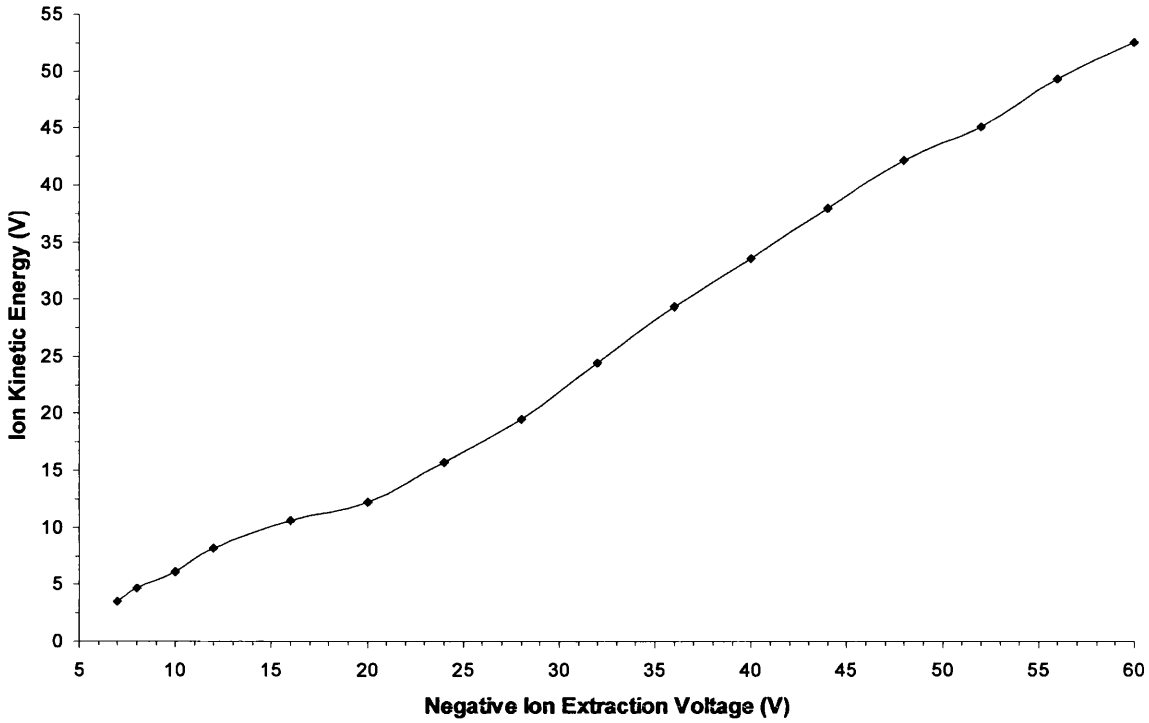

Figure 5.1: Effect of ion exit bias on $^{63}Cu^{+}$ kinetic energy recorded by Dash[1] (V_d = 680 V, I_d = 6 mA, P = 1.5 Torr, τ = 2 ms)

acquiring slightly different energies. It is typical of data published in the literature[7] and shows that the instrument is working properly. The ions are given their KE by a repeller voltage applied to accelerate the ions from the EI source. The KE measured corresponds to the KE lens bias required to optimise detection of the ions. This value should be equal in magnitude to the repeller bias applied to accelerate the ions.

Figure 5.2b illustrates a typical ion kinetic energy map of ions from the FFGD ion source, generated on application of a cell bias (accelerating potential, see chapter 3) of +70 V. In the new kinetic energy map there are two distinct maxima, A and B, indicating that ions may be formed in two different points in the system or via two different processes. The applied cone voltage was -60 V. Clearly "B" ions were formed inside the GD cell and accelerated across the cone sheath field, therefore giving excess energies over the accelerating potential of up to 20 eV (ions formed outside the GD cell and accelerated by V_{cell} would be expected to have a maximum kinetic energy equal to or less than that induced by the full magnitude of the accelerating potential). "A" ions were formed either at or beyond the ion exit aperture (when KE values < 70 eV are registered). The Ar^+ ions at "A" could have formed by symmetric charge transfer;

$$Ar^+_{\rightarrow} + Ar \rightarrow Ar_{\rightarrow} + Ar^+ \qquad \textit{(equation 5.1)}$$

as Ar^+ ions are accelerated through the aperture into the gas plume beyond. However, figures 5.3b and c show that Ar^{2+} and Cu^+ exhibit the same pattern. These ions could not both be formed by charge transfer in exactly the same way. It indicates therefore that there is a general ionisation beyond the ion exit aperture. This would be caused by two processes; (1) field-ionisation in the accelerating field, and (2) expansion of the plasma, leading to spontaneous (pressure) ionisation at low Rydberg densities (see section 2.7). To form Ar^{2+} outside the discharge cell it is likely to be due to ionisation of a "double Rydberg"[8] atom, i.e. an atom in which two electrons are excited to high n states. It is likely that formation of Ar^{2+} is enhanced on application of the accelerating field, as represented in equation 6.2.

$$Ar^{R*} + electric\ field \rightarrow Ar^{2+} + 2e^- \qquad \textit{(equation 5.2)}$$

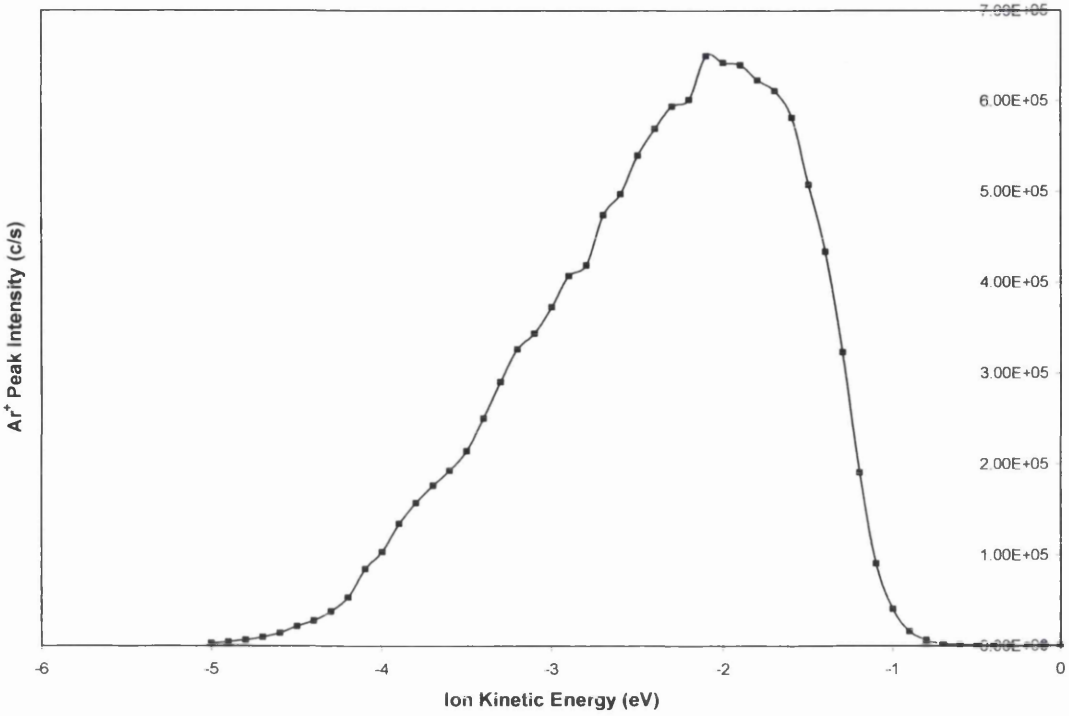

Figure 5.2a: Ar^+ kinetic energy map (argon only, electron energy = 20 eV, cage voltage = 0 V, tuned for Ar^+)

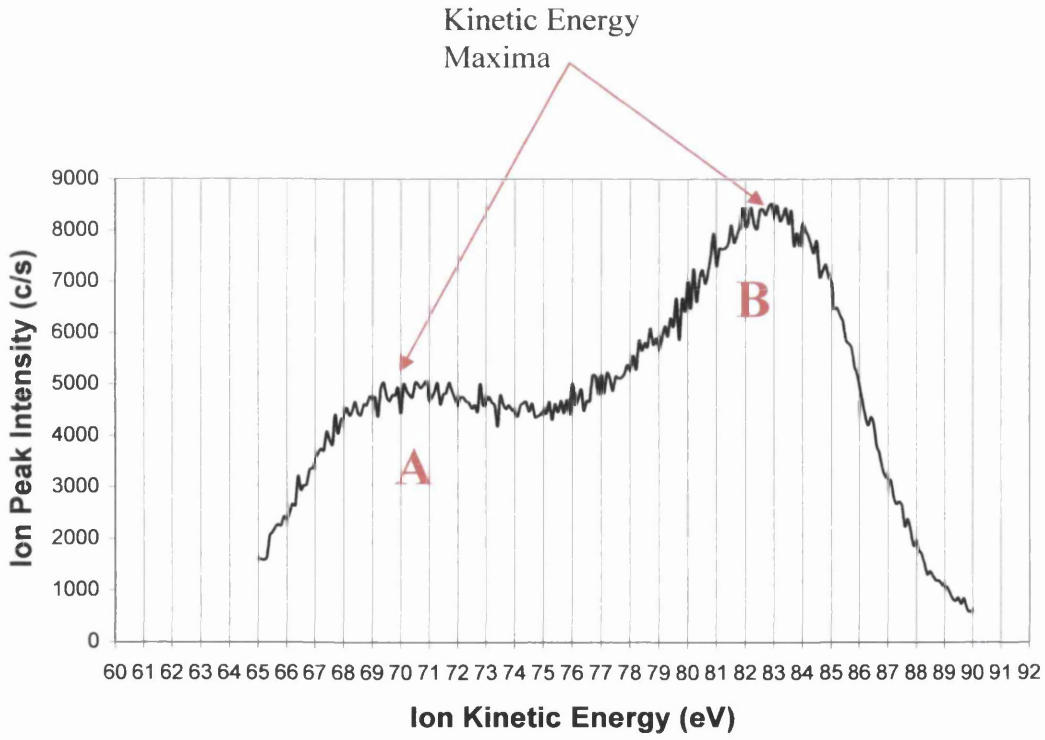

Figure 5.2b: Variation of argon ion intensity with kinetic energy of ions entering the mass analyser (V_d = 940 V, I_d = 5 mA, P = 0.8 Torr, F_{Ar} = 188 sccm, V_c = -60 V, V_{cell} = +70 V, $V_{cylinder}$ = -80 V, V_{einzel} = 0 V, optimised for Ar^+ detection)
A – ions formed outside source by field/pressure ionisation, B – ions formed and extracted from inside the GD cell

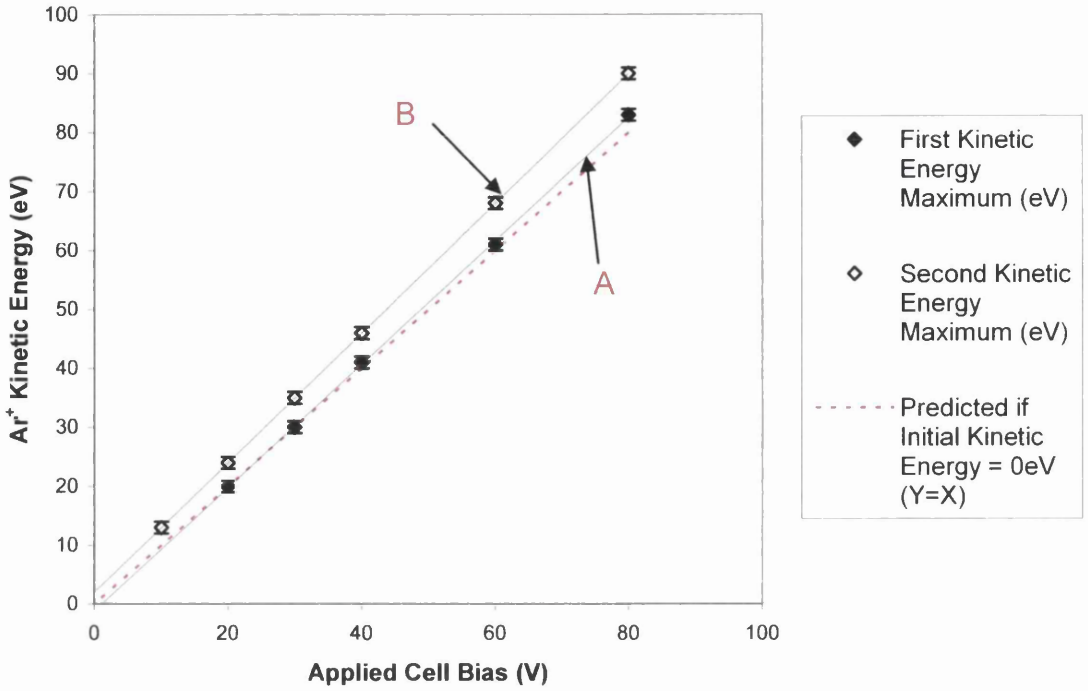

Figure 5.3a: Variation of Ar^+ kinetic energy with applied cell bias (V_{cell}) (V_d = 940 V, I_d = 5 mA, P = 0.8 Torr, τ = 5.68 ms, V_c = -60 V, $V_{cylinder}$ = -80 V, V_{einzel} = 0 V)

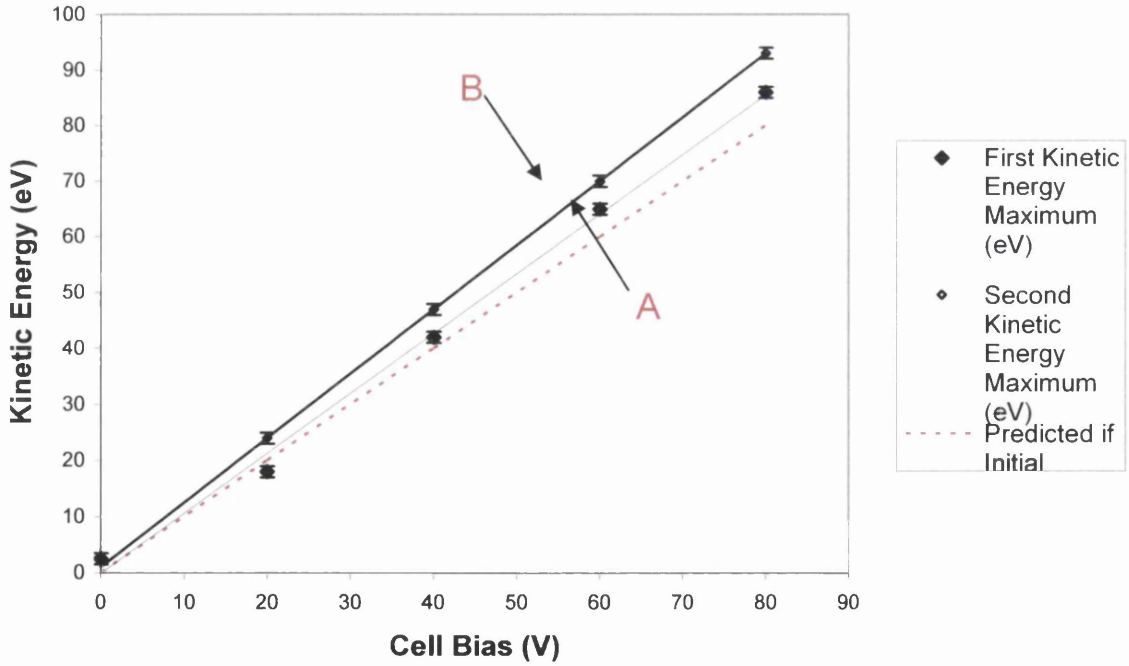

Figure 5.3b: Variation of Ar^{2+} kinetic energy with applied cell bias (V_{cell}) (V_d = 889 V, I_d = 5 mA, P = 0.8 Torr, τ = 5.68 ms, V_c = -60 V, $V_{cylinder}$ = -130 V, V_{einzel} = -10 V)

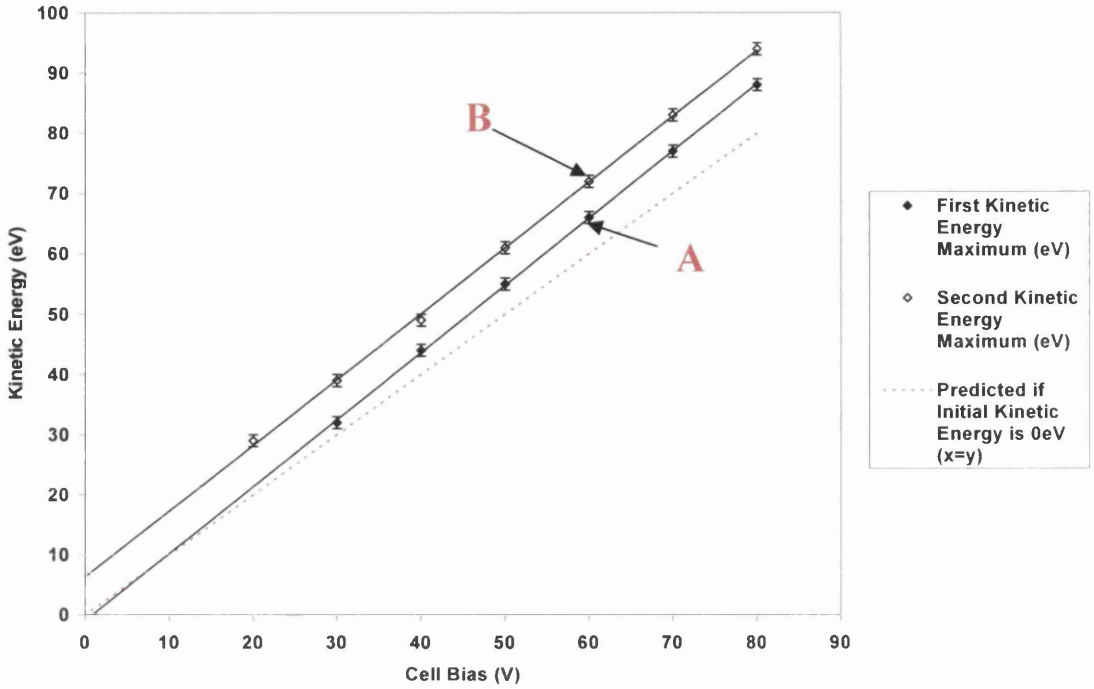

Figure 5.3c: Variation of Cu^+ kinetic energy with applied cell bias (V_{cell}) (V_d = 889 V, I_d = 5 mA, P = 0.8 Torr, τ = 5.68 ms, V_c = -60 V, $V_{cylinder}$ = -180 V, V_{einzel} = -10 V)

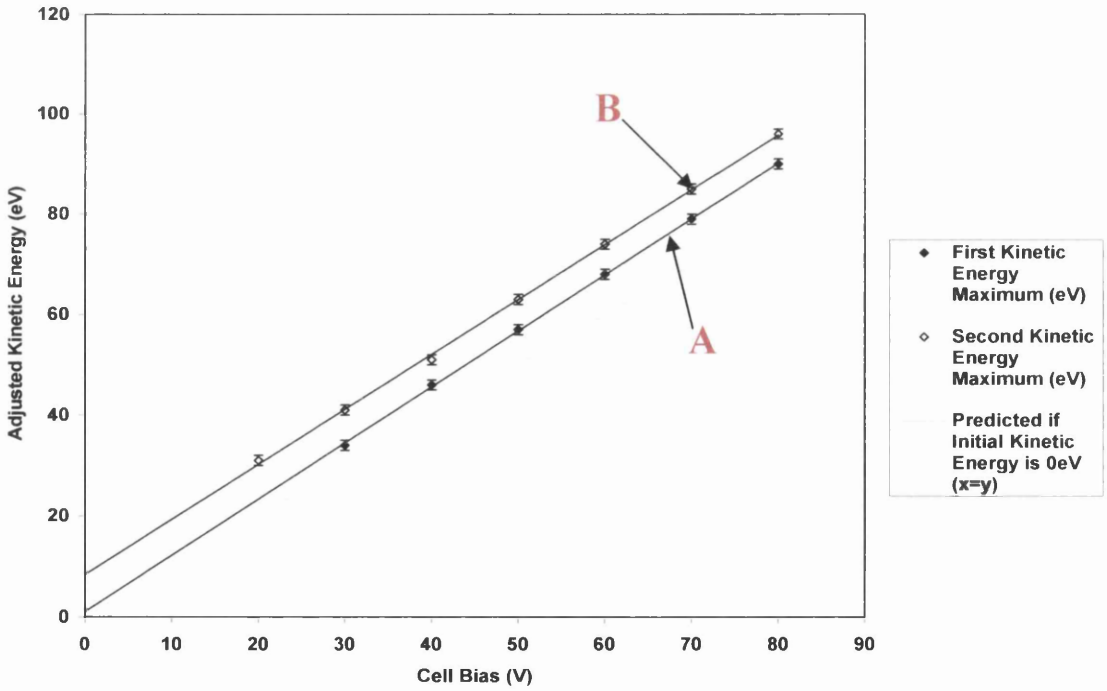

Figure 5.3d: Variation of corrected Cu^+ kinetic energy with applied cell bias (V_{cell}) (V_d = 889 V, I_d = 5 mA, P = 0.8 Torr, τ = 5.68 ms, V_c = -60 V, $V_{cylinder}$ = -180 V, V_{einzel} = -10 V)

Figure 5.3 shows the variation of the kinetic energy maxima, A and B (as indicated in figure 5.2b), as a function of the cell bias potential. The measured KE of the ions varies linearly with a gradient of approximately 1 eV per V, as expected. For each peak, the line of best fit predicts positive and negative intercepts for B and A respectively. A positive intercept implies that the ions had an initial kinetic energy on passing through the ion exit aperture, or that there was a zero error on the kinetic energy scale of the instrument. The negative intercept implies that ions were formed after leaving the ion exit aperture.

Using the electron impact source it was possible to form ions with known kinetic energy by setting the cage voltage to a known value. Figure 5.2a illustrates the variation of Ar^+ peak intensity with kinetic energy lens bias when the cage bias was set to 0 V. It was observed that when the cage (repeller) voltage was set to zero the ions appeared to have negative kinetic energy. This constitutes a zero error of -2 ± 0.2 eV. Thus, the negative intercept for the lower kinetic energy peak (A) is caused by a zero error on the kinetic energy scale. Ions therefore have little or no initial kinetic energy and are formed at, or beyond, the ion exit aperture. It was subsequently noted that the zero error of the kinetic energy scale varies with contamination of the lens stack e.g. due to oxidation or the build-up of organic materials or carbon (from methane addition) or sputtered metal on the lens surfaces.

Figure 5.3d illustrates the variation of the copper ion KE, adjusted to account for the zero error, as a function of V_{cell}. The intercept of the extrapolated line of best fit indicates that the lower KE species (A) have little KE prior to acceleration, whereas the higher energy species (B) had 8.4 eV. If figures 5.3a and b were similarly adapted, the kinetic energy of the "B" ions would be 4 eV for Ar^+ and 3 eV for Ar^{2+}. It is observed that the copper "B" ion KE was significantly higher, and therefore it is formed in the GD cell under the influence of the negative V_c, but the argon ions were formed closer to the ion exit aperture, possibly due to charge transfer (equation 6.1) as described above.

Chapter 4 describes how ionisation of Rydberg state species in the cone sheath field can lead to extraction of ions from the source and how the formation of a recombining plasma can lead to ion formation outside the source. Low energies of Ar^+ ions may be accounted for by symmetric charge transfer in the ion exit region. However, the same cannot be applied to Ar^{2+}, and therefore ion formation is shown to

occur outside the discharge cell. This result illustrates that ion-molecule processes cannot account for all observed results.

5.3 Summary

The results presented in this chapter clearly illustrate that the kinetic energy function of the mass analyser probe correctly measures changes to the ion kinetic energies. The main aim of this study was to determine where the ions detected were formed. It has been shown that ions can form inside or outside the discharge cell, as reflected in their kinetic energies. Ions formed outside the discharge cell have less than or equal to the maximum kinetic energy which can be achieved due to the accelerating potential (V_{cell}), whereas on application of a negative ion exit bias ions formed within the cell have a higher kinetic energy due to the negative potential drop across the cone sheath. This is indicated by two distinct ion signal maxima, as indicated in figure 5.2.

5.4 References

[1] I. P. Mortimer, PhD Thesis, University of Wales Swansea, 2000

[2] D. R. Williams, PhD Thesis, University of Wales Swansea, 2001

[3] D. J. Mitchell, PhD Thesis, University of Wales Swansea, 2002

[4] N. A. Dash, PhD Thesis, University of Wales Swansea, 2004

[5] K. Newman, PhD Thesis, University of Wales Swansea, 2005

[6] W. S. Taylor, J. G. Dulak and S. N. Ketkar, *J. Am. Soc. Mass Spectrom.*, **1**, 448, 1990

[7] Hiden EQP/EQS manual, Hiden Analytical Ltd., Warrington, UK

[8] T. F. Gallagher, *Rydberg Atoms*, Cambridge University Press, 1994

Chapter 6

Investigation of Ionisation Processes Downstream of the Active Discharge Region: Combined Mass Spectrometric and Electrical Studies

6.1 Introduction

This chapter details electrical and mass spectrometric results obtained with and without addition of secondary gases (hydrogen, methane and carbon tetrafluoride) to the FAG plasma of the new FFGD instrument (described in chapter 3). Simultaneous electrical and mass spectrometric studies allow direct comparison between results, and therefore aid understanding of the processes occurring within the plasma. Addition of secondary gases to the FAG plasma allows further chemical reactions to be studied. The new instrument has the advantage of allowing both cation and anion detection under the same discharge and ion extraction conditions. Therefore, it is possible to compare both sets of ion results directly with electrical probe results. Zero-current potentiometry enables the determination of local plasma potentials relative to a second electrode (discussed in more detail in section 2.8). Thus, potential gradients within the FAG plasma can be determined. The bracketed letters denote the two points in the plasma between which the zero-current potential was measured. The probe setup is illustrated in figure 3.10. The probes used in this study are probe A (A), probe B (B), the cone (C) and the cell wall (W). The potential of the first denoted probe relative to the second is illustrated, e.g. in figure 6.1c, Probe A is always more positive than B. The majority of results presented in this section were performed on application of a positive ion exit bias. For all results in this chapter secondary gases were added through probe B.

Addition of hydrogen and methane to the FAG of the FFGD plasma has been studied extensively within this group[1-12]. The majority of the work has focussed on positive ion mass spectrometry under negative or zero bias ion exit conditions. A brief study of negative ion formation from methane and hydrogen was carried out by Mortimer[2], but the influence of the discharge and ion extraction conditions was not examined. Mitchell[4] studied the variation of the cone current and probe potentials with V_d and argon residence time for the Cu/Ar FFGD plasma as well as the influence of the hydrogen addition to the FAG plasma. Dash[5] investigated the effect of concentrations of a range of gases, including hydrogen and methane, on the electrical properties of plasma and observed ion intensities. However, simultaneous studies of the effect of ion exit bias on spectrometric results and probe potentials on addition of secondary gases have not been performed.

6.1.1 Error Estimates

The key feature of the results in this chapter is how the intensities of the major ions vary with i) V_c (figures 6.1, 6.2, 6.8, 6.9, 6.12 and 6.16a), ii) V_d (figures 6.3, 6.4, 6.10, 6.13 and 6.16b) and iii) percentage addition of secondary gas (figures 6.5, 6.7, 6.11 and 6.15), and how changes in the ion intensities correspond to changes in the measured currents (I_c and I_d) and probe potentials. Very large variations in the absolute ion intensities (over 100% is possible) are observed due to the rapid deterioration of the performance of the new instrument and the low ion intensities measured, but the run to run patterns indicated in the figures were reproducible. The reproducibility of the measured currents and probe potentials is far better, with errors commonly within the region of ± 10%. Minor fluctuations are not reproducible between runs, unless stated, and no attempt has been made to rationalise them. A typical run to run reproducibility for a single ion and a current are given below:

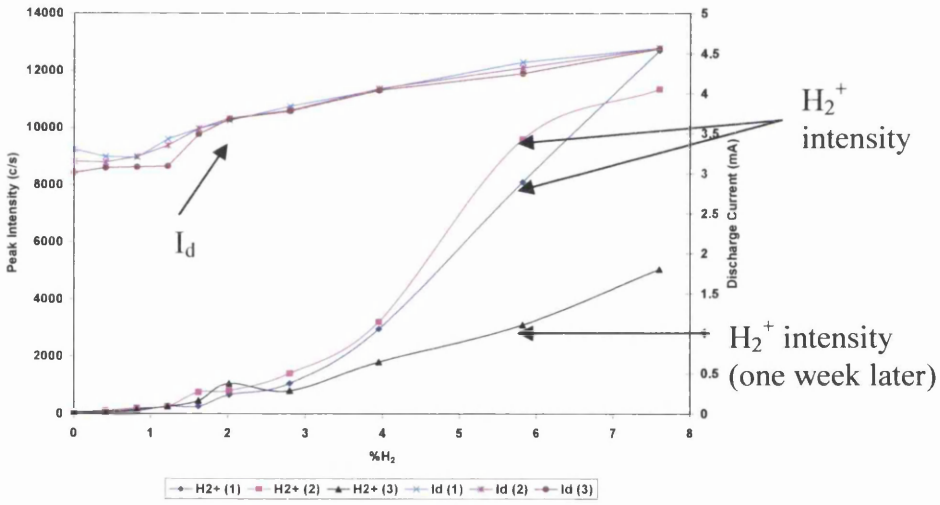

Run to run reproducibility of ion peak intensities and discharge current. It is clear that even for results recorded one week later the ion intensities were significantly lower, but the discharge conditions were unchanged. This figure is relevant to figure 6.11.

(V_d = 625 V, V_c = +30 V, P = 0.9 Torr, τ = 7.1 ms, V_{cell} = +70 V, Tuned for Ar^+)

6.2 No Secondary Gas Addition

Studies of ion formation on application of a positive V_c were performed without addition of secondary gas in order to determine the process by which ions are formed. On application of a positive, repulsive, ion exit bias one would not expect to detect cations formed within the discharge cell. Therefore it seems that the ions must be formed within or beyond the ion exit orifice. The Rydberg gas model presented in chapter four and sections 2.6 and 2.7 explains how cations could form in this system. It was thought that electrical probe results recorded in situ with mass spectrometric studies could provide valuable evidence in determining the validity of the model. The results presented here also describe the detection of negative ions.

6.2.1 Influence of the Applied V_c

6.2.1.1 Positive Ion Studies

Figure 6.1a illustrates the variation of observed cation intensities with changing V_c. This experiment was performed prior to modification of the instrument to improve ion transmission. On increasing V_c positively, the intensity of each ion showed a general increase. This obviously does not fit with conventional plasma theory, as the probability of a cation having enough energy to penetrate the repulsive field around the ion exit decreases with increasing positive V_c.

Figure 6.1b illustrates the variation of the same ion intensities for both positive and negative values of V_c after all modification of the instrument was completed. The maximum intensity of each ion was observed on application of a negative V_c, with the majority of ions reaching a maximum when V_c was -60 V. On application of a positive ion exit bias Ar^+ remained the major ion species and the other ion peaks were barely distinguishable from the background noise. As before, the argon ion intensity was observed to increase with increasing positive V_c.

Figure 6.1c illustrates the electrical probe studies performed in situ with this experiment. On application of a negative V_c, V(CB) is approximately equal to V_c. The model presented in chapter 4 shows that this is due to the formation of a large negative voltage drop across the narrow cone (cathodic electrode) sheath induced on application of a negative ion exit bias. However, on application of a positive ion exit bias the rate of increase of V(CB) decreases until a relatively stable value (~ +3 V) is

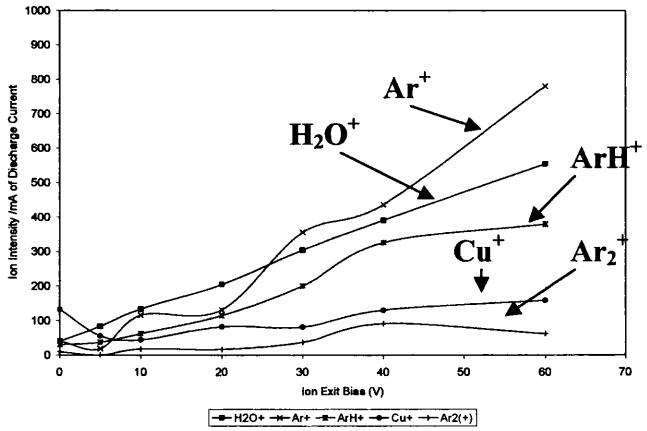

Figure 6.1a: Variation of ion peak intensities and plasma currents with V_c (V_d = 883 V, P = 0.75 Torr, τ = 3.6 ms, tuned for Ar^+)

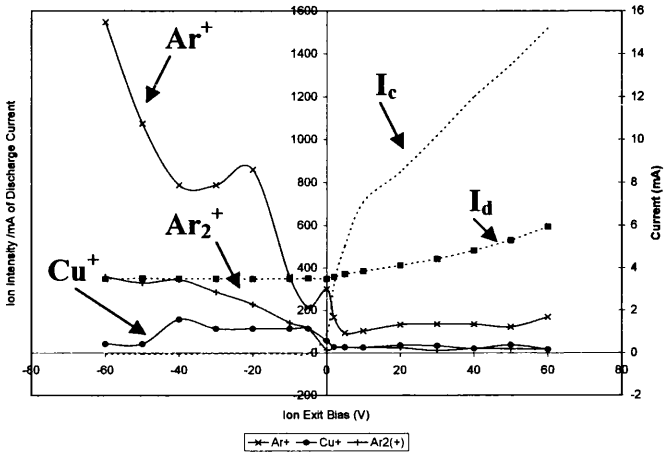

Figure 6.1b: Variation of ion peak intensities and plasma currents with V_c

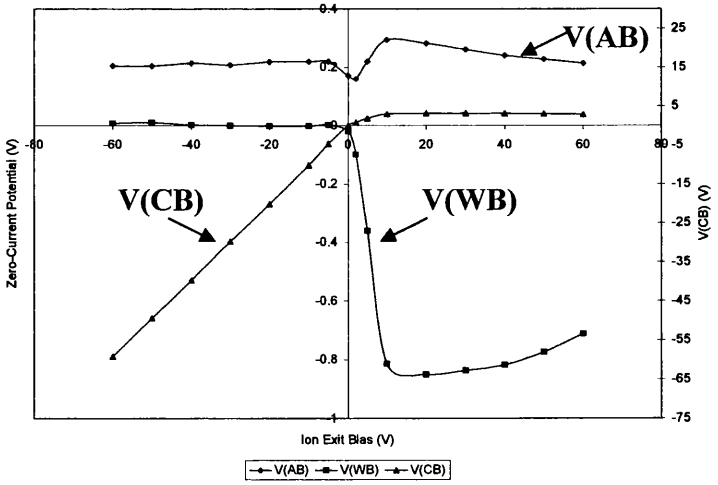

Figure 6.1c: Variation of zero-current potentials between electrical probes with discharge voltage
(V_d = 700 V, P = 0.9 Torr, τ = 7.1 ms, V_{cell} = +70 V, $V_{cylinder}$ = -180 V, V_{einzel} = +10 V, tuned for Ar^+)

reached. In chapter 4 it was described how on application of a positive V_c electron impact ionisation of Ar in the cone sheath leads to a constant V(CB) of 15 – 16 V. In this instance electron impact ionisation appears to occur when $V_c \sim +10$ V, and V(CB) is limited to approximately +3 V. For electron impact ionisation of Ar to occur in the cone sheath electrons energies of ~ 16 eV are required, and therefore this cannot be the case in this example. However, it is possible that that the same effect could be observed for ionisation of trace gases present (Ar^m, Cu, with ionisation energies of 4.2-4.4 and 7.72 eV)[19]. The conditions which favour this would therefore appear to be those that efficiently produce Ar^m in the cathode fall region of the main discharge.

When EI ionisation occurs in the cone sheath, a free ion-electron plasma forms and a negative potential drop to the cone results (see chapter 4). The products therefore represent the products of electron impact ionisation and recombination of the free ion-electron plasma back into a Rydberg gas as it passes through the aperture. Ar^+ is therefore the major reaction product, and the Cu^+ intensity remains approximately constant. Ar_2^+, also detected, we believe to be one of the products of associative recombination of Ar^+ to form Ar^R during recombination of the plasma as it passes through the aperture. Due to the high ionisation energy of water (12.6 eV)[19], H_2O^+ is probably a product of charge transfer.

Application of a positive V_c also induced a significant change to V(BW). In the model presented in chapter 4 it is suggested that on application of a positive V_c the Rydberg charge transfer chains are stabilised when carrying a current. The Rydberg atoms in the centre of the flow tube are likely to be more stable than those closest to W. As V_c is increased, more Rydberg atoms become involved in carrying the cone current, and therefore the density of Rydberg atoms close to B which can be ionised decreases. Thus, W becomes increasingly more negative than B (the effect is exaggerated somewhat due to the scale of the graph). Above $V_c = +10$ V, when EI ionisation appears to occur, there was very little change in V(WB).

In figure 6.1c V(AB) is positive for all values of V_c. When V_c is negative electrons flow from the cone to the anode (discussed in chapter 4), but the current is almost zero, and therefore the potential difference between A and B should be approximately zero. However, on application of a positive V_c, for electrons to flow towards the cone the potential at B should be more positive than at A (based on Ohm's law). In a Rydberg gas, the sheath potential at each probe is determined by the number of electrons released from Rydberg atoms at the probe surface. Since the

Rydberg density is higher at A (decaying plasma) one would again expect A to be more negative than B. It is therefore unusual that A is more positive than B for all values of V_c. It is possible that the ionisation of Rydberg atoms occurs more readily at B. As the plasma decays the density of Rydberg atoms decreases, and therefore the Rydberg atoms tend to expand, thereby increasing the n values. Assuming that overlap of Rydberg atoms is not possible (as assumed in the model described in section 2.7) the volume of the Rydberg atoms and therefore *n* (volume is proportional to n^6)[18] is limited by the space into which the Rydberg atoms can expand. As the plasma decays as it flows downstream the Rydberg density decreases, and therefore the *n* level of the Rydberg atoms is less restricted and excitation via energy transfer processes can occur. Thus, at the surface of probe B the atoms would be ionised more easily. However, we presume that the additional ionisation due to this effect would not have such a significant influence, and therefore it is likely that the value registered is evidence of a zero error in the measurement.

The results in this section cannot be explained by the conventional model of a GD plasma, but fit the Rydberg gas model described in chapter 4 well. Field ionisation is induced on application of an ion exit bias, and therefore on application of a negative V_c ions can be extracted from the cone sheath. Ionisation of Rydberg states, formed in a recombining plasma, outside the source can occur in the presence of an electric field (e.g. V_{cell}) or at low Rydberg concentrations (see section 2.7). Therefore, cations are still detected in the presence of a repulsive ion exit field.

6.2.1.2 Negative Ion Studies

Figure 6.2a illustrates the variation of the major anion intensities with V_c for a much lower V_d (and therefore plasma energy). There are two distinct regions for ion formation. The first ion intensity maximum occurred between $V_c = 0$ and +4 V. It is possible that, as concluded by Pinnaduwage et al.[13-16], ions are formed by dissociative attachment of free electrons to excited state species within the flowing plasma. However, as described in chapter 4, when V_c was > +16 V, the second region of anion detection, creation of an ion electron plasma occurs within the cone sheath and a negative field is created to the cone surface. This is indicated by the change to a maintained constant V(CB), as illustrated in figure 6.2b. Thus, negative ions should be repelled by the negative field that forms. However, based on the results of

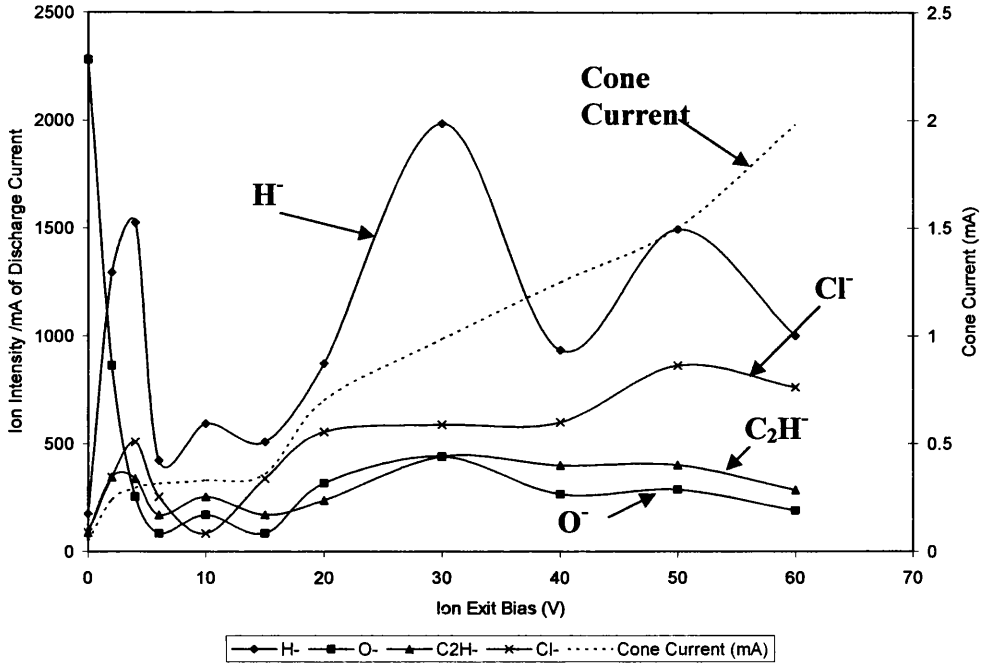

Figure 6.2a: Variation of negative ion peak intensities with V_c (no secondary gas)

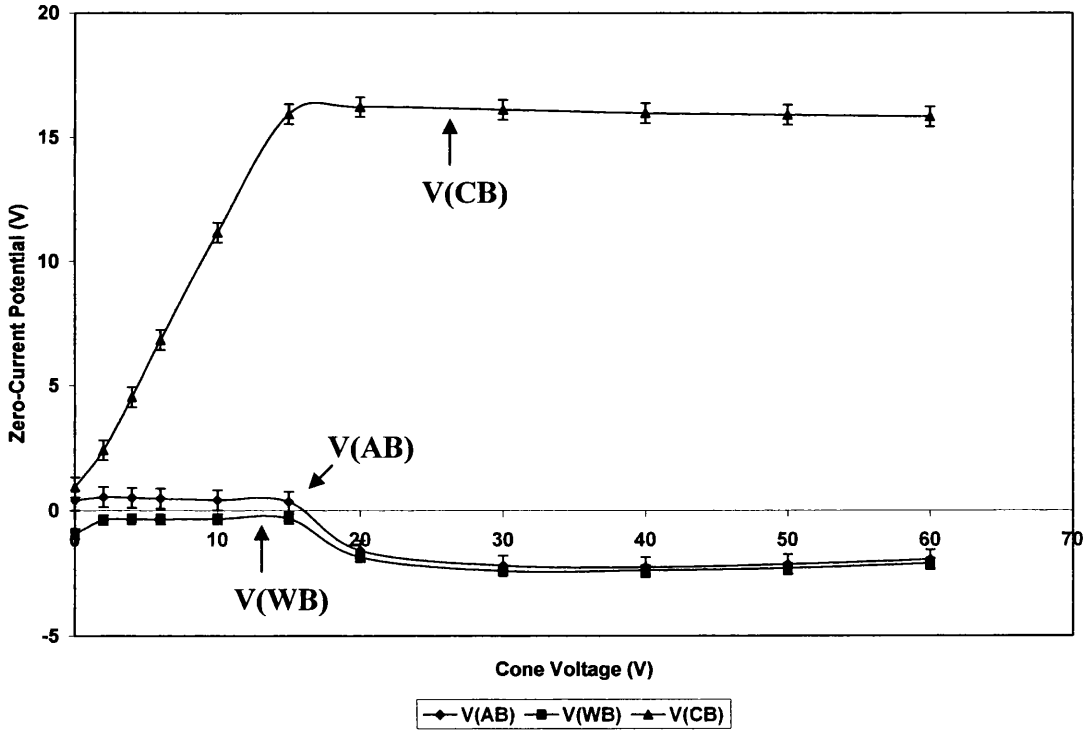

Figure 6.2b: Variation of probe potentials with V_c
(V_d = 490 V, P = 0.9 Torr, τ = 6.9 ms, V_{cell} = -70 V, $V_{cylinder}$ = +180 V, V_{einzel} = +10 V, tuned for H^-)

Mitchell[4], we believe that the field at the surface tends to go up and down as EI, ion migration and charge transfer compete. This may explain why the negative ion signals varied in the way observed.

It is also possible that negative ions could form via attachment of free electrons to Rydberg species in the recombining plasma outside the source, or that formation of both positive and negative ions could occur via electron transfer from a Rydberg atom. The valence electron of a Rydberg atom is very loosely bound and could therefore be transferred in a low energy collision (equation 6.1). The anions all result from the background gases, since these are the only species present with positive electron affinities. Cl^- (confirmed by isotope patterns) is intriguing since it can only be present in ultratrace levels in the reagent gases or as a result of out-gassing from the gas line or source components.

$$Ar^R + X \rightarrow Ar^+.X^- \rightarrow Ar^+ + X^- \qquad \textit{(equation 6.1)}$$

The major ion signals, as illustrated in figure 6.2a, are all fragment ions. This conforms to the dissociative electron attachment model of Pinnaduwage et al[13-16].

V(AB) and V(WB) were both approximately zero for $V_c < +15$ V, i.e. when EI ionisation of the discharge gas cannot occur. When V_c was increased from +15 to +20 V, both V(AB) and V(WB) became negative, as expected (see section 6.2.1.1).

6.2.2 Influence of V_d

6.2.2.1 Positive Ion Studies

Figure 6.3a illustrates the effect of V_d on the copper and argon cation intensities when V_c is small and positive. As V_d is increased, I_d increases, and therefore so does the Rydberg gas density. The results of the increases due to this effect are taken out of the plot by dividing the ion signals by the discharge current. It is then interesting that the Ar^+ intensity has been observed to increase almost linearly with increasing V_d, but the Cu^+ intensity remained approximately constant. It has been shown previously that when V_c is low, ionisation of Rydberg atoms passing through the ion exit aperture is predominantly responsible for Ar^+ and Cu^+ formation beyond the active discharge region[3,6,17]. The Ar^+ intensity is dependent on the Ar^R concentration, and therefore increases with increasing V_d. The formation of Cu^R is dependent on the

argon metastable and copper concentrations in the FAG plasma, and therefore the two effects are likely to differ. Thus, since the Cu^+ intensity remains constant, it appears that the Cu is completely ionised. The cone current increased with increasing V_d, i.e. as the Rydberg density increased.

Figure 6.3b shows that V(CB) was usually less than half of the applied cone bias (+4 V) and the value decreased with increasing V_d. The Rydberg gas model presented in chapter 4 illustrates that the magnitude of V(CB) is highly dependent on V_c. As V_c was very low in this experiment V(CB) was also low. V(WB) and V(AB) were both very small and little change was observed to either. The small reduction in each value may be indicative of the increased stability of the Rydberg gas, and therefore lower levels of ionisation at surfaces, when it carries a large current. As before, it is unclear why V(AB) was positive.

6.2.2.2 Negative Ion Studies

Figure 6.4a shows the variation of the major current-corrected anion peak intensities with increasing V_d without addition of secondary gas. The major ions observed were O^- from trace water, H^-, C_2H^- probably from residual hydrocarbons, and Cl^- (discussed above). Other ions observed include OH^-, CuO^-, CuO_2^- and H_3O^-. In fact, many of the ions detected are due to the presence of trace water in the cell. Two maxima were observed for each peak, when V_d = 460 and 675 V. Table 6.1 shows the electron affinities of species present within the FAG plasma. Cl (identified by its isotope pattern) has the highest electron affinity, and therefore even at ultratrace levels (Cl containing compounds had not been used in the instrument for over 2 years prior to this study) the Cl^- signal was the highest for almost the complete range of V_d. This is in part due to the fact the instrument was tuned for Cl^- detection. The electron affinity of O is ~0.37 eV lower than that of OH[19] and therefore one would expect OH^- to be more abundant if anions form by associative electron attachment (equation 6.2). However O^- was the dominant ion. This can be explained by dissociative electron attachment, as proposed by Pinnaduwage et al.[13-16] (equation 6.3). In this mechanism attachment of a slow electron to excited state water or OH occurs and rapid dissociation of the negative ion formed is induced. Since dissociation of H_2O^- or OH^- can lead to formation of O^- it is possible to form O^- in higher abundance. Pinnaduwage also states that the attachment of electrons to excited state species,

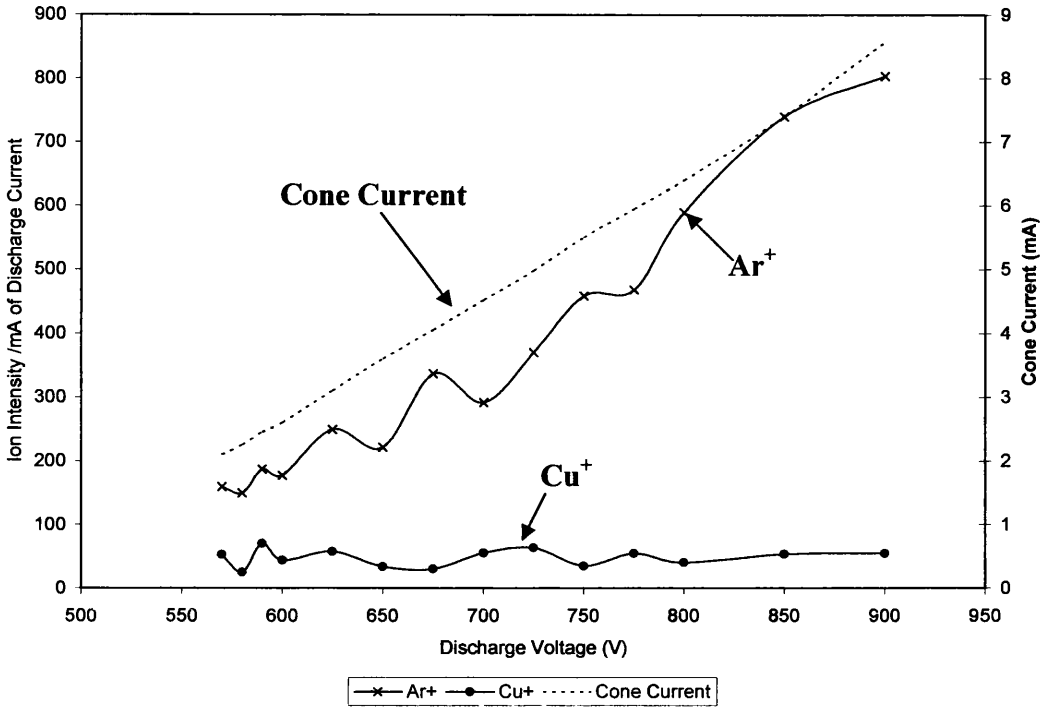

Figure 6.3a: Variation of ion peak intensities and plasma currents with discharge voltage

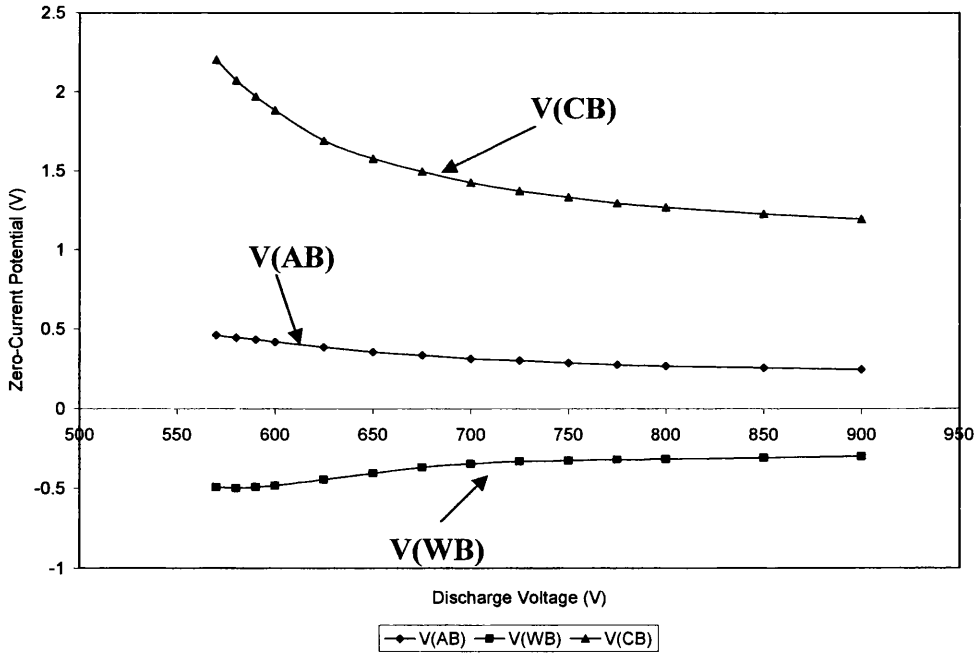

Figure 6.3b: Variation of zero-current potentials between electrical probes with discharge voltage
($P = 0.9$Torr, $\tau = 6.9$ms, $V_c = +4$V, $V_{cell} = +70$V, $V_{cylinder} = -180$V, $V_{einzel} = +10$V, tuned for Ar^+)

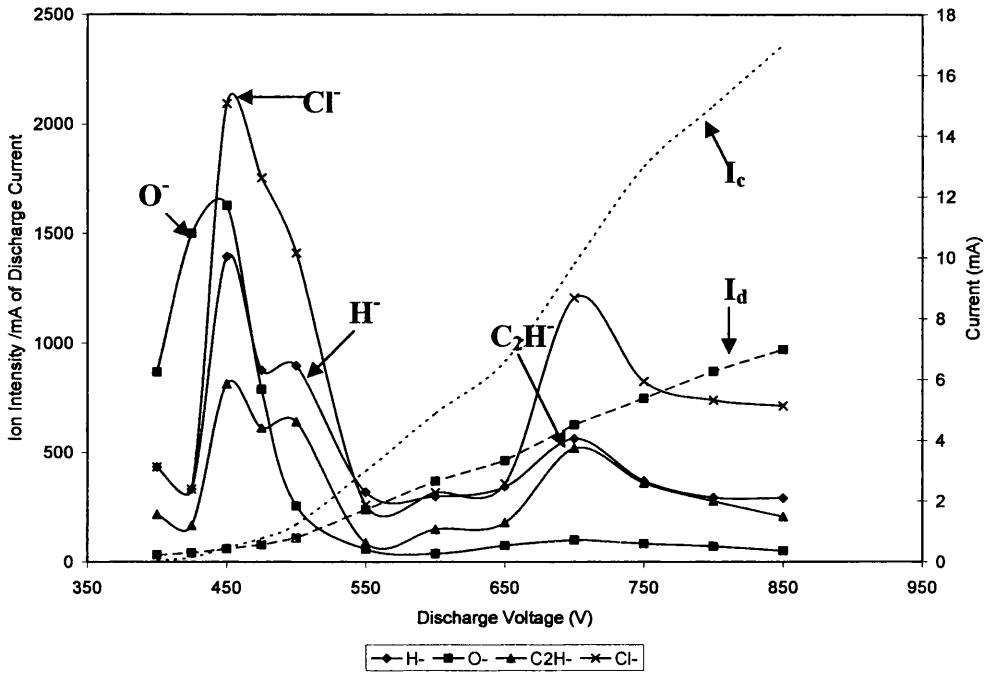

Figure 6.4a: Variation of negative ion peak intensities with discharge voltage, major ions (no secondary gas)

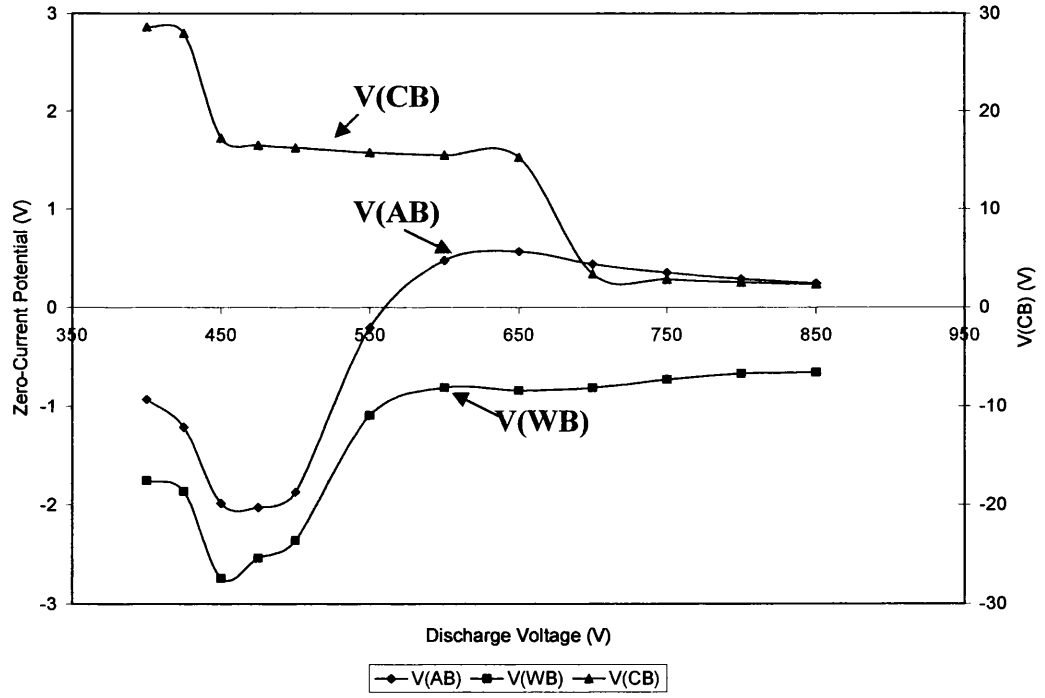

Figure 6.4b: Variation of probe potentials with discharge voltage
(V_c = +30 V, P = 0.9 Torr, τ = 6.9 ms, V_{cell} = -70 V, $V_{cylinder}$ = +180 V, V_{einzel} = +10 V, tuned for Cl^-, no secondary gas)

Species	Electron Affinity/eV[19]	m/z of Major Ion
H	0.75	1
C	1.26	12
CH	1.24	13
CH_2	0.65	14
N	Not Stable	14
CH_3	0.08	15
O	1.46	16
OH	1.83	17
F	3.4	19
C_2	3.27	24
C_2H	2.97	25
C_2H_2	0.49	26
O_2	0.45	32
$OH(H_2O)$	<2.95	35
Cl	3.61	35
Ar	Not Stable	40
CF_2	0.17	50
Cu	1.24	63
Cl_2	2.38	70
CuO	1.78	79

Table 6.1: Electron affinities of species which may be present in the FAG plasma[19]

particularly Rydberg state species, is far more efficient than to ground state atoms or molecules[16].

$$OH_x^* + e^- \rightarrow OH_x^- \quad \textit{(where } x = 0 \textit{ or } 1\textit{)} \quad \textit{(equation 6.2)}$$

$$OH_y^* + e^- \rightarrow [OH_y^{-*}] \rightarrow OH_y^- + H_z \quad \textit{(where } y = 1 \textit{ or } 2 \textit{ and } z = 0 \textit{ or } 1\textit{)} \quad \textit{(equation 6.3)}$$

It is also possible that transfer of a weakly held Rydberg electron could occur[18] within the FAG plasma (equation 6.4) in much the same way as the attachment of a slow electron.

$$OH_x^* + Ar^R \rightarrow [OH_x^{-*}] + Ar^+ \rightarrow OH_y^- + H_z \quad \textit{(equation 6.4)}$$

Figure 6.4b illustrates the variation of the probe potentials with V_d. At low values of V_d V(CB) was approximately equal to V_c, indicating that the majority of the applied potential is experienced over a narrow sheath close to the ion exit cone surface (see chapter 4). At low discharge voltages the discharge current was very low (~0.23 mA when V_d was 400 V) and the Rydberg atom density would also be expected to be low. In chapter 4 it was described how EI ionisation occurs in the cone sheath when $V_c > +16$ V. When V_d is low the Rydberg density in the cone sheath is low, and therefore EI ionisation may occur, but at a much slower rate. As V_d is increased the Rydberg atom density in the cone sheath increases and therefore the number of electrons released due to field ionisation of Rydberg state species increases. When $V_d = 450$ V there is a sharp decrease in V(CB), with V_c remaining approximately +16 to +17 V until $V_d = 650$ V. This clearly demonstrates the onset of EI ionisation in the cone sheath.

Within this range a negative field to the cone is created, and therefore no negative ions should be extracted from the FAG plasma. Anion detection is low for most of this range, but is optimised at the low V_d end of the range. Under these conditions ions are now thought to form from Rydberg state species formed in the recombining plasma outside the GD cell (see above). Both anions and cations could form as previously described in sections 6.2.1.1 and 6.2.1.2. Anions were also detected when V_d was < 450 V and > 650 V, i.e. when EI ionisation in the cone sheath is not important (at higher plasma densities a secondary discharge is thought to form between the anode and the cone, see chapter 4). When EI does not dictate the

electrical properties of the cone sheath there is a positive field gradient to the cone surface, and therefore anions could be extracted from the FAG plasma.

In figure 6.4b we note that V(AB) starts off negative at low V_d as expected for a Rydberg gas plasma. As V_d is increased, V(AB) initially becomes more negative, probably due to the increased Rydberg density at A and the increasing cone current (carried by the Rydberg gas). However, V(AB) then rises rapidly from -2 V to ~ +0.5 V. As explained above, A should not become positive with respect to B, and therefore the positive potential may be indicative of a zero error. The reduction of the magnitude of V(AB) can be explained by an increase in the stability of the charge transfer chains when carrying a large cone current. Over the same range V(WB) followed the same pattern as V(AB), and therefore the same conclusions can be drawn. The cell wall is always more negative than probe B. The potential of the sheath formed at the cell wall is effectively an average of the sheaths which would form if the wall was made up of a series of ring electrodes. In this hypothetical setup the wall potential at the upstream end would be higher than that at the downstream end, due to the higher Rydberg density, and therefore higher level of ionisation at the surface.

6.3 Addition of CH_4

Addition of methane to the FAG of the FFGD plasma has been performed by previous members of the group[1-6], mainly focussing on positive ion detection on application of a negative V_c. The main discharge related ions (Cu^+, Ar^+, ArH^+, etc) were observed as well as CH_x^+ (where x = 0 to 5). It was observed that the relative intensities of the ions were strongly influenced by the applied V_c. Application of a high negative V_c induced selective formation of fragment ions, whilst application of a low negative or low positive V_c increased the abundance of the molecular and protonated species[6]. This is investigated further in chapter 7.

6.3.1 Influence of Secondary Gas Concentration

6.3.1.1 Positive Ion Studies

Figure 6.5a illustrates the variation of the major ion intensities and the cone current on addition of CH_4 in the new instrument. The discharge current decreased

slightly on addition of methane (~ 0.3 mA at 12.8% addition), although addition of methane to the FAG plasma should not directly affect the active discharge. A greater decrease in I_c (0.95 mA) was observed over the same range. Addition of CH_4 directly into the FAG plasma induces quenching of the Rydberg state species proposed to be responsible for charge transfer through the afterglow region, and therefore a drop in I_c would be expected. At high levels of secondary gas addition it was thought that the cone current would be completely quenched due to the removal of the current carrying species. However, the Rydberg gas model presented in chapter 4 speculates that chains of polarised Rydberg species can form. It is likely that formation of such chains increases the stability of the charge-carrying Rydberg atoms to collisions. Previous experiments with H_2 gas indicated the relative unreactivity of the plasma when it is carrying a current. This could be a manifestation of the same phenomenon.

The partial quenching of the Rydberg gas also lifts V(CB) from +15 to +20 V (figure 6.5b). As the Rydberg atoms are quenched, the Rydberg density in the cone sheath decreases until there are insufficient electrons to generate a free ion-electron plasma by EI ionisation. The result is to lower the plasma potential (by the same amount as V(CB) increases). During this change we see cations generated. This corresponds to the point at which a negative field develops at the cone surface due to separation of charge. Therefore, a recombining plasma is created as discussed above.

The process responsible for the formation and detection of cations on application of a positive (repulsive) ion exit bias is discussed earlier in this chapter. Formation of ions related to the secondary gas occurs in the same way but collisional energy transfer from excited state Ar (including Rydberg states) must first occur (equations 6.5 and 6.6).

$$Ar^{**} + CH_4 \rightarrow Ar + CH_4^+ + e^- \rightarrow CH_4^R \qquad \textit{(equation 6.5)}$$

$$Ar^{**} + CH_4 \rightarrow Ar + CH_x^+ + H_y + e^- \rightarrow CH_x^R \qquad \textit{(equation 6.6)}$$

It is also possible for associative attachment of methane or radical species to the Ar^R (equation 6.7). Since the product is neutral it can escape through the ion exit aperture. Subsequent ionisation in the vacuum region can lead to the formation of both positive and negative ions (including equations 6.8 to 6.10).

$$Ar^R + CH_x \rightarrow Ar^R.CH_x \qquad \textit{(equation 6.7)}$$

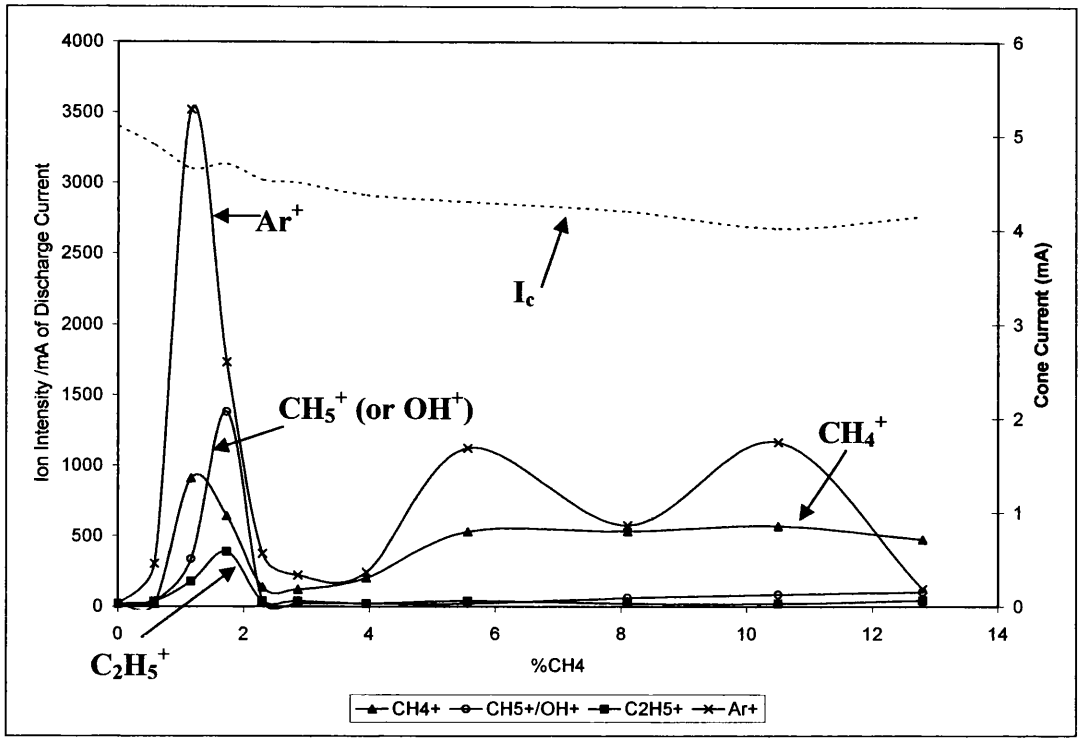

Figure 6.5a: Variation of ion peak intensities and cone current with CH_4 addition

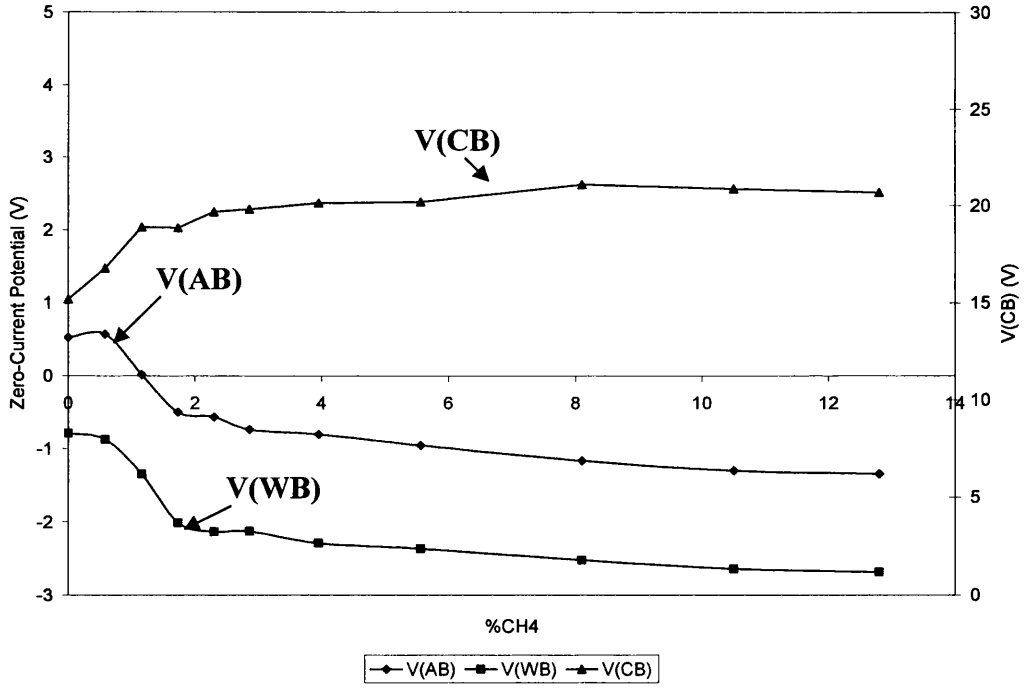

Figure 6.5b: Variation of zero-current potentials between electrical probes with CH_4 addition (secondary gas was added through probe B)

(V_d = 600 V, P = 0.9 Torr, τ = 7.1 ms, V_c = +30 V, V_{cell} = +70 V, $V_{cylinder}$ = -180 V, V_{einzel} = +10 V, tuned for Ar^+)

$$Ar^R.CH_x \rightarrow Ar^+ + e^- + CH_x \qquad \textit{(equation 6.8)}$$

$$Ar^R.CH_x \rightarrow Ar + e^- + CH_x^+ \qquad \textit{(equation 6.9)}$$

$$Ar^R.CH_x \rightarrow Ar^+ + CH_x^- \qquad \textit{(equation 6.10)}$$

It was also observed that V(AB) and V(WB) became increasingly negative with with addition of methane. Since the secondary gas is added through probe B, Rydberg atoms close to probe B are quenched, and therefore the field produced at B due to ionisation of Rydberg atoms at the probe surface would be reduced. Thus B becomes significantly less negative than A and W.

6.3.1.2 Negative Ion Studies

Formation of negative ions on addition of methane to the FAG plasma was previously studied by Mortimer using the first generation instrument[4]. The ions at m/z = 17 (OH^- or CH_5^-) and 25 (probably C_2H^-) had the highest abundances (figure 6.6a). Higher mass species, possibly due to polymerisation processes involving CH_x radicals, were also observed. Ion signals were found to decrease on application of a small positive or negative V_c. Mortimer[4] concluded that anion formation was likely to be due to low energy electron attachment, as reported by Pinnaduwage et al.[13-16] (equation 6.11), or electron transfer from Rydberg species (equation 6.12), with the latter being most likely.

$$e^- + CH_4 \rightarrow [CH_4^-] \rightarrow H_2 + CH_2^- \qquad \textit{(equation 6.11)}$$

$$Ar^R\,(Ar^+.e^-) + CH_4 \leftrightarrow Ar^+.e^-.\,CH_4 \rightarrow Ar^+ + CH_4^{R-} \rightarrow H_y + CH_x^- \qquad \textit{(equation 6.12)}$$

Figures 6.6b and c illustrate mass spectra produced on addition of CH_4 (4.5%) under the same discharge conditions (different to those used by Mortimer), but tuned for optimisation of different ions. Figure 6.6b was recorded tuning for the chloride ion. It was observed that species related to the added methane were only detected at low intensity, whereas products related to the cathode, water and chlorine were detected at relatively high intensity. The copper containing ions were observed by Mortimer[4] on addition of oxygen and hydrogen. It is likely that trace water from the walls of the discharge cell and the secondary gas were responsible for the oxide and hydroxide ions observed. On retuning for H^- detection, a significant increase in the intensities of

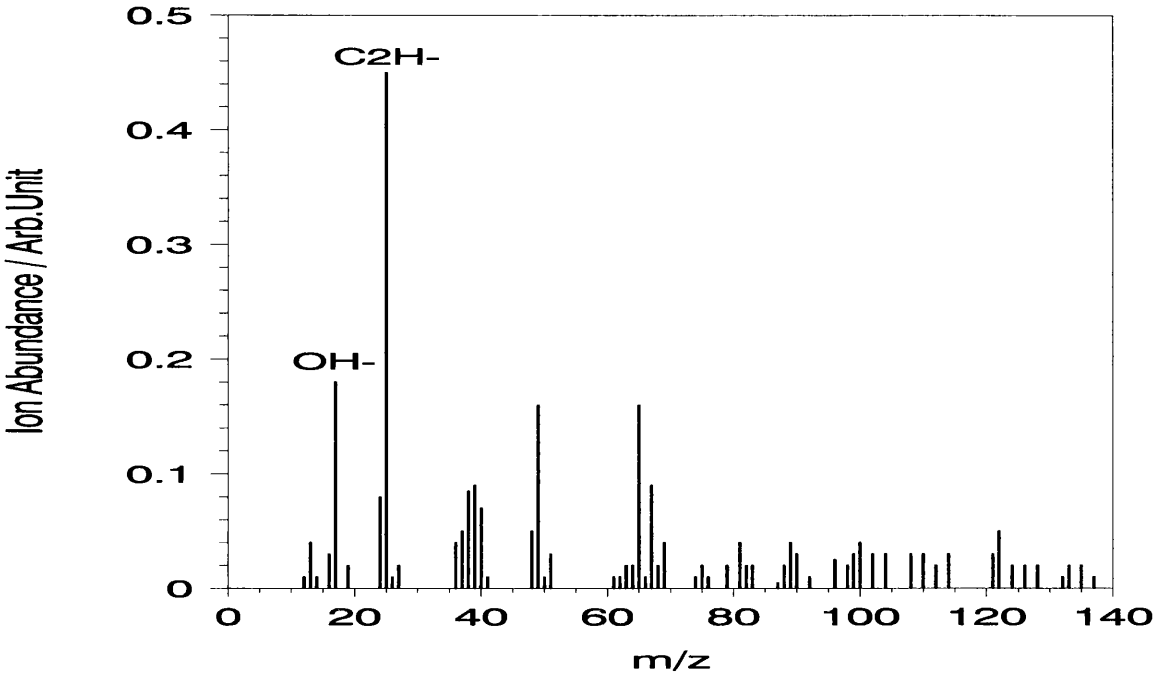

Figure 6.6a: Negative Ion Mass Spectrum of a Copper/Argon Glow Discharge with 23% CH_4 added at the ion exit (Mortimer - reference 4)
(V_d = 523 V, I_d = 2.77 mA, P = 2 Torr, V_c = 0 V, τ = 4.3 ms)

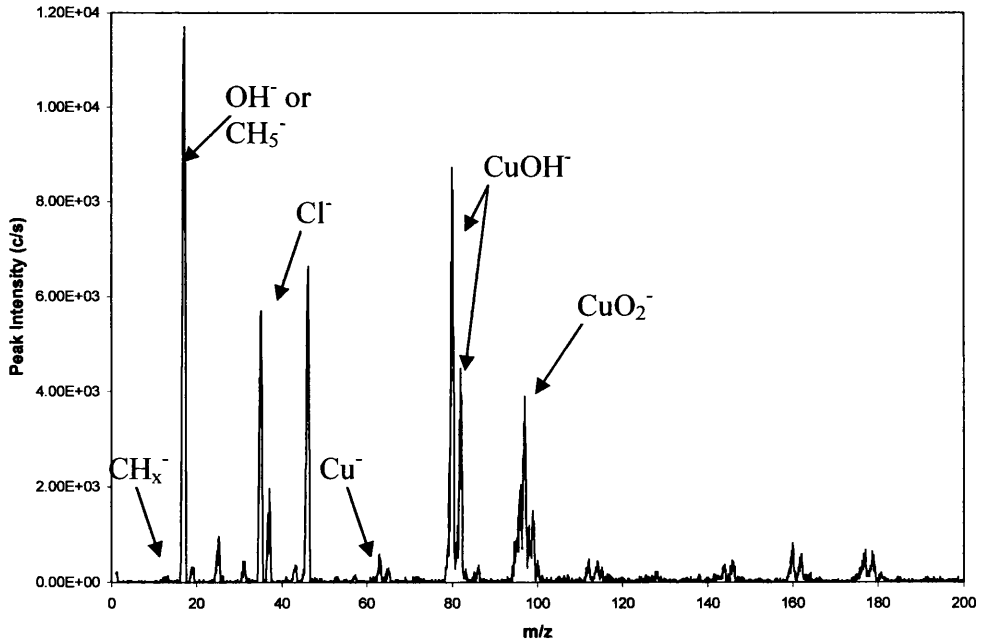

Figure 6.6b: Negative Ion Mass Spectrum of a Copper/Argon Glow Discharge with 4.5% CH_4, tuning for Cl^-
(V_d = 490 V, P = 0.9 Torr, τ = 7.1 ms, V_c = +30 V, V_{cell} = -70 V, $V_{cylinder}$ = +10 V, V_{einzel} = -20 V)

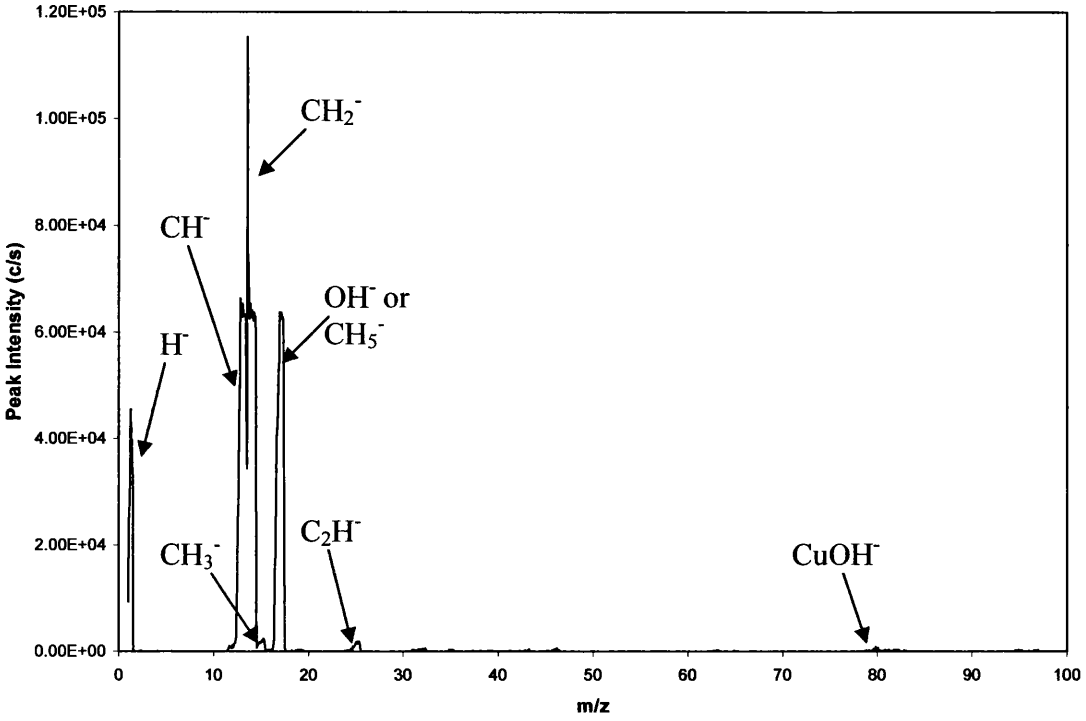

Figure 6.6c: Negative Ion Mass Spectrum of a Copper/Argon Glow Discharge with 4.5% CH_4, tuning for H^-
(V_d = 490 V, P = 0.9 Torr, τ = 7.1 ms, V_c = +30 V, V_{cell} = -70 V, $V_{cylinder}$ = +10 V, V_{einzel} = -20 V)

species related to the secondary gas was observed (figure 6.6c). The major ions observed were CH_2^-, CH^-, H^- and OH^-. The only other ion signals greater than $1/100^{th}$ of the CH_2^- intensity were CH_3^- and C_2H^-. No CH_4^- or H_2O^- ions were observed in this study, seemingly confirming the formation of anions via dissociative electron attachment[2,13-16]. It is interesting to note that the relative intensities of the anions detected were not directly related to the electron affinity (EA) of the corresponding neutral species. For instance, the EA of CH_2 is 0.65 eV[19], which is a little over half of that for CH. However, when tuning for detection of H^- (figure 6.6c) the intensity of CH^- is approximately two thirds of that for CH_2^-. Comparison of the electron affinities in table 6.1 with the mass spectra illustrated highlights several such inconsistencies. However, assuming the mechanism to be dissociative electron attachment, the ion intensities are dependent on the fragmentation induced after electron transfer and so discrepancies can arise.

Figure 6.7a illustrates the variation of the major ion intensities with addition of CH_4 for a low V_d (low Rydberg density). Maxima for ion detection occurred between approximately 1 and 2% addition of methane. Comparison with the cone current and V(CB) indicates that corresponds to the point at which all susceptible Rydberg atoms are quenched, and therefore the probability of charge transfer from the Rydberg atom to methane molecules is at its maximum. The sharp increase in V(CB), as previously discussed, is also indicative of increased quenching. Formation of negative ions for high levels of addition of methane is still possible due to continual regeneration of Rydberg species upstream.

6.3.2 Influence of the Applied V_c

6.3.2.1 Positive Ion Studies

Figure 6.8a illustrates the variation of ion intensities and the plasma currents with the applied ion exit bias. No ions were observed for $V_c < +15$ V. A general increase in the ion intensities was observed with increasing V_c for $V_c > +15$ V. The pattern again fits with the model presented in chapter 4, whereby application of $V_c > +16$ V induces EI ionisation close within the anodic (cone) sheath, leading to formation of a negative field gradient to the ion exit cone, when the level of positive ion detection is increased. This is also illustrated by the variation of V(CB), as illustrated in figure 6.8b. V(CB) initially increased before reaching constant value above $V_c = +25$ V.

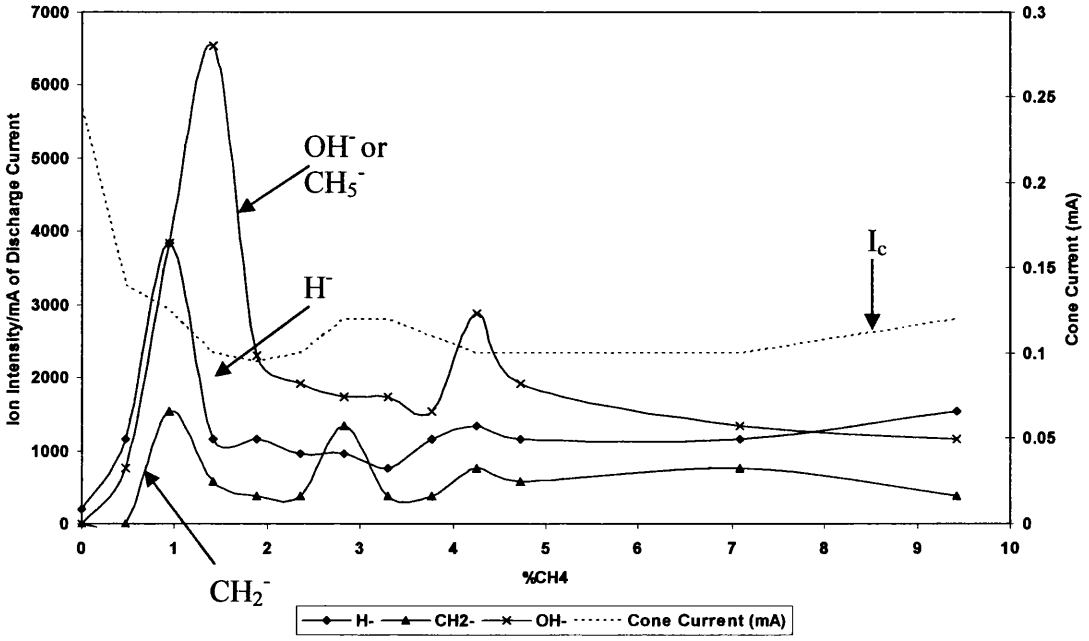

Figure 6.7a: Variation of negative ion peak intensities with %CH_4 when V_d = 440V

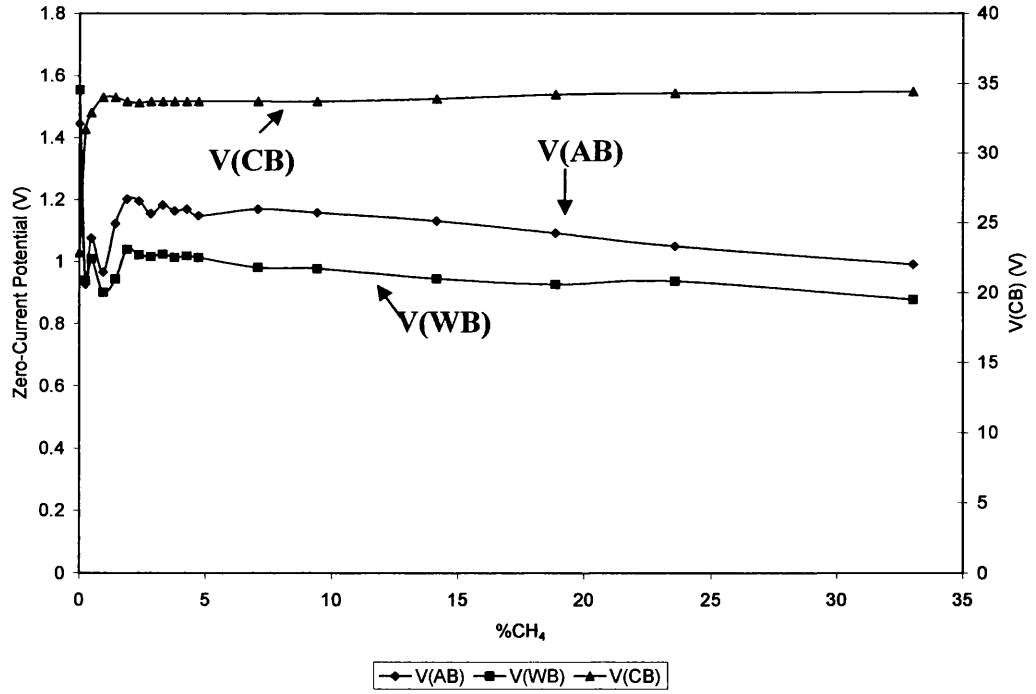

Figure 6.7: Variation of probe potentials with %CH_4 when V_d = 440V
(V_d = 440 V, P = 0.9 Torr, τ = 6.9 ms, V_c = +32 V V_{cell} = -63.3 V, $V_{cylinder}$ = +2.79 V, V_{einzel} = -3.96 V, tuned for OH^-)

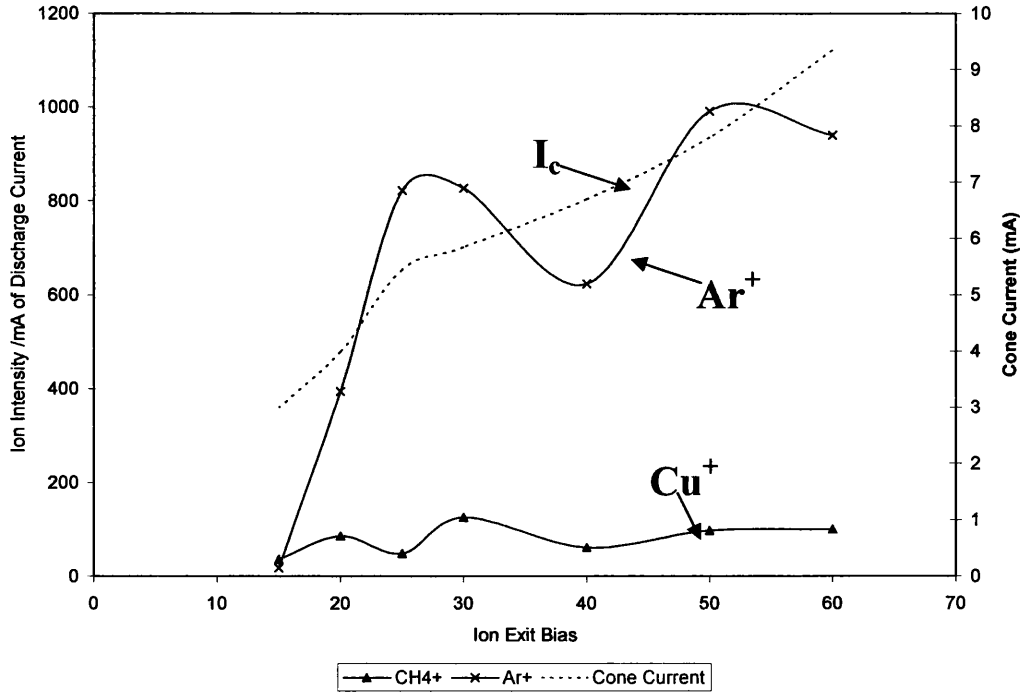

Figure 6.8a: Variation of ion peak intensities and plasma currents with V_c on addition of CH_4 (1.2%) (the drop in argon ion intensity when V_c = +40 V is most likely due to the effect of signal noise at such a low ion intensity)

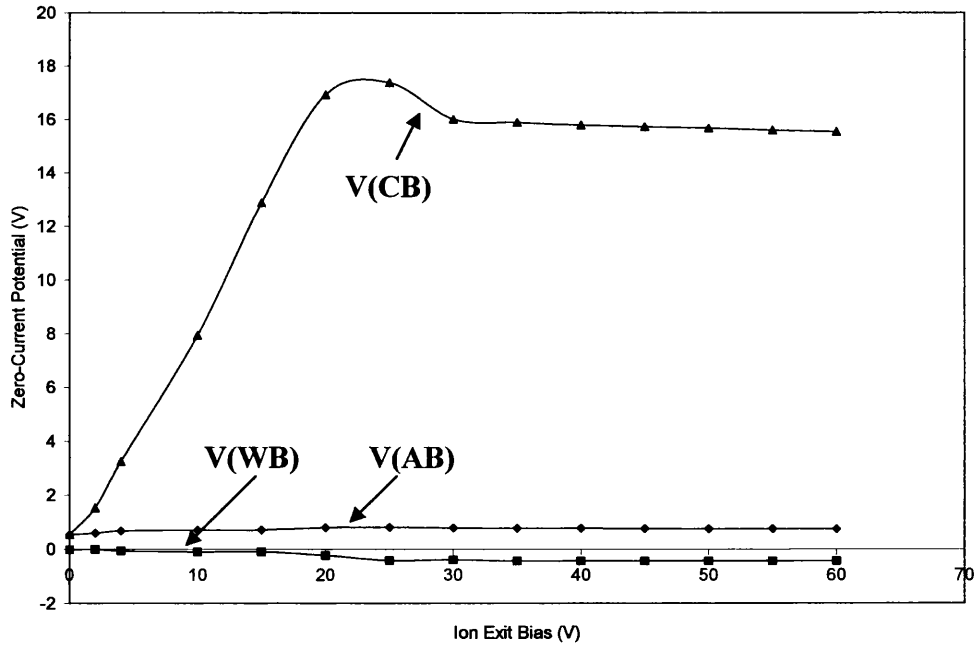

Figure 6.8b: Variation of zero-current potentials between electrical probes with V_c on addition of CH_4 (1.2%)
(V_d = 625 V, P = 0.9 Torr, τ = 7.1 ms, V_{cell} = +70 V, $V_{cylinder}$ = -180 V, V_{einzel} = +10 V, tuned for Ar^+)

This is very similar to results obtained without addition of a secondary gas (see chapter 4 and earlier in this chapter) and so it appears that the addition of 1.2% CH_4 has a minimal effect on the electrical properties of the plasma.

6.3.2.2 Negative Ion Studies

The results illustrated in figures 6.9a and 6.9b were collected in the same experimental run on variation of V_c. The results have been separated to illustrate an interesting aspect of the profile. Three regions were observed for optimum ion detection, when V_c was +4 V, +30 V and +60 V. It is interesting to note that the major ions observed on application of a low positive V_c were not observed in significant abundance when V_c was +30 V, and vice versa. No parent molecular ions (CH_4^+, H_2O^+) were observed, again supporting the previous conclusion that anions are formed by dissociative electron attachment.

It has been shown under different discharge conditions, figures 6.5b and 6.7b, that addition of 4% CH_4 is sufficient to quench nearly all susceptible Rydberg atoms. Therefore, the electron density due to ionisation of Rydberg atoms in the cone sheath is insufficient to allow formation of a free ion-electron plasma, leading to formation of a negative field at the cone surface. Thus, the magnitude of V(CB) (shown in figure 6.9c)increased with increasing V_c, until V_c = 40 V. It is expected that under these conditions there is a positive field gradient to the cone, and therefore ions could be extracted from the FAG plasma. This appears to be the case for the ions shown in figure 5.9b, because kinetic energy measurements for the OH^- were approximately 8 eV higher than the potential applied to accelerate the ions between the ion exit and mass analyser orifices (V_{cell}) for V_c > +20 V. However, the ions detected when V_c = +4 V had approximately zero kinetic energy and were therefore probably formed within or beyond the ion exit orifice.

6.3.3 Influence of V_d: Negative Ion Studies

Figure 6.10 illustrates the variation of the major ion intensities and CH_2^- with changing V_d. The ion maxima were observed for a relatively low V_d, though the corresponding V_d was dependant on the ion. For instance, the maximum current-corrected OH^- intensity was observed when V_d was 375 V, but the H^- maximum

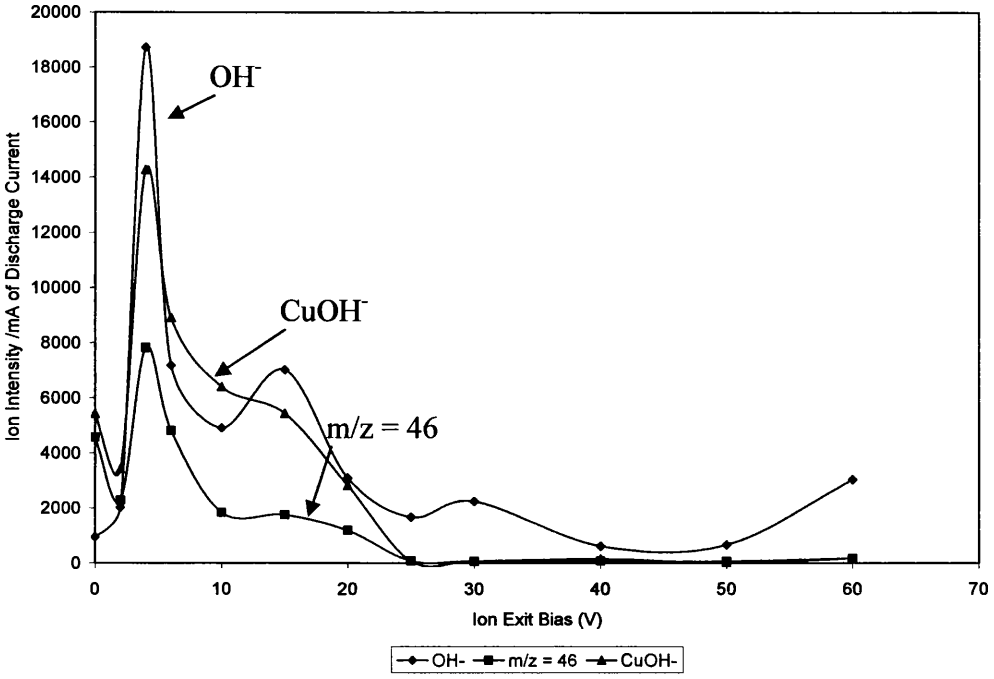

Figure 6.9a: Variation of negative ion peak intensities and ion kinetic energy with V_c on addition of CH_4

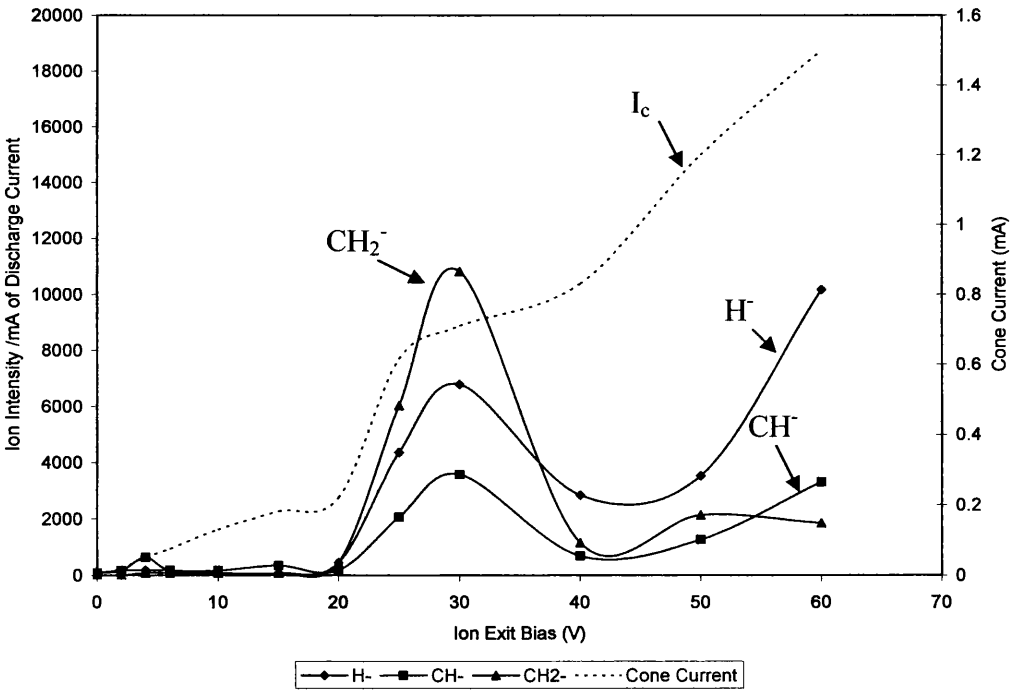

Figure 6.9b: Variation of negative ion peak intensities and ion kinetic energy with V_c on addition of CH_4 – same experimental run
(V_d = 490 V, P = 0.9 Torr, τ = 7.1 ms, V_{cell} = -70 V, $V_{cylinder}$ = +10 V, V_{einzel} = +10 V, 4% CH_4, tuned for OH^-)

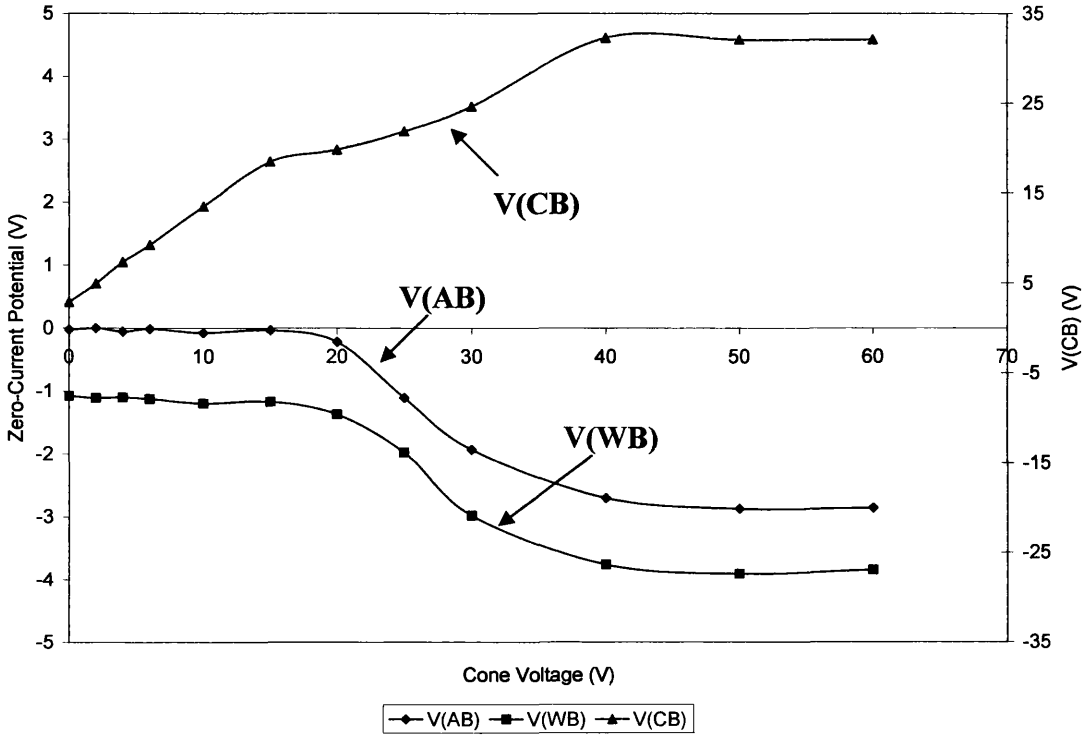

Figure 6.9c: Variation of probe potentials with V_d on addition of CH_4
(V_d = 490 V, P = 0.9 Torr, τ = 7.1 ms, V_{cell} = -70 V, $V_{cylinder}$ = +10 V, V_{einzel} = +10 V, 4% CH_4, tuned for OH^-)

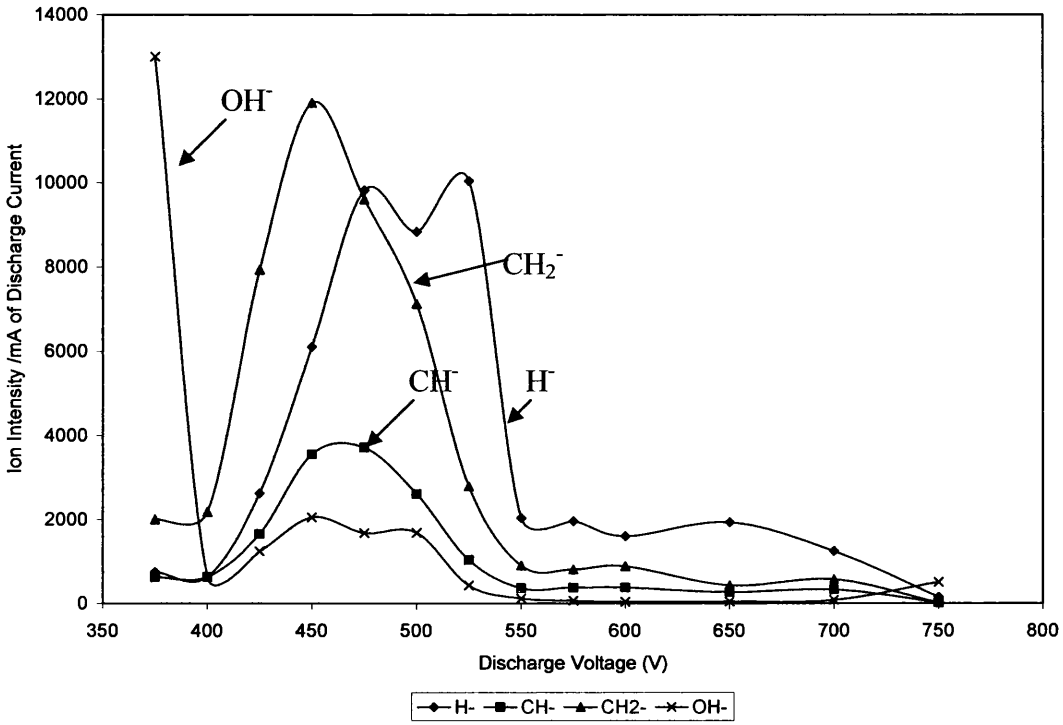

Figure 6.10: Variation of negative ion peak intensities with V_d on addition of 4% CH_4

(V_c = +30 V, P = 0.9 Torr, τ = 6.9 ms, V_{cell} = -70 V, $V_{cylinder}$ = +10 V, V_{einzel} = -20 V, tuned for CH_2^-)

occurred when V_d was 525 V. The probe potentials and cone current were not measured for this experiment, but for the same residence time and cone bias, without addition of secondary gas (figure 6.4), V_d = 450 V was the point at which EI ionisation occurred in the cone sheath and it was about this point that anion detection was optimised. This appears to be the case here, and therefore the mechanism should be the same. No CH_4^- or H_2O^- were observed, and again dissociative electron attachment is the most likely mechanism for anion formation.

6.4 Addition of H_2

The addition of hydrogen to the flowing afterglow plasma on application of a negative ion exit bias has been researched extensively within this group[1-12]. Addition of hydrogen is known to enhance the formation of certain ion species and reduce formation of others. For instance, addition of a small quantity of hydrogen often increases the formation of the cathode ion species, whilst the Ar^+ intensity is reduced to zero (discussed further in chapter 7). This is sometimes referred to as the "hydrogen effect". It has been proposed that the loss of the argon ion signal is due to efficient quenching of argon Rydberg states by the secondary gas[2,6]. In turn, this quenching process may produce the argon metastable state species believed to be responsible for formation of ions such as Cu^+ via Penning ionisation[3-6].

6.4.1 Influence of Secondary Gas Concentration

Figure 6.11a illustrates the variation of ion intensities and plasma currents with addition of hydrogen. In contrast to the addition of CH_4, addition of a small quantity of H_2 had very little effect on the cone current, and at higher levels of addition I_c actually increased. This is a remarkable result, as under the conditions of this investigation it seems that H_2 is largely unreactive with the Rydberg atoms carrying the current. As stated previously, we believe this to occur via a highly polarised structure of the gas. In this state the interactions between polarised Rydberg atoms are thought to be strong enough for collisions with secondary gas molecules to have relatively little effect. The increase in V(CB) does indicate some quenching, but the change is not as significant as observed on addition of CH_4 (figures 6.5 and 6.7), though the discharge conditions were not the same.

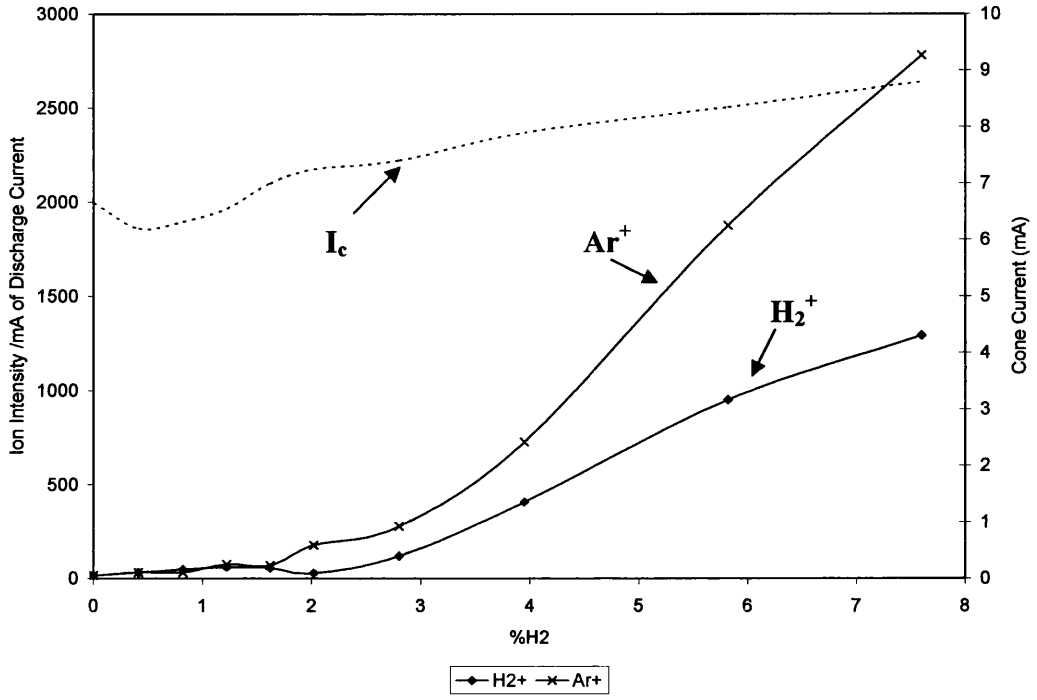

Figure 6.11a: Variation of ion peak intensities and plasma currents with addition of hydrogen

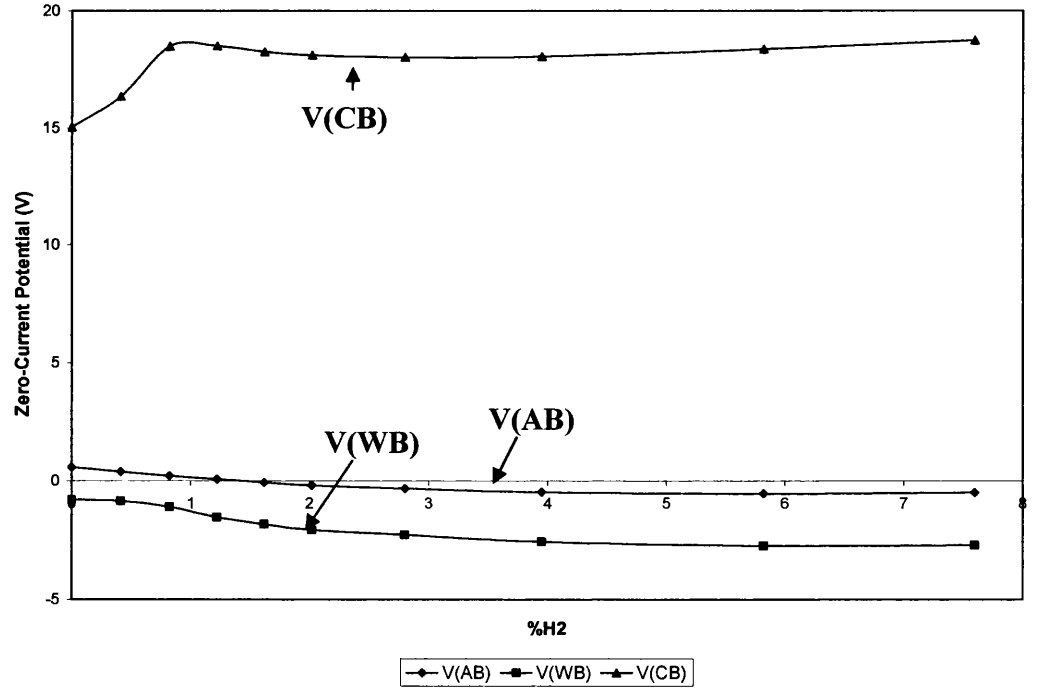

Figure 6.11b: Variation of zero-current potentials between electrical probes with addition of hydrogen

(V_d = 625 V, V_c = +30 V, P = 0.9 Torr, τ = 7.1ms, V_{cell} = +70 V, $V_{cylinder}$ = -180 V, V_{einzel} = +10 V, tuned for Ar^+)

The intensities of H_2^+ and Ar^+ increased with increasing addition of hydrogen. This result could be explained by the process shown in equations 6.13 and 6.14. Both processes involve quenching of argon Rydberg states which carry the plasma current, and therefore a corresponding drop in I_c would be expected. Initially a small drop in I_c was observed (figure 6.11a), but I_c increased again at higher levels of H_2 addition. This may be due to the ionisation induced by equations 6.13 and 6.14.

$$Ar^R + H_2 \leftrightarrow Ar^R.H_2 \rightarrow Ar^+ + H_2 + e^- \quad \textit{(equation 6.13)}$$

$$Ar^R + H_2 \leftrightarrow Ar^R.H_2 \rightarrow Ar + e^- + H_2^+ \quad \textit{(equation 6.14)}$$

The discrimination of the QMS towards lower mass species may contribute to the relatively high detection of H_2^+. It was suggested above that the negative shifts in V(AB) and V(WB) were due to increased quenching of Rydberg atoms close to probe B which would have been ionised at the surface, thereby reducing the sheath potential.

6.4.2 Influence of the Applied V_c

Figure 6.12a illustrates the variation of the major ion peak intensities with V_c on addition of 0.5% H_2. The changes in the ion intensities were very similar to those observed without addition of secondary gas. This was expected since so little hydrogen would not be expected to have a large effect on the ion intensities, as shown by figure 6.11a. The results in figures 6.12b are also very similar to results observed without addition of secondary gas (figure 6.12c). The mechanism responsible has been discussed in section 6.2.1.1.

6.4.3 Influence of V_d

Figure 6.13a illustrates the variation of the major peak intensities with discharge voltage on addition of 2.8% H_2. On addition of CH_4 (figure 6.4a) two maxima were observed for each ion, when V_d was 450 and 700 V. Similar results were observed on addition of H_2. Comparison with V(CB) shows that ion formation again corresponds with the onset of EI ionisation in the cone sheath, and therefore formation of ions from a recombining plasma beyond the ion exit orifice is the likely mechanism for cation formation.

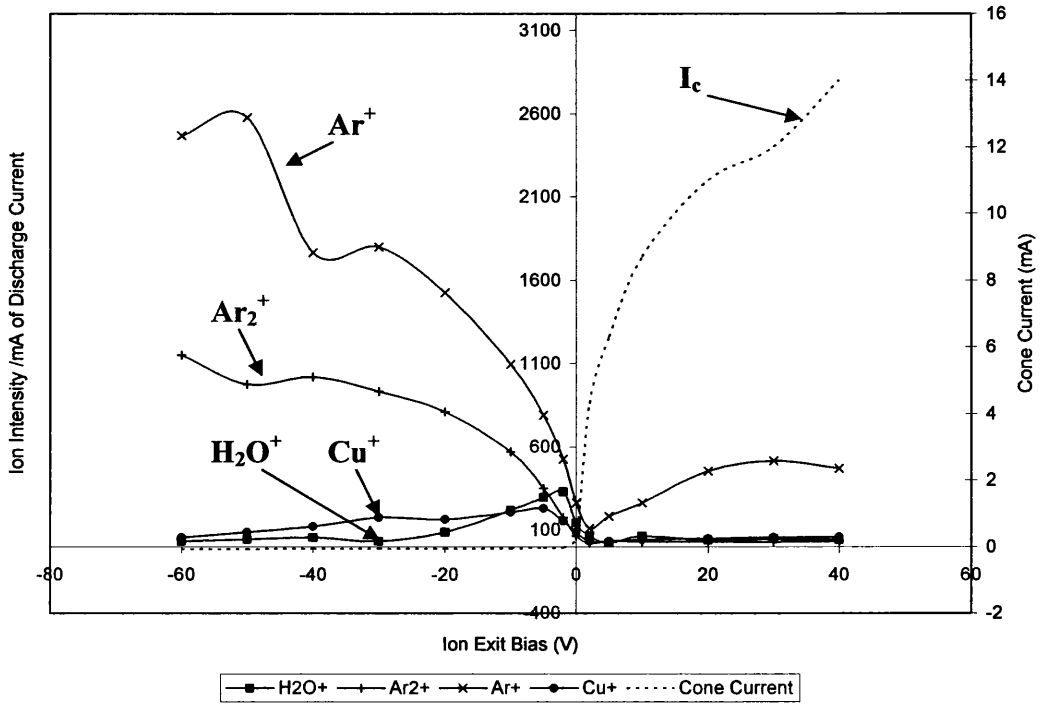

Figure 6.12a: Variation of ion peak intensities with V_c (0.5% H_2)

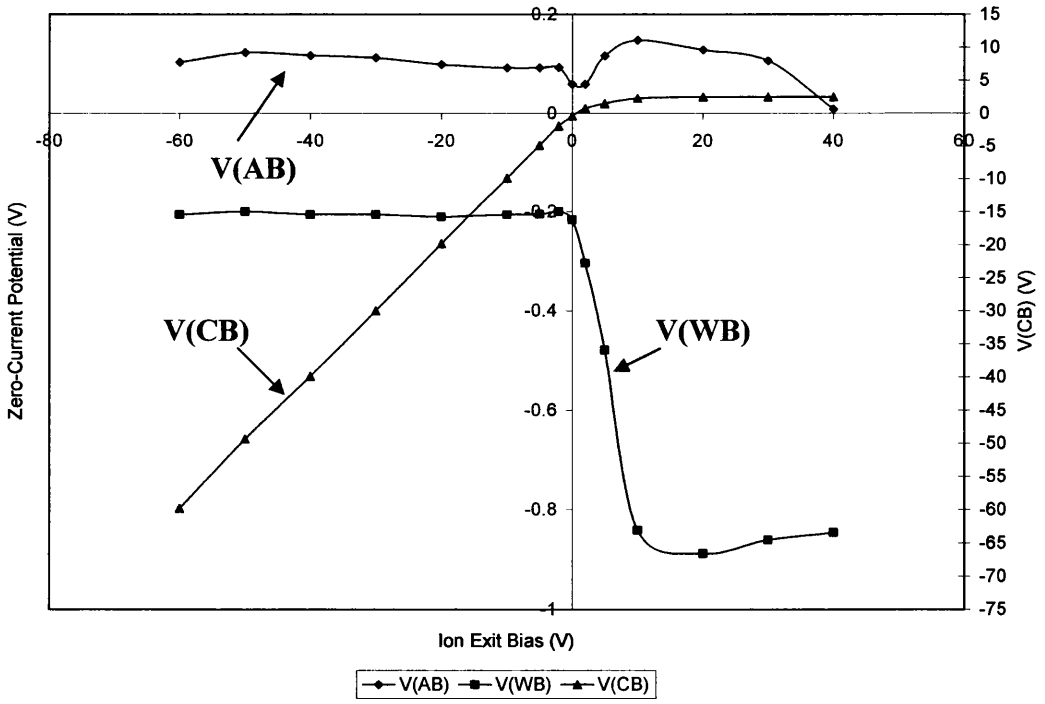

Figure 6.12b: Variation of zero-current potentials between electrical probes with V_c (0.5% H_2)

(V_d = 800 V, P = 0.9 Torr, τ = 6.4 ms, V_{cell} = +70 V, $V_{cylinder}$ = -180 V, V_{einzel} = +10 V, tuned for Ar^+)

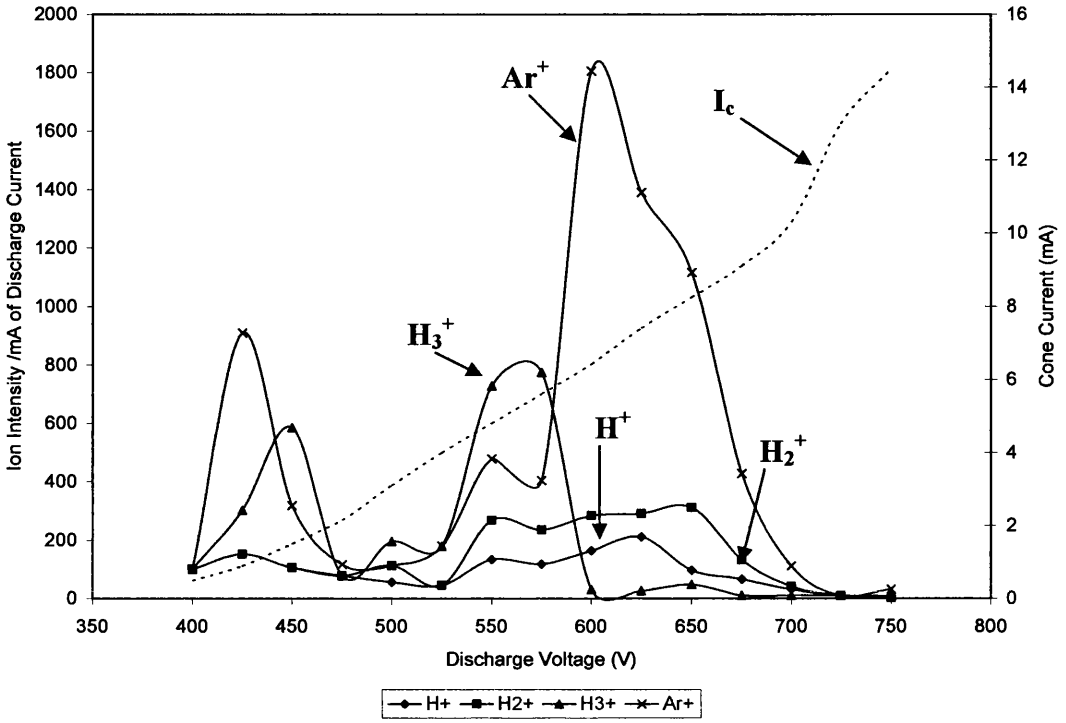

Figure 6.13a: Variation of ion peak intensities with V_d (2.8% H_2)

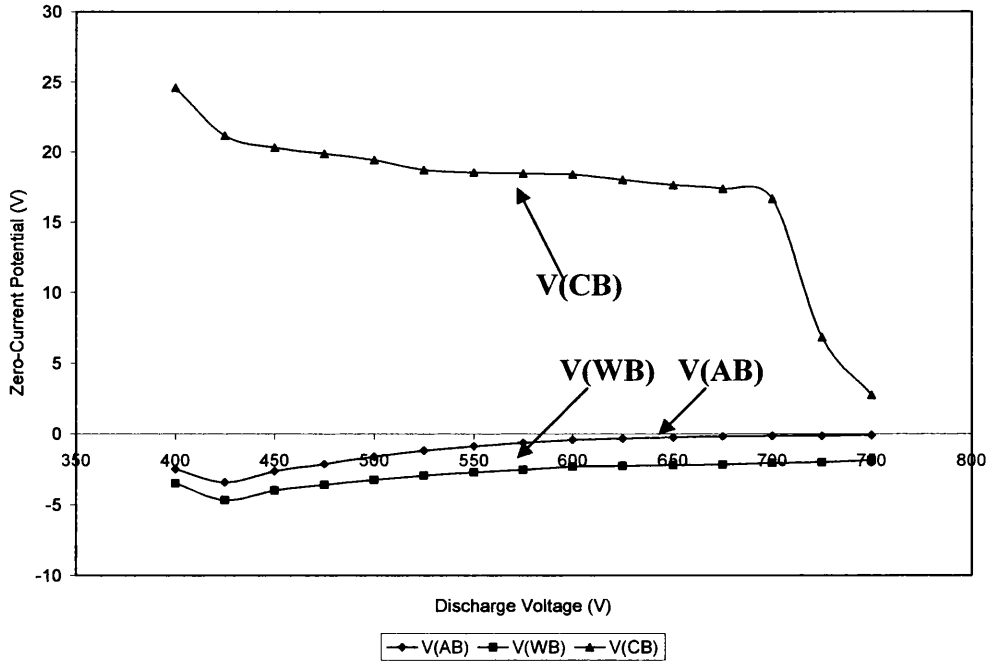

Figure 6.13b: Variation of zero-current potentials between electrical probes with V_d (2.8% H_2)

(V_c = +30 V, P = 0.9 Torr, τ = 7.1 ms, V_{cell} = +70 V, $V_{cylinder}$ = -180 V, V_{einzel} = +10 V, tuned for Ar^+)

6.5 Addition of CF_4

Mixed plasmas containing CF_4 have been studied by a number of authors[20-24] due to the use of fluorocarbons in Si and SiO_2 etching[25]. The major negative ions reported are CF_3^- and F^-.[20] Pinnaduwage et al.[13-16] reported the formation of anions via dissociative electron attachment involving high n excited state (Rydberg) species. They concluded that attachment of "slow" electrons to high n excited state molecules was more efficient than to ground state species. Electron attachment to free radical and Rydberg state species was found to ≥ 4 times higher than attachment to ground state species[23]. Pinnaduwage et al.[13-16] state that negative ions were formed by via negatively charged Rydberg species, also leading to formation of radical species.

Two groups have investigated negative ion formation from CF_4 via electron impact[26,27]. Both have reported that electron attachment to CF_4 can produce both ground state and excited state CF_4^-. Negative ion formation via the ground state CF_4^- was found to produce F^- and CF_3^- (equation 6.15), whereas dissociation of the excited state species produces only F^- (equation 6.16).

$$e^- + CF_4 \leftrightarrow CF_4^- \rightarrow CF_3 + F^- \text{ or } CF_3^- + F \quad \textit{(equation 6.15)}$$

$$e^- + CF_4 \leftrightarrow CF_4^{*-} \rightarrow CF_3 + F^- \quad \textit{(equation 6.16)}$$

6.5.1 Influence of Secondary Gas Concentration

Figure 6.14a illustrates a mass spectrum observed on addition of CF_4 to the FAG plasma when a positive ion exit bias was applied to the ion exit cone. Ar^+ was observed at high intensity, as well as peaks related to the reagent gas. Similarly to results observed by Olthoff and Wang[28] for both pure CF_4 and mixed CF_4:Ar plasmas, the CF_4^+ ion was not observed. The authors proposed that dissociative charge transfer between Ar^+ and CF_4 could explain the formation of CF_x^+ fragment ions. Several other ions such as COF_x^+ (where x is 0 to 2), H^+, H_3O^+, Ar^{2+}, N_2^+ and O_2^+ were also observed at significantly lower intensity (< 3000 c/s). However, ArH^+ and Cu^+ were not observed on application of a positive V_c, on addition of CF_4.

Under these conditions, prior to application of an ion accelerating voltage outside the cell, positive ions were not detected without addition of CF_4. If the conventional

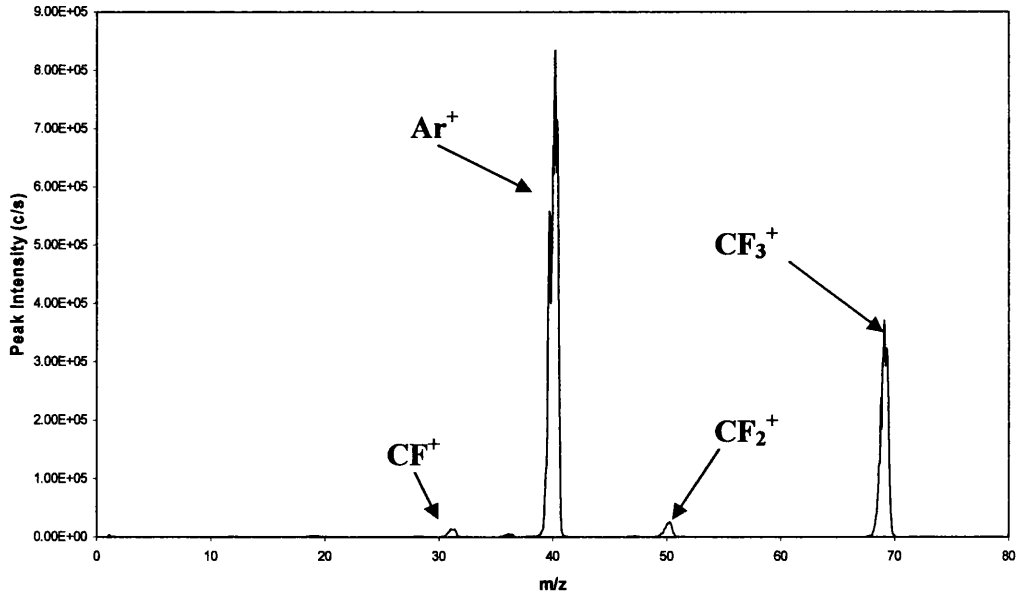

Figure 6.14a: Positive ion mass spectrum at positive ion exit bias on addition of CF_4 (V_d = 525 V, I_d = 2.25 mA, P = 1.4 Torr, τ = 8.5 ms, F_{CF4} = 19 sccm, V_c = +64 V)

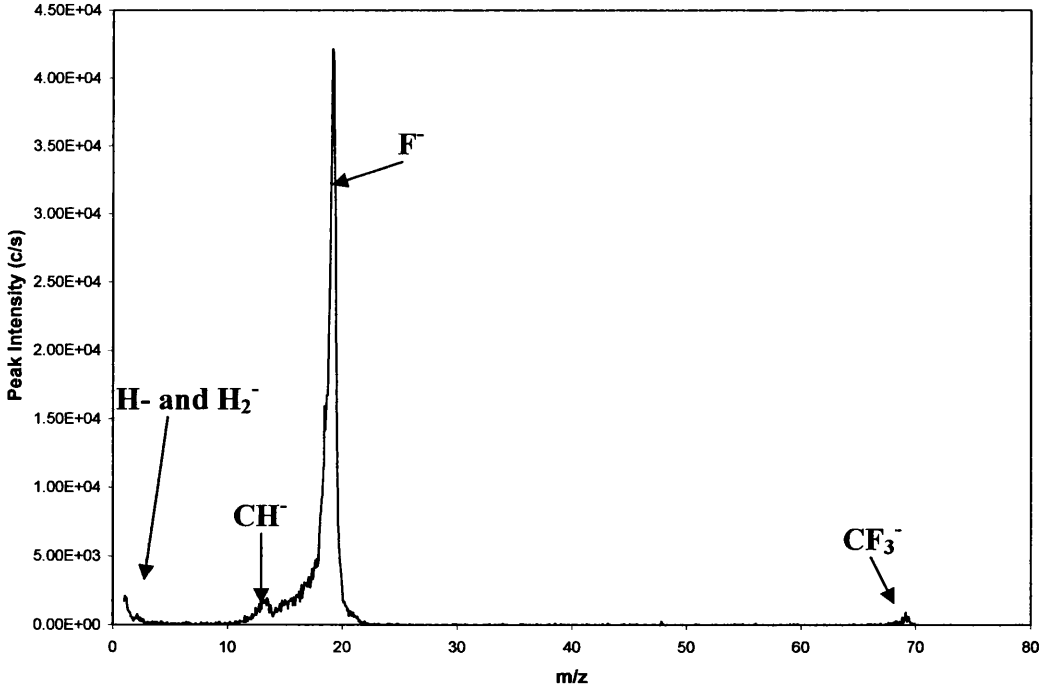

Figure 6.14b: Negative ion mass spectrum on secondary addition of 12.4% CF_4 (V_d = 525 V, P = 1.4 Torr, τ = 8.5 ms, V_c = +64 V, tuned for F^-)

ion-electron model of a plasma is applied to the system, all cations would be repelled by the positive ion exit bias and only negative ions could be detected. However, the Rydberg gas model presented in chapter 4 accounts for the detection of positive ions on application of a high V_c via formation of a potential drop to the ion exit orifice, creation of a recombining plasma, and ionisation of Rydberg species in the low pressure region beyond the ion exit.

Due to the high electron affinity (3.4 eV)[19] of fluorine (and halogen containing molecules) and low electronegativity of argon, transfer of the Rydberg state electron from Ar^R to ground or excited state species may occur[18] (equations 6.17 to 6.19). Rydberg atoms may be approximated to an ion/electron pair (e.g. $Ar^+.e^-$) since the outer electron approaches the ionisation level. For instance, electron attachment to F is energetically favourable because, assuming that approximately zero energy is required to ionise the Ar^R, ΔE for equation 6.18 is effectively equal to the electron affinity of F (3.4 eV in ground state, but expected to be higher when F is in an excited state[23]). The electron affinity of CF_3 is not quoted in reference 19).

$$Ar^R + CF_4^{0,*,R} \rightarrow Ar^+ + F^- + CF_3 \qquad \textit{(equation 6.17)}$$

$$Ar^R + F^{0,*,R} \rightarrow Ar^+ + F^- \qquad \textit{(equation 6.18)}$$

$$Ar^R + CF_3^{0,*,R} \rightarrow Ar^+ + CF_3^- \qquad \textit{(equation 6.19)}$$

The formation of ions related to the reagent (CF_3^+, CF_2^+, CF^+) could occur readily in the FAG plasma via Penning ionisation since CF (9.11 eV), CF_2 (11.42 eV) and CF_3 ($\leq$8.9 eV)[19] all have ionisation potentials lower than the argon $^3P_0$ and $^3P_2$ states (11.72 and 11.55 eV respectively). Again, one would expect such ions to be repelled by the positive field close to the ion exit cone. It is possible that these ions could form weakly bound pairs with negative ions formed within the discharge (predominantly F^-). These pairs would be neutrally charged and would therefore not be repelled by the positive V_c applied. These pairs could separate outside the source, therefore allowing detection of positive ions (equation 6.20).

$$F^- + CF_3^+ \leftrightarrow F^-.CF_3^+ \qquad \textit{(equation 6.20)}$$

A further possibility considered for formation of positive ions is electron impact close to or within the ion exit orifice. Under the conditions of figure 6.14a it is very likely,

though not confirmed by electrical probe measurements in this case, that EI ionisation occurs in the cone sheath as described in chapter 4, inducing the formation of a negative field to the cone surface. Therefore, Ar^+ formed in the cone sheath could be extracted as described in previous sections. However, it is unusual that no Cu^+ or water related peaks were observed. The electron impact spectrum of the residual gas of the flowing Cu/Ar plasma (figure 3.28b) contains relatively high intensity water related peaks and Ar^{2+}. The failure to observe the Ar^{2+} peak can be explained by the high energy required to remove two electrons (first ionisation energy = 15.76 eV, second = 27.63 eV)[19]. However, the ionisation energy of water (12.61 eV)[19] is lower than that of Ar, and so water related ion peaks should be observed.

Figure 6.14b shows a typical anion mass spectrum generated on addition of CF_4. No significant ion signals were observed above m/z = 70, therefore the parent molecular ion (m/z = 88) was not observed. It is likely that formation of F^- was favoured due to its high electron affinity (3.4 eV)[19]. The electron affinity for CF_3 has not been reported. In the example illustrated in figure 6.14b, the F^- intensity was 45 times that of CF_3^-. Peaks at m/z = 1 and 2, possibly H^- and H_2^-, are also observed, probably due to trace water presence. The formation of H^- by dissociative electron attachment to water or direct attachment to H radical (electron affinity = 0.754 eV)[19] are possible. No electron affinity for H_2 is presented in reference 19. The intensity of the peak at m/z = 2 is too high for D^- to be considered, and therefore the ion is most likely to be H_2^-, although the intensity may be exaggerated due to the bias of quadrupole mass spectrometers to low mass species. For a conventional ion-electron plasma negative ions would be expected to be extracted from the cell on application of a positive ion exit bias. However, it is possible that both positive and negative ions were formed via the formation of ion pairs similarly to equation 6.20.

Figure 6.15a illustrates the variation of the major anion and cation current-corrected peak intensities and the discharge current with addition of CF_4. Addition of CF_4 induced a sharp decrease in I_d for low percentage addition, but the current was approximately constant on higher addition. It has been shown earlier in this chapter that reagent gases quench Rydberg species which can carry current, but the effect is limited, probably due to the formation of stable Rydberg charge transfer chains. Unfortunately, the cone current was not measured in this experiment. On reduction of the discharge current a sharp increase in the major ion intensities was observed. The

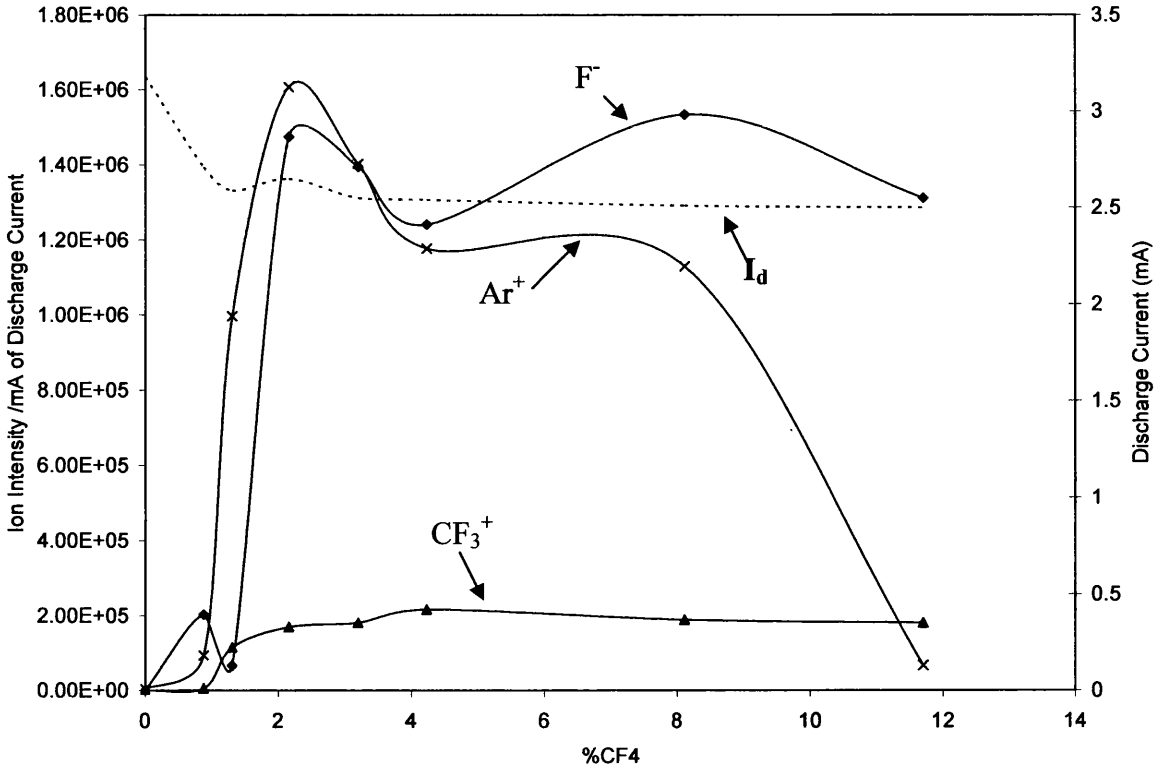

Figure 6.15a: Variation of ion peak intensities and discharge current with percentage addition of CF_4 (V_d = 525 V, P = 1.4 Torr, τ = 8.5 ms, V_c = +64 V, tuned for F^- and Ar^+)

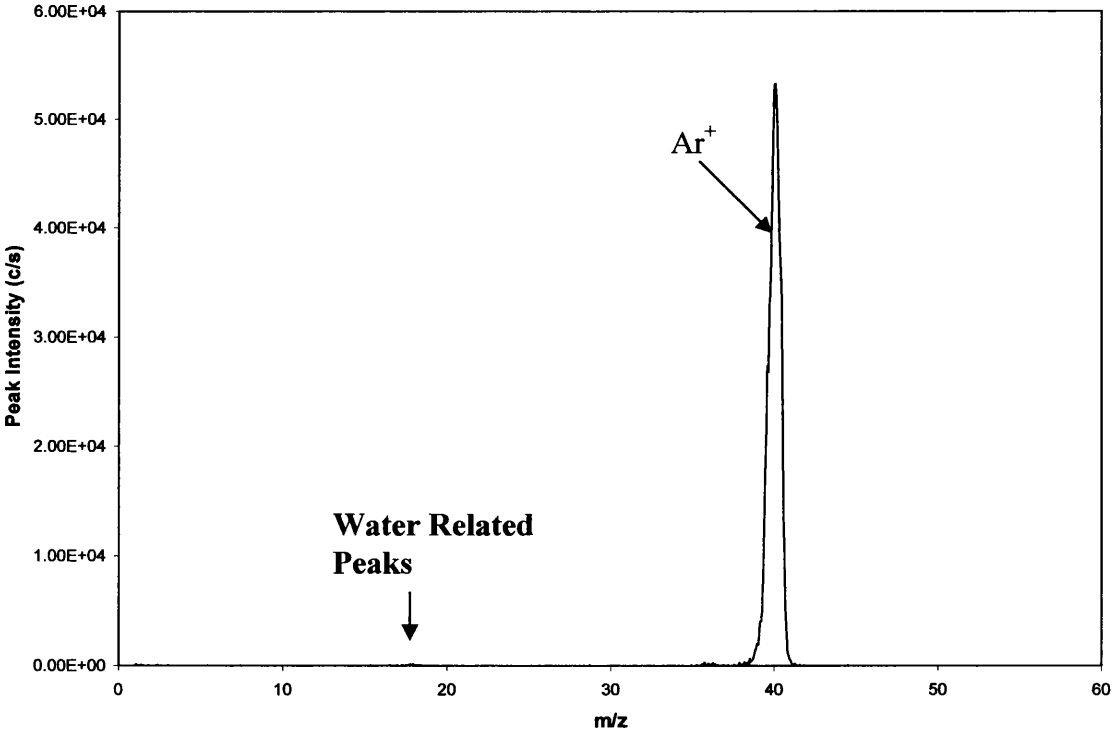

Figure 6.15b: Positive ion mass Spectrum taken without addition of CF_4 (V_d = 525 V, I_d = 2.92 mA, P = 1.4 Torr, τ = 6 ms, V_c = +60 V, tuned for Ar^+)

ions detected were clearly not formed in the active discharge region of the source, as a decrease in the observed ion intensities would be expected.

As the system was set up to allow negative ion studies, it is unusual that Ar^+ was detected at higher intensity than F^-, though the argon ion signal was rapidly quenched at higher levels of CF_4 addition. The CF_3^+ and F^- signals were not reduced as quickly. It is possible to explain this using the ion pair process shown in equation 6.20.

It is also possible for collisionally induced ionisation of the Argon Rydberg atom to occur[18] (equation 6.21), thereby allowing a higher level of cation formation, as observed at low levels of CF_4 addition (figure 6.15a). It appears, based on the results in figure 6.15a that anion and cation detection are optimised under the same conditions. The similarity between the Ar^+ and F^- peak intensities at low levels of CF_4 addition support the mechanism proposed in equation 6.17.

$$Ar^R + CF_4 \rightarrow Ar^R.CF_4 \rightarrow Ar^+ + e^- + CF_4 \quad \textit{(equation 6.21)}$$

For some time following the addition of CF_4 to the FAG plasma it was possible to detect Ar^+ at relatively high intensity (figure 6.15b). However, over time the Ar^+ intensity steadily declined. This is probably due to trace CF_4 presence gradually desorbed from the cell walls. Thus, as the walls degas the release of CF_4 into the plasma is gradually reduced, and therefore the observed ion intensities are also reduced.

6.5.2 Influence of the Applied V_c and V_d

Figure 6.16a illustrates the variation of F^- intensity with V_c. The increase in F^- intensity with increasing V_c implies that the ions are extracted from the source, rather than forming at or beyond the ion exit. An increase in the ion extraction potential would be expected to increase the efficiency of ion extraction. Due to problems with the ion kinetic energy function of the mass spectrometer this could not be corroborated by kinetic energy measurements.

Figure 6.16b illustrates the variation of the F^- peak intensity with V_d. The highest ion intensities were observed at a relatively low discharge voltage (< 500 V), with very little ion detection above V_d = 550 V. Based on the previous results in this chapter, the ion detection between V_d = 450 and 550 V is likely to correspond to the

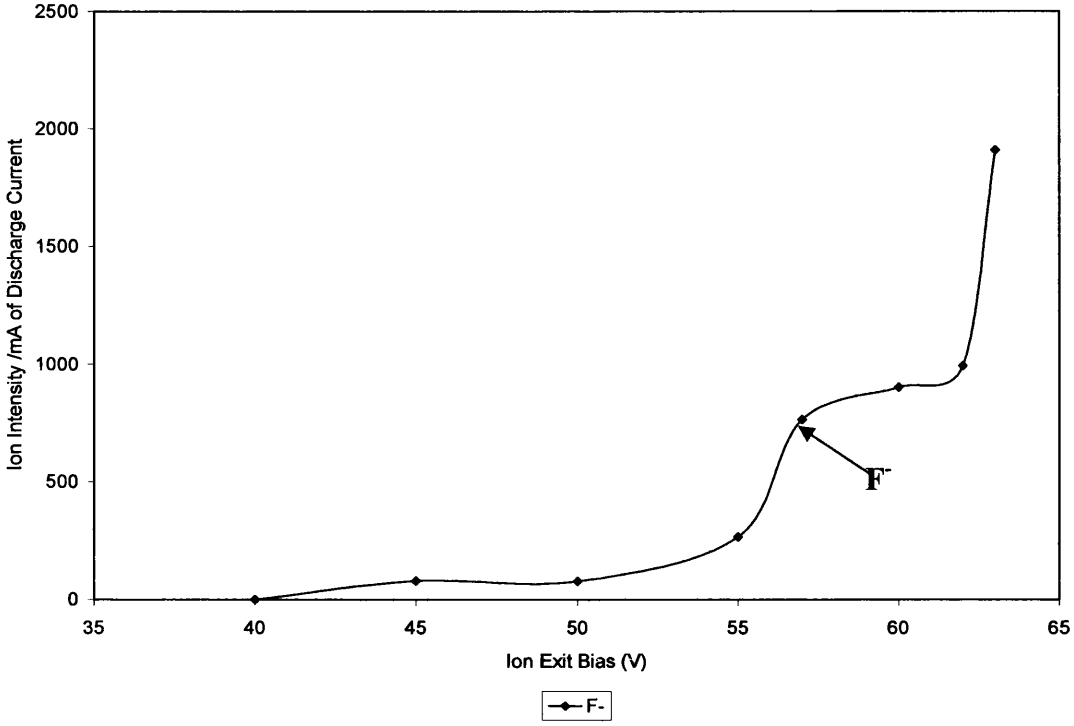

Figure 6.16a: Variation of ion peak intensities, discharge current and ion kinetic energy with V_c
(V_d = 525 V, P = 1.4 Torr, τ = 8.5 ms, V_c = +64 V, ~ 5% CF_4, tuned for F^-)

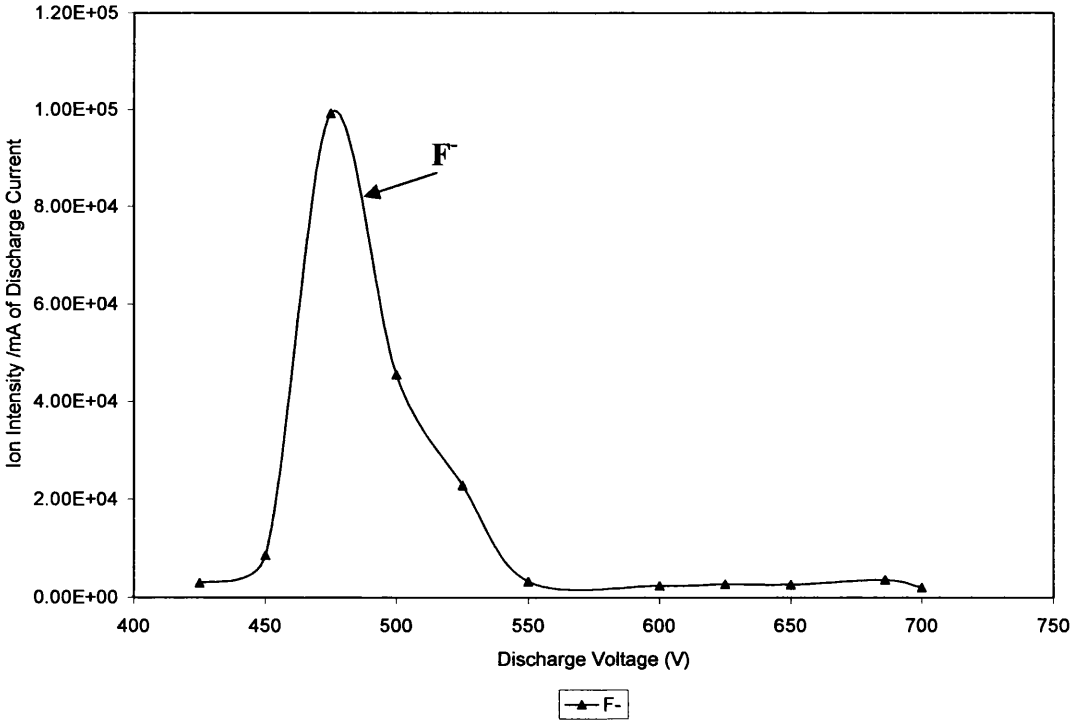

Figure 6.16b: Variation of ion peak intensities, discharge current and ion kinetic energy with V_d
(P = 1.4 Torr, τ = 8.5 ms, V_c = +64 V, ~ 5% CF_4, tuned for F^-)

onset of EI ionisation in the cone sheath, which has been common throughout this chapter.

6.6 Conclusions

It has been shown that the FFGD plasma does not fit the classical model of a plasma, but fits well with the Rydberg gas model developed within this group. The results presented in this chapter can all be explained by applying the new model, presented in chapter 4. The most basic problem with the conventional model is that it cannot explain the formation and detection of cations on application of a positive (repulsive) ion exit bias. That fact that cation intensities have been observed to increase with increasing positive V_c (figures 6.3a, 6.8a and 6.12a) opposes the ion-electron model completely. However, the Rydberg gas model illustrates how formation of a negative potential drop across the cone sheath, in response to changes in V_c and V_d, can allow cation extraction, and how ion formation via dissociation of Rydberg state species can occur in the resulting recombining plasma outside the discharge cell.

The plasma appears to become much less chemically reactive when a large current is flowing through it. Hence only limited quenching of the plasma occurs. This confirms data obtained by Mortimer[2] for the reaction with Hydrogen. We think that the Rydberg gas is stabilised in the form of highly polarised charge transfer chains when it is carrying a large current, and therefore very little quenching of the Rydberg gas can occur.

From the data in figure 5.5 it is clear that the optimum condition for the observation of anions occurs when a free ion-electron plasma forms in the anodic (cone) sheath, as is the case for observing cations. Since this is the condition where there is a negative field at the cone surface, the anions must be formed in the recombining plasma, probably via Rydberg processes, rather than electron impact. In general, anions reflect the presence of trace gas impurities with positive electron affinities, such as water, Cu, oxygen and a chlorine containing compound.

The addition of methane generates a range of hydrocarbon ions including CH_4^+, CH_5^+ and $C_2H_5^+$. It also helps release Ar^+ from the plasma. The former are detected under conditions where we expect the field at the cone surface to be negative.

Significant quantities of anions (CH_x^- and H^-) are also generated. Their detection optimises under conditions where a positive field at the cone surface is expected.

Addition of CF_4 leads to very significant simultaneous release of Ar^+ and F^-. This, we believe, is a reflection of a well known type of Rydberg gas reaction[18] (equation 6.17). A number of similar reactions have also been presented. Based on the results presented in this chapter and those of Pinnaduwage et al.[13-16], dissociative electron transfer is the principle mechanism for anion formation.

6.7 Summary

Although in some cases ion-molecule reactions can explain the formation and subsequent detection of ions, in many cases, such as when V_c is positive, ion formation can only be due to excited state reactions. It was described in chapter 5 how for a Rydberg gas plasma it is possible to form ions inside or outside the discharge cell. The Rydberg gas theory is seemingly confirmed by electrical (current and potential) measurements within the active discharge and the FAG plasma which cannot be explained in terms of an ion-electron plasma. It has also been shown that the Rydberg gas decays between the active discharge and ion exit cone, and the densities in the region of the probes can be calculated from the "plateau" currents. A model has been presented which explains how the magnitude and polarity of V_c influences the currents flowing through the FAG plasma and the sheaths at the anode and cone. Comparison of the model with mass spectrometric results indicates that on application of a positive V_c the ion intensities are maximised close to the point at which electron impact ionisation of Ar occurs in the cone sheath. It is thought that the majority of the ions detected under these conditions are formed by ionisation of the neutral Rydberg gas plume outside the discharge cell, but when electron impact occurs within the cone sheath a negative potential drop forms which could allow cations formed close to the on exit to be extracted. It appears that anions are formed by dissociative electron attachment either from Rydberg atoms or free electrons within the plasma.

6.8 References

[1] P. D. Miller, PhD Thesis, University of Wales Swansea, 1996

[2] I. P. Mortimer, PhD Thesis, University of Wales Swansea, 2000

[3] D. R. Williams, PhD Thesis, University of Wales Swansea, 2001

[4] D. J. Mitchell, PhD Thesis, University of Wales Swansea, 2002

[5] N. A. Dash, PhD Thesis, University of Wales Swansea, 2004

[6] K. Newman, PhD Thesis, University of Wales Swansea, 2005

[7] R. S. Mason, P. D. Miller, I. P. Mortimer, *Phys. Rev. E*, **55**, 7462, 1997

[8] I. P. Mortimer, D. J. Mitchell, N. A. Dash and R. S. Mason, *Proceedings of the XIVth International Conference on Gas Discharges and their Applications*, **2**, 260, 2002

[9] D. J. Mitchell, N. A. Dash and R. S. Mason, *Proceedings of the XIVth International Conference on Gas Discharges and their Applications*, **2**, 248, 2002

[10] R. S. Mason, P. D. Miller, I. P. Mortimer, D. J. Mitchell, N. A. Dash, *Phys. Rev. E*, **68**, 016408, 2003

[11] K. Newman, R. S. Mason, D. R. Williams and I. P. Mortimer, *JAAS*, **19**, 1192, 2004

[12] R. S. Mason, D. R. Williams , I. P. Mortimer, D. J. Mitchell and K. Newman, *JAAS*, **19**, 1177, 2004

[13] L. A. Pinnaduwage, W. Ding and D. L. McCorkle, *Appl. Phys. Lett.*, **71**, 3634, 1997

[14] W. Ding, D. L. McCorkle and L. A. Pinnaduwage, *J. Appl. Phys.*, **84**, 3051, 1998

[15] L. A. Pinnaduwage and P. G. Datskos, *J. Appl. Phys.*, **84**, 3442, 1998

[16] W. X. Ding, L. A. Pinnaduwage, C. Tav and D. L. McCorkle, *Plasma Sources Sci. Technol.*, **8**, 384, 1999

[17] R. S. Mason, D. M. P. Milton, M. Pichilingi, P. D. J. Anderson and M. T. Fernandez, *Rapid Comm. Mass Spectrom.*, **8**, 187, 1994

[18] T. F. Gallagher, *Rydberg Atoms*, Cambridge University Press, 1994

[19] D. R. Lide, *Handbook of Chemistry and Physics*, CRC Press, 1995

[20] M. V. V. S. Rao, S. P. Sharma, B. A. Cruden and M. Meyyapan, *Plasma Sources Sci. Technol.*, **11**, 69, 2002

[21] G. Cunge, P. Chabert and J.-P. Booth, *J. Appl. Phys.*, **89**, 7750, 2001

[22] B. Chervy, H. Riad and A. Gleizes, *IEEE Trans. Plasma Sci.*, **24**, 198, 1996

[23] M. Haverlag, A. Kono, D. Passchier, G. M. W. Kroesen and W. J. Goedheer, *J. Appl. Phys.*, **70**, 3472, 1991

[24] T. Kimura and K. Ohe, *J. Appl. Phys.*, **92**, 1780, 2002

[25] V. Georgieva, A. Bogaerts and R. Gijbels, *J. Appl. Phys.*, **93**, 2369, 2003

[26] M. V. V. S. Rao, S. P. Sharma, B. A. Cruden and M. Meyyappan, *Plasma Sources Sci. Technol.*, **11**, 69, 2002

[27] Y. Le Coat, J. Ziesel and J. Guillotin, *J. Phys. B*, **27**, 965, 1994

[28] J. K. Olthoff and Y. Wang, *J. Vac. Sci. Technol. A*, **17**, 1552, 1999

Chapter 7

Argon Rydberg Gas Reactions Studied in the 'PQ2' FFGD Mass Spectrometer; H_2, N_2, CO, CO_2 and CH_4

7.1 Introduction

This chapter extends work carried out previously to investigate the chemistry which occurs when a secondary gas is added to the afterglow of a fast flowing dc glow discharge plasma[1-12]. In this case, the second generation instrument, the 'PQ2' FFGD mass spectrometer has been used. The design is such that continuous addition of gases directly into the flowing afterglow (FAG) plasma is possible. As stated previously, addition of gases to the FAG plasma rather than mixing with the discharge gas allows the separation of the discharge processes (sputtering, electron impact, etc) from the chemistry involving secondary gas reactions with the plasma. The Rydberg gas model of the GD plasma used to interpret the data is discussed in detail in sections 2.6 and 2.7 and chapter 4.

Addition of secondary gases to a flow gas carrying excited states was carried out by Setser and co-workers[13-26], investigating the thermal rate constants for the quenching of noble gas metastable states (Ar $^3P_2$, Ar $^3P_0$, Kr $^3P_2$, Xe $^3P_2$,) by a range of organic and inorganic gases. The aim of Setser's work was to measure rate constants for quenching of specific excited metastable states. It was demonstrated that the rate at which the argon metastable states were quenched was dependent on the gas added. The approach of our experiments was to study the plasma which generates these excited states.

Many previous researchers have also reported on the effect of addition of secondary gases to glow discharge plasmas, but all of this work has involved premixing of the secondary with the discharge gas prior to entering the active discharge region. Wagatsuma and Hirokawa[27,28] studied the effects of oxygen and nitrogen directly to the active Ar/Cu discharge and observed a decrease in the Cu(I) emission intensity. It was proposed that the lower mass of nitrogen and oxygen relative to argon, and the corresponding decrease in momentum, reduced the sputtering efficiency and therefore release of $Cu_{(g)}$ from the cathode. It was also proposed that the oxide layer produced on addition of oxygen could further reduce sputtering. The reduction in sputtering rates for each system was corroborated by Fischer and co-workers[29], again using spectroscopic methods. It was also proposed that the formation of an oxide or nitride layer could reduce the secondary electron emission from the cathode surface therefore lowering the degree of excitation within the plasma. This was confirmed by Tochibuko[30] and co-workers who observed on

addition of nitrogen to a radio-frequency (rf) discharge a reduction in the argon metastable density. This fits with the proposals presented by a number of authors[3,31,32,33] for formation of Cu^+ through transfer of energy from argon metastable states i.e. Penning ionisation. Subsequent reduction in formation of excited states of argon would be expected to lead to a corresponding decrease in the formation of copper ions[31,34]. Similar reductions in sputtering[35,36] and argon metastable population[20,26,31,34,36,] have also been reported on addition of water vapour or methane to the argon glow discharge.

7.1.1 Effect of Ion Exit Bias

The effect of the ion exit bias on ions detected from the FAG plasma was investigated previously within this group[9,12] and from a 'static' gas GD by Taylor et al.[37]. The previous investigations have been predominantly limited to the effect of negative ion-exit biases since it was expected that a positive field at the ion exit would repel cations. Mitchell[9], however reported specific positive values for V_c at which ions were observed as a series of diffuse ionisation "resonances". Each resonance produced a release of ions whilst the regions between indicated very little ion formation. The resonances observed also appeared to be ion-specific, i.e. the resonances for Ar^+ differ from those for ArH^+ and those for Cu^+. As we have seen from chapters 4, 5 and 6, the ionisation at low positive V_c is the result of field ionisation of the Rydberg gas. However, we now know that on application of a higher V_c there is another region of ion detection, the result of electron impact ionisation and the development of a free ion-electron plasma within the anodic (cone) sheath.

Recent work by Newman[12] studying the influence of ion exit bias on the spectra recorded on addition of organic and organometallic vapours highlighted the fact that ions could often be more readily detected without application of an ion exit bias or on application of a small positive bias. A significant and important finding was that on application of a large negative ion exit bias the major ions observed were fragment ions. As the bias became less negative the fragment ions increased in size until application of a small negative, zero or small positive bias was applied, at which point the molecular ions (M^+) and protonated species (MH^+) reached their maximum intensities. It was proposed that under positive ion exit conditions ions detected were formed by ionisation of highly excited state species within the accelerating field

outside the source. However, it is possible that on application of a high negative ion exit bias ions were formed by collision induced dissociation (CID) close to the ion exit.

There are a number of processes which could determine the ionisation processes within the GD cell, many already described in chapters 5 and 6. Changing the magnitude of V_c may influence the following processes:

1) sampling efficiency – the observed positive ion intensities would be expected to increase with increasing negative V_c;
2) charge transfer (CT) – this is particularly efficient between Ar and Ar^+ at low ion kinetic energies, decreasing as the ion kinetic energy increases;
3) ion-molecule (I-M) processes;
4) collision induced dissociation (CID) – obviously only applicable to molecular ion processes;
5) electron impact (EI) ionisation – this requires the release of electrons either from the Rydberg gas (see below) or secondary electron emission from the cone surface when the bias is negative. The electrons are accelerated across the sheath field due to the bias on the cone;
6) field ionisation/Stark excitation of Rydberg species[38] – the field around the ion exit will induce ionisation of the highly excited state species;
7) mass discrimination at the orifice[39] – mass discrimination has been shown to favour transmission of low mass ions at the source pressure used in this investigation.

A Previous study established that the ion exit cone sheath thicknesses is ≤ 3 mm[10]. In plasma theory, these sheaths are believed to be almost collisionless. Therefore processes 2) to 5) will occur mostly by collisions occurring in the ion exit aperture. According to our experiments the main process is (6)[5-12] (discussed in chapters 2, and 4).

7.1.2 Addition of Hydrogen

The addition of hydrogen to a static argon glow discharge was first performed by Knewstubb and Tickner[40,41] in the 1960s. They observed that a 1.5% addition of hydrogen to the discharge gas lowered the charge density and that the argon ion concentration was significantly reduced. This was also observed by van de Sanden and co-workers[42,43] and was proposed to be caused by recombination processes. One example of a mechanism for reduction of charge density is illustrated by equations 7.1 and 7.2. The recombination coefficient of ArH^+ is many orders of magnitude larger than Ar^+ and it was therefore proposed that reaction 7.2 was the major process responsible for the observed decrease in charge density.

$$Ar^+ + H_2 \rightarrow ArH^+ + H \qquad \textit{(equation 7.1)}$$

$$ArH^+ + e^- \rightarrow Ar + H \qquad \textit{(equation 7.2)}$$

In contrast, the addition of hydrogen has been shown to increase the formation of the metal ions from the cathode[1-12,44]. Smithwick et al.[44] also observed that on addition of 1% H_2 for a number of metal samples the relative ion yields correlated better with theoretically calculated values than those using pure argon discharge gas.

The effect of addition of secondary hydrogen to the FAG plasma has been investigated extensively within this group both mass spectrometrically[1-12] and electrically[5,9,7], via double-probe studies, and it was this model which has been proposed to account for the variations in signal observed. The mechanisms for formation of the major discharge related ion species have been discussed in chapter 2.

7.1.3 Addition of Nitrogen

As discussed above, the quenching efficiency of nitrogen on the major plasma species has also been studied[3,27-29]. The effect of adding nitrogen to the flowing afterglow of the FFGD plasma was studied previously by Miller[1] and Mortimer[3] using the first-generation FFGD instrument, but only when V_c was negative or zero. Both concluded that the variations observed cannot be explained using ion-molecule kinetics, but that once more an excited state model fits the results well.

7.1.4 Addition of Carbon Monoxide

Mortimer[3] studied the addition of carbon monoxide. It was observed that initially Ar^+ was released, followed by rapid quenching of excited state argon species.

7.1.5 Addition of Carbon Dioxide

Mortimer[3] also studied the addition of carbon dioxide. Jogan et al.[45] report on the reaction of carbon dioxide in a Corona discharge mixture with argon whilst the decomposition in a pure CO_2 discharge[46,47] as well as CO_2/N_2[46], $Ar/CO_2/N_2/O_2$ [46] and CO_2/He mixtures[48] have been studied. The reaction of a CO_2/CH_4 mixture[49,50] to produce synthesis gas (syngas) is of interest since processes which decompose carbon dioxide, which is the major greenhouse gas, to form more useful species such as oxygen, carbon monoxide and hydrogen could be used to reduce the impact on the environment.

7.1.6 Addition of Methane

The addition of Methane to the flowing afterglow of a FFGD plasma has already been widely studied within this group[1,3,6,9,12]. Miller[1] investigated changes to the mass spectrum when varying the percentage addition of methane to the FAG plasma and proposed an excited state model to explain ion formation. This was continued by Mortimer[3] who repeated the results on application of both weak and strong ion exit fields. Mortimer[3] also studied the quenching efficiency of CH_4 by monitoring the variation in the cone current with increasing addition of the secondary gas to the FAG plasma as well as recording the negative ion spectrum.

The effect of methane addition on the electric fields and currents within the plasma was studied by Dash[9] using the electrical double probe technique described in chapters 2, 4 and 5. Dash[9] repeated the experiment performed by Mortimer[3] to determine the efficiency of quenching the argon Rydberg gas on addition of methane. Newman[12] also determined the quenching rate on addition of methane using the low voltage instrument described in this chapter. Some differences were found, and it was proposed that this was due to the sampling of a different Rydberg atom population because of the higher fields present in the accelerating region of the magnetic sector instrument compared with the fields within the low voltage quadrupole mass

spectrometer. Newman[12] also demonstrated the influence of the ion exit bias on the degree of fragmentation of methane observed, although a full study was not performed.

7.1.7 This Study

The results in this chapter report on using permanent gas additions. These gases have a range of unique physical properties and may therefore have different influences on the formation and removal of plasma species. The applied ion exit bias influences the flow of ions and electrons within the FAG plasma, as well as polarising excited state species, and therefore affects the chemical interactions which occur. Previously it has also been noted[4,12] that there can appear to be quite significant differences between the results from the low voltage (quadrupole) instrument and the pioneering work carried out on the modified high voltage (MS9) mass spectrometer based instrument. It was felt to be important to examine and understand these differences more fully. Therefore, some gases previously studies are included here for comparison.

7.2 Instrumentation

The experiments were performed using the second generation FFGD instrument built by Williams[4] and briefly described in section 3.2. The source design (figure 3.7) was based on that of the first generation instrument developed within this group[1,3], although there are a number of differences which are described below. The instrument was a modified VG PlasmaQuad II Inductively Coupled Plasma (ICP) mass spectrometer[4,51].

7.2.1 The FFGD Source

The GD source was used in its extended form as illustrated in figure 3.7. The design is very similar to that of the first and third generation instruments (discussed in chapter 3) and it had been expected that results should be directly comparable. Differences (provided the experimental conditions are the same) are then mostly due to the efficiency of ionisation of the plasma as it leaves the source and the efficiencies

of collection by the different mass spectrometers used. The discharge region is of co-axial design, i.e. the cathode pin extends through the centre of the cylindrical anode, and the discharge gas flows between the two. All metallic sections were produced from non-magnetic stainless steel (316grade[52]) unless otherwise stated. The high discharge gas flow rate extends the plasma downstream towards the ion exit cone to produce a flowing afterglow (FAG) plasma. Two cathode materials were used in this project – copper (Goodfellows[53], Cu rod; 99.99%) and vanadium (Goodfellows[53], V rod; 99.8%). Each cathode pin was 2 mm in diameter and 14 mm in length and was mounted in a brass sample holder. The brass sample holder was designed to allow incorporation of cathode pins up to 3mm diameter, and therefore it was necessary to wrap the base of the cathode pin with aluminium foil in order to hold the pin effectively. The presence of the foil does not affect the plasma as it does not extend into the discharge region. The cathode was insulated from the anode using ceramic and PEEK spacers. The spacers located into the brass sample holder aid centring of the cathode pin and restrict the exposed length of the sample pin to 7 mm. A seal is created through inclusion of a silicon O-ring directly between the anode and cathode surfaces and the cathode is held in place using a spring loaded clamp which also acts as the contact for the discharge power supply.

The anode is comprised of two sections; the anode body and an outer shell. The two sections were produced to promote even distribution of the discharge gas flow around the cathode pin from a single inlet, therefore allowing even sputtering of the cathode surface. The discharge gas inlet enters the anode via a 1/16" Cajon[54] fitting and is channelled into a 0.2 mm gap between the anode sections. The anode body had an interior diameter of 10 mm expanding to 20 mm to match the internal diameter of the flow tube. The anode is sealed to the flow tube using a Viton O-ring.

The flow tube was floated at anode potential due to the electrical contact between the two sections. This is significant, because the experiments reported by Mitchell[5] and Dash[9] were carried out with the body of the flow tube floating. As shown by Mitchell[5], the detailed effect of the ion exit voltage can be quite different when V_c is positive, although the general overall effects are very similar. This is because of the fields through the plasma affect the l and m values of the Rydberg population significantly[38]. As stated above, the source was operated in its extended form. The extension section was 20 mm long with an internal diameter of 20 mm and incorporated a Swagelok[54] (⅛" NPT) union through which the secondary gas inlet

passed. The gas inlet tubing was 1/16" diameter to prevent electrical contact between the inlet and the flow tube walls and therefore it was necessary to use a Vespel reducing ferrule to seal the fitting. To further reduce the possibility of disturbance to the plasma due to electric fields a short length of PTFE tubing was used to connect two lengths of stainless steel tubing together therefore forming a 'floating inlet'[12]. The flow of gas was actually delivered through a length of silica capillary tubing within the secondary gas inlet. This capillary (not illustrated in figure 3.7) terminates within 1 to 2 mm of the end of the tubing to prevent blockage due to deposition of sputtered cathode material and the inlet itself terminates 2 mm off the central axis. The gas is added 20 mm upstream of the ion exit cone to allow adequate time for thorough gas mixing.

The final section of the flow tube was sealed to the extension section using a Viton O-ring. This section incorporated a further Swagelok[54] fitting to allow secondary gases to be added closer to the cone (3.5 mm in front of the cone tip) or allow introduction of an electrical probe at the same point. For this investigation the fitting was blanked off as it was not used, and so has not been illustrated. A length of tubing (¼" diameter, 50 mm length) extended from the flow tube to a Baratron capacitance manometer (MKS Type 122 A[55], 0-10 Torr) used to monitor the source pressure off-axis. The use of wide bore tubing and positioning the pressure gauge off-axis helps minimise errors due to flow effects[56]. As the flow tube was electrically connected to the anode it was necessary to power the manometer using an isolated transformer.

The ion exit cone was produced from non-magnetic stainless steel and mounted onto a copper mounting plate. The cone had a flattened tip with a 0.3 mm orifice drilled centrally. The discharge gas was pumped from the source through the outlet illustrated in figure 3.7, and through the expansion chamber beyond the cone. The pumping outlet had a wide bore (¾") to allow the high throughput required and the pumping rate was controlled using a ball valve (Whitey[54] series 60). Using this system the source pressure could be varied for a given argon flow rate. A liquid nitrogen cold trap was incorporated into the line to prevent back diffusion of oil vapour to the source. The pump itself was an Edwards[57] E1M40 high capacity rotary pump. To allow improved pumping efficiency a second rotary pump (Edwards[57] E1M18), the original expansion chamber pump, was connected into the pumping line

beyond the ball valve. An isolation valve (Edwards[57] Speedivalve SP 25K) was incorporated to allow the second pump to be isolated when not in use.

7.2.2 Source Electronics

Figure 7.1 illustrates the electrical circuitry used to power the glow discharge and supply the ion exit bias. The glow discharge was powered by a Glassman[58] 0-1 kV, 0-300 mA direct current (dc) glow discharge power supply, operated in constant-voltage mode. The discharge voltage (V_d) was read off an analogue meter built into the power supply, whilst the discharge current (I_d) was displayed on a digital meter to allow more accurate measurement. The ion exit potential (V_c) was supplied by an Isotech[59] IPS 1603D power supply unit, which has a range of 0-60 V for a maximum current of 3 A. The ion exit cone was connected to the instrument earth and biased relative to the anode. The cone could be biased positively or negatively by switching the connections in the power supply. The ion exit bias was displayed on a digital readout on the power supply and more accurately on a digital multimeter (Wavetek DM 78A[59]).

7.2.3 Gas Transfer System

The gas transfer system (figure 7.2) is very similar in design to that for the third generation instrument detailed in chapter 3. All gas lines were produced from copper or stainless steel tubing (1/16" to ¼" according to availability and requirements of the fittings). A cryo-coil was incorporated into the secondary gas line in order to reduce the water levels in the reagent gases if required. The gas flow rates were monitored as they passed through individual mass flow meters (Tylan[60] FM360, 0-2000 sccm for the discharge gas and FM360 0-500 sccm for the secondary gas). The secondary gas mass flow meter was calibrated for nitrogen, and therefore a conversion factor (supplied by the company) was required when using another secondary gas. The gas flow rates were displayed as a voltage reading which could be converted directly to sccm values. The discharge gas flow rate, 0-2000 sccm, and secondary gas flow rate, 0-500 sccm, corresponded to a reading of 0-5V on the digital multimeter (Iso-Tech[60] IDM 201, supplied by RS Components Ltd.).

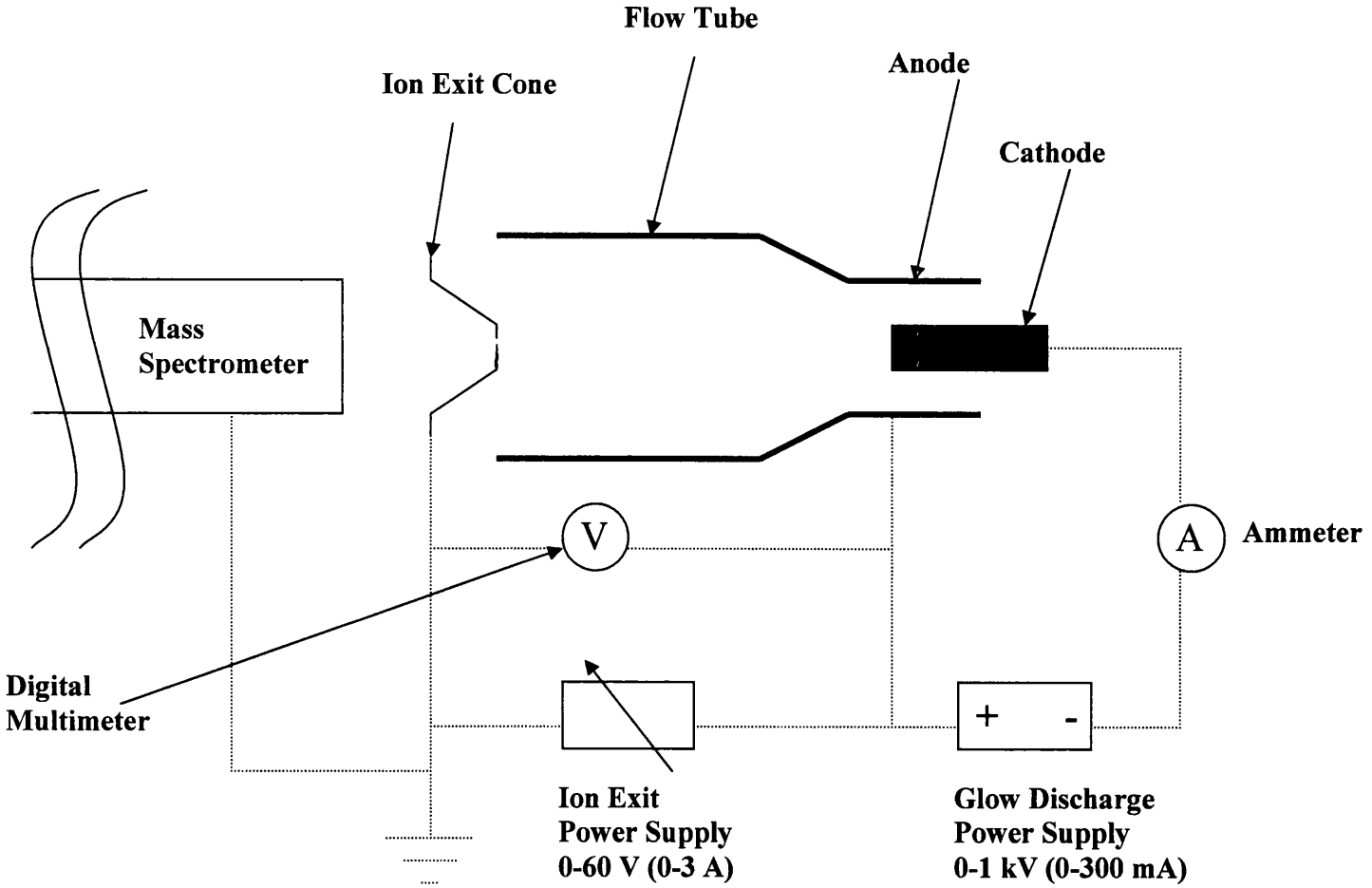

Figure 7.1: Schematic of the discharge and ion exit power supplies

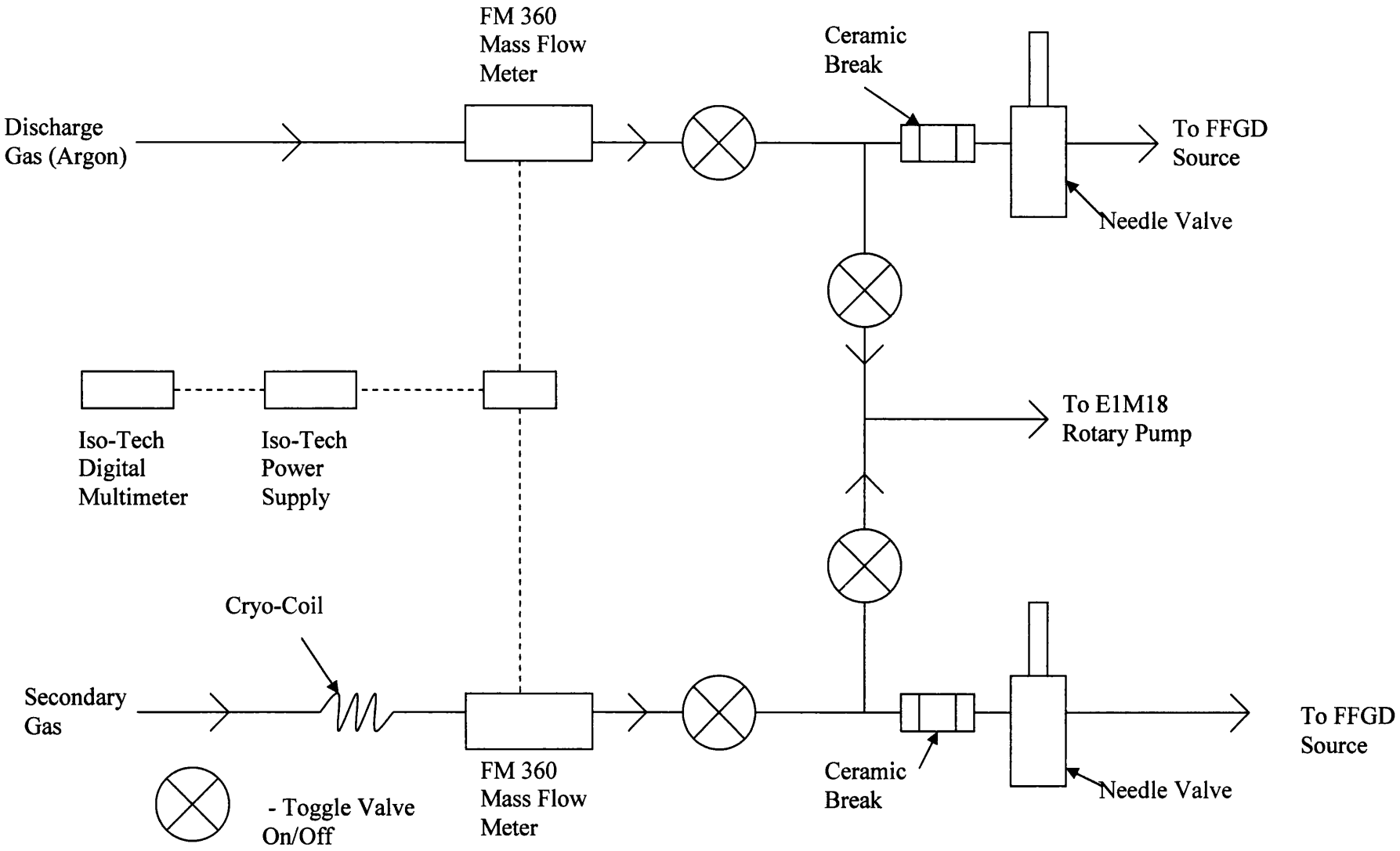

Figure 7.2: Gas Transfer System

The gases next passed through on/off toggle valves. After this point the gas lines were split to allow the gases to be directed to the source or for the gas lines to be evacuated via a purge line to the second source pump (Edwards[57] E1M18 rotary pump). The purge lines were controlled by further on/off toggle valves. The gas flow rates to the FFGD source were determined using fine control needle valves (Meggit Avionics[61] NV series). High voltage ceramic breaks (rated to 3 kV) were incorporated prior to the needle valves to prevent high voltages, due to gas lines floating at anode potential, short circuiting to the instrument earth. To prevent contact between the needle valves and the instrument they were mounted onto perspex and supported by Delrin rods. Delrin sleeves were fitted over the valve shaft to protect the operator from electric shocks.

The secondary gas inlet system was modified by Newman[12] to allow better control of low secondary gas flow rates, to allow addition of organic vapours from liquid samples and to use the mass spectrometer as a detector for gas chromatographic studies. Figure 7.3 illustrates the modified section of the secondary gas inlet which is incorporated between the needle valve and the glow discharge source.

To allow addition of gases the 3 way valve was set to direct the gas through the by-pass line (1/16" stainless steel tubing) into the GC oven. For the study of pure gas addition the oven was kept at room temperature. Within the oven the gas line is split into two silica capillaries[62] of equal internal diameter (i.d. = 250 μm, o.d = 350 μm) but one is one hundred times the length of the other. This required the use of a Swagelok T-piece and graphite reducing ferrules (1/16" to 0.4 mm). When the needle valve in the line to the rotary pump (Edwards E2M5[57]) was closed the gas flow was directed only to the source, and therefore the gas flow rate was equal to that measured. The gas passes through 5 m of capillary directly to the source as described in section 7.2.1, although to do so the tubing passes through a Swagelok union (1/16" to 1/16"), again fitted with a graphite reducing ferrule (1/16" to 0.4 mm) into a length of stainless steel tubing (1/16" o.d.) which protrudes from the opposite side. This allows the capillary to enter the secondary gas inlet whilst retaining a good vacuum seal.

The pumping line was incorporated to allow the gas flow to be split. By applying Poiseuille's formula (equation 7.3) whereby the flow rate of a fluid is related to the inlet and outlet pressures of the tubing and its length it was believed that if the pumping line and source pressure were equal the gas flow would be split 100:1 when the ratio of the lengths of the capillary were 5:500. The pumping line pressure was

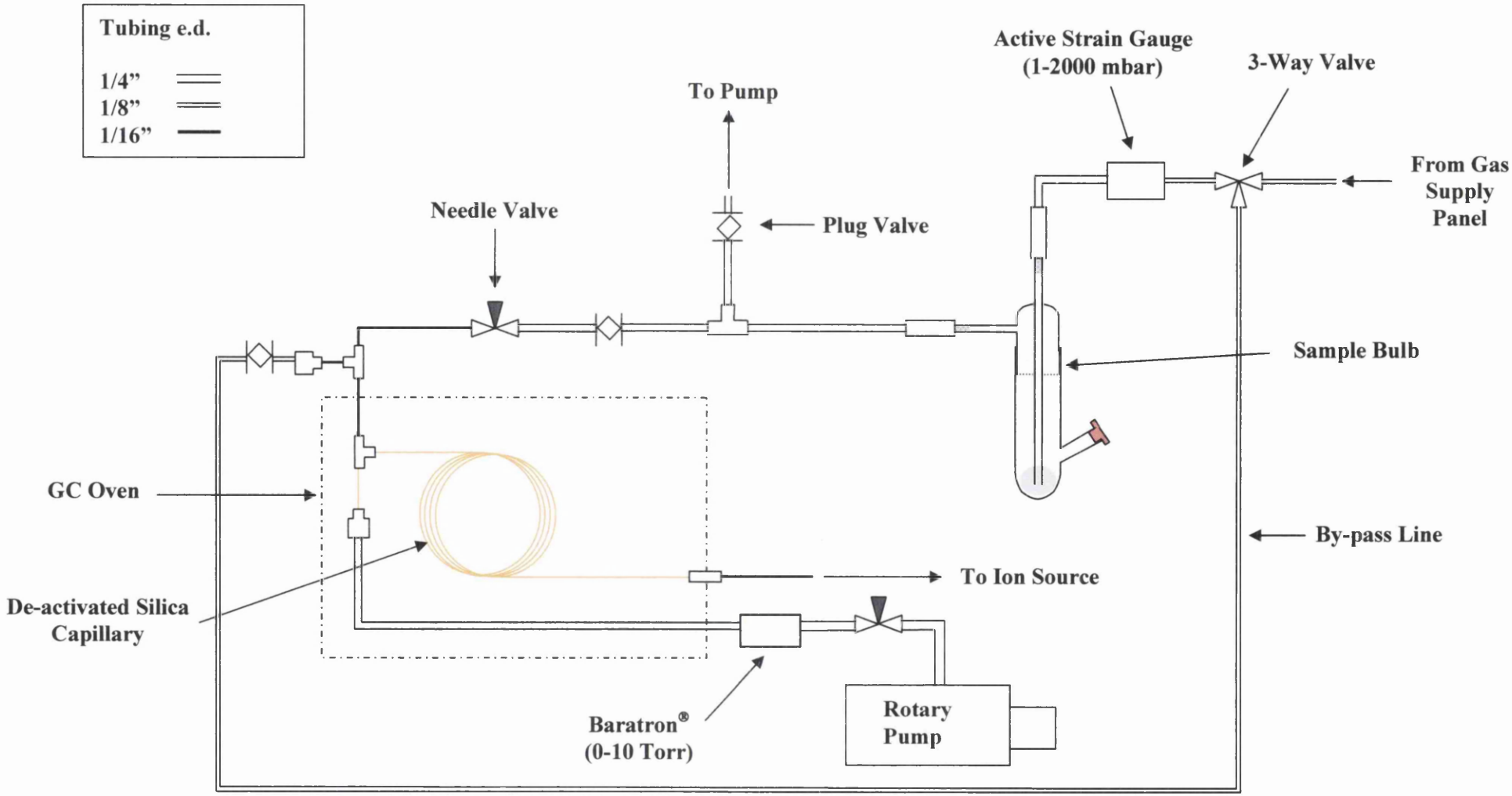

Figure 7.3: Schematic of the organic vapour inlet system (from reference 12)

controlled using a needle valve (Whitey 'D' Series SS14DKS4, non-rotating stem)[54] and measured using a baratron capacitance manometer (CDL1106, 0-10 Torr)[59].

$$\frac{dV}{dt} = \frac{(p_1^2 - p_2^2)\pi r^4}{16 l \eta p_0} \qquad \textit{equation 7.3}$$

where V is the volume flowing, p_1 and p_2 are the pressures at each end of the tube of length l, η is the viscosity, and p_0 the pressure at which the volume is measured.

Assuming the equation to apply to this system it was believed that it would be possible to reduce the minimum gas flow by a factor of one hundred, therefore allowing significantly improved control over low gas flow rates. However, it was discovered in this work by studying the hydrogen reaction that the split did not reduce the gas flow by the ratio estimated. On addition of hydrogen gas to the FAG the formation of ArH^+ is initially enhanced, reaching a maximum for less than 1% (of total gas flow) addition of hydrogen (reference 12 and figure 7.4a) and subsequently decreases on increasing the hydrogen flow. Figure 7.4a illustrates the effect of increasing hydrogen addition on the main ion peak intensities when the flow is direct (not split), whilst figure 7.4b illustrates the same effect using the split flow, assuming the split to be 100:1. It can be seen that the ArH^+ maximum under split flow conditions appears to occur at approximately one quarter of the addition of hydrogen compared with the not-split flow.

Two reasons were considered for this disparity: (i) it was found that the capillary tubing used does not have a constant internal diameter, and (ii) with the shorter length the "end-effects"[56] may be important. The gradients for the decay of the argon hydride ion signal were also compared, and again the ratio between the two determined as a comparison for the previous result. The split ratio was therefore estimated empirically by comparing the amount of hydrogen required to achieve the ArH^+ maxima for each process (split and normal flow). During the course of this work the short length of capillary was changed on several occasions both for repairs and in an attempt to increase the split ratio. It was discovered that the split ratio was always less than 50:1 and greater than 25:1 for the short lengths of capillary used (40-50 mm).

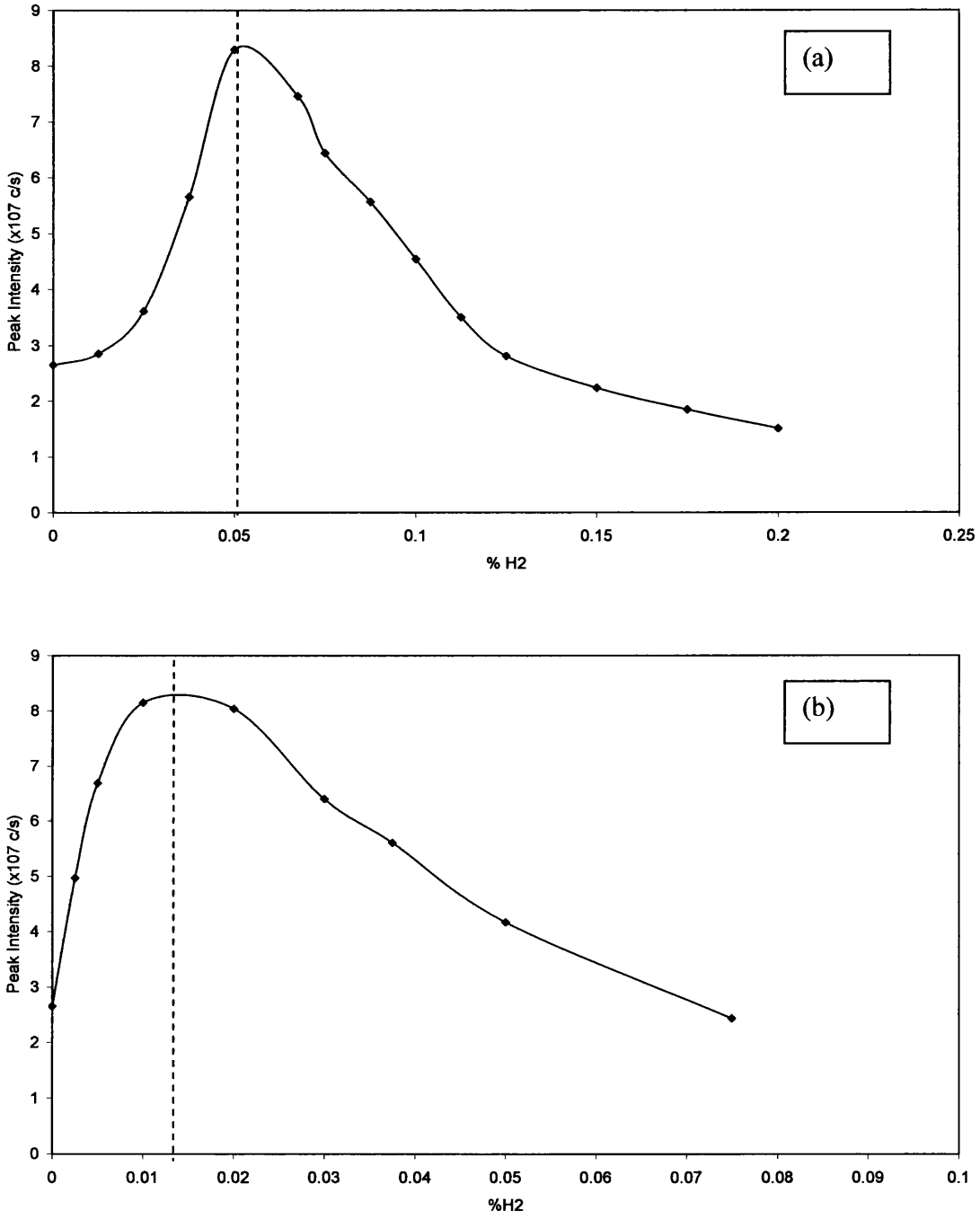

Figure 7.4: Comparison of ArH^+ ion current variation on addition of hydrogen to the FAG plasma using (a) not split and (b) split flows (V_d = 700 V, I_d = 2.5 mA, P = 1 Torr, F_{Ar} = 400 sccm, V_d = -20 V, τ = 2.1 ms, tuned for ArH^+ detection)

The secondary gas flow is expressed as a percentage of the total gas flow (argon and secondary gas) and was calculated using equation 7.4;

$$\%\ Secondary\ Gas = \left(\frac{F_{secondary}}{F_{secondary} + F_{Ar}} \right) \times 100 \quad \textit{(equation 7.4)}$$

where *%Secondary Gas* is the approximate percentage of the secondary gas contained within the plasma afterglow, $F_{Secondary}$ is the measured flow rate at which the secondary gas is admitted into the FFGD ion source and F_{Ar} is the measured flow rate at which the argon plasma support gas is admitted into the source. It should be noted that it is only possible to approximate the percentage of secondary gas added since for the equation to be true it is assumed that the gases mix homogeneously. Due to the manner of gas addition and the short residence times used it is very unlikely that this occurs.

7.2.4 Organic Vapour Inlet System

The inlet system illustrated in figure 7.3 was designed and built by Newman[12] to allow continuous addition of organic liquid samples to the FAG. FFGDMS was found to be an extremely sensitive technique for analysis of organic and organometallic compounds as a detector for Gas Chromatography (GC) and for the adapted continuous inlet system[12]. Continuous addition of the sample enabled the discharge conditions and focussing lenses to be tuned to achieve optimised ion signals and to allow improved speciation, and studies of the ionisation processes through ion exit bias induced fragmentation (discussed further in chapter 8).

7.2.5 The Mass Spectrometer

The instrument used was a modified VG PlasmaQuad II ICP quadrupole mass spectrometer[51], in which the ICP source had been replaced by the FFGD source described. All other regions of the spectrometer were used in their original configuration. The mass spectrometer (figure 7.5) consists of four regions:

1) the source;
2) intermediate pumped region;
3) analyser;
4) detector

The source (described previously) can be isolated from the pumped region through use of a slide valve (opened/closed by pneumatic pressure and controlled using the instrument software[63]), therefore allowing source maintenance without venting the whole instrument to atmospheric pressure.

The intermediate region was pumped using an Edwards[57] E1M18 rotary pump, which can also be used as a second source pump as described in section 7.2.1. The pressure within the intermediate region was typically $\leq 10^{-4}$ mbar, measured using a PRL 10 Pirani gauge[57] (range 10^{-4} - 10^{-3} mbar) and Edwards[57] 1105 vacuum controller. A trip relay in the vacuum controller was used to protect the instrument from sharp increases in pressure in the source by activating the slide valve. The intermediate chamber houses the first four lenses – extraction, collector, lens 1 and lens 2. The extraction lens is positioned 30 mm beyond the tip of the ion exit cone to direct the ion beam through the slide valve region to the collector lens, therefore reducing the loss of ions through diffusion.

The pressure in the analyser region must be significantly lower than the intermediate region, and therefore a 2 mm differential aperture was incorporated to reduce the gas flow. The analyser and detector regions were pumped by two Edwards Diffstack diffusion pumps backed by a single Edwards E1M18[57] rotary pump. Typical analyser pressures ranged from $0\text{-}5\text{x}10^{-8}$ mbar when the slide valve was closed to $1\text{-}3\text{x}10^{-7}$ mbar when the FFGD source was used. The analyser pressure was monitored using an Edwards CP25 Penning gauge[57] (pressure range 10^{-8} - 10^{-2} mbar), again connected to the 1105 vacuum controller. Three further trip relays within the vacuum controller were used to shut down the diffusion pumps and the multiplier if the pressure rose above a threshold value. The analyser region housed lens 3, lens 4 and the quadrupole mass analyser. With the exception of the extraction lens the ion focussing lenses were incorporated within a single assembly or 'stack'.

Typical tuning conditions for detection of cathode and argon ions with and without application of an ion exit bias are illustrated in table 7.1. However, the tuning conditions were very sensitive to varying conditions within the source and the tuning

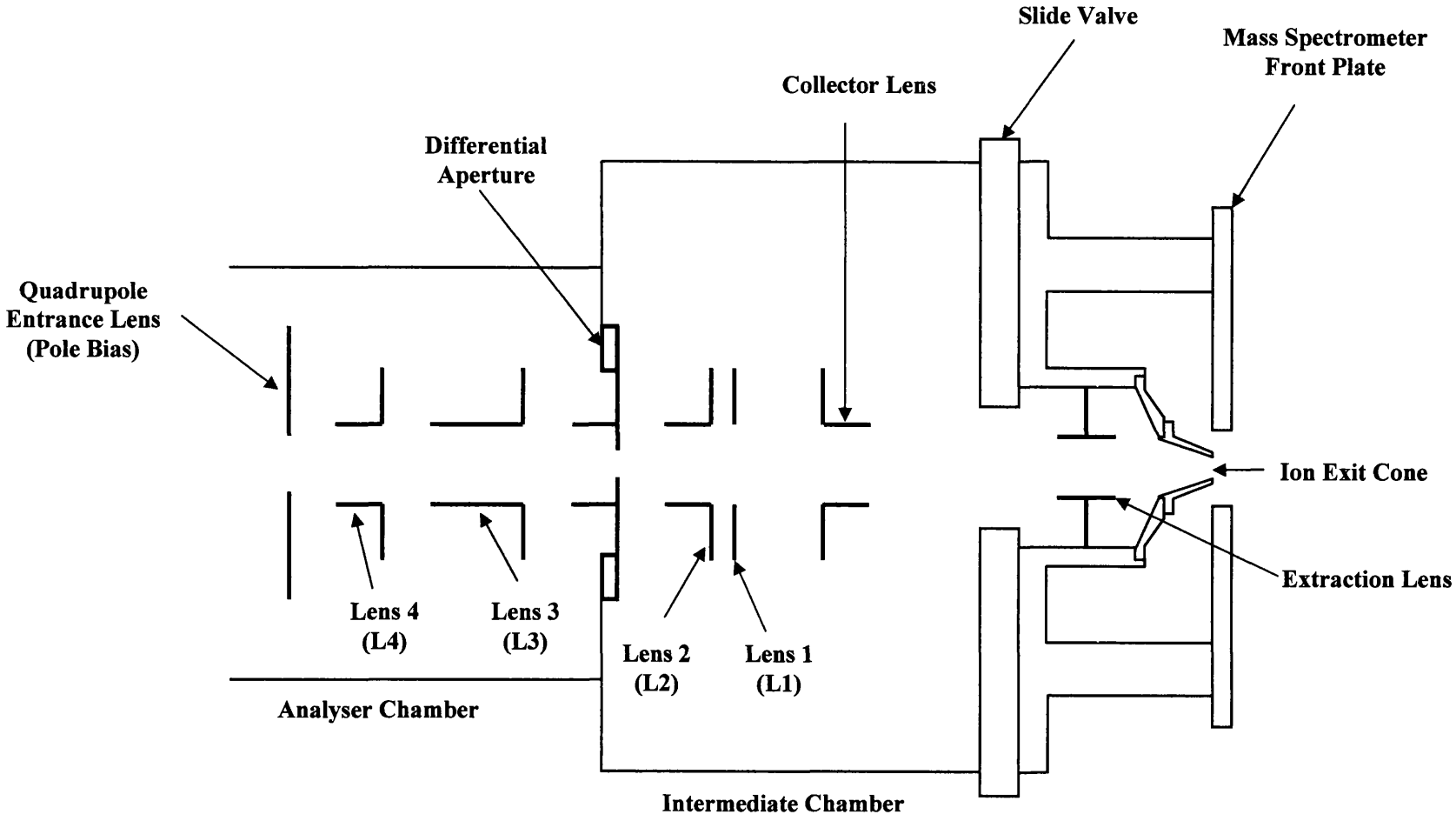

Figure 7.5: Schematic of the lens geometry (adapted from reference 12).

Lens	Copper ion			Argon ion		
	V_c = -20 V	V_c = 0 V	V_c = +2 V	V_c = -20 V	V_c = 0 V	V_c = +2V
Extraction	-250	-665	-820	-241	-840	-865
Collector	-18	-6	-6	-100	-30	-27
Lens 1 (L1)	+10	+2	+2	-7	-74	-70
Lens 2 (L2)	-29	-30	-30	-91	-67	-68
Lens 3 (L3)	+7	+21	+20	+14	+15	+15
Lens 4 (L4)	-100	-100	-100	-100	-100	-100
Pole Bias	+5.4	-17	-17	+3.5	-20	-25

Table 7.1: Typical lens and pole bias voltages

(P = 1.00 Torr, F = 400 sccm, V_d = 700 V)

of the other lenses. Lenses 1 and 2 focus the ion beam through the differential aperture and lenses 3 and 4 refocus the beam into the quadrupole entrance. The pole bias is set to accelerate or decelerate the ions through the quadrupole filter. Since the system was designed for positive ion detection, a negative pole bias would accelerate the ions and a positive bias would decelerate them.

As the analyser has a mass resolution of only 1 amu it was not possible in the work of this chapter to differentiate between ions with masses within +/- 0.5 amu of an integral value. This was only a problem in trying to distinguish between OH^+ and CH_5^+ (m/z = 17) and O^+ and CH_4^+ (m/z = 16). The QMF allows analysis of ions of up to 300 amu, and was therefore suitable for use in this study as the majority of the ions monitored had masses <100 amu.

Ions are detected by a single channel electron multiplier (Burle Channeltron model 4870v[64]) and the signal is processed using commercial software provided with the instrument. Using the software provided it is possible to operate the detector in three modes:

1) analogue mode;
2) pulsed mode;
3) dual mode.

In analogue mode the multiplier runs at a relatively low voltage (-1500 to -2000 V). This mode was incorporated to allow higher ion fluxes (such as Ar^+ when using the ICP torch[65] or Cu^+ when operating the FFGD source) without saturating the detector. Pulsed mode operates the multiplier at a high gain (10^7 to 10^8 at a multiplier voltage of -2500 to -3500 V) and allows detection of trace ion signals. This level of detection could be critical when analysing impurities within samples. Dual mode allows improved detection limits without saturating the detector. Using this method the computer software[63] uses a pre-scan to determine which ions to monitor in analogue and pulsed modes and by cross-calibration between the two it adjusts the analogue signal accordingly to fit the pulsed mass spectrum. The multiplier voltage can be adjusted manually should it be required.

7.3 Experimental Techniques

7.3.1 Discharge Conditions

For all of the following results the glow discharge was operated using the following conditions: V_d = 700 V, P = 1 Torr, F_{Ar} = 400 sccm, τ = 2.11 ms. The first set of experiments used a fixed ion exit bias (-20, -10, 0 and +2 V) and the percentage addition of secondary gas was increased. The second set of experiments used a fixed percentage of secondary gas (0.01, 0.1 and 1%) added and the ion exit bias was varied systematically, usually from -60 V through +10 to 20 V. For each change in ion exit voltage or secondary gas flow rate the focussing lenses were retuned and a spectrum (up to 130 amu due to settings in software[63], although signals for higher mass species were monitored where necessary) was recorded. Each set of results was recorded at least twice tuning on different ions to determine if the results were significantly influenced by tuning effects. The ions usually chosen for tuning were Cu^+ and ArH^+ as they have well separated masses, are both discharge related ions and usually appear in high abundance.

As secondary gases were added 20 mm upstream of the ion exit orifice the total reaction time, calculated using the residence time equation (equation 3.1), was ~1.2 ms; this assumes efficient mixing.

7.3.2 Reagent Gases

For this investigation all gases used were research grade, although there was a degree of variation in purity depending on the gas. Table 7.2 lists the gases used along with their corresponding purities[66].

Gas	Purity (%)
Argon	99.9995
Hydrogen	99.9995
Nitrogen	99.9995
Methane	99.995
Carbon Monoxide	99.97
Carbon Dioxide	99.999
Helium	99.9995

Table 7.2: Reagent Gas Purities[66]

7.3.3 Mass Calibration

During this investigation no mass drift was observed for the mass calibration and so mass calibration was not performed. However, mass calibration was performed by Newman[12] shortly before this work began. Mass calibration was performed operating the FFGD source using a cathode produced by twisting together a number of lengths of wire of different metals (Al, Ti, Cu, Ni, Cr, Ag, Sn, Ta, W, and Au). The ion signals corresponding to these metals, along with those related to the plasma gas (e.g. Ar^+), were used by the mass calibration programme to calculate the relationship between the true mass scale and the applied quadrupole fields. Frequent calibration (at least every 3-6 months, occasionally less) would be required when higher sensitivity is required as a small positive or negative shift in the mass corresponding to the detection maximum would reduce the observed peak intensity for a given mass.

7.3.4 Mass Spectrometer Maintenance

The rotary pump oil was changed every 12 months. The extraction lens was cleaned approximately every 6 months. The FFGD source was generally cleaned every 4-6 weeks. The long section of silica capillary in the inlet system was replaced once due to build up of organic material within the column. The shorter section of capillary was replaced several times in attempts to increase the gas split ratio.

7.3.5 Cathode Replacement

In order to remove effects due to cathode wear and the corresponding decrease in discharge current observed the cathode pin required regular replacement. When operating the source at room temperature the cathode was replaced at the start of each day and the discharge run for 45 minutes before any experiments were carried out to allow time for discharge stabilisation. Cathode replacement was required far less often using a heated discharge source (473 K for organic vapour addition; see chapter 8) as the discharge current and therefore sputtering rate were decreased. Due to this reduction in cathode erosion, and the disadvantages of repeated heating and cooling of the source required to allow maintenance to the source, cathode replacement was performed once a week. The addition of organic vapours is discussed in chapter 8.

7.3.2 Error Estimates

For figures 7.7, 7.9, 7.11, 7.13, 7.16, 7.19 the key feature of these results is how the measured intensities for the most abundant ions vary with the applied ion exit bias and how these variations in intensities are rationalised by the Rydberg gas model described in chapters 2 and 4. Although the general patterns remain the same, ion intensities have a reproducibility of ±40% (when tuning for the same ion mass) and occur within a range of $V_c \pm 10$ V. Minor fluctuations are often not reproducible between runs, unless stated, and no attempt has been made to rationalise them. A typical run to run reproducibility for a single ion is given below.

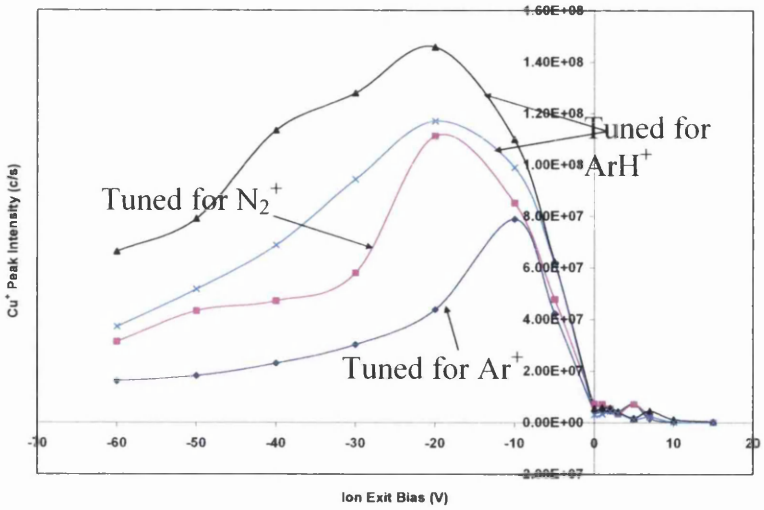

Run to run reproducibility of ion peak intensities (V_d = 700 V, P = 1 Torr, τ = 2.1 ms, 0.5% N_2). This example is relevant to figure 7.11.

For figures 7.8, 7.10, 7.12, 7.14, 7.15, 7.17, 7.18 the key feature of these results is how the measured intensities for the most abundant ions vary with the amount of secondary gas added. The reproducibility of the ion intensities is ±40%. The ion intensities are influenced greatly by small changes to the source conditions, especially the time since the ion exit cone was last cleaned. Extensive use of the source without cleaning lowers the measured ion signals significantly. Minor fluctuations in ion intensity are not reproducible, unless stated, and no attempt has been made to rationalise them.

7.4 Results and Discussion

7.4.1 Effect of Varying Ion Exit Bias with No Secondary Gas

This has previously been performed on this[4,12] and the high accelerating voltage (first generation) instruments[3,5]. Experiments on the high voltage instrument were run at significantly higher plasma residence time than those in this investigation (minimum of 4.3 ms compared with 2.1 ms) and therefore results differ from those taken previously on the low accelerating voltage (second generation) instrument. During investigations using the high voltage instrument each ion intensity was optimised individually for the applied V_c. Tuning for each individual ion was not performed in this investigation or those performed by Williams[4] or Newman[12], and this might influence the results obtained. One further significant factor is the

magnitude of the acceleration field outside the discharge cell of the high voltage instrument. Due to the strong electric field applied, field ionisation of excited state species emanating from the ion exit orifice is more probable. The electric field in the low voltage instrument is much smaller and therefore it had been thought previously that perhaps only the highest excited state species could be ionised efficiently.

Despite using very similar discharge conditions and performing the experiment in the same manner, results obtained by Mortimer[3] and Mitchell[5] on application of a negative ion exit bias differ. In fact, results obtained by Mitchell[5] when τ was 4.5 ms were similar to those taken by Mortimer[3] when τ was 6.3 ms. It is under these conditions that the results are most comparable with those observed by Williams[4] and Newman[12]. In each instance the Ar^+ peak intensity increased with increasing negative V_c ($V_c < 100$ V). However, the relative abundance of the argon ion was far greater in results taken on the high voltage instrument. This is probably due to the higher degree of field ionisation possible on that instrument. As argon was the most abundant species within the plasma the argon Rydberg atoms would be most affected by field ionisation. It has been observed on both instruments[4,5,12] that the argon ion intensity also has an increase in detection when V_c is close to 0 V (slightly negative or slightly positive). A similar effect was also observed for the argon dimer ion. The mechanisms for formation of these ions are discussed in chapter 2.

Both Mitchell[5] and Newman[12] have reported the detection of positive ions on application of a positive ion exit bias. Since positive ions would be repelled by a positive extraction bias, ion formation must occur within or beyond the ion exit orifice. Newman[12] reports positive ion detection up to $V_c \sim +10$ V, above which all ion signals were quenched. However, Mitchell[5] reported that, when using the high voltage instrument, discrete ranges of positive ion exit biases allowed detection of positive ions at high intensity. Figure 7.6 illustrates one such result. This is discussed further in chapter 8.

The Cu^+ ion intensity reached a maximum between $V_c = -20$ and -40 V, declining at higher and lower negative biases on both the high and low voltage instruments. Using the high voltage instrument[3,5] the ArH^+ signal increased with increasing negative V_c until a bias of > -80 V was applied, above which the signal began to drop. This differs from results observed on the low voltage instrument[4], for which the maximum ArH^+ peak intensity was observed when V_c was ~ -35 V. The detection of water related ions (H_2O^+ and H_3O^+) was found to be optimised at low values of V_c,

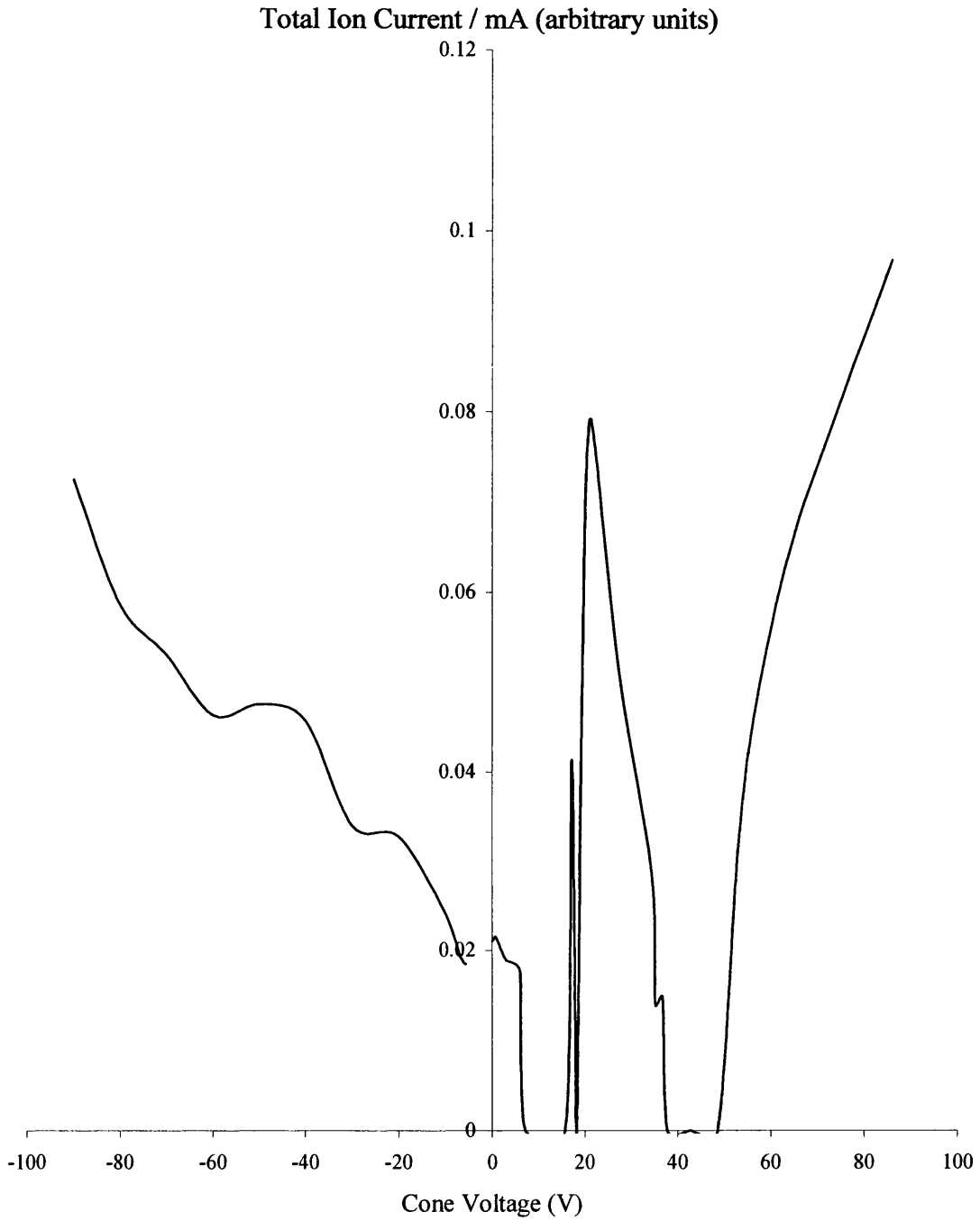

Figure 7.6: Plot showing that the total ion currents measured when positive and negative cone voltages are applied can be equivalent depending on the value of V_c (taken from reference 5)

F = 300 sccm, P = 1.6 Torr, τ = ~ 4.5 ms

from -5 V[3] to -20 V[4,12]. The presence of trace water has a significant influence on the magnitudes of the peak intensities, and variations in the detail may often be caused by this.

7.4.1.1 Results

The results obtained in this investigation agree well with the results reported by Newman[12] on the same instrument. Figures 7.7a and b illustrate the variation of detected ion signals from the discharge gas and its impurities as applied ion exit bias was varied. The discharge voltage, source pressure and argon residence time were kept constant throughout the work in this chapter (see section7.3), although variation in the magnitude of the discharge current occurred due to cathode wear, and over the time between anode cleaning. The discharge current was monitored and recorded throughout the investigation.

Figure 7.7a illustrates the variation of the major ion peaks. One might expect in a free ion electron medium, the magnitude of the ion peak intensities to increase with increasing negative ion exit bias as positively charged ions would become attracted more strongly to the ion exit, with no cation detection on application of a positive ion exit bias. The Ar^+ peak intensity initially appeared to follow this trend as it decreased almost linearly with decreasing V_c between -60 and -5 V. However, when $V_c = 0$ V the ion intensity observed was greater than that observed when $V_c = -40$ V and when $V_c = +1$ V the intensity was approximately equal to that when $V_c = -50$ V.

It has previously been proposed that the ions observed when $V_c = 0$ V or a small positive value the ions are not formed in the bulk plasma but within or beyond the ion exit orifice[3,4,5,9,12]. This argument is supported by a significant change in the ion optic tuning (table 7.1) for detection of ions on application of a positive or zero ion exit bias. Ions extracted from the source using a negative V_c would be expected to have a higher kinetic energy than those field-ionised outside the source. The degree of ion formation would also be expected to increase with a higher voltage applied to the cylindrical extraction lens (figure 7.5). Typical ion optic tuning conditions are illustrated in table 7.1. Thus, the voltage applied to the extraction lens for optimised ion detection on application of a positive or zero V_c was significantly higher (up to ~ 600 V) than that when V_c was -20 V. The applied pole bias voltage is directly related

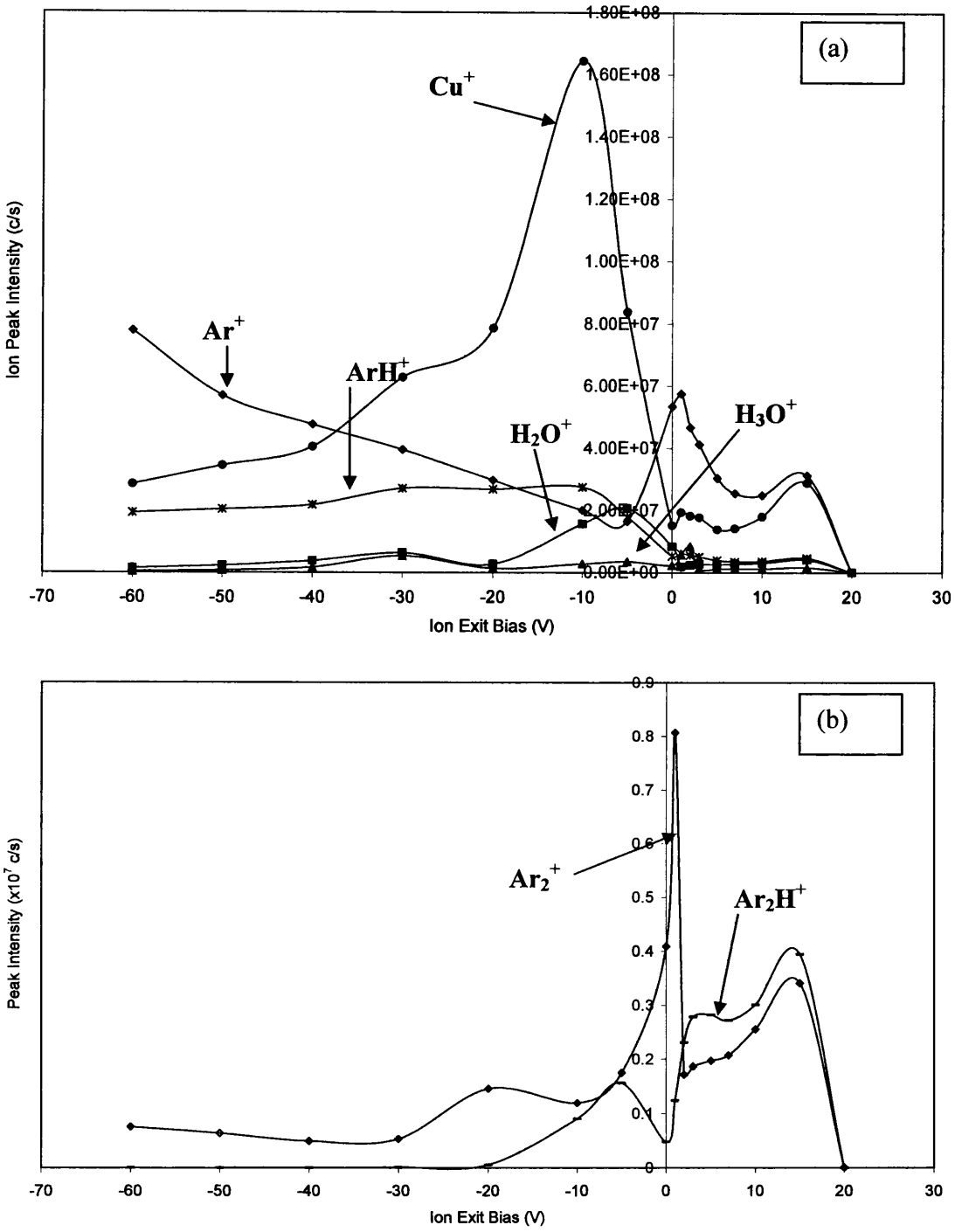

Figure 7.7: Variation of (a) major and (b) minor ion peak intensities from copper/argon glow discharge with ion exit bias (V_d = 700 V, I_d = 2.9 mA, P = 1 Torr, F_{Ar} = 400 sccm, τ = 2.1 ms, tuned for ArH^+)

to the kinetic energy of the ions being focussed. As expected, the ion kinetic energy was highly dependent on the ion exit bias.

Figure 7.7b illustrates the variation of the ion intensities of some less abundant ions, but nevertheless of some analytical interest. Both the argon dimer and dimer hydride ions were observed to have a low intensity when a negative V_c was applied, and their maxima were observed at V_c = +1 V and +3 V respectively. This was also observed by Newman[12] and illustrates the ability of the technique to form and detect molecular ions on application of a positive or low negative V_c.

7.4.1.2 Conventional Model

It is clear that extraction of ions from the FAG plasma is not solely responsible for the ions observed. The most conclusive evidence for this is the detection of positive ions on application of a positive, repulsive, ion exit bias. It was suggested above that if ions were extracted from within the cell, ion intensities would increase with increasing negative V_c, assuming the cone sheath to be collisionless. However, this was not the case. One other mechanism considered was electron impact ionisation within the ion exit orifice. On application of zero or a low positive ion exit bias the electron energies would be too low to induce ionisation of ground or metastable state species. Also, if EI was responsible for the ionisation observed then one would expect the Ar^+ ion to be significantly higher than the other ion signals since the plasma is mostly composed of Ar gas. Indeed, in chapters 4 and 6 we have outlined and can predict the conditions under which electron impact ionisation can be observed. Therefore, EI is not thought to be important in formation of the ions detected. No significant mass discrimination effects were observed.

7.4.1.3 Excited State Model

It has already been stated that ion extraction from the main plasma body is not possible on application of a positive (repulsive) ion exit bias, and therefore ion formation occurs via field ionisation of Rydberg state species outside the GD cell except under the conditions when EI ionisation can occur. Since the energies of Rydberg state species are close to the ionisation potential of the atom it is possible to induce ionisation by applying a small electric field. Though the threshold required is

low, the efficiency will depend on the strength of the field above the threshold, although we do not have a quantitative model for this. Thus, application of a high extraction lens bias was required to optimise ion detection on application of a positive or zero ion exit bias, as illustrated in table 7.1.

The applied ion exit field can influence Rydberg state species in two important ways. The first is field ionisation, leading to formation of free ions and electrons. On application of a positive bias the ions formed would be repelled towards the cathode. However, a second effect is to polarise the Rydberg atom by the Stark effect (equation 7.5). A proportion of the Rydberg atoms, e.g. $Ar^{R'}$ or $Cu^{R'}$, would therefore be more easily ionised in the accelerating field.

$$Ar^{R},\ Cu^{R} \rightarrow\ Ar^{R'},Cu^{R'} \qquad \textit{(equation 7.5)}$$

The observed ion intensities must be determined by these two processes. At low positive values of V_c the rate of excitation was greater than the rate of ionisation within the cell, and therefore all ion intensities increased. However, on application of a higher potential the rate of field ionisation became greater than the rate of excitation and therefore the ion intensity decreased because the ions formed inside the cell are turned back. There is a balance between the rates of ionisation inside and outside the source, and the efficiency of collection of ions from inside and outside the source, which can be described in the form of equation 7.6. The ion current detected is a function of;

a) concentration of Rydberg species at the ion exit, $[R]^{Exit}$, and the efficiency of their ionisation $\left(k_{ion}^{Exit}\right)$ and collection $\left(k_{tr}^{Exit}\right)$
b) concentration of Rydberg species inside the cell, $[R]^{Cell}$,and the efficiency of transmission $\left(k_{tr}^{Cell}\right)$ and subsequent collection $\left(k_{col}^{Cell}\right)$
c) concentration of ions inside the cell, [ion] and the efficiency of transmission $\left(k_{tr}^{Cell}\right)$

$$I_{signal} = [R]^{Exit}.k_{ion}^{Exit}.k_{tr}^{Exit} + [R]^{Cell}.k_{tr}^{Cell}.k_{col}^{Cell} + [Ion].k_{tr}^{Cell} \qquad \textit{equation 7.6}$$

All will be affected by the magnitude of V_c. When V_c is +20 V we now know from chapter 5 that the rate of field ionisation within the cell is saturated and hence no such ionisation can occur outside the source. The formation of the argon dimer ion is believed to occur via coupling of an argon Rydberg atom and a ground state argon atom (section 2.6), and this is chiefly responsible for the ionisation of Rydberg atoms when the Rydberg gas breaks down in the neutral plume, therefore we expect to see a higher Ar_2^+ abundance. The dimer does not easily survive a high negative sheath field, and therefore increased formation is observed particularly at low positive values of V_c due to the stability of the Ar Rydberg species.

On application of a negative V_c, extraction of ions from the GD cell and field ionisation of Rydberg states outside the source are both possible and therefore the two processes may "compete". Though not illustrated, this is reflected in the ion optic tuning conditions observed when V_c was -5 V. The tuning conditions were between those applied when V_c was -10 and 0 V. However, on application of more negative ion exit biases little adjustment of the ion optic tuning was required at each voltage to optimise ion detection. Similarly, very little retuning was required over the range of positive ion exit biases studied.

On application of a more negative ion exit bias the detected ions are formed and extracted from inside the GD cell, and hence have higher kinetic energies. The processes which may determine the ion intensities observed are illustrated in section 7.1.1. The magnitude of V_c influences a number of processes as follows:

1) The rate of field ionisation of Rydberg atoms in the ion exit field should increase with increasing V_c.
2) Excitation of Rydberg state species to red and blue states may occur as illustrated in equation 7.5.
3) The kinetic energy of cations is increased due to the application of an accelerating electric field.
4) Charge transfer may be induced as the ions are accelerated towards the ion exit (equation 7.7). If this were to occur in or beyond the ion exit orifice the ion kinetic energies would be low.

$$Ar^+_{\rightarrow} + Ar \rightarrow Ar_{\rightarrow} + Ar^+ \qquad \textit{(equation 7.7)}$$

5) When Rydberg species are field ionised close to the ion exit cone surface an electron is released. Acceleration of this free electron across the sheath towards the anode could lead to electron bombardment of Rydberg state species. Since Rydberg species do not require much additional energy to ionise electron impact ionisation may occur (equation 7.8).

$$e^-_{\rightarrow} + Ar^R \rightarrow Ar^+ + 2e^- \qquad \textit{(equation 7.8)}$$

For high negative ion exit biases the rate of ionisation of Rydberg species is likely to be greater than the rate of excitation and therefore processes 1) and 3) are very important. The decrease in the detected ion signals for the majority of the ions at high negative V_c is therefore probably due to the lower efficiency of transmission of high kinetic energy ions through the analyser[67]. The Ar^+ signal was not affected in this manner as Ar^+ can undergo rapid charge transfer (equation 7.7) within the cone sheath[80], therefore leading to a reduction in the ion kinetic energy. As the kinetic energy of the argon ion is lower its transmission coefficient will be different. This was reflected in the Pole bias voltage required to transmit the ions to the detector, which is different for Cu^+. One example of this, when V_c was -20 V, is illustrated in table 7.1.

7.4.2 Addition of Hydrogen to the Flowing Afterglow (FAG) Plasma

The addition of hydrogen to the FFGD plasma was studied previously[1-12], with particular attention paid to the effect of the hydrogen flow rate on quenching of excited state neutral species within the FAG plasma. In each investigation the addition of a small amount of hydrogen (a fraction of a percent of the total flow) was observed to rapidly reduce the Ar^+ signal, whilst increasing the intensities of the Cu^+ and ArH^+ peaks. The latter quickly disappeared on further H_2 addition. It was concluded that the reduction in the argon ion intensity was due to quenching of the precursor to Ar^+ formation, argon Rydberg states. Equation 7.9 illustrates the quenching process:

$$Ar^R + H_2 \rightarrow Ar^* + H_2^{*'} \qquad \textit{(equation 7.9)}$$

where * and *' are unspecified excited states. One possible product of this reaction is, ultimately, the argon metastable state (Ar^m), which is believed to be involved in the formation of copper ions and other Rydberg states. This is discussed in more detail in chapter 2.

On higher levels of H_2 addition the copper ion intensity was found to vary very little, whereas all the other major ion signals (ArH^+, H_2O^+, etc) were rapidly reduced. This implies that the precursors for formation of these ions are highly excited (higher than metastable) states of Ar which are efficiently quenched on the addition of hydrogen, except when carrying a high current through the plasma (see chapter 6). Without addition of secondary gas the formation of argon hydride ion is believed to occur via reactions between argon Rydberg states and water vapour. On addition of hydrogen, the argon hydride ion intensity rose sharply. Previous studies have shown that this cannot be due to ion-molecule reactions[2,11]. It is possible that the formation of ArH^+ was increased by trace levels of water present in the hydrogen reagent gas. However, it is very likely that formation of argon hydride also occurs via interaction of argon Rydberg state species with hydrogen gas (equation 7.10). As no change to the plasma potentials occurred it was proposed that the product of this reaction was ArH^R.

$$Ar^R + H_2 \rightarrow ArH^R + H \qquad \textit{(equation 7.10)}$$

This supports the conclusion that the argon ion signal was quenched due to removal of the argon Rydberg state, the precursor to argon ion formation.

Mitchell[5] reported the influence of the ion exit bias on the major ion intensities for a set argon residence time on application of both positive and negative ion exit biases using the high voltage instrument. The variation patterns for the Cu^+ and ArH^+ peak intensities were found to differ on addition of hydrogen, but the Ar^+ variation occurred as with the pure gas.

In contrast to the results presented by Mitchell[5], Williams[4] observed that, with the exception of Ar_2^+, the variation of all major discharge related ion intensities with negative V_c was very similar with and without addition of hydrogen gas. This difference may be due to the high accelerating field within the high-voltage instrument used by Mitchell[5]. Neither author studied the variation of the major ion intensities as a function of hydrogen flow for different ion exit biases. Newman[12]

recorded the variation of different cathode ion intensities with hydrogen flow when V_c was 0 V and -20 V for low percentage addition of hydrogen. The exact range of gas addition is not known due to the problems with the split flow technique indicated in section 7.2.3. However, results for the other major plasma related ions were not presented.

This investigation follows on from the work performed by Newman[12] and Williams[4], studying the influence of the hydrogen gas flow rate and V_c individually for low reagent gas flow rates using the same low voltage instrument.

7.4.2.1 Effect of Varying Hydrogen Flow Rate at Different Fixed Ion Exit Bias Values

A number of the ion signals were quenched for less than 1% addition of hydrogen to the FAG plasma, therefore studies of the ion intensities below this level provide the most information about the plasma chemistry in the GD cell. The results shown in this section are very similar to the results of Williams[4] and Newman[12], using the low voltage instrument. Figure 7.8 illustrates the variation of the major ion species as a function of hydrogen when V_c was (a) -10 V, (b) 0 V and (c) +2 V. The experiment was also repeated at V_c = -20 V, but the results were omitted due to the similarity to those when V_c was -10 V. It can be observed that despite the differences in absolute ion intensity induced by changing V_c the variation of the major ion intensities was very similar in each case. This indicates that the magnitude of V_c has no effect on the chemistry occurring within the flowing plasma.

In figure 7.8a the argon ion peak intensity has been omitted and in figures 7.8b and c the copper ion peak has been omitted due to their low intensity. It is clear from figure 7.8a that the formation of Cu^+ and ArH^+ cannot be accounted for if the plasma was an ion-electron medium, because there was no corresponding loss of ion intensity to balance the increases observed. The ions therefore emerge from excited state neutral reactions. However, the formation of H_3O^+ appears to correspond to loss of H_2O^+. This may be due to direct reaction between H_2O^R and the reagent gas as shown in equation 7.11. The same pattern was also observed when V_c was 0 V and +2 V (figures 7.8b and c respectively), and this may also be accounted for by the excited state reaction.

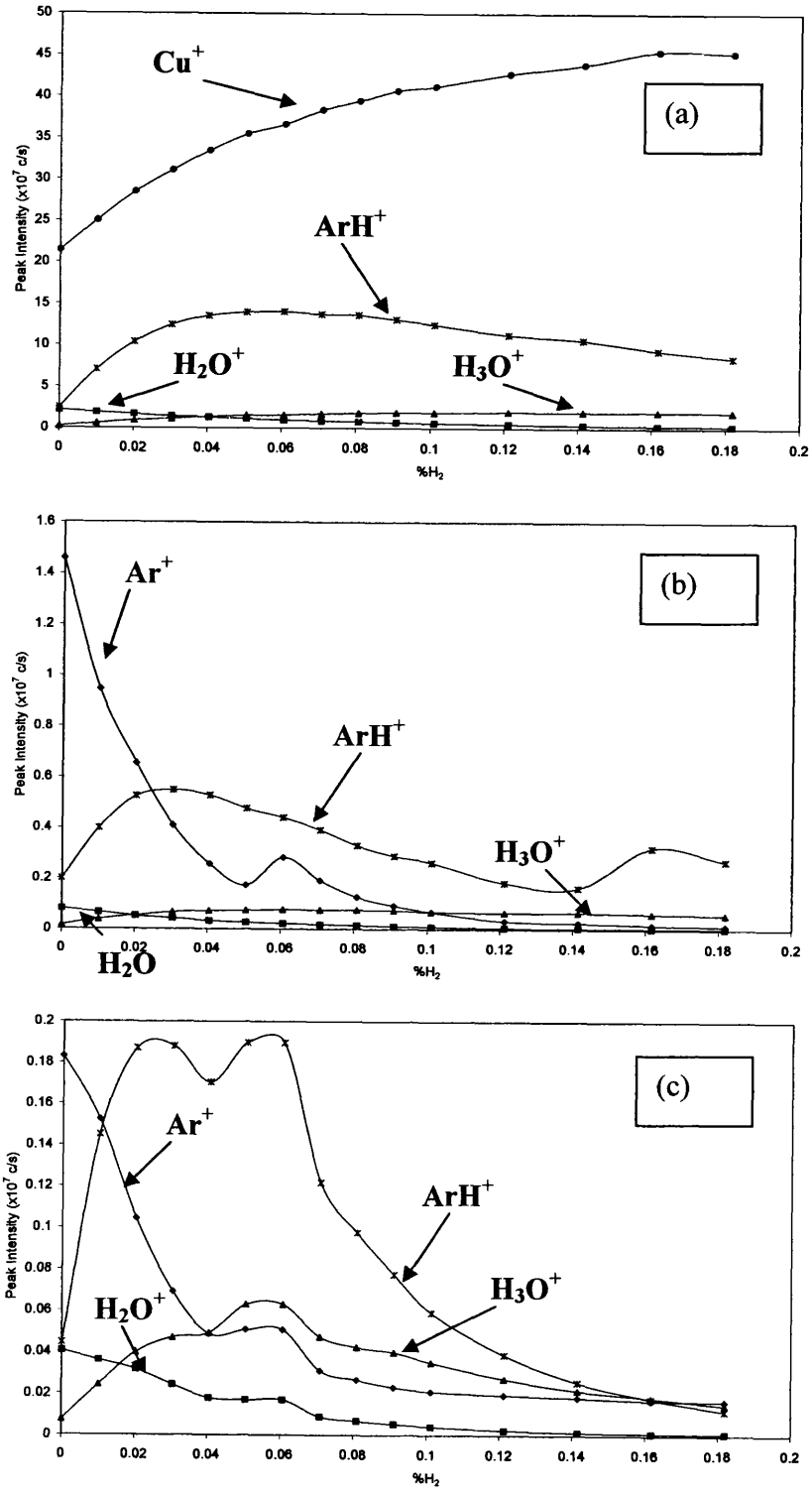

Figure 7.8: Variation of major ion peak intensities with percentage addition of hydrogen when V_c is (a) -10 V, (b) 0 V and (c) +2 V
(V_d = 700 V, I_d = 2.5 mA, P = 1 Torr, F_{Ar} = 400 sccm, τ = 2.1 ms, tuned for Cu^+)

$$H_2O^R + H_2 \rightarrow H_3O^R + H \qquad \textit{(equation 7.11)}$$

It is now thought that all of the ions detected on application of a small positive ion exit bias were formed by field ionisation of Rydberg state species outside the glow discharge source. When V_c was negative the ion exit field allowed extraction of ions from the flowing plasma and therefore the ion optic tuning conditions for optimised ion transmission were significantly different. However, when V_c was 0 V to -5 V the tuning conditions were between the two extremes and therefore it is quite likely that ions detected were formed both inside and outside the GD cell. This is also true on addition of hydrogen. The tuning conditions were very similar to those observed without addition of secondary gas. The variation of the ion peak intensities as a function of hydrogen addition followed the same patterns at V_c = -20, -10, 0 and +2 V. This is not surprising since the reaction is with the Rydberg gas before it gets to the cone sheath.

7.4.2.2 Effect of Varying Ion Exit Bias for a Fixed Hydrogen Flow Rate

The variation of the major ion peak intensities as a function of ion exit bias at a fixed hydrogen flow rate has already been studied within this group[3,5]. The results obtained in this investigation (figure 7.9) were very similar to those without addition of a secondary gas (figure 7.7) and those observed by Williams[4] for negative ion exit biases using the same low voltage instrument. The variation of the Cu^+ and ArH^+ intensities with V_c matched very closely with previous results[4]. The variation of the ArH^+ intensity with V_c is known to differ using the high voltage instrument (section 7.4.1). Mitchell[5] observed that, contrary to results presented here, the variation of the ArH^+ peak intensity with V_c was influenced by the addition of H_2. He observed that with H_2 present the argon hydride peak intensity increased until V_c was ~ -30 V, before remaining approximately constant at higher biases. However, without addition of H_2 the ArH^+ intensity increased with increasing V_c over the range studied. The Ar^+ intensity increased with increasing negative V_c in each investigation. The results for the minor ion formation have been omitted since there was no significant difference between their variations with V_c with and without addition of hydrogen.

On application of a V_c < -20 V Williams[4] reported complete loss of all ion signals. This may be due to the ion optic tuning conditions, the higher source pressure

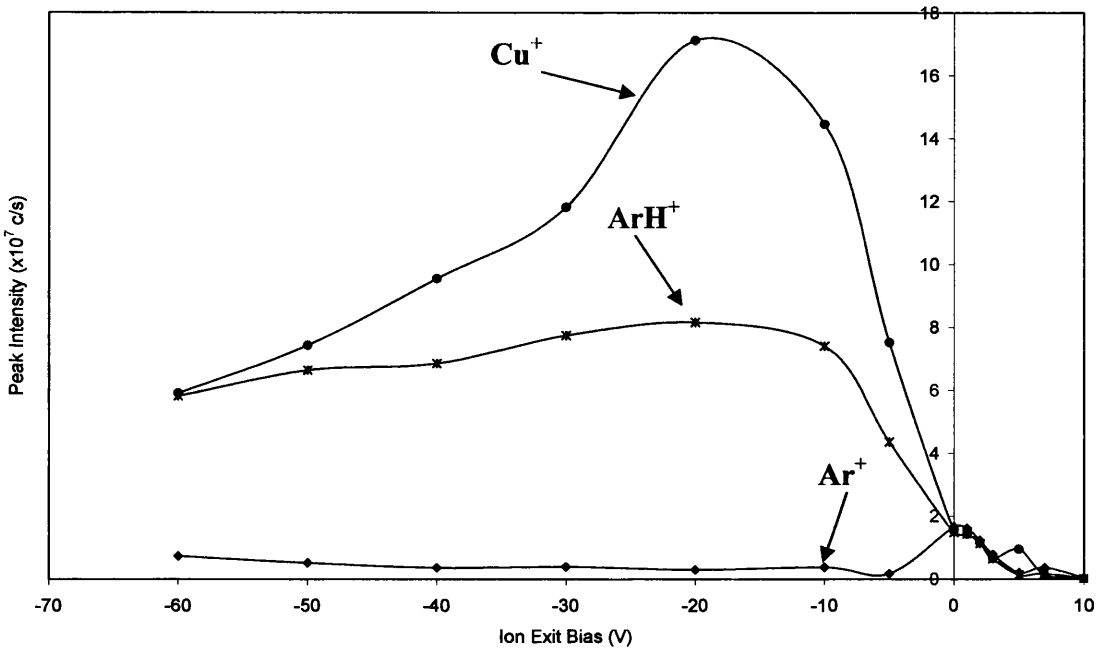

Figure 7.9: Variation of major ion peak intensities with ion exit bias for addition of 0.1% hydrogen
(V_d = 700 V, I_d = 2.7 mA, P = 1 Torr, F_{Ar} = 400 sccm, τ = 2.1 ms, tuned for ArH^+)

and lower discharge voltage used in the previous investigation. The variation of the major ion signals as a function of positive V_c on addition of hydrogen has been previously studied by Mitchell[5] using the high voltage instrument. Within the V_c range of this investigation the Cu^+ peak intensity was observed to initially increase on application of a positive bias before the loss of the signal above $V_c \sim +5$ V. In contrast, the Ar^+ and ArH^+ peak intensities decreased with increasing positive V_c until the signal was lost at $V_c \sim +5$ to +7 V. Similar results were observed in this investigation, but the Cu^+, Ar^+ and ArH^+ peak intensities all decreased with increasing positive V_c before the signals were lost at $V_c \sim +10$ V.

The tuning conditions for both Cu^+ and ArH^+ (not shown) were very similar to those without addition of secondary gas (table 7.1). On application of a high negative V_c ions were extracted from the source, and therefore had an initial kinetic energy due to acceleration across the sheath field. However, on application of zero or a small positive V_c application of a large potential to the extraction lens was required. This is thought to aid ionisation of Rydberg state species. The pole bias voltage indicated that these ions had very low initial kinetic energy, as expected. The addition of H_2 changes the relative ion intensities, but does not influence the processes responsible for ion formation (e.g. field ionisation in the cone sheath or extraction lens region).

7.4.3 Addition of Nitrogen to the FAG Plasma

This study extends work performed by Miller[1] and Mortimer[3] using the high voltage FFGD instrument. These previous investigations focussed on the variation of the observed ion intensities as a function of the nitrogen flow rate. Due to a flaw in the original source[1,3] design for the high voltage instrument the secondary gas was actually added downstream of the ion exit orifice position and therefore back-diffusion of the gas was required to allow the reaction to be monitored. In this investigation the gas was added 20 mm upstream of the ion exit orifice and therefore a reaction time of ~ 1.2 ms was allowed. This means that significantly less gas was required to induce changes in the mass spectra.

7.4.3.1 Effect of Varying Nitrogen Flow Rate for a fixed Ion Exit Bias

The variation of the discharge gas and cathode ion intensities as a function of nitrogen addition was very similar in two previous studies[1,3]. In each study the copper ion intensity remained approximately constant. The principal reaction believed to be responsible for the formation of Cu^+ (and the intermediate Rydberg state species) is Penning ionisation via energy transfer from an argon atom excited to a metastable state (see section 2.5). The fact that the Cu^+ peak intensity varied very little indicates that the argon metastable and other excited precursor state populations were approximately constant. In this investigation the variation of the Cu^+ intensity appears to be dependent on the applied ion exit bias (figure 7.10). When V_c was 0 V the Cu^+ peak intensity was approximately constant, whereas when V_c was -10 V the intensity dropped with increasing nitrogen addition, and when V_c was +2 V the intensity increased by approximately 50% on ~ 1.1% nitrogen addition.

When V_c was -10 and 0 V (figures 7.10a and b), the Ar^+ intensity was approximately constant up to > 1% N_2 addition. This indicates that there was no significant change to the Ar^R density in the plasma. The quenching efficiency of nitrogen would be expected to be low since the cross section for energy transfer to a small, non-polar molecule is normally low[38]. An interesting effect is that when V_c was +2 V (figure 7.10c) the Ar^+ peak intensity initially increased on addition of nitrogen gas (31% increase on addition of 1.16% N_2). This contrasts with the addition of hydrogen (section 7.4.2) when the Ar^+ signal decreased sharply. The latter is thought to be caused by quenching of argon Rydberg state species in collisions with hydrogen molecules. This being the case, an increase in the Ar^+ peak intensity implies either an increase in the argon Rydberg state population or an increase in the ionisation efficiency of the existing Rydberg population. Under low positive V_c conditions ion formation can occur only by expansion of the gas and field ionisation of Rydberg state species in the expanding gas outside of the GD cell (see chapter 4). Mortimer[3] determined that the quenching efficiency of nitrogen was one of the lowest in the investigation, and similar to that of helium and argon. However, nitrogen will aid ionisation of argon Rydberg states. The principle mechanism by which ionisation of Rydberg atoms can occur is by associative ionisation[38] (equation 7.12). This is improved by adding N_2 (equation 7.13)[38].

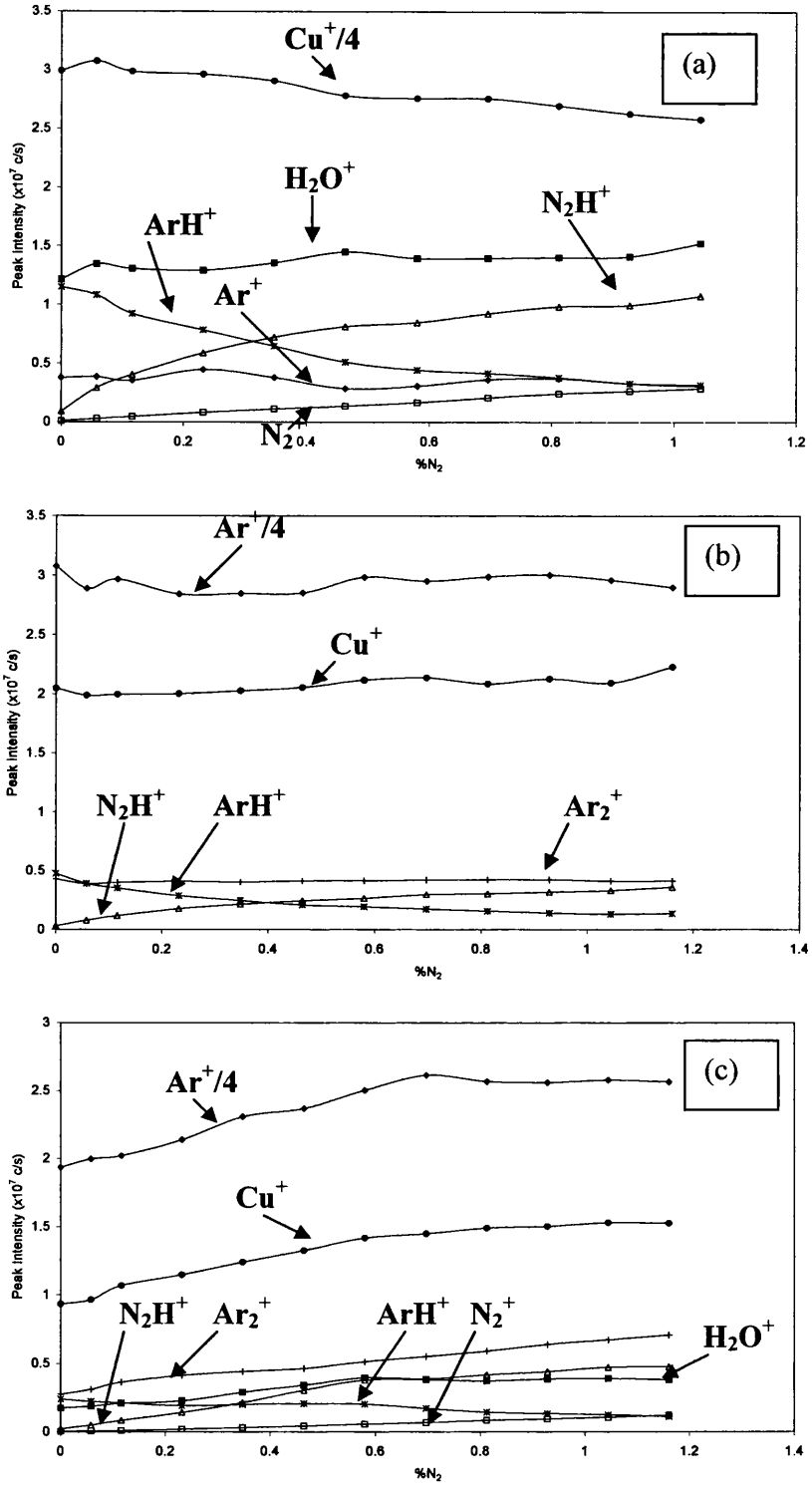

Figure 7.10: Variation of major ion peak intensities with percentage addition of nitrogen when V_c = (a) -10 V, (b) 0 V and (c) +2 V
(V_d = 700 V, I_d = 1.6 mA, P = 1 Torr, F_{Ar} = 400 sccm, τ = 2.1 ms, tuned for Cu^+)

$$Ar^R + Ar \leftrightarrow Ar_2^R \rightarrow Ar^+ + Ar + e^- \quad \textit{(equation 7.12)}$$

$$Ar^R + N_2 \leftrightarrow ArN_2^R \rightarrow Ar^+ + N_2' + e^- \quad \textit{(equation 7.13)}$$

One further mechanism is rotational energy transfer[38]:

$$Ar^R_n + N_2(J) \rightarrow Ar^+ + N_2(J\text{-}1) + e^- \quad \textit{(equation 7.14)}$$

This is efficient where rotational energies are a close match for Δn changes in Rydberg atoms.

In the absence of efficient quenching, the net effect is to cause an increase in Ar^+ formation in the expanding plasma as it leaves the cell. The same result is not observed when V_c is negative because ionisation occurs inside the cell. Once ionised it is possible that Ar^+ can react by charge transfer to produce species such as N_2^+. Very little N_2^+ was formed because the I-M reaction rate is very slow[78].

The reaction rates are presumably also influenced by the presence of a field, which affects the energies and stabilities of the different l and m levels of the Rydberg atom states[38]. For example, this is observed to be a strong effect when the plasma carries a large current[5]. The quenching efficiency of H_2 is very low towards what are thought to be the l = 1 Rydberg states, which are very likely the current carriers (see chapter 4). Since the ion exit field does not extend very far into the plasma[10], any such effects can only affect reactions occurring close to the ion exit cone.

In each of the investigations the ArH^+ peak intensity decreased with increasing nitrogen addition. ArH^+ is formed due to the trace levels of water vapour present in the gases and source materials. Therefore, greater levels of secondary gas addition (carrying trace water impurity) might be expected to increase the formation of ArH^+. The variation of the argon hydride peak intensity with nitrogen addition was also not influenced by the magnitude of V_c.

The most probable reaction leading to a reduction in ArH^+ is the direct reaction of either the ArH^+ ion or ArH^R with nitrogen. Since the increase in N_2H^+ ion intensity corresponds to a similar decrease in the ArH^+ peak intensity proton transfer is possible (equation 7.15).

$$ArH^+ + N_2 \rightarrow Ar + N_2H^+ \quad \textit{(equation 7.15)}$$

However, for this to be true when V_c was +2 V, both formation of ArH^+ and subsequent proton transfer must occur outside the discharge cell. It is possible for N_2H^+ to capture an electron, leading to formation of a Rydberg state species (equation 7.16) which could undergo field ionisation outside the discharge cell.

$$N_2H^+ + e^- \leftrightarrow N_2H^R \qquad \textit{(equation 7.16)}$$

When V_c = +2 V the N_2H^+ appears to form in response to the increase in water content.

7.4.3.2 Effect of Varying Ion Exit Bias for a Fixed Nitrogen Flow Rate

Analysis of the variation of the major ion peak intensities with V_c for constant addition of nitrogen to the FAG plasma has not been performed previously. Figure 7.11 illustrates the variation of the major ion intensities with V_c on addition of 0.1% N_2. The experiment was repeated for 0.01% and 1% addition, and the profile was the same in each instance. It has already been argued that ion-molecule reactions cannot fully account for the observed variations in ion intensity due to the repulsive field on application of a positive V_c. On addition of nitrogen the major discharge related ion intensities varied with V_c in the same way observed in previous sections (figures 7.7 and 7.9).

It has been observed in work by Newman[12] (see also chapter 8) that the magnitude of V_c can be tuned to allow detection of fragment or parent molecular ions. Some evidence of this can be observed in figure 7.11. The maxima for detection of N_2^+ and N^+ were observed at V_c = -20 V and -60 V respectively. The low intensity of the N^+ ion even on application of a high negative ion exit bias is probably due to the high bond strength of the nitrogen molecule (9.8 eV[68]). Very little bond breakage would be expected even at high collision energies.

7.4.4 Addition of Carbon Monoxide to the FAG Plasma

The addition of CO to the FAG plasma of a fast flowing GD was an experiment performed by Mortimer using the high voltage instrument[3]. The variation of the major ion peak intensities was recorded as a function of CO addition at different

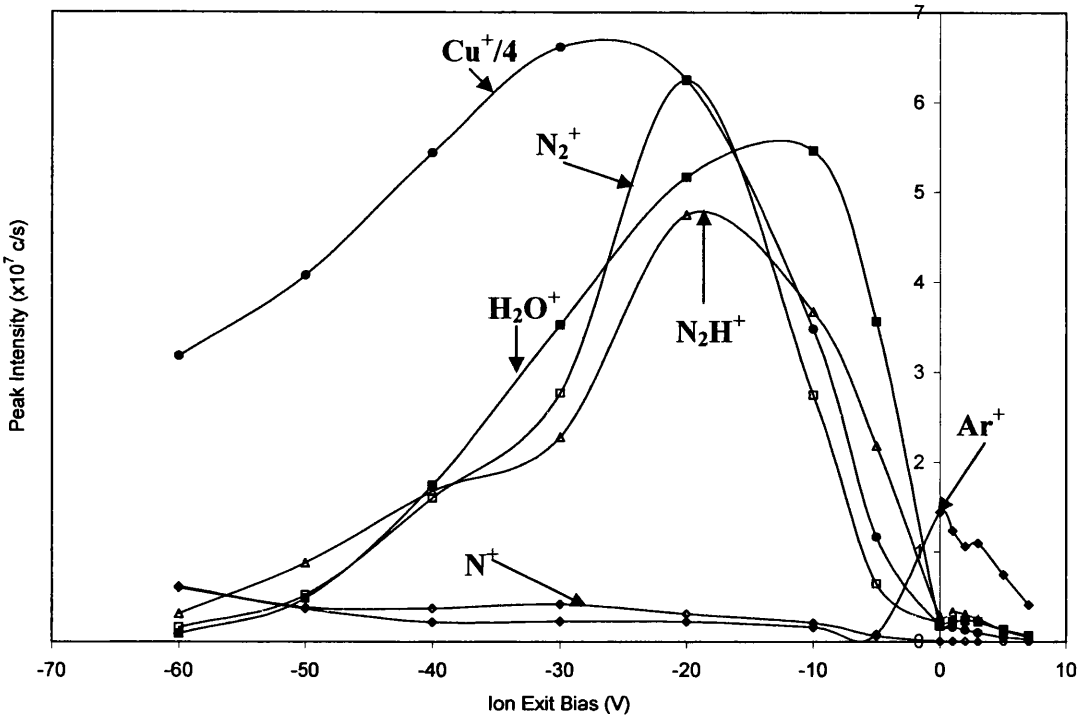

Figure 7.11: Variation of major ion peak intensities with ion exit bias for 0.1% addition of nitrogen
(V_d = 700 V, I_d = 1.6 mA, P = 1 Torr, F_{Ar} = 400 sccm, τ = 2.1 ms, tuned for Cu^+)

argon residence times. However, the effect of the ion exit bias on the ion signals has not been investigated. No studies have been conducted using the low voltage instruments.

7.4.4.1 Effect of Varying Carbon Monoxide Flow Rate for a Fixed Ion Exit Bias

Mortimer observed that the discharge related ion signals were all rapidly quenched on addition of CO, whilst the carbon monoxide related ion intensities (CO^+ and CHO^+) initially increased sharply, but decreased again on higher levels of addition. In this investigation very similar results were observed (figure 7.12). However, the intensity of the Cu^+ peak was initially observed to increase at low levels of CO addition before decreasing again at higher levels. The same patterns were observed when V_c was -20, -10, 0 and +2 V, indicating again that the magnitude of V_c does not influence the reactions occurring within the FAG plasma.

As previously discussed, the ion-electron model of the GD plasma cannot easily be applied to explain ion detection when V_c was positive, since ion transmission from the source is discouraged. Besides that, when V_c was -10 V large increases to the Cu^+, CO^+ and HCO^+ ion intensities were observed without similar decreases in other ion intensities. This once again demonstrates that ions are created in substantial quantities from highly excited neutral species, not from I-M reactions or EI ionisation (since the maximum electron energy allowed by acceleration across the ion exit sheath when V_c is -10 V is 10 eV, and is therefore insufficient to ionise CO by EI)[69].

The reduction in the Ar^+ and ArH^+ peak intensities can be rationalised as the quenching of Ar and ArH Rydberg state species (e.g. equation 7.17), leading to formation of CO^+ and CO^R. This is reflected in the sharp increase in the CO^+ peak intensity observed for low percentage addition of CO.

$$Ar^R + CO \rightarrow Ar + CO^+ + e^- \rightarrow CO^R \quad \textit{(equation 7.17)}$$

For very low addition of CO the Ar^+ peak intensity was initially approximately constant (see figure 7.12b). This is also observed in other FFGD systems and probably indicates release of Ar^+ ions in collisions of Ar^R with CO (equation 7.18) as well as quenching of Ar^R states. It is also likely that formation of lower energy argon states would occur, as represented in equation 7.19.

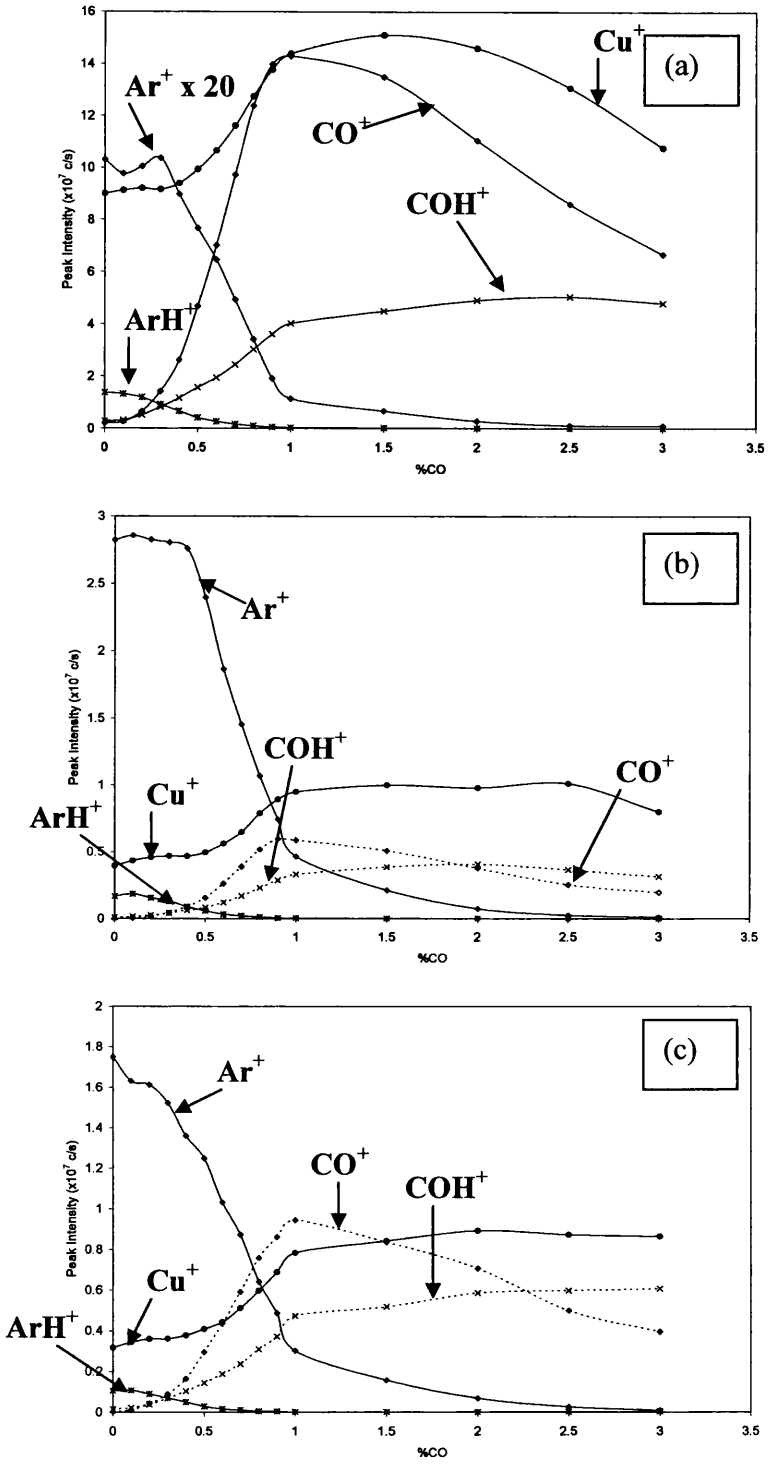

Figure 7.12: Variation of major ion peak intensities with percentage addition of carbon monoxide when V_c = (a) -10 V, (b) 0 V and (c) +2 V
(V_d = 700 V, I_d = 1.8 mA, P = 1 Torr, F_{Ar} = 400 sccm, τ = 2.1 ms, tuned for Cu^+)

$$Ar^R + CO \rightarrow Ar^+ + CO\ (J\text{-}1) + e^- \quad \textit{(equation 7.18)}^{38}$$

$$Ar^R + CO \rightarrow Ar^* + CO^* \quad \textit{(equation 7.19)}$$

The decrease in the Ar^+ intensity also coincides with an increase in Cu^+ detection, which suggests that the lower excited and metastable states responsible for Cu ionisation are also populated by the CO reaction (in a similar manner to H_2):

$$Ar^* + CO \rightarrow Ar^M + CO^* \quad \textit{(equation 7.20)}$$

The observed increase in CHO^+ peak intensity corresponds to a reduction in both the ArH^+ and H_2O^+ peak intensities. Each species is formed due to reactions with trace water (as described in the previous sections), and therefore addition of CO would reduce the formation of water related and hydride ions.

These results support previous results presented by Mortimer[3] indicating that CO quenches Rydberg states of argon much more effectively than nitrogen. As discussed in section 7.4.3.1, the interaction of nitrogen molecules with the Rydberg state electron in Ar^R is limited to close range interactions as nitrogen has no dipole[38]. Since CO has a natural dipole the cross section for collisions with the Rydberg electron are greater[38].

7.4.4.2 Effect of Varying Ion Exit Bias for a Fixed Carbon Monoxide Flow Rate

Figure 7.13 illustrates the effect of the ion exit bias on the ion intensities of the major ion species with ion exit bias on 0.1% addition of CO. The experiment was repeated on addition of 0.01% and 1% CO. As the variations in the major ion intensities observed were the same these results have been omitted. The variation of the major discharge related ion species with V_c was very similar to that observed without addition of secondary gas. However, no increase in the Ar^+ peak intensity was observed when V_c was 0 V or positive. This could be because the reaction with CO has removed those Ar Rydberg atoms which already respond under these conditions.

Optimised detection of the CO^+ and CHO^+ peak intensities was observed under similar conditions to that for Cu^+, i.e. when V_c was -10 to -20 V. As discussed

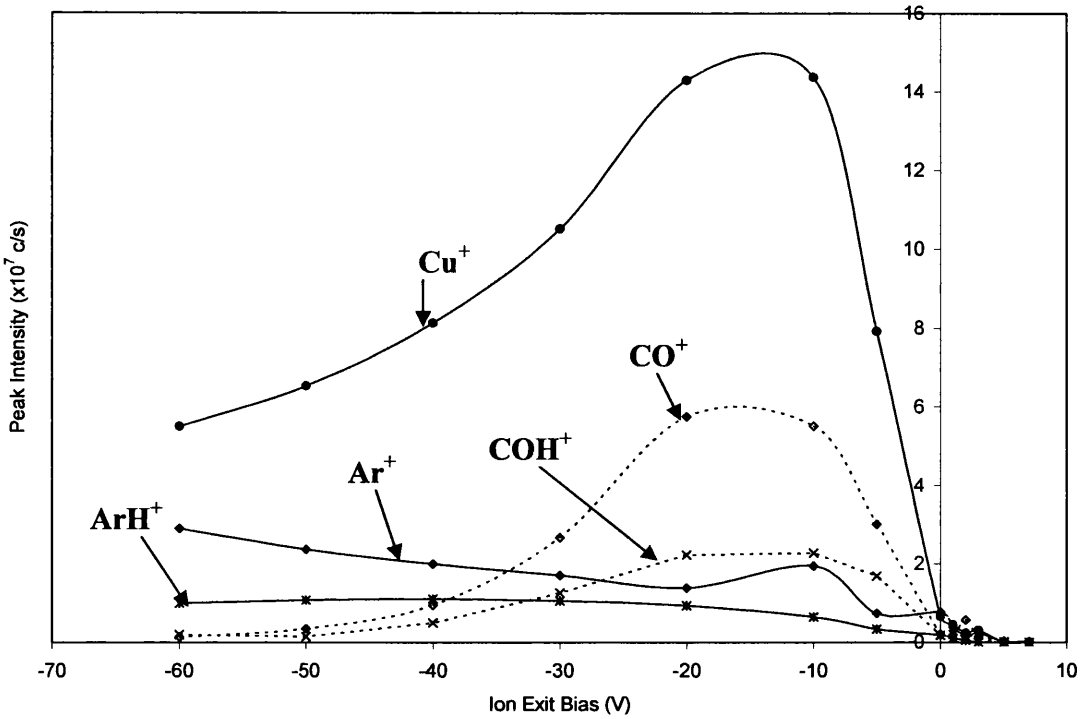

Figure 7.13: Variation of major ion peak intensities with ion exit bias for 0.1% addition of carbon monoxide
(V_d = 700 V, I_d = 2.5 mA, P = 1 Torr, F_{Ar} = 400 sccm, τ = 2.1 ms, tuned for Cu^+.)

previously, ion detection when V_c is negative is likely to be primarily due to ionisation, and subsequent extraction of ions from within the ion exit field. Thus, the higher the extraction bias the higher the ion kinetic energies. At high ion kinetic energies the ion beam is less efficiently focussed using quadrupole instruments[68] and the signal decreases.

7.4.5 Addition of Carbon Dioxide to the FAG Plasma

The addition of CO_2 to the FAG plasma of a fast flowing GD was an experiment performed by Mortimer using the high voltage instrument[3]. The variation of the major ion peak intensities was recorded as a function of CO_2 addition at different argon residence times. The effect of the ion exit bias on the ion signals was not investigated. No studies have been conducted using the low voltage instruments.

7.4.5.1 Effect of Varying Carbon Dioxide Flow Rate for a Fixed Ion Exit Bias

Results presented by Mortimer were similar to those presented for addition of hydrogen and carbon monoxide in the same study[3]. In each case the Ar^+ ion signal was rapidly reduced on addition of secondary gas. However, on addition of H_2 the ArH^+ peak intensity initially increased, as discussed previously (section 7.4.2.1). On addition of CO and CO_2 the ArH^+ peak intensity decreased rapidly with addition of the secondary gas. One other point of interest on addition of CO_2 is the increase in Cu^+ detection at low residence times for low gas flow rates. This suggests increased formation of argon excited state species involved in Cu^+ formation via quenching of Rydberg state species, as for the H_2 reaction.

Similar patterns for CO_2^+ and CO_2H^+ were observed to those for CO^+ and CHO^+, i.e. the peak intensities initially increased on addition of CO_2 but subsequently fell on addition of higher quantities. It appears that CO^+ and CO_2^+ were formed in the same manner, and the same applies for CHO^+ and CO_2H^+.

The patterns of behaviour measured in this study (figures 7.14 and 7.15) agree with the previous study by Mortimer[3]. When V_c was -10 V (figure 7.14) the increase in the Cu^+ and CO_2^+ intensities were both significantly higher than the loss in the Ar^+ and ArH^+ intensities over the same range, again evidence of neutral chemi-ionisation processes. When V_c was 0 V (figure 7.15a) the loss of the argon ion signals was

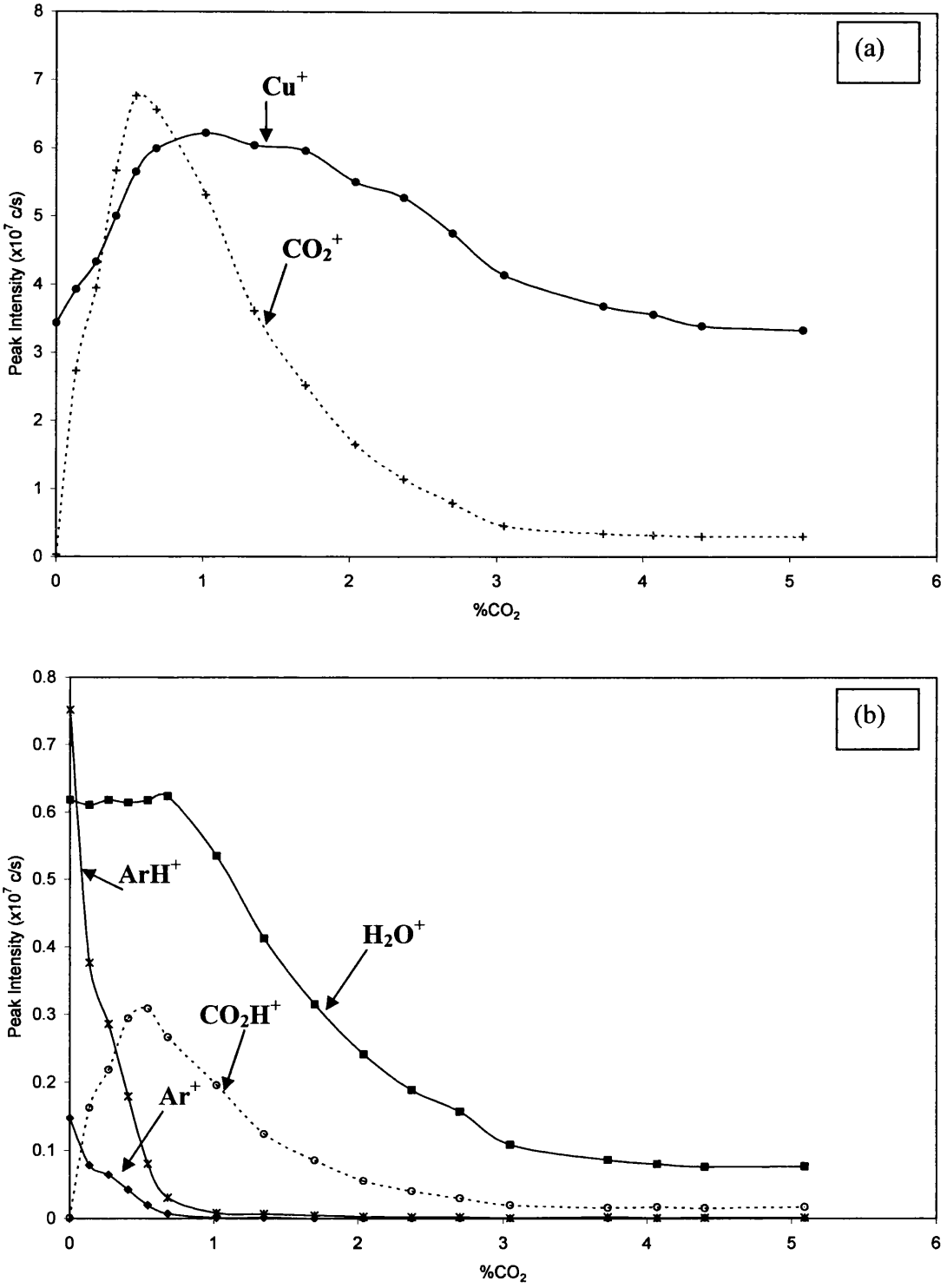

Figure 7.14: Variation of (a) major and (b) minor ion peak with percentage addition of carbon dioxide when V_c = -10 V
(V_d = 700 V, I_d = 1.7 mA, P = 1 Torr, F_{Ar} = 400 sccm, τ = 2.1 ms, tuned for Cu^+.)

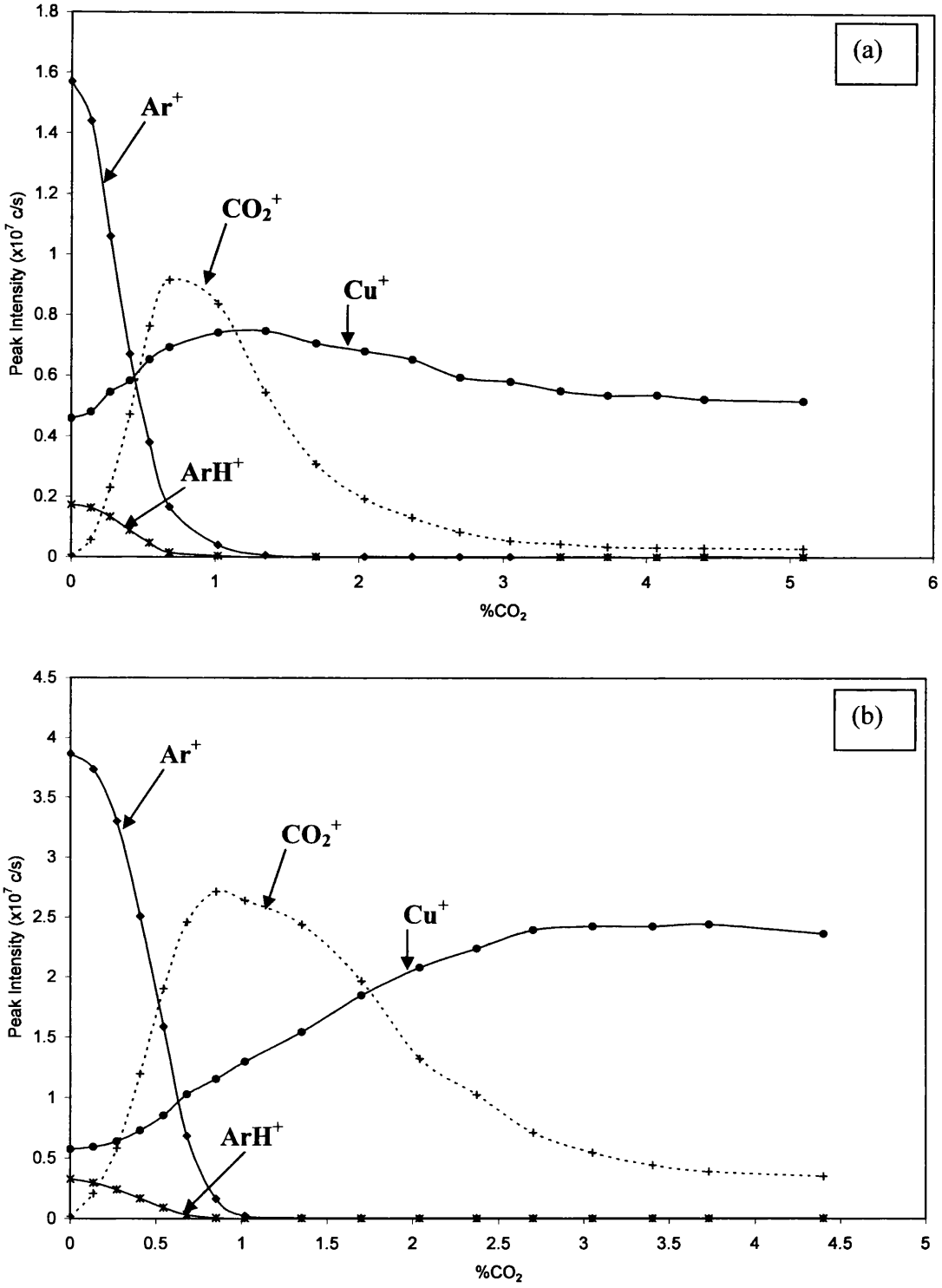

Figure 7.15: Variation of major ion peak intensities with percentage addition of carbon dioxide when V_c = (a) 0 V and (b) +2 V
(V_d = 700 V, I_d = 1.7 mA, P = 1 Torr, F_{Ar} = 400 sccm, τ = 2.1 ms, tuned for Cu^+)

similar to the increase in the Cu^+ and CO_2^+ intensities. Similar results were observed when V_c = +2 V. The loss of CO_2^+ ion signal on addition of higher quantities of CO_2 was not compensated by any increase in the intensities of other ion species.

In the previous sections it has been illustrated that the loss of Ar^+ signal and increase in reagent gas and copper ion intensities is predominantly due to the quenching or Ar Rydberg states in reactions involving secondary gases. A reaction scheme for addition of CO_2 is illustrated in equations 7.21 to 7.23 below:

$$Ar^R + CO_2 \rightarrow Ar + CO_2^+ + e^- \rightarrow CO_2^R \quad \textit{(equation 7.21)}$$

$$Ar^R + CO_2 \rightarrow Ar^+ + CO_2\,(J\text{-}1) + e^- \quad \textit{(equation 7.22)}^{38}$$

$$Ar^R + CO_2 \rightarrow Ar^* + CO_2^* \quad \textit{(equation 7.23)}$$

Though CO_2 has no permanent dipole, it does have an oscillating dipole, and this increases the cross section for collisions with the argon Rydberg electron[38]. Energy transfer from or to the Rydberg state atom can occur via vibrational or rotational modes.

7.4.5.2 Effect of Varying Ion Exit Bias for a Fixed Carbon Dioxide Flow Rate

The effect of ion exit bias on the detected ion intensities has been investigated on addition of 0.01, 0.1 and 1% gas addition and the effects observed were found to be the same. Figure 7.16 illustrates the variation of the major ion intensities with V_c on 0.1% addition of carbon dioxide. The variation of the major discharge related ion intensities was the same as that on addition of each of the previous gases and will not be discussed again. The variation of the Ar^+ signal has been omitted due to its low intensity. As reported in section 7.4.4.2 for addition of CO, there was no increase in the Ar^+ signal when V_c was 0 V. This is presumably due to the high quenching efficiency of CO_2, compared to its ionising efficiency over the time scale of the reaction.

7.4.6 Addition of Methane to the FAG Plasma

The addition of methane to the flowing afterglow of the FFGD plasma has been studied within this group before, using both high voltage[1,3,9] and low voltage[12]

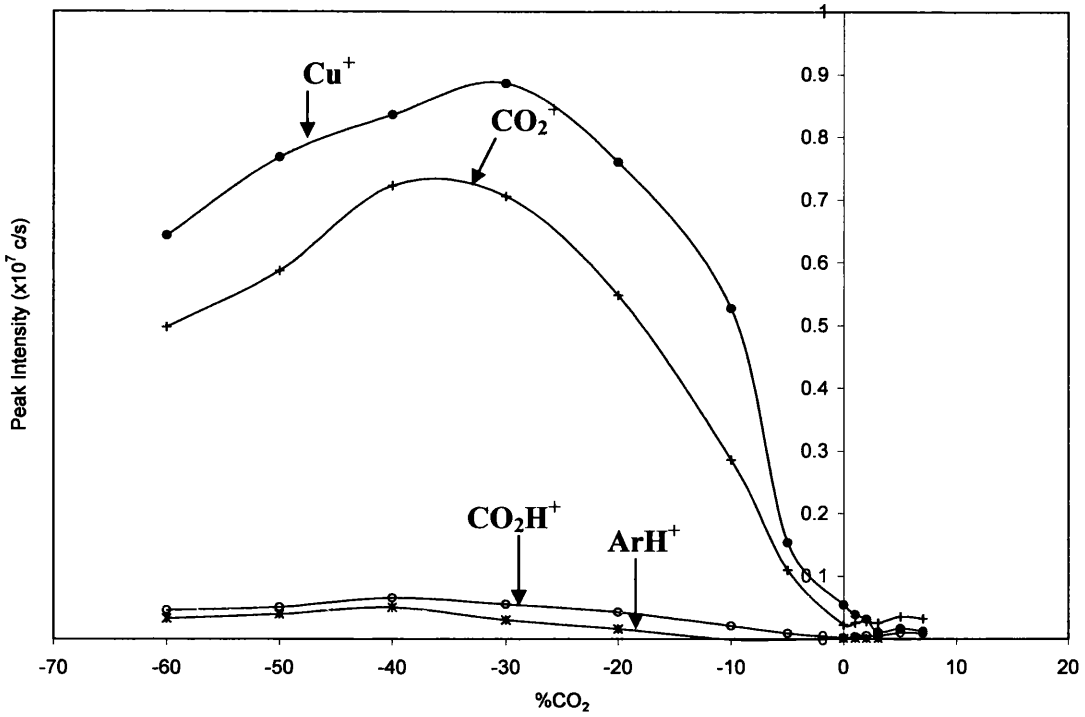

Figure 7.16: Variation of major ion peak intensities with ion exit bias for 0.1% addition of carbon dioxide
(V_d = 700 V, I_d = 1.5 mA, P = 1 Torr, F_{Ar} = 400 sccm, τ = 2.1 ms, tuned for Cu^+)

instruments. Dash[9] and Newman[12] have each measured the efficiency of quenching of the argon Rydberg gas by various gases including methane. Mortimer[3] investigated the influence of magnitude of the applied ion exit field strength on ion formation using the high voltage instrument. Newman[12] also performed a preliminary investigation into the influence of V_c on the mass spectra observed. The study reported here is the first investigation into the effect of the methane flow rate on the observed ion intensities, and the first detailed study of the influence of the ion exit bias, using the low voltage instrument.

7.4.6.1 Effect of Varying Methane Flow Rate for a fixed Ion Exit Bias

The results presented by Miller[1], Mortimer[3] (under weak exit field conditions) and Dash[9] illustrate the same variation of ion intensities with methane flow rate. Again, the Ar^+ peak intensity was rapidly reduced on addition of methane. Miller observed that for low levels of CH_4 addition the Cu^+ peak intensity was slightly increased, but not to the levels observed on addition of CO, CO_2 or H_2[1]. The investigation by Mortimer[3] indicated a reduction in Cu^+ intensity under weak ion exit field conditions, but an increase (x1.5 at V_c = -100 V) was observed on application of an ion exit bias of -100 V.

Figures 7.17 and 7.18 show the variation of the major ion peak intensities observed in this investigation. The ArH^+ and Ar^+ intensities followed the trends observed by previous authors[1,3,9]. The Cu^+ peak intensity also increased on addition of CH_4 when V_c was 0 or +2 V (x4.8 and x2.9 at respective maxima), but no significant change occurred at V_c = -10 V. This indicates that the processes responsible for enhancement occur at the ionisation stage, because when V_c = -10 V there is no enhancement, and we presume that all Cu^R are ionised by the 10 V ion exit field effects. This is a different effect to those observed on addition of H_2, CO and CO_2. These previous reactions were consistent with quenching of Ar Rydberg states, which under favourable circumstances leads to formation of lower argon excited state species (including Ar^m), the precursors to Cu^R formation. This could occur in the plasma or cone sheath, and hence shows up at all V_c values. The increased Cu^R formation, and subsequent ionisation in the sheath field would be expected to enhance the Cu^+ signal on application of V_c = -10 V, but this was not the case.

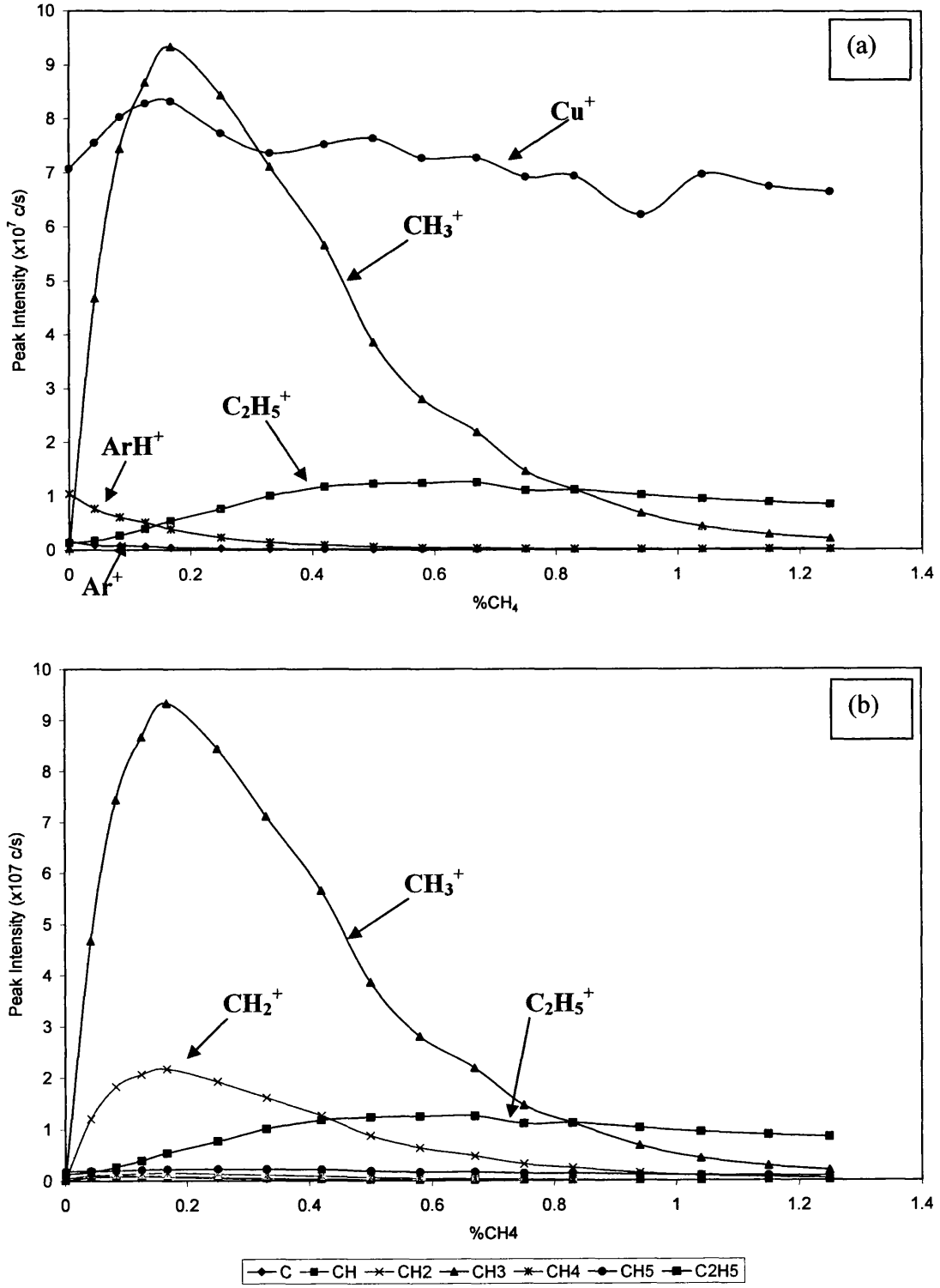

Figure 7.17: Variation of (a) major and (b) methane related ion peak intensities with low percentage addition of methane when V_c = -10 V
(V_d = 700 V, I_d = 2.1 mA, P = 1 Torr, F_{Ar} = 400 sccm, τ = 2.1 ms, tuned for Cu^+)

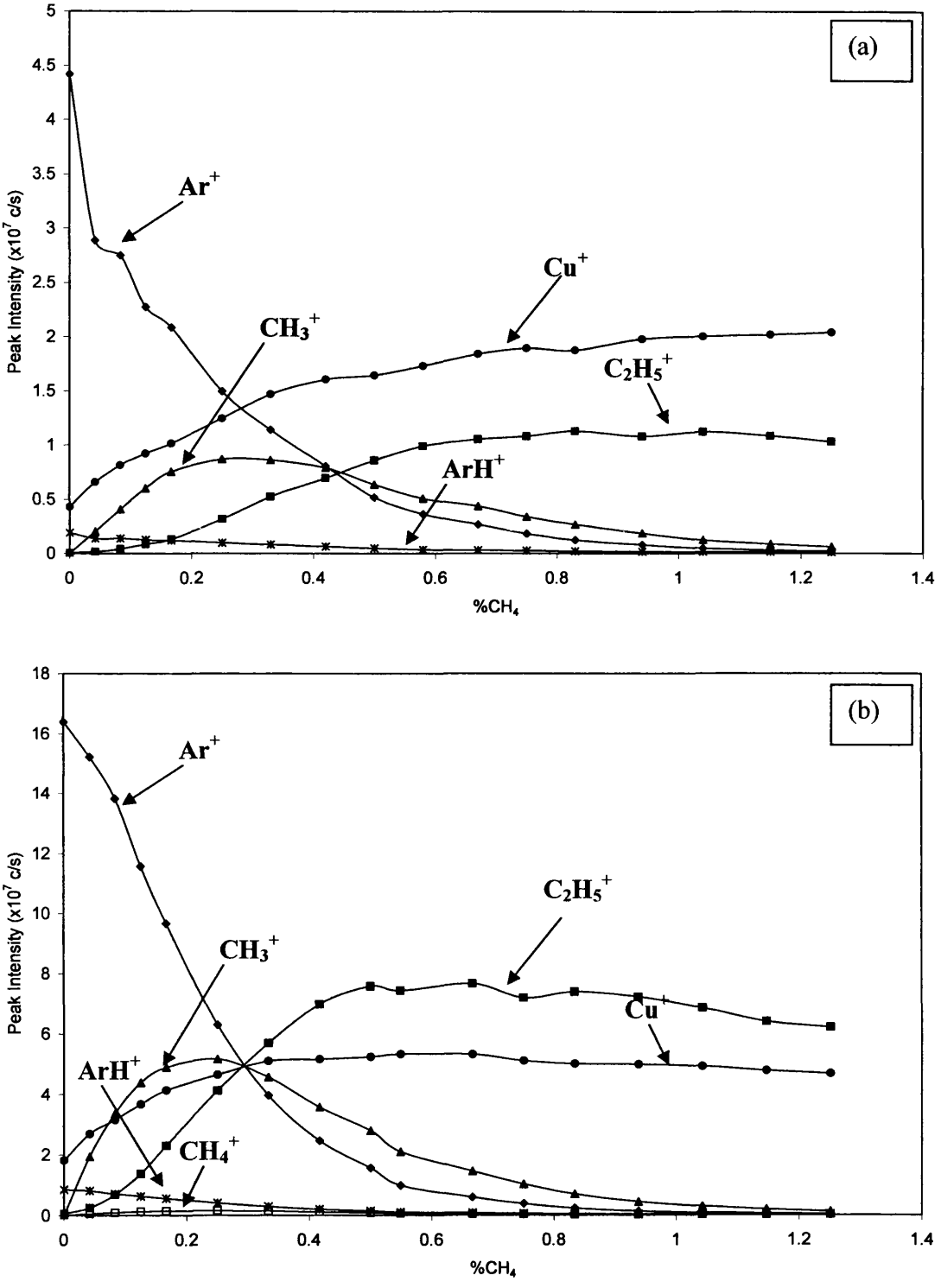

Figure 7.18: Variation of methane related ion peak intensities with low percentage addition of methane when V_c = (a) 0 V and (b) +2 V
(V_d = 700 V, I_d = 2.1 mA, P = 1 Torr, F_{Ar} = 400 sccm, τ = 2.1 ms, tuned for Cu^+)

Thus, the effects when V_c = 0 and +2 V are due to enhanced ionisation of Cu^R states by CH_4 (equation 7.24):

$$Cu^R + M \leftrightarrow CuM^R \rightarrow Cu^+ + e^- + M \quad \textit{(equation 7.24)}$$

where M = N_2, CH_4, etc. No effect on the Cu^+ intensity was observed in the presence of the high accelerating field (MS9 instrument)[3], because the accelerating field was strong enough to completely ionise the Cu^R.

In each previous investigation[1,3,9] the intensity of the CH_x^+ peaks increased sharply on addition of a small amount of CH_4 and decreased on higher CH_4 addition. $C_2H_x^+$ ions were also formed, increasing more slowly but reaching a maximum intensity for a higher CH_4 flow rate than that for the CH_x^+ ions. Very similar results, illustrated in figures 7.17 and 7.18, were observed in this investigation. When V_c was 0 V (figure 7.18a) the increase in the CH_x^+ and Cu^+ intensities could be explained by charge transfer processes since a significant reduction in the Ar^+ peak intensity was observed. The loss of CH_x^+ signal on higher levels of CH_4 addition could be explained by the continued increase in the $C_2H_x^+$ and Cu^+ peak intensities. However, when V_c was +2 V (figure 7.18b) similar effects were observed, when ion-molecule reactions are ruled out because the applied V_c discourages extraction of positive ions from the GD cell. The effects observed on application of a negative ion exit bias (figure 7.17) also cannot be explained by an I-M process as the massive increase in the formation of CH_3^+ on addition of 0.2% CH_4 was greater than the loss in all ion signals combined.

Ionisation (equation 7.25) or fragmentation (equation 7.26) of the methane molecule may occur in collisions between Ar^R and CH_4 (in ground or excited states). It is possible for further fragmentation to occur than is indicated in equation 7.26.

$$Ar^R + CH_4 \rightarrow Ar + CH_4^+ + e^- \rightarrow CH_4^R \quad (\Delta E = -309.1\ kJ\ mol^{-1}) \quad \textit{(equation 7.25)}$$

$$Ar^R + CH_4 \rightarrow Ar + CH_3^+ + H + e^- \quad (\Delta E = -132.6\ kJ\ mol^{-1}) \quad \textit{(equation 7.26)}$$

Equation 7.26 appears to dominate since, when V_c = -10 V the CH_3^+ intensity is significantly higher (can be by a factor of 65) than that of CH_4^+. On application of a negative V_c, the higher levels of fragment ion detection can in part be explained by CID within the cone sheath. However, when V_c is +2 V (figure 7.18b), when the ions

formed are indicative of the plasma composition, the CH_3^+ intensity was up to 32 times higher than CH_4^+. Thus, both reactions probably occur. It is also possible that neutral decomposition occurs to form radicals which become ionised or excited in subsequent collisions. It should be noted at this point that the CH_4^+ peak cannot be distinguished from that of O^+ in the mass spectrum (the same applies to CH_5^+ and OH^+), and therefore the CH_4^+ intensity may actually be lower than that indicated in figures 7.17b and 7.18b. One problem associated with this is discussed in section 7.4.6.2 below.

Neutral fragments (CH_x, where x is 0 to 3) can be ionised by energy transfer from argon Rydberg or metastable state species (Ar^m) (equation 7.27) as their ionisation energies, listed in table 7.3, are lower than that of the argon $^3P_2$ and $^3P_0$ states (11.55 eV and 11.72 eV respectively). The ionisation potential of CH_4 is greater than that argon metastable state energy and therefore cannot be ionised by this process.

$$Ar^m + CH_3 \rightarrow Ar + CH_3^+ + e^- \leftrightarrow CH_3^R \quad \textit{(equation 7.27)}$$

Ion-electron recombination could lead to the formation of CH_x Rydberg state species which would be ionised in the ion exit or accelerating fields.

x	Ionisation Potential (eV)
0	11.26
1	10.64
2	10.4
3	9.84
4	12.51

Table 7.3: Ionisation potentials of CH_x species[68]

Miller[1] reported that the observed intensities for CH^+, CH_2^+ and CH_5^+ were significantly higher than those for C^+ and CH_3^+. Since the energy required to form C^+ is so high, requiring cleavage of 4 C-H bonds and subsequent ionisation, it is not surprising that this ion was observed at low intensity. However, the maximum intensity of the CH_3^+ ion was approximately 60% of that for the C^+ ion and less than $1/5^{th}$ of the other CH_x^+ fragment ions[1]. In this investigation, the maxima for all CH_x^+

intensities were observed for the same amount of CH_4 addition and the ion intensity maxima increased with increasing x (x = 0 to 3). It is possible that the observed difference between the two systems is due to the much higher accelerating field applied in the high voltage instrument and the different reaction conditions used by Miller[1] (higher pressure, lower V_d, etc).

Formation of larger hydrocarbon species such as $C_2H_5^+$ could occur via I-M processes[3] e.g.:

$$CH_3^+ + CH_4 \rightarrow C_2H_5^+ + H_2 \qquad \textit{(equation 7.28)}$$

$$C_2H_5^+ + e^- \leftrightarrow C_2H_5^R \qquad \textit{(equation 7.29)}$$

Ion-electron recombination produces Rydberg molecules which can be ionised within the sheath field or outside the discharge cell. Since gas discharges are sources of free radicals[69] it is possible that radical reactions occur. One possible sequence is shown below:

$$CH_3^R + M \rightarrow CH_3^{\cdot} \qquad \textit{(equation 7.30)}$$

$$CH_3^{\cdot} + CH_4 \rightarrow C_2H_5^{\cdot} + H_2 \qquad \textit{(equation 7.31)}$$

$$C_2H_5^{\cdot} + Ar^R \rightarrow C_2H_5^+ + e^- + Ar \leftrightarrow C_2H_5^R \qquad \textit{(equation 7.32)}$$

Pinnaduwage et al.[71-73] have also illustrated how electron attachment to highly energetic species leads to formation of fragment ions (positive and negative) and radical species. This was discussed in detail in chapter 6.

7.4.6.2 Effect of Varying Ion Exit Bias for a Fixed Methane Flow Rate

The influence of the ion exit bias on ions formed from organic molecules was recently reported by Newman[12]. It was observed that the formation of fragment ions was induced on application of a high negative V_c, whereas application of small negative, zero or small positive voltage led to detection of the parent molecular ion. It was also observed that the degree of fragmentation increased with increasing negative V_c. Blom and Munson[73] reported on the formation of various hydrocarbon ions from methane using a high pressure chemical activation (HPCA) source. It was observed that the magnitude of the field strength applied within the drift cell directly influenced

the degree of fragmentation observed, with higher field strengths inducing higher levels of fragmentation. Mortimer[3] performed a similar experiment using the high voltage FFGD instrument, and also found that the degree of fragmentation observed increased with increasing V_c (ion exit field strength).

In this investigation the degree of ionisation was again observed to increase with increasing negative V_c. It was also observed that the $C_2H_x^+$ ion species reached their maximum intensities on application of a low negative ion exit bias, and $C_2H_5^+$ was one of the most abundant ion species on application of a positive V_c. The variation of the discharge related ion intensities with V_c (figure 7.19a) was the same as observed in previous sections. Figure 7.19b illustrates the variation of the hydrocarbon ion intensities with the applied ion exit bias on addition of 0.1% CH_4. The same results were observed on addition of 0.01 and 1% CH_4 and have therefore been omitted. It has been noted above that using the PQ2 mass analyser it is not possible to differentiate between ions of the same mass, such as CH_4^+ and O^+ (m/z = 16), or CH_5^+ and OH^+. The result of this is that two maxima for ion detection of both masses m/z = 16 and 17 (figure 6.18b). Application of a high negative ion exit bias has been shown to induce fragmentation of methane, and a range of organic and organotin compounds[12], and therefore the ion intensity maxima on application of a high negative V_c probably correspond to O^+ and OH^+, whilst the maxima on application of a low negative V_c probably correspond to CH_4^+ and CH_5^+.

Mortimer[3] concluded that the increase in the detection of hydrocarbon fragment ions with increasing V_c was due to increased sampling of ions formed upstream of the ion exit, close to the active discharge region, due to interaction between highly excited states of argon and the added methane. However, we now know this should not occur, as back diffusion of gases is limited due to the fast argon flow and, most importantly, the drop in voltage and therefore field ionisation of the Rydberg gas occurs over a distance < 3 mm from the cone surface[10].

Electron bombardment close to the ion exit orifice was considered. Electrons formed close to the surface would be accelerated away from the ion exit cone on application of a negative ion exit bias and the kinetic energy of the electron is determined by the applied bias. Therefore, on application of an ion exit bias of -60 V the maximum electron energy allowed is 60 eV and formation of any of the fragment ions is possible. However, formation of CH_3^+ and CH_2^+ ions was observed when V_c was -5 V. The maximum electron energy would therefore have been 5 eV and

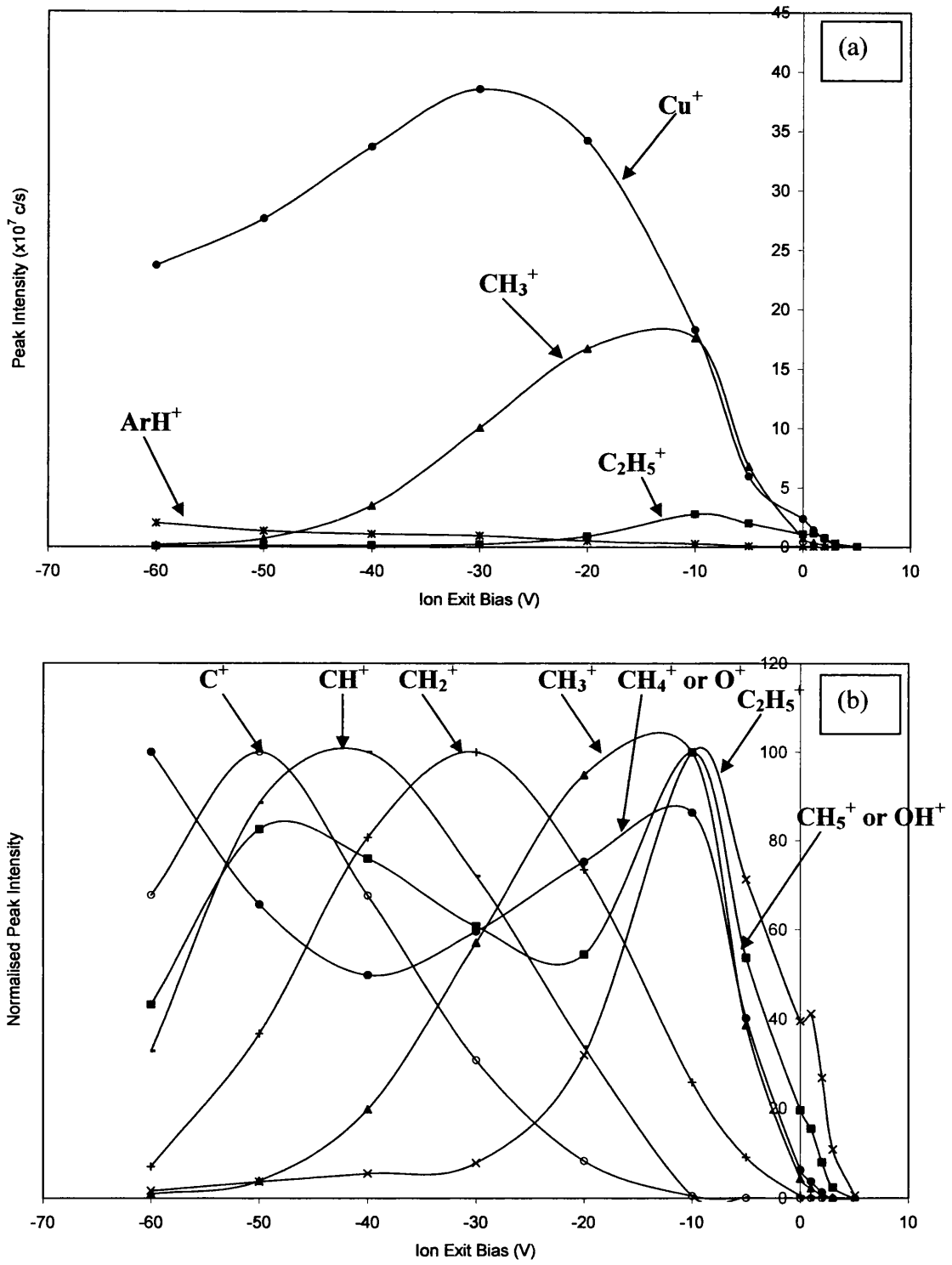

Figure 7.19: Variation of (a) major and (b) methane related ion peak intensities with ion exit bias on 0.1% addition of methane
(V_d = 700 V, I_d = 2.1 mA, P = 1 Torr, F_{Ar} = 400 sccm, τ = 2.1 ms, tuned for Cu^+)

insufficient to induce ionisation of ground state neutral species (table 7.3). However, it is possible that excited state neutral radicals could be ionised in this manner (equation 7.33):

$$CH_3^* + e^- \rightarrow CH_3^+ + 2e^- \qquad \textit{(equation 7.33)}$$

In section 7.4.6.1 it was illustrated that fragment ions could be formed by energy transfer processes involving both argon Rydberg and metastable state species.

Figure 7.20a shows a NIST library EI spectrum[74]. It is clear that the fragment ion intensities decline with increasing fragmentation due to the higher energies required. Figure 7.20b is a spectrum recorded during this investigation on application of a high negative V_c (-60 V). In this spectrum the C^+ ion is the highest intensity of the C_1 ions, with CH_4^+ the lowest in intensity. Clearly the two spectra cannot be formed by the same ionisation process. Figure 7.20b also shows the C_2 ion peaks, of which the lower mass species are formed in preference to the higher mass species (such as $C_2H_5^+$).

One further possibility, and the most likely, is collision induced dissociation (CID) within the cone sheath. As ions are accelerated through the sheath field they can collide with neutral species converting the kinetic energy of the molecule into internal energy (equation 7.34). If the increase in internal energy is sufficient then fragmentation can occur[75] (equation 7.35). Therefore, increasing the ion exit bias increases the kinetic energy of the ion, and a greater degree of fragmentation can occur.

$$CH_4^+{}_{\rightarrow} + Ar \rightarrow CH_4^{*+} \qquad \textit{(equation 7.34)}$$

$$CH_4^{*+} \rightarrow CH_3^+ + H + 2e^- \qquad \textit{(equation 7.35)}$$

Similarly, dissociation due to bombardment by Ar^+ ions formed at the sheath boundary by the process shown in equation 7.36 occurs:

$$Ar^+{}_{\rightarrow} + CH_4 \rightarrow Ar + CH_x^+ + H_y + e^- \qquad \textit{(equation 7.36)}$$

This process is similar to the electron impact process above, and therefore the energy of the ions due to acceleration across the cone sheath will be determined by the

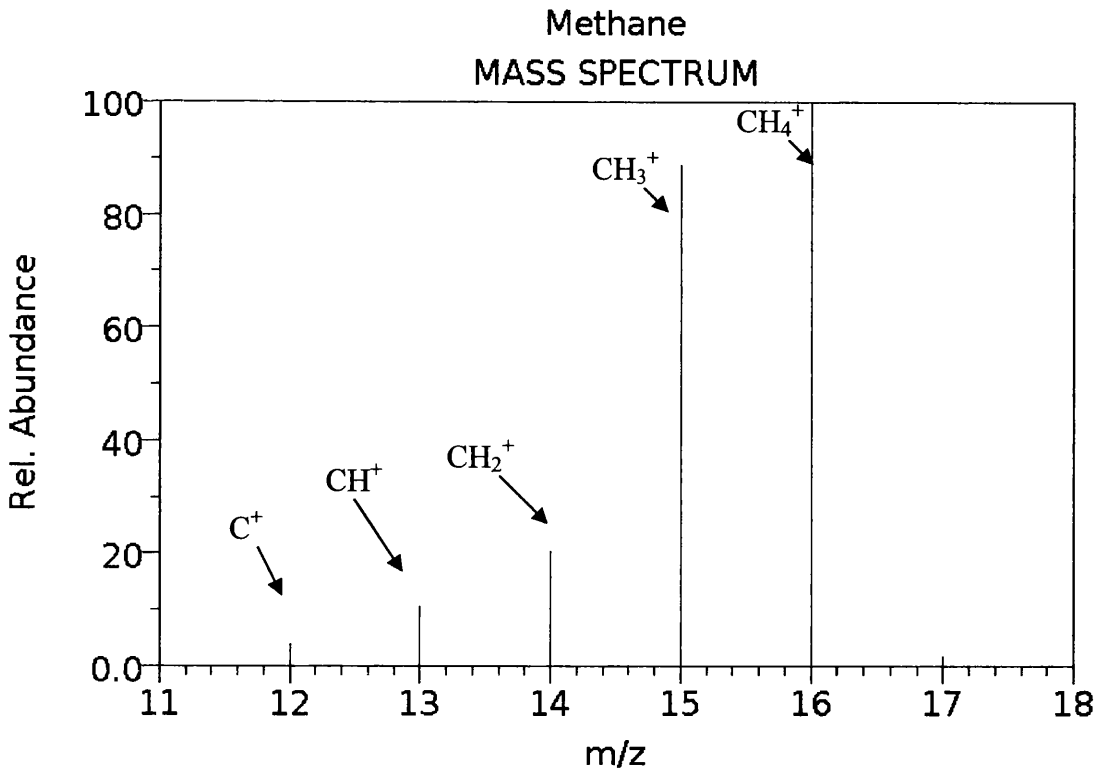

Figure 7.20a: NIST library mass spectrum of methane[76]

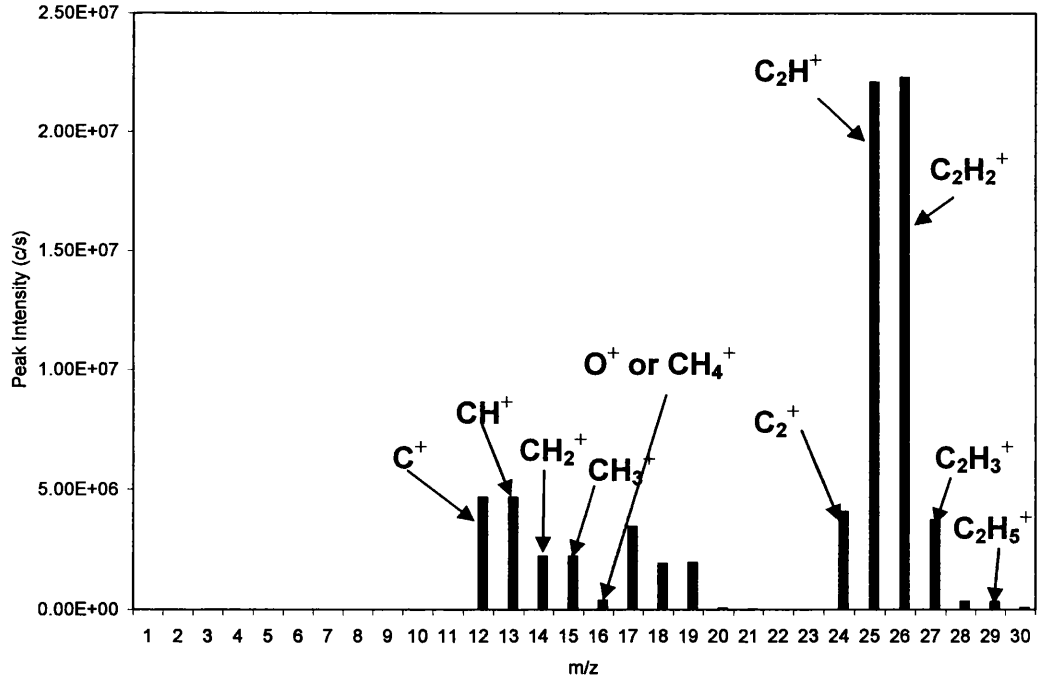

Figure 7.20b: Mass spectrum recorded when V_c was -60V on addition of methane to the FAG plasma
(V_d = 700 V, I_d = 2.1 mA, P = 1 Torr, F_{Ar} = 400 sccm, τ = 2.1 ms, tuned for Cu^+)

magnitude of the ion exit field and the distance the ion travels before collision. Thus, as V_c is increased the degree of fragmentation also increases (figure 7.19b).

On application of a small positive ion exit bias it is possible that neutral Rydberg species undergo the Stark effect within the ion exit field[76], encouraging ion formation via field ionisation outside the cell. On application of higher potentials (> +5 V) it appears that ionisation was induced by the ion exit field, and therefore no ions were detected. The ions detected on application of a positive V_c are indicative of the species present within the FAG plasma and those formed in the expanding gas outside the discharge cell. The implications of this as a tuneable process for chemical speciation are discussed in more detail in chapter 8 and references 12, 76, 77 and 78.

The results presented here are similar to the CID results described by Munson et al.[73], though in their work C^+ was not observed even at field strengths of 200 V cm^{-1}. In both investigations the degree of fragmentation increased with the ion exit field strength, and fragment ion formation has been ascribed to CID in the ion exit field. This indicates that the sheath layer must be very narrow, to allow most of the voltage drop to be transferred as KE to the accelerating ions.

7.5 Quenching Rate Constants

Rate constants for removal of Ar^+ from the mass spectrum by addition of secondary gases have been calculated within this group[3,9] and compared against quenching rate constants for the Ar $^3P_2$ state reported by Setser et al.[26]. The rate constants reported by Mortimer[3] cannot be trusted as the secondary gas was added downstream of the ion exit orifice and therefore it was not possible to determine the absolute concentration of secondary gas added or reaction time. However, the relative quenching efficiencies of the reagent gases may be comparable with reactions where the gas was added upstream of the ion exit.

In this investigation the rate constants for removal of Ar^+ from the mass spectrum on addition of a number of reagent gases added to the FAG plasma were estimated and compared against those for charge transfer processes[79] (equation 7.37 where M is the reagent gas). However, in this system the formation of Ar^+ is believed to occur via field ionisation of argon Rydberg states, and therefore the rate constant calculated should correspond to quenching of these states (equation 7.38). It is also possible that collisional excitation of Ar^R could induce ionisation via a ΔJ-1 rotational

transition[38,80] (equation 7.39) and therefore it is the net quenching rate constant that is calculated.

$$Ar^+ + M \rightarrow Ar + M^+ \qquad \textit{(equation 7.37)}$$

$$Ar^R + M \rightarrow Ar^* + M^* \qquad \textit{(equation 7.38)}$$

$$Ar^R + M_{J+1} \rightarrow Ar^+ + M_J + e^- \qquad \textit{(equation 7.39)}$$

The rate equation for quenching of the Ar^+ ion signal is expressed as:

$$\frac{-d[Ar^+]}{dt} = k\,[M][Ar^+] \qquad \textit{(equation 7.40)}$$

At a source pressure of 1 Torr the density of the discharge gas in the FFGD cell was calculated using equation 7.41:

$$\frac{n}{V} = \frac{P}{RT} = \frac{1\times101325\times6.022\times10^{23}}{760\times8.314\times310\times10^{6}} = 3.12\times10^{16}\ molecules\,cm^{-3} \quad (equation\ 7.41)$$

where P is the source pressure, R is the gas constant and T is the temperature of the gas in the source (previously determined to be 310 K[4])

Therefore for 0.1% addition of M, as a percentage of the total gas flow rate, *[M]* is equal to $3.12\text{x}10^{13}$ molecules cm^{-3}, assuming ideal gas mixing. The pseudo first order rate law for the reduction in Ar^+ intensity with addition of M is therefore:

$$\ln[Ar^+]_t = \ln[Ar^+]_0 - k\Delta t[M] \qquad \textit{(equation 7.42)}$$

where Δt is the reaction time, assumed to be the residence time of the reagent gas, calculated as 1.2 ms. As $ln[Ar^+]_0$ is constant, plotting $ln[Ar^+]_0$ against *[M]* predominantly produced straight line plots where the gradient is equal to $-k\Delta t$.

It has been illustrated in this chapter that the magnitude of V_c directly influences the magnitude of the observed ion peak intensities due to ionisation of Rydberg state species in the ion exit field. For this investigation V_c was set to 0 V throughout to prevent the ion exit bias influencing the reaction process in the FAG plasma.

7.5.1 Results

The quenching rate coefficients calculated from the plots in figure 7.21 are shown in table 7.4 and compared against gas phase ion-molecule reaction rate constants[79] and those measured by Dash[9] and Newman[12] in previous investigations. The discharge conditions for the experiments performed by Dash[9] were: P = 2 Torr, V_d = 500 V, reaction time = $\Delta t = 9.2 \times 10^{-4}$ s. The conditions used by Newman were similar to those used in this investigation, but V_d was 650 V and V_c was -20 V, therefore some discrepancy between previous results and those calculated in this investigation was expected.

Reagent Gas	k (Charge Transfer)[79] ($x10^{-11}$ molecule^{-1} cm^3 s^{-1})	k (Dash [9]) ($x10^{-11}$ molecule^{-1} cm^3 s^{-1})	k (Newman[12]) ($x10^{-11}$ molecule^{-1} cm^3 s^{-1})	k (This Work) ($x10^{-11}$ molecule^{-1} cm^3 s^{-1})
H_2	82	32 (± 15%)	27 (± 0.2)	112 (±10%)
N_2 (max)	1	-	-	0.138 (±10%)
CO	3.8	-	-	5.92 (±17%)
CO_2	71	-	-	17.5 (±21%)
CH_4	95	24.4 (±8%)	16 (± 0.2)	11.4 (±5%)

Table 7.4: Rate Constants for Loss of Ar^+ Ion Signal on Addition of Reagent Gases (This investigation - P = 1 Torr, V_d = 700 V, V_c = 0 V, $\Delta t = 1.2^{-3}$ s, tuned for Cu^+)

The addition of hydrogen to the FAG plasma has been investigated extensively within this group and its quenching efficiency is known to be high[1-12]. Previous results presented by Dash[9] indicate that the rate constant was lower than that expected for removal of Ar^+ via a charge transfer process[79]. Dash[9] illustrated that increasing the plasma residence time decreased the rate constant. In this investigation τ was approximately half of that used in the previous investigations. In the previous investigation[9] it is also possible that ion formation occurred via field ionisation of excited state species below Rydberg levels due to the high accelerating field. This would therefore lead to a reduction of the calculated rate constant. The results of this investigation indicate that the quenching rate constant of hydrogen is higher than that

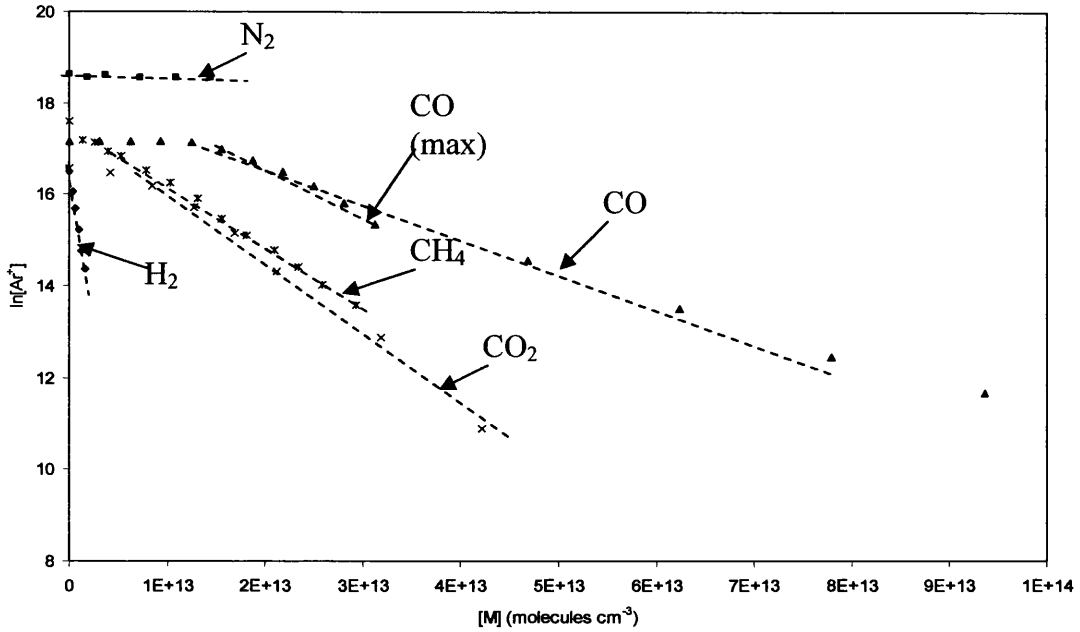

Figure 7.21: Reagent gas quenching plots
(Source Conditions: V_d = 700 V, P = 1 Torr, F_{Ar} = 400 sccm, τ = 2.1 ms, $\Delta t = 1.2^{-3}$ s, tuned for Cu^+)

for a charge transfer process. This is likely to be due to the efficient energy transfer to hydrogen rovibrational levels.

The rate constant measured on addition of hydrogen was significantly higher than that measured by Newman[12] (> factor of 4 higher) using the same instrument under similar discharge conditions. The major difference between the two sets of conditions is that Newman applied an ion exit bias of -20 V, and therefore the ions monitored were formed within the cone sheath and accelerated into the mass analyser. In this investigation V_c was 0 V, and therefore ions were formed (mostly) by field ionisation of Ar^R outside the discharge cell. This increases the time over which quenching, and also charge transfer, reactions could occur.

The rate constant on addition of nitrogen was by far the lowest measured in this study. As described in section 7.4.3.1 the interaction between nitrogen and the argon Rydberg electron is long range as N_2 has no dipole, and therefore the quenching efficiency is low[38]. The rate constant measured in this study (table 7.4) agrees well with this. Over the range of nitrogen addition specified, very little reduction of the Ar^+ signal was observed, and therefore the quenching rate constant was very low.

In this investigation the quenching rate constant on addition of CO was estimated to be significantly higher than that observed for N_2 and significantly lower than that for H_2 (table 7.4). However, three distinct regions to the graph line were observed, possibly indicating competing processes. In section 7.4.4 it was suggested that the initial constant Ar^+ intensity could be due to the competing collisional excitation/ionisation and quenching of Ar^R. Thus, initially the Ar^+ intensity was approximately constant, due to a balance between the competing processes. However, as the CO concentration is increased, the quenching rate becomes greater than the excitation rate and therefore the Ar^+ intensity declines. Due to the inconsistency of the gradient, two quenching rate constants have been measured as indicated in table 7.4 and figure 7.21. The lower rate constant measured was similar to the charge transfer rate constant[79].

As CO has a permanent dipole, interactions with the argon Rydberg electron occur readily, and therefore the collisional cross section would be expected to be greater than that for N_2. However, H_2 has no dipole and therefore interactions between hydrogen and the Rydberg state electron would be expected to be short

range. It is therefore unusual that hydrogen is far more efficient at quenching argon Rydberg states. Charge transfer processes were ruled out since no corresponding increase in the CO^+ peak intensity was observed (figure 7.12b).

The rate constant measured on addition of CO_2 was significantly lower than that for the charge transfer process[79] (table 7.4). The rate constant was however greater than that for CO. Though CO_2 does not have a permanent dipole, it does have an oscillating dipole which should allow a relatively large cross section for collision with the argon Rydberg electron. Also, the larger physical size of the molecule, compared with CO, allows improved energy transfer due to the larger range of rotational and vibrational states to which it can be excited[38].

The charge transfer rate constant for the methane is greater than those for CO, CO_2 and even H_2[79]. In this investigation the quenching rate constant was estimated to be between those for CO_2 and CO, and the value was close to a factor of ten lower than the charge transfer rate constant. This again illustrates that charge transfer is unlikely to be responsible for the observed reduction in Ar^+ intensity. The rate constant measured in this investigation is approximately half of that measured by Dash[9]. The rate constant was also approximately ¼ of that measured by Newman[12] using the low voltage instrument. As described above, Newman[12] applied V_c = -20 V, and therefore it is believed that Ar^+ was formed by field ionisation of Ar^R within the cone sheath. In this investigation ionisation has been shown to mostly occur outside the discharge cell, and therefore the results were expected to differ. Methane is again limited to short range interactions with the Rydberg state electron[38]. Therefore, the quenching efficiency was lower than that of the more highly polarised CO_2 molecule. However, this is compensated for in part by the size of the methane molecule, and the greater number of rotational and vibrational modes, and therefore the quenching efficiency was slightly higher than that for CO.

7.5.2 Summary

In this section, rate constants have been estimated for the reduction of the Ar^+ intensity by a number of secondary gases, and compared with results obtained in previous investigations[9,12] and charge transfer rate constants[79]. The results did not

match accurately with those measured by other members of the group, predominantly due to the differences in conditions used. Below are a series of relative rate constants for a) charge transfer[79], and from various studies within this group – b) Mortimer[3], c) Dash[9], d) Newman[12] and e) this study:

a) $CH_4 > H_2 > CO_2 > CO >> N_2$
b) $H_2 > CO_2 > CH_4 > CO > N_2$
c) $H_2 > CH_4$
d) $H_2 > CH_4$
e) $H_2 >> CO_2 > CH_4 > CO >> N_2$

Despite the problems with the setup used by Mortimer[3], the relative quenching rate constants measured agree with the results in this investigation and those measured by Dash[9] and Newman[12]. However, there is poor agreement between the relative, as well as measured values, of the charge transfer rate constants and the results of this investigation. Thus, it is highly unlikely that charge transfer processes were responsible for the observed quenching of the Ar^+ signal.

7.6 Conclusions

The reactions of N_2, H_2, CO, CO_2 and CH_4 with the plasma give essentially the same ion intensity profiles, whether using the high voltage, MS9, instrument or the quadrupole (VG PQII) mass analyser used in the present study. This is despite differences in the source pressure (2 Torr and 1 Torr respectively), plasma residence times (4.3 to 6.3 ms and 2.1 ms respectively), reaction times, trace water content and the electric fields within the flow tube (flow tube in MS9 instrument was floating, at anode potential in this study). The conditions outside the discharge cell also differ, with the quadrupole instrument having an intermediate region of approximately 1 mTorr pressure, which contains a cylindrical extraction lens (operated up to 1000 V). The ion acceleration region (accelerating potential = 4 kV) lies immediately beyond the source of the MS9 instrument and is at a pressure of approximately $2x10^{-6}$ Torr when the source is in use[9]. Any differences in the profile details are assumed to be due to these differences in operating conditions.

One exception to this is the magnitude and response of the Ar^+ signal on variation of the ion exit bias. Previously this was proposed to be due to the more efficient ionisation of Ar^R in the accelerating field of the high voltage MS9 instrument compared to the low field in the quadrupole instrument when V_c is low. However, it should also be noted that symmetric charge transfer in argon is very efficient, and therefore most Ar^+ ions emerging from the source will have been formed close to the ion exit. This means that the Ar^+ kinetic energy is likely to be lower than that of other ions, and discrimination against the Ar^+ ion is very likely when tuning for any other ion in the mass spectrum, unless V_c is low (the lower kinetic energy of Ar^+ is discussed in chapter 5).

Many of the ionic reaction products could be produced via ion-molecule (e.g. charge transfer) or Rydberg atom reactions. It is not always possible to distinguish which occurs. Exceptions to this include:

(1) Formation of Ar^+ on addition of N_2 and CO, which conforms to the known Rydberg atom ionisation reaction[38];
(2) CO^+ and $C_xH_y^+$ (from methane reaction) are sometimes created in excess despite the removal of other ions from the mass spectrum, which might be their ionic precursor. This again supports the Rydberg gas model.
(3) Each reaction gave cationic products on application of a positive ion exit bias, demonstrating that ionisable neutral species, such as Rydberg atoms, exit the discharge cell.

The rate constants measured for removal of the Ar^+ from the mass spectrum by the reagent gases are of a similar order of magnitude to the literature values of the charge transfer rate constants[79]. However, the magnitudes and particularly relative Ar^+ removal efficiencies measured differ significantly from those in reference 79. For H_2 and CO addition the estimated values are greater, but for N_2, CO_2 and CH_4 they are substantially less than the charge transfer rate constants[79]. However, the rate constants measured by Newman[12] and Dash[9] on addition of hydrogen were significantly lower than the charge transfer values. This is likely to be due to differences in the source conditions used. The relative rate constants are in agreement with determined by Mortimer[3], despite the differences between the instruments and the discharge conditions used.

The Cu^+ signal is enhanced by the addition of H_2, CO and CO_2 for all V_c values studied. In these cases the signal reaches a maximum and is removed at higher added gas concentrations. This is consistent with a neutral excitation, ionisation and quenching mechanism already described in a paper detailing the hydrogen reaction[81]. However, on addition of N_2 and CH_4 the Cu^+ intensity is enhanced at low V_c values, but not at high negative V_c values. This indicates that the gases specifically aid ionisation of Cu^R atoms. For more negative ion exit biases this makes little difference because it is presumed that all the Cu^R atoms are ionised in the ion exit field.

There is a very distinct fragmentation pattern for methane when the negative V_c is increased. This is similar to results presented by Newman for 'breakdown' of organometallic[12,78], and organic compounds[12]. Comparison with experiments of Munson et al.[73] indicates that much lower voltages were required in our experiments to induce the same effect, even though the gas pressure is significantly higher. This gives clear evidence that a) collision induced decomposition (CID) is responsible for the fragmentation observed, and b) that the region over which the ion exit potential drop occurs is virtually collision free, and hence almost the full energy of the voltage drop is available to the collision. This is discussed further in chapter 8.

Generally, the variations of ion intensity with V_c indicate that, for all the gases studied in this chapter, ions have much higher signals when V_c is negative. This implies that ionisation in, and subsequent transmission of ions from the sheath region is more efficient than the same processes in the neutral plume. This is not true of the Ar_2^+ and Ar_2H^+ signals. The argon dimer ions are likely to form by associative ionisation in the neutral plume. Similarly, findings in chapter 8 indicate that formation of molecular, pseudo molecular and dimer ions occur more readily in the neutral plume than in the sheath field.

7.7 Summary

The quenching rate constants for removal of Ar^+ from the mass spectrum measured in this investigation differ significantly from the charge transfer rate constants in the literature[79]. Thus it was concluded that the quenching of the Ar+ signal could not be explained in terms of ion-molecule reactions. This is also evident from the mass spectra because the reduction of the Ar^+ is not always balanced by a corresponding increase in other ion signals. However, it has been shown that, with

reference to well known Rydberg atom collision processes[38], that the discrepancies between the charge transfer rate constants and the values measured in this investigation (such as the unexpectedly high quenching efficiency of H_2) can be explained if the plasma is a Rydberg gas. The relative quenching rate constants measured for the gases added in this investigation agree well with the results of Mortimer[3], but the magnitude of the quenching rate constants differ due to differences between the experimental conditions used.

As in the previous chapters it has been illustrated that ions form outside the discharge cell on application of a positive V_c and that on application of a negative V_c ions are predominantly formed in the ion exit field and extracted from the discharge cell. It was also observed that the magnitude and polarity of V_c directly influences the fragmentation of the added gases. The degree of fragmentation increased with increasing negative V_c, and the parent molecular ion species was commonly observed on application of a small positive V_c. This is discussed in greater detail in chapter 8.

7.8 References

[1] P. D. Miller, PhD Thesis, University of Wales Swansea, 1996

[2] R. S. Mason, P. D. Miller, I. P. Mortimer, *Phys. Rev. E*, **55**, 7462, 1997

[3] I. P. Mortimer, Ph.D Thesis, University of Wales Swansea, 2000

[4] D. R. Williams, Ph.D Thesis, University of Wales Swansea, 2001

[5] D. J. Mitchell, Ph.D Thesis, University of Wales Swansea, 2002

[6] I. P. Mortimer, D. J. Mitchell, N. A. Dash and R. S. Mason, *Proceedings of the XIVth International Conference on Gas Discharges and their Applications*, **2**, 260, 2002

[7] D. J. Mitchell, N. A. Dash and R. S. Mason, *Proceedings of the XIVth International Conference on Gas Discharges and their Applications*, **2**, 248, 2002

[8] R. S. Mason, P. D. Miller, I. P. Mortimer, D. J. Mitchell, N. A. Dash, *Phys. Rev. E*, **68**, 016408, 2003

[9] N. A. Dash, Ph.D Thesis, University of Wales Swansea, 2004

[10] R. S. Mason, D. R. Williams , I. P. Mortimer, D. J. Mitchell and K. Newman, *JAAS*, **19**, 1177, 2004

[11] K. Newman, R. S. Mason, D. R. Williams, et al., *JAAS*, **19**, 1192, 2004

[12] K. Newman, Ph.D Thesis, University of Wales Swansea, 2005

[13] D. H. Stedman and D. W. Setser, *Prog. React. Kinetics*, **6**, 4, 1971

[14] J. A. Coxon, D. W. Setser and W. H. Deuwer, *J. Chem. Phys.*, **58**, 2244, 1973

[15] L. G. Piper, D. W. Setser and M. A. A. Clyne, *J. Chem. Phys.*, **63**, 5018, 1975

[16] L. A. Gundel, D. W. Setser, M. A. A. Clyne, J. A Coxon and W. Nip, *J. Chem. Phys.*, **64**, 4390, 1976

[17] D. L. King, L. G. Piper and D. W. Setser, *J. Chem. Soc. Faraday Trans. 2*, **73**, 1977

[18] J. H. Kolts, H. C. Brashears and D. W. Setser, *J. Chem. Phys.*, **67**, 2392, 1977

[19] M. A. A. Clyne, P. Monkhouse and D. W. Setser, *Chem. Phys.*, **28**, 447, 1978

[20] L. G. Piper, J. E. Velazco and D. W. Setser, *Chem. Phys.*, **59**, 3323, 1973

[21] L. G. Piper, W. C. Richardson, G. W. Taylor and D. W. Setser, *Discuss. Faraday Soc.*, **53**, 100, 1972

[22] J. E. Velazco and D. W. Setser, *Chem. Phys. Lett.*, **25**, 197, 1974

[23] J. E. Velazco, J. H. Kolts and D. W. Setser, *J. Chem. Phys.*, **65**, 3468, 1976

[24] J. E. Velazco, J. H. Kolts and D. W. Setser, *Chem. Phys. Lett.*, **46**, 99, 1977

[25] J. H. Kolts and D. W. Setser, *J. Chem. Phys.*, **68** 4848, 1978

[26] J. E. Velazco, J. H. Kolts and D. W. Setser, *J. Chem. Phys.*, **69**, 4357, 1978

[27] K. Wagatsuma and K. Hirohawa, *Anal. Chem.*, **61**, 325, 1989

[28] K. Wagatsuma and K. Hirokawa, *Anal. Chim. Acta*, **306**, 193, 1995

[29] W. Fischer, A. Naoumidis and H. Nickel, *J. Anal. Atom. Spectrom.*, **9**, 375, 1994

[30] F. Tochibuko, Z. L. Petrovic, S. Kakuta, N. Nakuno and T. Makabe, *Jpn. J. Appl. Phys.*, **33**, 4271, 1994

[31] M. K. Levy, D. Serxner, A. D. Angstadt, R. L. Smith and K. R. Hess, *Spectrochim. Acta B*, **46**, 253, 1991

[32] W. W. Harrison and F. L. King, *Mass Spectrom. Rev.*, **9**, 285, 1990

[33] W. Vieth and J. C. Huneke, *Spectrochim. Acta B*, **46**, 941, 1993

[34] R. L. Smith, D. Serxner and K. R. Hess, *Anal. Chem.*, **61**, 1103, 1989

[35] P. L. Larkins, *Spectrochim. Acta B*, **46**, 291, 1991

[36] P. H. Ratcliff and W. W. Harrison, , *Appl. Spectrosc.*, **49**, 863, 1995

[37] W. S. Taylor, J. G. Dulak and S. N. Ketkar, *J. Am. Soc. Mass Spectrom.*, **1**, 448, 1990

[38] T. F. Gallagher, *Rydberg Atoms*, Cambridge University Press, 2005

[39] P. R. Klinsman and J. A. Rees, *J. Phys. E*, **3**, 444, 1970

[40] P. F. Knewstubb and A. W. Tickner, *J. Chem. Phys.*, **36**, 674, 1962

[41] P. F. Knewstubb and A. W. Tickner, *J. Chem. Phys.*, **36**, 684, 1962

[42] R. F. G. Meulenbroeks, A. J. van Beek, A. J. G. Helvoort, M. C. M. van de Sanden and D. C. Schramm, *Phys. Rev. E*, **49**, 4397, 1994

[43] M. J. de Graaf, R. Severens, R. P. Dahiya, M. C. M. van de Sanden and D. C. Schramm, *Phys. Rev. E*, **48**, 2098, 1993

[44] R. W. Smithwick III, D. W. Lynch and J. C. Franklin, *J. Am. Soc. Mass Spectrom.*, **4**, 278, 1993

[45] K. Jogan, A. Mizuno, T. Yamamoto and J. Chang, *IEEE Trans. Ind. Appl.*, **29**, 876, 1993

[46] I. Maezono and J. Chang, *IEEE Trans. Ind. Appl.*, **26**, 651, 1990

[47] D. D. Hsu and D. B. Graves, *Plasma Chem. Plasma Proc.*, **25**, 1, 2005

[48] J. Wang, G. Xia, A. Huang, S. L. Suib, Y. Hayashi and H. Matsumoto, *J. Catalysis*, **185**, 152, 1999

[49] C. Qi, D. Wei, T. Xumei, Y. Hui, D. Xiaoyan and Y. Yongxiang, *Plasma Sci. Technol.*, **8**, 181, 2006

[50] A. M. Ghorbanzadeh, S. Norouzi and T. Mohammadi, *J. Phys. D*, **38**, 3804, 2005

[51] Thermo Elemental Ltd. (formerly VG Elemental Ltd.), 3 Ion Path Road, Winsford, Cheshire, UK

[52] Baco Metals, Bridgend, South Wales, UK

[53] Goodfellows Metal Ltd., Cambridge, UK

[54] Bristol Fluid System Technologies Ltd. (Swagelok), Bristol, UK

[55] MKS Instruments Ltd., Cheshire, UK

[56] N. Harris, *Modern Vacuum Practice*, Mc-Graw-Hill, 1989

[57] BOC Edwards, Crawley, West Sussex, UK

[58] Glassman Europe Ltd., Basingstoke, Hampshire, UK

[59] RS Components Ltd., Corby, Northants., UK

[60] Tylan General (UK) Ltd., Swindon, Wiltshire, UK

[61] Meggit Avionics, Fareham, Hampshire, UK

[62] SGE Europe Ltd., Milton Keynes, UK

[63] PQ Vision v4.4 (Supplied by VG Elemental Ltd.)

[64] Kore Technology Ltd., Ely, Cambridgeshire, UK

[65] VG PlasmaQuad System Manual, Version 2b, 1989

[66] BOC Ltd., BOC Special Products, Guildford, Surrey, UK

[67] E. de Hoffman and V. Stroobant, *Mass Spectrometry: Principles and Applications 2nd edition*, John Wiley & Sons Ltd., 2002.

[68] D. R. Lide, *Handbook of Chemistry and Physics*, CRC Press, 1995

[69] M. Schmidt, R. Foest and R. Basner, *J. Phys. IV*, **8**, 231, 1998

[70] L. A. Pinnaduwage, W. Ding and D. L. McCorkle, *Appl. Phys. Lett.*, **71**, 3634, 1997

[71] W. Ding, D. L. McCorkle and L. A. Pinnaduwage, *J. Appl. Phys.*, **84**, 3051, 1998

[72] P. G. Datskos and L. A. Pinnaduwage, *Phys. Rev. A*, **55**, 4131, 1997

[73] K. Blom and B. Munson, *J. Am. Chem. Soc.*, **105**, 3793, 1983

[74] NIST library mass spectrum, *http://webbook.nist.gov/chemistry*

[75] J. R. Chapman, *Practical Organic Mass Spectrometry*, John Wiley & Sons, New York, 1985

[76] K. Newman and R. S. Mason, *Rapid Commun. Mass Spectrom.*, **20**, 2067, 2006

[77] K. Newman and R. S. Mason, *JAAS*, **19**, 1134, 2004

[78] K. Newman and R. S. Mason, *JAAS*, **20**, 830, 2005

[79] Y. Ikezoe, S. Matsuoka, M. Takebe and A. Vigiano, *Gas Phase Ion-Molecule Reaction Rate Constants Through 1986*, Mazuren Co. Ltd. Tokyo, Japan, 1987

[80] H. Hotop and A. Niehaus, *J. Chem. Phys.*, **47**, 2506, 1967

[81] K. Newman, R. S. Mason, D. R. Williams and I. P. Mortimer, *JAAS*, **19**, 1, 2004

Chapter 8

Analysis of Organic Vapours

8.1 Introduction

Chemical identification is very important in many fields including analytical, environmental, pharmaceutical, and nutritional chemistry[1]. A wide range of mass spectrometric techniques have been developed to allow quantitative and qualitative analysis. The technique chosen for analysis is dependent on a number of factors including; sample state (solid, liquid, gas), cost, molecular mass, required accuracy of qualitative or quantitative results, etc. It is desirable to develop a versatile technique which allows analysis of small quantities of a wide range of samples with fast sample interchange. Chemical speciation is also simplified by acquisition of elemental and structural (i.e fragmentation) information, as well as the parent molecular mass. However, most techniques do not provide all three.

The most common ionisation method is electron impact (EI) ionisation[2], in which collisions of fast electrons with gaseous molecules induce formation of fragment ions. Fragmentation patterns provide structural information and can allow identification of functional groups. However, molecular ion peaks are often observed in low abundance, if at all. The reproducibility, and unique character of EI results allows comparison of observed fragments with library spectra, enabling fast matching.

Inductively coupled plasma (ICP) mass spectrometry can be used to determine the elemental composition of molecules. The high power of the ICP source, often exceeding 1000 W, can induce complete atomisation and ionisation of the sample[2,3]. Reduction of the ICP power can enable detection of larger fragment ions[4], but molecular ion detection is not possible. ICP mass spectrometry is relatively versatile and has excellent sensitivity (sub parts per billion) for liquid or gaseous samples. Determination of molecular mass can be readily achieved using chemical ionisation (CI) mass spectrometry. CI is a 'soft' ionisation technique, and therefore little fragmentation is observed[5].

Glow discharge (GD) techniques have been widely utilised due to their application for direct analysis of solid samples[6]. Application of GD-MS and GD-OES (optical electronic spectroscopy) for analysis of both conducting and non-conducting samples is possible and allows determination of the sample material and trace impurities[7]. Depth profiling is also possible since sputtering of the cathode sample predominantly induces vaporisation of atoms from the surface layer. The recent development of pulsed GD ion sources enables determination of elemental, structural

and molecular ion information[1,2]. The authors also report on the application of this pulsed GD-MS as a detector for GC. The pulse cycle can be separated into three distinct temporal regions; the pre-peak, plateau region and post-peak[8,9]. It is thought, by the authors, that ions detected in the pre-peak range are mainly formed due to EI ionisation, and predominantly elemental ions are observed[2]. Ions in the plateau region are thought to be formed by a combination of EI, charge transfer and Penning ionisation (PI) processes[1,10,11], and therefore fragment and molecular ions are observed. After the GD pulse the plasma relaxes, and therefore in the post-peak region EI ionisation is not possible and PI, i.e. energy transfer from metastable states of the plasma gas, is proposed to dominate, yielding parent molecular ions. During a single experimental run for GC analysis of an organic mixture it was possible to obtain elemental, structural and parent molecular information for each compound[1]. Minimum detection limits for the compounds analysed were in the range 392 ng to 2.44 μg range.

Determination of molecular ion, fragment and elemental information could also be achieved using a tandem mass spectrometer system, wherein molecular ions are initially generated but fragmentation can be induced in an intermediate collision cell[12].

The FFGD ion source developed by Mason et al.[13-20] is low power (<5 W) and is therefore less destructive than the ICP technique. Newman[19,20] demonstrated the capability of this source to detect fragment or molecular ions by selectively tuning the bias applied to the ion exit, and investigated the use of the FFGD-MS technique as a detector for gas chromatography (GC). The sensitivity of the technique was determined to be high enough to allow speciation studies at sub-picogram levels. However, addition of the sample via GC is transient, and therefore an inlet system was designed to allow continuous introduction of organic vapour to the FAG plasma, in order to study the ionisation process in more detail under continuous flow conditions[19].

The inlet system (figure 7.3) was similar to that used by Mortimer[15] to transfer carbon tetrachloride vapour and allows addition of small quantities of organic and organometallic vapours from liquid samples with reasonably high vapour pressures. Variation of V_c over negative and positive ranges allowed potentially rapid and simple scanning of fragmentation patterns and molecular ions. This was done for only a limited range of molecules to demonstrate the principle. These included ethanol,

bromobenzene, fluorobenzene and 1-bromobutane, which were also studied in this investigation. In each instance it was observed that the degree of fragmentation increased with increasing negative ion exit bias, whereas application of a small positive ion exit bias allowed detection of the parent molecular ion with very little fragmentation.

Analysis of many of the compounds investigated in this chapter using GD ion sources has not been reported in the literature. Togashi et al.[21] report on the fragmentation of methanol, methane and benzene on addition to the afterglow of an ICP plasma. Charge exchange was determined to be the dominant process for ion formation, but Penning ionisation was also thought to be significant. Song et al.[22] analysed benzene via GD-ion trap mass spectrometry (ITMS). The ITMS mass spectrum illustrated in reference 22 displays the parent molecular and fragment ion peaks but little or no elemental data. Similar results were also presented for toluene and cyclohexane addition. Lewis and co-workers[1,2] analysed a number of the compounds studied in this investigation via pulsed GD-MS: methanol, 2-butanol, benzene and chlorobenzene. It was demonstrated that elemental, structural and parent molecular ion information could be gathered within the pre-peak, plateau and post-peak regions respectively (as discussed above).

CI has been widely used as an ion source for organic mass spectrometry[23] since parent molecular ion identification is readily achieved with very little fragmentation. One author illustrates significantly lower detection limits allowed by CI-ITMS compared with common CI and EI techniques for analysis of chloroaromatic compounds[24]

In this chapter the work has been extended to a much wider range of organic compounds. It is still limited by the inlet system and the mass range of the instrument. The most limiting feature of the inlet design is the length of gas line between the sample bulb and the GC oven, which was at room temperature and therefore allowed deposition of lower vapour pressure compounds on the surfaces. This was reflected in the lower ion intensities observed and interference in the subsequent experiments. Heating tape was used to raise the temperature, but no improvement was observed. Deposition within, and subsequent blockage of the silica capillary was also a problem. This appeared to be predominantly induced during addition of less volatile compounds, particularly phenol.

Work has also been carried out to determine whether the technique could be used to distinguish between isomers. Controlled fragmentation could induce different fragmentation patterns in molecules containing side chains or differing functional group positions on a benzene ring (i.e. ortho-, meta- or para-) depending on the relative bond energies. One further aim was to determine whether the technique could be used to distinguish between isomers better than EI or other fragmentation techniques. It was also of interest to determine the ionisation processes occurring e.g. EI, Penning, CID or ion-molecule.

In chapter 7, on addition of methane, it was concluded that application of a negative ion exit bias leads to CID in the ion exit sheath, and that the magnitude of the negative bias determines the degree of fragmentation observed. However, on application of zero or a positive ion exit bias, the parent molecular ion intensity maximum was observed. The Ar^+ and Ar_2^+ maxima were also observed for $V_c = 0$ V or a positive bias, and therefore it was concluded that ion formation occurred in the Rydberg gas plume outside the cell, and was indicative of the plasma composition and associative ionisation products formed in the expanding gas. This is in line with the Rydberg gas model presented in chapter 4.

8.2 Experimental Technique

A description of the second generation FFGD instrument and general operating and maintenance procedures are presented in chapter 7. The coaxial FFGD source was used in its extended form (figure 3.7) as for addition of secondary gases to the FAG plasma. The discharge voltage (V_d), source pressure (P) and argon residence time (τ) were kept constant throughout, although the discharge current (I_d) varied slightly due to cathode wear, and on application of a positive ion exit bias (V_c). V_d = 700 V, P = 1 torr and τ = 2.24 ms.

The continuous flow organic vapour inlet system shown in figure 7.3 was designed to allow analysis of organic compounds with relatively high vapour pressures. To prevent condensation and subsequent deposition of the compound within the inlet system or the source the majority of the inlet system and the source were heated. The FFGD source and the gas line between the GC oven and the source were heated to 473 K and the GC oven was set to heat the capillary to 373 K. The

source temperature was restricted by the upper temperature limit of the Viton O-rings used to seal the source.

The organic vapour was generated by injecting a liquid sample into the sample bulb. 0.1 to 0.2 μL of each liquid sample was injected through a 10 mm turnover type Suba-Seal. Helium gas flowing over the sample carried vapour into the FFGD source. A plug of quartz wool was placed in the base of the bulb to provide a large effective surface area, and therefore allowed rapid equilibration of the organic sample/helium mixture. Heating or cooling of the sample bulb using a water or ice-water bath allowed the vapour pressure of the sample to be varied. Decreasing the temperature of the sample allowed the vapour pressure to be lowered, therefore reducing the sample flow rate. The vapour pressures of the organic samples and the sample bulb temperature for each sample, where known, are given in table 8.1. The sample purities are illustrated in table 8.2.

Prior to injection of the sample, the bulb was isolated and evacuated via the incorporated pumping line. After injection of the sample, the 3 way valve was set to direct the helium carrier gas to the sample bulb and the bulb filled to a pressure of 800-1300 mbar, measured by an active strain gauge[30]. The mixture was then allowed to equilibrate for at least 15 minutes at the selected bulb temperature. The flow of helium gas into the sample bulb was controlled by a Negretti[31] needle valve in the same manner described in chapter 3. A helium flow rate of 1 sccm was chosen because it allows transfer of a suitable amount of the organic sample without significant disturbance to the plasma[19]. The sample flow rate from the bulb was controlled by a second needle valve, and the gas flows were balanced to maintain a constant sample bulb pressure in the range indicated above.

The sample flow rate was dependent on the helium gas flow rate, the vapour pressure of the organic sample and the sample bulb pressure. The flow rate (F_{sample}, in sccm) was calculated using equation 8.1 (assuming the sample liquid and vapour phases to be in equilibrium)[20]:

$$F_{sample} = \frac{VP_{sample}}{P_{bulb}} \times F_{He} \qquad \textit{(equation 8.1)}$$

where VP_{sample} is the sample vapour pressure (mbar) at a given temperature, P_{bulb} is the sample bulb pressure (mbar) and F_{He} is the carrier gas flow rate (in sccm). The

Compound	Vapour Pressure/mbar	Bulb Temperature/K
Benzene	104	294
Bromobenzene	4.4	294
1-Bromobutane	42.3	294
1-Bromopropane	53.7	273
1-Butanol	1.05	273
t-Butylchloride	139	294
Chlorobenzene	12.6	294
1-Chlorobutane	37.37	273
2-Chlorobutane	64.1	273
1-Chloropropane	150	273
1,3-difluorobenzene		294
Ethanol	15.75	273
Ethylene Glycol		348
Fluorobenzene	83.79	294
1-Iodopropane	46.73	294
Methanol	39.94	273
m-Fluorotoluene	23.25	294
p-Fluorotoluene	22.48	294
Phenol	15.3	348
1-Propanol	4.3	273
2-Propanol	9.5	273
1,3,5-trifluorobenzene	113	294

Table 8.1: Vapour pressures of the organic compounds at the operating sample bulb temperature

Vapour pressures obtained from NIST Standard Reference Database[25] and Knovel Critical Tables[26]. All values were calculated using the Antoine Equation:

$$\log_{10}(P) = A - \frac{B}{(T + C)}$$

where P = vapour pressure (in bar) and T = temperature (in K). The constants A, B and C were taken from the above databases. Values in red indicate that the temperature fell just outside the range of values for which constants A, B and C are available in the literature[25,26]. Unfortunately, calculations performed using A, B and C for different temperature ranges indicate no consistent vapour pressure and no consistent increase or decrease in the calculated vapour pressure when calculating in a higher temperature range. In the calculations performed variations of up to 13% for the vapour pressure (under the experimental conditions) were possible depending on the literature source. These values are therefore only rough estimates included to give an idea of how the vapour pressures of the compounds compare with others used in this investigation.

Compound	Purity	Supplier
Benzene	99.9	Sigma-Aldrich[27]
Bromobenzene	97	BDH[28]
1-Bromobutane	99	Sigma-Aldrich
1-Bromopropane	99	Sigma-Aldrich
1-Butanol	99.92	Fischer Scientific[29]
t-Butylchloride	99	Sigma-Aldrich
Chlorobenzene	99	Sigma-Aldrich
1-Chlorobutane	99	Sigma-Aldrich
2-Chlorobutane	98	Sigma-Aldrich
1-Chloropropane	98	Sigma-Aldrich
1,3-difluorobenzene	99	Sigma-Aldrich
Ethanol	99.99	Fischer Scientific
Ethylene Glycol	99	Sigma-Aldrich
Fluorobenzene	99	Sigma-Aldrich
1-Iodopropane	99	Sigma-Aldrich
Methanol	99.99	Fischer Scientific
m-Fluorotoluene	99	Sigma-Aldrich
p-Fluorotoluene	97	Sigma-Aldrich
Phenol	99.5	BDH
1-Propanol	99.5	BDH
2-Propanol	99.8	Fischer Scientific
1,3,5-trifluorobenzene	97	Sigma-Aldrich

Table 8.2 Sample purities and suppliers

flow rate, calculated from equation 8.1, was expressed as a percentage of the Ar discharge gas flow rate, given by equation 8.2.

$$\%\ Organic\ Sample = \left(\frac{F_{sample}}{F_{sample} + F_{Ar}} \right) \times 100 \quad (equation\ 8.2)$$

where F_{Ar} is the discharge gas flow rate (in sccm). The split gas flow technique detailed in chapter 7 could allow lower levels of sample addition but was not used in this investigation. Splitting of the gas flow requires the pressure of the gas transfer line to be maintained at the source pressure. This process can be very time consuming due to fluctuations in the pressure. Also, regular calibration of the split ratio would have been required to account for the reduction of the capillary internal diameter on any deposition of material. Thus, splitting the gas flow was deemed to be unnecessary.

The glass sample bulb consists of two sections separated by a ground-glass joint and sealed using silicone high vacuum grease. The design allows easier cleaning between samples over a one piece bulb. The bulb sections were cleaned using a 5% solution of Decon 90 solution, followed by successive rinses with distilled water and methanol (AnalR, Fischer Scientific)[29]. Silicone grease was reapplied, and the quartz wool replaced, between samples. The sample bulb was isolated from the gas inlet system for cleaning by closing the adjacent plug valve[32] and turning the three-way valve[32] to redirect the gas flow through the bypass line. Use of the bypass line allowed continuous flow of the helium carrier gas through the capillary and into the discharge cell.

The cathode material used could be selected to reduce interference due to formation of ions of the same mass. Vanadium (m/z = 51) was commonly used due to its relatively low erosion rate and minimal interference of its isotopes with species of interest. Due to the low natural abundance of ^{50}V (0.25%) this isotope caused very little interference. Copper was also used due to its very low cost and its availability within the laboratory. Copper has only two isotopes (m/z = 63 and 65), and therefore interference was again minimal. However, cathode ion masses for both copper and vanadium do correspond to fragment ions from larger molecules such as phenyl compounds (e.g. m/z = 51 corresponds to both C_4H_3 and ^{51}V). Due to the relatively poor mass resolution allowed by the quadrupole instrument it was not possible to

distinguish between the two ions. Due to the low cathode erosion rate at elevated temperatures, and the problems caused by repeated heating and cooling of the source (to allow maintenance), cathode replacement was commonly performed once a week, depending on use.

Ion intensities were normalised relative to the maximum intensity for each ion using equation 8.3;

$$Normalised\ Ion\ Intensity = \frac{X^+\ Intensity}{Maximum\ X^+\ Intensity} \times 100 \quad \textit{(equation 8.3)}$$

where X^+ is the ion for which the peak intensity is being normalised. This improves the clarity of the fragmentation patterns and allows all of the ions monitored to be displayed on the same scale regardless of their relative intensities.

8.2.1 Error Estimates

In this chapter the key feature of the results (figures 8.1, 8.2, 8.5, 8.6 and 8.9-8.17) is the fragmentation pattern for each organic molecule added, determined from the relative positions of the ion intensity maxima for the fragment and parent molecular ions. The voltages which correspond to the ion intensity maxima commonly have a reproducibility of ± 10 V, but the overall fragmentation patterns are not changed. The minor fluctuations in intensity off maxima are not reproducible, unless discussed in the results section, and no attempt has been made to rationalise these fluctuations. A typical run to run reproducibility for a single ion is given below.

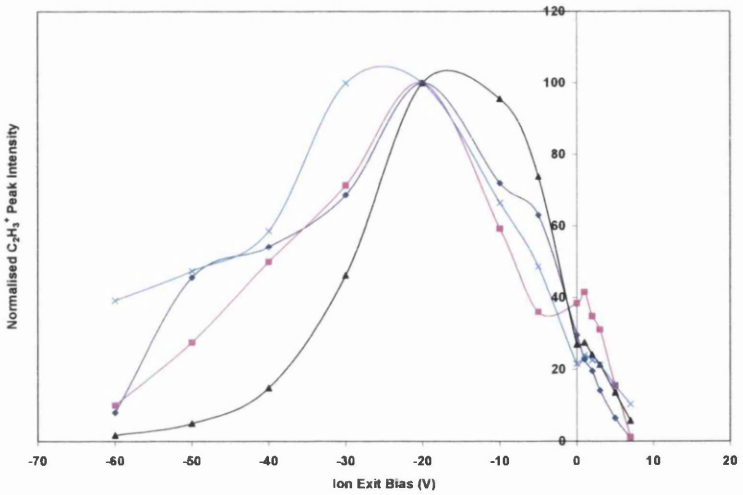

The diagram illustrates the run to run reproducibility of the normalised $C_2H_3^+$ peak intensity variation with V_c and the position of the ion intensity maximum. This example is relevant to figure 8.6.
(V_d = 700 V, P = 1 Torr, τ = 2.1 ms, addition of propanol)

8.3 Results

To determine the flexibility of the technique a wide range of compounds with different vapour pressures were analysed (table 8.1). It was possible to analyse low vapour pressure species such as terpenes and phenol by heating the sample bulb, but due to deposition of sample material within the gas line sustained gas flow or cleaning of the gas line was required to remove this material. Thus, the experiment turnaround time was significantly increased.

8.3.1 The Discharge Related Ions

The variation of the major discharge related ions with V_c was discussed in section 7.4.1 and illustrated in figure 7.7. Figure 8.1a illustrates the variation of the major discharge related ions with V_c on addition of methanol. The addition of methanol, or any of the other samples analysed, did not significantly influence the pattern of discharge ion variation, although it did have a significant effect on the ion intensities. The patterns and relative ion intensities observed varied slightly depending on the ion for which the ion optic lenses were tuned.

It is significant that molecular ion (Ar_2^+, H_2O^+, etc) detection maxima were observed on application of a small negative or even positive V_c. As discussed in previous chapters, this is probably due to ionisation of molecular Rydberg species outside the FFGD cell, rather than extraction of ions from the source. It is believed that application of a high negative V_c induces collision induced dissociation (CID) within the thin cone sheath, and therefore a greater degree of fragmentation occurs. On application of a small positive V_c, positive ions formed within the source cannot be sampled from the plasma due to the repulsive field around the ion exit, and therefore the ions detected must have been formed within, or beyond the ion exit orifice.

A Rydberg gas mechanism was proposed in chapter 4 which can account for the detection of positive ions on application of both negative and positive ion exit biases. On application of a negative ion exit bias, ions are formed by field ionisation in the cone sheath field and are subsequently accelerated across the field to the ion exit orifice. Field ionisation occurs in a similar manner on application of a small positive ion exit bias. However, on application of a low positive V_c there is a positive field gradient to the cone surface, and therefore cations are repelled back into the bulk plasma. Therefore, ions can only form via ionisation of Rydberg atoms in the intermediately pumped region of the mass spectrometer by field-, spontaneous- (pressure ionisation due to the low Rydberg density – see section 2.7) or auto-ionisation. It was concluded from the increase in the extraction lens bias required to maximise ion detection on application of 0 V or a positive V_c (chapter 7) that field ionisation is the dominant mechanism under these conditions. The kinetic energy, as determined from the pole bias voltage, also indicates that ionisation occurred outside the source under these conditions, but occurred within the source on application of a negative V_c.

Figure 8.1b illustrates the variation of the major discharge related ion intensities on addition of methanol over a wider V_c range. The range V_c = -60 to +17 V has already been discussed. In chapter 4 it was illustrated how the character of the cone sheath field changes on application of a higher positive V_c, allowing a fraction of the ions formed within the sheath to be extracted. It was also described how ions can be formed from the recombining plasma that results. Figure 8.1b shows that when V_c was greater than +20 V the ion intensities began to increase again, with several ions reaching their maximum intensity when V_c was +60 V. This is believed to be within

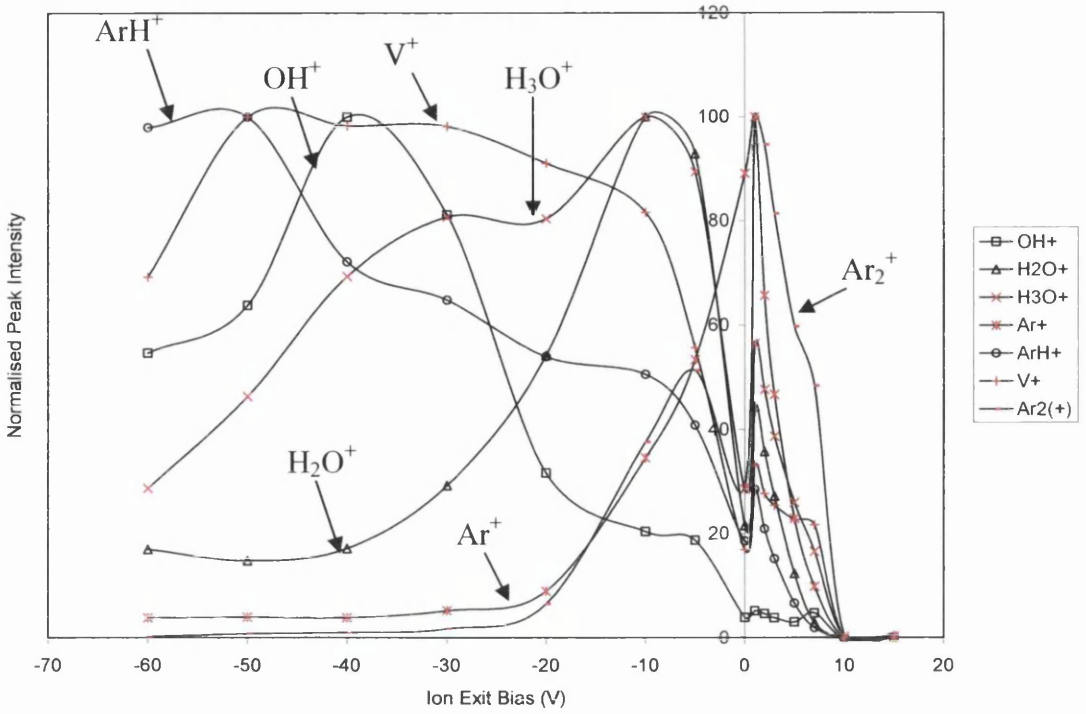

Figure 8.1a: Variation of normalised discharge and water related ion intensities with applied V_c

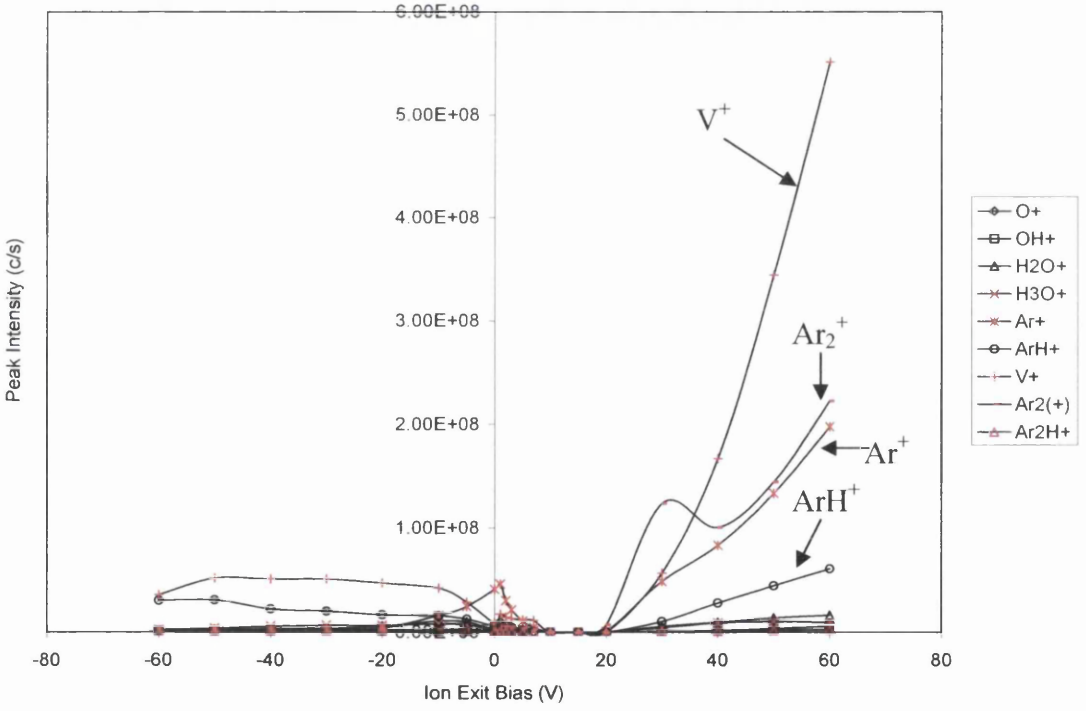

Figure 8.1b: Variation of discharge and water related ion intensities with applied V_c
(V_d = 700 V, P = 1 Torr, τ = 1.39 ms, methanol addition = 94.2 ppm, tuned for $^{51}V^+$)

the range of conditions under which EI ionisation occurs within the cone sheath, with creation of a negative field at the cone surface. The extraction lens and pole bias voltages were very similar to those used under low positive V_c conditions, indicating that field ionisation of Rydberg states in the neutral Rydberg gas plume was the dominant ionisation mechanism.

It can be seen in figure 8.1b that the V^+ ion signal increased the most on application of a high positive V_c. Assuming ion formation to occur via field ionisation of highly excited (Rydberg) state species one might expect Ar^+ to be the most abundant ion observed since the argon discharge gas constitutes the majority of the flowing plasma. However, the level of Ar_2^+ detection was also higher than that for Ar^+ at high positive V_c. Three mechanisms for Ar_2^+ formation have been proposed. The Hornbeck-Molnar[33] process (equation 8.4) is a two-body collision process, in which at least one of the argon atoms is in an excited state. The second is a three-body process[34,35] involving two ground state atoms and either an argon ion (equation 8.5) or Rydberg state species (equation 8.6).

$$Ar^* + Ar^{(*)} \rightarrow Ar_2^+ + e^- \qquad \textit{(equation 8.4)}$$

$$Ar^+ + 2Ar \rightarrow Ar_2^+ + Ar \qquad \textit{(equation 8.5)}$$

$$Ar^R + 2Ar \rightarrow Ar_2^+ + Ar + e^- \qquad \textit{(equation 8.6)}$$

It is possible that a collision between argon atoms in the ground and Rydberg states could lead to the formation of a short-lived excited neutral dimer which could traverse the ion exit field. Field ionisation of this excited state could explain the high levels of Ar_2^+ observed on application of a positive V_c (equation 8.7). A similar mechanism, shown in equation 8.8, is the likely source of Ar^+ from its Rydberg atom precursor.

$$Ar^R + Ar \rightarrow Ar_2^R \rightarrow Ar_2^+ + e^- \qquad \textit{(equation 8.7)}$$

$$Ar^R + Ar \rightarrow Ar_2^R \rightarrow Ar^+ + Ar + e^- \qquad \textit{(equation 8.8)}$$

8.3.2 Alcohols

A range of alcohols were selected because of their ready availability within the laboratory. Due to the high sensitivity of the technique, most of the alcohol samples

investigated were cooled to 273 K by immersing the sample bulb in an ice/water bath to reduce their vapour pressures. However, due to their low vapour pressures at room temperature, phenol and ethylene glycol were heated to 348 K.

8.3.2.1 Methanol

The variation of the normalised methanol related ion intensities with V_c is illustrated in figure 8.2a. As observed by Newman[19] and on addition of methane (section 7.4.6), the degree of fragmentation increased with increasing negative V_c, and parent molecular ion detection was optimised on application of a small positive V_c. Due to the poor mass discrimination of the quadrupole mass filter (QMF) it is not possible to distinguish between ions of equal mass, and therefore it is unclear whether the ions observed at m/z = 29 correspond to CHO^+ or $C_2H_5^+$. Formation of larger hydrocarbon ions has previously been reported on addition of methane[13,15,19] (section 7.4.6) with $C_2H_3^+$ and $C_2H_5^+$ the major C_2 ions. On addition of methanol it is likely that both CHO^+ and $C_2H_5^+$ ions were formed.

Figure 8.2b illustrates the variation of the methanol related ion intensities with V_c, over an extended range. As observed for the major discharge ions (figure 8.1) all ion signals were quenched above V_c = +10 V but increased sharply on application of V_c > +20 V. This effect has been discussed in section 8.3.1 for the detection of the major discharge related ion species. Very little fragmentation was observed on application of a high positive V_c. It is significant that the intensities of the molecular and pseudo-molecular ion maxima occurred when V_c was ≥ +30 V. In fact, when V_c was +30 V, the molecular ion peak intensity was approximately double that when V_c was +3 V. In the previous study by Newman[19], detection limits for analysis of organic and organometallic vapours were estimated on application of a small positive V_c. Clearly, in this case the detection limit would be improved if V_c was set to +30 V.

The variation of the degree of fragmentation can also be observed in the spectra illustrated in figure 8.3. The discharge related ions OH^+, H_2O^+, H_3O^+, Ar^{2+}, Ar^+, ArH^+, V^+, Ar_2^+ and Ar_2H^+ have been removed to improve the clarity of the spectra. When V_c was -60 V CH_x^+ ions dominated the spectrum. At -30 V CH_3^+ was the major ion species, but higher mass species such as CH_3O^+ were more abundant than at V_c = -60 V. When V_c was +2 V CH_3^+ was the only significant CH_x^+ (x = 1 to 3) ion with M^+, $[M+H]^+$ and $[M-H]^+$ (where M is methanol) the major ions.

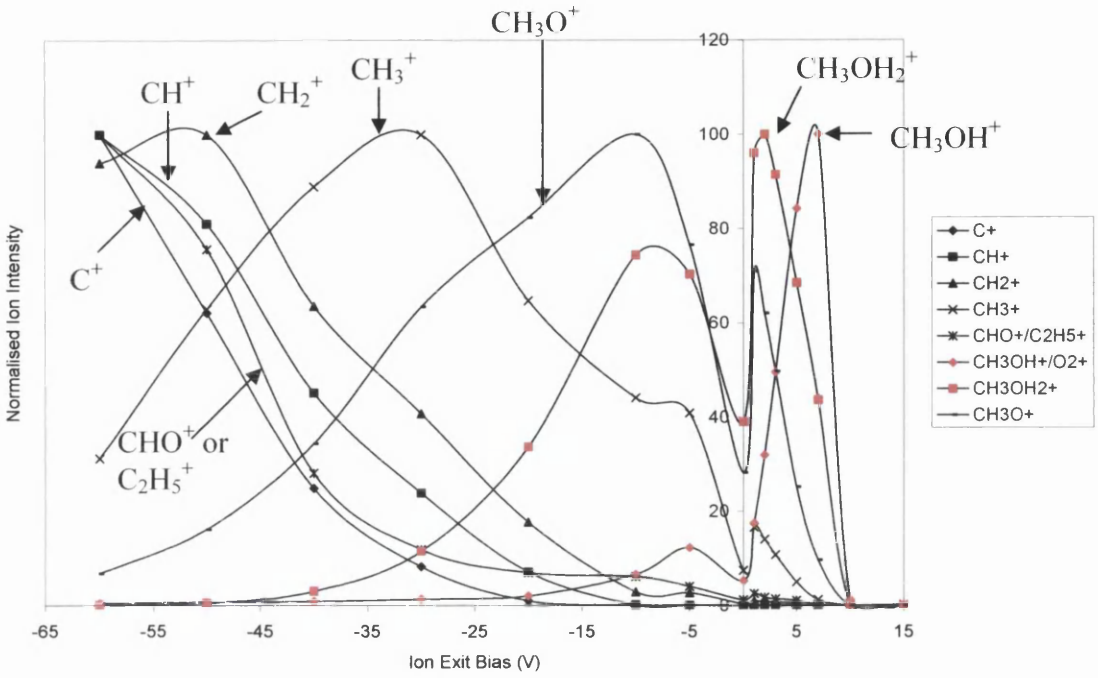

Figure 8.2a: Variation of normalised methanol related ion intensities with applied V_c (this spectrum has been reproduced many times with very little deviation)

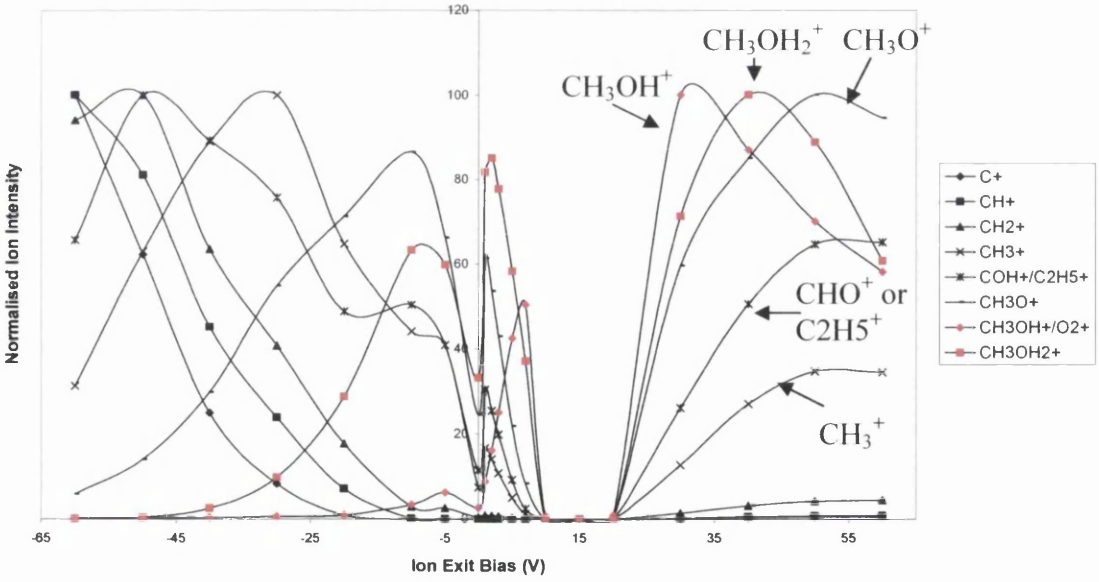

Figure 8.2b: Variation of normalised methanol related ion intensities with applied V_c
(V_d = 700 V, P = 1 Torr, τ = 1.39 ms, methanol addition = 94.2 ppm, tuned for $^{51}V^+$)

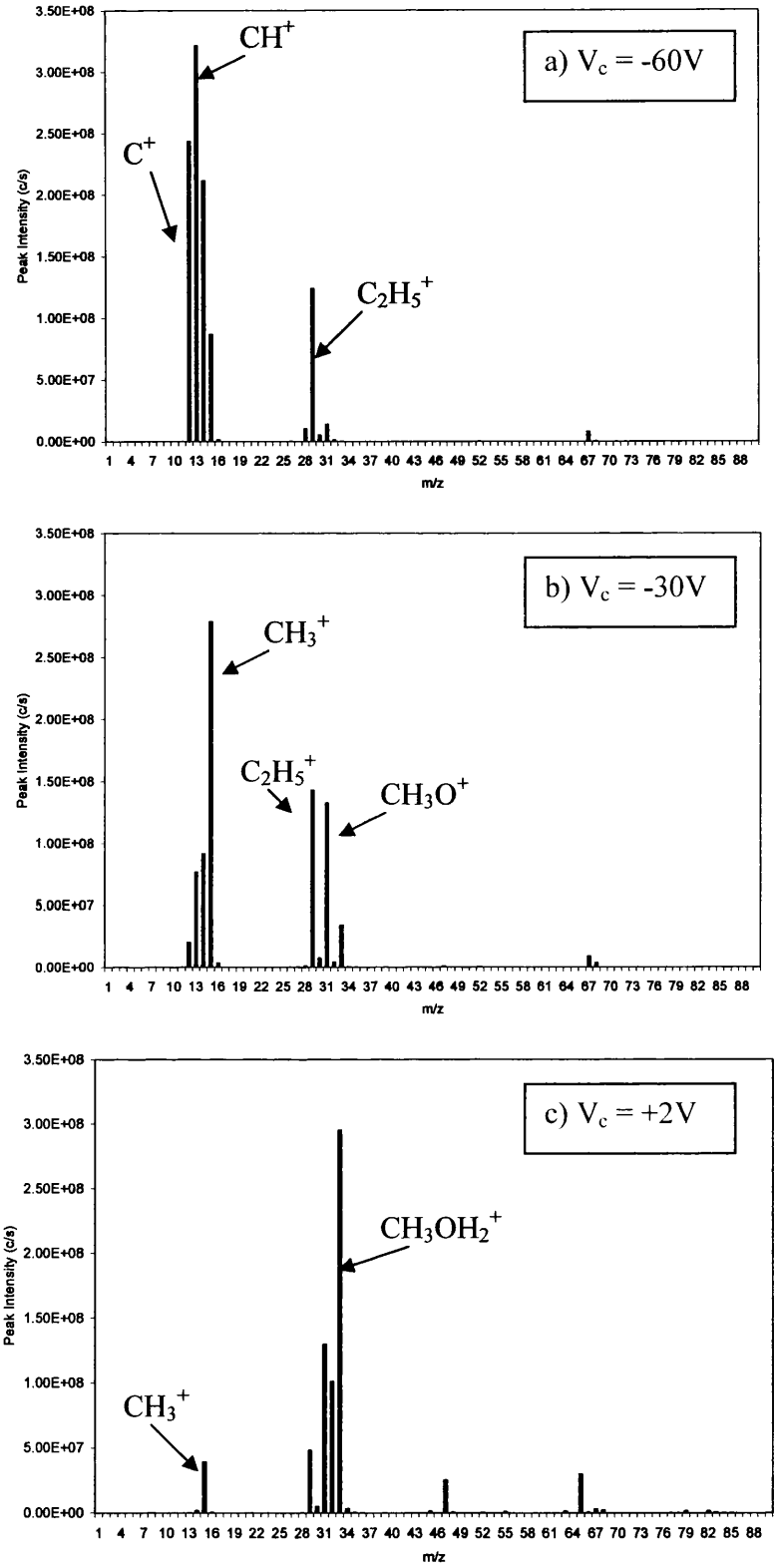

Figure 8.3: Methanol FFGD mass spectra dependence on the ion exit bias (V_d = 700 V, P = 1 Torr, τ = 1.39 ms, methanol addition = 94.2 ppm, tuned for $^{51}V^+$)

The 70 eV EI spectrum for methanol is illustrated in figure 8.4[25]. It is clearly distinguishable from each of the spectra shown in figure 8.3. The degree of fragmentation on application of V_c = -60 or -30 V (figures 8.3 a and b) is far greater than that induced by EI ionisation. Also, the maximum ion signal observed on application of V_c = +2 V was $CH_3OH_2^+$, which is not seen in the EI spectrum. Therefore, EI is not responsible for the observed fragmentation and ionization.

8.3.2.2 Ethanol

Figure 8.5a illustrates the variation of the major ethanol related ion species with V_c. It is clear that, as observed on addition of methanol, the degree of fragmentation was increased with increasing negative V_c and that detection of the molecular ion species was favoured on application of a small positive bias. In this example, the parent molecular ion signal was very low for all negative values of V_c, but was significantly enhanced on application of a small positive bias, reaching a maximum when V_c was +7 V. The fragmentation pattern in figure 4.5a is not as clear as was observed for methanol. In fact, ions assumed to be $C_2H_5^+$ and CH_2OH^+ were both observed at high intensity on application of a small positive V_c as well as a negative V_c. However, results of repeat runs indicate that clear fragmentation patterns can be observed with ethanol. One such result is shown in figure 4.5b, but whilst this level of clarity is common for the majority of the compounds analysed, this is not true for ethanol.

As observed on addition of methanol, when V_c was between +10 and +17 V all ion intensities were very low (figure 4.5c). Above +17 V the ion signals began to increase again, with the majority of the ions plotted reaching their maximum intensity when V_c was between +40 and +60 V. Formation of larger fragment ions and the molecular ion was strongly favoured under high positive V_c conditions. As described above, under high positive V_c conditions, the detection limits for GC analysis could be significantly improved. In this case, the $C_2H_5O^+$ peak intensity was approximately a factor of 3 higher when V_c = +60 V compared with that when V_c = +5 V, and the parent molecular ion intensity when V_c = +60 V was more than double that when V_c = +7 V.

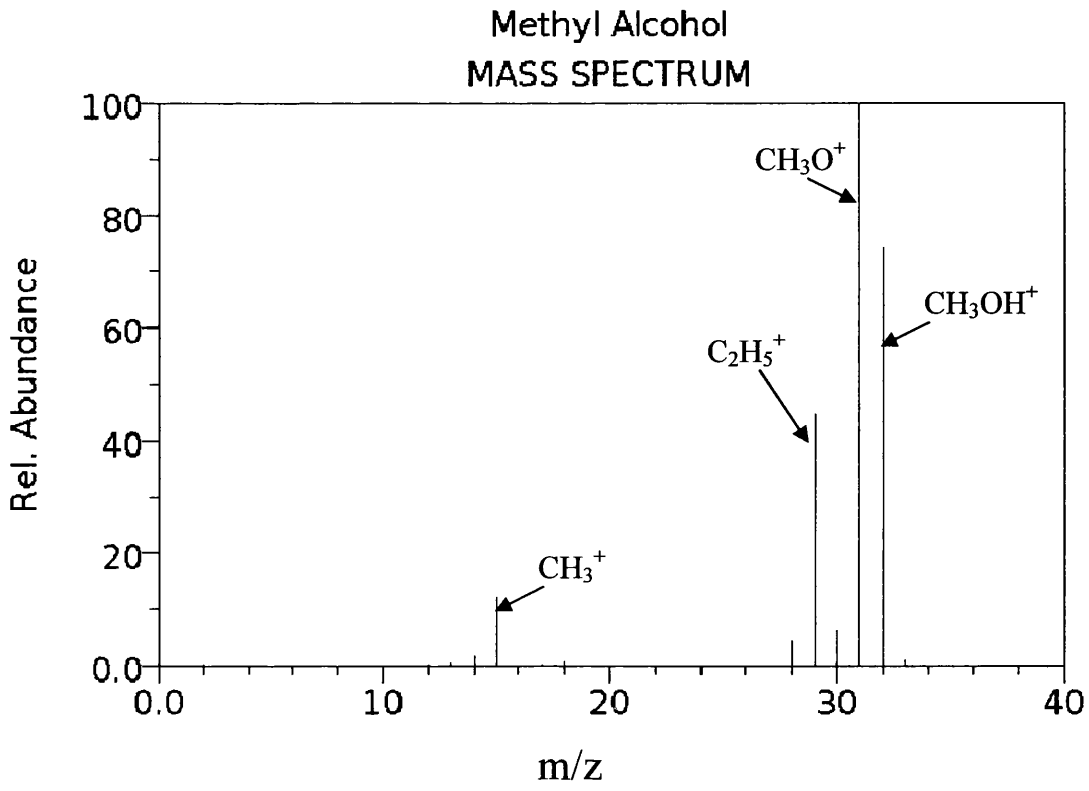

Figure 8.4: 70 eV electron impact spectrum of Methanol[25]
(http://webbook.nist.gov/chemistry)

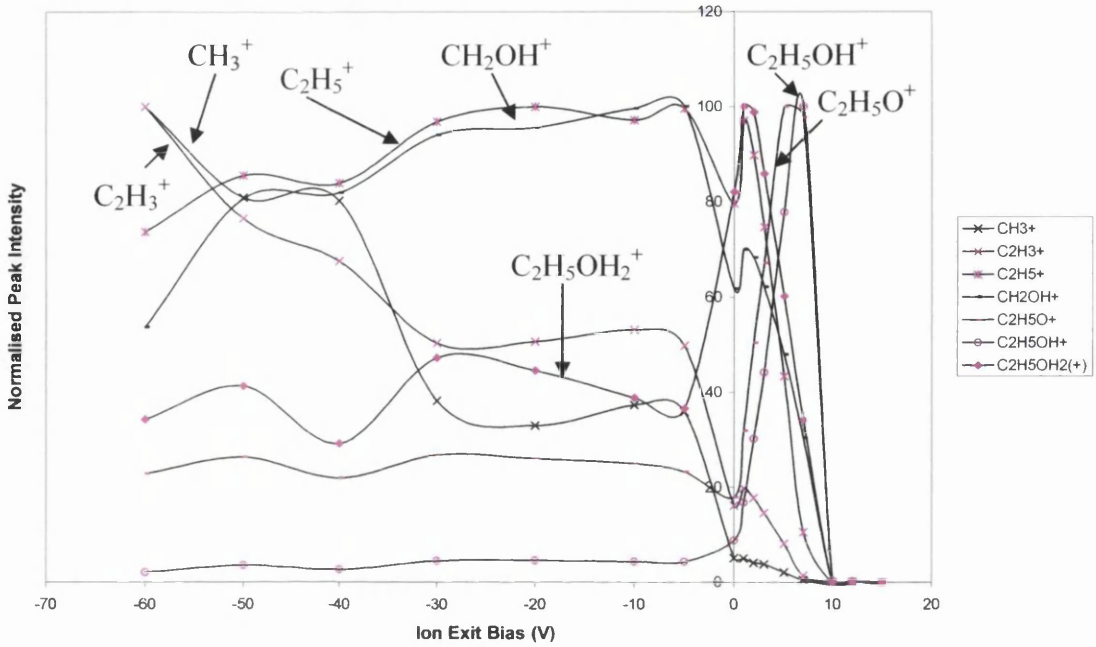

Figure 8.5a: Variation of normalised ethanol related ion intensities with applied V_c

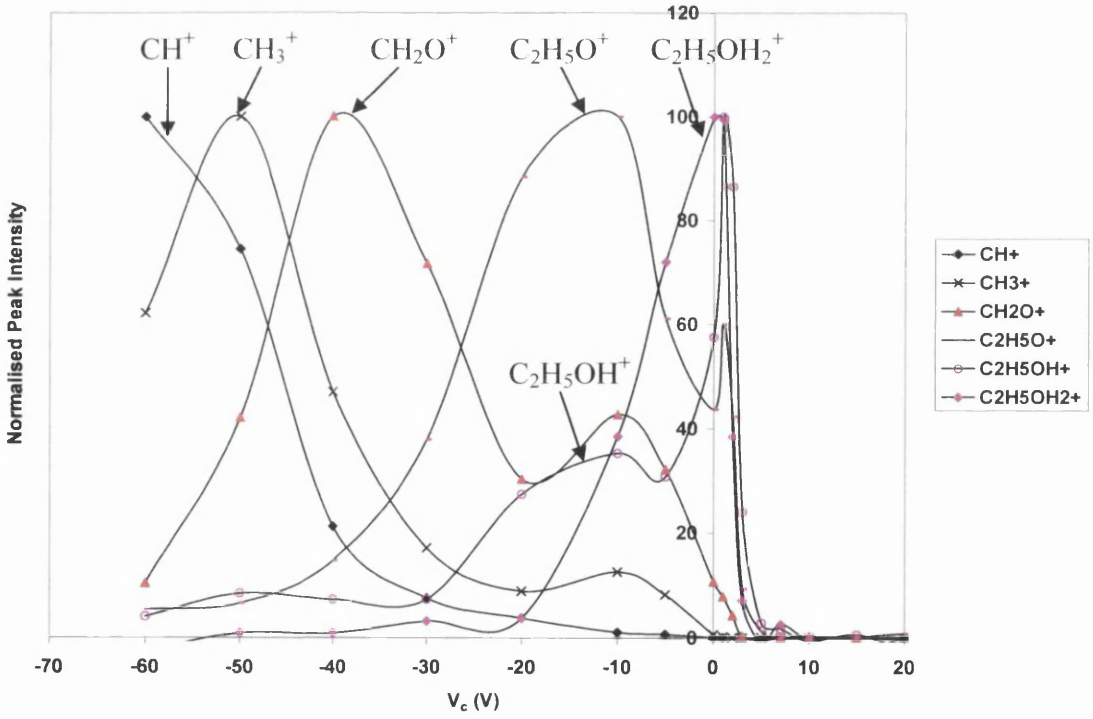

Figure 8.5b: Variation of normalised ethanol related ion intensities with applied V_c. Illustrates that results on addition of ethanol can follow the same fragmentation pattern as for the majority of compounds added to the FAG plasma)
(V_d = 700 V, P = 1 Torr, τ = 1.39 ms, ethanol addition = 37.2 ppm, tuned for $^{51}V^+$)

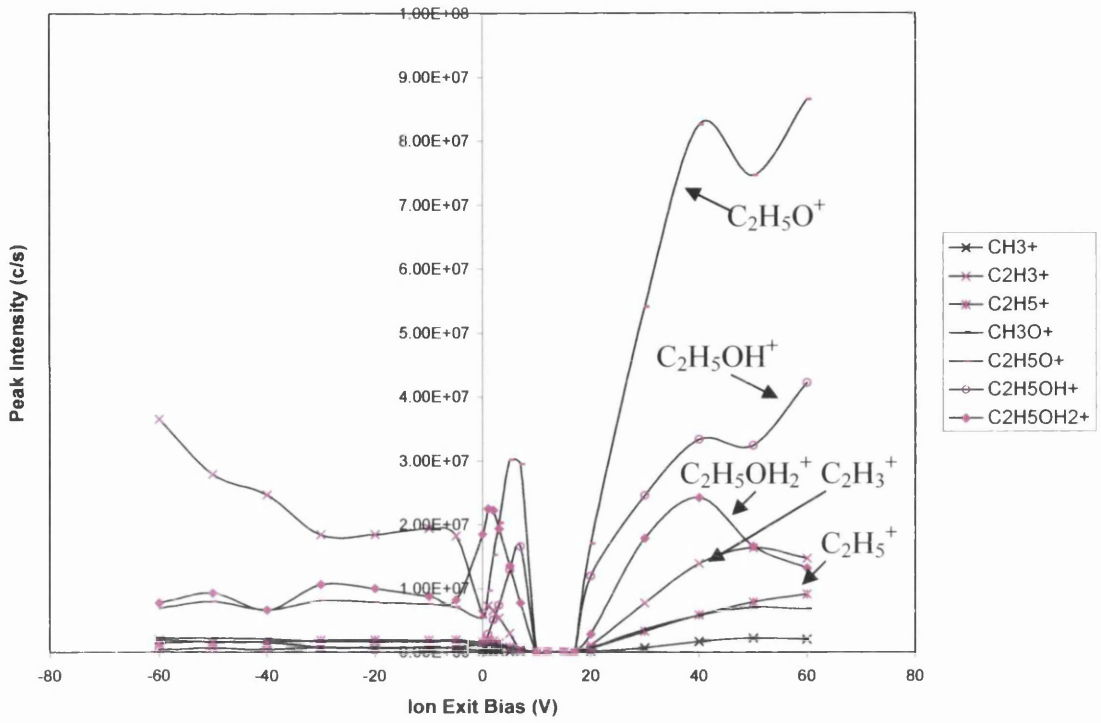

Figure 8.5c: Variation of ethanol related ion intensities with applied V_c (V_d = 700 V, P = 1 Torr, τ = 1.39 ms, ethanol addition = 37.2 ppm, tuned for $^{51}V^+$)

8.3.2.3 1- and 2-Propanol

One challenge for organic speciation is to differentiate between isomers. This may be possible due to the slight differences between bond energies in branched and straight chain molecules. However, a high energy environment such as a GD plasma may not afford the level of control required to distinguish between the two.

Figures 8.6a and b illustrate the variation of the major ion species normalised peak intensities with V_c. The only significant difference between the fragmentation spectra of the two compounds is the variation of the $C_2H_3^+$ ion intensity. On addition of 1-propanol the maximum $C_2H_3^+$ intensity was observed when V_c was -40 V, whereas, on addition of 2-propanol the maximum $C_2H_3^+$ intensity was observed when V_c was – 20 V. However, the maximum $C_2H_3^+$ intensity has been observed over a range of negative values of V_c on addition of 2- and 1-propanol, as indicated in figure 8.6. That being said, the degree of fragmentation was always seen to increase with increasing negative V_c, with the parent molecular ions reaching their maxima for a small positive V_c.

Figures 8.7 and 8.8 illustrate spectra observed for 1- and 2- propanol respectively. As above, the major discharge related ions have been removed. There are a number of differences between the spectra which could be indicative of the bond energies in each molecule. Comparison of figures 8.7b and 8.8b clearly shows that the relative intensities of $C_2H_3^+$ and the peak at m/z = 32 (CH_3OH^+ or O_2^+) are dependent on the isomeric form of propanol. Also, the formation of $C_2H_5O^+$ appears to be favoured on addition of 2-propanol under the same conditions. On application of V_c = +3 V, the most abundant mass detected on addition of 1-propanol was m/z = 32, whereas for 2-propanol the most abundant ion detected was $C_2H_5O^+$. The differences may, in part, be due to the higher addition of 2-propanol to the FAG plasma. However, this is unlikely to be solely responsible.

8.3.2.4 1-Butanol

Figure 8.9 illustrates the variation of a selection of butanol related ion normalised peak intensities with V_c. As with the previous compounds, the degree of fragmentation increases with increasingly negative values of V_c. However, unlike the previous examples illustrated, the parent molecular ion reached a maximum intensity

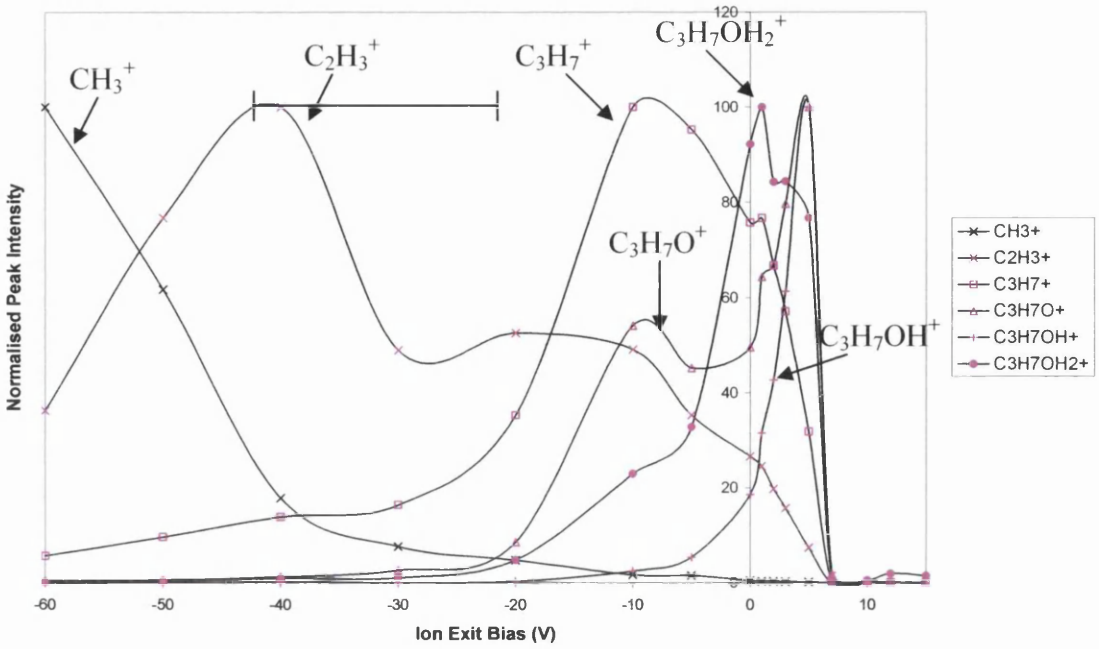

Figure 8.6a: Variation of normalised propan-1-ol related ion intensities with applied V_c

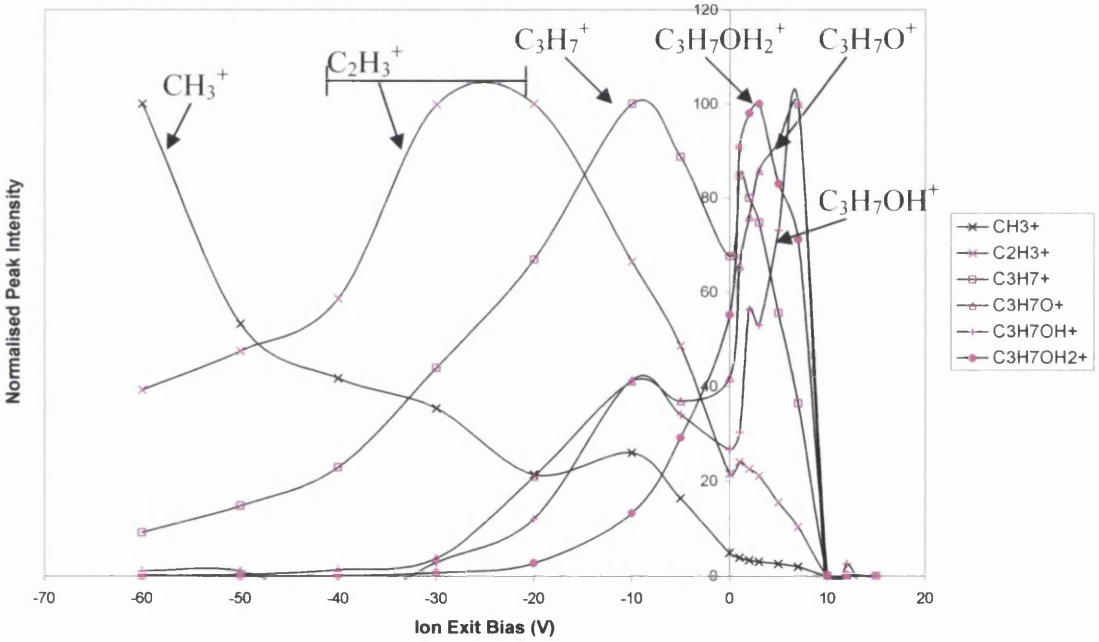

Figure 8.6b: Variation of normalised propan-2-ol related ion intensities with applied V_c
(V_d = 700 V, P = 1 Torr, τ = 1.39 ms, propan-1-ol addition = 11 ppm, propan-2-ol addition = 21.8 ppm, tuned for $^{51}V^+$)

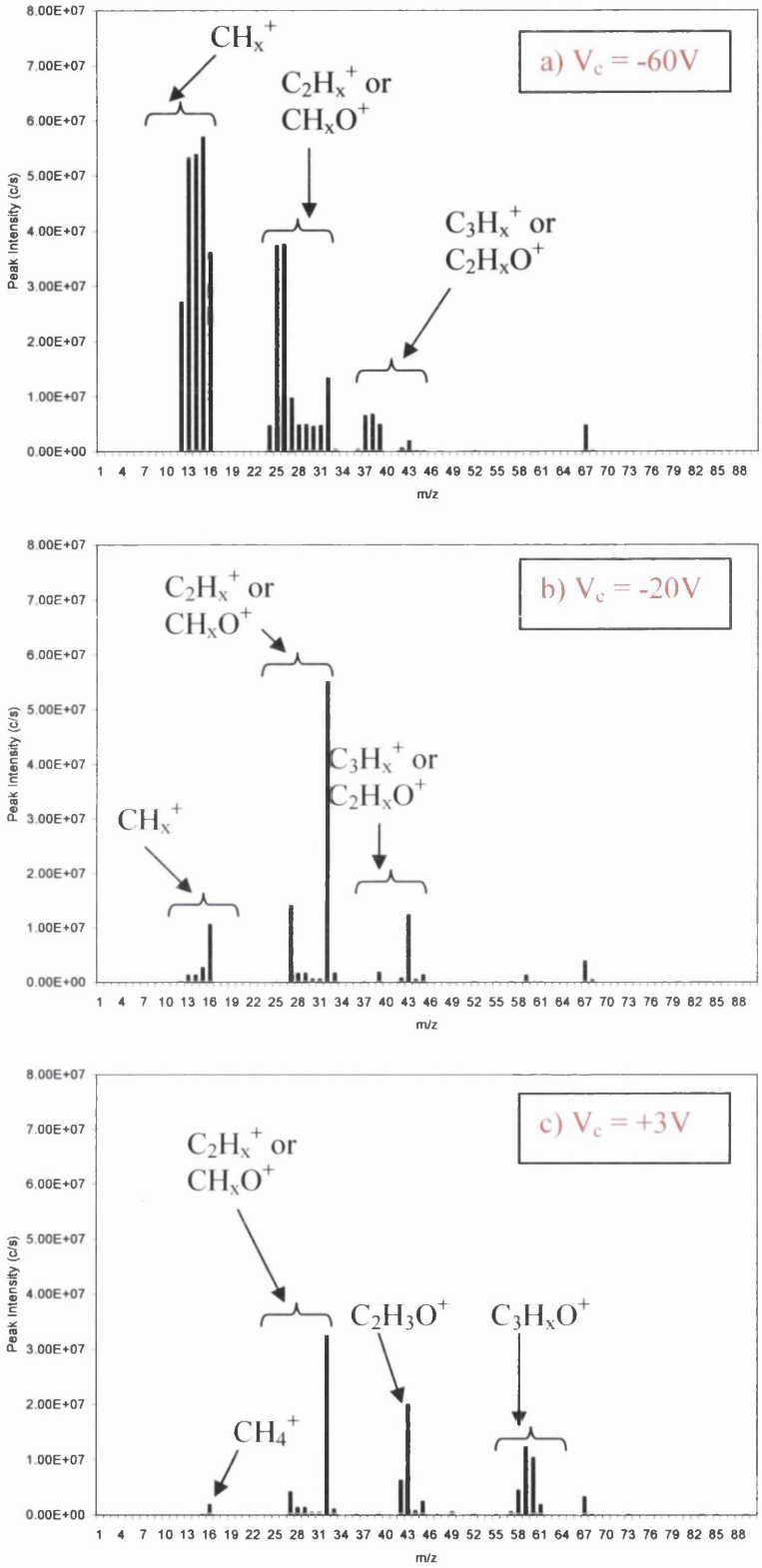

Figure 8.7: Propan-1-ol FFGD mass spectra dependence on the ion exit bias (V_d = 700 V, P = 1 Torr, τ = 1.39 ms, propan-1-ol addition = 11 ppm, tuned for $^{51}V^+$)

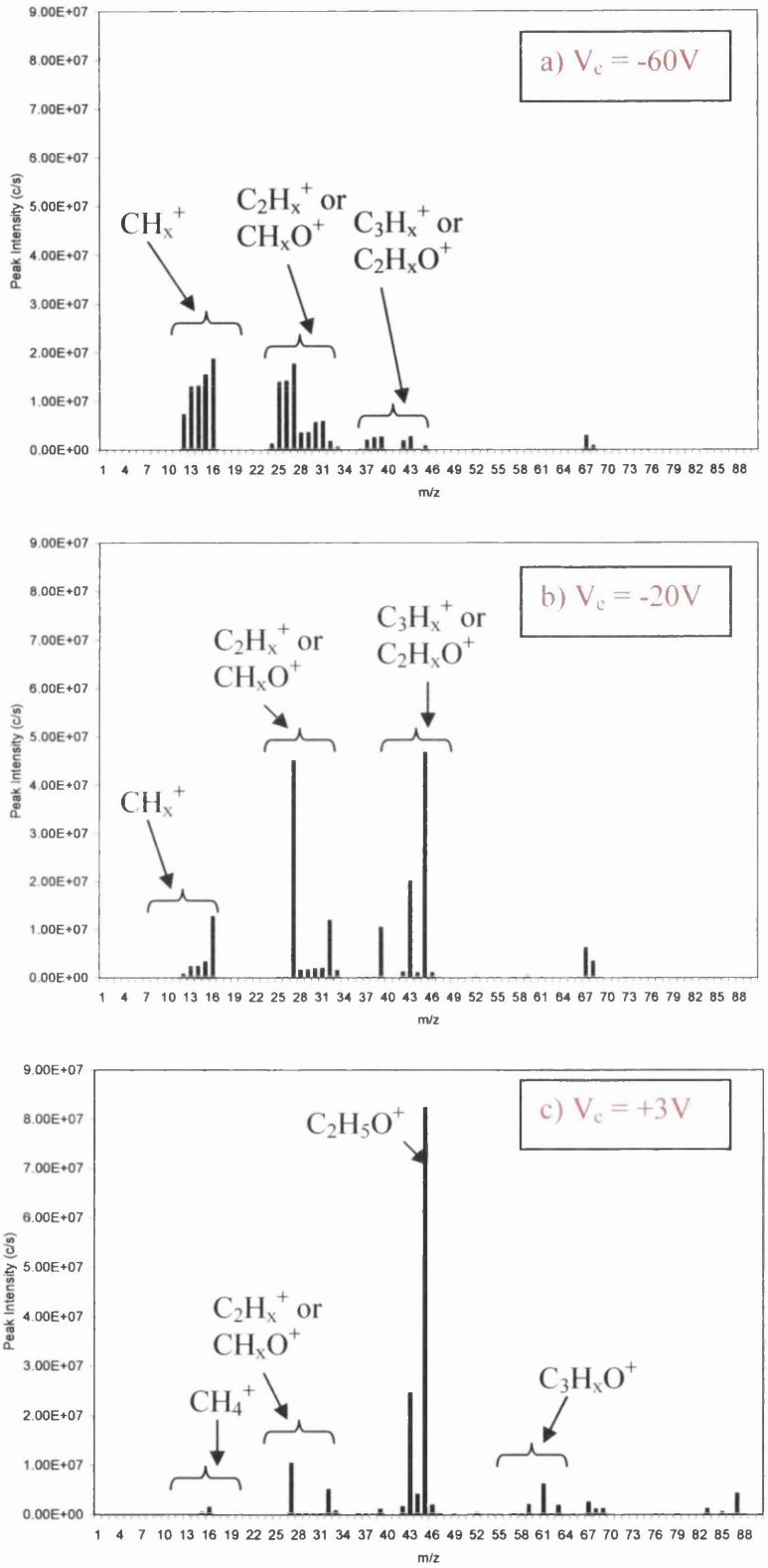

Figure 8.8: Propan-2-ol FFGD mass spectra dependence on the ion exit bias (V_d = 700 V, P = 1 Torr, τ = 1.39 ms, propan-2-ol addition = 21.8 ppm, tuned for $^{51}V^+$)

when V_c was 0 V and the $[M-H]^+$ ion maxima occurred when V_c was -5 V. Similar results had been observed on addition of ethanol and methanol and small variations were therefore expected.

8.3.2.5 Addition of Ethylene Glycol and Phenol

It has been previously stated that addition of lower vapour pressure compounds was problematic due to the necessity of heating the sample to allow adequate addition for mass spectrometric analysis. In particular, on addition of phenol the deposition of sample within the transfer line prior to the GC oven and within the heated capillary led to both undesirable signals in subsequent experimental runs and blockage of the capillary.

Prior to this discovery, a number of less volatile compounds were run to determine the range of compounds which can be analysed using this technique. Two such compounds were ethylene glycol and phenol. By heating the sample bulb to 348 K it was possible to analyse both compounds, and the results are illustrated in figure 8.10a and b respectively. As in previous examples, the degree of fragmentation increased with increasing negative V_c. However, each figure illustrates differences compared with the previous examples. On addition of ethylene glycol, the parent molecular ion was not observed above background noise levels for any value of V_c. On addition of phenol the parent molecular ion was observed but all ion maxima were observed on application of a negative V_c, with the majority of the ion signals quickly quenched on application of a positive bias. One possible reason for the observed maximum on application of a negative bias is that ionisable Rydberg molecules exit the source as dimers on application of a positive V_c. This has not been confirmed for phenol, but results on addition of benzene (section 8.3.3) indicate that this is likely.

8.3.2.6 Discussion

With the exception of ethanol, a clear increase in fragmentation with increasing negative V_c was observed. It has been shown that the ions observed on addition of methanol were not formed by EI ionisation. The electron impact mass spectra for FFGD and EI do not match under any of the conditions investigated. Also, due to the high argon gas flow, one would expect the Ar^+ ion to be the dominant ion under

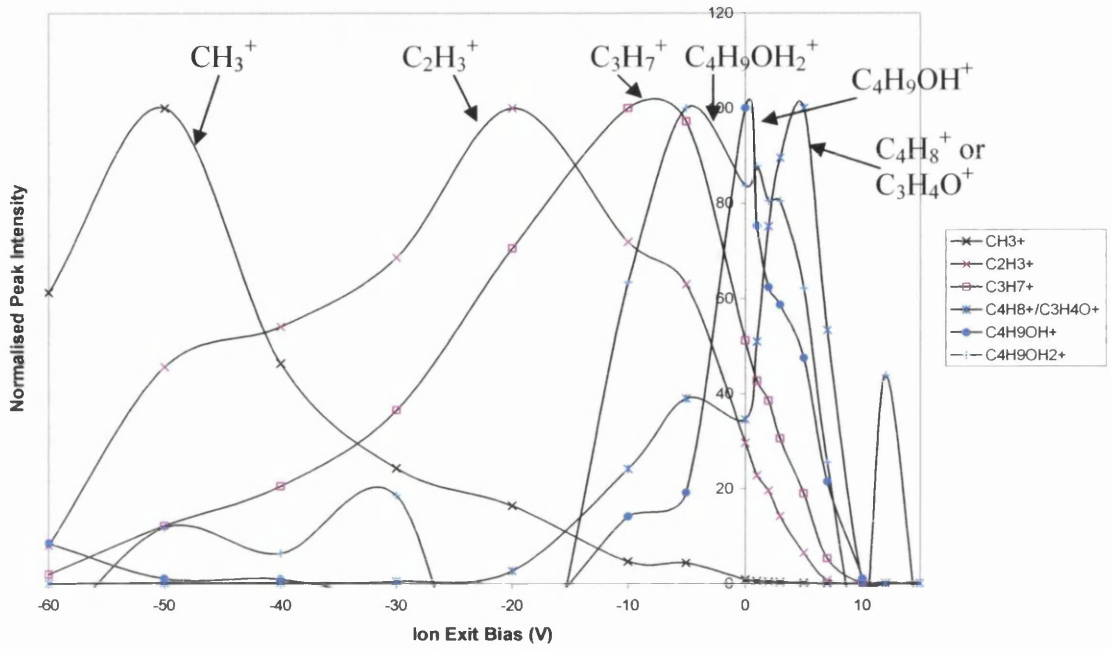

Figure 8.9: Variation of normalised butan-1-ol related ion intensities with applied V_c.
(V_d = 700 V, P = 1 Torr, τ = 1.39 ms, butan-1-ol addition = 2.43 ppm, tuned for $^{51}V^+$)

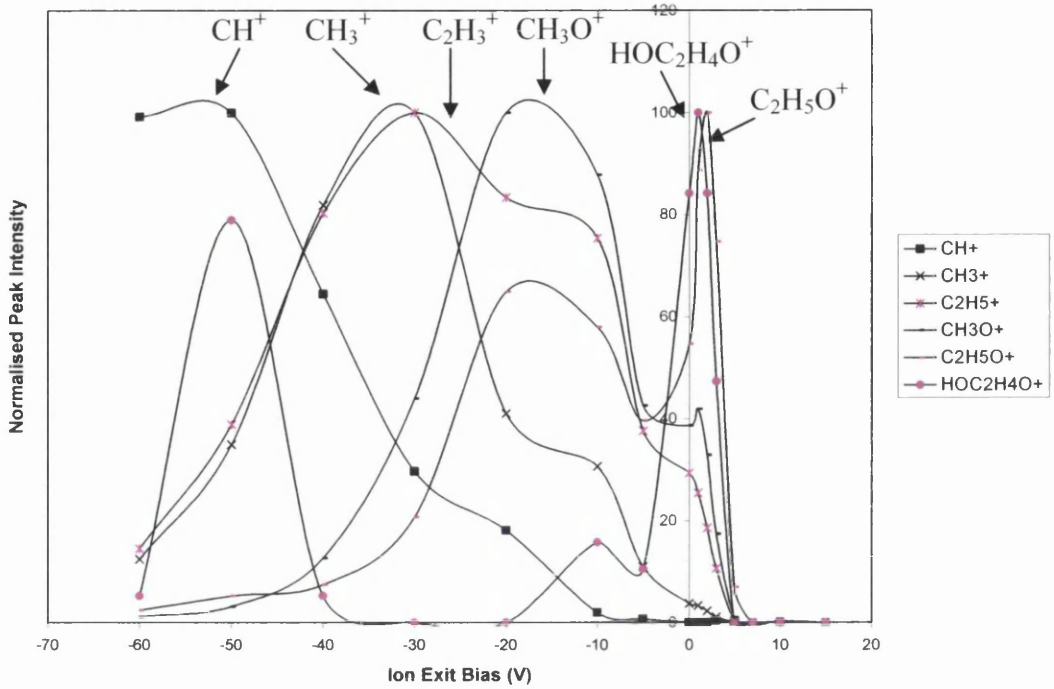

Figure 8.10a: Variation of normalised ethylene glycol related ion intensities with applied V_c

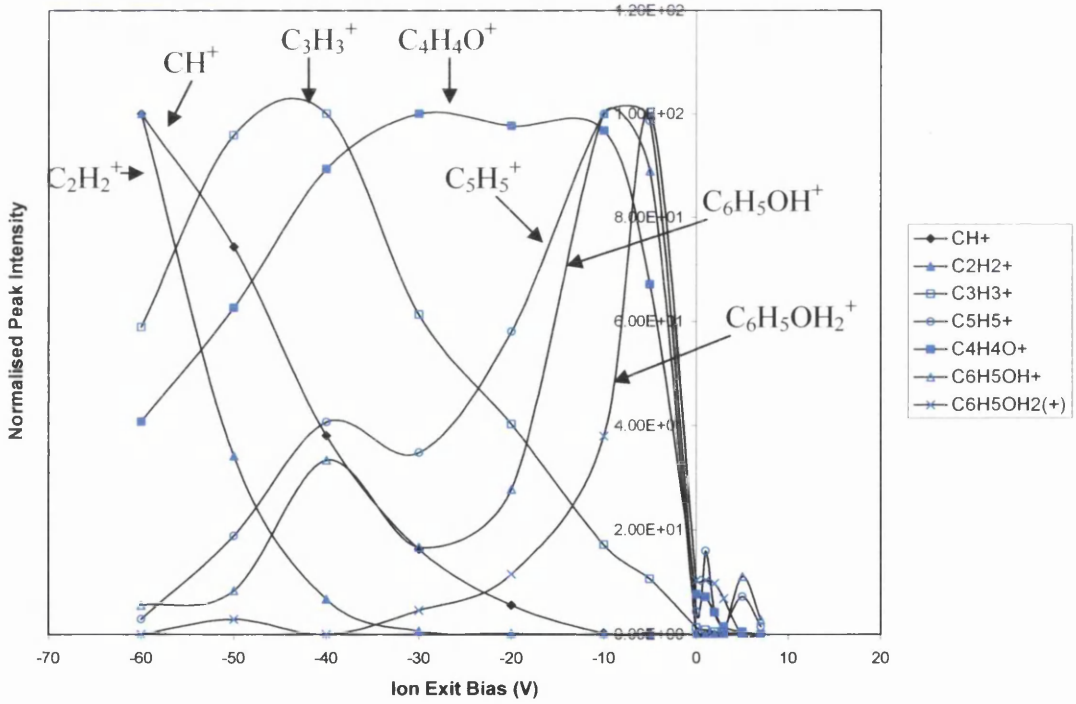

Figure 8.10b: Variation of normalised phenol related ion intensities with applied V_c (V_d = 700 V, P = 1 Torr, τ = 1.39 ms, phenol addition = 36.1 ppm, tuned for $^{51}V^+$)

negative V_c conditions, but this was not observed. With the exception of ethanol, the results are very similar to those observed on addition of nitrogen or methane to the FAG plasma. We therefore conclude that CID within the cone sheath is responsible for the fragmentation observed on application of a negative V_c. We also conclude that ion formation on application of a positive V_c is due to field ionisation of Rydberg state species outside the discharge cell, and that the ions observed are indicative of the plasma composition and products of associative ionisation in the expanding Rydberg gas plume outside the discharge cell. Therefore, it appears that the plasma is predominantly composed of larger fragment and parent molecular Rydberg species and that the vast majority of fragmentation occurs within the ion exit sheath.

Why then does the pattern differ for ethanol? Assuming the same mechanism applies, ethanol may be broken down within the flow tube of the discharge cell. It is possible that catalysed thermal decomposition occurs at the walls of the vessel, although Meot-ner and Sieck[36] previously showed that thermal decomposition occurs at temperatures above 550 K. This is higher than the temperature of the discharge cell. It is also possible that Penning type energy transfer aids fragmentation, though this would be expected to contribute to the fragmentation of the other alcohols.

It was possible to determine breakdown patterns and parent molecular ion species for each of the compounds analysed, with the exception of ethylene glycol. Therefore, in some instances chemical speciation may not be possible, though information about the chemical structure can still be determined.

8.3.3 Addition of Benzene

As discussed in section 8.3.2.5, the maximum detection of the phenol parent molecular ion occurred on application of a negative V_c. This was also observed for benzene (figure 8.11a). However, the $C_6H_6^+$ signal reached a second maximum, 94% of the maximum intensity, on application of V_c = +5 V. Also observed (figure 8.11b) was the formation of dimer ions, the intensities of which again reach maxima on application of a positive and a negative V_c. It is possible that a collision between two benzene molecules in ground and Rydberg states could lead to formation of a highly excited neutral dimer which could be field ionised in the extraction field beyond the ion exit (equation 8.9):

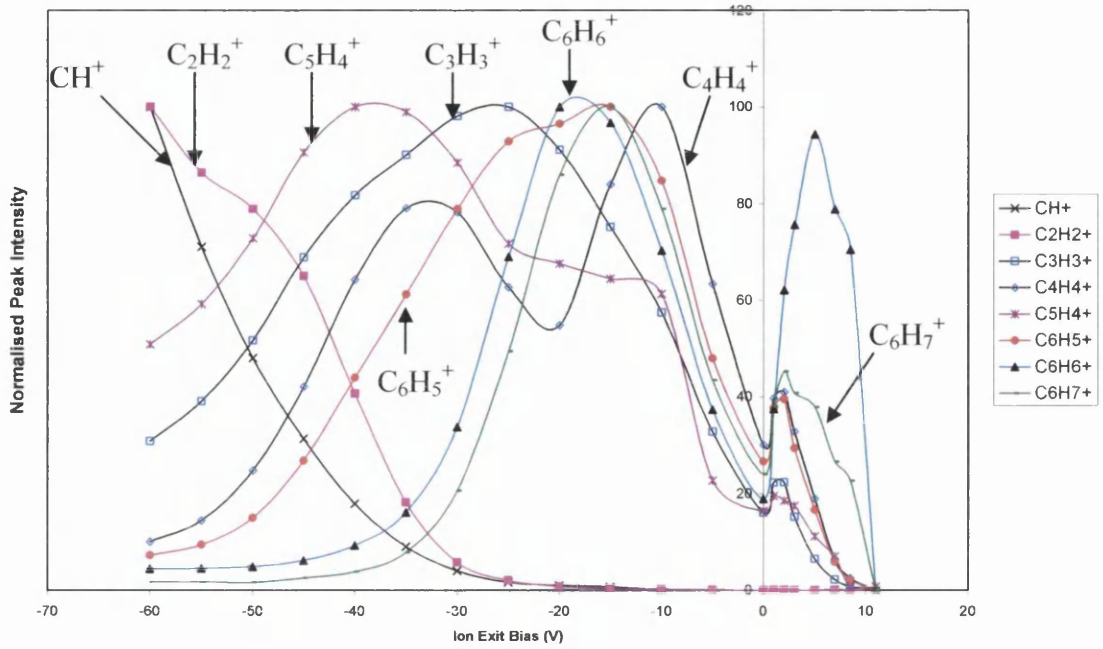

Figure 8.11a: Variation of normalised benzene related ion intensities with applied V_c

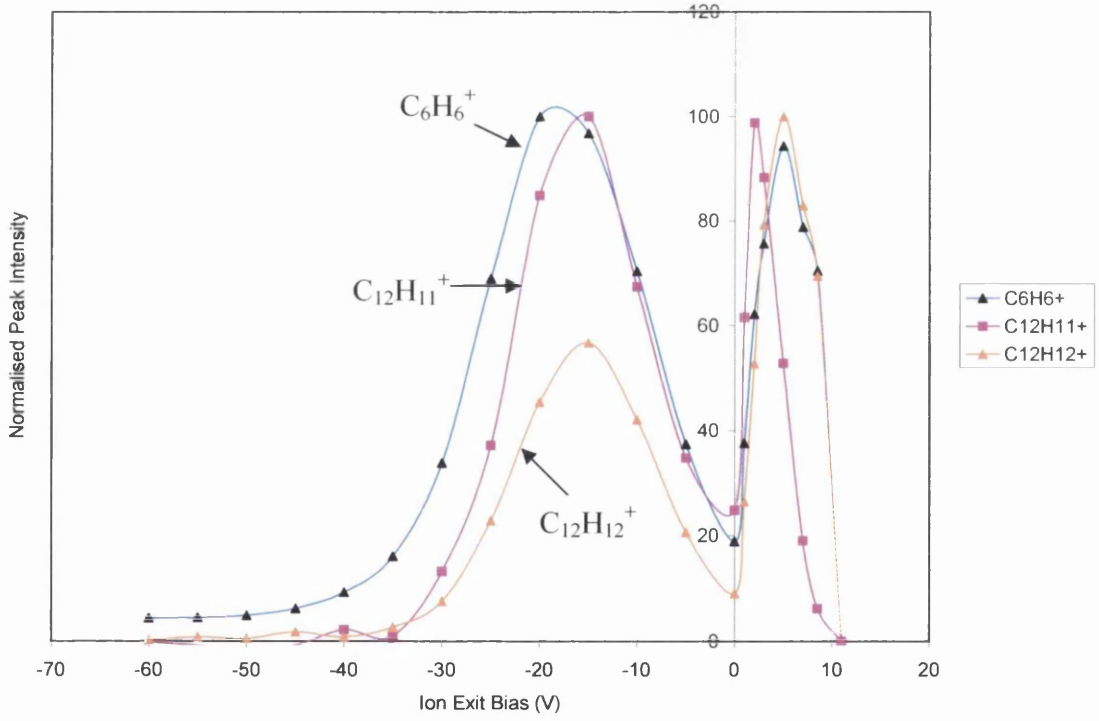

Figure 8.11b: Variation of normalised benzene related ion intensities with applied V_c
(V_d = 700 V, P = 1 Torr, τ = 1.39 ms, benzene addition = 259.9 ppm, tuned for $C_6H_6^+$)

$$B^R + B \rightarrow B_2^R \rightarrow B_2^+ + e^- \qquad \textit{(equation 8.9)}$$

where B is a benzene molecule. This is similar to the mechanism proposed for formation of Ar_2^+. However, it is also thought likely that the formation of the benzene dimer ion can occur via a large complex which can be broken down on application of a negative V_c. It was initially speculated that a benzene trimer cluster could be the precursor, but on analysis of the mass spectrum generated on application of a positive V_c (which should be indicative of the plasma composition) the trimer ion was not observed. However, the B_2Cu^+ and BCu^+ ions were both observed. Identification was possible due to the copper isotope ratio. Therefore, it appears that a diphenyl copper complex forms within the FAG plasma, and it is this which is fragmented in the ion exit field.

8.3.4 Addition of Halides

8.3.4.1 Halopropane

The variation of selected ion intensities with V_c on addition of 1-chloropropane is illustrated in figure 8.12a. As with the previous examples, the degree of fragmentation increased with increasing negative V_c, this time with the molecular ion peak intensity optimised when V_c was -5 V. It is possible that this is due to the formation of dimers or clusters in the FAG plasma, though no evidence of such species was observed. No Cl^+ was observed under the conditions used in this investigation, probably due to the high ionisation potential of Cl (table 8.3). On application of a positive V_c there was also evidence of formation of $(C_3H_7)_2Cl^+$, although it is not clear whether Rydberg precursor forms within the source or the neutral gas plume beyond the ion exit.

X	Electron Affinity of X (eV)	Ionisation Energy of X (eV)
H	0.75	13.6
F	3.40	17.4
Cl	3.61	13.0
Br	3.36	11.8
I	3.06	10.5

Table 8.3: Electron Affinities and Ionisation Potentials[37]

Figures 8.12b and c illustrate the variation of the variation of bromopropane and iodopropane (respectively) reaction products with V_c. In both instances there is evidence of increased fragmentation with increasing negative V_c, though it is not as clear in figure 8.12a. In contrast to the reaction with chloropropane, Br^+ was observed for -60 V $\leq V_c <$ +7 V, and I^+ was observed over the whole of the V_c range studied. The ionisation potential of I (table 8.3) is lower than the first metastable state energies of argon, and therefore Penning type ionisation reactions may occur (equation 8.10).

$$Ar^* + I \rightarrow Ar + I^+ + e^- \qquad \textit{(equation 8.10)}$$

Optimisation of the parent molecular ions for the bromo- and iodo- compounds was achieved on application of +3 V and -10 V respectively. The bromopropane result agrees with the many of the results in this investigation and that of Newman[19], and again shows that the ions detected on application of a positive ion exit bias are indicative of the Rydberg gas composition and associative reaction products from the neutral plume. Similarly, on application of a small positive V_c, $C_3H_8I^+$ and $(C_3H_7)_2I^+$ were detected. Thus, it is possible that detection of the $C_3H_7I^+$ maximum on application of a negative ion exit bias is due to fragmentation of C_3H_8I and $(C_3H_7)_2I$ formed within the FAG plasma.

8.3.4.2 Fluoro-compounds

It has already been demonstrated in chapter 6 that addition of fluorides to the FAG plasma of the FFGD leads to significant production of F^- due to the high electron

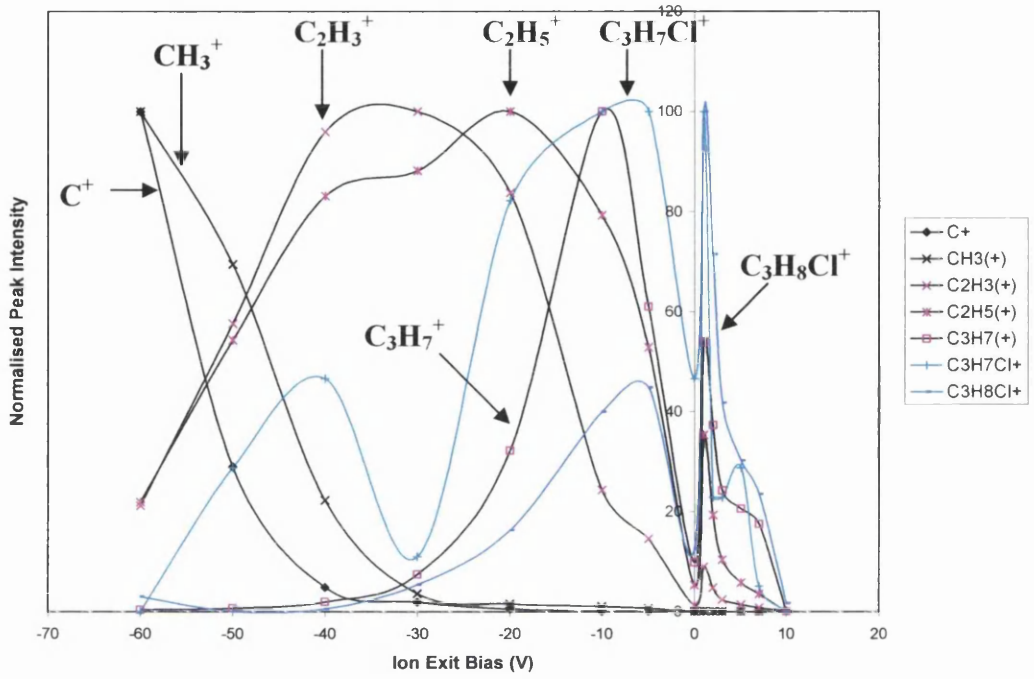

Figure 8.12a: Variation of normalised 1-chloropropane related ion intensities with applied V_c (1-chloropropane addition = 337 ppm, tuned for Cu^+)

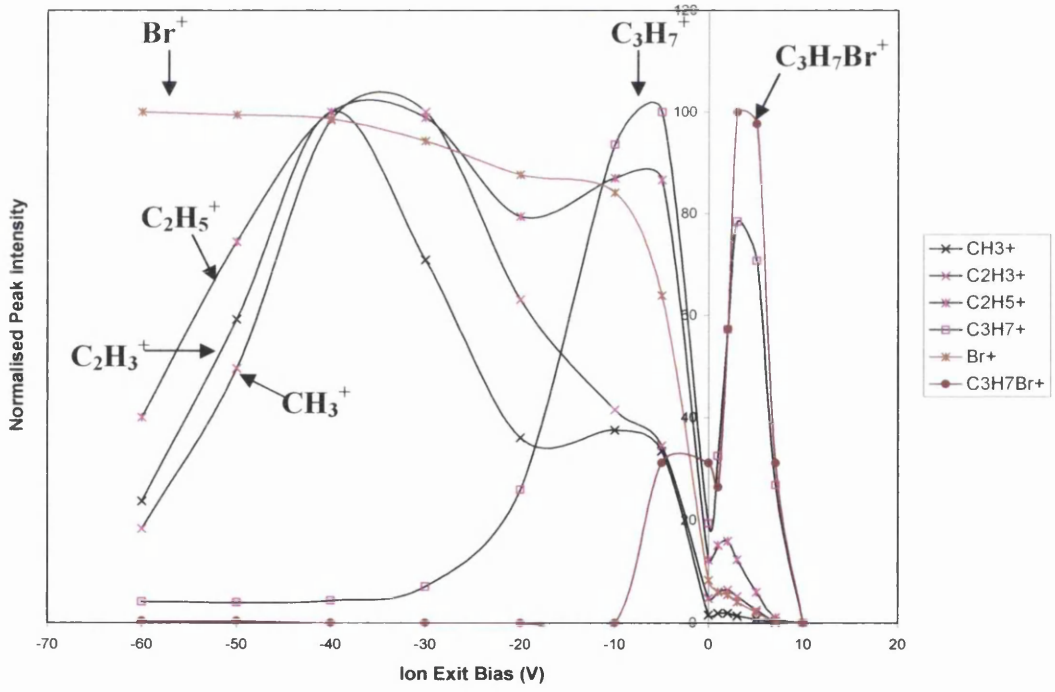

Figure 8.12b: Variation of normalised bromopropane related ion intensities with applied V_c (1-bromopropane addition = 133.9 ppm, tuned for V^+)
(V_d = 700 V, P = 1 Torr, τ = 1.39 ms, iodopropane addition = 111.8 ppm, tuned for $^{63}Cu^+$)

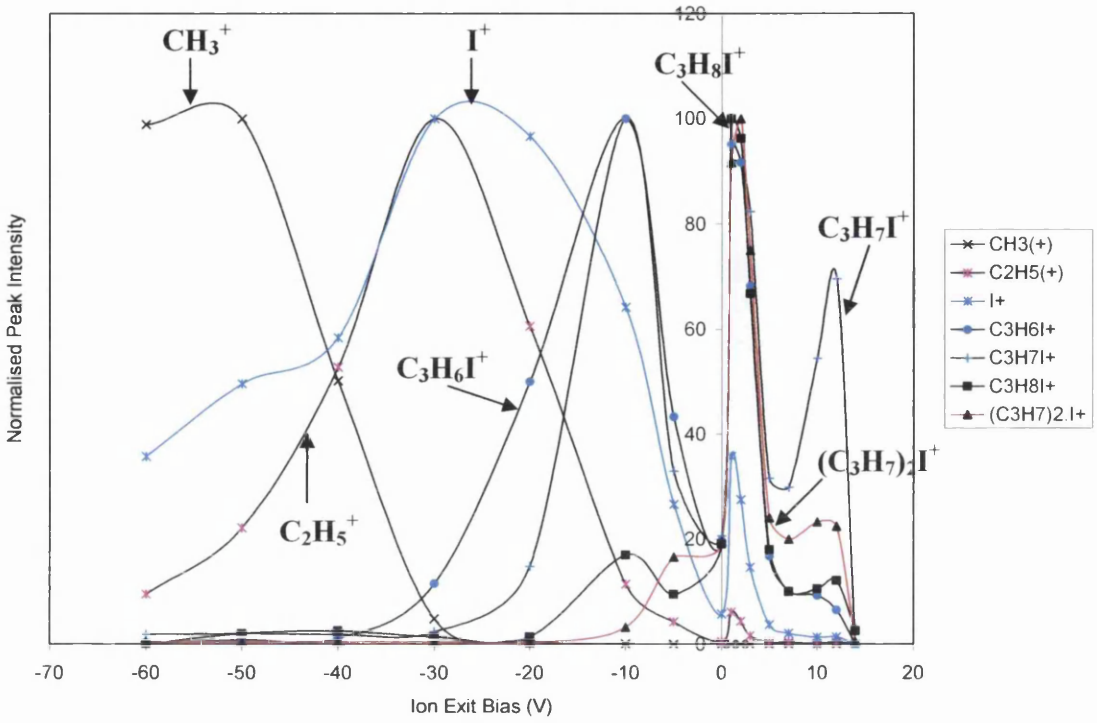

Figure 8.12c: Variation of normalised Iodopropane related ion intensities with applied V_c
(V_d = 700 V, P = 1 Torr, τ = 1.39 ms, iodopropane addition = 111.8 ppm, tuned for $^{63}Cu^+$)
The Br^+ and I^+ peak intensities, particularly on application of a high negative Vc, are strongly influenced by tuning for different ions.

affinity of fluorine. This, coupled with the high ionisation energy of F meant that F^+ was not observed in this investigation. Formation of VF^+ was observed on addition of fluorobenzene, possibly due to associative ionisation in the neutral gas plume (equation 8.11):

$$V^R + F \rightarrow VF^+ + e^- \qquad \textit{(equation 8.11)}$$

Figures 8.13 a to c show the variation of the selected fluorobenzene, m-fluorotoluene and p-fluorotoluene ion intensities, respectively, with V_c. As observed for each organic molecule studied, the degree of fragmentation increased with increasing negative V_c. In each instance molecular, or pseudo-molecular ion intensities were optimised on application of a negative V_c. For the reaction of benzene this was attributed to the formation in the plasma, and subsequent fragmentation of dimers in the cone sheath. It is thought likely that this could occur here, but due to time constraints this has not been investigated. It is also possible that the stability of the benzene ring reduces the degree of fragmentation observed.

On application of a positive V_c (figure 8.13a) the fluorobenzene parent molecular ion peak intensity was over six times the magnitude of that for the next most abundant ion (VF^+) and this would therefore aid speciation, although the absolute intensity was approximately a factor of 5 lower than that when V_c was -20 V. Comparison of figures 8.13b and c indicates that it may be possible to distinguish between m- and p-toluene based on their fragmentation patterns. In particular, the variation of the parent molecular ion signal may allow this. However, due to the limited nature of this investigation, further study is required before a conclusion can be reached.

Further evidence of the different effect observed on addition of benzene ring containing molecules is shown in figures 8.14a and b on addition of di- and tri-fluorobenzene respectively. In each example the maximum parent ion intensity was observed when V_c was -20 V, at which point the parent molecular ion was the major ion observed in the mass spectrum. In these examples formation of small fragments such as CH^+ was not favoured even when V_c was -60 V. This is indicative of the stability of the compound analysed. On addition of trifluorobenzene few ions were observed above the level of background noise on application of a positive V_c.

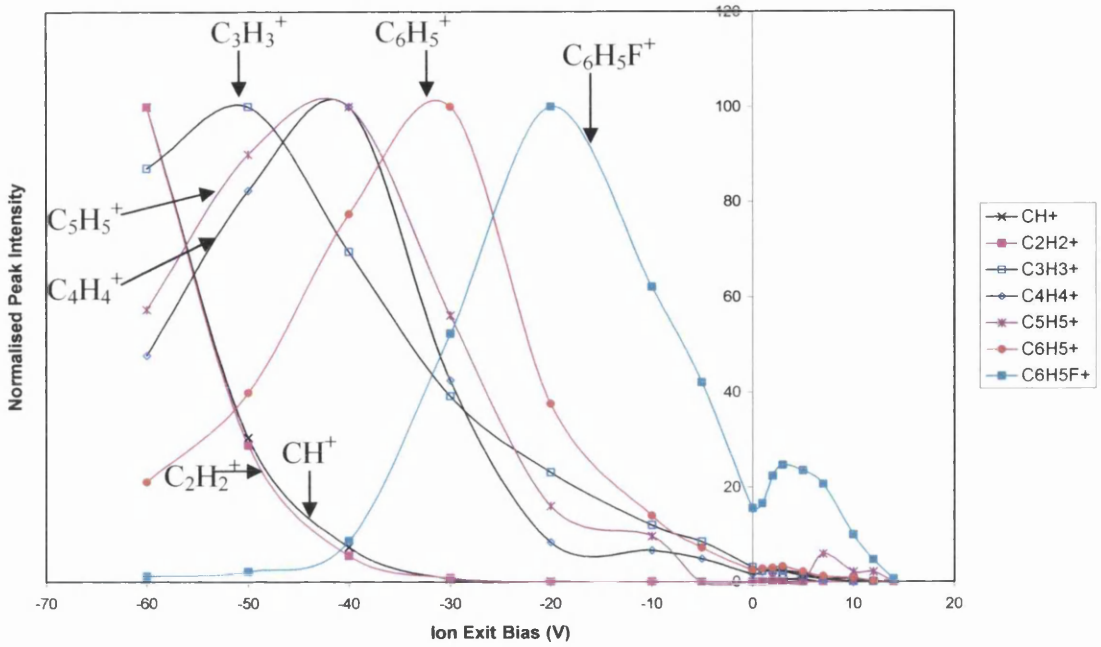

Figure 8.13a: Variation of normalised fluorobenzene related ion intensities with applied V_c (fluorobenzene addition = 220.2 ppm)

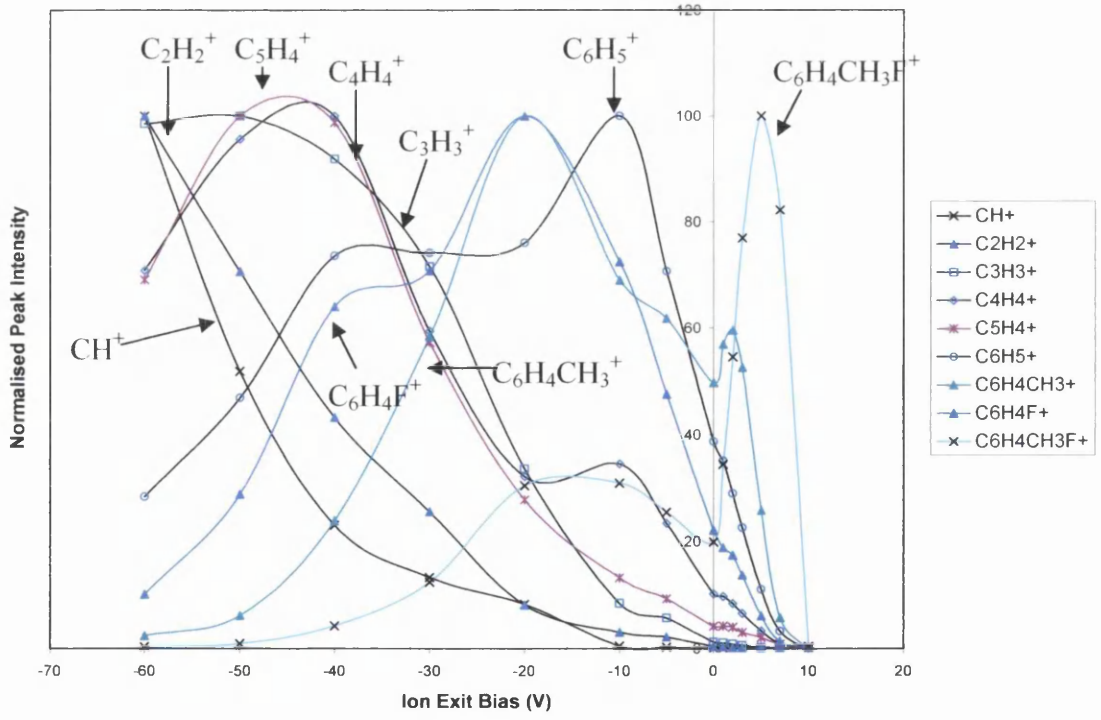

Figure 8.13b: Variation of normalised m-fluorotoluene related ion intensities with applied V_c (m-fluorotoluene addition = 58.1 ppm)

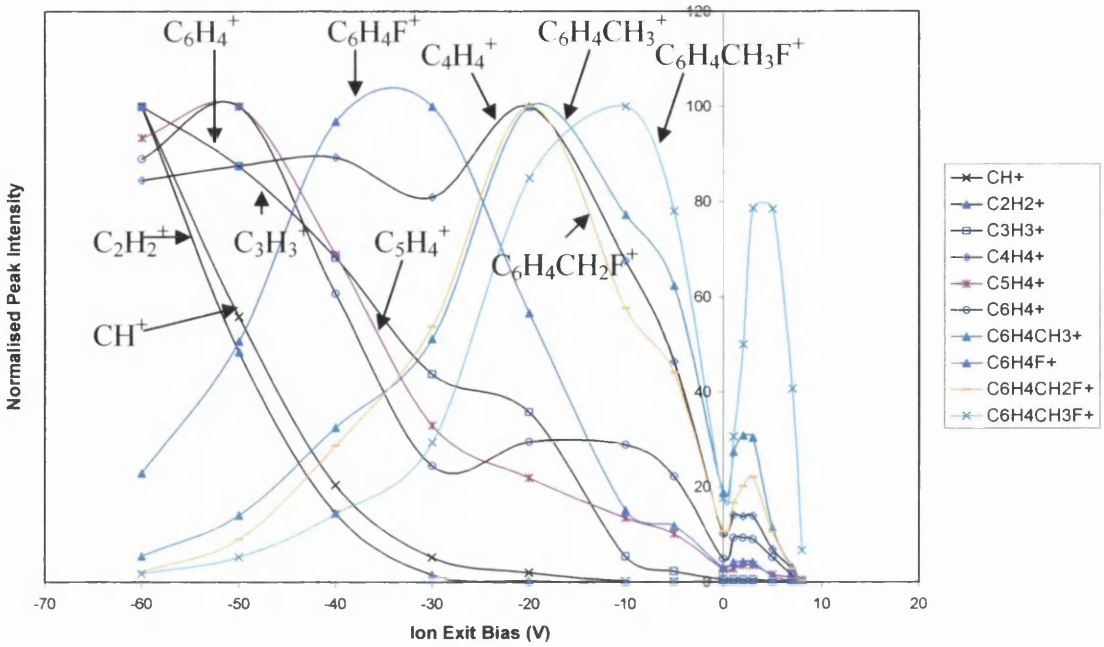

Figure 8.13c: Variation of normalised p-fluorotoluene related ion intensities with applied V_c (p-fluorotoluene addition = 54.2 ppm)
(V_d = 700 V, P = 1 Torr, τ = 1.39 ms, tuned for V^+)

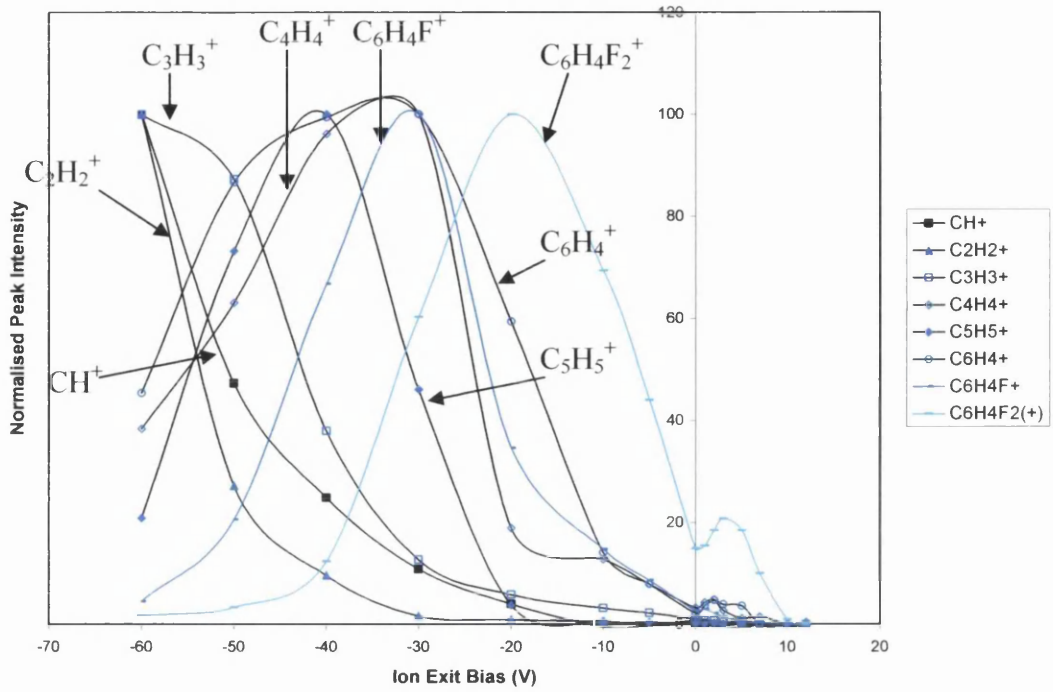

Figure 8.14a: Variation of normalised difluorobenzene related ion intensities with applied V_c (tuned for $C_6H_4F_2^+$)

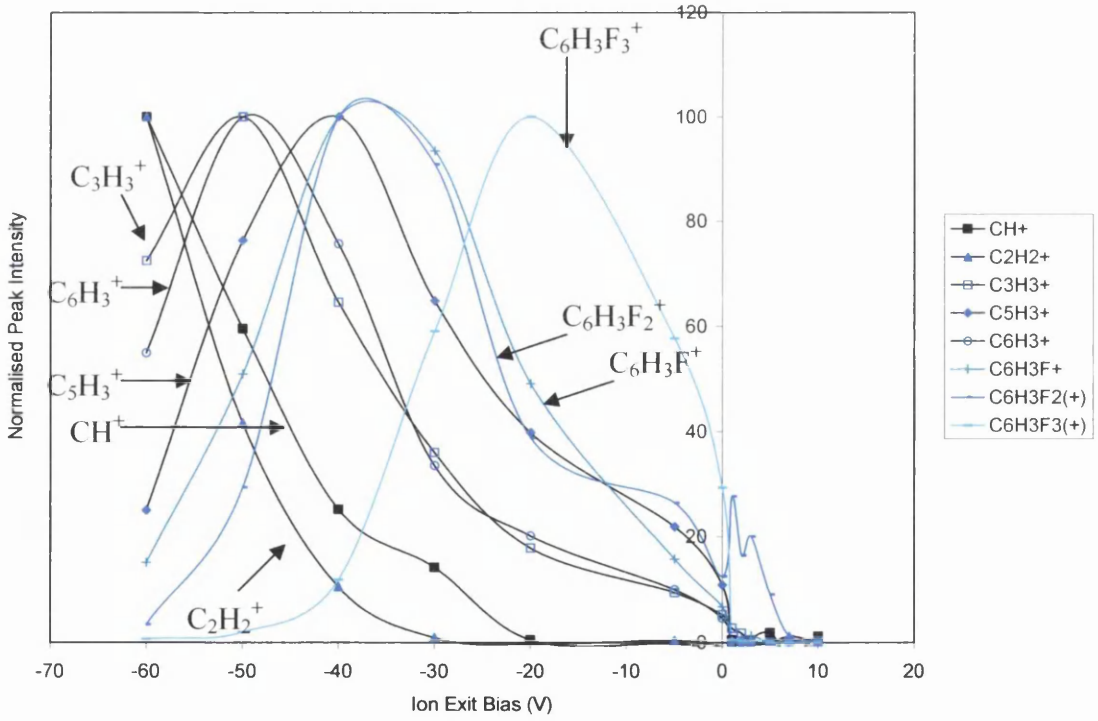

Figure 8.14b: Variation of normalised trifluorobenzene related ion intensities with applied V_c (trifluorobenzene addition = 275 ppm, tuned for $C_6H_3F_3^+$)
(V_d = 700 V, P = 1 Torr, τ = 1.39 ms)

8.3.4.3 Chloro-compounds

The variation of 1-, 2-, and t- butylchloride related ion intensities with V_c are illustrated in figures 8.15a, b and c respectively. A significant difference was observed between the $C_3H_7^+$ ion intensity profiles for analysis of the 1- and 2- isomers (figures 8.15a and b). However, this result was not common, and therefore it is not currently possible to distinguish between the two species using this technique. It may be significant that, as noted below figure 4.15c, it was more difficult to get a good fragmentation pattern for 2-chlorobutane than for either other isomer. Further investigation is required to determine whether this is significant. The profile observed for variation of t-butylchloride parent molecular peak intensity with V_c was significantly different to that for the 1- and 2- compounds, with the maximum intensity observed when V_c was -30 V. It is possible that the difference observed for the t-butylchloride parent molecular ion could be due to the low intensities measured. The ratio of the peaks at m/z = 92 and 94, due to the two Cl isotopes, was not consistent and was rarely close to 3:1, and therefore background noise was a significant problem in this instance. The low abundance of Cl containing cations is probably due to dissociative electron attachment as described in chapter 6. The electron affinity of chlorine (3.61 eV)[37] is very high, and therefore formation of Cl^- and chlorine containing fragment anions is highly likely.

The variation of chlorobenzene related peak intensities with V_c is illustrated in figure 8.16. The maximum parent molecular ion intensity was observed when V_c was -20 V. This fits with the results for other phenyl compounds, but it is not known if dimerisation occurs. The degree of fragmentation of each chlorine containing compound increased (generally) with increasing negative V_c, as expected.

8.3.4.4 Bromo-Compounds

The variation of a selection of ions related to bromobutane and bromobenzene with V_c are illustrated in figures 8.17a and b respectively. In each example the maximum bromine intensity was detected for a negative V_c. Again, the degree of fragmentation showed a general increase with increasing negative V_c. In contrast to other phenyl compounds, the maximum intensity of the bromobenzene parent molecular ion was observed on application of a positive V_c. However it was also

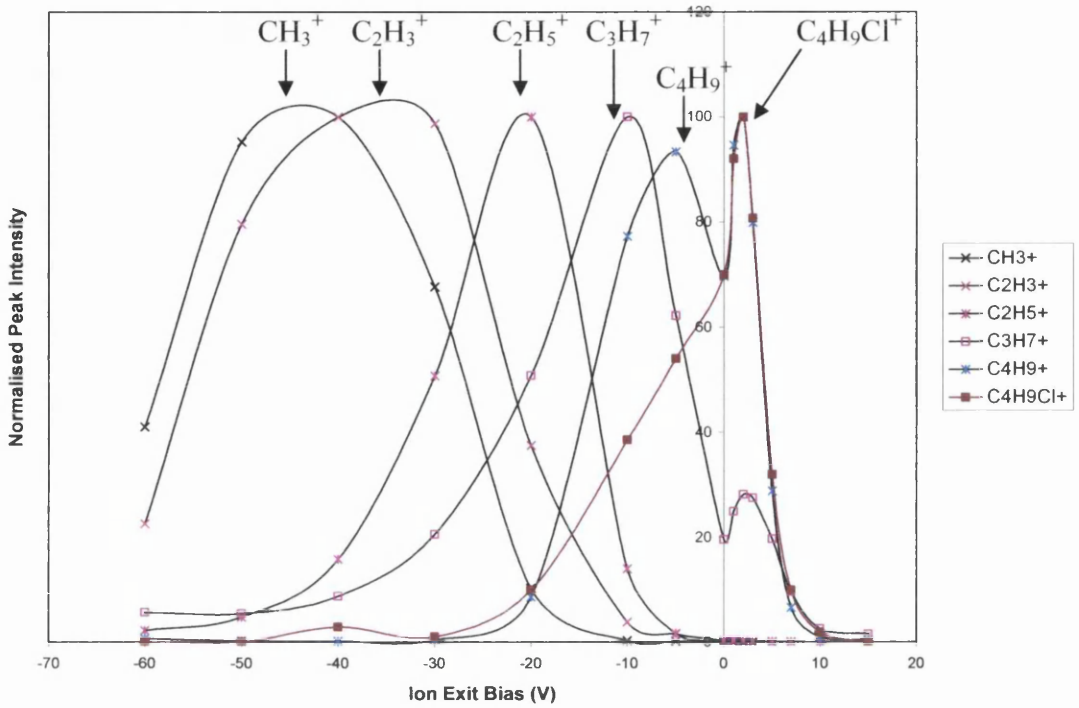

Figure 8.15a: Variation of normalised 1-chlorobutane related ion intensities with applied V_c (1-chlorobutane addition = 379.4 ppm, tuned for V^+)

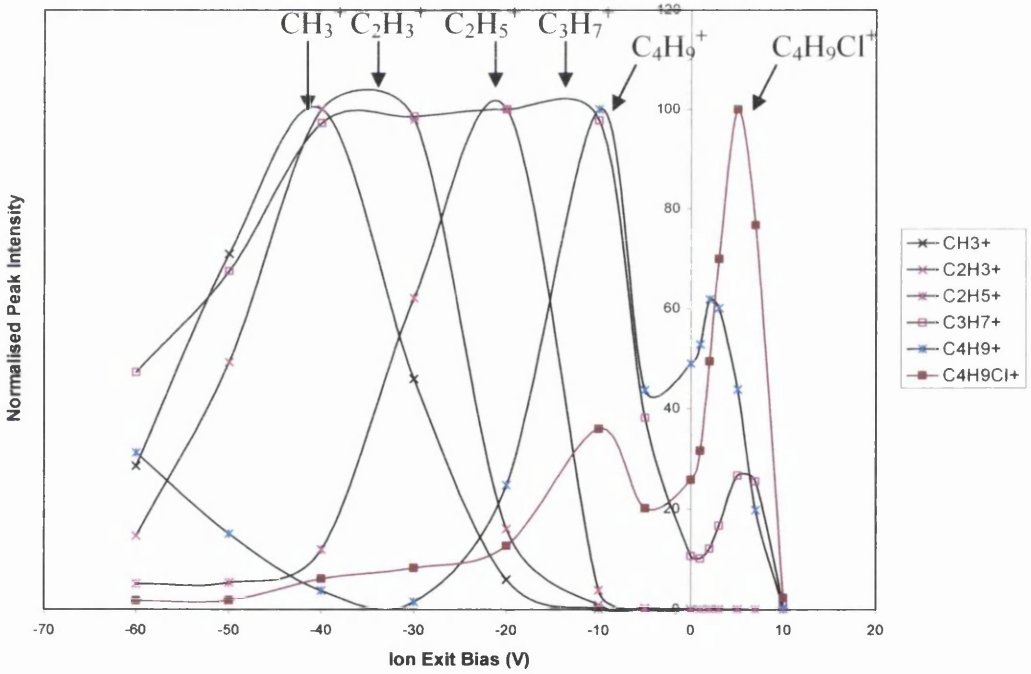

Figure 8.15b: Variation of normalised 2-chlorobutane related ion intensities with applied V_c (2-chlorobutane addition = 160 ppm, tuned for V^+)
(V_d = 700 V, P = 1 Torr, τ = 1.39 ms)

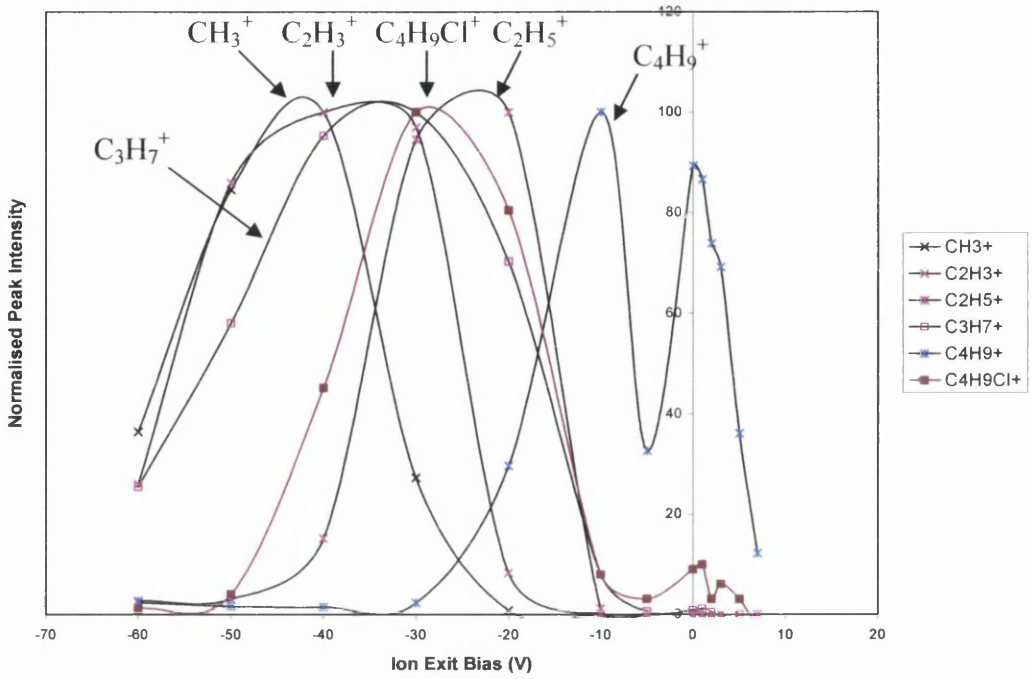

Figure 8.15c: Variation of normalised t-butylchloride related ion intensities with applied V_c (t-butylchloride addition = 365.7 ppm, tuned for V^+)
(V_d = 700 V, P = 1 Torr, τ = 1.39 ms)

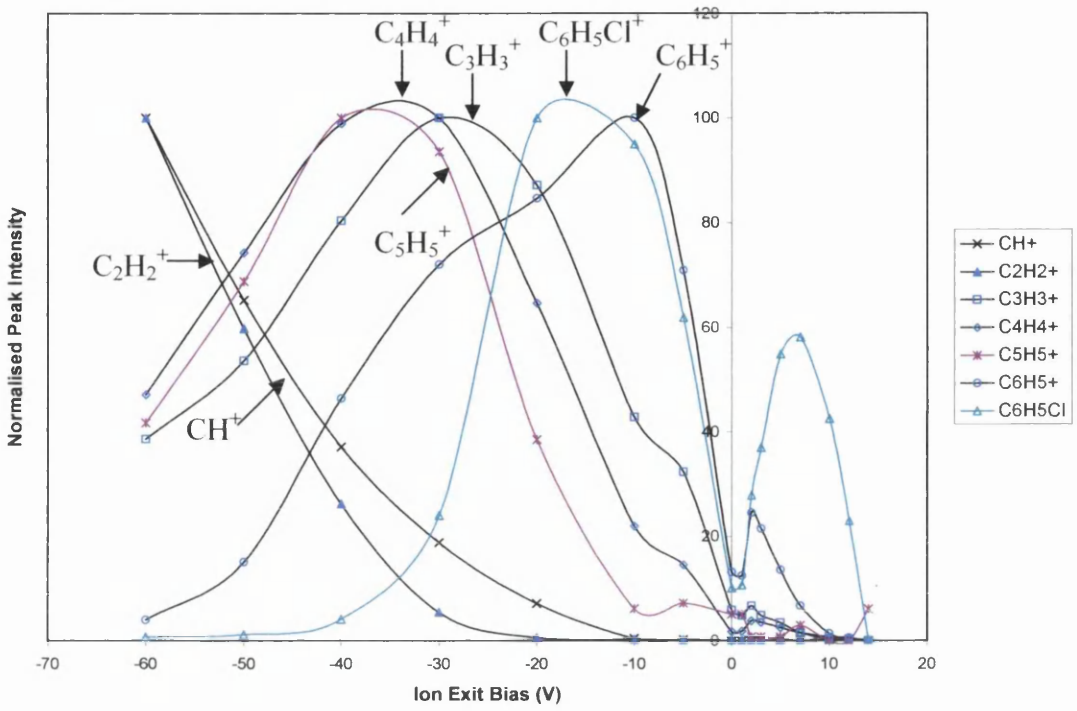

Figure 8.16: Variation of normalised chlorobenzene related ion intensities with applied V_c
(V_d = 700 V, P = 1 Torr, τ = 1.39 ms, chlorobenzene addition = 30 ppm, tuned for V^+)

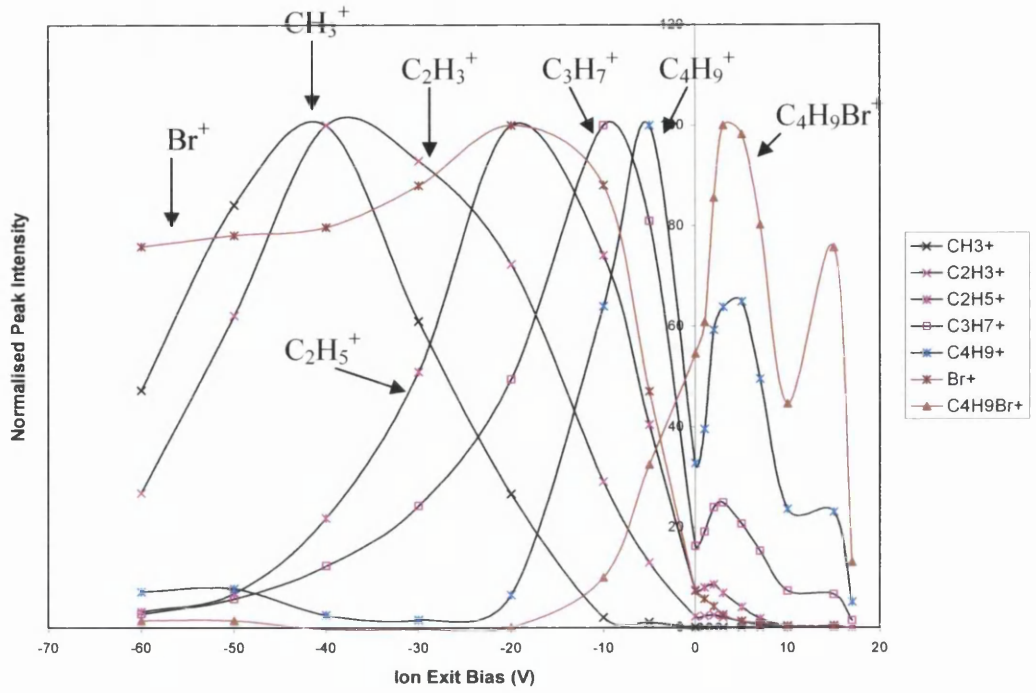

Figure 8.17a: Variation of normalised bromobutane related ion intensities with applied V_c (1-bromobutane addition = 120.2 ppm, tuned for V^+)

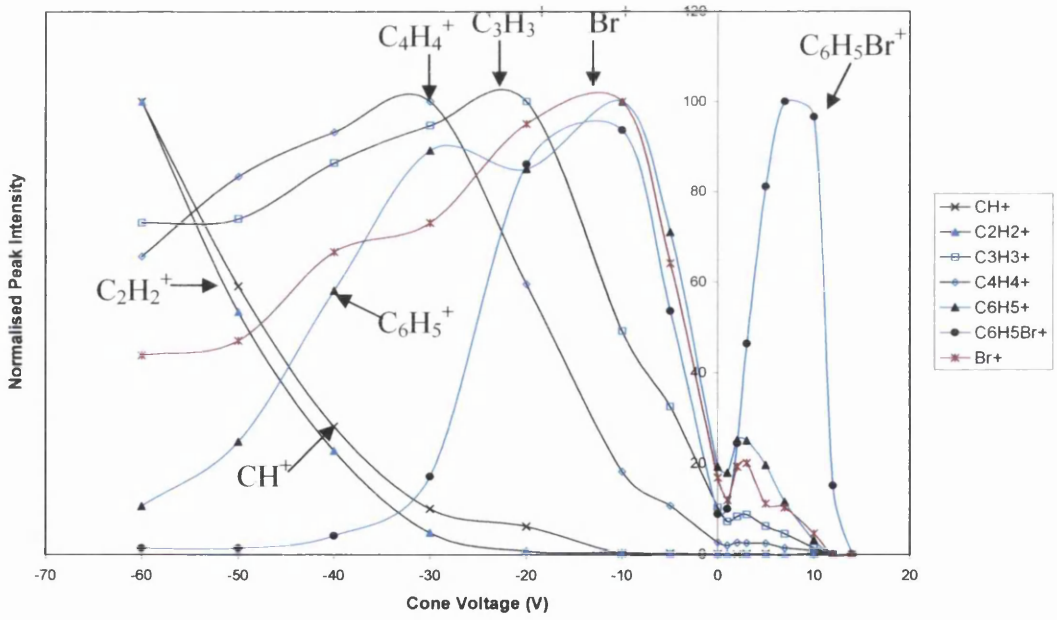

Figure 8.17b: Variation of normalised bromobenzene related ion intensities with applied V_c (bromobenzene addition =10.8 ppm, tuned for $C_6H_5^+$)
(V_d = 700 V, P = 1 Torr, τ = 1.39 ms)

observed at > 90% of the maximum ion intensity when V_c = -10 V, and therefore dimer formation may again be important.

8.3.5 Terpenes

Three terpenes were selected for analysis due to their equal mass and same chemical composition but sometimes very different structure. As with the previous examples, the degree of fragmentation increased with increasing negative V_c. The molecular ion peak (m/z = 136) for each structure was observed on application of zero or a positive V_c but at very low intensity. α- and γ-terpinene (figures 8.18 and 8.19 respectively) each contain a six membered carbon ring with two double bonds whilst myrcene (figure 8.20) is a branched compound without a carbon ring. It was thought that differences between the structures of myrcene and the terpinenes would lead to different fragmentation mass spectra. Due to the similarity between α- and γ-terpinene, the fragmentation patterns for these molecules were expected to be the same.

Though there were differences between the spectra for α- and γ-terpinene, changes were observed on repeat reaction, and it is unlikely that they can be used to distinguish between the two. However, the high degree of fragmentation, and the higher molecular ion peak intensity, of myrcene on application of a positive V_c means that it is possible to distinguish between the terpinenes and myrcene using this method. For each molecule the smallest fragment ion (C_1 and C_2) were not observed in significant abundance when V_c = 0 V, but for myrcene the intensity increased again on application of V_c = +2 V. Due to the low intensity of the parent molecular ion it would also be difficult to identify the molecular mass, therefore making speciation very difficult. A further drawback for analysis of terpenes is their low vapour pressure, though this would not be a problem using the GC-MS system built by Newman[19].

8.4 Conclusions

Based on the observations by Newman[19,20] it was proposed that coupling of the new vapour inlet system with the FFGD instrument could be a useful tool for study of ionisation processes on addition of organic and organometallic vapours. Controlling

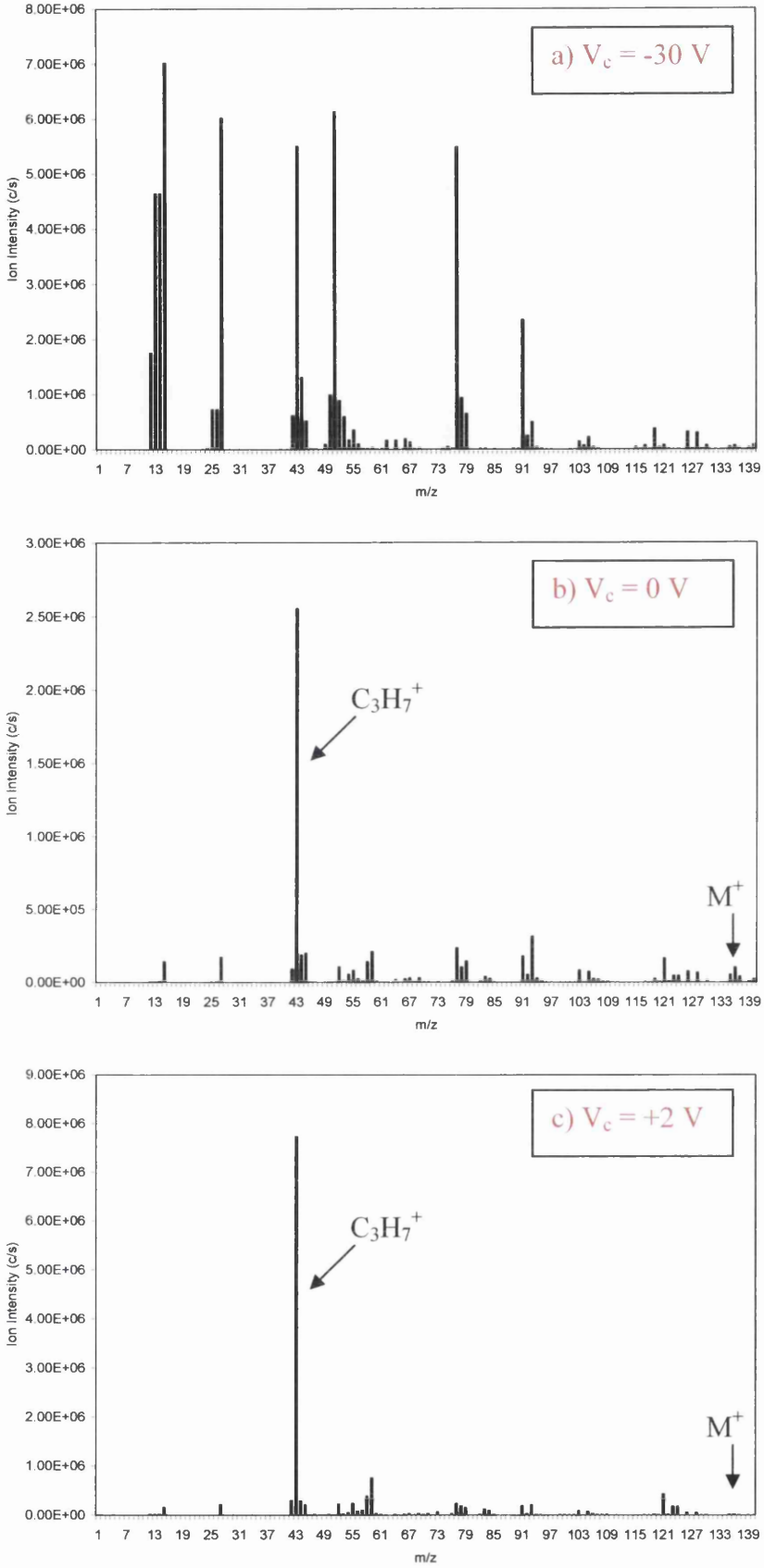

Figure 8.18: α-terpinene FFGD mass spectra dependence on the ion exit bias (V_d = 700 V, P = 1 Torr, τ = 1.39 ms, tuned for m/z = 121)

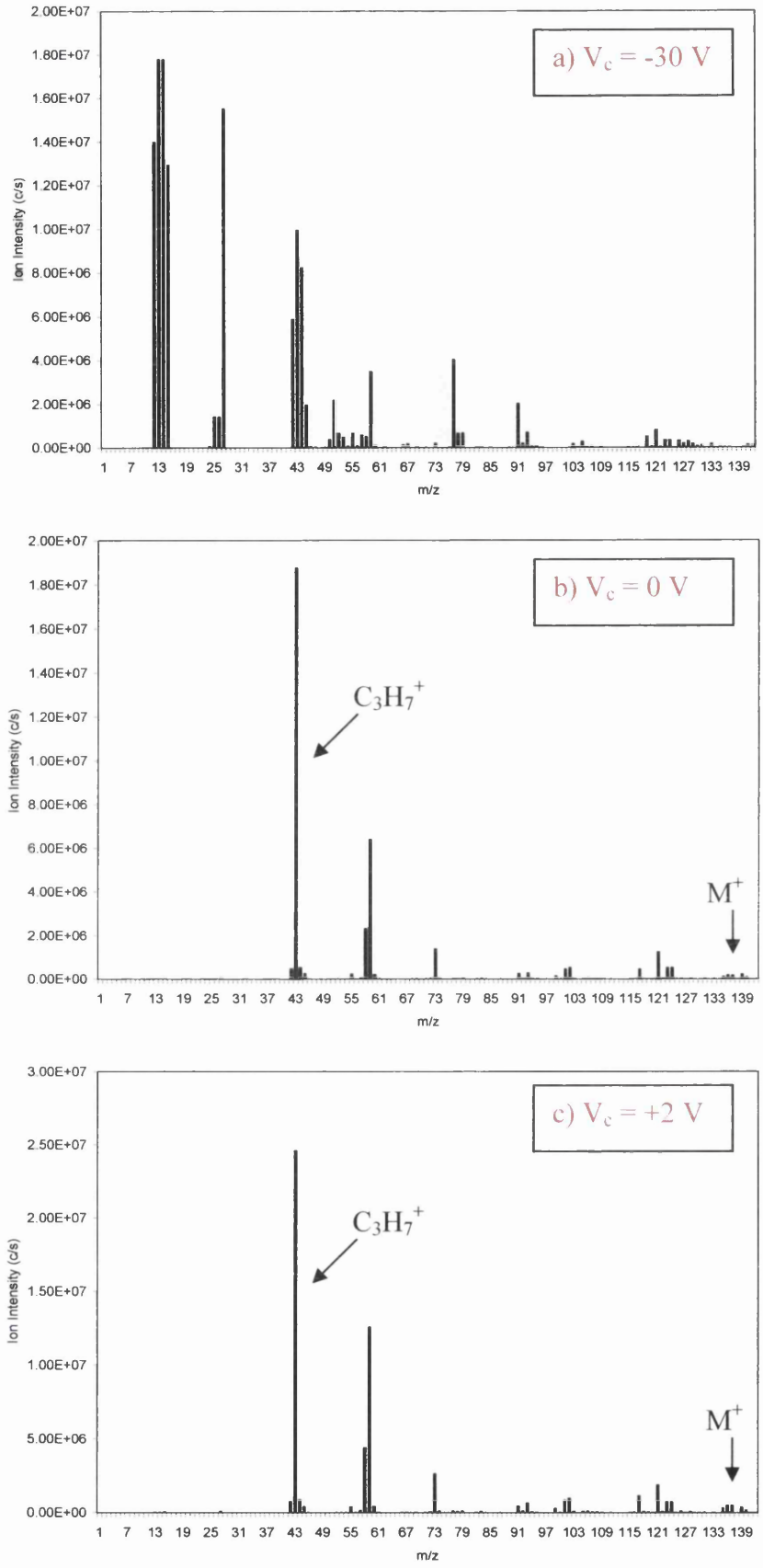

Figure 8.19: γ-terpinene FFGD mass spectra dependence on the ion exit bias (V_d = 700 V, P = 1 Torr, τ = 1.39 ms, tuned for m/z = 121)

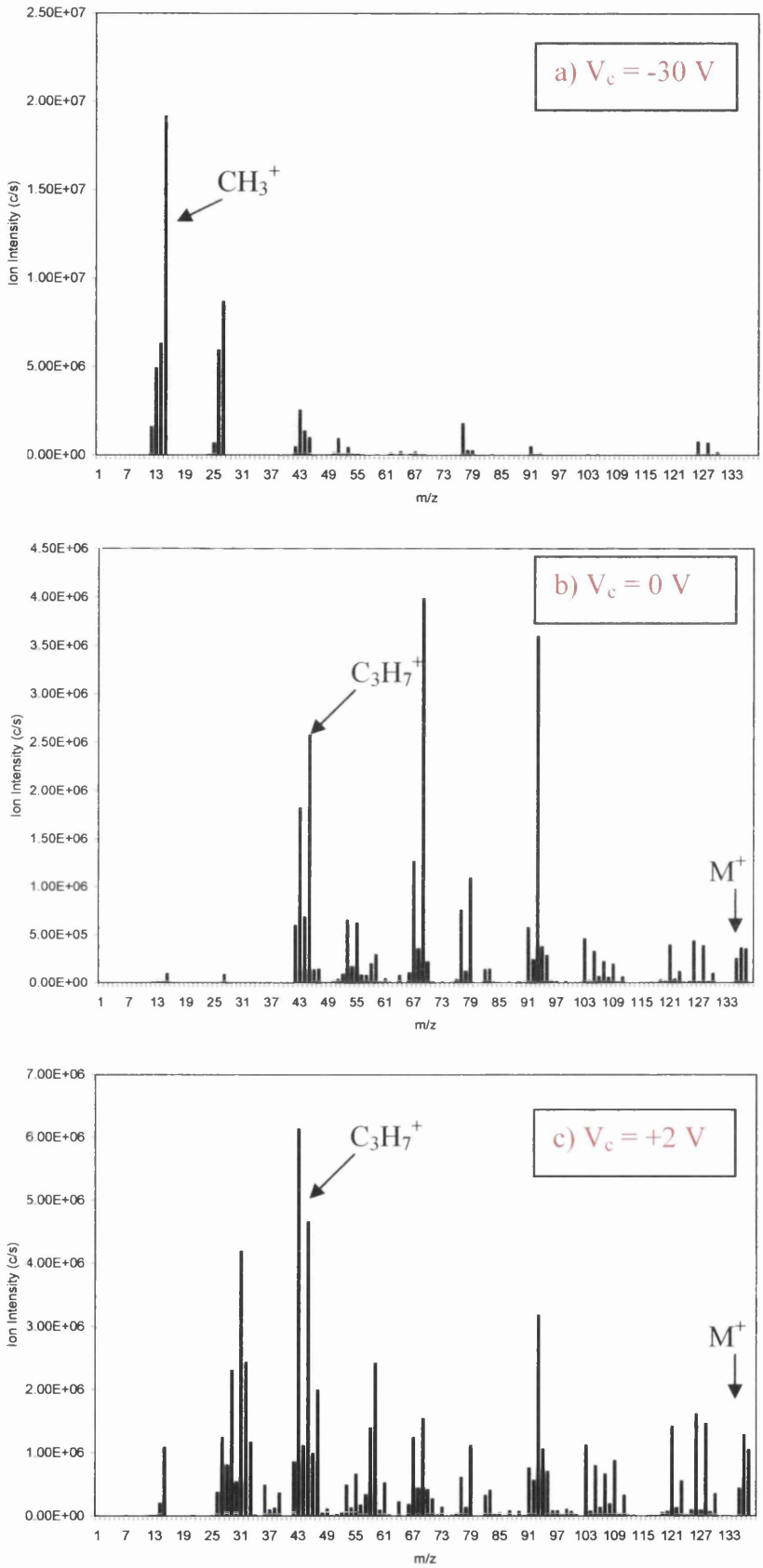

Figure 8.20: Myrcene FFGD mass spectra dependence on the ion exit bias (V_d = 700 V, P = 1 Torr, τ = 1.39 ms, tuned for $^{63}Cu^+$)

the degree of fragmentation allows determination of elemental, structural and parent molecular ion information. The vapour inlet system also allows a continuous flow of the sample, permitting ion optic tuning whilst the sample is added.

In each example in this study the degree of fragmentation generally increases with increasing negative V_c, though the voltage at which the molecular ion peak intensity is maximised is highly dependent on the chemical structure. It has been confirmed that the spectra observed cannot be explained by ion-molecule, Penning or EI processes. For instance, if EI was the mechanism for ion formation one would expect Ar^+ to be significantly higher, since the discharge gas was Ar. The mechanism for fragmentation is the same as that proposed for methane in chapter 7, whereby CID was almost certainly induced in the cone sheath on application of a negative V_c. Ionisation of Rydberg state species in the accelerating field outside the cell is the proposed mechanism on application of a positive V_c, hence the greater tendency to form ions indicative of the plasma composition (e.g. molecular ions). This agrees well with the Rydberg gas theory presented in chapters two and four.

In some instances, such as the reaction of ethanol, the breakdown patterns are not as clear. This is probably due to breakdown of the molecule in the FAG plasma before reaching the cone sheath. When V_c is positive the ions detected are representative of the Rydberg gas composition. Therefore fragment ions, formed by ionisation of excited state neutral fragments outside the cell, are observed at a higher intensity than expected.

It has been shown that the vapour inlet system can be used for analysis of a range of organic compounds, often allowing determination of the parent molecular ion species. However, it has also been illustrated that the parent molecular ion is sometimes not observed. This is true of some chlorine containing compounds. Since Cl^+ was not observed, it would be difficult to definitively determine the molecular structure using the information obtained. Using fragmentation spectra it may be possible to distinguish between isomers, though further study is required for a definite conclusion to be reached. However, based on the results obtained in this study it is unlikely that the technique can compete with EI mass spectrometry for identification of isomers.

It may be possible to use negative ion analysis to aid identification, since many of the compounds analysed contained electronegative elements (F, Cl, etc). The third generation FFGD instrument was shown to produce a high abundance of negative ions

on addition of carbon tetrafluoride (chapter 6), including F^-, and CF_x^- fragment ions. However, the parent molecular ion species was not detected. This is believed to be due to ion formation via dissociative electron attachment[38-40], possibly via collisions with argon Rydberg atoms, in which the outer electron is very weakly bound.

The technique could be further improved by coupling the FFGD cell to a mass spectrometer with higher mass resolution. The VG Plasmaquad II[41] quadrupole mass spectrometer used in this investigation is only capable of mass discrimination to the nearest mass unit. Therefore, it was not possible to differentiate between ions of very similar masses e.g. $^{81}Br^+$ and Ar_2H^+. The first generation FFGD-MS instrument incorporated a magnetic sector mass analyser capable of mass discrimination to several decimal places and would be able to distinguish between ions of similar mass. However, coupling the new inlet system to a high voltage instrument would not be as simple since the original source was floated at a high potential.

When Newman[19] determined the high sensitivity of this technique, experiments were run for a small positive ion exit bias. Figures 8.2 and 8.5 illustrate that sensitivities could possibly be improved even more ($\geq$ a factor of 2) if a higher positive V_c (> +30 V) was used. It is likely that the improved sensitivity is caused by the occurrence of efficient low energy EI ionisation in the cone sheath region, which was studied in chapters 4 to 6. The results of Newman[19] already indicate that the sensitivity of the FFGD technique is better even than that of the pulsed GD technique developed by Lewis et al[1,2], which itself is more sensitive that EI or CI, whilst still providing elemental, structural and parent molecular ion information within a single experimental run. Automation of the technique (acquiring mass spectra over a range of V_c) could reduce the time in which the information is gathered, therefore potentially allowing the chemical formula and structure to be determined within a single GC run, as is possible using the pulsed technique[1].

8.5 Summary

The results presented in this chapter extend the work carried out by Newman and illustrate much the same effect for each organic vapour added. For an increasing negative V_c the degree of fragmentation increases, with the parent molecular ion signal usually maximised on application of a small positive, zero or small negative V_c. Fragmentation of the molecule is thought to be due to collisions within the cone

sheath field induced by acceleration of ions towards the cone surface and therefore when V_c is more negative the kinetic energy of the ions is higher and the energy transferred in a collision, and thus the degree of fragmentation, also increases. In some instances the parent molecular ion maximum is observed on application of a relatively large negative V_c (e.g. benzene maximum when V_c = -20 V). This has been shown to be due to the formation of dimers, and possibly larger species, within the FAG plasma which break down in the ion exit field.

Though the sensitivity of the technique has been shown to be very good[19], there are several limitations to the technique which limit its use for chemical identification. For example, in some instances the parent molecular ion peak was not observed, Cl^+ and F^+ were not observed and it may often not be possible to use the technique to distinguish between isomers. On the other hand, the structural, elemental and parent molecular ion information which can be collected in most cases is very useful. The use of gas chromatography in place of the continuous flow inlet system greatly increases the range of compounds which can be added.

8.6 References

[1] D. Fliegel, R. Waddell, V. Majidi, D. Gunther and C. L. Lewis, *Anal. Chem.*, **77**, 1847, 2005

[2] C. L. Lewis, M. A. Moser, D. E. Dale Jr., W. Hang, C. Hassell, F. L. King and V. Majidi, *Anal. Chem.*, **75**, 1983, 2003

[3] T. J. Cleland and F. R. Meeks, *Spectrochim. Acta B*, **51**, 1487, 1996

[4] J. W. Waggoner, L. S. Milstein, M. Belkin, K. L. Sutton, J. A. Caruso and H. B. Fannin, *J. Anal. At. Spectrom.*, **15**, 13, 2000

[5] B. Munson, *Int. J. Mass Spectrom.*, **200**, 243, 2000

[6] W. W. Harrison, C. Yang and E. Oxley, *Glow Discharge Plasmas in Analytical Spectroscopy*, ed. R. K. Marcus and J. A. C. Broekaert, John Wiley & Sons, 2003

[7] V. Hoffmann, M. Masik, P. K. Robinson and C. Venzago, *Anal. Boanal. Chem.*, **381**, 173, 2005

[8] J. A. Klingler, C. M. Barshick and W. W. Harrison, *Anal. Chem.*, **63**, 2571, 1991

[9] R. E. Steiner, C. L. Lewis and F. L. King, *Anal. Chem.*, **69**, 1715, 1997

[10] B. Chapman, *Glow Discharge Processes*, Wiley & Sons, New York, 1980

[11] A. Bogaerts and R. Gijbels, *Spectrochim. Acta B*, **55**, 279, 2000

[12] E. de Hoffman and V. Stroobant, *Mass Spectrometry: Principles and Applications 2nd edition*, John Wiley & Sons Ltd., 2002.

[13] P. D. Miller, PhD Thesis, University of Wales Swansea, 1996

[14] R. S. Mason, P. D. Miller, I. P. Mortimer, *Phys. Rev. E*, **55**, 7462, 1997

[15] I. P. Mortimer, Ph.D Thesis, University of Wales Swansea, 2000

[16] D. R. Williams, Ph.D Thesis, University of Wales Swansea, 2001

[17] D. J. Mitchell, Ph.D Thesis, University of Wales Swansea, 2002

[18] N. A. Dash, Ph.D Thesis, University of Wales Swansea, 2004

[19] K. Newman, Ph.D Thesis, University of Wales Swansea, 2005

[20] K. Newman and R. S. Mason, *Rapid Commun. Mass Spec.*, **20**, 2067, 2006

[21] H. Togashi, A. Hashizume and Y. Niwa, *Spectrochim. Acta B*, **47**, 561, 1992

[22] K. Song, H. Cha, H. Park and S. C. Lee, *Microchemical J.*, **70**, 285, 2001

[23] R. Srinivas, A. R. Devi and G. K. V. Rao, *Rapid Comm. Mass Spectrom.*, **10**, 12, 1996

[24] Y. Hashimoto, M. Yamada, M. Suga, K. Kimura, M. Sakairi, S. Tanaka, M. Mizumoto and M. Sakamoto, *Bunseki Kagaku*, **19**, 49, 2000 a

[25] *NIST Chemistry Webbook, NIST Standard Reference Database Number 69,* ed. P.J. Linstromand, W.G. Mallard, National Institute of Standards and Technology, Gaithersburg, MD, 20899, (http://webbook.nist.gov), 2003

[26] *Knovel Critical Tables,* 2003 (http://www.knovel.com/knovel2/Toc.jsp?BookID=761)

[27] Sigma-Aldrich Company Ltd., Poole, Dorset, UK

[28] BDH Chemicals Ltd. Poole, Dorset, UK

[29] Fischer Scientific UK Ltd., Loughborough, UK

[30] BOC Edwards, Crawley, West Sussex, UK

[31] Meggitt Avionics, Fareham, Hampshire, UK

[32] Bristol Fluid System technologies Ltd. (formerly Bristol Valve and Fitting Co.), Avonmouth, Bristol, UK

[33] J. A. Hornbeck and J. P. Molnar, *Phys. Rev.*, **84**, 621, 1951

[34] P. F. Knewstubb and A. W. Tickner, *J. Chem. Phys.*, **36**, 674, 1962

[35] P. F. Knewstubb and A. W. Tickner, *J. Chem. Phys.*, **36**, 684, 1962

[36] M. Meot-ner, and L. W. Sieck, *Int. J. Mass Spec. Ion Proc.*, **92**, 123, 1989

[37] D. R. Lide, *Handbook of Chemistry and Physics*, CRC Press, 1995

[38] L. A. Pinnaduwage, W. Ding and D. L. McCorkle, *Appl. Phys. Lett.*, **71**, 3634, 1997

[39] W. Ding, D. L. McCorkle and L. A. Pinnaduwage, *J. Appl. Phys.*, **84**, 3051, 1998

[40] P. G. Datskos and L. A. Pinnaduwage, *Phys. Rev. A*, **55**, 4131, 1997

[41] Thermo Elemental Ltd. (formerly VG Elemental Ltd.), 3 Ion Path Road, Winsford, Cheshire, UK

Chapter 9

Conclusions and Further Work

9.1 Introduction

This chapter is a summary of the conclusions drawn from the studies reported within this thesis. The studies presented here were conducted to extend the understanding of the physical and chemical properties of the FFGD plasma, with particular emphasis on Rydberg gas reactions with secondary gases and organic vapours. One further aim was the development of the new FFGD instrument to improve analytical sensitivity, remove problems and to allow electrical probe studies. Suggestions for further work are also presented.

9.2 Summary of Conclusions

9.2.1 Development of the Prototype FFGD Instrument

In the course of this investigation a number of improvements were made to the design of the new FFGD source, removing problems highlighted by Dash[1], as well as those identified during this study. The modifications to the source design all had a positive effect: improved vacuum seal, prevention of short-circuiting, etc. Several of the changes did not have a quantifiable influence on results, such as removal of magnetic stainless steel and PVC from the discharge cell, but served to prevent potential experimental error. The production of a new flow tube to allow electrical probe studies has proved vital in confirming results obtained on the high voltage instrument[1,2] and extending the Rydberg gas theory, though it is unfortunate that extensive in-situ mass spectrometric and electrical probe studies were not possible in this investigation.

A number of changes aimed at improving ion transmission to the quadrupole mass analyser were made, with varying degrees of success. Acceleration of the ion beam across the ion exit to mass analyser orifice (inter-orifice) gap was found to improve ion transmission significantly. Indeed, after reduction of the inter-orifice gap the accelerating potential, V_{cell}, was essential for detection of ions (excluding use of the EI source within the mass analyser). The accelerating potential also served as a reference for testing the performance of the kinetic energy lens of the mass analyser, which was found to correctly

measure changes in the kinetic energy, but the absolute values were not reliable. However, the measured values served to indicate the point at which ions were formed, and therefore the mechanisms for ion formation.

The application of biases to the cylinder lens, $V_{cylinder}$, and Einzel lens, V_{Einzel}, also increased the measured ion intensities, though not as significantly as V_{cell}. There is still some question as to the whether applying a large voltage between the ion exit cone and the cylinder lens accelerates ions, induces ionisation of Rydberg state species, or both. For optimum ion transmission the overall potential difference between the two points was in excess of 270 V. Therefore, it is possible that ionisation of a range of excited states in the expanding gas plume could occur under these conditions. Unfortunately, the advantages gained through acceleration and improved focussing of the ion beam were negated on reduction of the inter-orifice gap. The character of the mass spectra also changed, with Ar^+ and Ar^{2+} becoming the dominant ion signals, rather than Cu^+ and ArH^+. Reversing the changes to the instrument did not reverse the changes to mass spectra and ion intensities, and it is not clear why. However, it is likely that a reduction in pumping efficiency, evidenced by the lower gas flow rates which could be used, was at least partly responsible.

9.2.2 Fundamental Studies

In chapters 4 and section 2.7 extensions of the Rydberg gas model developed within this group are described, with particular emphasis on the ion exit bias effect and calculations used to determine the kinetic and thermodynamic validity of the model. Chapter 4 also contains results from a series of experiments run during this investigation that corroborate the ion exit bias effect on a Rydberg gas. It is shown that many of the results cannot be explained by the conventional ion-electron plasma model[3], though collisions involving ions and electrons cannot be ignored, particularly within the ion exit sheath field. The conditions of the FFGD plasma are shown to stabilise the Rydberg gas. However, ionisation of the Rydberg gas can occur in the presence of an electric field or at very high or very low Rydberg densities.

It has been shown that the Rydberg gas is capable of carrying large currents, probably by charge transfer between adjacent Rydberg atoms, on application of a positive V_c. The current under positive ion exit voltage conditions is induced by field ionisation in the anodic (cone) sheath, and is balanced by ionisation of Rydberg atoms in the cathodic sheath, and movement of ions to the cathodic surface. On application of $V_c >$ +16 V results indicate that electron impact ionisation of Ar occurs in the anodic sheath, and the subsequent separation of charge creates a negative field at the cone surface, thereby allowing extraction of cations formed within the anodic sheath. Thus, cations can be detected on application of a positive (repulsive) ion exit bias. On application of a much higher V_c it appears that a secondary discharge forms between the anode and the ion exit cone. It has been shown that under positive V_c conditions ions are formed outside the discharge cell. This is probably due to ion-electron recombination as the gas exits the source. Rydberg atoms formed by this process can be ionised in the expanding neutral gas plume.

Ion kinetic energies presented in chapter 5 show that on application of a negative ion exit bias, using the new FFGD source, ions were formed both inside and outside the discharge cell. Ions formed within the cone sheath are subsequently accelerated across the sheath and therefore have an initial kinetic energy. However, ions formed in the accelerating field outside the GD cell had no initial kinetic energy and therefore any kinetic energy was due to the applied V_{cell}. The kinetic energy of Ar^+ is lower than that for Cu^+ due to symmetrical charge transfer within in the cone sheath.

Chapter 6 details the chemistry and electrical properties of the flowing plasma in the new FFGD source with and without secondary gases. If the plasma was an ion-electron medium one would expect the addition of a gas to quench the plasma current. Though there is sometimes a small initial drop (small increase on addition of H_2), even for large additions of secondary gas (several %) the changes to the cone and discharge currents were insignificant. After the initial drop the currents remained approximately constant, indicating that the gas could only remove a fraction of the current-carrying species. This is explained by the presence of charge transfer chains of Rydberg atoms which are not quenched by the added gas. However, the added gas can quench Rydberg atoms outside these chains.

Direct correlation between formation, and subsequent loss of Ar^+ and F^- was observed on addition of CF_4 to the FAG plasma (same source conditions), leading to the conclusion that the two are likely to be formed together. One possible mechanism for this is electron transfer from Ar^R to F or CF_x (the latter is dissociative electron attachment). This is a typical Rydberg gas process, and could occur in the neutral gas plume outside the discharge cell.

Chapter 7 also details the addition of secondary gases to the FAG plasma, but on a second low voltage instrument. The Ar^+ removal rate constants were calculated in the same way as performed by Mortimer[4], Dash[1] and Newman[5] for comparison with literature values of the charge transfer rate constants[6] and the rate constants previously measured within this group[1,4,5]. The order of quenching efficiency of the gases was in agreement with the study by Mortimer[4], though the absolute intensities were significantly different due to a design flaw in the source used in the previous study. The relative quenching efficiencies did not match with those for charge exchange[6]. However, the differences can be explained by the relative efficiencies of quenching of Rydberg states by the different gases. For instance, nitrogen has no dipole and so the cross section for collisions is very low[7]. Thus, the quenching efficiency of nitrogen is also very low. On the other hand, hydrogen has no dipole and the quenching efficiency is therefore much higher than expected. This is likely to be due to the efficient energy transfer to hydrogen rovibrational levels[1,4,5]. It has even been suggested that ionisation or fragmentation of the collision partner could enhance the quenching efficiency[5].

The influence of each gas added on the ion intensity profiles was essentially the same as the results obtained using the high voltage instrument[1,2,4,8], despite changes to the source conditions and electric fields within the instrument. It was concluded that, although many of the reaction products could be formed by ion-molecule reactions, there were several cases where ion-molecule reactions definitely could not be responsible. Again, the detection of cations on application of a positive V_c was highlighted as evidence for a Rydberg state mechanism.

On addition of N_2 and CH_4 clear fragmentation patterns were observed on variation of V_c. This result is similar to results presented by Newman[5,9,10] on addition of organic and organotin compounds in the same way. On application of a negative V_c the

secondary gas was subjected to collisionally induced fragmentation in the ion exit sheath. Rydberg state species are ionised in the ion exit field and accelerated across the sheath. The maximum energy of the ion is determined by the magnitude of the ion exit field, and therefore the degree of fragmentation increases with increasing negative V_c. However, on application of a low positive V_c the formation of the molecular ion and argon dimer ion was enhanced. This is thought to be due to field ionisation and associative ionisation[7] processes involving Rydberg state species outside the discharge cell. Monitoring the extraction lens (induces field ionisation) and pole bias (related to ion kinetic energy) voltages seemingly confirmed this supposition.

This ability of the technique to fragment molecules has been described as an alternative to established techniques, such as EI, for chemical speciation. Newman[5,9-11] describes how the technique can be applied to analysis of organic or organotin compounds using a continuous flow organic vapour inlet system or via a GC interface. The continuous flow inlet system allows extended study of reactions in the FAG plasma. Chapter 8 details the addition of a range of organic vapours in such a manner, and the effect of V_c on ion intensities. In each case a general increase in the degree of fragmentation was observed with increasing negative V_c, with the molecular ion intensity maximum observed at low negative to low positive ion exit biases. In the case of benzene, the molecular ion maximum was observed at a surprisingly high negative V_c. Further analysis indicated that the dimer ion maximum was observed when V_c was positive. Thus, it appears that the dimer forms within the FAG plasma and is fragmented in the ion exit sheath on application of a negative V_c, whereas, on application of a small positive V_c, the mass spectrum is indicative of the composition of the plasma and associatively ionised products formed in the neutral gas plume. However, a second maximum for the benzene dimer ion was observed for a negative V_c, implying that the dimer was itself a product of fragmentation. Further investigation led to the discovery of a higher mass product, believed to be $(Benzene)_2Cu^+$, on application of a positive, but not negative V_c.

In some instances the parent molecular ion was not observed or was observed at very low intensities, making speciation more difficult. Also, on addition of chlorides, the Cl^+

ion was not observed. The problems associated with identification of chloro- and fluoro-compounds may be overcome by anionic mass spectrometry.

Throughout this thesis it has been illustrated that conventional plasma theory[3] cannot account for all of the results observed. However, the anomalous results can be explained if the plasma is considered to be a Rydberg gas medium.

9.3 Suggested Further Work

Due to the deterioration of the performance of the new FFGD instrument and the time constraints of this investigation there are several points of interest which could not be investigated. One of the primary reasons for the development of the new FFGD instrument was to perform negative ion studies of organic samples. However, due to the deterioration of the ion transfer efficiency, this became impossible. Study of the negative ion mass spectra in conjunction with electrical properties of the plasma could be significant in proving the mechanism by which ions are formed, particularly under positive ion exit bias conditions, where positive and negative ions are both detected. Comparison of the positive and negative ion signals on addition of carbon tetrafluoride has already shown some correlation between the formation of, and subsequent loss of positive and negative ions, under the same conditions. Continuation of the studies using the organic vapour inlet system constructed by Newman[5], comparing the negative ion and electrical studies with the previous results obtained for organic and organometallic compounds is likely to provide very valuable information about the plasma chemistry.

Also prevented by the time constrictions of this project was determination of absolute detection limits for the organic compounds used. It was planned to repeat the addition using the GC inlet system designed and constructed by Newman[5]. Newman[5] previously reported detection limits for organotin compounds at sub picogram levels, making the FFGD technique more sensitive than many other techniques. A comparison of the detection limits for different compounds would also be of interest. Further study of molecular ion detection on application of a high positive bias would also be of interest because it has been shown that the molecular ion peak intensities can be increased on

application of $V_c > +30$ V. Based on the results in figures 8.2b and 8.5b, it is thought that it may be possible to improve the detection limit significantly.

One suggestion made in Newman's thesis is the extension of the technique to study other organometallic compounds such as organomercury. Further study of the dimerisation, and possible cluster formation on addition of organic compounds, illustrated clearly on addition of aromatic compounds (chapter 8), should also provide further evidence of the chemistry of the FAG plasma. It would also be useful to develop a system for heating the sample bulb and gas transfer line of the continuous flow organic inlet system, possibly through incorporation inside the GC oven, to prevent deposition of less volatile compounds within the gas line.

One other aspect considered in this study was the development of the new discharge source to allow spectroscopic studies. This was previously planned by Dash[1], and was reflected in the prototype source design. However, the spectroscopic equipment within the laboratory could not be used, and replacement equipment is expensive. Optical studies of the flowing afterglow and the ion exit sheath would again aid fundamental studies of the processes occurring and species present within the flowing plasma. Further, result permitting, it may serve to remove the doubt expressed about the validity of the Rydberg gas model.

9.4 References

[1] N. A. Dash, Ph.D Thesis, University of Wales Swansea, 2004

[2] D. J. Mitchell, Ph.D Thesis, University of Wales Swansea, 2002

[3] B. Chapman, *Glow Discharge Processes*, Wiley & Sons, New York, 1980

[4] I. P. Mortimer, Ph.D Thesis, University of Wales Swansea, 2000

[5] K. Newman, Ph.D Thesis, University of Wales Swansea, 2005

[6] Y. Ikezoe, S. Matsuoka, M. Takebe and A. Vigiano, *Gas Phase Ion-Molecule Reaction Rate Constants Through 1986*, Mazuren Co. Ltd. Tokyo, Japan, 1987

[7] T. F. Gallagher, *Rydberg Atoms*, Cambridge University Press, 2005

[8] P. D. Miller, PhD Thesis, University of Wales Swansea, 1996

[9] K. Newman and R. S. Mason, *Rapid Commun. Mass Spec.*, **20**, 2067, 2006

[10] K. Newman and R. S. Mason, *JAAS*, **20**, 830, 2005

[11] K. Newman and R. S. Mason, *JAAS*, **19**, 1134, 2004

Appendix – Argon: Excited States and Orbital Theory

The ground state electronic configuration of Ar is $1s^2\ 2s^2\ 2p^6\ 3s^2\ 3p^6$.
Each atomic orbital is defined by a series of quantum numbers. These quantum numbers are[1,2,3,4];

1) principal quantum number, n, defines groups of orbitals which are distinguished, within each group, by the values of l, m_l and m_s. For a hydrogen atom this indicates the energy of the electron (related to its distance from the nucleus), where $n = 1$ is the ground state, $n = 2$ is the 1st excited state, $n = 3$ is the 2nd, and so on (figure A1);
2) l is the angular momentum quantum number, which specifies the magnitude of the electron's orbital angular momentum, where $l = 0, 1, 2....n-1$;
3) m_l is the magnetic quantum number, which specifies the orientation of the electron's orbital angular momentum, where $m_l = l, l-1, l-2, \ldots, -l$;
4) m_s is the spin quantum number and specifies the orientation of the electron's spin angular momentum, where m_s for an electron = $\pm\frac{1}{2}$.

Taking hydrogen as an example, since there is only one electron to consider, in the ground state; $n = 1$ (figure A1), therefore l can only equal 0, $m_l = 0$ and $m_s = \pm\frac{1}{2}$. $l = 0$ indicates that the electron resides in an s orbital. However, for the outer electrons of argon, e.g. when $n = 3$, l can be equal to 0, 1 or 2, and for a p-orbital where $l = 1$, $m_l = 1, 0$ or -1. As before $m_s = \pm\frac{1}{2}$. However, in the ground state of argon each orbital contains a pair of electrons, and therefore the net spin of the outer orbital is zero.

Each electronic state can be represented by a state notation called a term symbol[1] of the form:

$^{2S+1}L_J$

where 2S+1 is the multiplicity, L is the total orbital angular momentum quantum number and J is the total angular momentum quantum number[1,2]. S is the sum of the electron spins in the atom, therefore when all electrons are paired the net spin is zero

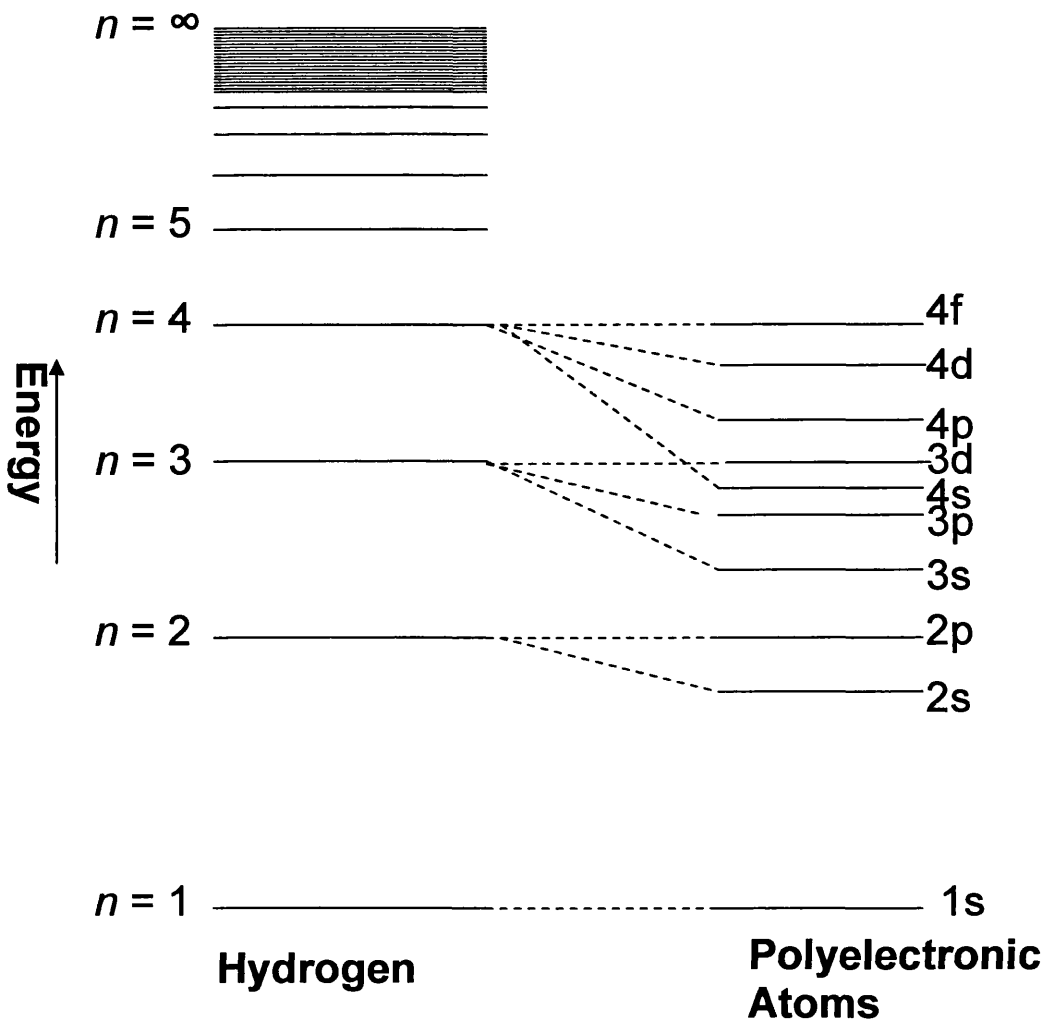

Figure A1: Energy levels in hydrogen ($1s^1$) and polyelectronic atoms including the breakdown of degeneracy in polyelectronic atoms. (The order of the 4s and 3d orbitals is dependent on the nuclear charge)

and the multiplicity = 0. This state is referred to as a singlet state. For one unpaired electron S = ½, and therefore the multiplicity is 2. This state is referred to as a doublet state. For an atom two unpaired electrons for which the spins are parallel, i.e. a triplet state, the multiplicity is 3.

Individual l values of the valence electrons combine to give L, where $L = l_1 + l_2$, $l_1 + l_2 - 1, \ldots . |l_1 - l_2|$. Each value of L is a positive integer and is assigned a symbol as below[1,2]:

L = 0, 1, 2, 3, 4, etc
Symbol = S, P, D, F, G, etc

The total angular momentum quantum number $J = L + S, L + S - 1, \ldots |L - S|$.

The ground state of argon has a net spin of zero, and hence is a singlet state ($2S + 1 = 1$). Since in the ground state configuration of Ar all electrons are paired and all orbitals filled (closed shells), the angular momenta cancel out, therefore giving L = 0. Thus the minimum, and only, value J can take = $|L - S| = |0 - 0| = 0$. The term symbol is therefore:

$^1S_0$

The lowest unoccupied orbital in Ar is the 4s orbital and thus excitation of an electron from the 3p to 4s orbital produces the first excited state:

$1s^2\ 2s^2\ 2p^6\ 3s^2\ 3p^5\ 4s^1$

Since the first electronic excited state of argon has 2 unpaired electrons it is possible for the spins the net spin can be equal to either 1 or 0, thus giving triplet and singlet states respectively. The singlet state ($2S + 1 = 1$) can only form if the electron spins are opposed. Since l for an electron in an s orbital = 0 and for an electron in a p orbital = 1, L = 1. L cannot equal zero as the minimum value for $L = |l_1 - l_2| = |0 - 1| = 1$. The maximum J value for the singlet state is therefore $L + S = 1 + 0 = 1$. Thus the term symbol is:

$^1P_1$

For the triplet state the maximum J value = 1 + 1 = 2, the minimum = |L - S| = 0 and J = 1 is also possible. There are therefore 3 possible triplet states:

$^3P_2$, $^3P_1$ and $^3P_0$

The lifetimes of these states are determined by a number of factors described by a series of selection rules governing the transitions between states[1-4]. The spin selection rule states that $\Delta S = 0$. The law of conservation of momentum must be applied, and as such $\Delta L = 0, \pm 1$ and $\Delta l = \pm 1$. Due to this, $\Delta J = 0, \pm 1$, except when J = 0, in which case $\Delta J = 0$ does not apply.

Of the four excited states discussed so far, the transition from the singlet excited state to the ground state obeys the spin selection rule, and therefore decay back to the ground state via emission of a photon can occur readily. However, the transition from a triplet state to a singlet state requires $\Delta S = 1$ and is therefore forbidden. Argon triplet states would therefore be expected to be metastable (long lived) excited states. Relaxation from both the singlet and triplet states obey the $\Delta L = 0, \pm 1$ and $\Delta l = \pm 1$ rules. However, for the ground state J = 0, and therefore transitions between the singlet excited state and $^3P_1$ state are allowed (though still spin forbidden). Therefore the $^3P_2$ and $^3P_0$ are the most stable excited states. The argon $^3P_1$ state is a radiant resonance level and decays to the ground state with emission of a photon, but the $^3P_2$ and $^3P_0$ states are both metastable[6].

Further examples of excited states occur when a 3p electron is excited to a 4p orbital. As before, it is possible for the resulting spin, S, to be equal to 0 or 1, and thus, it is possible for the excited state to exist in a singlet or triplet state (2S + 1 = 1 or 3 respectively). For a p orbital $l = 1$, and therefore L can be equal to 0, 1 and 2, represented by the symbols S, P and D respectively.

Singlet State: When S = 0 and L = 0 the J value can only be 0. When S = 0 and L = 1 the J value = 1, and when S = 0 and L = 2 the J value = 2. Thus, the singlet state can exist in the forms: $^1S_0$, $^1P_1$ and $^1D_2$.

Triplet State: When S = 1 and L = 0 the J value = 1. This is written as $^3S_1$. When S = 1 and L = 1 the J value = 2, 1 or 0. These are represented by the notations $^3P_2$, $^3P_1$ and $^3P_0$ respectively. When S = 1 and L = 2 the J value = 3, 2 or 1. These are represented by the terms $^3D_3$, $^3D_2$ and $^3D_1$.

As noted for excitation of an electron to the 4s orbital relaxation to the ground state may not be allowed by the spin and angular momentum selection rules. In the ground state configuration the total spin, S, is zero, and therefore only relaxation from the singlet state (in which the electron spins oppose each other) to the ground state is allowed by the $\Delta S = 1$ selection rule. Of these states only transitions from $^1S_0$ and $^1P_1$ to the ground state are allowed by the $\Delta L = 0, \pm 1$ selection rule, but neither of these is allowed by the $l = \pm 1$ selection rule, as is indeed true of all the transitions from a 4p to a 3p orbital, since $l = 1$ for all p electrons.

It is possible for relaxation to the 4s orbital to occur, but as described above, only relaxation of the singlet state to the ground state is allowed by the selection rules (although relaxation from the $^3P_1$ orbital may be possible if the $\Delta S = 0$ selection rule is relaxed – i.e. the atom is sufficiently heavy). Relaxation to the $^1P_1$ state is only possible from another singlet state. Any of the transitions from the singlet states is allowed by the selection rules, and therefore none of the singlet states are metastable.

According to Bohr's theory[5], the radius of an atom (for an electron with circular orbit) is proportional to n^2. Therefore, when $n = 2$ the atomic radius, r, is 4 times that when $n = 1$. Similarly, when $n = 10$, r is 100 times that when $n = 1$. Figure A2 shows the increase in the atomic radius of hydrogen with increasing n. This is due to the decrease in electrostatic attraction between the nuclear and electronic charges as their separation increases[1]. However, we now know that this, rather than being at a constant distance from the nucleus, the electron distribution is given by a probability distribution where the Bohr radius is a measure of the most likely distance of a hydrogenic electron from the nucleus.

The energy of each n level is related to n. In this case the energy of an electron relative to the ionisation potential, E_n, is determined using the equation[1];

$$E_n = -(Z^2\mu e^4/32\pi\varepsilon_0\hbar).1/n^2 = -hcR/n^2$$

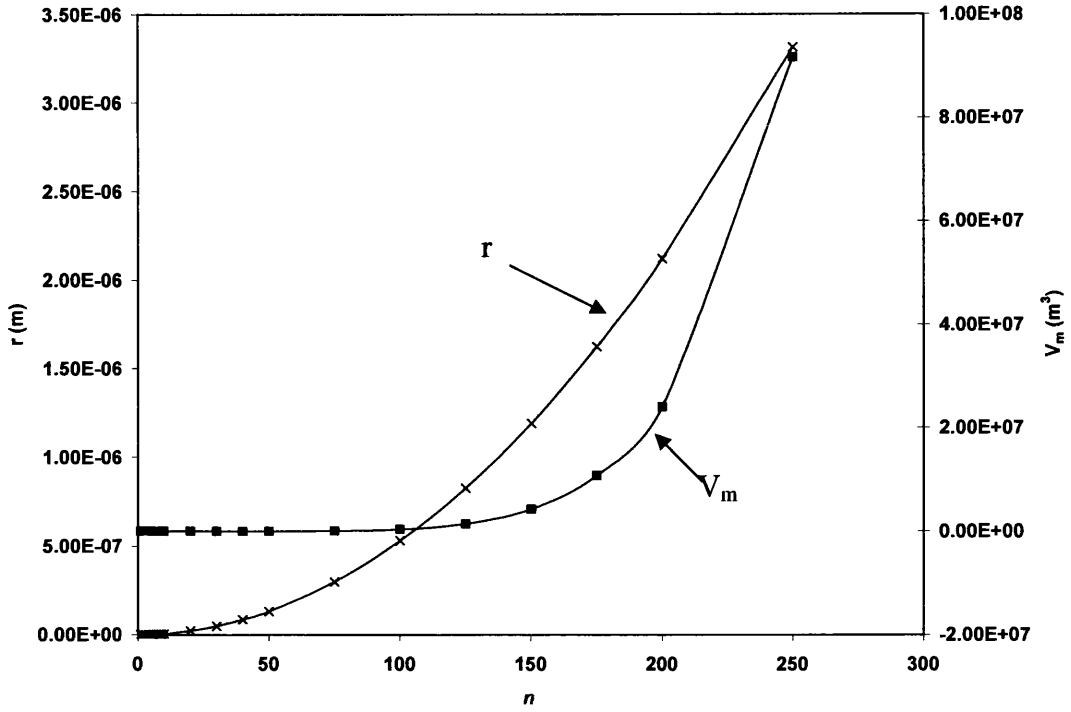

Figure A2: Variation of the atomic radius, r, and molar volume, V_m, at 298K as a function of *n* using Bohr radius.

where Z is the atomic number, μ is the reduced mass, e is the charge on an electron (or proton), ε_0 is the vacuum permittivity, $\hbar = h/2\pi$, where h is Planck's constant, c is the speed of light and R, in this instance, represents the Rydberg constant for Ar. Figure A3a shows the variation of E_n with n. Also shown on the same diagram is a standard energy level diagram to illustrate how such diagrams are generated. Figure A3b is an adaptation of figure A3a and is included to indicate more clearly how n influences the ionisation potential. As n is increased the energy gaps between different n levels is rapidly reduced. At high n the electron is very close to the ionisation potential (i.e. when $-E_n/hcR = 0$).

For a hydrogenic atom an atomic orbital is a one-electron wavefunction (Ψ) that describes the distribution of an electron in an atom[1]. The wavefunction of an electron is calculated using the equation:

$$\Psi_{n,l,m} = R_{n,l}Y_{l,m}$$

where R is the hydrogenic radial wavefunction (description of the motion of a particle of mass μ in a one dimensional region) for a given n and l and Y is the spherical harmonic for an orbital with given l and m_l[1]. Values for these can be obtained from physical chemistry textbooks such as references 1 and 2. A plot of the 1s wavefunction for a hydrogenic atom is shown below:

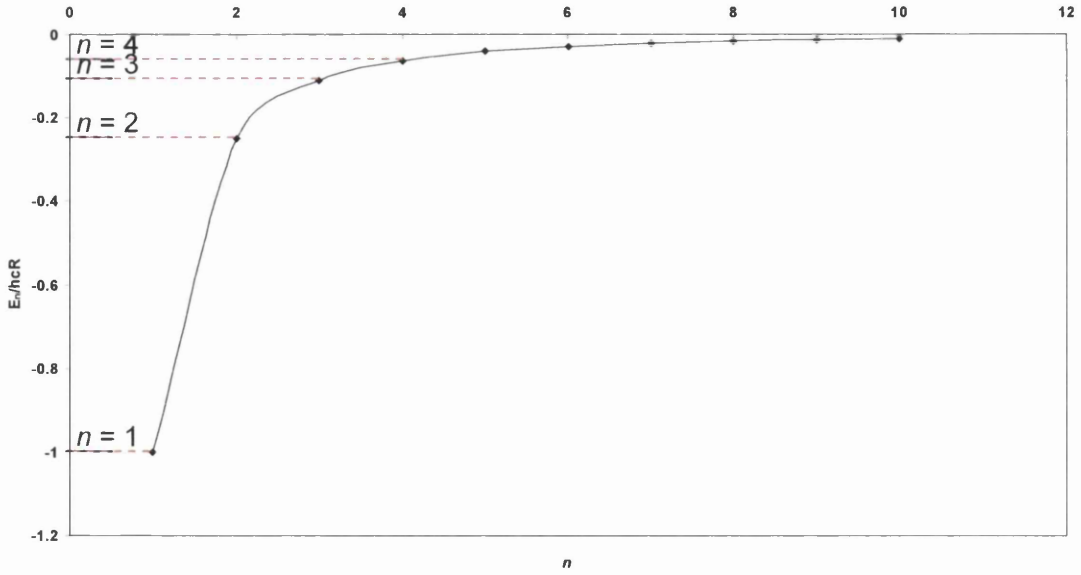

Figure A3a: Variation of electron energy for a given *n* level (divided by hcR, where R is the Rydberg constant) below ionisation potential with *n*. The lines on the left hand side of the diagram illustrate the data as a typical energy level diagram similar to that in figure A1.

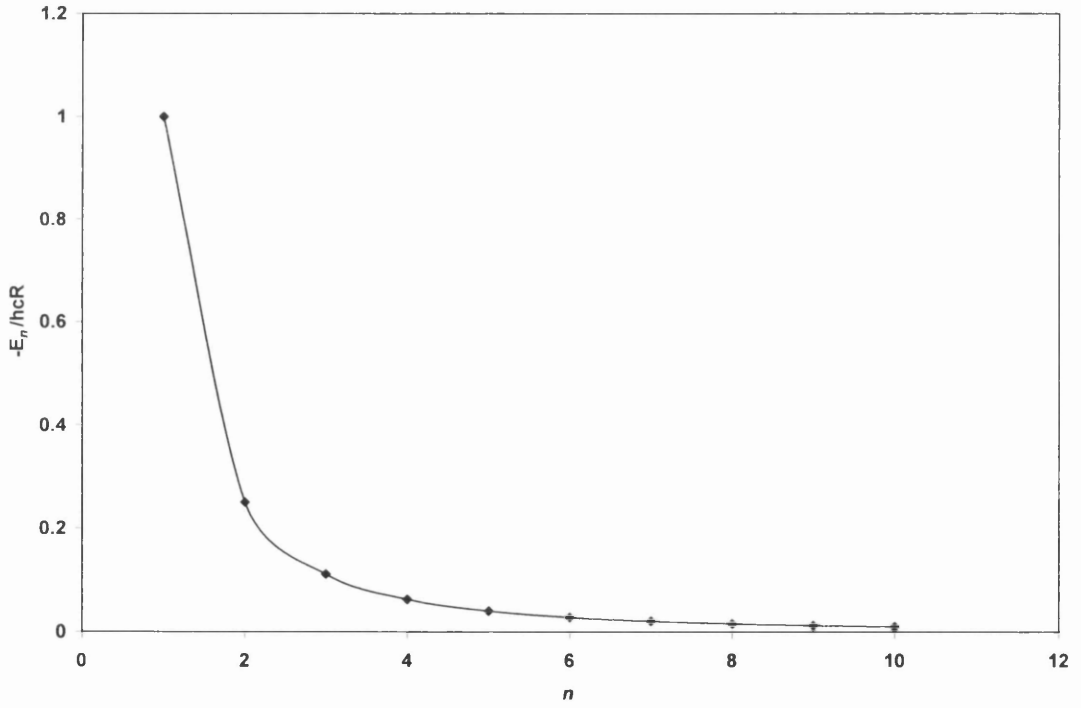

Figure A3b: Variation of ionisation energy for an electron in a given *n* level (divided by hcR, where R is the Rydberg constant)

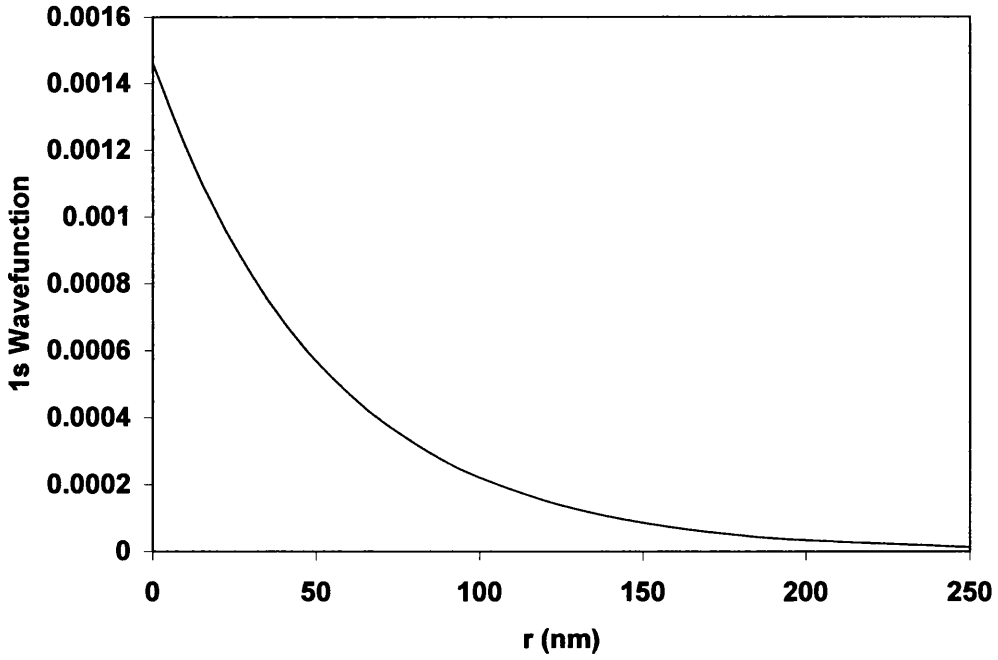

Figure A4: Variation of the 1s orbital wavefunction as a function of distance from the nucleus, r.[2]

This does not indicate how the electron probability density varies with increasing distance from the nucleus. This is shown by plotting the radial distribution function, *RDF*, where;

$RDF = 4\pi r^2 \Psi^2$

against r, as shown below[2]:

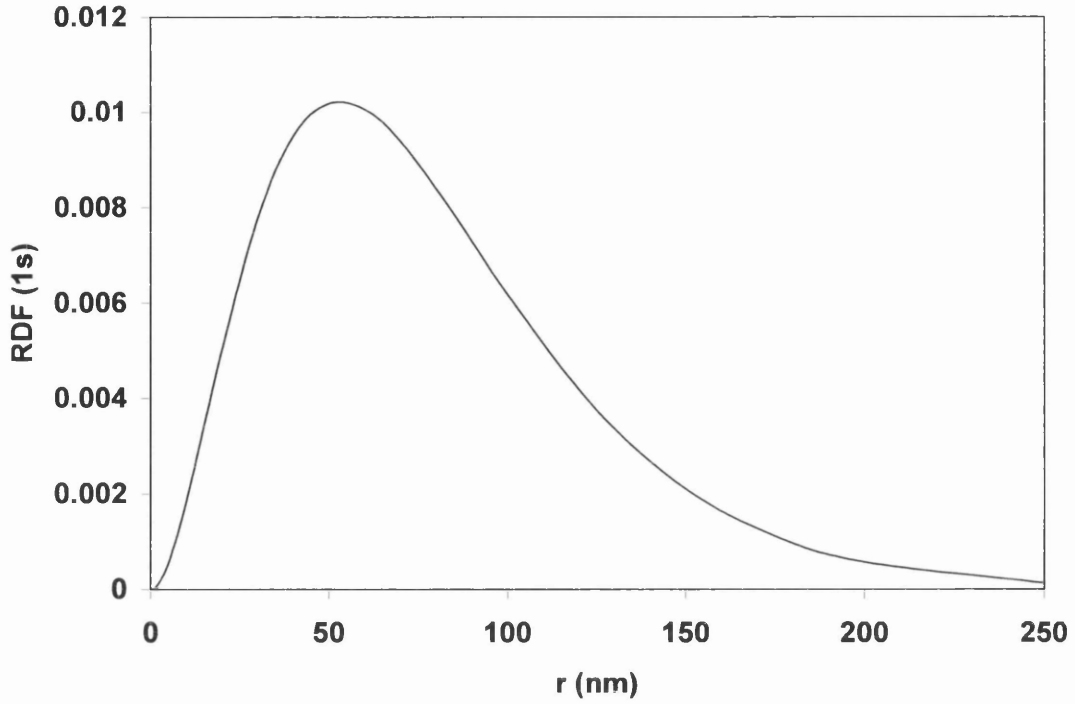

Figure A5: Variation of the RDF for the 1s orbital of a hydrogenic atom as a function of r.[2]

From the graph above it can be seen that the highest probability of finding the electron occurs when r ~ 52 pm. Orbitals are commonly represented in the form of a "boundary surface" in which there is a 95% probability of finding the electron[1,2]. For the hydrogen 1s orbital this is spherical and has a radius of 160 pm[2]. The boundary surface for the orbital is:

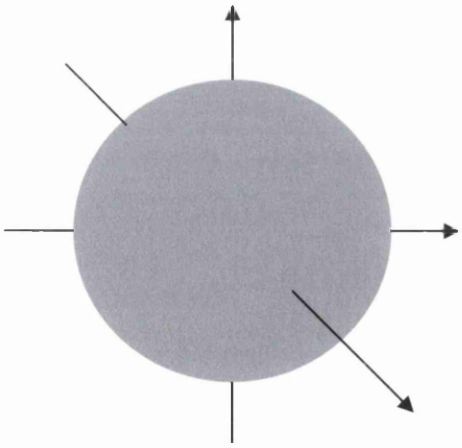

Figure A6: Boundary surface of the hydrogen 1s orbital[1,2]

All s orbitals are spherically symmetric, but differ in the number of radial nodes – points at which the wavefunction passes through zero[1]. An electron density diagram for the hydrogen 2s orbital is shown below. Again, the probability of finding the electron is highest close to the nucleus, but there is a node (pale band) which represents region of very low probability.

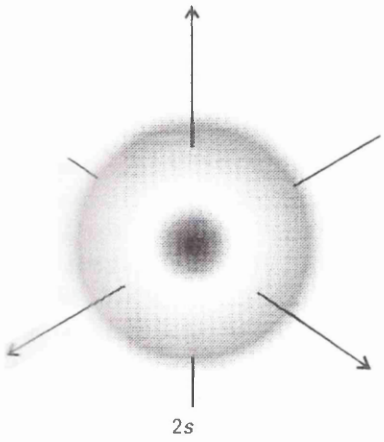

Figure A7: Electron density diagram for the hydrogenic 2s orbital.

The radius of the boundary surface of the 2s orbital is larger than that for the 1s orbital, and therefore the average distance of the 2s electron from the nucleus is greater[1].

In quantum mechanical terms the size of the atom would occur when the wavefunction is zero. However, this only occurs at an infinite distance from the nucleus[2]. Due to this, it was necessary to determine a practical method of indicating the atomic/ionic size. There are 4 common radii definitions:

1) Atomic Radius – half the interatomic distance between 2 adjacent atoms.
2) Covalent Radius – half the covalent bond distance of a molecule.
3) Ionic Radius – an approximation based on the minimum distance measured between ions using x-ray crystallography. This cannot be applied to compounds which display a degree of covalency.
4) Van der Waals Radius – half the distance between two atoms of an element which are as close to one another as possible without being bonded by anything other than Van der Waals forces.

For the sake of simplicity the Bohr radius has been used to represent atomic size throughout the work in this thesis.

The diagram below shows how the hydrogenic radial wavefunctions, R, of the hydrogenic 2s and 2p orbitals vary with ρ, a dimensionless variable that is directly proportional to r. Unlike the s obitals, the wavefunction for a 2p orbital is zero when ρ, and therefore r, is zero[1]. This can be explained in terms of the centrifugal effect of the angular momentum of p orbitals, when tends to "fling" the electron away from the nucleus[1].

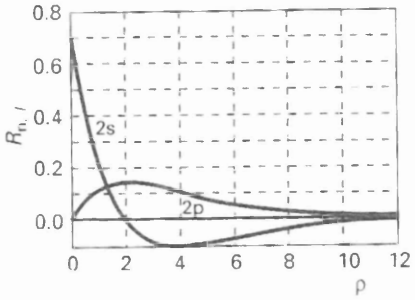

Figure A8: Variation of the 2s and 2p radial wavefunctions as a function of ρ.

The boundary surfaces for the 2p orbitals are illustrated below. It is clear from the probability of finding the electron close to the nucleus is far lower than that for the 1s and 2s orbitals.

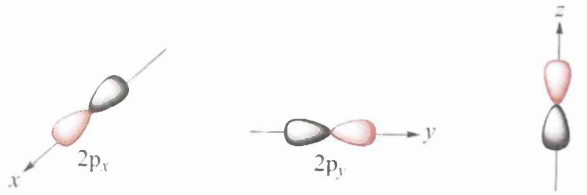

Figure A9: Boundary surfaces of the hydrogen 2p orbitals[2]

The two different colours used (these are often replaced by + and -) represent the opposite sign of the wavefunction for each region. The three 2p orbitals are distinguished by the three different values of m_l when $l = 1$. The different values of m_l denote orbitals with different angular momenta around the z-axis, but the same magnitude of momentum[1].

When $n = 3$ there are also five d orbitals, each with different angular momenta around the z-axis. As with the p orbitals, the probability of finding the electron close

to the nucleus is very low[1,2]. The boundary surfaces for the five 3d orbitals are shown below:

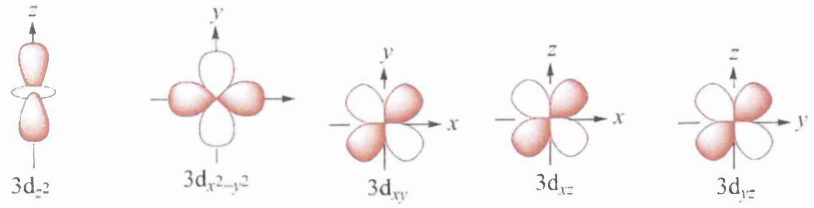

Figure A10: Boundary surfaces of the hydrogen 3d orbitals[2]

The Scrödinger equations (from which the wavefunction equation is derived) for many-electron atoms are very complicated due to the interaction between the electrons[1]. It is generally accepted that orbitals of polyelectronic atoms have spatial distributions similar to those of the hydrogen atom[2], but the nuclear charges are modified by the presence of all the other electrons[1].

Orbitals which have identical energies are said to be degenerate[2]. In hydrogen all orbitals for a given principal quantum number have the same energy, and therefore the degeneracy increases with increasing n. When n = 1 the degeneracy is 1 as only one s orbital is available. When n = 2 there is one s and three p orbitals of the same energy, and therefore the degeneracy = 4. When n = 3 there is one s, three p and 5 d orbitals of the same energy, and therefore the degeneracy = 9. The number of degenerate orbitals in the excited state = n^2 (figure A11)[2].

In polyelectronic atoms this rule breaks down[2]. Figure A1 shows how the energy of the s, p and d differ in polyelectronic species, therefore reducing the degeneracy. In the absence of an externally applied magnetic field, the orbitals possessing a given *l* value are degenerate. Figure A1 shows that in polyelectronic atoms orbitals of different *l* differ in energy. It can also be seen that orbitals of higher *n* states can have energies lower than orbitals of lower *n* states e.g. 4s can be lower in energy than 3d. This effect becomes more important with increasing *n*. The loss of degeneracy is due to orbital penetration effects[2]. It is known from the radial distribution functions that electrons in s orbitals have a considerably larger probability near the nucleus than in a p orbital. Thus, s orbitals have lower energies. Electrons are held in orbit by the Coulombic attraction between the nucleus and the electron, but when another electron

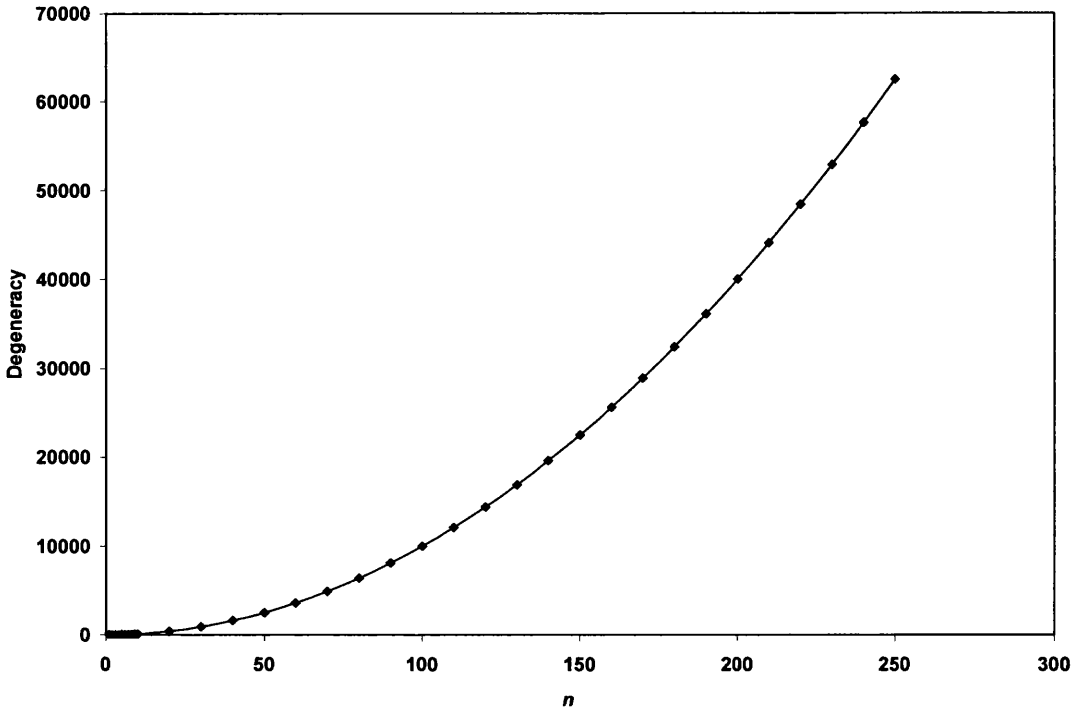

Figure A11: Variation of degeneracy in a hydrogen atom with n. The number of orbitals of the same energy increases as n^2.

is present the two electrons repel each other. One electron effectively shields the outer electron from the nuclear charge and so the electron only experiences the effects of a fraction of the nuclear charge, the effective nuclear charge, Z_{eff}^2. Thus, electrons with better penetration towards the nucleus, such as s orbitals, are less shielded from the nuclear charge. This effect therefore enhances the effect due to the radial distribution functions described above.

However, for high *n*, Rydberg, states the electron spends most of its time a long way from the nucleus, and therefore the orbital penetration effects become negligible. As the electron effectively experiences the effect of a point charge (nucleus), the degeneracy reverts back to the hydrogenic model described above, i.e. the degeneracy approaches n^2.[5]

References

1 P. W. Atkins, *Physical Chemistry 5th edition*, Oxford University Press, Oxford, 1997

2 J. Barrett, *Atomic Structure and Periodicity*, RSC, UK, 2002

3 K. J. Laidler and J. H. Meiser, *Physical Chemistry 3rd edition*, Houghton Mifflin Company, New York, 1999

4 R. J. Silbey and R. A. Alberty, *Physical Chemistry 3rd edition*, John Wiley & Sons, Inc. , 2001

5 T. F. Gallagher, *Rydberg Atoms*, Cambridge University Press, 1994